



The University of
Nottingham

CREEP OF WELDED BRANCHED PIPES

by
Glen Rayner BEng

**Thesis submitted to the University of
Nottingham for the Degree of Doctor of
Philosophy, May 2004**

This thesis is dedicated to my parents

TABLE OF CONTENTS

Abstract	vi
Acknowledgements	vii
Nomenclature	viii
CHAPTER ONE INTRODUCTION	1
1.1 General	1
1.2 Creep of power plant pipelines	3
1.2.1 General	3
1.2.2 Understanding of creep in steam plant applications	5
1.3 Branched pipes	7
1.3.1 General	7
1.3.2 Connection types and geometry	8
1.3.3 Creep failure	10
1.4 Motivation, objectives and scope of thesis	11
CHAPTER TWO LITERATURE REVIEW	26
2.1 Introduction	26
2.2 Microstructural and mechanical behaviour under creep in metals.....	26
2.3 Mathematical modelling of creep.....	29
2.3.1 Introduction	29
2.3.2 Steady-state creep modelling.....	30
2.3.3 Continuum damage mechanics modelling.....	33
2.3.4 The reference stress method.....	36
2.3.4.1 General.....	36
2.3.4.2 R5 reference stress approach.....	39
2.4 Creep of welds	43
2.4.1 Introduction	43
2.4.2 Metallurgical and mechanical behaviour.....	45
2.4.3 Creep performance and failure of welds.....	47
2.4.4 Experimental methodologies and studies of weldments.....	50
2.5 Numerical analysis of welded pipes.....	53
2.5.1 General	53

2.5.2	Effect of material mis-match on stress.....	58
2.5.3	Effect off weldment geometry and loading on stress.....	62
2.5.4	Failure behaviour of weldments.....	63
2.6	Creep of branched pipes.....	65
2.6.1	Introduction.....	65
2.6.2	In-service experience & experimental studies of branched pipes.....	67
2.6.3	Numerical analysis of branched pipes	72
2.6.3.1	Homogeneous studies.....	72
2.6.3.2	Weldment studies	76
2.7	Conclusions.....	80

CHAPTER THREE CREEP BEHAVIOUR OF HOMOGENEOUS BRANCHED PIPES.....118

3.1	General	118
3.2	Background theory.....	121
3.3	Geometries and FE models.....	122
3.4	Material properties.....	126
3.5	Results.....	126
3.5.1	Stress distributions	127
3.5.2	The effects of material properties	129
3.5.3	The size effects of the branch.....	130
3.5.4	The effect of weld size	133
3.5.5	Comparison with British Standards and Booth's operating stresses..	133
3.6	Discussion and conclusions.....	136

CHAPTER FOUR CREEP BEHAVIOUR OF HETEROGENEOUS WELDED BRANCHED PIPES.....151

4.1	Introduction	151
4.2	Geometry and material properties.....	153
4.3	FE models	154
4.4	Stress distributions and high stress regions.....	155
4.4.1	Branched flat end cap.....	155
4.4.2	Branched hemispherical end cap.....	157
4.4.3	Isolated branched main pipe.....	159

CHAPTER SEVEN	EVALUATION OF THE R5 CREEP LIFE ASSESSMENT APPROACH FOR SINGLE AND MULTI-MATERIAL COMPONENTS.....	284
7.1	Introduction	284
7.2	Background.....	285
7.3	Overview of the R5 life assessment approach	286
7.3.1	R5 application to homogeneous components	286
7.3.2	R5 application to multi-material components	289
7.4	Single-material components	293
7.4.1	General	293
7.4.2	Analytical formulations and FE models.....	293
7.4.3	Results	299
7.5	Multi-material components.....	299
7.5.1	General	299
7.5.2	Analytical formulations and FE models.....	300
7.5.3	Results	307
7.6	Discussion.....	314
7.6	Conclusions.....	318
CHAPTER EIGHT	DISCUSSION AND CONCLUSIONS.....	345
8.1	General discussion.....	345
8.2	General conclusions	349
CHAPTER NINE	FUTURE WORK	353
9.1	Parametric study of the creep behaviour for thick-walled branched steam pipes with additional loading	353
9.2	The creep behaviour of thin-walled branched pipes.....	354
9.3	The interaction effects between branch pipes.....	354
9.4	Assessment of R5 stress redistribution factors for weld zones.....	354
REFERENCES	357
APPENDIX 1	373

ABSTRACT

Creep failure of welds in high-temperature power plant steam piping systems is known to be a potential cause of plant failure. Creep behaviour of plain pipes with circumferential welds and cross-weld specimens have received fairly extensive attention. However, research into the creep behaviour of welded thick-walled branched steam pipes has received less attention. Consequently, this thesis addresses improving the understanding of the creep behaviour for this type of geometry. Numerical and analytical methods are used to assess the creep behaviour of typical power plant branched pipe geometries.

The effects of various geometric and material parameters on the creep stress and creep life behaviour of the connections are studied. In particular, the effect of the differing creep properties associated with the various material regions of the weld are investigated. The importance of incorporation of weld properties in creep life assessments is thus assessed.

Finite element steady-state and continuum damage mechanics creep analyses have been used to identify the relative creep strength of typical connections compared to plain pipes. The work identifies typical creep rupture locations within branched pipe welds and the associated damage accumulation at and around these positions.

Various creep life assessment methods/procedures are used in practise; these are mainly the British Standard codes, British Energy's R5 procedure, steady-state creep approaches and continuum damage mechanics approaches. The relative accuracy and conservatism of these distinct approaches are addressed for the application to typical branched pipes.

The general formulation of steady-state creep stress is applied to the parametric study of weld materials in a typical multi-material welded branched pipe. An approximate interpolation technique for power-law creep is implemented to reduce the number of analyses needed to span a wide range of material parameters. The method is used to estimate the creep stresses and lives at several critical regions within the various material zones of the weld. The advantages of the technique are related to the small number of analyses required and the simple and compact way of presenting the results for weld design and life assessment purposes.

ACKNOWLEDGEMENTS

First of all, my deepest thanks go to Professor Tom Hyde and Dr Seán Leen, my supervisors, who not only provided me with a sound backdrop of academic and engineering experience and knowledge, but also, genuine care, guidance and encouragement.

Similar thanks also go to Dr Wei Sun, who has provided me with non-stop support, wisdom, and most importantly, friendship.

I would like to express my gratitude to Dr Adrian Williams for lending me his expertise and advice.

Acknowledgements go to my sponsors, British Energy, PowerGen and Innogy for their financial support of the work. In particular, special thanks go to Dr Peter Budden, Dr David Allen and Dr Steve Brett.

Thanks go to Adam, my twin brother, and all of the family, for supporting me throughout the years. To Claire, her encouragement, companionship and love have helped lead me through the ‘twists and turns’ that are a PhD. Finally, to Mum and Dad, who I feel completely indebted to. They have provided me with much love and support throughout my life. So this PhD is justly dedicated to them.

Nomenclature

ENGLISH SYMBOLS

a_1, a_2, a_3	cross-sectional area of bars in multi-bar structures
a, b, b_1	branched pipe weld geometry parameters
A, A', C, E, G	constants in creep constitutive equations
\bar{b}_1, \bar{b}_2	widths of material zones in a beam
b_x, b_y	branch pipe weld width and height, respectively
c_i, e, g, j_i	constants in creep constitutive equation
Ca_1	branch modification geometric factor
d, d_i, d_m	branch pipe outer, inner and mean diameters, respectively
\bar{d}	beam depth
dim	non-dimensional functions of dimensions
D, D_i, D_m	main pipe outer, inner and mean diameters, respectively
E_i	Young's modulus
$f_1(\sigma), f_2(t), f_3(T)$	stress, time and temperature dependence, respectively
h	heat-affected zone width
H	activation energy
k	stress redistribution factor
L_1, L_2, L_3	length of bars in multi-bar structures
m, M	CDM material constants
\hat{M}, \hat{M}_l	bending moment and limit bending moment, respectively

n, n', n_i	stress exponent in Norton's and CDM laws
p_i	internal pressure
P, P_L	load and limit load, respectively
R	Boltzmann constant
r_0, r_l	branched pipe weld radii
r, r_i, r_m	branch pipe outer, inner and mean radii, respectively
R, R_i, R_m	main pipe outer, inner and mean radii, respectively
s	branch pipe spacing
S_{ij}	deviatoric stress
t	branch pipe wall thickness or creep time
$t_f, t_{CD}, t_{f,mdh}$	failure life, creep damage life and failure life based on the mean diameter elastic hoop stress of the main pipe, respectively
$t_{r(SS)}, t_{r(CDM)}, t_{r(R5)}$	steady-state, CDM and R5 rupture life, respectively
t_r^*	assessment time
T	main pipe wall thickness or temperature
w	Branch pipe weld width on the inside bore
w_o	plain pipe butt weld width
\dot{u}, \dot{u}_{nom}	deformation rate and nominal deformation rate
$\bar{U}, \bar{U}_i, \bar{U}_{EL}, \bar{U}_T,$	deformation, initial elastic or elastic-plastic
$\bar{U}_{SS}, \bar{U}_{SR}$	deformation, the elastic deformation, total deformation, steady-state deformation and redistribution deformation, respectively

GREEK SYMBOLS

α	multi-axial material constant or stress scaling factor
α_R	reference scaling factor
β	branched pipe internal weld angle
χ, ϕ	CDM material constants
δ_{ij}	Kronker delta
$\varepsilon, \varepsilon_{ij}, \varepsilon^C$	strain, strain tensor and creep strain, respectively
$\dot{\varepsilon}_o$	constant in Norton's creep power law
$\dot{\varepsilon}^C, \varepsilon_{ij}^C$	creep strain rate and creep strain rate tensor, respectively
γ	system loading factor
η	Branch ligament efficiency
λ, λ_i	stress concentration factor
θ_0	plain pipe butt weld angle
θ	branched pipe external weld angle
$\sigma, \sigma_{ij}, \sigma_i, \sigma_{nom}$	stress, stress components, principal stress components and nominal stress, respectively
$\sigma_a, \bar{\sigma}_a$	mean axial end load
$\bar{\sigma}_{el,max}$	maximum elastic stress
$\sigma_{eq}, \bar{\sigma}_{eq}$	equivalent stress and normalised equivalent stress, respectively
$\sigma_1, \bar{\sigma}_1$	maximum principal stress and normalised maximum principal stress, respectively

$\sigma_{ref}, \sigma_{ref}^R$	reference stress and rupture reference stress, respectively
$\sigma_r, \bar{\sigma}_r, \sigma_r^P, \sigma_{r(SS)}$	rupture stress, normalised rupture stress, peak rupture stress and steady-state rupture stress, respectively
σ_b	design operating stress
σ_{mdh}	mean diameter hoop stress
τ, τ_{ij}	Shear stress and shear stress component, respectively
$\omega, \dot{\omega}$	damage and damage rate, respectively
ξ, ψ, ζ	constants in creep constitutive equations

ABBREVIATIONS

BS	British Standard
CDM	continuum damage mechanics
CMV or CrMoV	denotes typical CrMoV power plant steels, e.g. $\frac{1}{2}\text{Cr}\frac{1}{2}\text{Mo}\frac{1}{4}\text{V}$
CEGB	Central Electricity Generating Board
FE	finite element
HAZ, HAZ ^b , HAZ ^P	heat-affected zone, branch pipe and main pipe HAZ, respectively
PM, PM ^b , PM ^P	parent material, branch pipe and main pipe parent material, respectively
PWHT	post weld heat treatment
SS	steady-state creep
Type IV	Type IV HAZ heat-affected weld zone
WM	weld metal

Note – Tables and figures are placed at the end of the text in each chapter

CHAPTER ONE

INTRODUCTION

1.1 General

Many technological advances of the nineteenth and twentieth century have led to a dependency on the use of power. The use of power is diverse, whether it's electricity for televisions, natural gas for central heating or crude oil for powering anything from lawnmowers to fighter jets, the developed world cannot exist without it. The importance of the role of power stations within the developed world can never be underestimated; they are and probably will be at the forefront of modern civilisation for many years to come. The dependency on power stations to create electricity to help run industry, services, domestic appliances and society as a whole is tremendous. With this dependency come large requirements for the reliable operation of the plant to constantly supply power but also to maximise its profitability as an industry, while at the same time keeping a safe operating environment. The reliable and safe operation of power plant is mainly dependent on the understanding of the power generation process. One area of this understanding is how component failure within the plant occurs, whether failure occurs by human misuse or by normal operating conditions. It is this latter topic that is of importance within this thesis. Under normal operating conditions, failure within the plant can endanger human life, as well as being economically expensive due to the replacement of failed equipment and loss of earnings due to shutdown. Failures can occur in many

areas of the plant, for instance the steam generation equipment can fail by corrosion, thermal fatigue or creep. The causes of such failure are often complex and are not yet fully understood; therefore it is of interest to power companies to increase plant safety and profitability by gaining knowledge of all potential failure areas.

Common failure mechanisms of plant components under normal operating conditions include thermal fatigue and creep, which generally limit the life of the plant to around 15 to 25 years [1]. As of May 2002, around 50% of operational fossil-fuelled power stations within the UK with an installed capacity of over 100MW are twenty years old or more and can produce just over 43% of the country's installed electricity capacity [2]. The extent of the number of ageing fossil-fuelled power plants is not just confined to the UK, as similar situations in many other countries exist. Many nuclear-fuelled power stations in the UK are also nearing the end of their design lives, with more than 50% of such plants, responsible for the production of around 10% of the UK's electricity, are over twenty years old. Obviously, the plants are very close to or have overrun their design lives and have carried on in operation due to the power companies deciding via risk assessment techniques and extensive research programmes that the plants are still safe and reliable for extended use. However, over the last decade or so the appearance of substantial cracking in many plant steam-piping components has been reported and understanding of this particular problem is required to extend the life of plants still further, while maintaining safety and improving future design. Gaining knowledge of the

cracking has been mainly directed towards understanding the problems caused by high-temperature creep.

1.2 Creep of power plant pipelines

1.2.1 General

Fossil and nuclear power plants generate electricity using several integral steps, as described using the example of a coal-fired power plant diagram shown in Figure 1.1. Put simply, coal is burnt to heat water until it has turned to steam. The boiler typically contains hundreds of kilometres of tubing, which carries and heats the water to produce steam. A photograph of a typical boiler room is shown in Figure 1.2 and a typical layout of a boiler with reheater is shown in Figure 1.3. The water is heated around the boiler walls until it has turned to relatively low temperature steam. The steam is then transferred from the tubing on the boiler walls to the superheater, where it is heated further to produce very high temperature and high pressure steam, typically around 550°C and 17MPa, respectively. The superheater contains very thick pipework to heat the steam due to the extreme temperatures and pressures involved in the process. The steam then enters the high-pressure turbine to release its heat and pressure energy by rotating large turbine blades, which in turn rotates an AC generator to produce electricity, the steam then leaves the high-pressure turbine at typically less than 0.001 MPa pressure. The steam can then typically be reheated in a reheat boiler and used with intermediate and low-pressure turbines to generate additional electricity and improve the power plant efficiency.

The high temperatures and pressures exerted on constitutive parts of the boiler, superheater and turbine stages of power plant reduce the life of these components and often control plant failure and plant life. The failure mechanism that often controls these components is high temperature creep. The steam pipelines within the superheater section is considered the area of greatest risk from creep failure within the plant.

Creep is defined as the time-dependent deformation of a material held under a constant stress, which is below the yield stress of the material [6]. Creep can occur within a wide range of materials at a wide range of temperatures, but generally for metallic creep within engineering metals and alloys, creep is considered important at temperatures above 0.4 times the melting temperature of the metal [7]. After a sustained period of time the metal can creep no longer and consequently will fail by creep rupture.

The steam piping section contains many different types of geometry, such as plain pipes, pipe bends and branched pipes. Welds are commonly used to connect these together and are known to be a common site of pipeline failure due to creep [8,9]. The weld contains relatively weak heat-affected zones produced by the welding process. Figure 1.4 shows a typical example of the failure of a power plant plain pipe section by creep rupture of the weld. However, due to a lack of understanding about the creep of welds present design codes and life assessment procedures generally only consider the

weakening effect of welds in power plant piping in a simplified way, e.g. in terms of a basic strength reduction factor.

The weakening effect of the weld's material inhomogeneity can be exacerbated by the stress concentration effects of different geometry types, such as welded branched pipe connections.

1.2.2 Understanding of creep in steam plant applications

The understanding of high temperature metallic creep in power plant applications has continuously been improved since the problem first surfaced and much knowledge has been gained. Understanding of how the geometry, materials and loading affect the creep and failure behaviour of typical components, such as plain pipes, pipe bends, turbines blades have been used to improve plant design and lifing codes. Mathematical models have been created to model creep to investigate such effects and these have been used extensively over the last decade or so in computer modelling packages such as finite element software to improve knowledge on creep. However, the creep and creep failure of components is a complex and difficult problem to fully understand in a number of ways. Firstly, the study of the creep failure of plant components is very difficult experimentally since under in-situ loadings and temperatures failure typically requires a time-scale of decades. Experimental testing has been carried out on typical components but the temperatures or loadings had to be increased compared to in-situ conditions to achieve relatively short failure times; the failure lives were then extrapolated backwards to estimate failure lives for in-situ conditions. Such results are

generally used cautiously due to the extrapolation procedure. Secondly, while such experimental tests can be carried out for isolated geometry, material and loading circumstances, it is certainly prohibitive to encompass the wide range of geometry, loading and material combinations used within power plants. Thus, the effects of the interaction of all three are still unclear for many situations. Thirdly and lastly, materials testing of tensile test pieces are commonly used to obtain material creep properties for mathematical modelling to extrapolate creep failure lives of components. However, the material properties are idealised since tensile creep tests generally use uni-axial loading, whereas, in reality, power plant components experience complex multi-axial stress-states. Multi-axial properties have been produced for multi-axial modelling, giving improved life and creep predictions, [e.g. 10]. These are just some of the complications involved in understanding creep behaviour and failure of high-temperature plant components. Nevertheless, the problems associated with the first and second points described can be reduced by the use of computer software, such as finite element analyses, where by the geometry, materials and loading effects of components can be varied more easily and cheaply than equivalent experimental tests. However, the accuracy of computational modelling is dependent on the third point described, i.e. the requirement for accurate and representative mathematical models and material properties.

1.3 Branched pipes

1.3.1 General

Branched pipe connections (also known as tees or cylinder-cylinder intersections) are commonly used within power plant systems to transfer steam by either combining or splitting the flow. Branched pipes are used to collect steam in the superheater and reheater sections of plant and can be found along main pipe sections, or headers or other pressure vessel equipment. Figure 1.5 shows a typical superheater header with three parallel layers of small branches and a larger branch on the end cap. The vast majority of branched pipes used within power plant applications are constructed by welding of the adjoining pipes. Although some forged branched pipe connections are used, they are not considered within the present work as they are relatively rare.

Welded branched pipes are generally considered to be weaker than plain pipe sections in terms of creep strength for two main reasons: (i) the presence of the weld produces an inherent weakness due to material inhomogeneity in the heat-affected zones which are generally weaker than the base material of the pipes, thus producing a material mismatch and a common area of creep failure, and (ii) the inherent geometric stress concentrations associated with such connections, e.g. discontinuities at weld toes and necks, and high stresses at inner crotch corners.

However, quantitative knowledge of the weakening effect of such connections was relatively poor when many plants were designed and constructed in the

1960s and 1970s. Design codes lacked incorporation of accurate creep behaviour of branched pipes and the weakening effect of the weld. Design codes such as BS 5500 [11] and BS 1113 [12] consider work which is based on 1960s and 1970s studies on the elastic strength and basic materials creep strength of branched pipes. Creep life assessment procedures, such as the R5 [13] are commonly based on the reference stress technique which can be applied to complex components, such as branched pipes, to give more accurate creep lives. However, these lifing procedures can generally only be applied to homogeneous components, so that there is no incorporation of the weakening effect of the weld. The main reason for this lack of understanding about the creep of welded branched pipes compared to other components, such as plain pipes, is the complexity of the component, such as the geometry, the number of variables, which includes the diameters of branch and main pipe, thicknesses of branch and main pipe, weld size and angle and so on, and variation of material properties due to the weld.

1.3.2 Connection types and geometry

There are many different types of branched pipes in service. As explained earlier, the critical branched pipes that are affected by creep are situated in superheater and reheater sections of plant, where the temperatures and pressures of steam are typically around 550°C and 17MPa, respectively. Thick-walled branched pipes are mainly used to collect steam from small tubing pipes found in these sections via the use of inlet and outlet header tanks. Figure 1.5 and Figure 1.6 show typical examples of a superheater and a reheater header used in plant, respectively. There are two main types of

connections used within headers and used in the majority of plants. The first are rows of small branches positioned along the length of the header used to combine heated steam from furnace tubing in the header. The second type are larger branches, these are used mainly for transporting the collected steam from the header to the turbine section of the plant, as shown in the reheater header of Figure 1.6. The sizes vary for these two types of connections with header size, for UK fossil-fuelled plants, the smaller branch pipes are typically less than 100mm outer diameter and around 10mm to 20mm wall thickness, compared to the headers outer diameters of around 300mm to 500mm and wall thicknesses of around 60mm. The larger branch pipes normally have dimensions of around a third of the header outer diameter and wall thickness. Hence, the work presented in this thesis will generally only consider branch sizes within these ranges of sizes.

There are generally two types of welded branched pipes in use, dependent on the way the connections are made, namely 'set-in' or 'set-on' connections. 'Set-in' connections have the branch pipe set into the main pipe and welded from the outside surface. 'Set-on' connections have the branch pipe set on the top of the main pipe and welded from the outside surface. Both branch weld types are shown in Figure 1.7. 'Set-on' branch connections are more common in power plant since they are easier to construct and repair if cracking occurs in the weld region. The present work therefore focuses on 'set-on' connections.

A common approach used to strengthen branched pipes and increase their creep performance is to use reinforcement by increasing either the branch pipe

thickness, the main pipe thickness or both. A diagram displaying branched pipe strengthening is shown in Figure 1.8.

Figure 1.9 shows the geometric notation used to describe simple welded branched pipes. The basic dimensions used for the component are as follows:

1. Main pipe outside diameter D
2. Main pipe mean diameter D_m
3. Main pipe inside diameter D_i
4. Branch pipe outside diameter d
5. Branch pipe mean diameter d_m
6. Branch pipe inside diameter d_i
7. Main pipe wall thickness T
8. Branch pipe wall thickness t

The main non-dimensional parameter ratios used to define a particular connection geometry are: d/D , D/T , d/t and t/T .

1.3.3 Creep failure

In-situ and branched pipe test components have indicated that creep failure around the weld region can occur before other remote regions such as the header or plain pipe sections [16]. Such failure can occur in different positions depending on materials, loading and geometry. The most common creep failure locations found within typical high temperature coal-fired branched pipes are displayed in Figure 1.10 [19,20]. Failure within the weld itself is common. Cracks on the outside of the weld surface at the weld foot and weld toe are shown in Figures 1.10a and 1.10b. Creep crack growth on the inside

bore of the connection is also common, especially within the heat-affected zone of the weld (Figure 1.10c) and near the inner crotch corner of the base metal (Figure 1.10d).

1.4 Motivation, objectives and scope of thesis

Extensive research on material creep behaviour and the creep of simple components such as welded plain steam pipes has been carried out previously [19-26] and substantial understanding has been gained about the effects of materials, geometry and loading. Including knowledge of the variation of stress, strain and displacement distributions and their effect on failure life and position within welded components has helped to improve plant safety and validate life extension. However, experience within the power industry has shown that although failure within welds of branched connections are common and more premature than in welded plain pipes [17,18,27], there is still a lack of knowledge on the creep behaviour of such components. There is therefore a requirement for improved understanding of the creep behaviour of branched pipes. The effect of stress distributions on this creep behaviour is an important aspect of improving understanding. The inherent complexity of these components and their associated weld regions leads to experimental testing being very time-consuming and expensive, closed-form analytical solutions not existing and realistic numerical investigations using such tools as finite element (FE) analysis being time consuming. Although creep analyses of branched pipes using FE is intensive, the method is still drastically cheaper and less time consuming than experimental testing. Standard FE packages, e.g. Abaqus [28], commonly utilise popular mathematical creep models such as steady-state

power laws, e.g. Norton's law, and corresponding material creep properties obtained from experimental creep testing, e.g. uni-axial tests [29,30]. FE packages typically allow user programming of more complex and accurate mathematical models, such as the continuum damage mechanics (CDM) approach [31,32,33].

The aim of this thesis is to investigate multi-material creep within welded branched pipes across a range of material properties, geometries and connection types. This will provide insight into the strength reduction and failure behaviour effects caused by the weld and branch, which will in turn permit assessment of present design and lifing methods with respect to such failure. The work is entirely computational in nature, including FE analyses, both steady-state and CDM, and the application of design and creep life codes.

Chapter Two of this thesis reviews the current literature on the creep of welds, describing details of the mechanical and metallurgical characteristics of welds, the failure behaviour and performance of welds and the methods currently used in the study of the creep of welds. In the latter sections, a more detailed review of the creep of welded branched pipes and welded plain pipes is presented, in relation to experimental, analytical and numerical studies carried out.

Chapter Three assesses the steady-state creep stress distribution behaviour and failure lives for typical UK fossil-fuelled isolated welded branched pipes using a steady-state rupture approach [33,34]. Firstly, the effect of varying geometric

parameters on the steady-state stress variation in the connection and peak stresses within homogeneous branch connections are investigated.

Chapter Four assesses the effect of the presence of inhomogeneous weld material properties on the steady-state stress distributions and failure behaviour of typical welded branched pipe configurations. Comparisons are made with homogeneous failure lives and positions to evaluate the importance of the weld and its role in life prediction.

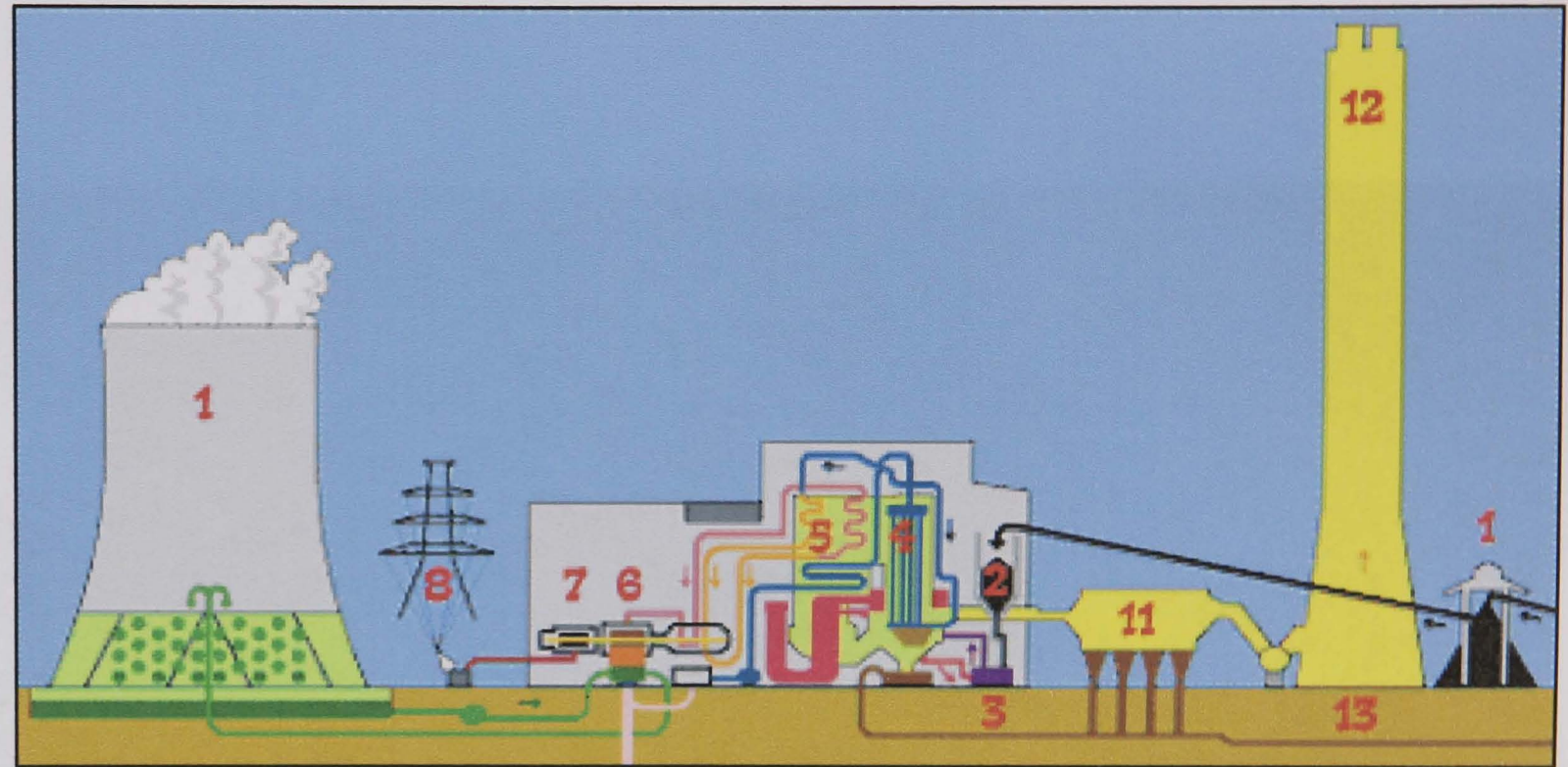
Chapter Five provides assessment and validation of the application of a general formulation approach for steady-state stress prediction in a multi-material component using FE analyses as proposed by Tang [35] to a typical three-material isolated welded branched pipe. The method is used to conduct a steady-state creep parametric analysis of the multi-material behaviour of the stresses in the weld, allowing for the stress predictions to be assessed in a compact and easy manageable way using a relatively small number of FE calculations. The method is combined with a simple approximate rule based on the linear behaviour of creep stresses with the inverse of the materials creep exponent values, n , from Norton's power law to reduce the number of required FE calculations still further. The accuracy of the stress predictions produced from the general formulation approach combined with the $1/n$ approximation, are assessed by comparison with FE steady-state solutions for typical in-situ materials. A detailed study of the stress variation with parent material, heat-affected zones and weld metal material properties is presented at several positions of interest around the weld region. The results are used to

demonstrate the accuracy and effectiveness of the combined general formulation approach and modified Calladine approximation method [36] for branched pipe weld assessment and design purposes, as well as to investigate weld behaviour on stress distributions.

In Chapter Six a comparison of steady-state rupture and continuum damage mechanics (CDM) failure predictions for realistic three-material isolated welded branched pipes is presented. Comparing the failure lives and positions of the two approaches for two different weldment material property sets assesses the effect of ignoring the tertiary creep stage in steady-state assessments. The CDM results provide a means of assessing the accuracy of the less computationally intensive FE steady-state rupture predictions.

Chapter Seven provides a wide-ranging comparison of three popular creep life assessment techniques for the purpose of addressing the relative accuracy of each. The steady-state rupture approach, British Energy's R5 rupture reference stress approach and the CDM approach are assessed for a wide range of single and multi-material components. The components considered range from relatively simple idealised structures, e.g. a beam in bending, to more realistic applications, e.g. a multi-material welded branched connection. The aim is to provide an assessment and guidance on the use of the R5 approach for both single and multi-material components.

Chapter Eight presents a general discussion and the main conclusions that can be drawn from the work presented in the thesis. Finally, Chapter Nine identifies future work required, based on the findings of the present study.



1. Coal Stockpile, 2. Boiler Bunker and coal feeder, 3. Pulverisers, 4. Boiler, 5. Superheater, 6. Turbine, 7. Generator, 8. Generator transformer, 9. Cooling towers, 10. Condenser, 11. Electrostatic Precipitators, 12. Chimney, 13. High concentration slurry disposal

Figure 1.1. Diagram of the basic processes within a coal-fired power plant (Energex plc [3]).

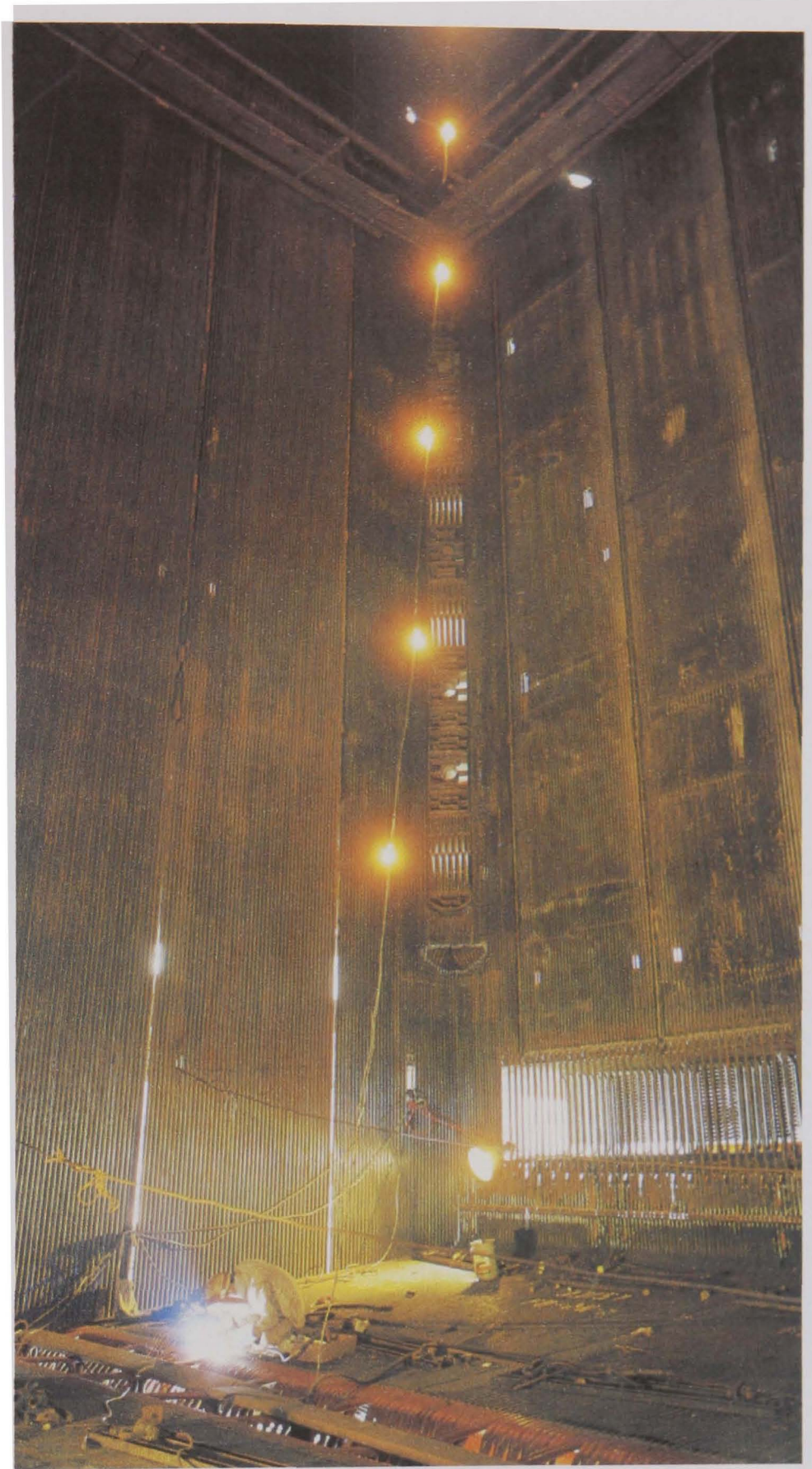
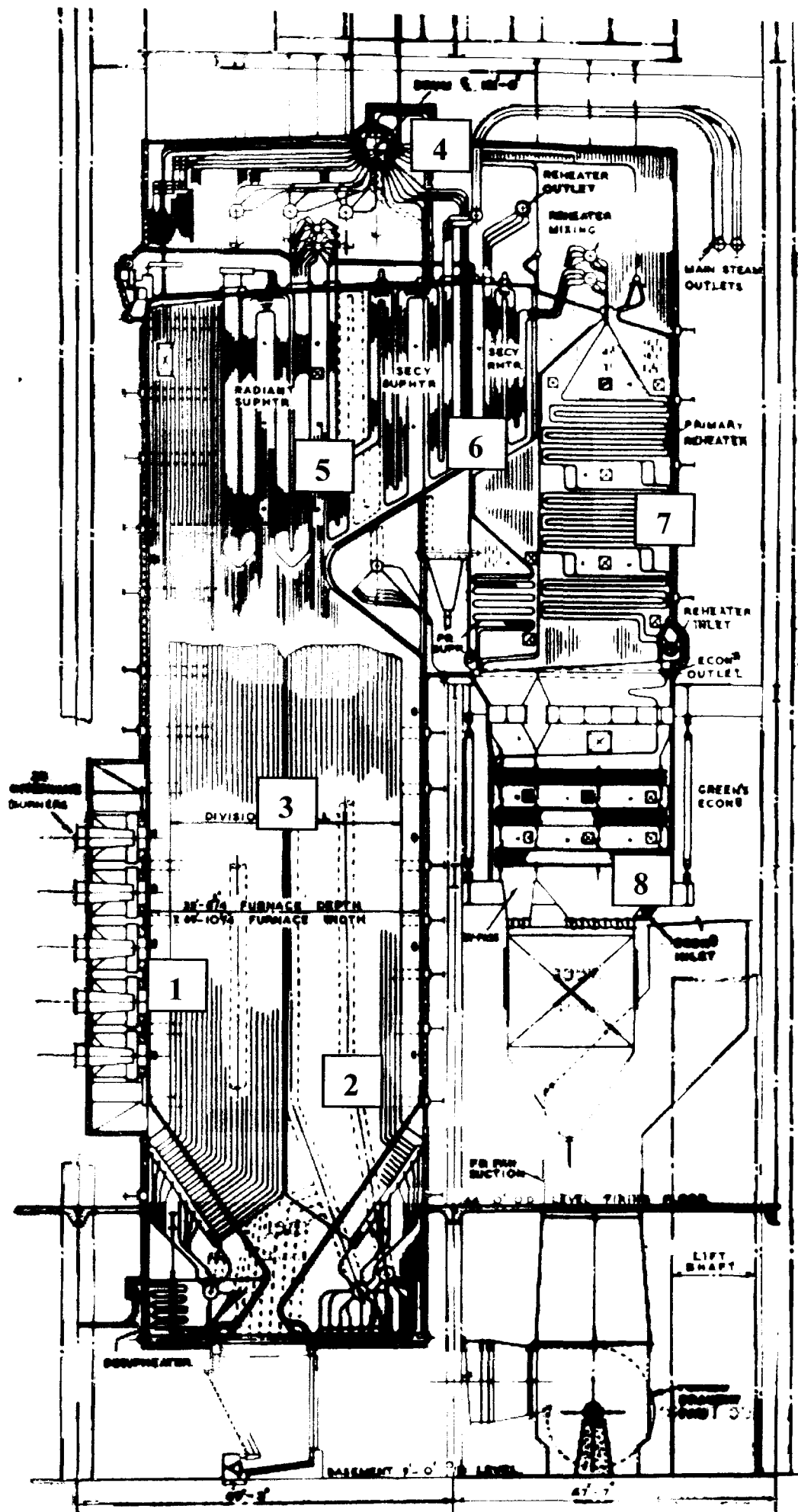


Figure 1.2. Furnace wall tubing in a boiler section of a fossil-fuelled power plant (PowerGen plc. [4]).



1. Intervane burners, 2. Furnace, 3. Waterwall tubes, 4. Boiler drum, 5. Platen superheater, 6. Final superheater, 7. Reheater, 8. Economiser.

Figure 1.3. Set-up of a boiler with reheat section (CEGB [5]).

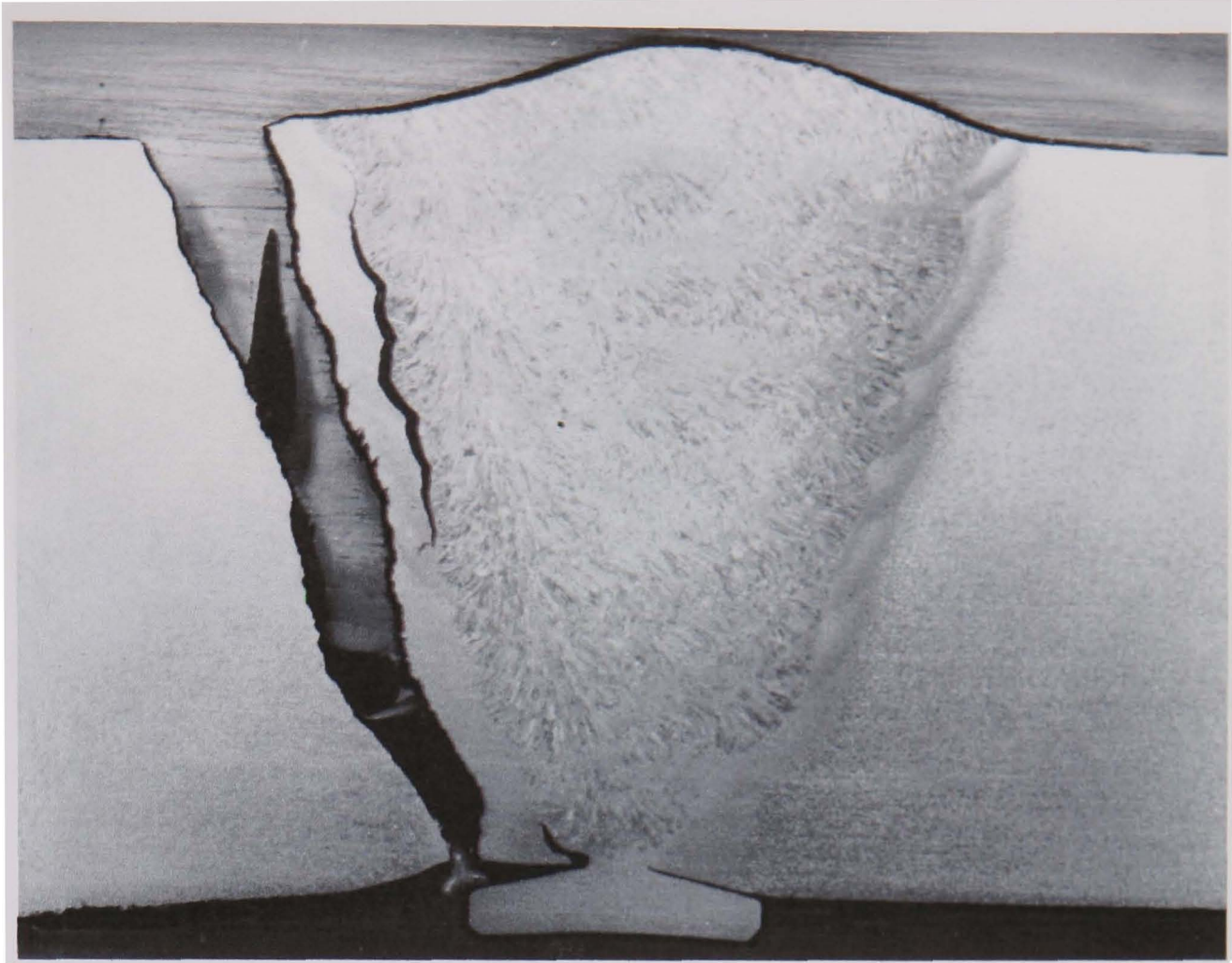


Figure 1.4. Cracks found in the heat-affected zone of a weld from a main steam plain pipe (PowerGen plc. [4]).

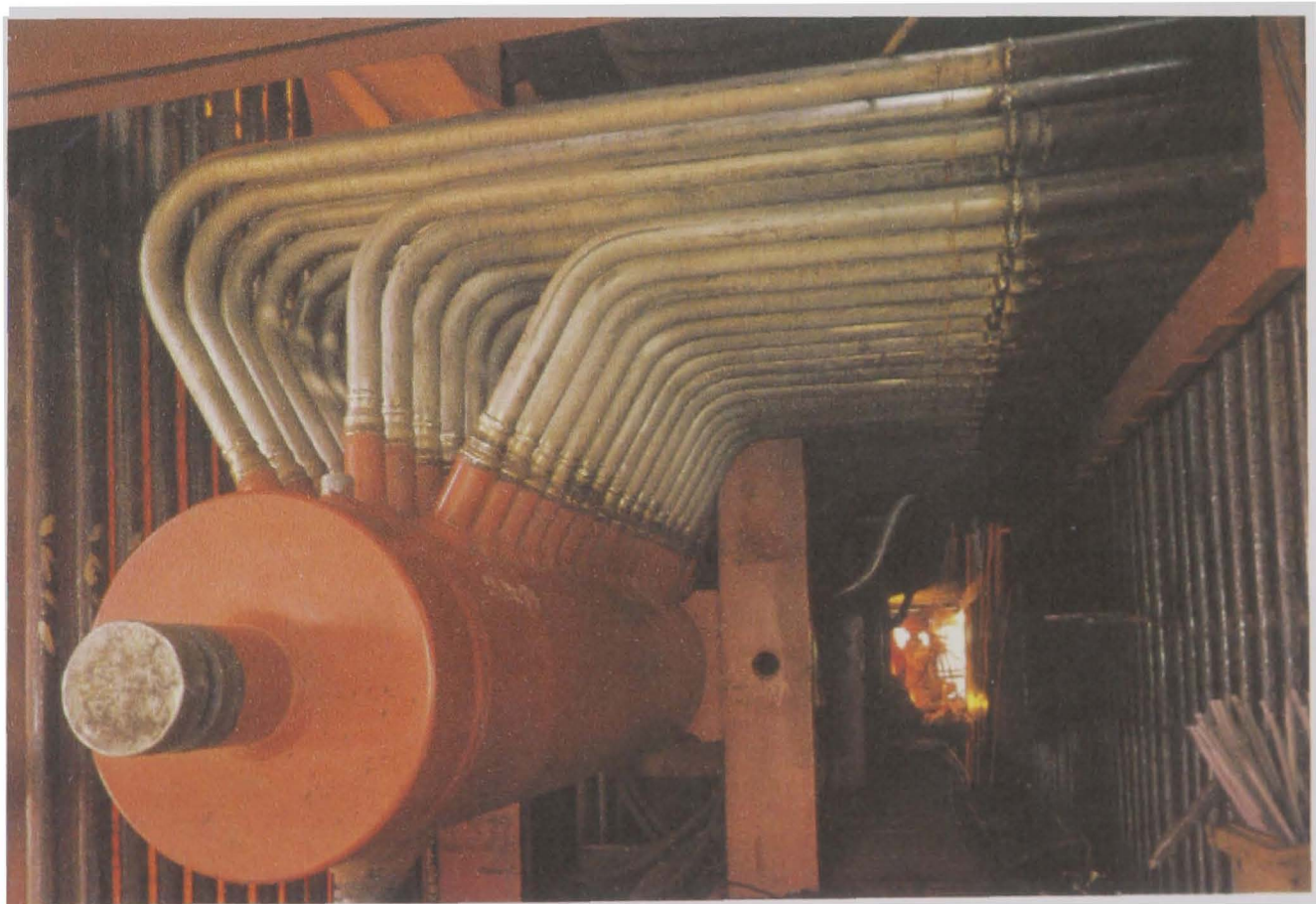
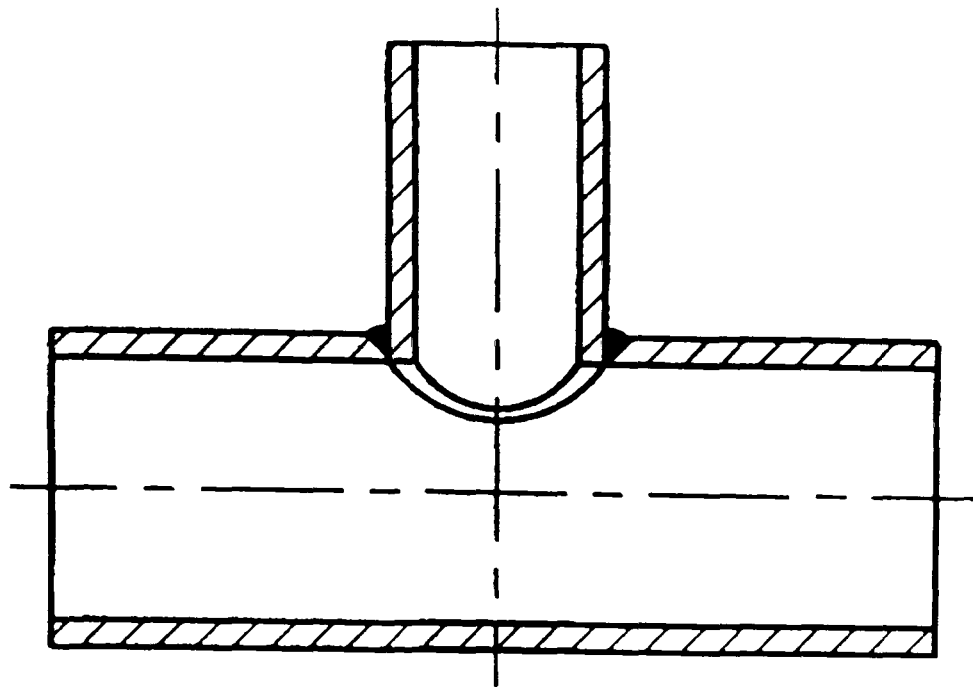


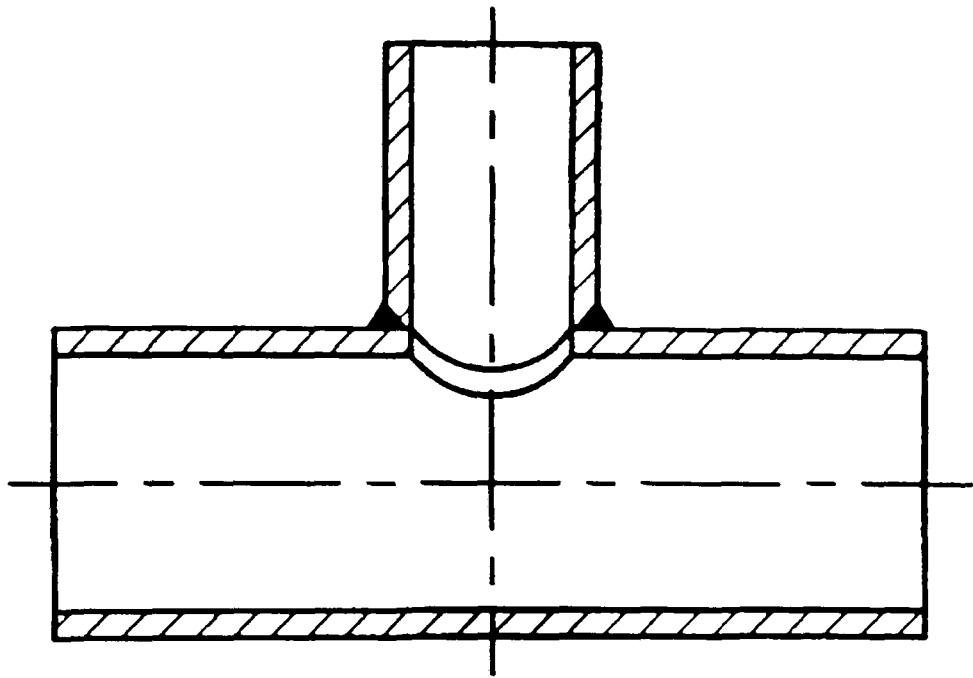
Figure 1.5. Superheater header (Nippon Steel Corp. [14]).



Figure 1.6. Reheat header (PowerGen plc. [4]).



Set-in



Set-on

Figure 1.7. Main welded connection types of branched pipe (Lynch [15]).

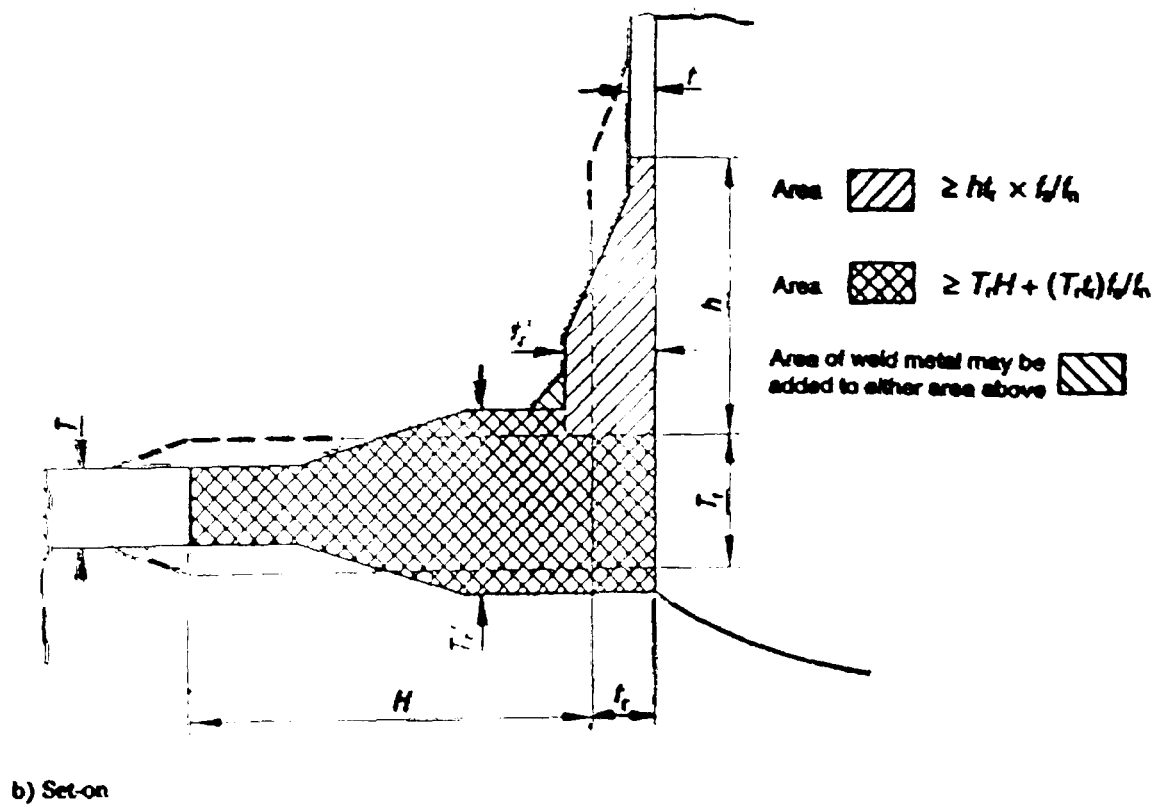
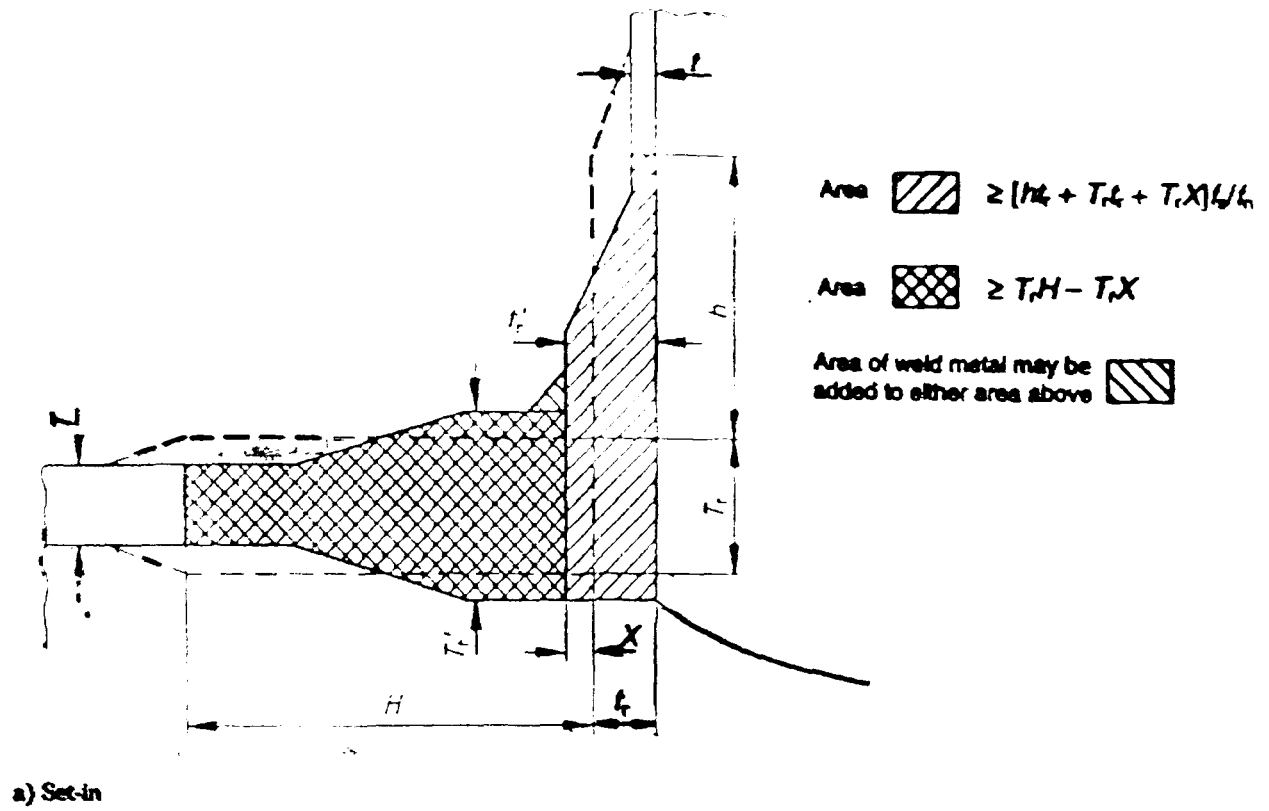


Figure 1.8. Variables for branched pipe strengthening (from BS5500 [11]).

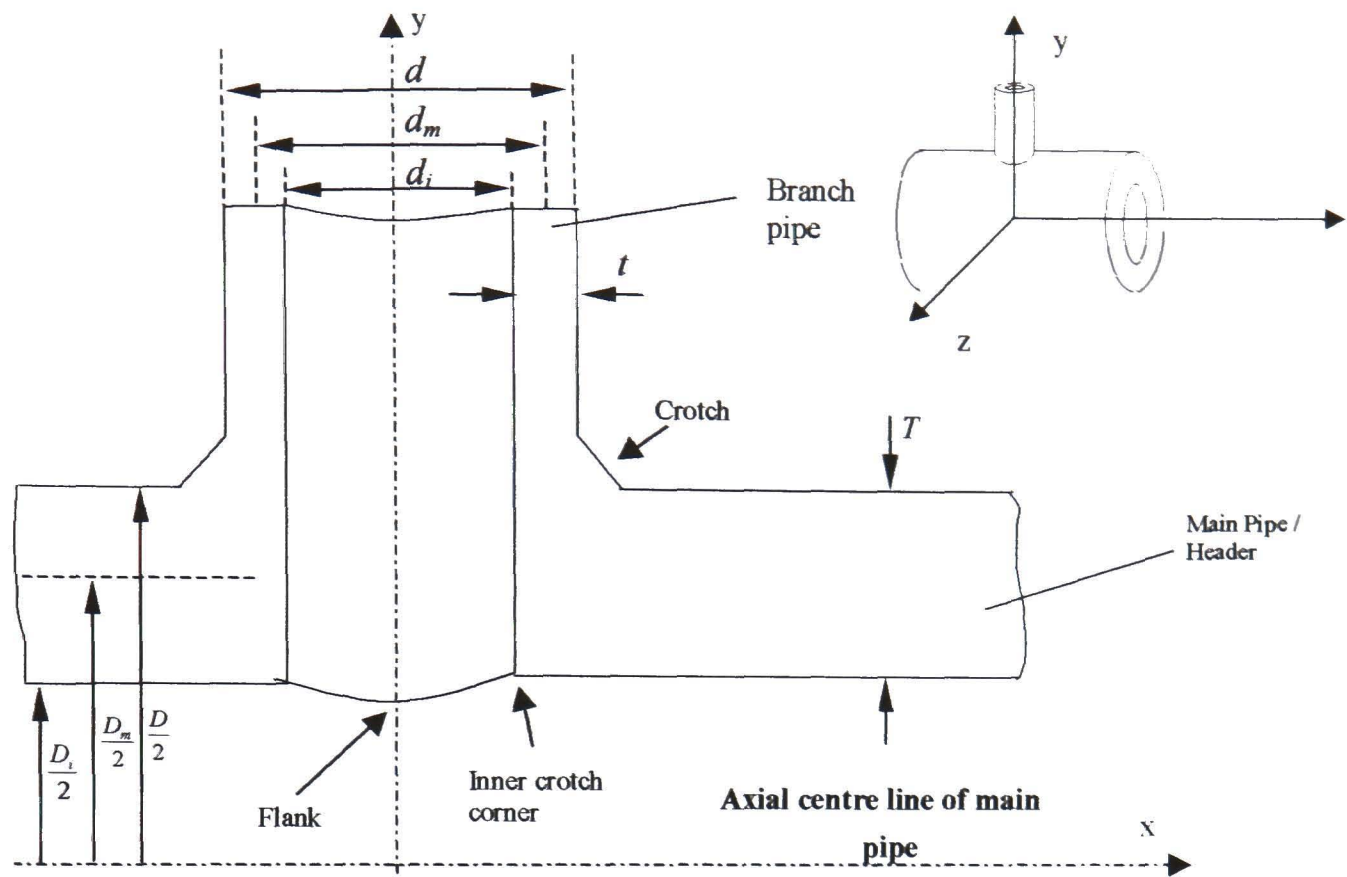


Figure 1.9. Geometric notation of welded branched pipes.

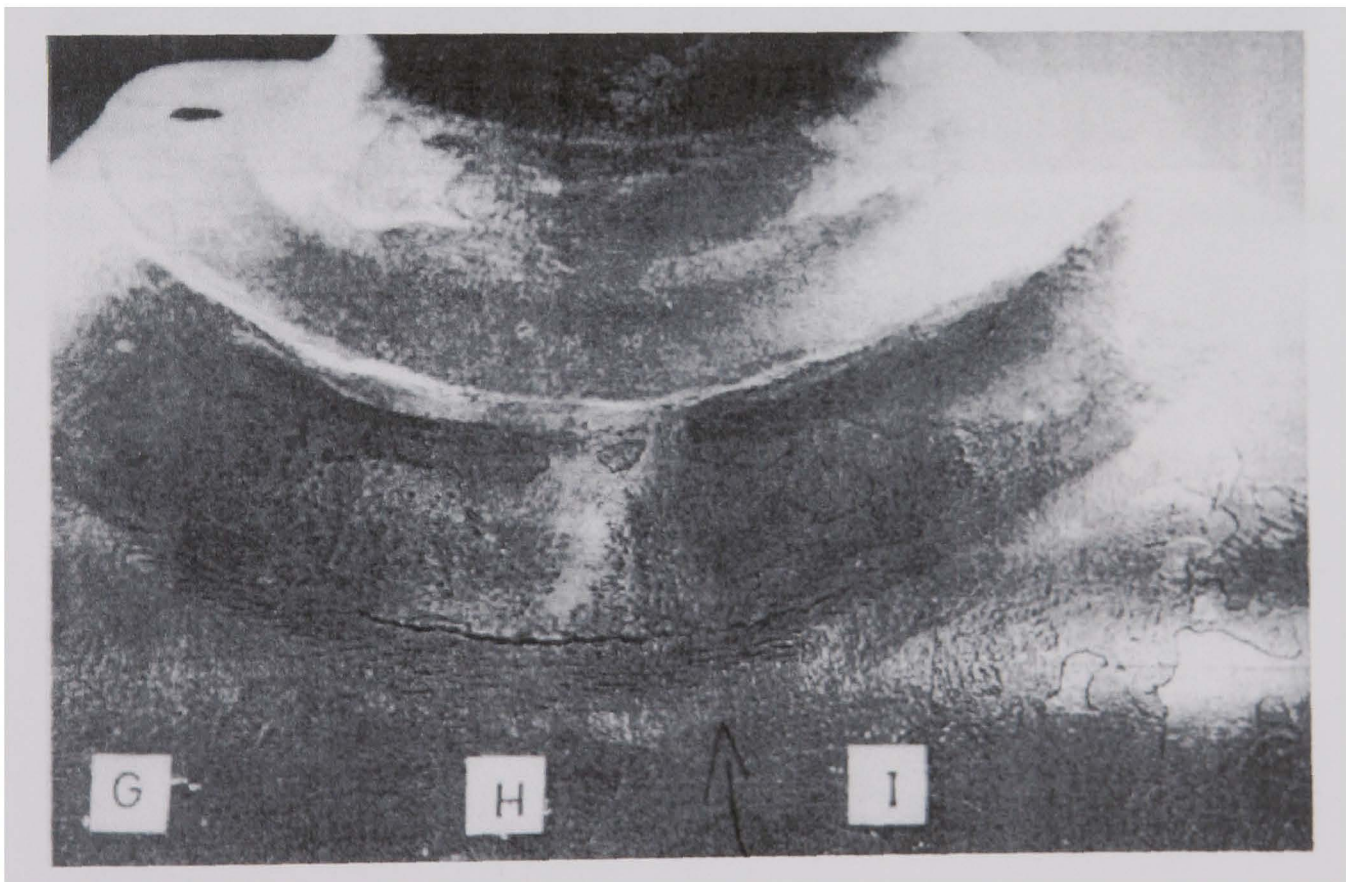


Figure 1.10a. Circumferential creep cracks at the weld foot on the outside surface of the weld of a branched pipe (Sys [17]).



Figure 1.10b. Gross circumferential and transverse creep cracks on the outside surface of the weld of a branched pipe (Day et al [18]).



Figure 1.10c. Parallel creep cracks within the weld at the inside bore of a branched pipe (Sys [17]).

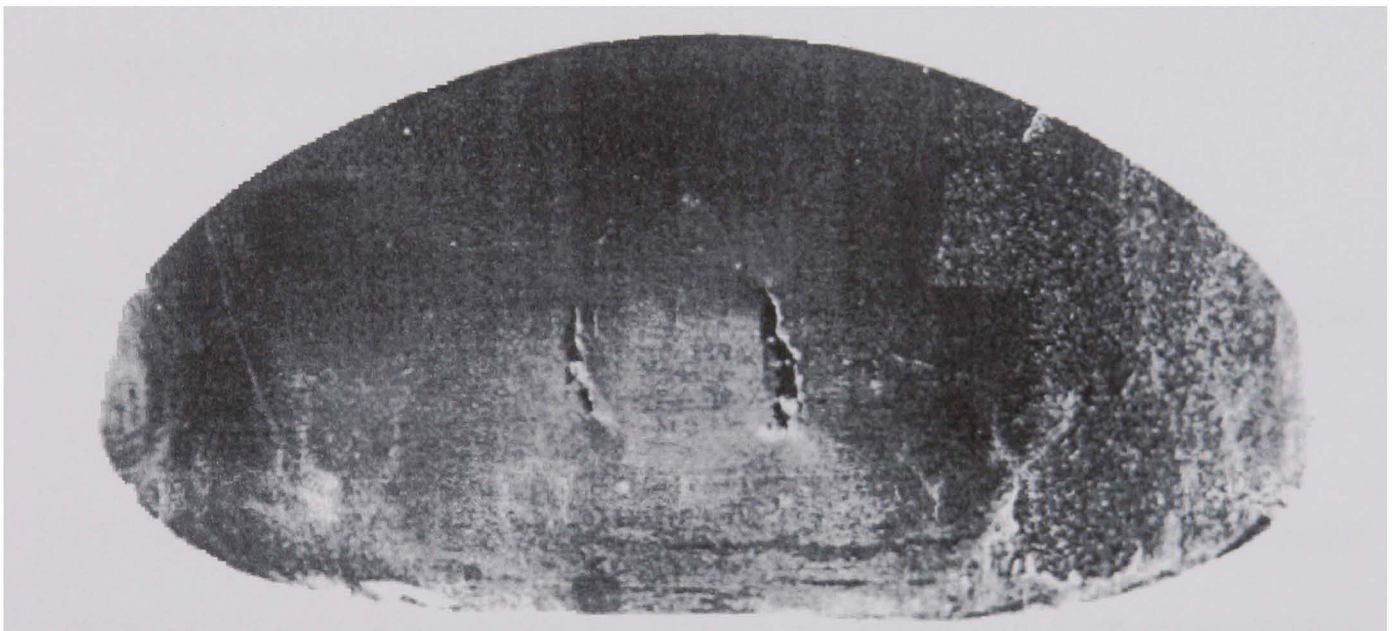


Figure 1.10d. View of a through-thickness creep crack near the inside crotch corner of the weld at the inside bore of a branched pipe (Sys [17]).

CHAPTER TWO

LITERATURE REVIEW

2.1 Introduction

Creep is defined as the time-dependent deformation of a material at an applied stress less than the yield strength. At high temperatures, creep can produce significant continuous viscoplastic strains within metallic components that eventually lead to failure. The extent of creep and the time to failure depend on the material, the operating temperature, the applied stress history and the geometry of the component.

2.2 Microstructural and mechanical behaviour under creep in metals

Although some metals such as lead, copper and mild steel can creep at room temperatures, the phenomenon is normally associated with high temperatures, typically greater than 40% of the absolute melting temperature of a metal [37]. On a microstructural level, there are two dominant creep mechanisms namely dislocation creep and diffusional creep [37]. Diffusion occurs when vacancies exist in the metal crystal lattice. An atom can move into a neighbouring vacancy when it has enough thermal (activation) energy. Dislocation creep is related to dislocations within the crystal lattice of the metal overcoming the natural stiffness of the crystal lattice structure or other obstacles such as

precipitates to move through the lattice, giving rise to 'slip'. Both mechanisms produce creep deformation and dislocations also join together to produce damage and form cracks.

Mechanisms of metallic creep on the macroscopic level start with the accumulation of creep strain with time at a given stress and temperature. Creep generally consists of three distinct stages, as shown in Figure 2.1 [38]. The immediate effect of an applied load will introduce initial elastic strain. Thereafter, a region of increasing creep strain at a decreasing creep strain rate occurs, known as the *primary* creep stage. Following this stage, is a region of constant creep strain rate, called the *secondary* creep stage or *steady-state* creep stage. The third and final stage consists of a region of progressively increasing strain rate, known as the *tertiary* creep stage, where the creep strain rate increases rapidly. After some time, the material fails by creep fracture or rupture [37,38]. The three main stages are described below in more detail:

Primary creep is a period of work-hardening in which the creep rate decreases with time. As a result, the material becomes harder to deform as the internal stress increases with the dislocation density.

Secondary creep (steady-state creep) is a period of balance between work-hardening and thermal softening. The latter is a recovery process activated by the energy from the dislocation structure. This results in a region of constant creep rate and the material becomes neither harder nor softer. This stage is normally used as the basis of engineering

design and life assessment for creep, as it is commonly the dominant region over the design life of components.

Tertiary creep results from necking, cracking and metallurgical instability. It is characterised by an increasing creep strain rate culminating in fracture.

Differences in the creep response of a material may arise when one stage dominates under a particular stress or temperature combination [39], the basic shape of the creep curve remains unaltered. For instance, the CrMoV alloys used for fossil-fuelled power plant steam piping systems, which usually experience stresses lower than 100MPa and temperatures around 550°C, generally have short *primary* creep stages, long *secondary* creep stages and short *tertiary* creep stages. Typical creep behaviour for a $\frac{1}{2}\text{Cr}\frac{1}{2}\text{Mo}\frac{1}{4}\text{V}$ alloy is shown in Figure 2.2 [26] for an accelerated temperature of 640°C. Note that as the stress is decreased the *secondary* creep rate reduces, while the failure life increases. Each curve shows a negligible *primary* creep stage, while the *secondary* creep stage dominates the creep curve and the *tertiary* creep stage is substantial for all three stress levels, but reducing in prominence for lower stresses. The secondary creep stage dominates each creep curve by constituting around 70% of the materials creep life. As the graph shows for this material, at this accelerated temperature, for higher stresses the tertiary creep stage becomes more prominent. Likewise, if creep tests were performed at three different temperatures and at a constant stress level similar behaviour would be found.

2.3 Mathematical modelling of creep

2.3.1 Introduction

Many simplified creep constitutive relations have been proposed to describe the nature of the three different regions of the creep curve. As described earlier, creep strain, ε^C , is dependent on three main parameters: stress, time, and temperature, denoted σ , t and T , respectively. A generalised creep strain law can therefore be shown in the form of

$$\varepsilon^C = f_1(\sigma)f_2(t)f_3(T) \quad (2.1)$$

where $f_1(\sigma)$, $f_2(t)$ and $f_3(T)$ can be separated to give distinct relationships for each of the three parameters on creep strain. Previous work has suggested many forms for $f_1(\sigma)$, $f_2(t)$ and $f_3(T)$ [38,39], as follows:

For the stress dependence, $f_1(\sigma)$:

$$f_1(\sigma) = A\sigma^n \quad \text{Norton [40]}$$

$$f_1(\sigma) = C \sinh(\xi\sigma) \quad \text{McVetty [41]}$$

$$f_1(\sigma) = E \exp(\psi\sigma) \quad \text{Dorn [42]}$$

$$f_1(\sigma) = C[\sinh(\zeta\sigma)]^e \quad \text{Garofalo [43]}$$

where A , C , E , ξ , ψ , ζ , e and n are material constants. Suggestions for the time dependence, $f_2(t)$:

$$f_2(t) = bt^k \quad \text{Bailey [44]}$$

$$f_2(t) = E(1 - e^{-qt}) + Gt \quad \text{McVetty [41]}$$

$$f_2(t) = \sum_i c_i t^{j_i} \quad \text{Graham and Walles [45]}$$

where E , G , c_i , b , g , j_i and q are constants, which could depend on temperature. Suggestions for the temperature dependence, $f_3(T)$:

$$f_3(T) = t \exp(-\Delta H / \dot{R}T) \quad \text{Dorn [42]}$$

where t is time, ΔH is the activation energy, \dot{R} is the Boltzmann constant and T is the absolute temperature.

2.3.2 Steady-state creep modelling

One of the simplest and most commonly used creep law relating creep strain to applied stress is Norton's power law [40]

$$\dot{\epsilon}^C = A \sigma^n \quad (2.2)$$

where A and n are material creep properties, determined from creep test data. n is generally called the creep exponent or creep index value. This relationship describes the variation of minimum creep strain rate with applied constant stress for the secondary (steady-state) creep stage for uniaxial stress behaviour. $f_2(t)$ is assumed to equal unity. Temperature dependence is not explicitly defined in this law: the equation is used for constant temperature conditions. However, the effect of different temperatures can be captured through the material constants A and n . For power plant applications, temperature and load remain practically constant for prolonged periods of time and the steady-state creep stage dominates the creep curve of the material, so that the use of Norton's law is valid for such analyses [38,39].

Since true uniaxial states of stress are rare it is important to treat creep as a multiaxial problem. The application of plasticity yield criteria to creep behaviour for multi-axial stress states is widely accepted and modified versions of uniaxial creep constitutive equations have been derived and used successfully [38,39]. For steady-state creep, a commonly used law [46] relating multiaxial stress and creep strain rate is the multiaxial generalisation of the Norton law, as follows:

$$\dot{\varepsilon}_{ij}^c = \frac{3}{2} A \sigma_{eq}^{n-1} S_{ij} \quad (2.3)$$

where $\dot{\varepsilon}_{ij}^c$ is the creep strain rate tensor, S_{ij} is the deviatoric stress, defined as:

$$S_{ij} = \sigma_{ij} - \frac{1}{3} \sigma_{kk} \delta_{ij} \quad (2.4)$$

where δ_{ij} is the Kronecker delta which is equal to 1 when $i = j$ and 0 when $i \neq j$.

The multiaxial creep stress state can be treated using the concept of equivalent stress, σ_{eq} , defined similar to that of the theory of plasticity [47-49] as:

$$\sigma_{eq} = \frac{1}{\sqrt{2}} [(\sigma_x - \sigma_y)^2 + (\sigma_y - \sigma_z)^2 + (\sigma_z - \sigma_x)^2 + 6(\tau_{xy}^2 + \tau_{yz}^2 + \tau_{zx}^2)]^{1/2} \quad (2.5)$$

where $\sigma_x, \sigma_y, \sigma_z$ are the Cartesian normal stress components acting in the x, y and z planes, respectively, and $\tau_{xy}, \tau_{yz}, \tau_{zx}$ are the shear stress components.

Similarly, an equivalent creep strain can be derived.

Stress redistribution and strain accumulation are important phenomena associated with creep over time following initial elastic response [38,39,46].

An example of this behaviour is shown in Figure 2.3 [39], which represents a typical time history of deflection and stress at a position of interest for a

constant load. The redistribution of stress due to the time-dependent relationship between strain and stress and the spatial distributions of stress and strain within a component are shown. For all but the simplest components [35,39], numerical techniques such as finite element (FE) analysis are required to quantify the redistributed, steady-state stresses. For multi-material, welded branched pipe components this is specifically true: hence, the present work is based on FE modelling. In addition, for such multi-material components as welded pipes, with significant differences in creep properties between weld zones, the determination of stress-redistribution and resulting steady-state stresses is a complex process, e.g. [23,35].

An important relationship in steady-state creep of homogeneous components, first proposed by Calladine [36], is the approximately linear relationship between maximum steady-state creep stress in a component and inverse of Norton creep exponent, n . Calladine showed that the maximum stress for six components, as shown in Figure 2.4, under different stress states, an approximately linear variation with $1/n$, as shown in Figure 2.5, where $m=1/n$. Calladine proposed that the relationship held generally for any component experiencing power-law creep. The maximum steady-state stress in any component can thus be found for any arbitrary value of Norton creep exponent by interpolating between any two known stress values corresponding to two different n values, say $n=1$ and $n=10$. The relationship has been incorporated into creep life assessment procedures that use a maximum steady-state creep stress to predict a rupture life, e.g. British Energy's R5 procedure [13], which is based on the reference stress method [39,50].

2.3.3 Continuum damage mechanics modelling

Continuum damage mechanics (CDM) applied to creep problems can model primary, secondary and tertiary creep in the form of damage accumulation [39]. It is based on a time-dependent accumulation of creep damage within the material at high temperature leading to failure or rupture. The interest here is in damage accumulation during the tertiary creep stage. Other types of damage at high temperature relate to corrosion, spalling, fatigue etc [37,38]. On a macroscopic scale, damage due to creep generally represents the growth of internal voids in and around the grains of a metallic structure at high temperature, due to nucleating cracks and cavities, examples of which are shown in Figure 2.6 [51]. Creep damage localisation has been observed in both engineering practice and laboratory simulation [37,51]. Put simply, growth of voids in a material will lead to an effective loss in material cross-section. As a result, the stress acting over this cross-section for a constant applied load and temperature will increase with time as damage increases. Penny and Marriott [39] recommend the model proposed initially by Kachanov [31] and the later modifications to this by Rabotnov [52] as the most robust of models for creep damage growth. The finalised versions of the Kachanov and Rabotnov models are based on a power law which incorporates a damage parameter, denoted by ω . As damage accumulates with time, the strain rate at a point in the material also increases with time, resulting in continuous stress redistribution. A CDM law for multiaxial creep strain rate, $\dot{\epsilon}^C$, [53] is as follows

$$\dot{\epsilon}_{ij}^c = \frac{3}{2} A' \left[\frac{\sigma_{eq}}{1-\omega} \right]^{n'} \frac{S_{ij}}{\sigma_{eq}} t^m \quad (2.6)$$

where A' , n' and m are material creep properties determined from experimental creep data, S_{ij} is the deviatoric stress and σ_{eq} is the equivalent stress of Equation 2.5. When creep initiates in the un-damaged material at time equal to zero, the damage level is zero, $\omega=0$. As creep time increases, the damage and strain rate at a position will increase, and ω tends to unity and the strain rate to infinity. The condition $\omega = 1$ corresponds to material failure. A second equation is coupled with Equation 2.6 to represent the evolution of damage with time [52,53], as follows

$$\dot{\omega} = \frac{M\sigma_r^\chi}{(1+\phi)(1-\omega)^\phi} t^m \quad (2.7)$$

where $\dot{\omega}$ is the damage rate and M , ϕ and χ are material constants, which can be determined from experimental creep rupture data. The creep rupture stress [10], σ_r , is based on the tri-axial creep behaviour of a material, and is calculated using the equivalent stress, σ_{eq} , and maximum principal stress, σ_1 , as follows

$$\sigma_r = \alpha\sigma_1 + (1-\alpha)\sigma_{eq} \quad (2.8)$$

where α is a material constant, which ranges from 0, for cases where σ_{eq} dominates to 1, for cases where σ_1 is dominant.

CDM analyses will produce a creep rupture life for a component when the material across its section has reached $\omega = 1$, i.e. failure, but only at the cost of extensive computational time, since modelling of damage evolution requires

very small time increments due to the compatibility of strain and stress-redistribution. An alternative approach is to use the steady-state stress with the integrated form of Equation 2.7 with respect to time, giving

$$t_f = \left[\frac{1+m}{M(\sigma_r)^\chi} \right]^{1/(1+m)} \quad (2.9)$$

to predict a lower bound failure time. Where lower bound denotes that the failure life will be more conservative than the equivalent failure time based on the CDM prediction using Equations 2.6 and 2.7.

To predict rupture lives using the material rupture properties and the rupture stress based on steady-state creep stresses, as shown in previous studies, e.g. [23,34]. This latter approach has been shown to give reasonably conservative estimates for the failure times of power plant weldments compared to the alternative damage mechanics approach. Damage analysis has its limitations because often the material constants required (i.e. A' , n' , M , m , ϕ , χ) may not be widely available and tend to be difficult to attain. Additionally, standard FE packages such as Abaqus [28] and Ansys [54] do not offer “in-built” CDM material constitutive equations, such as Equations 2.6 to 2.8, in their software and sub-routines must be written to model CDM. However, CDM life predictions can be used to benchmark simpler methods, such as lives estimated using steady-state creep stresses [34].

2.3.4 The reference stress method

2.3.4.1 General

The idea of the reference stress method (RSM) was first proposed by Soderberg [55] and later additions made were by MacKenzie [56], Sim [50] and others. The method is widely used for analysis and design of engineering components under creep conditions [39,58-60]. The method has been used to estimate creep deformation, creep stresses and rupture lives of components [39,58-60]. The approach predicts relatively accurate results and because of its simplified nature compared to other approaches it is therefore commonly used. The R5 creep life assessment method for power plant components is based on the use of reference stresses.

On initial loading of a component, instantaneous generalised deflection vector, \bar{U}_i is obtained at a position of interest. This vector is a function of the component dimensions and the elastic or elastic-plastic behaviour of the material. A second, steady-state creep deformation occurs, which is time-dependent, namely, \bar{U}_{SS} . This deformation increases at a steady rate, $\frac{d\bar{U}_{SS}}{dt}$.

A third deformation is due to creep during the stress redistribution phase, \bar{U}_{SR} . These three sources of deformation are shown in Figure 2.7 to characterise the general component behaviour [39]. Thus, the total deformation, \bar{U}_T , at the position will be accumulated as

$$\bar{U}_T = \bar{U}_i + \frac{d\bar{U}_{SS}}{dt}t + \bar{U}_{SR} \quad (2.10)$$

For some simple components, $\frac{d\bar{U}_{ss}}{dt}$ can be obtained. e.g. [61], in the general form of

$$\frac{d\bar{U}_{ss}}{dt} = f_1(n) f_2(\text{dim}) A \sigma_{nom}^n \quad (2.11)$$

where $f_1(n)$ is a function of Norton stress exponent, n , $f_2(\text{dim})$ is a function of component dimensions and σ_{nom} is a convenient nominal stress dependent on the loading of the component.

Mackenzie [56] proposed the use of a scaling factor, α , in Equation 2.11 for the purpose of simplifying the solution for finding the displacement rate using a reference stress for the component, σ_{ref} , so that Equation 2.11 becomes

$$\frac{d\bar{U}_{ss}}{dt} = \frac{f_1(n)}{\alpha^n} f_2(\text{dim}) A (\alpha \sigma_{nom})^n \quad (2.12)$$

When $\alpha = \alpha_{ref}$ (a constant reference factor), so that the function $\frac{f_1(n)}{\alpha^n}$ is

independent of n and $\frac{d\bar{U}_{ss}}{dt}$ in Equation 2.12 becomes simplified, so that

$$\frac{d\bar{U}_{ss}}{dt} = \bar{D} A (\sigma_{ref})^n \quad (2.13)$$

where \bar{D} is a reference multiplier, equal to $\frac{f_1(n)}{\alpha^n} f_2(\text{dim})$ and $A (\sigma_{ref})^n$ is the

steady-state creep strain rate at the reference stress, σ_{ref} , which is thus equal to

$$\alpha_{ref} \sigma_{nom} \cdot$$

For a component with an analytical solution in the form of Equation 2.12, the value of α_{ref} can be obtained by using trial and error with Equation 2.12 for two values of n until a value of α is found for which $\frac{f_1(n)}{\alpha^n}$ is independent of n . The α value thus found is taken as the α_{ref} value, the σ_{ref} and \bar{D} values can then also be determined.

For components without analytical solutions, which cover the vast majority of structures, numerical methods have been suggested. Sim [50] proposed a method based on approximate solutions using limit loads. This method

consists of plotting $\log \left[\frac{d\bar{U}_{ss}/dt}{A(\alpha\sigma_{nom})^n} \right]$ for a range of α values against n to find

α_{ref} , the value for which $\frac{d\bar{U}_{ss}/dt}{A(\alpha\sigma_{nom})^n}$ is independent of n , as shown in Figure

2.8. The y -axis intercept gives the log of the reference multiplier parameter, \bar{D} .

Sim [50] used the similarities between (i) the time-independent (static) elastic and time-dependent creep $n=1$ solutions and the (ii) time-independent elastic-perfect-plastic (EPP) and time-dependent creep $n=\infty$ stress distributions to give an approximate method for determining the reference stress and displacement rate, as follows:

$$\sigma_{ref} = \frac{P}{P_L} \sigma_y \quad (2.14)$$

and

$$\bar{D} \approx \frac{\bar{U}_i^{EL}}{(\sigma_{ref} / E)} \quad (2.15)$$

where P is the applied operating load, P_l is the limit load of the component, σ_y and E are yield stress and Young's modulus, respectively, and \bar{U}_i^{EL} is the initial elastic deflection of the component.

2.3.4.2 R5 reference stress approach

The most common use of the R5 lifing technique [13] is for homogeneous (single) material defect-free components under steady-load. The R5 approach however is based on a modified version of Equation 2.14, which leads to more accurate predictions of failure lives [60,62-64], as described below.

Equation 2.14 generally provides a lower bound on the actual reference stress for rupture assessment purposes [60]. However, comparison of experimental and rupture calculations for numerous structures made from creep ductile materials (defined as rupture by gross creep deformation) indicate that Equation 2.14 provides accurate predictions of life for materials with similar shape rupture and deformation surfaces [62]. An extensive evaluation of predicted rupture lives and experimental data for components in various stress-states led to the generation of the R5 approach [13], which is summarised below.

It has been shown [64] that the estimated time for a structure to fail by the spread of creep rupture damage, t_{CD} , is less than the estimated time to rupture obtained from uniaxial stress rupture data at the reference stress, $t_r(\sigma_{ref})$, of Equation 2.14, i.e.

$$t_{CD} \leq t_r(\sigma_{ref}) \quad (2.16)$$

R5 argues that the difference between t_{CD} and $t_r(\sigma_{ref})$ is due to stress concentration effects in the component [62,63]. A stress concentration factor, λ , is thus defined as

$$\lambda = \frac{\bar{\sigma}_{el,max}}{\sigma_{ref}} \quad (2.17)$$

where $\bar{\sigma}_{el,max}$ is the maximum value of the elastically calculated equivalent stress in the component. The equivalent stress is used to account for both uni-axial and multi-axial states of stress within components. Calladine [36] deduced that the maximum steady-state stress in a component varies approximately linearly with the inverse of Norton creep exponent value, n . The maximum steady-state stress at $n = \infty$ is the reference stress and at $n = 1$ is the maximum elastic stress. This relationship gives rise to a rupture reference stress, σ_{ref}^R , used within the R5 approach defined as

$$\sigma_{ref}^R = \left(1 + \frac{1}{n}(\lambda - 1)\right) \sigma_{ref} \quad (2.18)$$

The rupture reference stress therefore augments the reference stress to account for the effect of stress concentrations within a component.

Volume 7 of R5 states that Equation 2.18 should be used for creep brittle materials (defined as rupture by negligible creep deformation), where overall creep rupture of a component may be assumed to occur when local rupture at the stress concentration occurs, i.e. $t_{CD} \approx t_r(\sigma_{ref}^R)$. However, it is argued that for creep ductile materials (R5 states ductile materials with n values less than 7) significant time is taken for damage to spread before fracture occurs after damage initiation, so that Equation 2.18 is overly conservative. R5 thus defines an improved empirical estimate of the rupture reference stress, σ_{ref}^R , as follows:

$$\sigma_{ref}^R = (1 + 0.13(\lambda - 1)) \sigma_{ref} \quad (2.19)$$

The component failure life, t_f , is then calculated using a life equation based on the reference rupture stress, such as

$$t_r = \frac{(\sigma_{ref}^R)^{-\chi}}{M} \quad (2.20)$$

where M and χ are material rupture properties, obtained from uniaxial rupture test data.

Under creep and constant loading conditions, stresses in weldments redistribute across the different material zones of a weld due to mis-match in creep properties and the requirement for strain compatibility within the component. This primarily occurs due to parallel loading to the weld direction, e.g a pressurised butt-welded straight pipe [13]. Volume 7 of the R5 procedure describes two approximate procedures for predicting the creep life of welded components. The first procedure considers the stress redistribution for each constituent zone by modifying the homogeneous reference stress (Equation 2.14) by multiplying with a zone-specific stress redistribution factors, k , and then calculating the life using the usual procedure as for a homogeneous component, as detailed above. The k factors are based on the stress redistribution of parent material, weld metal, coarse HAZ and Type IV HAZ material behaviour of straight welded pipes made of either $\frac{1}{2}\text{Cr}\frac{1}{2}\text{Mo}\frac{1}{4}\text{V}$ parent material with a $2\frac{1}{4}\text{CrMo}$ weld metal or with both $2\frac{1}{4}\text{CrMo}$ parent and weld metals. The approach firstly requires the knowledge whether the weld will fail by hoop stress dominance or by axial stress dominance. Under the latter, the axial stress would be significantly larger than the hoop stress and would therefore control the weld failure. Since the HAZ and Type IV zones are very thin, the amount of stress redistribution in the axial direction (transverse to the weld) of a straight pipe weld would be very small, since redistribution is limited to the material local to the weld zones interfaces. For this later case of

transverse loading (transverse to the weld fusion line) dominance, the R5 allocates the k values for all weld zones as unity, i.e. no stress redistribution within all zones. Under hoop stress control, the reverse is true and all zones have a significant size in the radial direction and stress redistribution would occur by weaker materials off-loading to stronger zones. In this case, k factors with non-zero values are defined. For example, a $\frac{1}{2}\text{Cr}\frac{1}{2}\text{Mo}\frac{1}{4}\text{V}:2\frac{1}{4}\text{CrMo}$ weldment has k values of 1, 0.7, 1 for the PM, WM and Type IV HAZ regions. The second R5 multi-material method calculates reference stresses for each weld zone using a mis-match limit load, which uses a separate rupture strength stresses for each weld zone, dependent on the zones creep rupture strength. The method is described in more detail later in Chapter 7, where it is evaluated.

The physical basis for use of the reference stress method with multi-material components is less clear. Fundamental work by Yehia [65] applied the reference stress method successfully to simple multi-material components to predict reference stresses and displacements for materials with different Norton A constants. However, the study did not apply different Norton exponents, n , values in relation to each material, therefore its application to realistic multi-material components, which often have materials with different n values, is somewhat limited. Other published literature on the physical basis and the successful application of the RSM to multi-material components has not been found. A simplified method proposed by the Volume seven of the R5 procedure [13] for predicting reference stresses in multi-material components is discussed in the next section.

2.4 Creep of welds

2.4.1 Introduction

Welds are of utmost importance in power plants and other installations, often operating at high temperature under constant loading. Components used for high temperature plant are mainly complex and large in nature, because of this, connection of smaller components by welding is common practise, since forging or casting is generally much more expensive. Hence, welded joints are a frequent occurrence in every stage of plant operation. The high temperature performance of power-generation components and plant is generally limited by the creep life of the weldments, so that safe and reliable performance of all welded components is essential for effective plant operation. However, the creep behaviour of welded plant components is complex, due to the effects of material inhomogeneity of the weld, component geometry and loading.

Welds are complex in structure with different creep property zones produced by the welding process and are often weaker than that of the parent material of the component. The difference in creep strength between these different weld zones, known as weld mis-match, as well as the individual strengths of the zones, control the strength of the weld. The effect of welds on the creep failure lives of different power-plant components, such as straight pipe sections, pipe bends, end caps, branched pipes etc., is still not fully understood. Conversely, the effects of geometry, loading, creep properties and mathematical models on weld design and life assessment are still needy areas of research.

Distinct problems relating to the creep of welded components. i.e. the distinct creep strength of each weldment material and the combined effect on creep stress and strain distributions and failure behaviour. This has led to extensive research on this topic, including subjects such as the simulation of weldment performance, e.g. [10,26,34,53,66], residual life assessment, e.g. [34,58,60,67], improving weld design methods, e.g. [35,64], the effects of weld repair, e.g. [9,33,68] and others. The main approaches employed in creep of welds studies are based on experimental, analytical and numerical methods.

The majority of research has concentrated on two main areas. Firstly, the creep of uniaxial cross-weld test specimens used to provide indications of real component behaviour and for the generation of material properties [39]. Secondly, the creep behaviour of straight pipe steam sections with circumferential weldments has been extensively studied using experimental and numerical techniques to understand material mis-match behaviour and attain creep life predictions of the components, e.g. [33,34,69]. However, the creep of other important welded components, such as welded branched steam pipes, has had less attention. This is due to welded straight pipe sections being the most common welded component in power plant and also having relatively simple geometries. By comparison, welded branched pipes are less common than straight pipes and have relatively complex geometries.

Previous work relevant to the creep of welds and welded branched pipes is now described. Firstly, general work on the creep of welds is reviewed in this section and in Section 2.5; focusing on metallurgical and mechanical features

of weldments, weld performance and failure and previous studies and methodologies used to investigate creep of welds. Secondly, a review of the literature relating to branched steam pipes is presented in Section 2.6.

2.4.2 Metallurgical and mechanical behaviour

The welding process involves the deposition of very hot weld metal (WM), called a weld bead, onto the cooler parent material (PM) of the components to be connected together. For large welded regions, many weld beads will be laid to complete the weldment. The PM adjacent to the weld bead is subjected to numerous heating and cooling cycles as each weld bead is laid down, producing a different structured material compared to the PM away from the weld. This region is known as the heat-affected zone (HAZ) and its microstructure is dependent on the welding temperature magnitude and time at this temperature, number of heating cycles, the cooling rate, the material and the metallurgical state. Figure 2.9 displays the different material zones, each with varying grain size, in (a) a deposited single weld bead and (b) multiple weld beads, due to a single weld heating cycle and multiple heating cycles, respectively [70]. The number of material zones related to the single weld bead is five; weld metal (WM), parent material (PM) and three different heat-affected zones (HAZ)(Coarse, fine and intercritical grained). The multiple bead welds have an additional three heat affected weld metal zones produced from the heat-treating process from the deposition of an adjacent weld bead, these are known as the coarse columnar, recrystallised coarse and fine zones. Hence, a weldment is inherently inhomogeneous in structure and shows a structured distribution of varying metallurgical structures. Each of these

different microstructural zones has its own stress, strain and rupture behaviour. The extent of which is dependent on the particular parent material, weld metal and welding conditions used for the component. A typical example of the use of multiple weld beads to produce a weldment along main steam pipe sections for a fossil-fuelled power plant butt weld is shown by a cross-section of its macrostructure in Figure 2.10 [4].

Differences in thermal properties, e.g. expansion coefficient, of the various microstructural zones of the weld induce residual stresses across the weld during the welding process. This can be unfavourable to weld performance if the weld is left untreated in high stress and high temperature conditions, such as power plant piping. Hence, post weld heat treatment (PWHT) is commonly applied to the weld region to relieve, i.e. reduce, the residual stress state, to decrease the general stress levels and also to temper the weld microstructure.

Since the microstructure varies significantly across the weld, the mechanical properties of these distinct regions also change significantly. The ultimate tensile stress (UTS), the yield stress and the ductility all vary substantially after the welding process is complete [71]. The values of these properties often vary at different locations within the weld, the PM, WM and HAZ are all affected for typical engineering steel alloys [71]. These zones also commonly have significantly different creep properties, for instance minimum creep strain rate, rupture strength. For example, generally for low carbon steels the intercritical HAZ region is the weakest in terms of creep and rupture strength and has a higher ductility compared to the PM. The WM strength and ductility can vary

compared to the PM depending on material choice. e.g. [30,72,73]. Additionally, creep crack growth rates within the different regions of the weldment can vary significantly; it may be very high in the WM region, producing a brittle mode of failure, while in regions such as the PM, crack growth is generally slow and controlled by a ductile failure mode.

To effectively study creep failure of welds it is important that all of these metallurgical and mechanical characteristics of weld behaviour are considered.

2.4.3 Creep performance and failure of welds

Low alloy steels are often used for power plant piping sections, since they offer good creep performance at reasonable cost [71]. The alloys are based on chromium and molybdenum mixtures and sometimes including usage of vanadium to increase the creep strength of the alloy still further. For instance, power plants in the UK often use $\frac{1}{2}\text{Cr}\frac{1}{2}\text{Mo}\frac{1}{4}\text{V}$ steels for high-temperature piping. Power generation plants contain tens of thousands of welded components within boiler, superheater, reheater and turbine sections, which are usually designed for 100,000 to 200,000 hours of operation without failure [1]. Creep failures of weldments have been experienced in plant [74,75] and are becoming more frequent for ageing power stations due to nearing or passing the end of their design creep lives. The high temperature and pressure of the steam, plus additional axial end loads acting on the pipes are the primary causes of these failures.

The formation of weld cracks is the primary failure mode for power plant piping under normal operating conditions. Crack initiation can be attributed to numerous cases, including poor welding practices, inadequate post weld heat treatment (PWHT), ill-designed levels of material mis-match and the accumulation of creep damage. Worldwide adoption of a classification for weld cracking in power plant piping has been established [74,76]. Four main types of crack are described. The classification of the locations and orientations of weld cracking is shown in Figure 2.11 as illustrated by Schuller et al [76]. Crack Types I, II and III are all related to inadequate welding procedures, e.g. inadequate PWHT. These occur relatively early in plant service and can be repaired by local welding or rewelding of the whole weldment. Cracking Types I and II are found to initiate in the WM from the interaction of residual stresses produced from welding with the low-ductility of WM regions, thus producing circumferential 'reheat' and transverse WM cracks in the WM (Type I) and through WM, HAZ and PM (Type II) regions. The cause of Type III cracking is similar to that of Type I and II, i.e. poor PWHT through the interaction of residual stresses and brittle material regions and can be detected and repaired after PWHT. However, Type III cracks are located circumferentially in coarse grain regions of the HAZ.

Type IV and Type IIIa cracks are medium and long-term service crack growth controlled by creep damage accumulation due to high temperatures and loadings. The Central Electricity Generating Board (CEGB), adopted an additional variety of the Type III crack, denoted Type IIIa [74]. This circumferential crack variety is found in the fine-grained region of the HAZ.

instead of the coarse grained region for Type III cracks (see Figures 2.9 and 2.11). Type IV cracks are located in the intercritical region of the HAZ on the PM boundary and grow circumferentially around the weldment. Both Type IIIa and Type IV cracks occur as a result of the interaction of system stresses, predominately axial and/or bending stresses, with the relatively high ductility of the regions in the HAZ. Creep cavitation followed by macroscopic crack growth is the known failure mechanism involved with these types of cracks [74,77].

Creep failure of power plant piping made of ferritic steel alloys are most often controlled by Type IV cracking in the weld, compared to Type IIIa. Recent experimental studies on full-scale butt-welded main pipes and test specimens have generally concluded that the creep failure of welds using CrMoV materials, e.g. [21,74,77-80], and the newer power plant materials using higher content levels of chromium, e.g. P91, [79,80] is controlled by Type IV cracking. An example of this fact is shown in Figure 2.12, which displays the cumulative CrMoV butt-weld repairs made to the UK's Innogy plc. (formerly National Power plc.) plant piping due to Type IIIa and IV cracking [74]. Around 85% of these repairs are related to Type IV cracking, compared to 15% for Type IIIa.

The introduction of a weld in a structure usually results in a decrease in creep rupture life, compared to a homogeneous structure made of the same parent material. The extent of the decrease in life is dependent on the performance of the metallurgical and mechanical features of the weld. Weld creep failure

location does not always occur in the weaker material, since stress and strain redistribution also controls the weldment strength [71].

2.4.4 Experimental methodologies and studies of weldments

A number of test methods are used for experimental creep testing of welds. These include; cross weld tests, welded tube tests, model pipe weld tests and full-scale component testing. They differ in complexity and this in the accuracy with which they can model a real welded component. Since, under normal operating temperatures and loads of say 568°C and 16.55MPa internal pressure [81], respectively, steam pipes creep lives are expected to be around 20 to 25 years, experimental creep testing must take significantly shorter times. Hence, testing is generally carried out under accelerated stress or temperature conditions and the data is extrapolated to the other stress or temperature levels. Two popular experimental creep testing techniques are now described, namely; cross weld creep testing and full-scale component creep testing.

The expense and difficulties of experimental testing full-scale welded components has lead to the wide use of simpler experimental techniques, such as uniaxial cross weld rupture tests. This test uses welded specimens, which normally are machined parallel across the weld or sometimes at an oblique angle across the weld. An example of the geometry of a cross weld specimen is shown in Figure 2.13 for two different cross weld angles [35]. The weld is positioned at the centre of a uniaxial creep specimen and is loaded at constant stress and constant temperature conditions. The tests are relatively easy to perform, providing a certain level of understanding about rupture and creep

behaviour of the weld, and have been used to obtain the material constants in creep constitutive equations [30,72,81,82], e.g. Equations 2.2, 2.6 and 2.7, to aid in the study of creep behaviour of in-situ welded components. Additionally, they are used simply to determine the weakening effect of the weld. This is normally achieved by producing failure life data over a range of stresses and temperatures and comparing to homogeneous PM or WM uniaxial creep test life data for the same range of stresses and temperatures e.g. [80, 83]. Attempts by Etienne and Heerings [83] to define life reduction factors for in-situ weldments from cross-weld test data have been made. Hyde and Tang [84] reviewed the current status of cross-weld creep test data and showed that cross weld specimen life can be estimated from understanding of the constitutive laws of the different weld zones. Additionally, the work [84] recommended that the failure mode of the test specimen should be identical to that of the component under assessment, for instance Type IV cracking in a circumferential straight steam pipe weld with additional axial loading or bending. However, due to the uniaxial nature of this test method the direct application of such test data to in-situ components with multi-axial loading must be accompanied by a certain amount of caution.

Full-scale component creep testing is a more realistic test method for welded components. Such tests are generally carried out for the purpose of validating design codes, remaining life rules and numerical analysis predictions. These tests are complex, require purpose built facilities and are expensive, so that only a limited number of tests have been carried out. The components are commonly tested under in-service conditions replicating pressurised steam

temperatures and loadings, e.g. internal pressure and, commonly, additional axial or bending loads. The creep behaviour of the weld and component are tested, monitoring strain accumulation, crack growth data and other important information.

Previous full-scale steam plant component testing has been carried out by the CEGB, reported by Coleman *et al* [21, 85], and Williams [86]. Coleman *et al* [21,85] described a number of CEGB testing programmes to ensure of the integrity of welded pipework components. Non-defective (un-cracked) and defective (cracked) welded components from fossil-fuelled plant were tested. The main bulk of the work compared the experimental stress, strain and failure behaviour of two full-size thick-walled $\frac{1}{2}\text{Cr}\frac{1}{2}\text{Mo}\frac{1}{4}\text{V}$ butt-welded pressure vessels with uniaxial creep test predictions using four different weld metal materials, each constituting two weldments for each vessel at a temperature of 565°C and an accelerated pressure of 455 bar. The four types of weld metals considered, namely mild steel, $\frac{1}{2}\text{Cr}\frac{1}{2}\text{Mo}\frac{1}{4}\text{V}$, 1CrMo and 2CrMo were typical of those used in UK power plant. The geometry of one of the vessels is shown in Figure 2.14, displaying the weldment detail and strain and crack monitoring positions [21]. It was found that the uniaxial life predictions based on uniaxial creep properties and the mean diameter elastic hoop stress, were overly conservative relative to the measured test lives. The experimental mild steel pipe weld failed at around 24,000 hours compared to a uniaxial life prediction of 100 hours. The 1CrMo and 2CrMo weldments developed axial creep cracking in the weld metal at around 30,000 hours and still hadn't failed after 45,000 hours compared to the uniaxial mean diameter hoop stress life

prediction of 3,000 hours and 34,000 hours, respectively. The $\frac{1}{2}\text{Cr}\frac{1}{2}\text{Mo}\frac{1}{4}\text{V}$ weld metal didn't failed either, nor initiated significant damage after 45,000 hours, the uniaxial data estimated the creep failure life of the weld to be 6,000 hours. The conservatism of the predicted creep life based on uniaxial data and the mean diameter elastic hoop stress highlighted the inadequacy of this form of life prediction and the importance of the inclusion of stress redistribution, multi-axial stress states and material mis-match behaviour in creep design and life assessment methods. Additionally, several experimental contingency creep tests were carried out on ex-service fossil-fuelled pressure vessels with creep cracks already present in the components at normal operating temperature and pressure of 565°C and 159bar and at a downrated condition of 540°C and 159bar, respectively. The residual stresses present in the weld, including the HAZ, of a new weld on one of the vessels were examined at various times over the test period using a hole drilling technique. The main findings were that the residual axial stresses present in the weld decayed from 130MPa to -15MPa after 16,000 hours of testing and that no creep crack growth or initiation was observed in the vessel, leading to the conclusion that continued operation of similar power plant components was supported, even with crack defects present.

2.5 Numerical analysis of welded pipes

2.5.1 General

Due to the complexities of welded pipes, exact analytical creep solutions are not typically available. Hence numerical methods are commonly used for

specific material, geometry and loading combinations. Finite element (FE) modelling is the most commonly used approach, in conjunction with mathematical creep models, such as the ones described in Section 2.3. Before accurate modelling can be performed, the material properties for each material zone within the weld must be determined.

CDM constitutive equations have been presented in many forms for use with modelling of damage accumulation in welds within straight pipe sections. The generation of CDM constitutive laws by Hayhurst and co workers for FE modelling [10,53,67,69,87] are the most widely used, the simplest of which uses a one state variable as shown in Equations 2.6 and 2.7 [10,53]. This set of coupled CDM equations have been applied extensively and successfully to typical CrMoV welds of straight pipe sections, e.g. [20,26,34,88], as shown for example in Figure 2.15 [89]. Damage levels, ω , greater than 0.55 has accumulated in the WM and HAZ regions along the HAZ/WM boundary, peaking at the outside surface (right hand side), which agrees with full-scale CEGB creep tests reported by Coleman *et al* [85].

As mentioned earlier, the so-called steady-state creep rupture approach [23,34] and the reference stress approach are less time consuming than the CDM approach and require less material data, although they are less accurate since the tertiary creep stages is ignored. Nonetheless, they have been commonly used for creep assessments of weldments in straight pipe sections of power plant [e.g. 26,18,66,24,90-94].

For example, a popular steady-state creep law is Norton's law, shown as Equation 2.4 in Section 2.3.2, which is often included in creep modelling using standard FE packages, e.g. [28,54]. An effective FE-based steady-state life prediction technique which only requires four material properties for each weld zone technique using Norton law and the integrated damage law, Equations 2.4 and 2.9, respectively, has been shown by Hyde and co-workers [26,30,33,34] to be conservative compared to CDM predictions for a variety of typical CrMoV weldment materials, for aged, as-new and repaired, different straight pipe geometries. The predicted creep life is based on the use of a peak steady-state rupture stress [10], σ_r , as defined in Equation 2.8, for each material weld zone, using the distinct creep rupture properties for each zone and Equation 2.9. The component failure life and initiation position is then taken as the lowest life over all weld zones and positions of peak rupture stress, σ_r . The component life predictions were generally found to be 40% conservative for welded pipes relative to corresponding CDM predictions [33]. This conservatism is attributed to CDM predictions including stress reduction at the failure position of the pipe weld during the tertiary creep stage of stress redistribution.

One of the first FE weld studies was conducted by Walters and Cockcroft [95] in 1972 modelling two material zones, the PM and the WM. Later studies have also included the HAZ, e.g. Coleman *et al* [85], Hall and Hayhurst [20] and Sun [23]. More recent work uses four-material CDM models by Perrin and Hayhurst [69] to improve understanding on Type IV cracking by including coarse-grain and Type IV HAZ regions. A typical example of the pipe and

weld geometry and FE three-material mesh used for a typical $\frac{1}{2}\text{Cr}\frac{1}{2}\text{Mo}\frac{1}{4}\text{V}$ parent material and $2\frac{1}{4}\text{CrMo}$ weld metal thick-walled straight pipe weldment with closed end pressurised conditions used for such studies is shown in Figure 2.16 [33]. The Norton creep properties A and n , and A' and n' of Equations 2.4 and 2.6, respectively, and for the PM and WM are obtained from homogeneous uniaxial creep tests carried out at various levels of stress, which provides the minimum creep strain rate, $\dot{\epsilon}_c$ for each stress level, e.g. [23,51]. Plotting the log of the $\dot{\epsilon}_c$ values against the log of the various stress range values provides the n value, which is the gradient of the line and the A value which is the inverse-log of the $\dot{\epsilon}_c$ -intercept. Similarly the M and χ of Equations 2.7 and 2.9 are obtained by plotting the log of the rupture life, t_r , for each test carried out at a different stress against the log of the stress value. The gradient of the straight line is the χ value of the material and the inverse-log of the t_r -intercept of the line is the M value. The damage parameters, from Equations 2.6 and 2.7, m and ϕ are found for each material by curve fitting of the primary and tertiary creep stages from $\dot{\epsilon}_c$ and time plots, respectively. The creep rupture multiaxiality parameter, α , from Equation 2.8 is determined from either notched or waisted cross-weld creep specimen tests for the HAZ material or homogeneous specimens for the PM and WM and FE CDM calculations [96,97]. It is very difficult to determine the creep and rupture properties (A , n , M , χ , m and ϕ) for the different HAZ regions, due to their small size (typically about 1.5mm in width) [71,82]. Some specialised techniques have been developed to determine these properties such as the impression creep test technique of Hyde *et al* [96], which also makes use of the

reference-stress method. The material properties for the steady-state law of Equations 2.4 are obtained by indenting a small HAZ test piece under high temperature and using the creep deformation-time record for several pressures in conjunction with the RSM to find uniaxial-stress and uniaxial creep strain rate and therefore constants A and n . The damage constants of Equations 2.6 and 2.7, i.e. M , χ , m and ϕ are obtained in a similar manner as described above for the PM and WM but a trial and error process of comparing experimental failure times at different stresses for cross-weld creep tests of notched and waisted specimens with the results of FE damage modelling using estimated constants is used [96,97].

To simplify the modelling of the differences in creep strength and the stress distribution within the different zones of weldments during creep, the R5 procedure [13,98] suggests that a factor k is used to modify the σ_{ref} of Equation 2.14 for each zone. The material zones which deform relatively slowly in creep, such as the coarse-grained HAZ, pick up stress from zones which deform faster, whereas as the intercritical HAZ, Type IV HAZ zones relatively to the PM offload stress. The k factors for a straight pipe weld are; $k=1$ for the PM, Type IV HAZ and refined HAZ, 0.7 for the WM, and 1.4 for the Coarse HAZ and around 1.3 for the mixed HAZ [98]. The modified σ_{ref} for each zone are then used to predict a σ_{ref}^R using Equations 2.18 or 2.19 for each zone and then a failure life for each zone using a rupture life equation based on each materials rupture properties, such as Equation 2.9. However, the values of these k factors have only been described for straight pipe welds, under hoop-stress control, and not other types of components [13]. This is due

to the simple understanding of the stress distribution and redistribution behaviour of each weld zone in the hoop and axial directions of the pipe [85,99]. For more complex components, such as welded branched pipes, the effects of geometry on the stress redistribution behaviour of each weld zone are less well understood. Another method of assessing the relative creep strength and stress-redistribution within the weldment zones is described in the R5 [13], this updates the σ_y value, from Equation 2.14, for each zone, using each materials rupture strength. A limit analysis of the welded component using the numerous σ_y values for each zone is then carried out and a resulting σ_{ref} value is calculated using the limit load and material σ_y value for each zone type. The resulting σ_{ref}^R and t_r are then calculated in the normal way, as for homogeneous components, but each zone has its own predicted failure life using its own rupture properties. The smallest life from all zone life predictions is then taken as the component failure life. However, there are no publications assessing the accuracy of this particular multi-material R5 method.

2.5.2 Effect of material mis-match on stress

An important aspect of material mis-match relates the stress redistribution effects between the different weld-related material regions, i.e. PM, WM and HAZ. For a straight pipe stress redistribution gives lower stresses in weaker material zones and higher stresses in stronger zones. Parametric studies on varying strengths of weld materials and its effect on stress distributions across the weld have been presented previously, e.g. [85,99,100]. Coleman *et al* [85] studied a V-welded thick-walled pressurised main steam pipe, modelling the

PM, HAZ and WM. The Norton constant A for the WM zone was varied, keeping the Norton exponents constant for all zones and all equal to 4. A_{WM} / A_{PM} values of 1, 5, 14, 1688 were studied, representing typical weld mismatch behaviour for $\frac{1}{2}\text{Cr}\frac{1}{2}\text{Mo}\frac{1}{4}\text{V}$, $2\frac{1}{4}\text{Cr}1\text{Mo}$, $1\text{Cr}\frac{1}{2}\text{Mo}$ and mild steel WM, respectively, welded to a $\frac{1}{2}\text{Cr}\frac{1}{2}\text{Mo}\frac{1}{4}\text{V}$ PM; while A_{PM} / A_{HAZ} was kept constant at a value of 4. For all the A_{WM} / A_{PM} values, the hoop stress was significantly larger than the axial stress at all material positions considered. For all A_{WM} / A_{PM} weld situations the maximum hoop and equivalent stresses were in the HAZ and these stresses increased slightly with increasing A_{WM} / A_{PM} . The peak axial stress was predicted in the HAZ for $A_{WM} / A_{PM} < 800$ and in the remote PM regions for $A_{WM} / A_{PM} > 800$. Examples of these results are shown in Figure 2.17. Similar observations were reported by Law and Payten [99] and Browne et al [101]. Law and Payten [99] concluded that for creep-hard weldments (e.g. $A_{WM} / A_{PM} < 1$) the highest stresses were found in the WM. For creep-soft weldments (e.g. $A_{WM} / A_{PM} > 1$) the highest stresses occur in the HAZ near the PM boundary on the outer surface.

To fully understand the effect of material mis-match with respect to creep behaviour the weld zones Norton exponent, n , also needs to be varied. Initial work on this aspect has been carried out by Tu *et al* [66]. More recent work has been carried out by Hyde and co-workers [35,100,102], who proposed a general formulation procedure for parametric multi-material analyses for steady-state creep conditions.

The general formulation is obtained by an induction process, from analytical solutions for stress and deformation of some simple two and three-material structures, e.g. loaded two and three bar structures, two and three material beams in pure bending and two and three-material thin and thick cylinders under internal pressure [102]. Thus, for a component of p materials obeying power law creep of the form $\dot{\epsilon}/\dot{\epsilon}_o = (\sigma/\sigma_{nom})^n$, and for an arbitrary position of interest, e.g. material 2, for example, the stress, σ_i , is given by the following equation:

$$\begin{aligned}
& f_1(n_1, n_2, n_3, \dots, n_p, \text{dim}) \left(\frac{\dot{\epsilon}_{oi}}{\dot{\epsilon}_{o1}} \right)^{\frac{1}{n_1}} \left(\frac{\sigma_i}{\sigma_{nom}} \right)^{\frac{n_1}{n_1}} + \\
& f_2(n_1, n_2, n_3, \dots, n_p, \text{dim}) \left(\frac{\dot{\epsilon}_{oi}}{\dot{\epsilon}_{o2}} \right)^{\frac{1}{n_2}} \left(\frac{\sigma_i}{\sigma_{nom}} \right)^{\frac{n_1}{n_2}} + \\
& f_3(n_1, n_2, n_3, \dots, n_p, \text{dim}) \left(\frac{\dot{\epsilon}_{oi}}{\dot{\epsilon}_{o3}} \right)^{\frac{1}{n_3}} \left(\frac{\sigma_i}{\sigma_{nom}} \right)^{\frac{n_1}{n_3}} + \dots \\
& \dots + f_p(n_1, n_2, n_3, \dots, n_p, \text{dim}) \left(\frac{\dot{\epsilon}_{oi}}{\dot{\epsilon}_{op}} \right)^{\frac{1}{n_p}} \left(\frac{\sigma_i}{\sigma_{nom}} \right)^{\frac{n_1}{n_p}} - 1 = 0
\end{aligned} \tag{2.21}$$

and the deformation rate, \dot{u}_i , as follows

$$\begin{aligned}
& g_1(n_1, \text{dim}) \left(\frac{\dot{\epsilon}_{oi}}{\dot{\epsilon}_{o1}} \right)^{\frac{1}{n_1}} \left(\frac{\dot{u}_i}{\dot{u}_{nom}} \right)^{\frac{1}{n_1}} + \\
& g_2(n_2, \text{dim}) \left(\frac{\dot{\epsilon}_{oi}}{\dot{\epsilon}_{o2}} \right)^{\frac{1}{n_2}} \left(\frac{\dot{u}_i}{\dot{u}_{nom}} \right)^{\frac{1}{n_2}} + \\
& g_3(n_3, \text{dim}) \left(\frac{\dot{\epsilon}_{oi}}{\dot{\epsilon}_{o3}} \right)^{\frac{1}{n_3}} \left(\frac{\dot{u}_i}{\dot{u}_{nom}} \right)^{\frac{1}{n_3}} + \dots \\
& \dots + g_p(n_p, \text{dim}) \left(\frac{\dot{\epsilon}_{oi}}{\dot{\epsilon}_{op}} \right)^{\frac{1}{n_p}} \left(\frac{\dot{u}_i}{\dot{u}_{nom}} \right)^{\frac{1}{n_p}} - 1 = 0
\end{aligned} \tag{2.22}$$

where $\dot{\epsilon}_{o1}, \dot{\epsilon}_{o2}, \dot{\epsilon}_{o3}, \dots, \dot{\epsilon}_{op}$ and $n_1, n_2, n_3, \dots, n_p$, are material constants for the material zones 1 to p , and σ_{nom} and \dot{u}_{nom} are a conveniently defined

nominal stress and a displacement rate dependent on the load level, respectively. $f_1, f_2, f_3, \dots, f_p$ and $g_1, g_2, g_3, \dots, g_p$ are unknown functions dependent on the Norton exponents n_i and the non-dimensional functions of dimensions, dim . The stress or displacement rate can be any component, e.g. equivalent stress, maximum principal stress or radial displacement rate. For a given σ_{nom} , the $\dot{\epsilon}_{o1}, \dot{\epsilon}_{o2}, \dot{\epsilon}_{o3}, \dots, \dot{\epsilon}_{op}$ constants are obtained from the material constants, A_i , such that $\dot{\epsilon}_{oi} = A_i \sigma_{nom}^{n_i}$. Knowing the $f_1, f_2, f_3, \dots, f_p$ and $g_1, g_2, g_3, \dots, g_p$ values for a particular set/combination of $n_1, n_2, n_3, \dots, n_p$ values allows the σ_i and \dot{u}_i values to be determined from the above two equations. Hyde *et al* however have previously applied Equations 2.21 and 2.22 to simplify parametric analyses of welded components, a three-material cross-weld uniaxial creep specimen [35,102] and a welded straight pressurised steam pipe [102-104]. The procedure simplifies parametric analyses by drastically reducing the number of FE calculations required to investigate the effect of varying $\dot{\epsilon}_{oi}$ and n_i values for each material zone.

Hyde *et al* [100,102,103] presented the variation of f_1, f_2, f_3 and g_1, g_2, g_3 functions for a range of n_i from 3 to 9, Figure 2.18 shows the f functions at a HAZ Type IV position, Position A, in a three-material welded thick-wall straight pipe [35,100]. The same smooth variation was obtained for the g_1, g_2, g_3 functions [103]. Hyde *et al* then proposed interpolation using curve-fitting or surface-fitting of the known f_1, f_2, f_3 and g_1, g_2, g_3 functions for any combination of the materials properties. Complete parametric analyses for

stress or displacement rate can thus be easily performed within the chosen range of n , say 3 to 9. A three-material analysis using this procedure to find the stress and displacement rate would require eighty-one steady-state FE calculations to interpolate for any combination of n_1 , n_2 , n_3 or $\dot{\epsilon}_{oi}/\dot{\epsilon}_{o1}$, $\dot{\epsilon}_{oi}/\dot{\epsilon}_{o2}$ and $\dot{\epsilon}_{oi}/\dot{\epsilon}_{o3}$ ratios. The f_1 , f_2 , f_3 functions were then used by Hyde *et al* [100] to investigate the mis-match effects of the three materials, A and n values, on the steady-state creep stress in the pipe weld. The investigation was aimed at studying Type IV cracking. The equivalent stress results showed a strong dependence on weld mis-match. When the HAZ is creep 'soft', the stresses in the HAZ were generally low, and when creep 'hard', the stresses were generally high. This relationship agrees with findings by other researchers, e.g. Coleman *et al* [85], Law and Payten [99]. The equivalent stress is also significantly dependent on $\dot{\epsilon}_{o2}/\dot{\epsilon}_{o1}$, $\dot{\epsilon}_{o2}/\dot{\epsilon}_{o3}$, n_1 and n_2 , but practically independent of n_3 . Figures 2.19 and 2.20 show some typical results [35,100]. The stress and displacement rate predictions using the obtained f_1 , f_2 , f_3 functions were accurate to within 3% of separate FE results [35,100]. To fully exploit the results of the parametric capability of the procedure, Tang [35] proposed the use of an electronic database with a computer program.

2.5.3 Effect of weldment geometry and loading on stress

Figure 2.16(a) displays a typical power plant V-shaped straight pipe weld geometry, used to investigate weld parameters, such as the weld width, the weld interface angle and the HAZ width, and system loadings such as internal pressure and additional axial and moment loads [33]. Vazda [24], Hyde *et al*

[90] and Law and Payten [99] have studied the effects of weld angle and concluded no significant effect on peak stress levels for internal pressure only. However, if additional axial end loading is present the peak stresses do increase significantly [90]. For weld angles greater than 15° the peak stress increased by over 20% for axial loads greater than 0.66 of σ_{mdh} . The peak stress position changed from the WM boundary to the PM boundary in the HAZ, typical of Type IV creep cracking. This is attributed to the hoop stress becoming less dominant compared to the axial stress as axial end load increases [105,106]. The effect of weld width on peak steady-state stress was also studied by Vazda [24] and Hyde *et al* [93]. Vazda [24] showed an insignificant weld width effect on stresses, for weld widths between 2mm to 8mm. Similar findings were concluded by Hyde *et al* [93] for welds between 8mm to 12mm wide. Vazda [24] also found that the effect of HAZ width on peak creep stress was greater than that for the weld width, but less than the effect of weld interface angle. It was found that smaller HAZ widths produce slightly higher stresses and the influence is only of importance for pipe welds with high axial end loads.

2.5.4 Failure behaviour of weldments

CDM has been used previously to predict failure lives and positions of straight pipe welds [20,26,34,88], where component failure is normally defined as the time when a high level of damage, i.e. $\omega > 0.9$, has spread across the bulk of the wall thickness [20,26]. These CDM studies have mainly considered damage accumulation for typical pipe V-weldment geometries and CMV materials with three-material zones, (i.e. PM, HAZ and WM).

Hall and Hayhurst [20] were among the first to predict damage accumulation, failure life and failure position for such pipe welds under an internal pressure of 45.5 MPa. The CDM model in this case was used to replicate pipe weld test failure as reported by Coleman *et al* [85]. CDM predicted component failure in the WM on the HAZ boundary (i.e. fusion line), initiating near the outer surface, which was in agreement with the test result. The CDM failure life was 27% lower than that of the test life, giving confidence in the constitutive laws and material properties used for the CDM calculation. Perrin and Hayhurst [69] also considered CDM pipe weld calculations using four material zones, inclusive of a Type IV-intercritical HAZ region and, again, found similarities with in-service Type IV failure location cracking in the intercritical HAZ region, along the HAZ/PM boundary for additional axial loadings.

Extensive CDM parametric material studies by Storesund *et al* [88] and Wang and Hayhurst [107] using eleven and forty different weldment material combinations, respectively, both found that good WM and HAZ creep rupture strength and ductility, relative to the PM, optimises weld creep life. Storesund *et al* [88] also concluded that when creep ductility in the WM and/or HAZ is relatively low compared to the PM increased axial stresses in the weld region are predicted to occur for pressure-only pipe welds. Noting that this would lead to Type IV cracking failure behaviour.

Hyde *et al* [94,106] showed that CDM failures were predicted to initiate near the outer surface of the pipe in the HAZ, on the PM boundary, and spread to

the inner surface for two typical thick-walled V-shape welds under an internal pressure of 16.55 MPa and an operating temperature of 640 °C. The position and damage accumulation behaviour in the HAZ replicated Type IV cracking, which again agrees with in-situ failures [74,77] and numerical studies [20,33,88]. It was also shown by Hyde *et al* [26,34,106] that significant damage accumulation commences at around 80% to 90% of the CDM component failure life of the plain pipe welds considered.

Steady-state creep life estimates for thick-walled welded steam pipes using Equation 2.9, predict failure initiation sites identical to those of CDM [34,94]. Life underestimates of around 30% to 40% were obtained relative to the CDM predictions, establishing the steady-state rupture approach as an alternative, conservative approach [33]. R5 creep life assessments, using Equation 2.19, by Goodall and co-workers, e.g. [60,62-64], of components with a range of stress-states, including typical power plant components gave conservative estimates of rupture life compared to experimental and steady-state creep estimates.

2.6 Creep of branched pipes

2.6.1 Introduction

As explained in Section 2.4.1, only a small amount of literature has been published on the creep behaviour of branched pipes and there are several reasons for this. Firstly, studies of creep in branched pipes differ from straight pipe sections, since the effect of geometry on the stress-state behaviour is more

complex. Experimental testing can be carried out using full-scale components under either accelerated temperatures or pressures. This is expensive, hence only a handful of full-scale branched pipe testing programmes have been published [9,17,18,108,109]. Secondly, published literature on numerical studies, e.g. finite elements, of the creep behaviour of branched pipes is rare. This again is due to the complexity of the problem, branched pipe FE models require large three-dimensional meshes with mesh refinement concentrated in high stress concentration regions such as the weld region and the inside bore [e.g. 108-110]. Such large FE meshes require extensive user and computational time for studying branched pipe creep behaviour; computational resources have not met the criteria for undertaking such studies, until only recently [87]. Numerical creep studies of branched pipes using steady-state creep laws, continuum damage mechanics and reference stress approaches are required to understand the geometric, loading and material behaviour on creep stresses, strains and failure, similar to the studies which have been carried out for straight pipe sections, as detailed in Section 2.5.3. However, a lack of literature covering these topics has been found, therefore addressing the need for further understanding. An essential part of this work must consider the effect of weldment properties, since weldments can reduce the strength of components under creep conditions considerably [74-77]. The published literature that concerns the creep of branched pipes, with concentration made on the effect of the weld, is now described and discussed in two sections, (i) experimental and in-situ studies and (ii) numerical methodologies and studies.

2.6.2 In-service experience & experimental studies of branched pipes

Sys [17] presented the results of one of the first full-scale experimental test programmes on the creep rupture of typical branched pipes from UK power plant. The programme considered six thick-walled branched pipes made of 2¼Cr1Mo parent and weld metal material, the geometry of two connections are shown in Figure 2.21. All six connections had the same main pipe and branch pipe dimensions. The creep tests were carried out until failure using a temperature of 575°C and two pressure-only loadings of 15.3MPa and 13.1MPa, details of the test conditions, failure life and position are shown in Table 1. The type of intersection described in Table 1 as “fig. 3” denotes pad reinforced and “fig. 4” denotes thickness-reinforced, see Figures 2.21a and 2.21b, respectively, for the reinforced branched pipe geometries studied. For four of the six branches, failure initiated in the weld at or just below the inside surface, near the crotch corner (P1 in Figure 2.21), by numerous parallel cracks and on the outside surface by a through crack, also on the crotch corner side (P2 in Figure 2.21). Photographs of the cracks are shown in Figure 2.22. The actual cracking location within the specific weld region was not described in the study. However, it was stated that the cracking had initiated and confined itself to the weld metal or fused zones, i.e. heat-affected zones (HAZ). Additional circumferential cracking parallel to the weld was also found on the outside surface at the weld toe, on the flank side, for both reinforced branch pipe configurations (P3 in Figure 2.21). It was found that these cracks did not significantly penetrate the wall thickness of the connection, (Figure 2.22c). The other two branched pipe cases, i.e. cases K4 and K5 of Table 1 failed by extensive deformation in the main pipe section causing instability and hence

cracking (Figure 2.23). Instability was caused by deformations causing a decrease in wall-thickness and increase in radius therefore increasing hoop stress, which lead to failure. However, cracking was found at the same positions as the other four connections, i.e. near the crotch corner on the inside bore surface in the weld and at the weld foot. Sys described these two large deformation branched pipe failures as unrealistic with respect to in-situ creep failure, since failures in-service occur at relatively low strain levels. However, the other four failures, which occurred in the weld at the crotch corner, were described as a likely in-service failure mode. Sys concluded that when failure occurs near the crotch corner, cracking is confined to the weld. However, the use of relatively brittle weld metal compared to the more ductile parent material does not affect the lifetime of the connection significantly. Additionally, Sys [17] compared the failure lives of the tested branched pipes with the creep rupture lives estimated from uniaxial cross-weld specimen tests performed at the mean diameter hoop stress as the main pipe of the connections and at the same temperature as the tests. The results showed that the branched pipes failure lives were within $\pm 25\%$ of the uniaxial predicted failure lives.

Similar crack and failure sites were again found by Day *et al* [18] from full-scale tests on an ex-service multiple 1Cr $\frac{1}{2}$ Mo thick-walled branched outlet header. The test was carried out at the same in-service pressure and temperature of 550°C for 3000hours, and then at 575°C until failure, i.e. occurrence of steam leakage. The geometry and dimensions of the main header body and the numerous branched pipes/stubs are shown in Figure 2.24. The failure of the test vessel was 9170 hours and had occurred in the weld at

the branch weld/body intersection, approximately in the axial direction of the header in the crotch corner plane of the connection of, i.e. similar to branched pipe failure found by Sys [17], of the largest branched pipe, at the centre of the header, see Figure 2.24. This failure by weld cracking is shown in Figure 2.25 and was first detected after 8199 hours of testing and quickly propagated 1500 hours after this point, leading to failure. Additional circumferential and transverse cracking were also found at numerous locations around the large branch weld and stub welds, as shown for example in Figure 2.26 for the large branch. A diagram showing the size and locations of these cracks over the testing period found on the largest, central branched pipe is shown in Figure 2.27, including the crack that lead to component failure. No cracks had extended between the stub penetrations on the header in the axial plane of the header, showing the weakening on the header body region by multiple penetrations was insignificant compared to the cracking modes associated with the individual penetrations. Detailed findings of damage and crack initiation sites within different weldment regions of the branched pipes was not reported on, i.e. HAZ damage and cracks. However cracking was all confined to the welded region, which includes weld metal and HAZ. As well as reporting cracking history Day *et al* [18] reported on strain and branch ovality measurements at various locations around the header. The measurements showed that the vessel generally experienced steady-state creep conditions throughout the test period.

Again, similar findings to Sys [17] and Day *et al* [18] of full-scale branched pipe creep tests was reported on by Storesund *et al* [111]. In this case,

microstructural examination of the weld region was reported on as well as crack sites, including the effect of the HAZ on cracking and damage levels. The creep tests considered six ex-service T-joint isolated and double joined branched pipes made of $2\frac{1}{4}\text{Cr}1\text{Mo}$ and $\frac{1}{2}\text{Cr}\frac{1}{2}\text{Mo}\frac{1}{4}\text{V}$ steels. The branched pipes had operated at 530°C and 13MPa pressure and were tested at 510°C and at the same operating pressure. The geometries of the branched pipes differed somewhat from typical in-service and other tested components [e.g. 17,18] since the weldments were located above the saddle position due to a flanged and forged branch connection, as shown in Figure 2.28. The microstructural examinations found that maximum damage and cracking sites were found in the coarse-grained HAZ and the weld metal, perpendicularly along the fusion line of the weldments at the crotch side of the weldment, deep through the wall thickness, i.e. similar positions to [17,18]. It was explained that creep damage was slightly lower in the intercritical HAZ (Type IV region) weldment crotch position regions since the weldment was positioned above the saddle position, due the flanged connection. It was noted and referenced [112] that if this was not the case, higher damage and cracking is more likely to occur in the intercritical HAZ (Type IV region). It was suggested that more detailed testing and studies on the effect of weld materials on creep damage accumulation was necessary to understand the failure behaviour and residual life of branched pipe service-exposed weldments. More recent full-scale branched pipe creep testing by van-Wortel and co-workers [9,113] concluded similar microstructural examination findings that maximum damage was again confined to the HAZ (Type IV) and WM regions of the weld, at the weld toe and neck on the crotch and saddle planes. A typical example of the thick-walled CMV branched pipe

header geometry used is shown in Figure 2.29 [9] and typical cracks from the tests at the weld foot are shown in Figure 2.30 [113]. Table 2.2 shows the microstructural damage examination of one of the tested branched pipe weld on the saddle and crotch plane within the different weld regions at times of 8000, 15000 and 21000 hours, in which the later was assumed to be the failure life. The table provides damage level information according to the VGB-TW 507 Dutch code which ranges from 1 to 5, where the numbers denote the type of damage, i.e. 1 (no creep cavities), 2 (single creep cavities), 3 (coherent cavities), 4 (micro creep cracks) and 5 (macro creep cracks), and the letter denotes the degree of damage, i.e. A (small extent) and B (medium extent). The table displays the repaired and unrepaired branched pipe damage information, of which the latter is of interest in the present work.

Other full-scale branched pipe component creep tests have been carried out and reported on previously, for example, Patel *et al* [108] creep tested thinner-walled branched connections, which obey thin shell theory and is of less interest to the present work, as thick-walled connections are the subject matter. Other publications have highlighted that the weld is the common failure position in in-service branched pipe of variable sizes, for example Mitchell and Brett [68], described the main creep crack site and position of small branched connections, e.g. stubs, to be in the intercritical HAZ /Type IV region at the weld toe circumferentially around the branch.

In conclusion, for thick-walled branched pipes, the common creep failure and cracking positions are confined to the weldment, this is due to the weak HAZ

or WM related to the weld. The crack sites in the HAZ or WM were generally found on the crotch and saddle planes of the connection; at the outside surface (weld toe and neck) and near the inside surface and these can grow through the wall thickness to produce failure by leakage. The tests have shown that for a wide variety of materials used, i.e. from low chromium steels, e.g. $\frac{1}{2}\text{Cr}\frac{1}{2}\text{Mo}\frac{1}{4}\text{V}$, to high chromium steels, e.g. 13CrMo44, crack/failure positions are common throughout. However, it has been shown that the choice of steel used for the parent material and weld metal to construct the branched pipes is important in relation to the component creep life, even though they share common failure positions. The effects of weld geometry, mis-match and loadings on creep life using experimental creep tests and in-situ experience is still relatively unknown compared to straight welded pipes since only a few connections have been tested and more understanding is required.

2.6.3 Numerical analysis of branched pipes

2.6.3.1 Homogeneous studies

Only a few homogeneous steady-state creep studies of branched pipes have been reported on, which are relevant to the present work. The study reported by Budden and Goodall [114] investigated creep stresses and failure lives in thin-walled branched connections. Two typical branch connections were considered, Vessels A and B, the dimensions of which are given in Table 2.3. A graph showing a survey by the UK's CEGB on in-service header R/T (radius to thickness) ratios was shown in the work, see Figure 2.31. It is clear that the majority of headers are thick-walled (i.e. R/T approximately less than 5) and

therefore providing evidence that concentration should be made on this type of geometry. As well as presenting stress and life predictions from homogeneous steady-state creep calculations for the two vessels, FE limit load analyses were conducted for use with the R5 life assessment approach, and also stress and life predictions based on the inverse use of British Standards BS5500 [11] and BS1113 [12] as detailed by Booth [115]. All three life prediction approaches were then compared to experimental full-scale component creep testing reported on by Brown [116] for the same branch pipe components to assess the accuracy and validity of the approaches. The steady-state creep analyses were based on Norton's law and typical power plant creep conditions of 550°C and internal pressures of 17.58MPa and 13.79MPa for vessels A and B, respectively. The vessels parent material was typical of power plant steel, using ½Cr1Mo. The three-dimensional FE mesh used for Vessel B is shown in Figure 2.32, it is clear that mesh refinement was used around the connection region, a similar mesh was used for Vessel A. It is clear from Figures 2.33 and 2.34 that the highest steady-state stress concentrations were found at the weld toes on both planes, while the inner crotch corner and inner surface flank stresses were slightly lower, and weld neck stresses were relatively small. Similar behaviour was shown for the creep strain concentrations for these two planes for Vessel B. It was concluded that life predictions produced using peak steady-state creep stresses at the weld toes on the crotch plane and flank plane were relatively close to R5 and British Code predictions, and all were conservative by around 40% to 60% compared to the experimental failure lives reported by Brown [116], these comparisons are shown in Tables 2.4a and 2.4b. It was also noted that FE elastic stress concentrations and steady-state

strain rate results taken at the crotch and flank mid-wall positions agreed well with measured values taken from the experimental full-scale creep tests by Brown [116] for both vessels. This provides evidence that the steady-state Norton creep law model gave good agreement with the real-life creep behaviour of the component, as well as the failure behaviour of the vessels. It was suggested that further investigation into the effect of weldment regions on failure behaviour was required to improve predictions.

More recent branched pipe life assessments by Budden and co-workers using the R5 approach concentrated on validating the approach [98,108] against experimental full-scale creep tests. One such example [108], which was very similar to that of the investigation by Budden and Goodall [114], as previously explained, except in this case the R5 approach was assessed against experimental creep lives for a typical welded thin-walled branched pipe using the modification of predicting a rupture reference stress, σ_{ref}^R , for each weld zone, using a stress-distribution k factor [13,98], as explained in Section 2.5.1, and then a rupture life for each zone using the representative rupture data for each zone instead of just a homogeneous PM life as in [114]. It was assumed that the stress distribution factor, k , for each weld zone, in this case PM, WM and Type IV HAZ, was equal to unity as FE analysis showed that the maximum principal stress was transverse to the weld fusion boundary and that little stress distribution would occur in creep, therefore all zones σ_{ref}^R value were equal. The experimental failure of the welded connection was in the Type IV HAZ weld region, due to a large through-wall crack, the FE R5 approach predicted failure to occur in the Type IV zone at a life which was

20% lower than the test life. The R5 failure prediction was therefore relatively accurate in both life and weld zone region.

Other research has been carried out on limit loads of branched pipes e.g. [15,117-120], which can be used to predict the R5's rupture reference stress [13], with mainly thin-walled connections being considered. The work by Moffat and co-workers, e.g. [15,117,118], has extensively investigated the effects of geometric parameters and crack size and location on the effects of limit pressures and moments for branched pipes using experimental and FE analyses. The work was aimed at the prediction of plastic-collapse loads for use with low-temperature fracture assessments, such as British Energy's R6 procedure, as well as high-temperature creep crack growth assessments, such as the methods described in British Energy's R5 procedure [13], the work was not however aimed at assessments of creep rupture.

Published work on the interaction effect on the creep behaviour of multiple-branched pipes is very scarce. The CEGB [120] and the British Standards BS5500 [11] and BS1113 [12] recommend that the axial and circumferential distance between the branches be kept to a certain level, dependent on the ligament efficiency and the limit pressure of the component, where these are dependent on the space between the branches, the diameters and thickness' of the header/main pipe and branches and the loadings. The interaction between branches, as defined by BS5500 [11], becomes significant when the spacing, s , is less than $2\sqrt{DT}$, where D and T are the header/main pipe diameter and wall-thickness, respectively, and a ligament efficiency, η , defined as $\frac{s-d}{s}$,

where d is the branch diameter, is used to increase the operating stress of the connection and therefore compensate for additional stresses produced by the interaction. However, these recommendations are generalised and concluded from mainly elastic-plastic behaviour of the thin-walled connections and not the creep behaviour. Hence, further work is required to investigate the creep behaviour of multiple branched pipes.

2.6.3.2 Weldment studies

One of the earliest studies investigating the influence of the weldment properties for thin-walled branched pipes was reported by Dhalla [121]. This work considered the effect of HAZ, PM and WM material weldment zones on stress and failure location using finite element analysis (FE) validated by experimental full-scale component creep testing. Comparisons with the ASME creep life prediction code were also made based on a homogeneous material connection. The vessel geometry used is shown in Figure 2.35. HAZ creep cracking was found on all experimentally tested branched pipes except the hemi-spherical branched pipe (N-1), the locations were mainly parallel and perpendicular to the weld in at the saddle positions on the outer surface, but not at the right-angled positions, as shown in Figure 2.35. An example of the mesh used is shown in Figure 2.36. The effects of primary and secondary creep were considered in the FE analysis using a simplified polynomial creep law, as well as the effect of residual stresses created by the welding process, which was modelled by adding an initial high-temperature profile reflecting this. It was concluded that the 3-material FE model predicted the correct cracking location at the saddle positions in the HAZ using the uniaxial creep properties and that

creep of the welds was of primary importance compared to the effect of the residual stresses on the failure behaviour of the connection. Figures 2.37 and 2.38 show typical results of the effects of the inclusion of residual stresses and multi-material creep properties in FE modelling, respectively. The work also showed that the FE calculations of the weld residual stresses, within the weld, relaxed rapidly during creep conditions and that the life prediction based on multi-material weld creep behaviour was reasonable compared to ASME code predicted lives and experimental full-scale failure lives.

~~A branched pipe creep life assessment study reported by Li [122] considered a~~
2-material weld FE model, of a service-exposed 10CrMo910 parent material and weld metal and new weld metal from a weld repair using either 10CrMo910 or 10CrMo44 filler. This work is one of the most detailed in describing the effect of weld mis-match and its effect on creep-rupture life. The geometry of the thick-walled branched pipe and weld are shown in Figures 2.39 and 2.40. The loading condition used in the study was for a temperature of 600°C and internal pressure of 19MPa. The two materials were modelled using uniaxial data, with Norton creep law properties. Creep rupture data was used to obtain material constants for the exposed material and new WM, to predict rupture times. Figure 2.41 displays the FE mesh used and the maximum principal elastic stress distribution. Figure 2.42 shows the steady-state creep stress distribution, at the saddle position of the weld. From the results, it was concluded that the choice of weld metal was very important in increasing the creep life of the component, in this case an under-matched

13CrMo44 without PWHT weld repair produced a longer-lasting weldment than the matched 10CrMo910 with PWHT.

Wortel and co-workers [9,123] used FE one- and two-material steady-state creep studies based on Norton's law to predict rupture initiation and therefore failure life. The life predictions were based on several life assessment approaches and compared with full-scale experimental rupture/crack growth and failure life data. The FE model was three-dimensional and included parent and weld metal material regions. For the majority of the components, it was shown that steady-state creep was shown to be predominant over the operating lives of the connections. One-material FE models used with rupture and damage approximate prediction methods such as the Inverse British Code [115] and simplified Kachanov CDM [31] methods significantly over-predicted the failure lives compared to that of the life of the experimentally tested component. Two-material FE failure life predictions were better than the one-material predictions, however they still over-predicted the life. Other work by Wortel [123] described the use of two-dimensional FE steady-state creep results using three materials, inclusive of fine-grain HAZ material, PM and WM. The results and details of the FE calculations were not given, but it was shown that the failure location of the FE model was identical to that of the full-scale tested branched pipe, i.e. the HAZ material on the saddle plane on the connection. The effect of material mis-match was noted to be significant, but only given in qualitative form; a creep under-matched weld gave longest life, compared to creep matched and over-matched for the 2¼Cr1Mo parent

material connection. Additional FE investigations concluded that smooth weld edge grinding lowered creep stresses and therefore increased lifetime.

Hayhurst and co-workers have modelled creep damage accumulation within a thin-walled branched pipe [87,124]. The CDM constitutive laws used three state variables to model primary and tertiary stage damage accumulation in the micro-structure due to dislocations and cavitations produced by material softening during service-aging. The welded branched pipe was made of $\frac{1}{2}\text{Cr}\frac{1}{2}\text{Mo}\frac{1}{4}\text{V}$ parent material and $2\frac{1}{4}\text{Cr}1\text{Mo}$ weld metal and loaded by a temperature of 590°C and a constant pressure of 4MPa. The materials, and temperature used were typical of UK power plant, but the pressure and thin-walled pipes were more representative of reheat boiler piping than that of main steam pipework. The branched main steam pipe geometry was idealised as a cylinder-sphere intersection to permit the use of the more simple axisymmetric analysis. The model considered four material zones, the PM, WM, HAZ and intercritical/Type IV HAZ, as shown in Figure 2.43. Figure 2.44 displays the creep damage accumulation in the mesh after 14,759 hours, where the maximum damage denoted by red regions is equal to 0.99 and is located in the intercritical/Type IV HAZ weld regions. The high damage is concentrated across the majority of the spherical vessel wall in the lower main pipe Type IV HAZ region. These results, though useful, are somewhat unrealistic for typical power plant geometries, due to the axisymmetric cylinder-sphere intersection assumption. As a branch pipe connected perpendicular to the header/main pipe longitudinal axis will have a very different tri-axial stress state and is likely to have different damage distributions and high damage sites and failure life.

CDM calculations for a three-dimensional thick-walled perpendicular joining branch connection to a header/main pipe's longitudinal axis is therefore required for more typical power plant life assessment purposes.

2.7 Conclusions

There remains a significant gap in understanding of the weakening effect due to the connection geometry and inferior creep properties of the weldment zones in respect to the creep of branched pipes. Welded branched pipe creep investigations are therefore required, similar in style to the investigations carried out for welded straight pipes (Section 2.5), as well as supplementary studies. The gaps in knowledge surrounding the creep of branched pipes are discussed below.

Firstly, studies based on investigating the effect of the presence of the weldment are required, concentrating on the possible reduction in life caused by the weaker materials and weld-mismatch and whether or not such analysis detail is required. In addition, the effects of different weldment geometry and filler materials require investigation. It is not fully understood how different materials, which may have significantly different creep properties, affect the stress distributions and load redistribution within different regions and how this can affect the failure life and position of the weldment. Parametric material analyses investigating the effect of different weldment properties are therefore required to improve understanding. Previous research has mainly used the R5 procedure [13] for branched pipes. This approach, as well as the inverse use of the British design codes [115], are generally based on homogeneous material

properties and exclude the effects of the strength reduction due to weldment properties. These approaches may therefore be non-conservative in predicting failure life for some cases. Validation of these homogeneous approaches is therefore required against other approaches, such as multi-material steady-state and CDM predictions.

Secondly, the effects of geometric parameters (such as branch and main pipe diameters, thicknesses, weld size etc.), additional loadings such as moment loads, as well as the interaction of branches along multiple branched headers/main pipes require consideration. Previous work has mainly concentrated on thin-walled connections. The creep behaviour of thick-walled connections is likely to be significantly different to that of thin-shell connections. Parametric analyses of geometric parameters for realistic branched pipes are therefore required for greater understanding. Assessment of the commonly used inverse use of the British Standard code method [115] (BS5500 [11] and BS1113 [12]) and R5 procedure [13] are also required to understand whether they predict relatively accurate lives for varying geometric parameters compared to other creep life assessment methods, such as steady-state and CDM approaches.

Table 2.1. Creep rupture test details performed on five welded branched pipes (Sys [17]).

Specimen No.	Type of intersection	Diameter ratio	Temp. °C	Internal pressure kg/cm ²	Time to leakage	Location of the through crack
K2	fig. 3	0.35	575	153	2760	crotch corner-weld material
K3	fig. 4	0.35	575	131	13128	crotch corner-weld material
K4	fig. 4	0.35	575	153	3529	side face – parent material
K5	fig. 4	0.35	575	153	2156	side face – parent material
K6	fig. 4	0.35	575	131	11127	crotch corner-weld material
K7	fig. 4	0.35	575	153	4682	crotch corner-weld material

Table 2.2. Damage evolution levels at the right-angled and saddle points of a 2¼Cr1Mo welded branched pipe (Rotvel *et al* [9]).

Replica location:	Right angle, tensile side						Saddle points					
	unrepaired			repaired			unrepaired			repaired		
Inspection at (10 ³ h)	8	15	21	8	15	21	8	15	21	8	15	21
Base metal header	2A	2A	2A	2A	2A	2A	2B	2B	2B	2A	2A	2A
FGHAZ header	3A	3A	3B	2A	2B	3A	3A	3A	3B	2A	2A	2B
CGHAZ header	3A	3A	3A	2A	2B	3A	3A	3A	3B	2A	2A	2B
Repair weld	-----			2A	2A	2A	-----			2A	2A	3A
FGHAZ in old weld	-----			2A	5	5	-----			2A	5	5
Old weld metal	3A	5	5	3A	3A	5	3A	5	5	3A	3B	5
CGHAZ nozzle	3A	3A	3B	3A	3A	3B	3A	3A	5	3A	3A	3B
FGHAZ nozzle	3A	3B	5	3A	5	5	3A	3B	5	4	5	5
Base metal nozzle	2B	2B	2B	2B	2B	2B	2B	2B	2B	2A	2B	2B

Table 2.3. Dimensions of branched pipe test vessels (mm) (Budden & Goodall [114]).

	R	T	r	c	c/T	r/R	R/T	P(MPa)
A	97.7	19.6	61.15	12.2	0.62	0.62	4.99	17.58
B	98.0	13.0	61.15	13.0	1.00	0.62	7.54	13.79
C	97.7	19.6	61.15	10.0	0.51	0.62	4.99	17.58

Table 2.4. Branched pipe creep life estimates based on (a) experimental, BS inverse codes rule and R5, and (b) steady-state creep analysis (Budden & Goodall [114]).

(a) experimental and analytical (* with 1.2 safety factor)

Vessel	A	B	C
stress (failure time)			
Experimental (6)	112 (8000)	131 (4310)	122 (5640)
inverse codes	138 (3439)	148 (2617)	151 (2462)
Limit load	135 (3794) 162 (1845)*	133 (3988) 160 (1938)*	152 (2374) 182 (1165)*

(b) based on finite-element analysis

Vessel	A	B	
stress (failure time)			
Crotch vessel weld toe (P ₁)	σ_e	140 (3286)	170 (1525)
	σ_1	153 (2313)	210 (662)
Flank vessel weld toe (P ₃)	σ_e	139 (3380)	144 (2940)
	σ_1	162 (1845)	173 (1423)
Average stress (S6)	σ_e	131 (4273)	135 (3794)
	σ_1	145 (2860)	154 (2254)
Average stress (S3)	σ_e	74 (40837)	98 (13455)
	σ_1	67 (60481)	94 (15864)

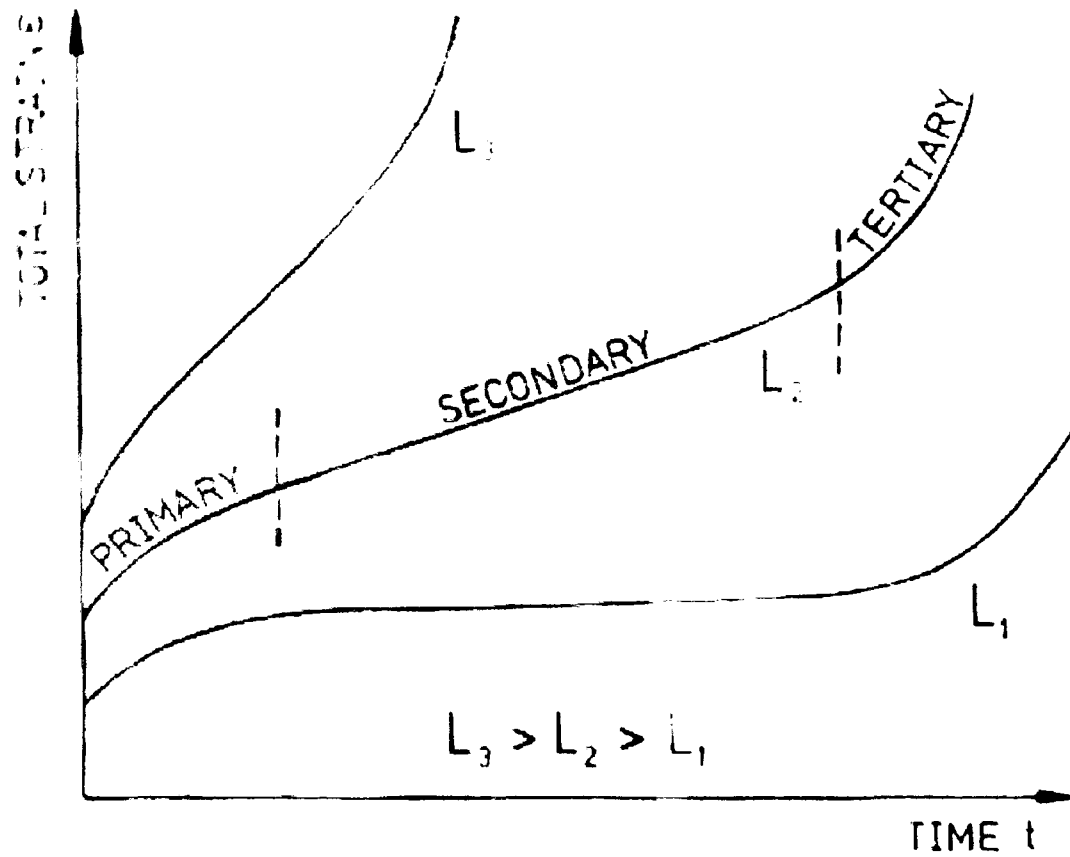


Figure 2.1. Typical creep curves for different constant load, L , and temperature (Boyle & Spence [38]).

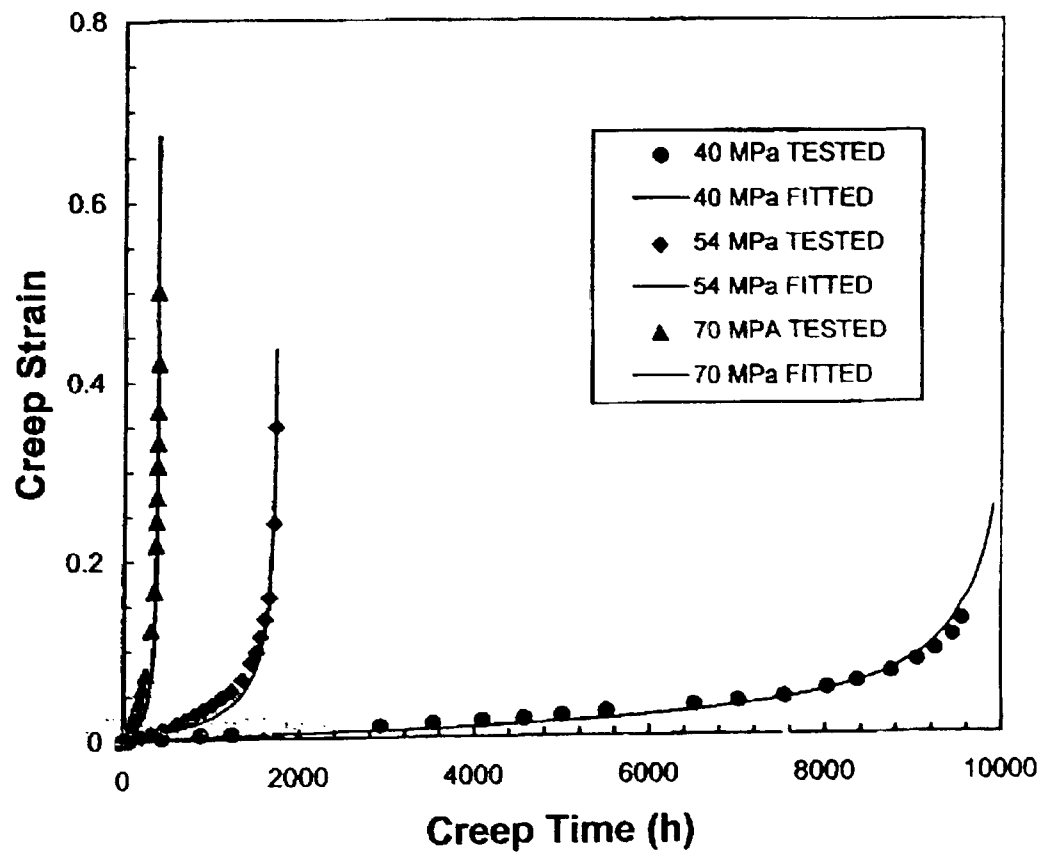


Figure 2.2. Creep curves for three different stress levels for a $\frac{1}{2}\text{Cr}\frac{1}{2}\text{Mo}\frac{1}{4}\text{V}$ alloy at 640°C (Hyde & Sun [26]).

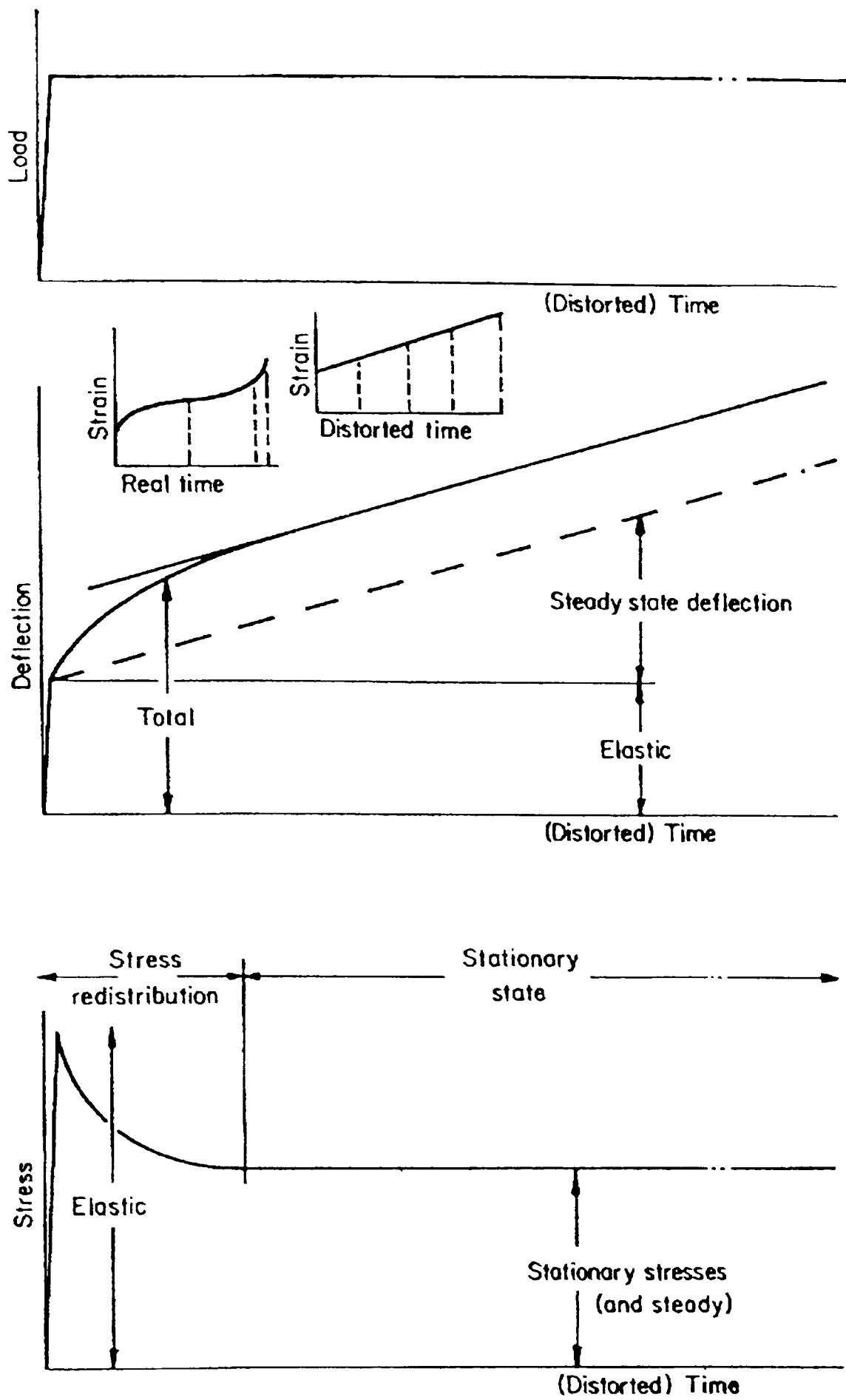


Figure 2.3. Stress redistribution and strain accumulation for steady-state creep following elastic loading (Penny & Marriott [39]).

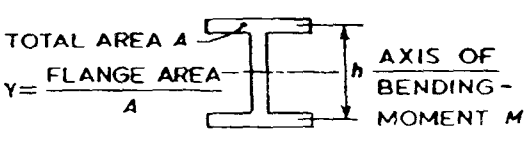
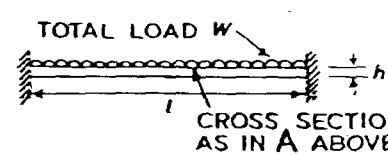
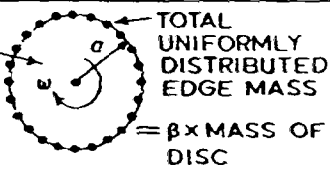
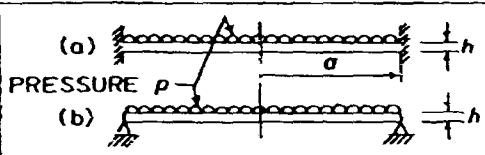
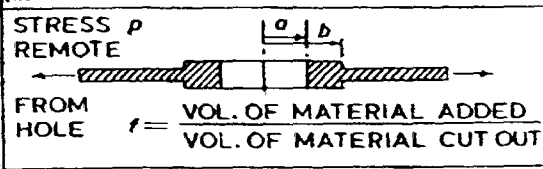
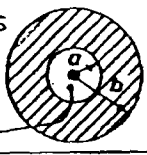
A	 <p>TOTAL AREA A $Y = \frac{\text{FLANGE AREA}}{A}$ AXIS OF BENDING-MOMENT M</p>	$\sigma_{\max, n=1} = \frac{M}{Ah} \cdot \frac{6}{2Y+1}$
	I — SECTION IN PURE BENDING	
B	 <p>TOTAL LOAD W l CROSS SECTION AS IN A ABOVE</p>	$\sigma_{\max, n=1} = \frac{Wl}{Ah} \cdot \frac{1}{2Y+1}$
	UNIFORMLY LOADED BEAM WITH CLAMPED ENDS	
C	 <p>MASS DENSITY ρ TOTAL UNIFORMLY DISTRIBUTED EDGE MASS w $= \beta \times \text{MASS OF DISC}$</p>	$\bar{\sigma}_{\max, n=1} = \frac{\rho a^2 w^2}{g} \left(\frac{7}{16} + \frac{\beta}{2} \right)$
	ROTATING PARALLEL-SIDED DISC	
D	 <p>(a) PRESSURE p (b) PRESSURE p</p>	$\begin{aligned} \text{(a)} \quad \bar{\sigma}_{\max, n=1} &= p \frac{a^2}{h^2} \cdot \frac{3\sqrt{3}}{8} \\ \text{(b)} \quad \bar{\sigma}_{\max, n=1} &= p \frac{a^2}{h^2} \cdot \frac{21}{16} \end{aligned}$
	UNIFORMLY LOADED CIRCULAR PLATE (a) CLAMPED EDGE (b) SIMPLY SUPPORTED EDGE	
E	 <p>STRESS ρ REMOTE FROM HOLE $f = \frac{\text{VOL. OF MATERIAL ADDED}}{\text{VOL. OF MATERIAL CUT OUT}}$</p>	$\bar{\sigma}_{\max, n=1} = \rho \frac{2}{1 + \frac{3}{4} \cdot \frac{fa^2}{b^2}}$
	SYMMETRICALLY STRETCHED SHEET WITH HOLE AND RING REINFORCEMENT	
F	 <p>CLOSED ENDS INTERNAL PRESSURE p</p>	$\bar{\sigma}_{\max, n=1} = p \cdot \frac{b^2 \sqrt{3}}{b^2 - a^2}$
	THICK-WALLED TUBE UNDER INTERNAL PRESSURE	

Figure 2.4. Details of six different components used in the study by Calladine [36].

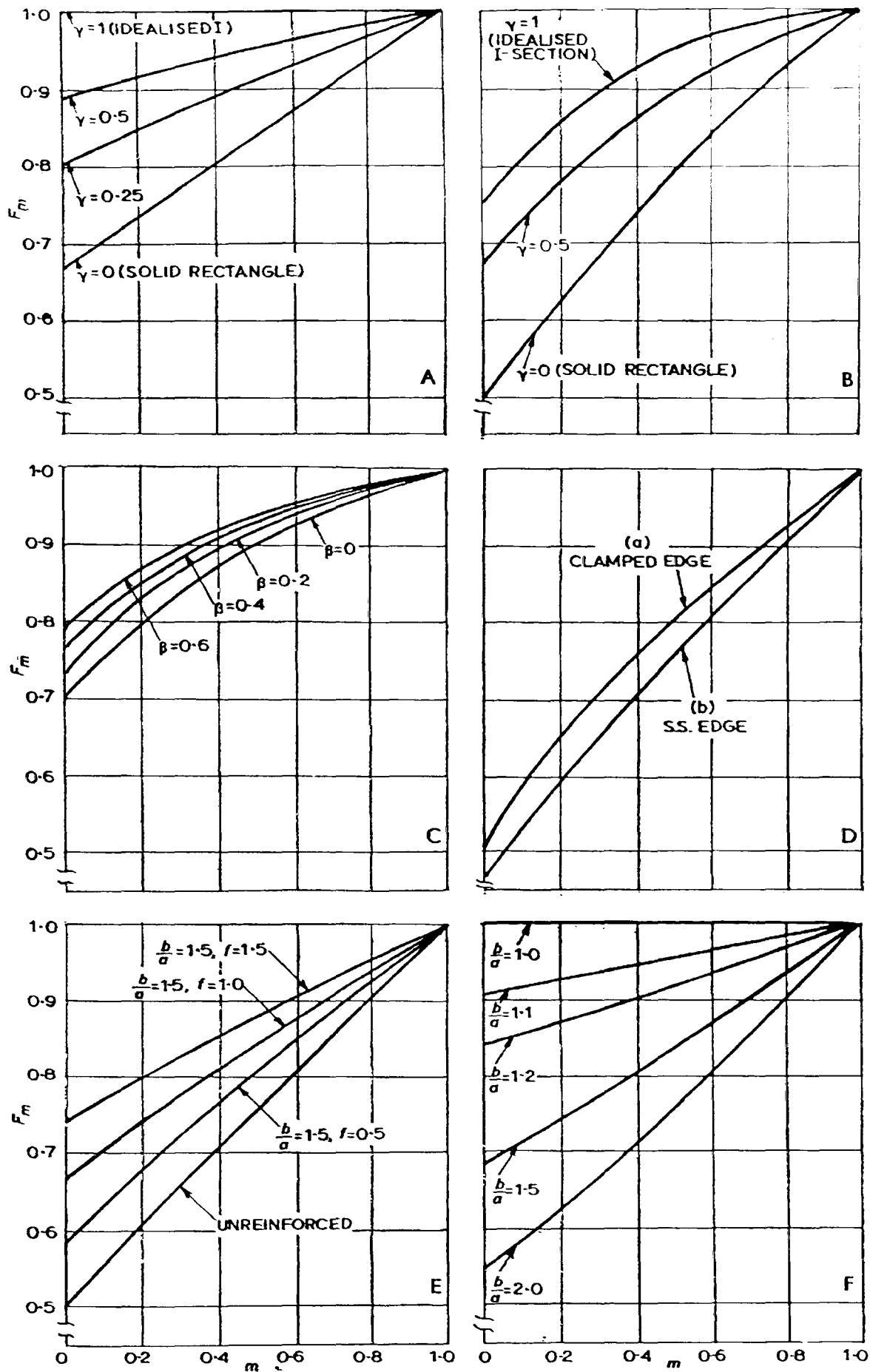


Figure 2.5. Variation of stress with the inverse of Norton's creep exponent value for six different components shown in Figure 2.4 (Calladine [36]).

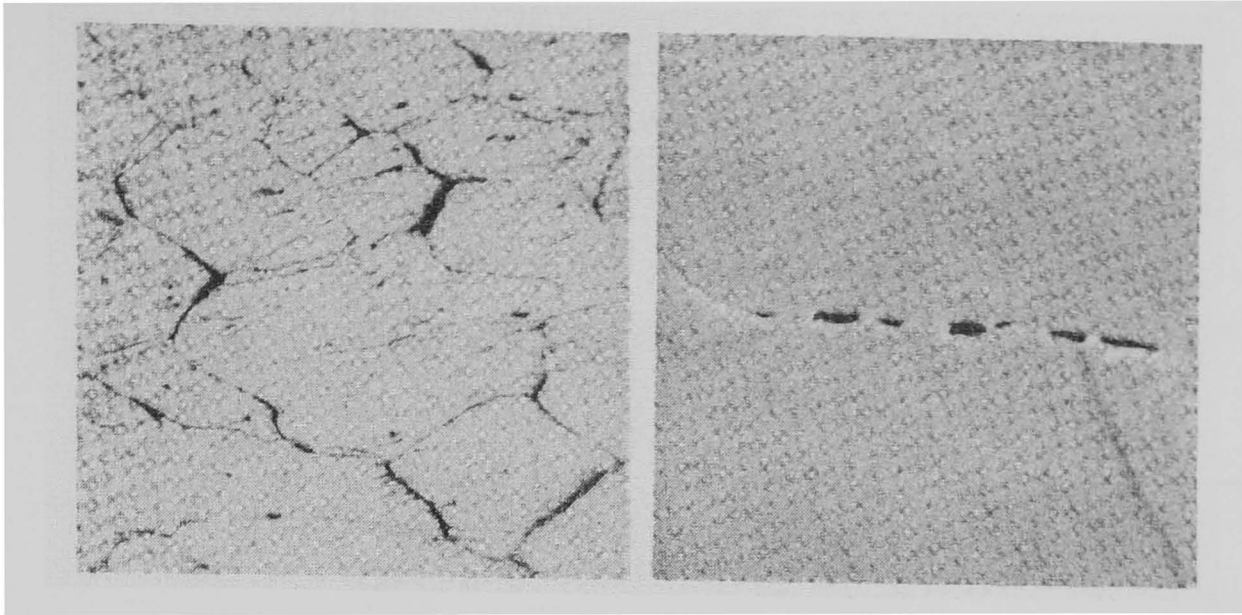


Figure 2.6. Typical microstructural high temperature creep damage associated with tertiary creep by intergranular cracking and cavities (Evans and Wilshire [51]).

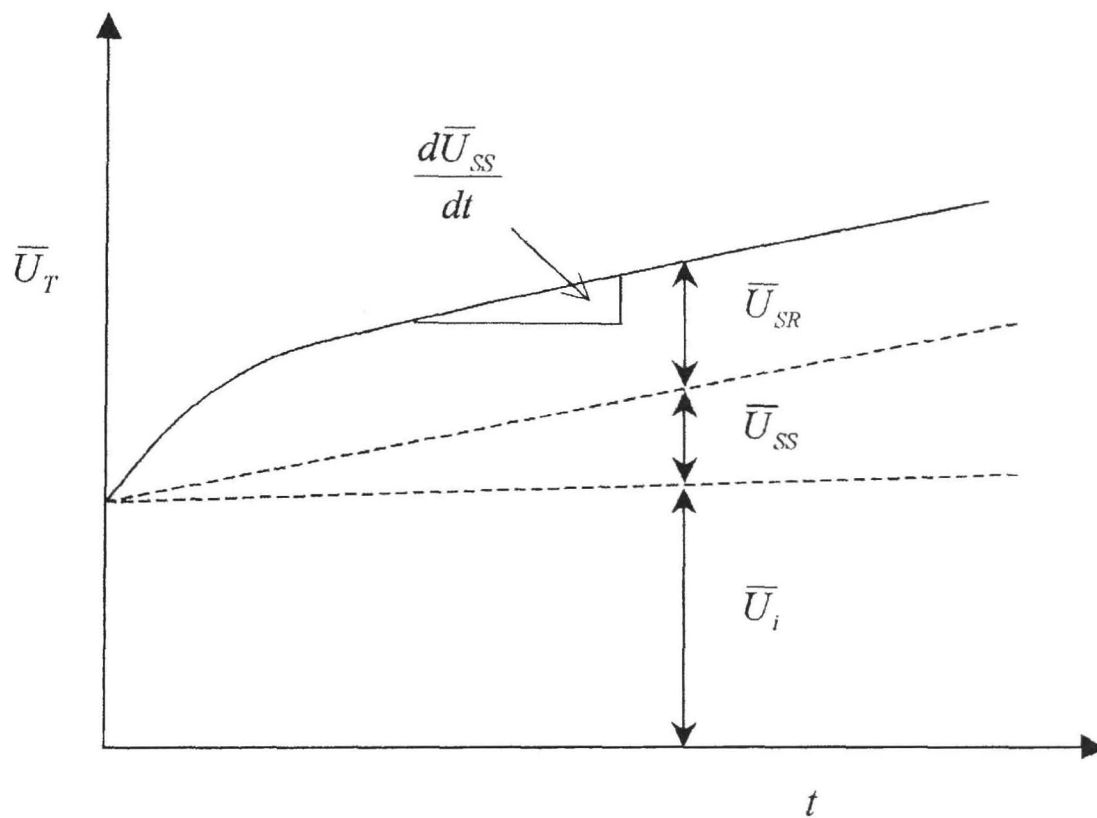


Figure 2.7. General shape of creep deflection during steady-state creep (Penny & Marriott [39]).

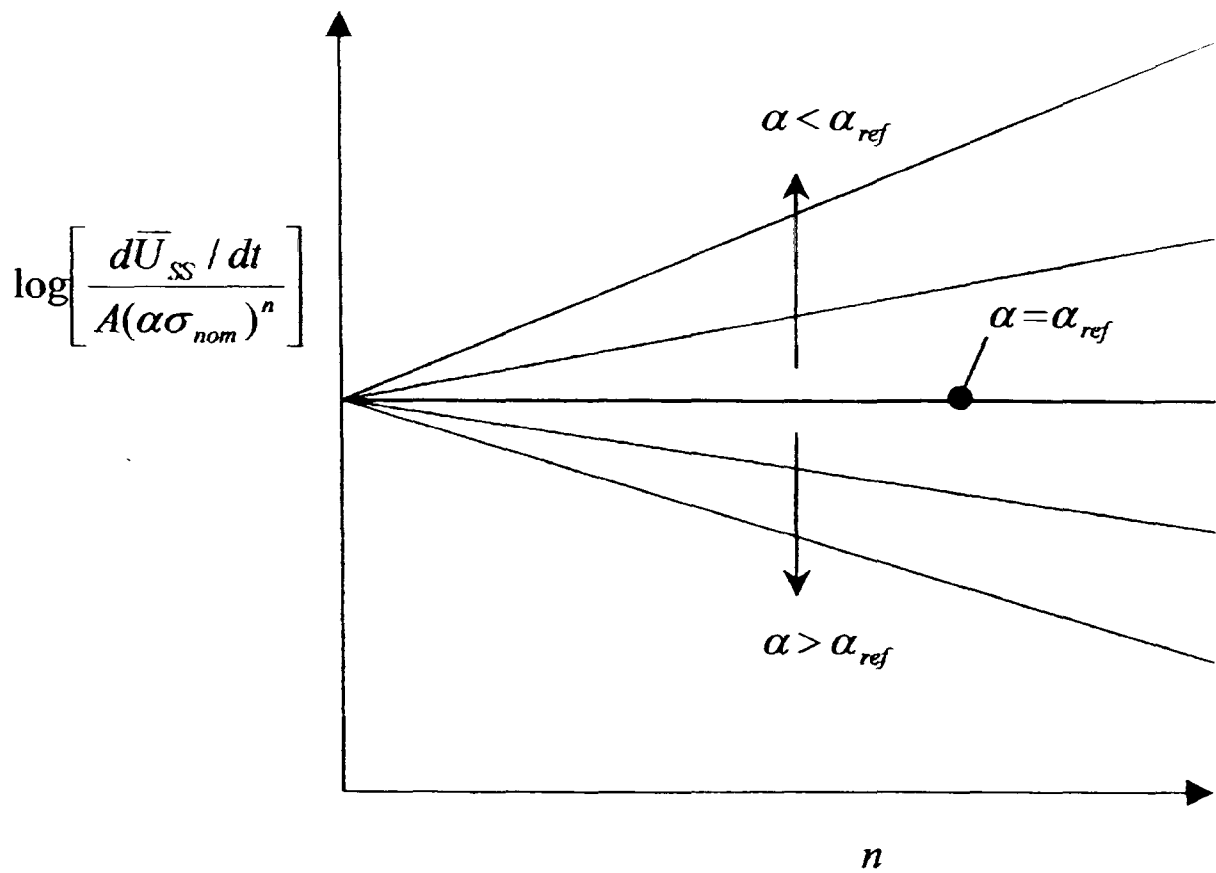


Figure 2.8. Illustration of the calculation of the reference stress by varying parameters α and n to find α_{ref} .

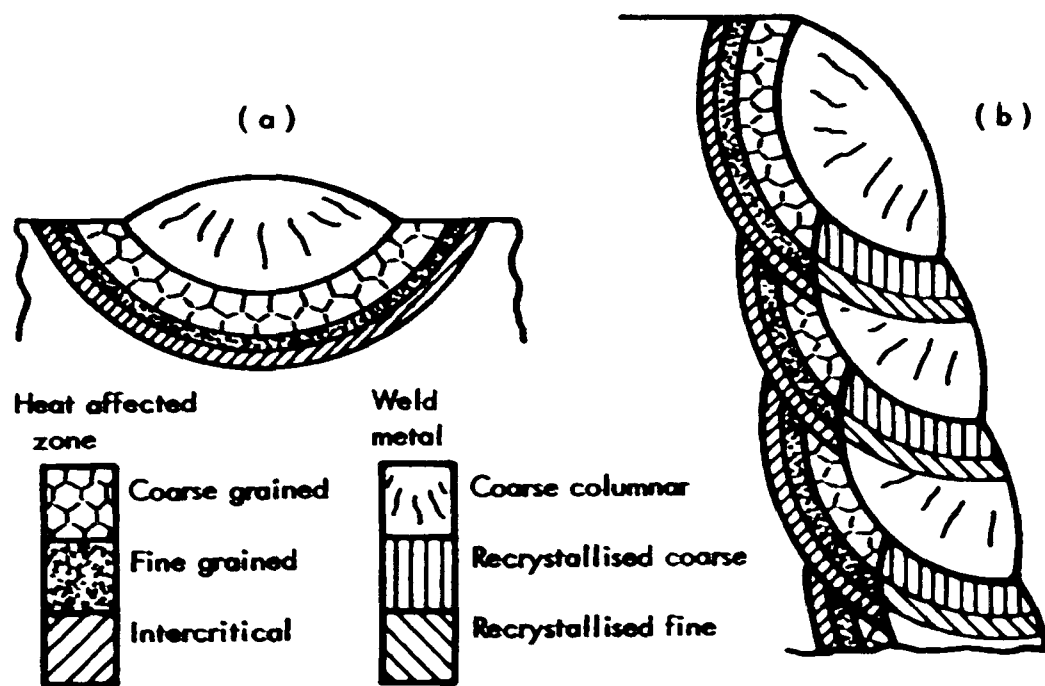


Figure 2.9. Schematic diagram representing the variation of microstructure in (a) a single weld bead and (b) multiple weld beads (Coleman [70]).

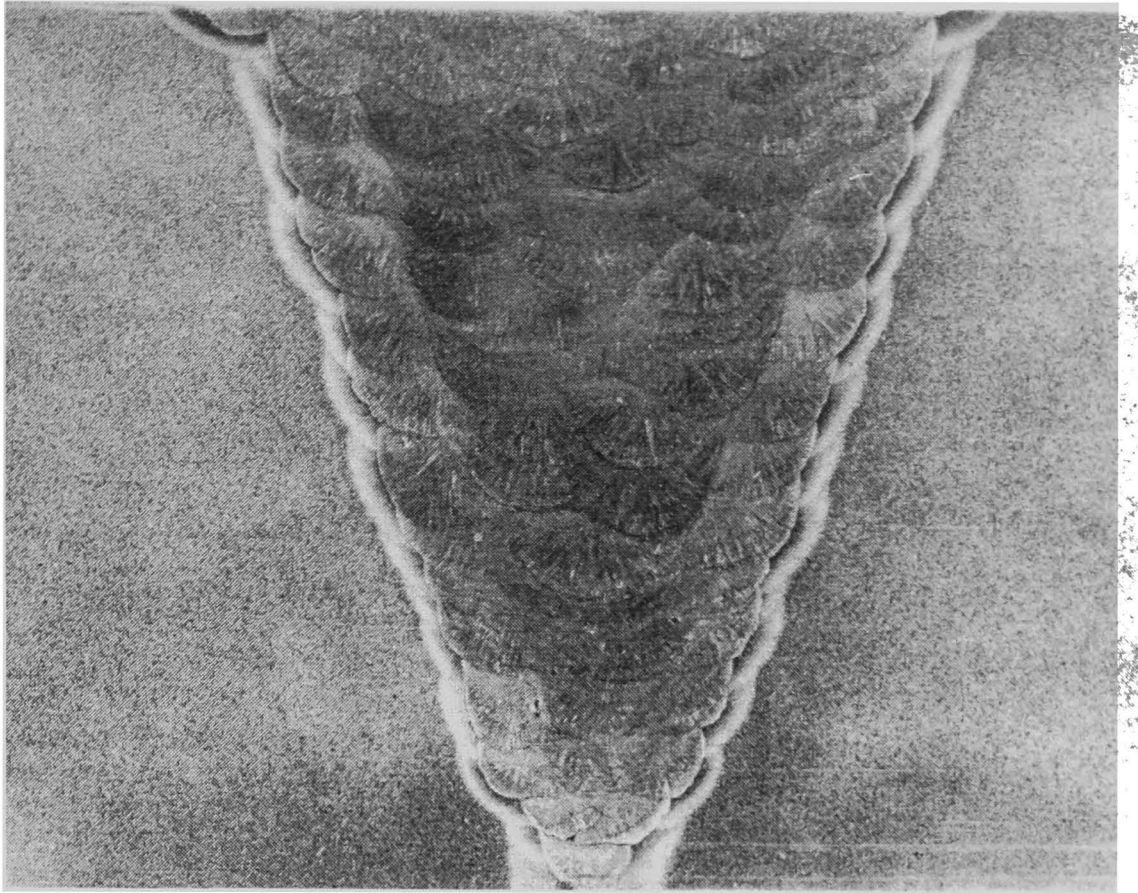


Figure 2.10. Macrostructure of a typical butt weld for a main straight pipe section in fossil-fuelled power plant (Powergen Plc. [4]).

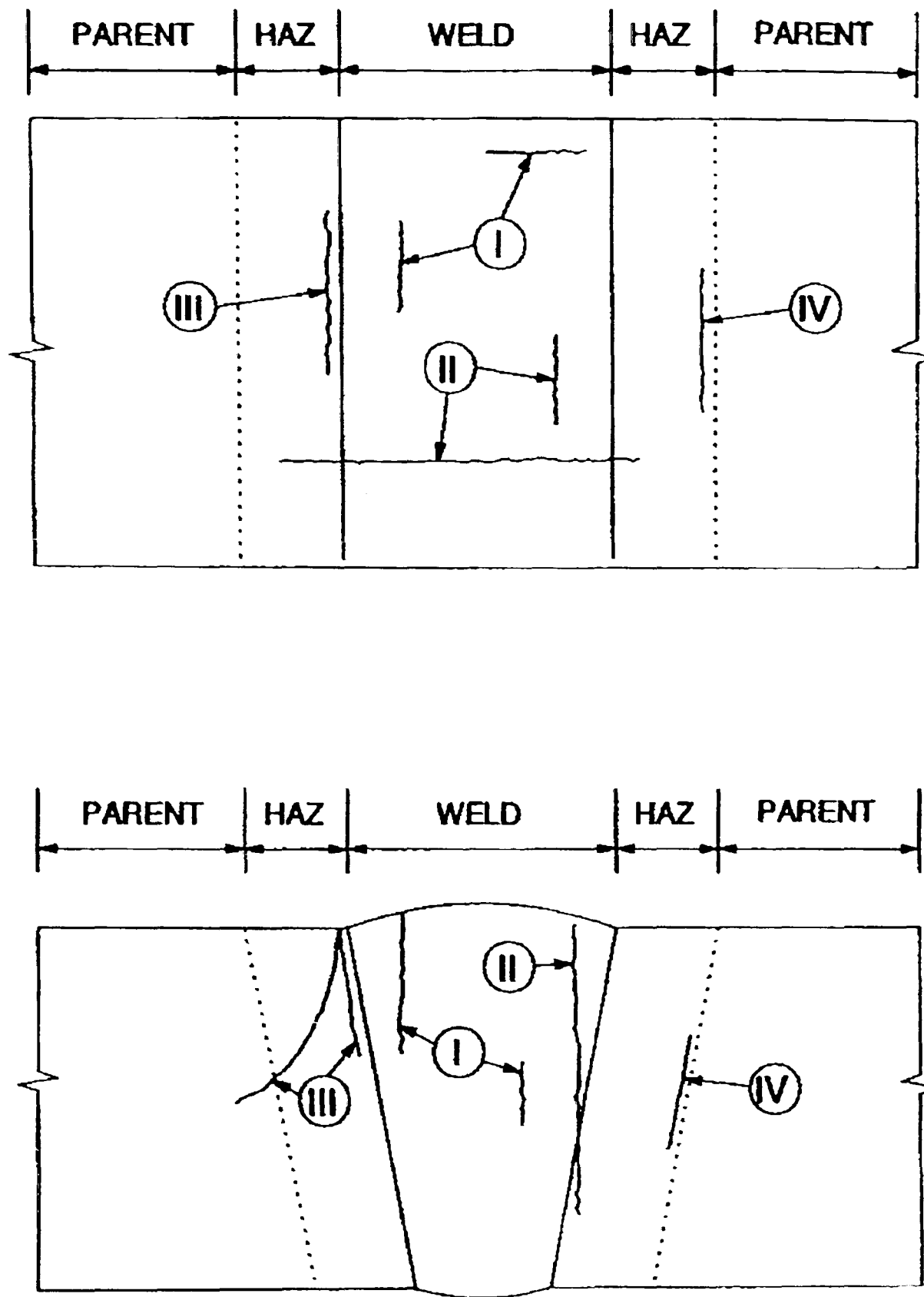


Figure 2.11. Classification of cracking in weldments (Schuller *et al* [76]).

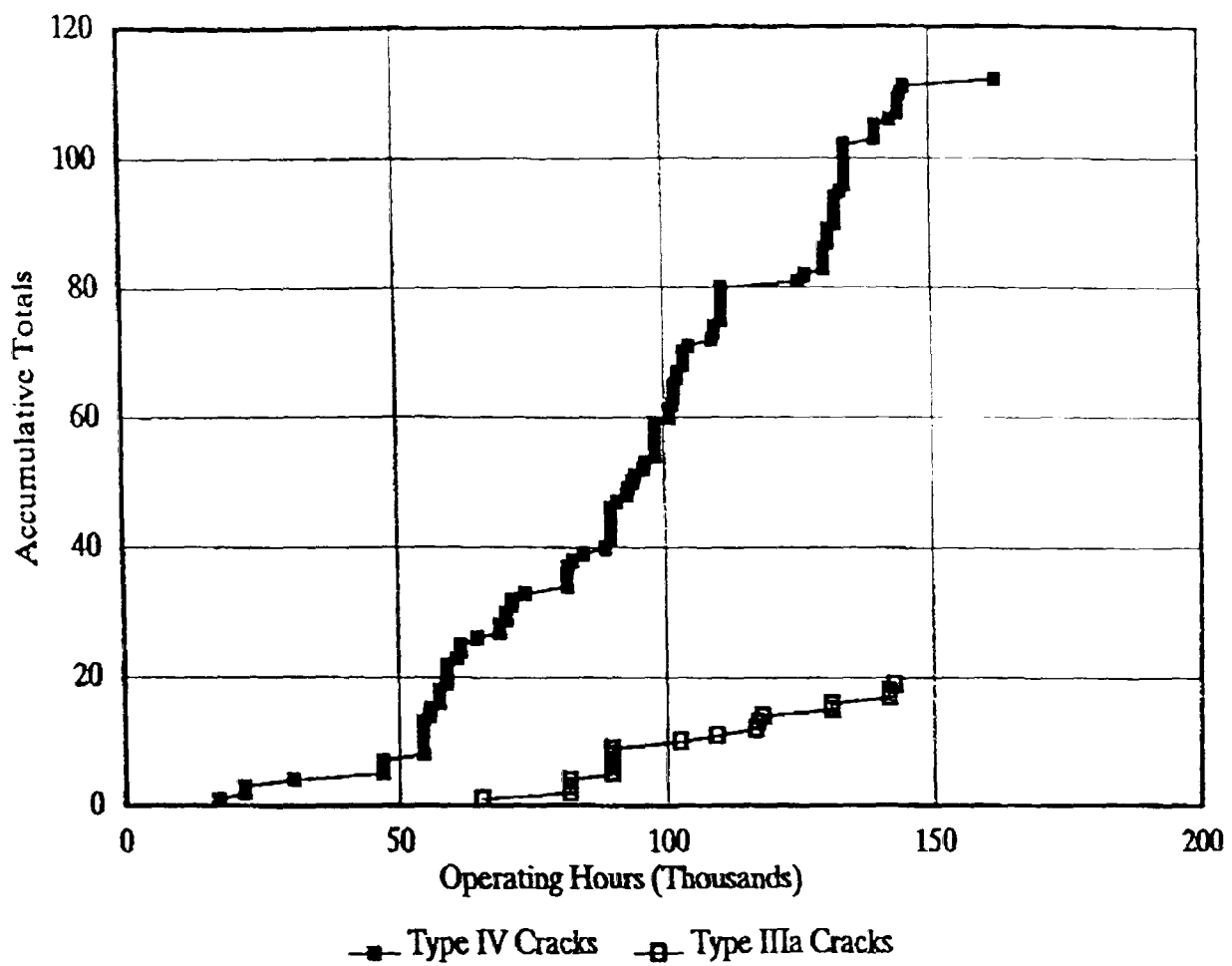


Figure 2.12. Crack incidences data for CrMoV circumferential butt-welded steam pipes, 2.25Cr1Mo:VrMoV welds (Brett [74]).

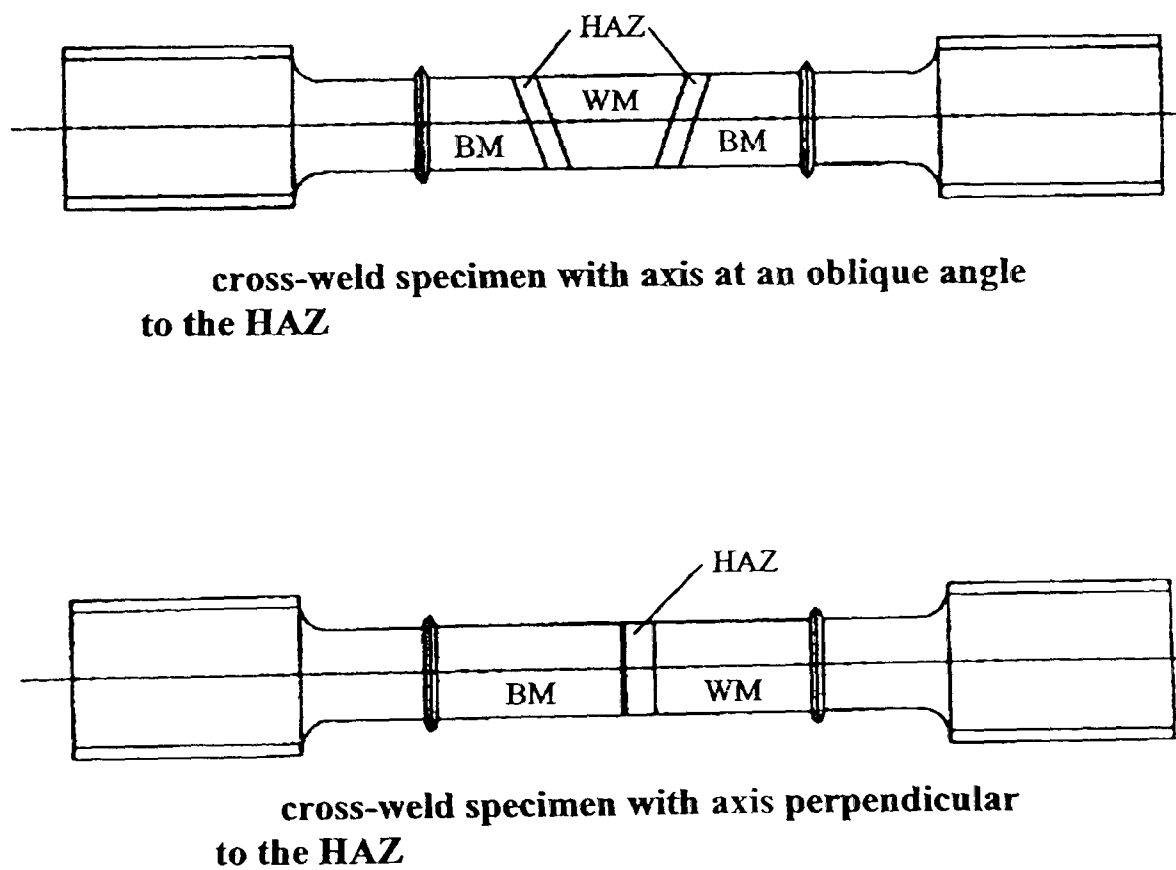


Figure 2.13. Typical cross weld creep test specimens (Tang [35]).

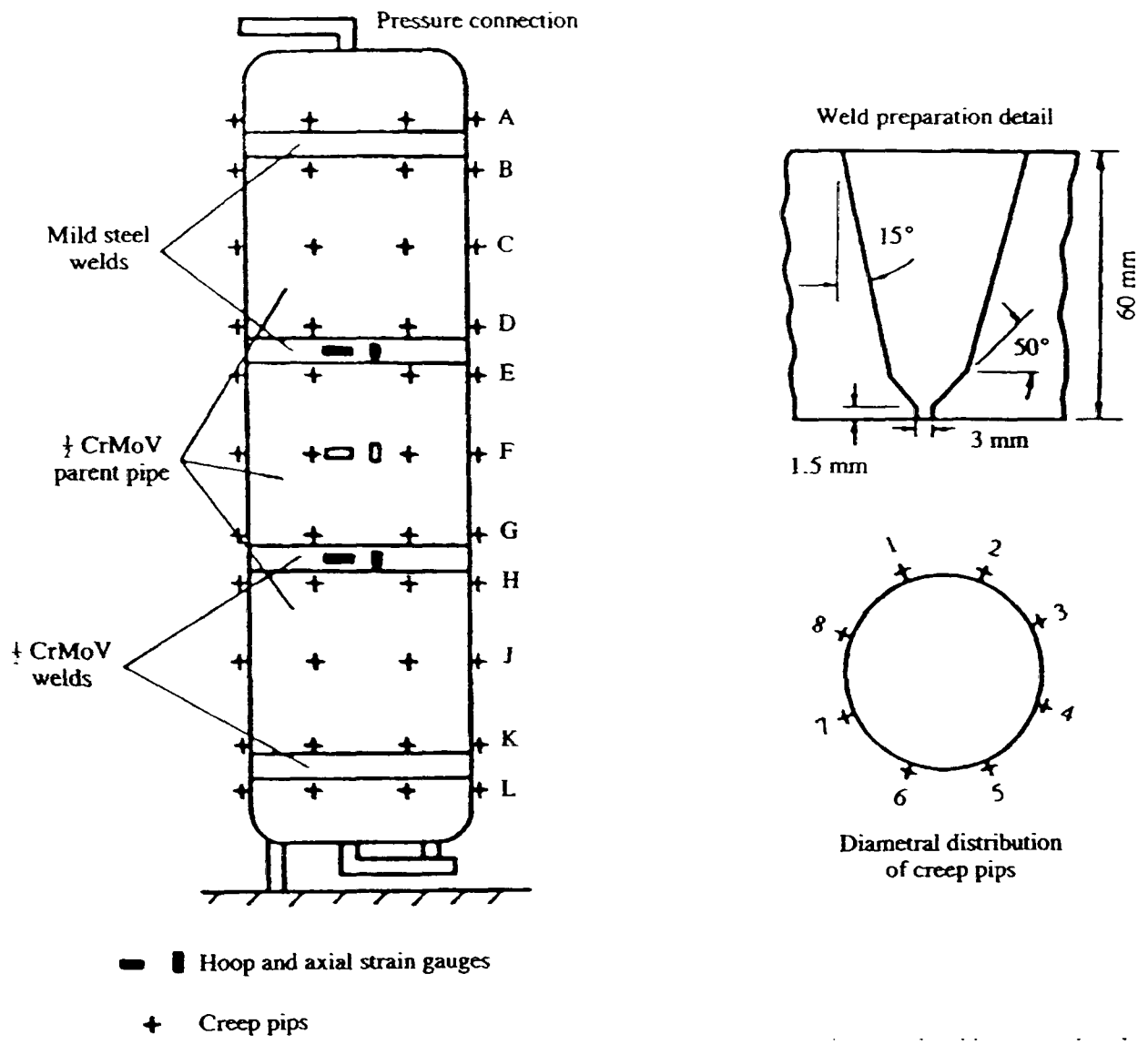


Figure 2.14. Butt welded pressure vessel pipe showing weld details and monitoring positions (Coleman and Fidler [21]).

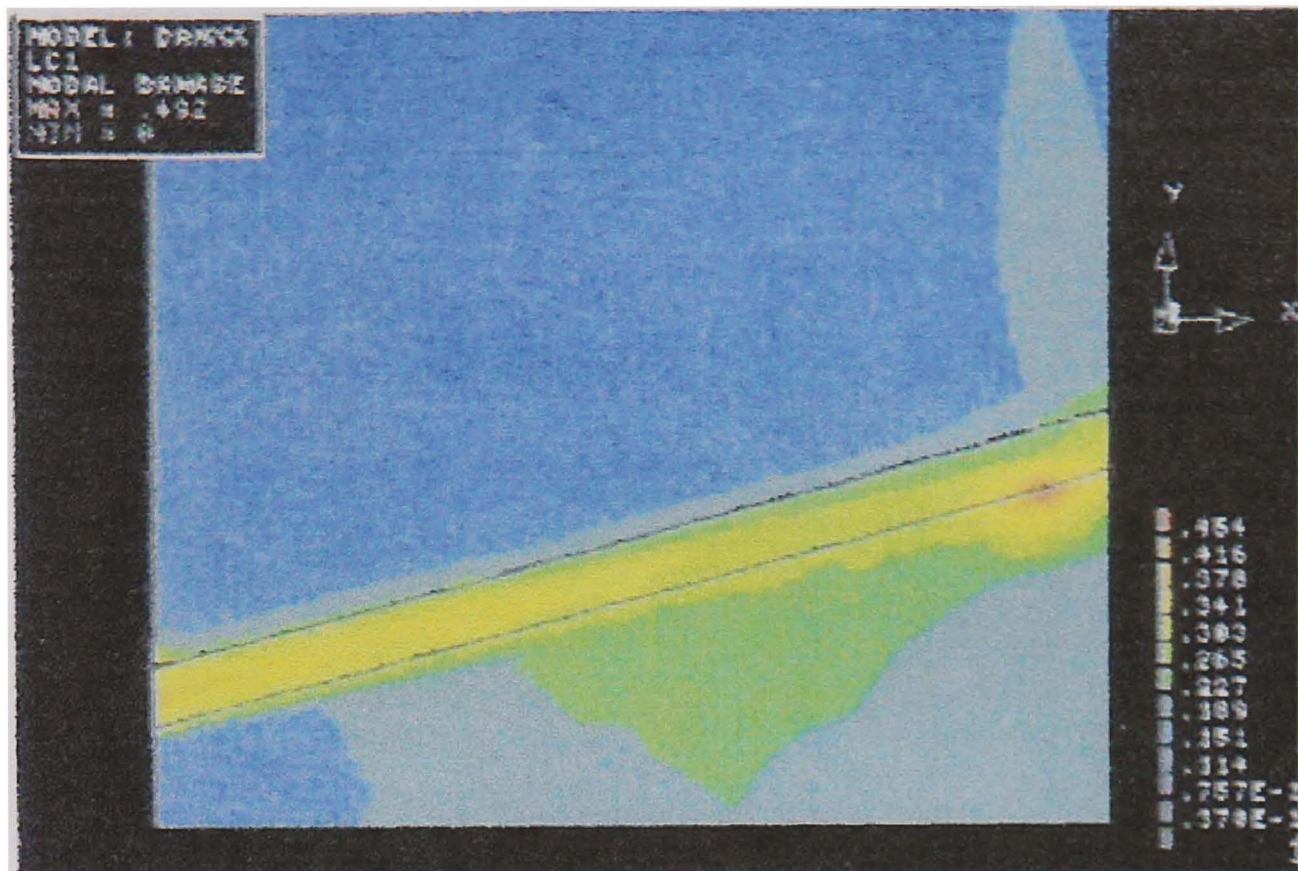


Figure 2.15. CDM damage distribution in a butt-welded CrMoV straight pipe section (Perrin *et al* [89]).

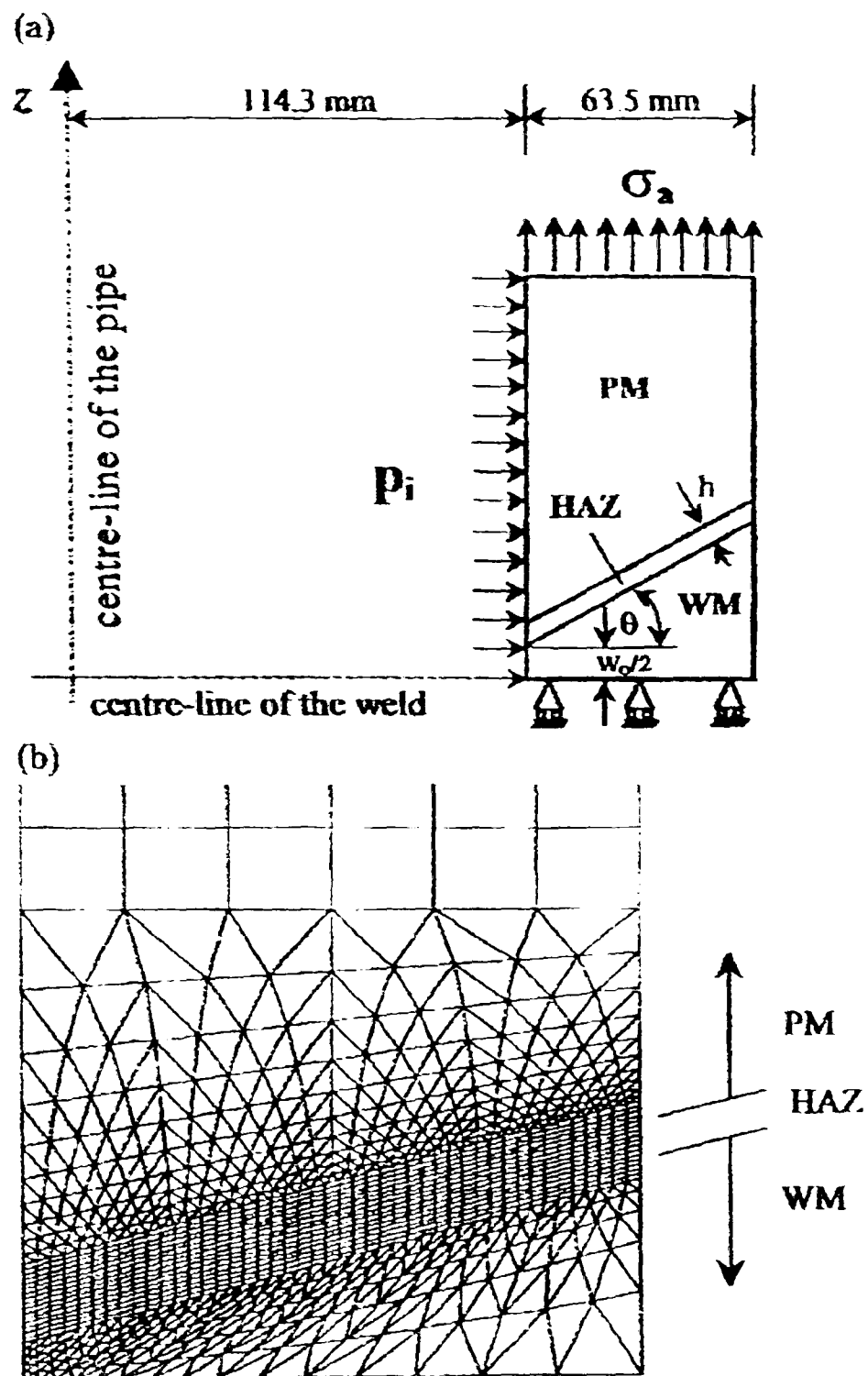


Figure 2.16. (a) Dimensions and loading and (b) FE mesh of the CrMoV straight pipe weld used for steady-state and CDM calculations (Sun *et al* [33]).

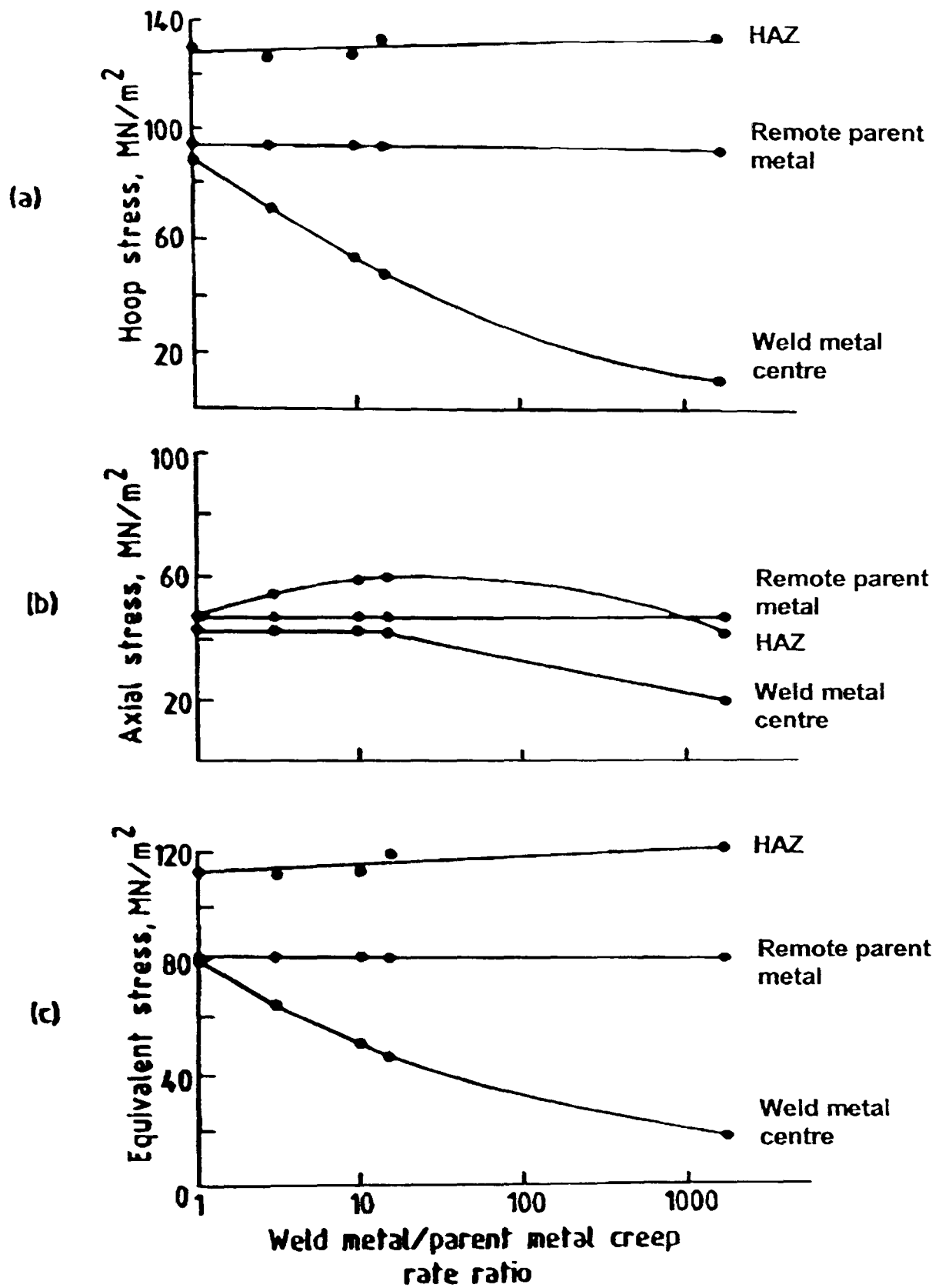


Figure 2.17. Variation of (a) hoop, (b) axial and (c) equivalent stresses with weld metal to parent material creep rate ratio (A_{WM} / A_{PM}) at three positions on the outer surface of the pipe (Coleman *et al* [85]).

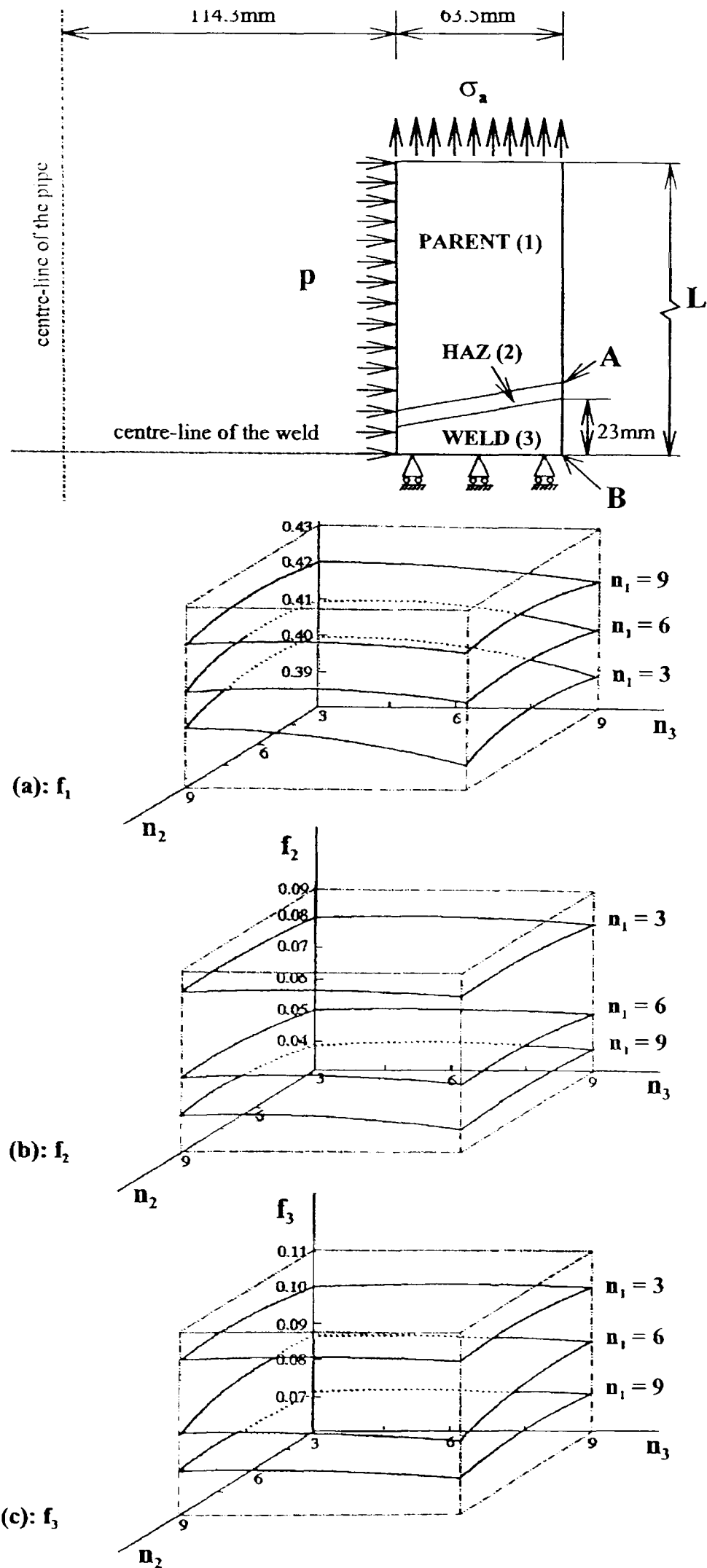
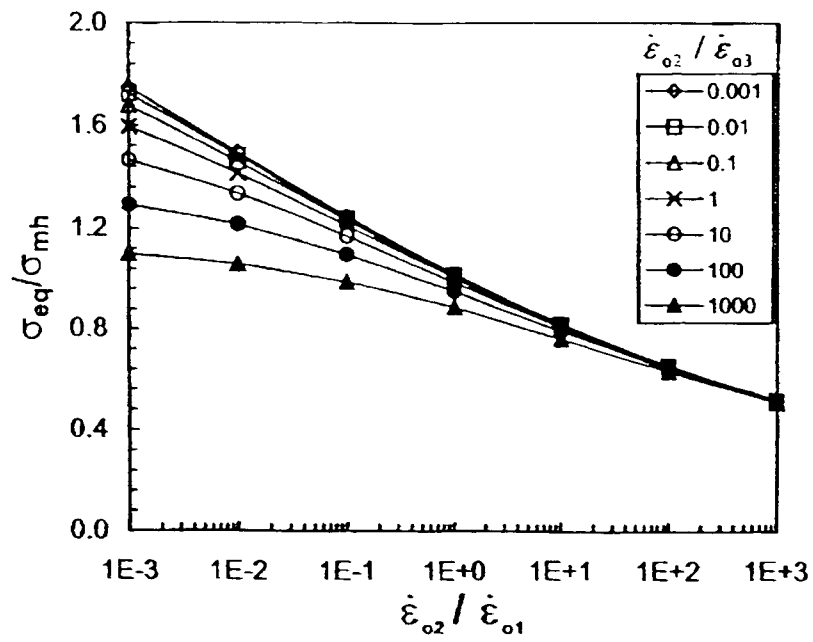
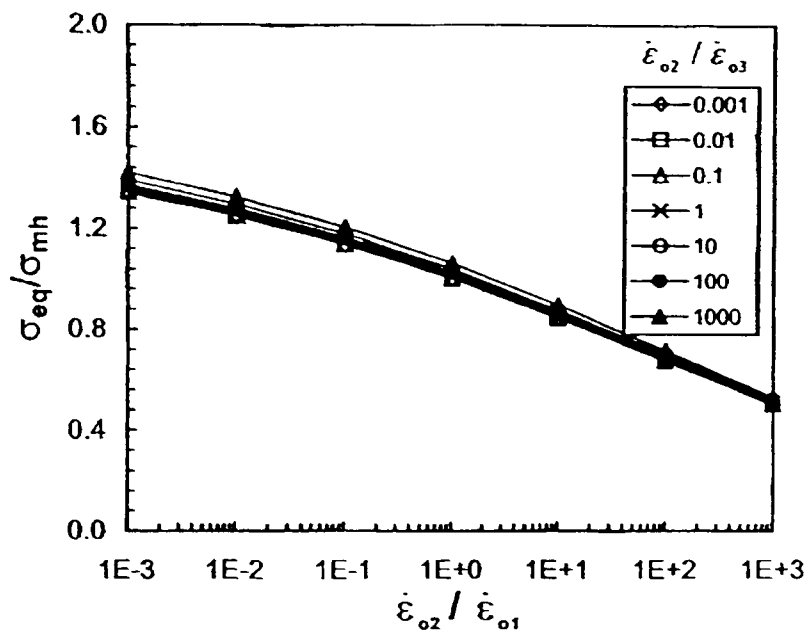


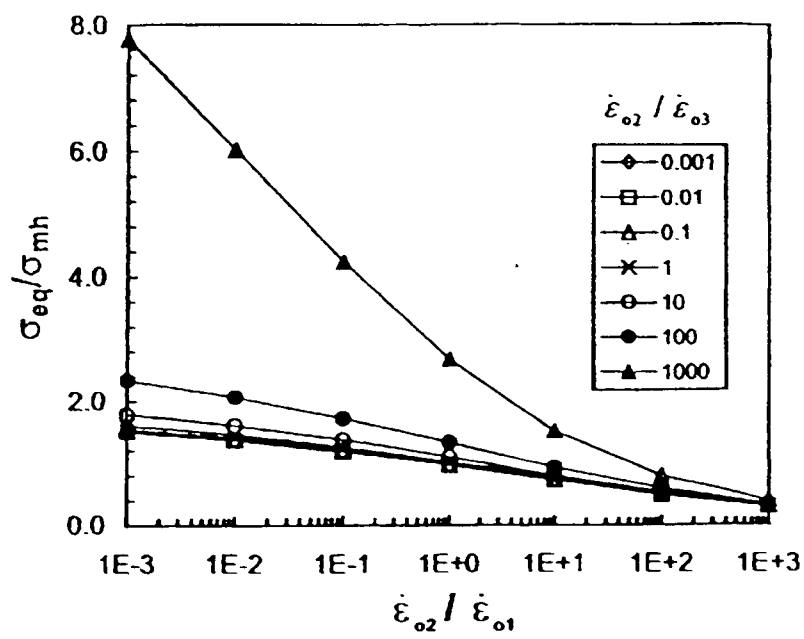
Figure 2.18. Variation of (a) f_1 , (b) f_2 and (c) f_3 value for the equivalent stresses at Position A in the HAZ on the outer surface of the pipe, as shown above (Hyde *et al* [100]).



(a) $n_1 = 3, n_2 = 9, n_3 = 3$

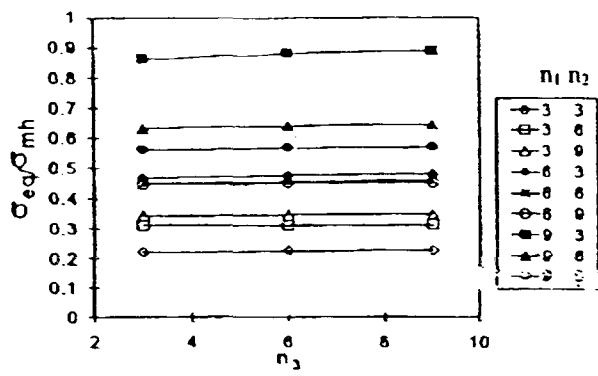


(b) $n_1 = 9, n_2 = 3, n_3 = 9$

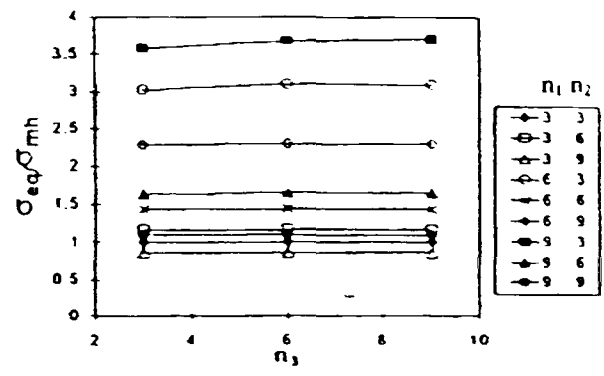


(c) $n_1 = 6, n_2 = 3, n_3 = 3$

Figure 2.19. Variations in the normalised equivalent stress at Position A in the HAZ Type IV region of outer surface of the pipe (Tang [35]).

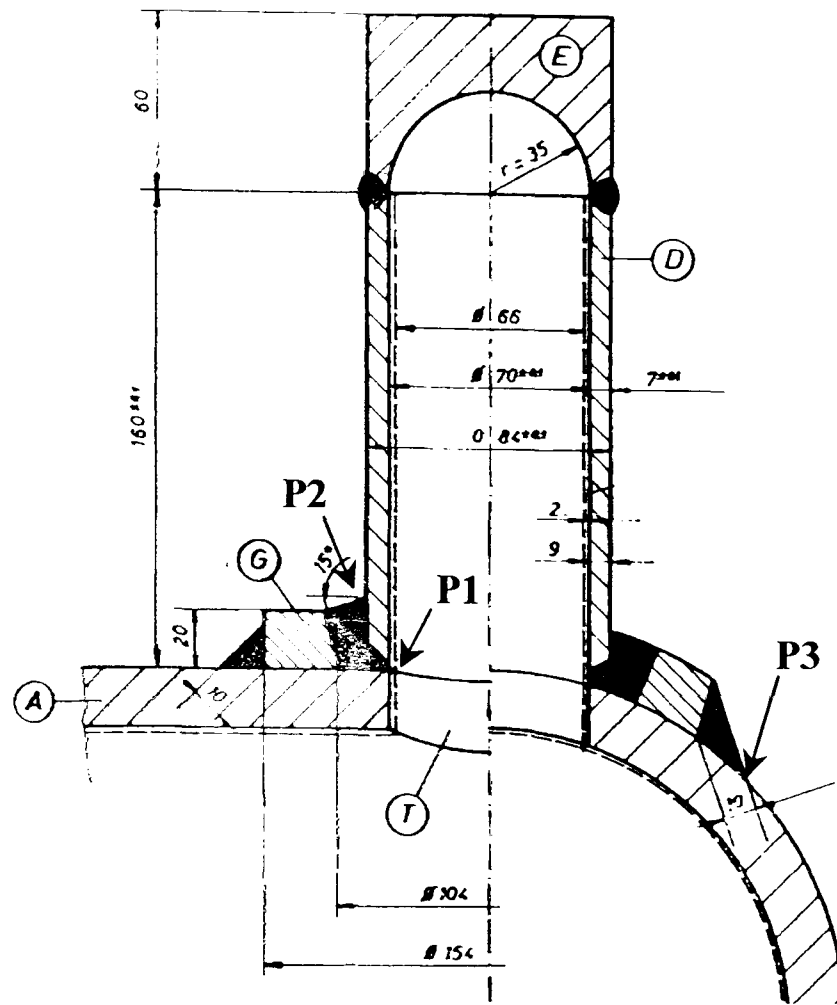


(a): $\dot{\epsilon}_{o2} / \dot{\epsilon}_{o1} = 100$ and $\dot{\epsilon}_{o2} / \dot{\epsilon}_{o3} = 0.01$

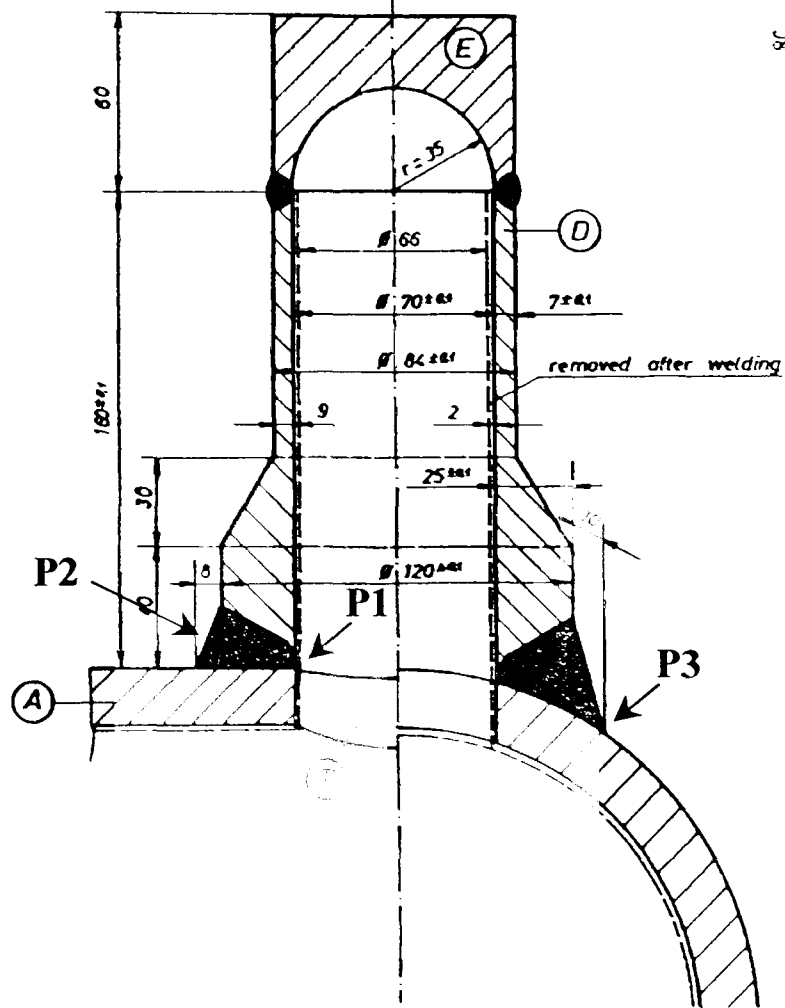


(b): $\dot{\epsilon}_{o2} / \dot{\epsilon}_{o1} = \dot{\epsilon}_{o2} / \dot{\epsilon}_{o3} = 0.01$

Figure 2.20. The effect of n_3 on the normalised equivalent stress at Position A in the HAZ Type IV region of outer surface of the pipe for a range of n_1 and n_2 combinations (Hyde *et al* [100]).



(a)



(b)

Figure 2.21. Detail of branch geometry and type of connection reinforcement (a) pad-reinforced and (b) branch-thickening reinforced used by Sys [17] in full-scale creep rupture tests.

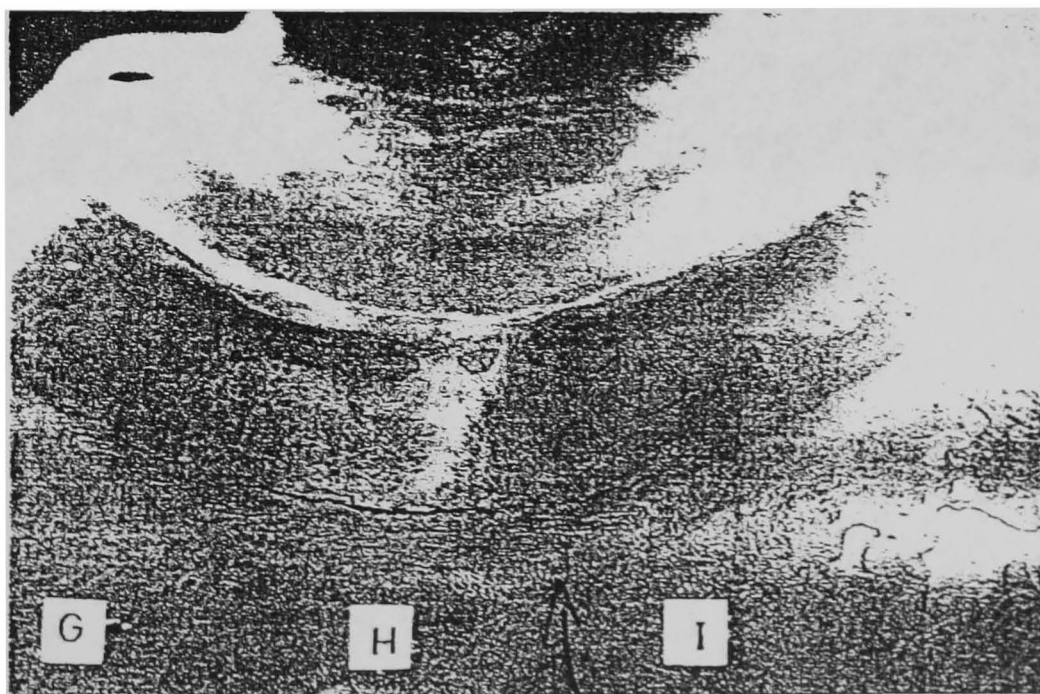
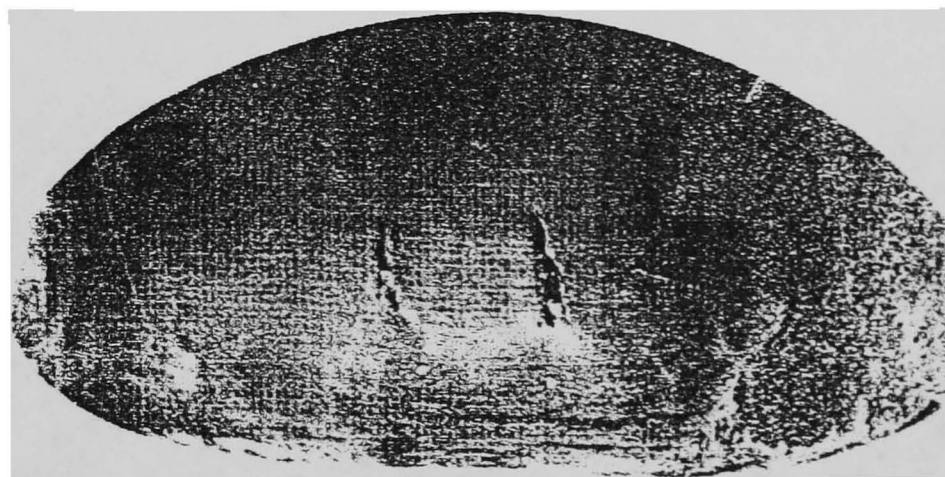
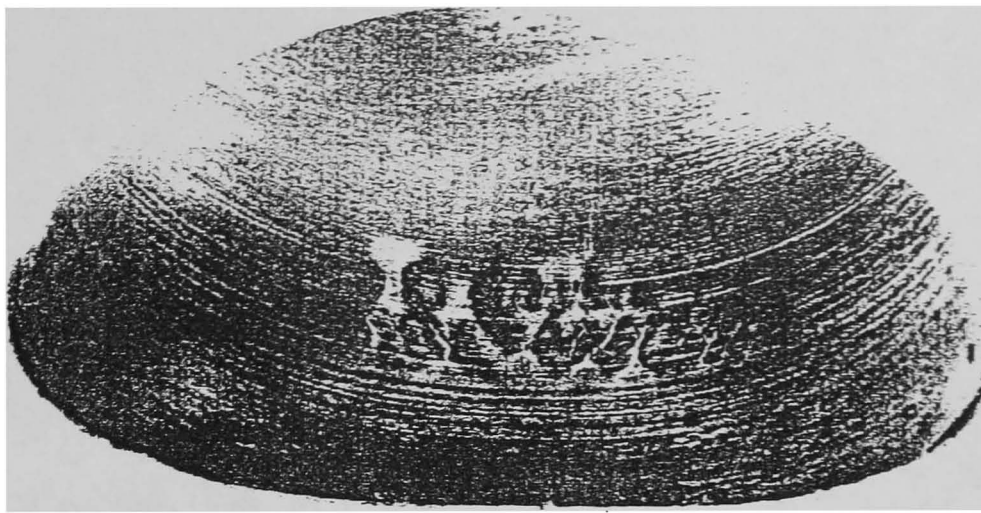


Figure 2.22. Different cracking modes found by Sys [17] on experimentally tested full-scale failed branched pipes; parallel cracks on the inside surface on the crotch corner side (top), through crack on the outside surface on the crotch corner side (middle) and cracks at the weld foot on the flank side, outer surface (bottom).

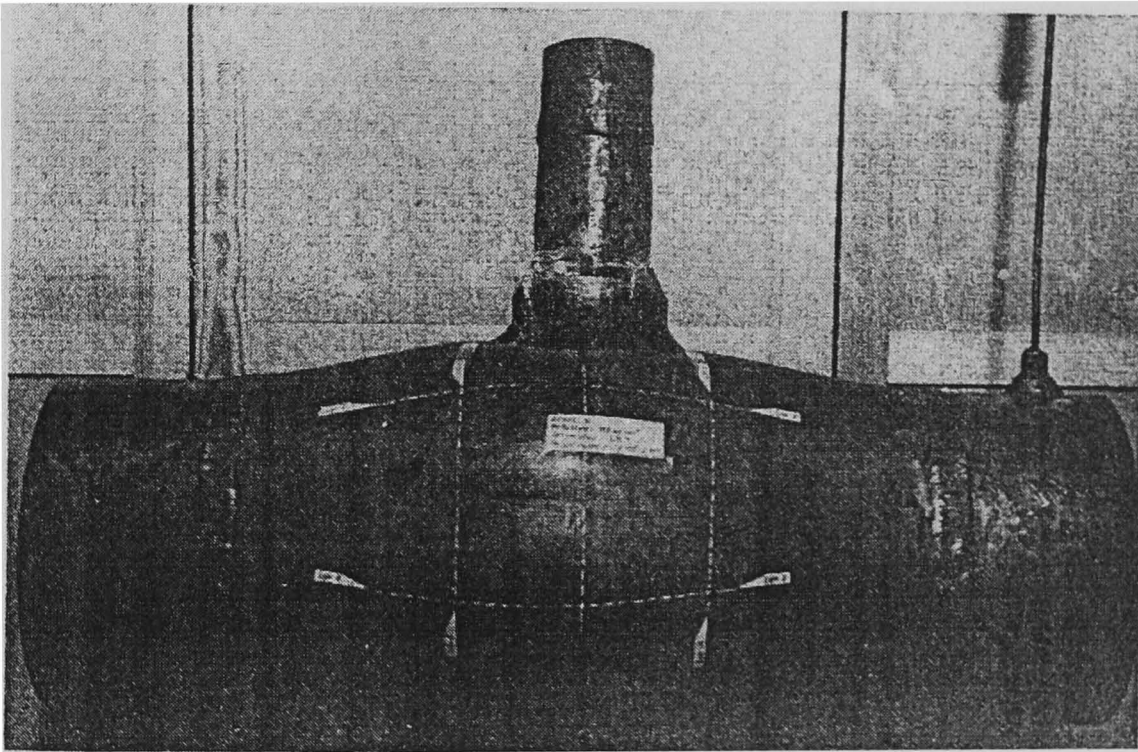


Figure 2.23. Large deformation failure in the main pipe section of test components K4 (top) and K5 (bottom) (Sys [17]).

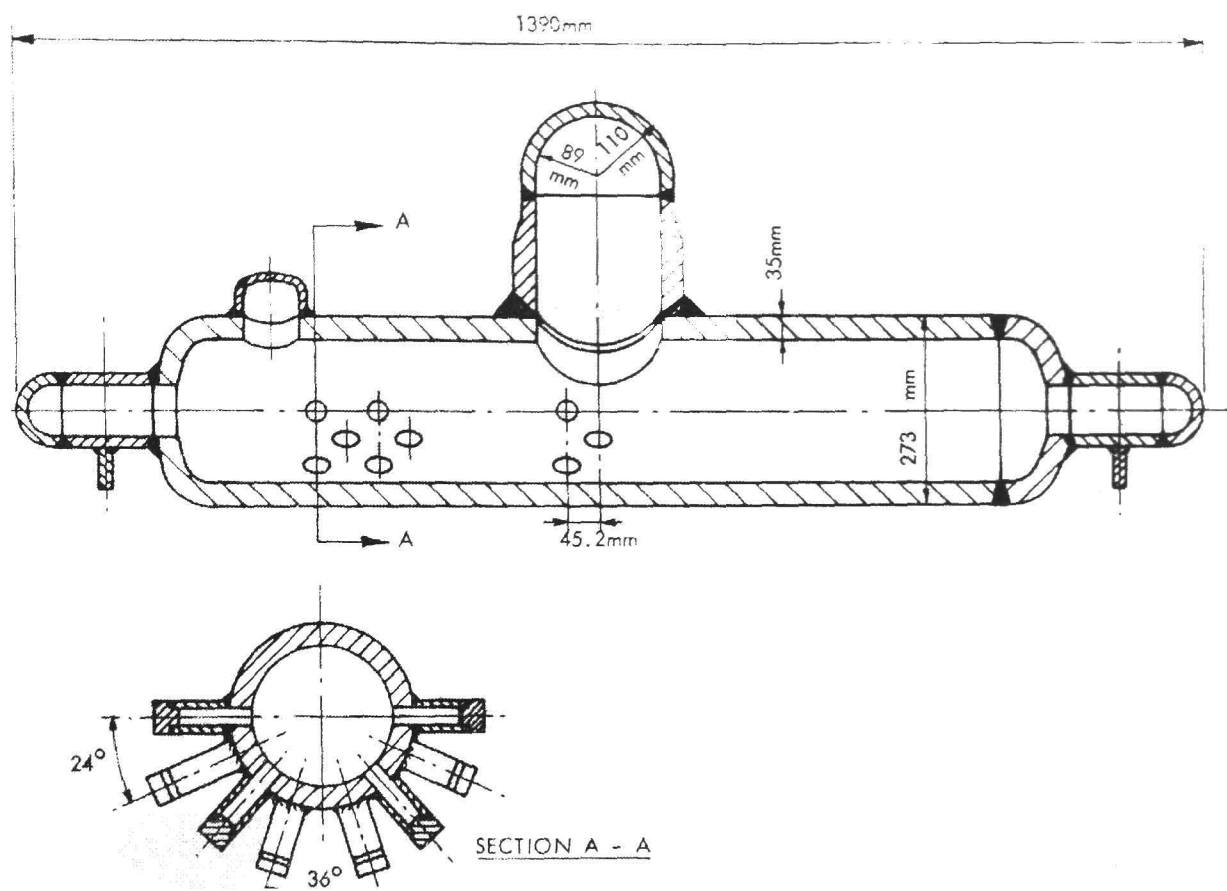


Figure 2.24. Details of branched header full-scale creep test vessel used by Day *et al* [18]).

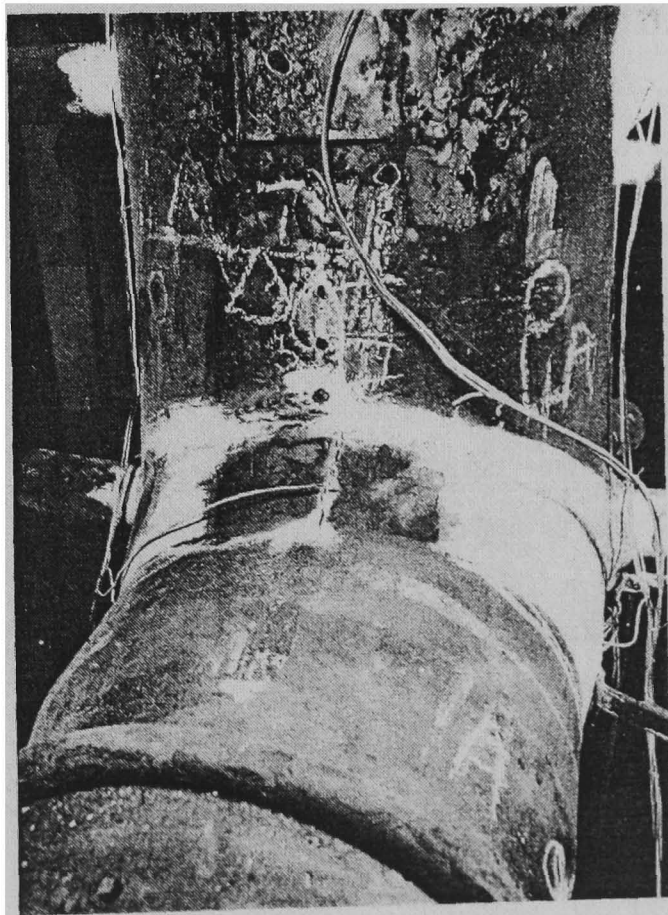


Figure 2.25. Failure location on the large, centre-length branch weld, transverse weld metal cracking on the crotch corner plane, Day *et al* [18]).

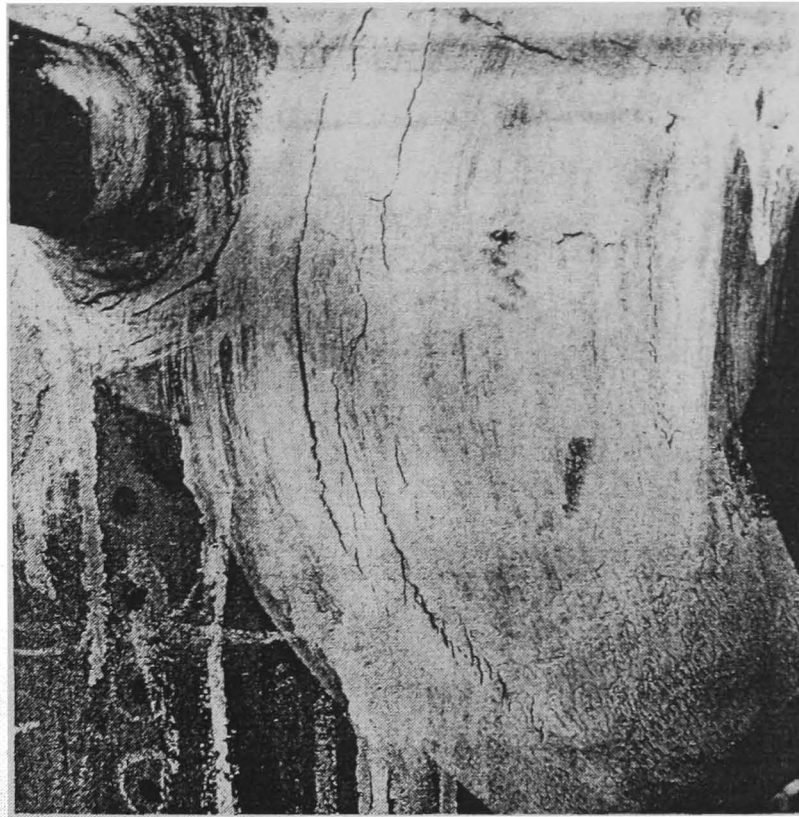


Figure 2.26. Additional cracking locations on the large, centre-length header branch weld, circumferential and transverse weld metal cracks around the weld, Day *et al* [18]).

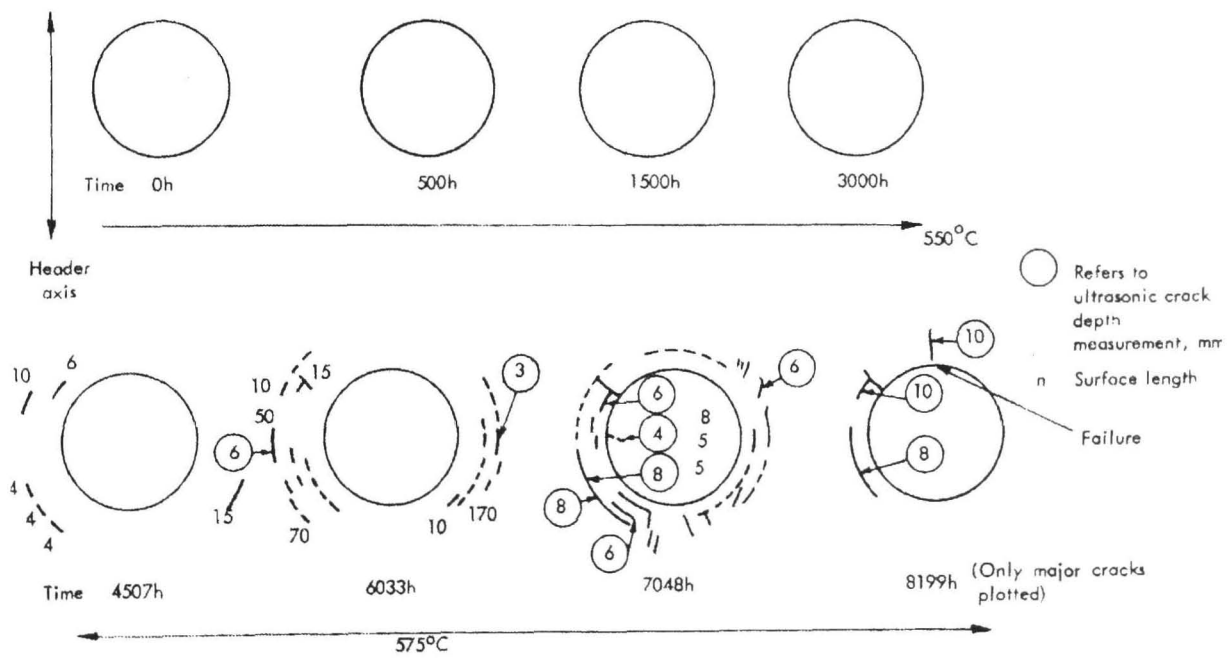


Figure 2.27. Cracking history of large, centre-length header branch weld, Day *et al* [18]).

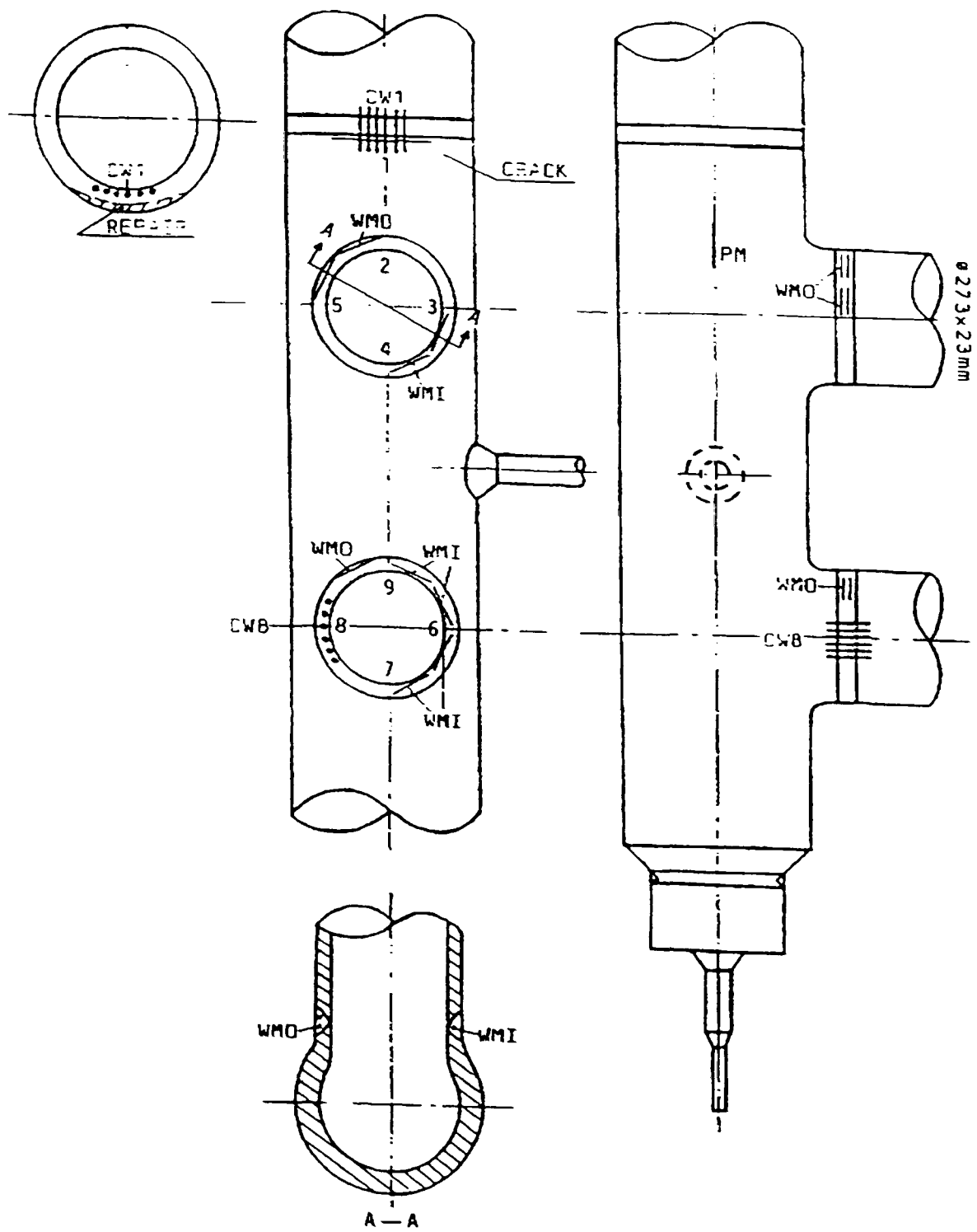


Figure 2.28. Geometry of double-branched T-joint used by Storesund *et al* [111] for full-scale component creep testing.

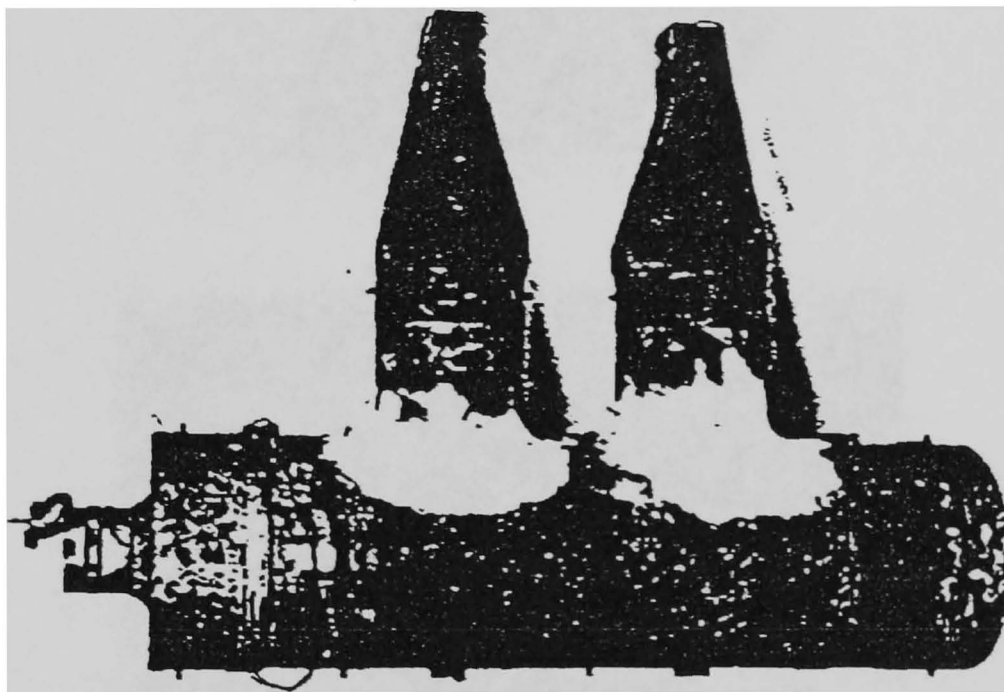
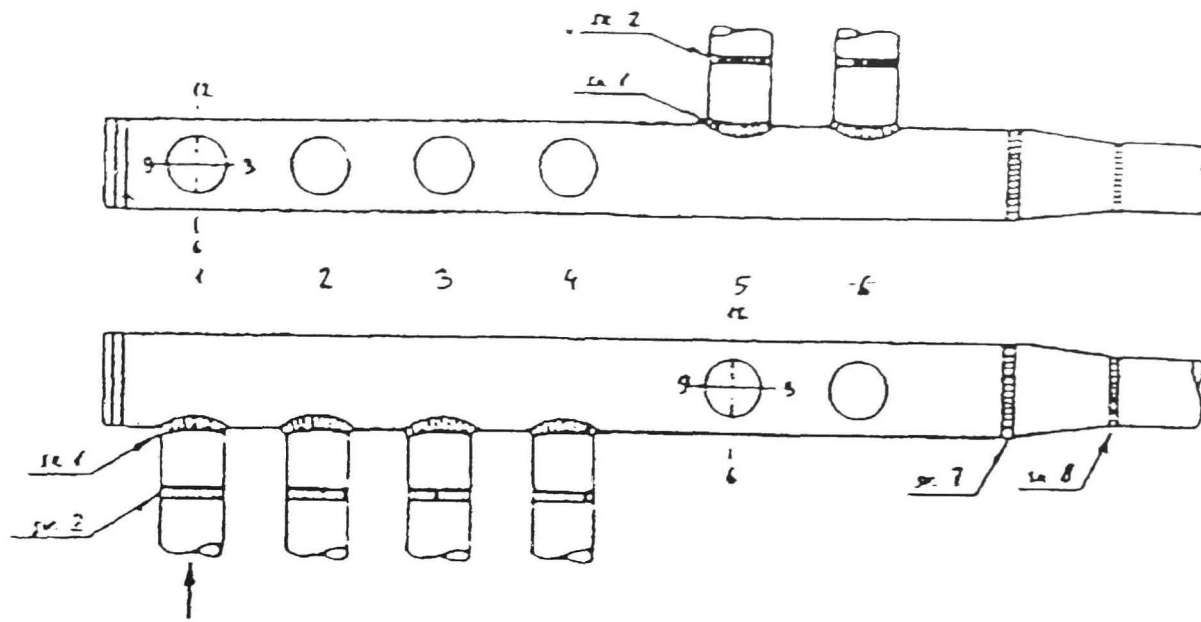


Figure 2.29. Geometry of T-branched branched header (top) and the double-branched $2\frac{1}{4}\text{Cr1Mo}$ T-branched test vessel (bottom) made from the header and creep tested by Rotvel *et al* [9].

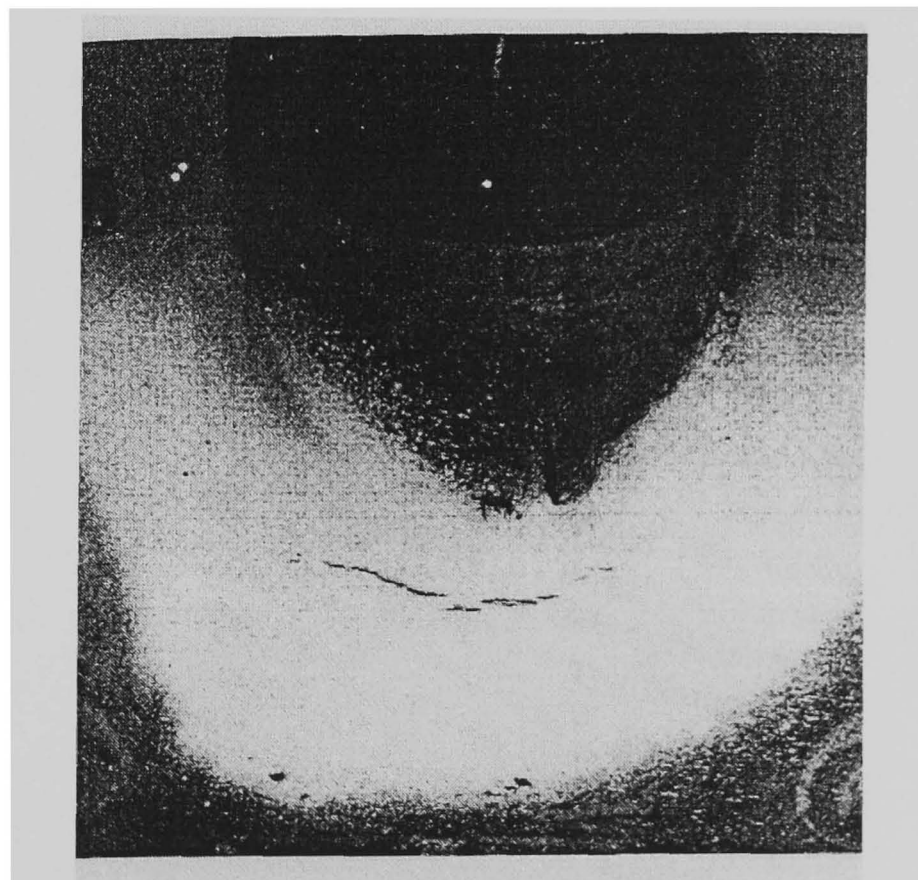
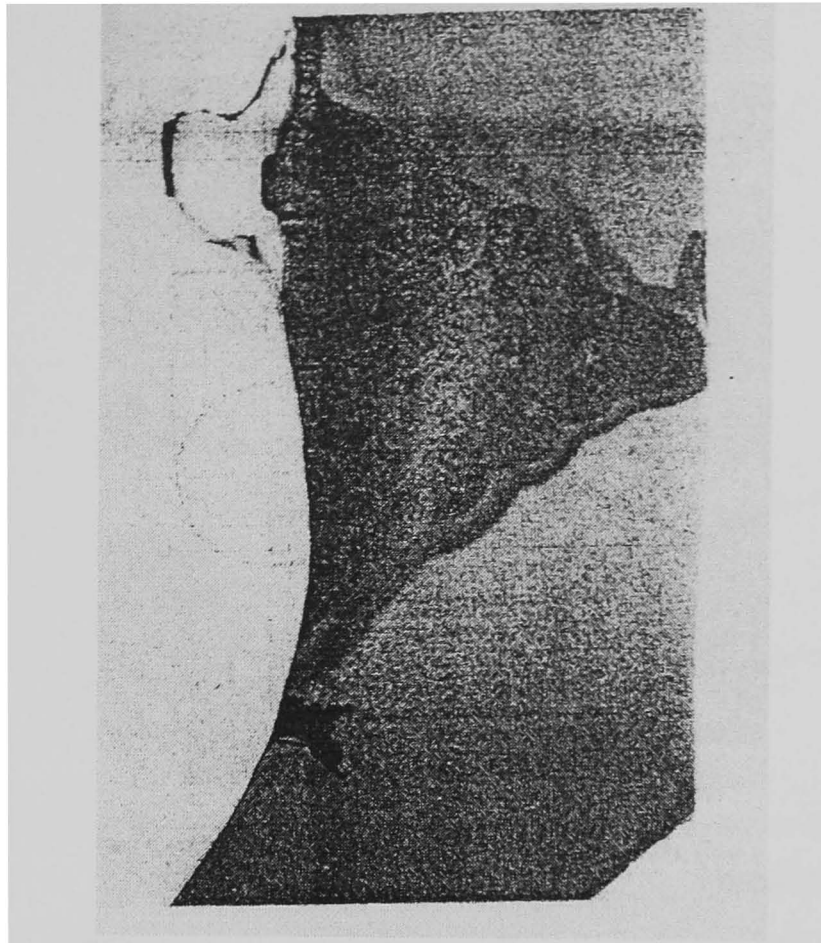


Figure 2.30. Cross-section (top) and face on view (bottom) of creep cracks at the weld foot saddle position of the $2\frac{1}{4}\text{Cr1Mo}$ T-branched test vessel in the fine-grained HAZ region of the weld (van Wortel and Arav [113]).

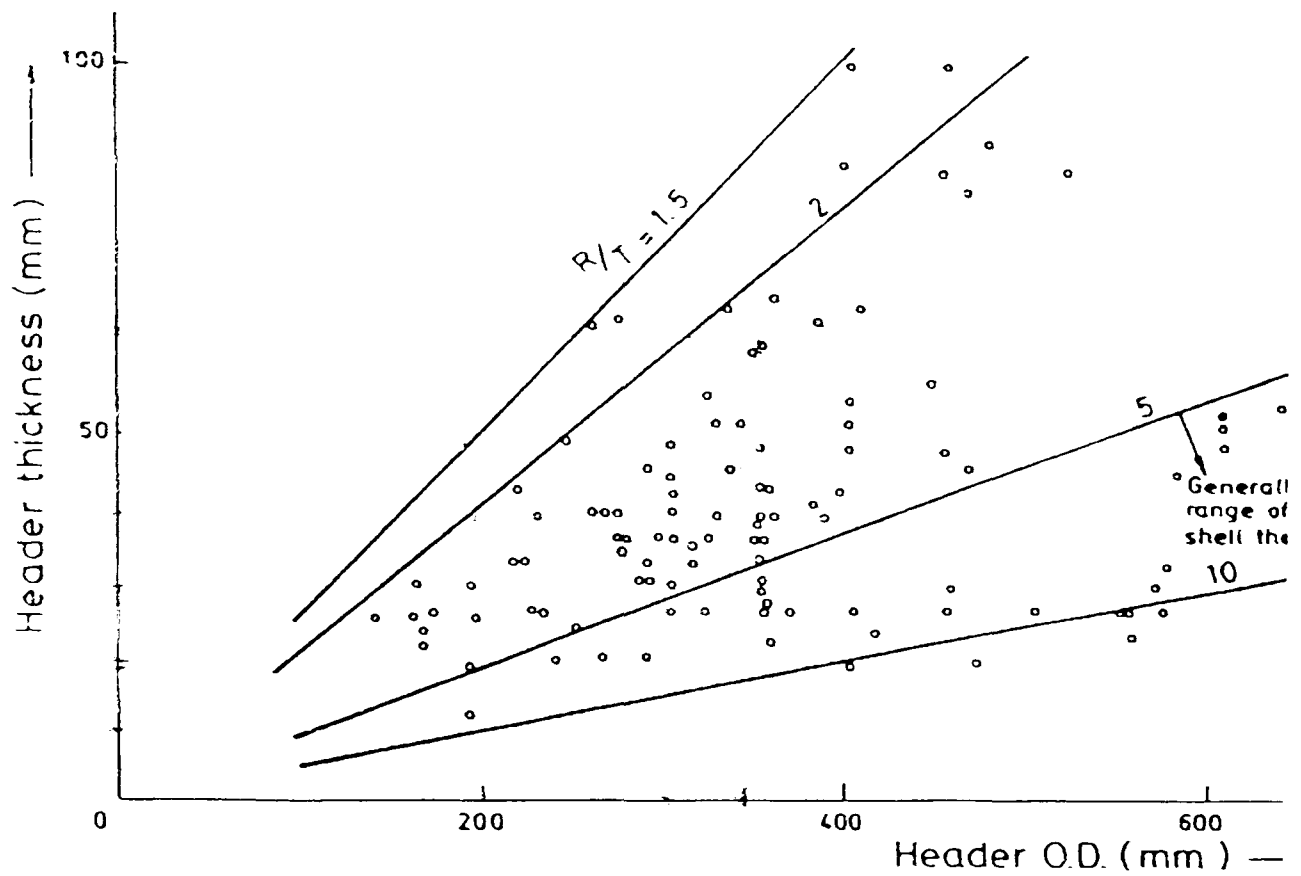


Figure 2.31. Typical power plant header geometries (Budden & Goodall [114]).

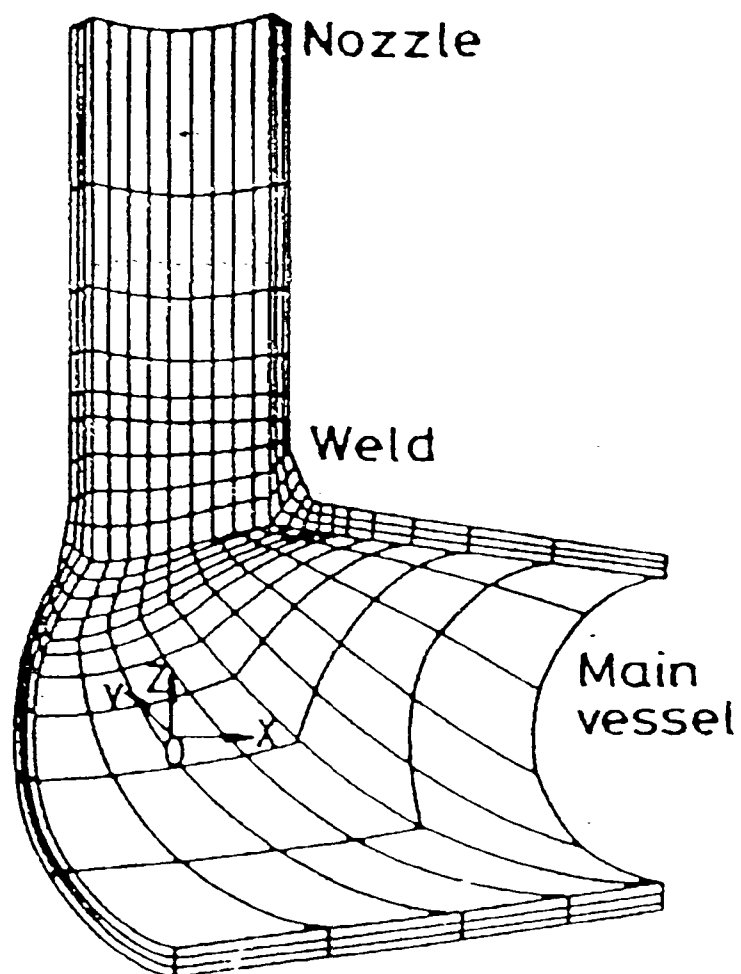


Figure 2.32. Finite element mesh for branched pipe Vessel B (Budden & Goodall [114]).

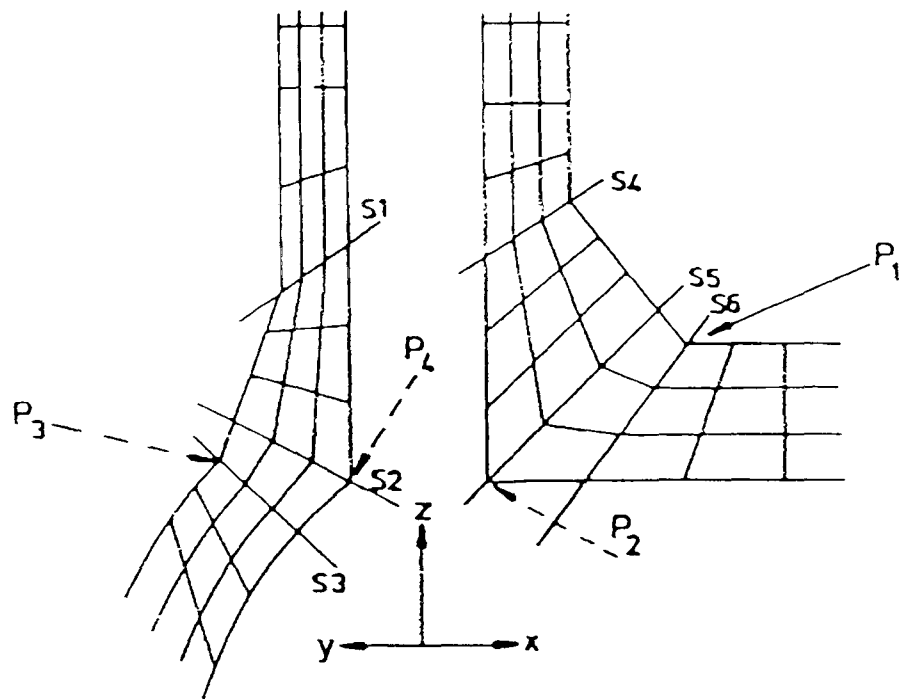
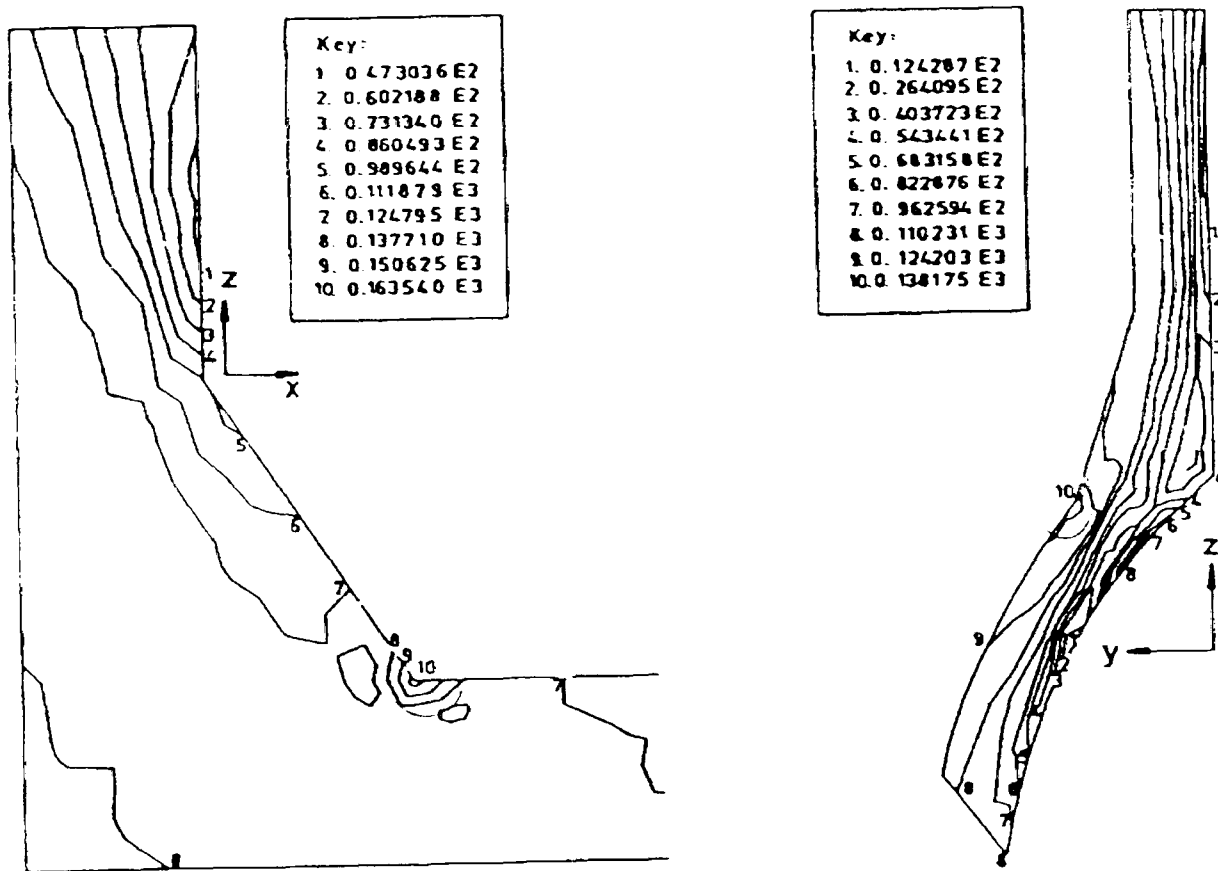


Figure 2.33. Close up of the flank (left) and crotch (right) connection regions of the finite element mesh of the branched pipe Vessel B (Budden & Goodall [114]).



Finite element results for vessel B at 246h
 (a) equivalent creep strain on x-z plane,
 (b) equivalent creep strain on y-z plane,
 (c) equivalent stress on x-z plane,
 (d) equivalent stress on y-z plane

Figure 2.34. Equivalent steady-state creep stress contour plots of the crotch (left) and flank (right) planes of the branched pipe Vessel B (Budden & Goodall [114]).

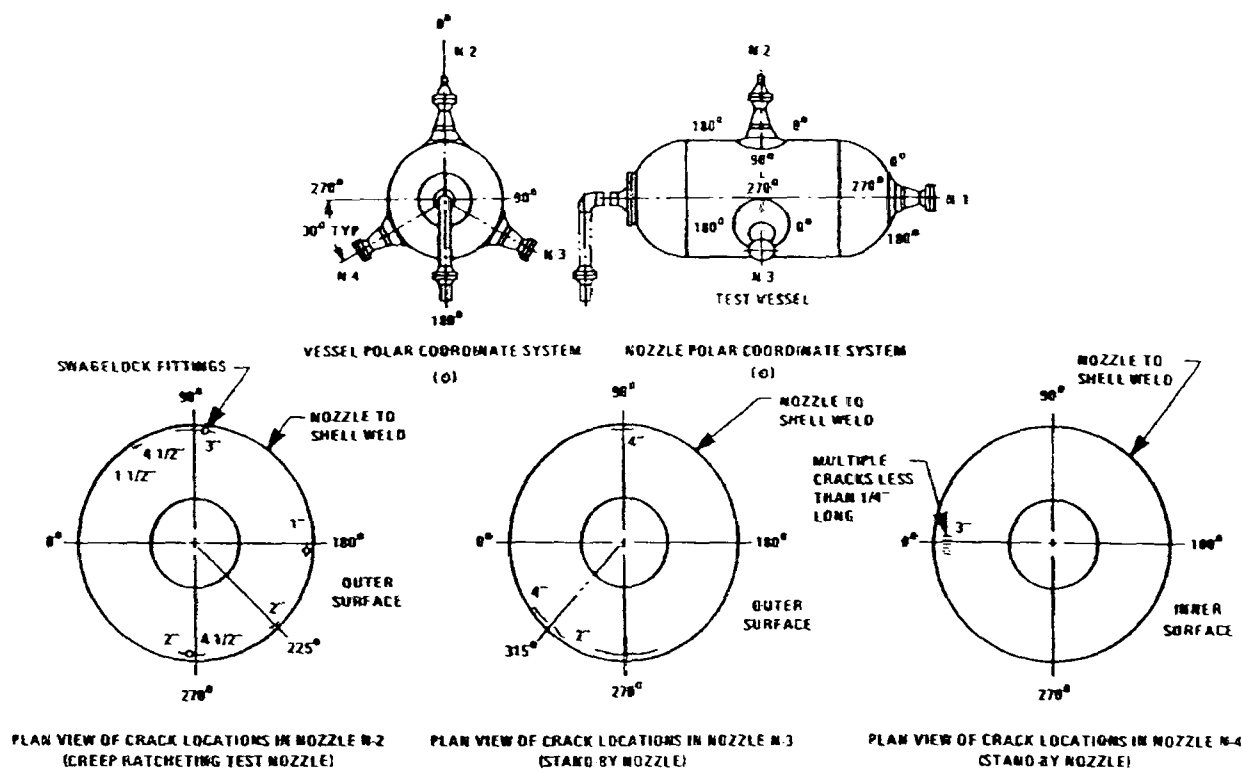


Figure 2.35. Geometry of test vessel and HAZ creep crack locations for the Type 304 stainless steel T-branched test vessel (Dhalla [121]).

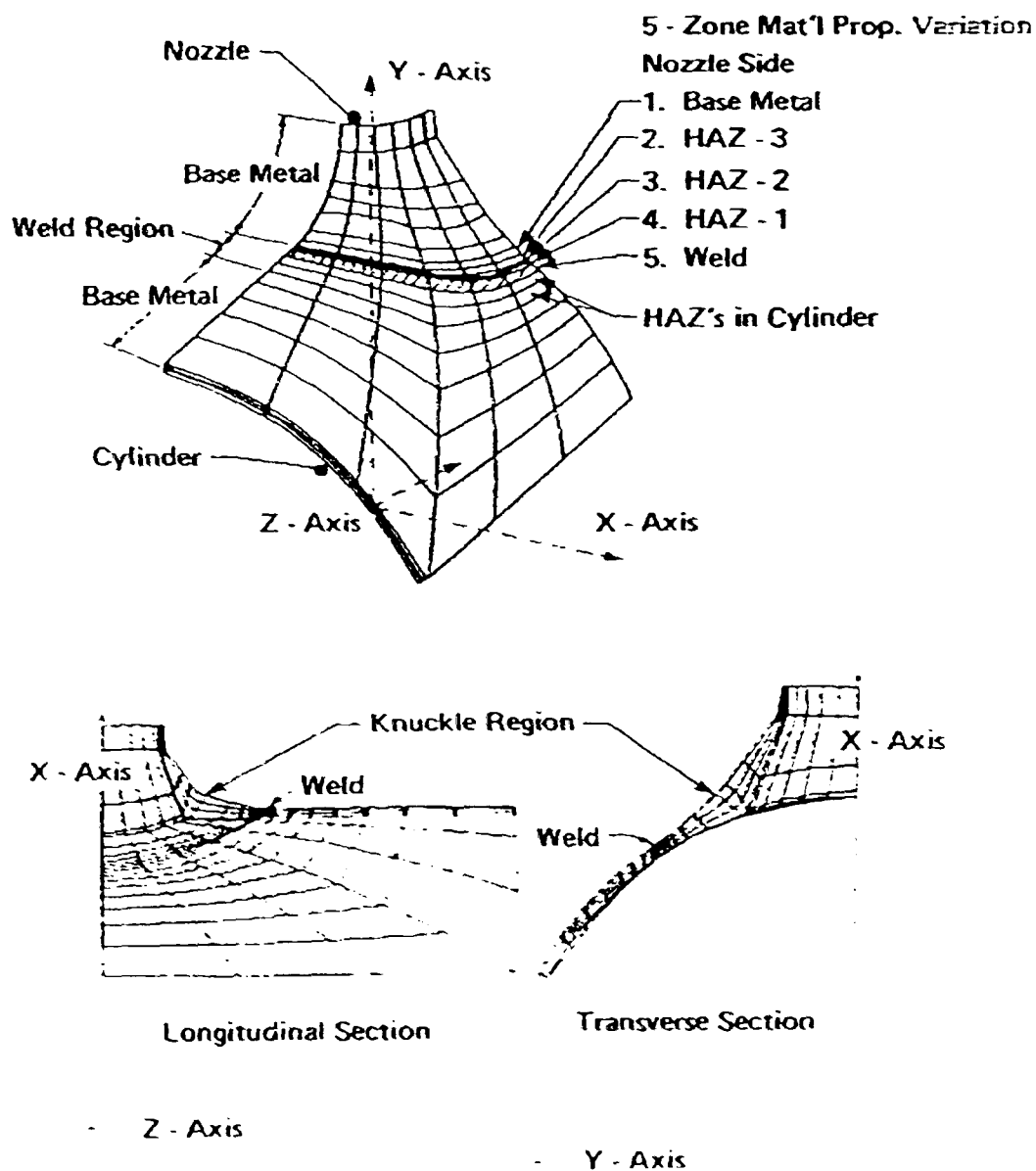


Figure 2.36. FE model of branched pipe, including weldment material zones for the Type 304 stainless steel T-branched test vessel (Dhalla [121]).

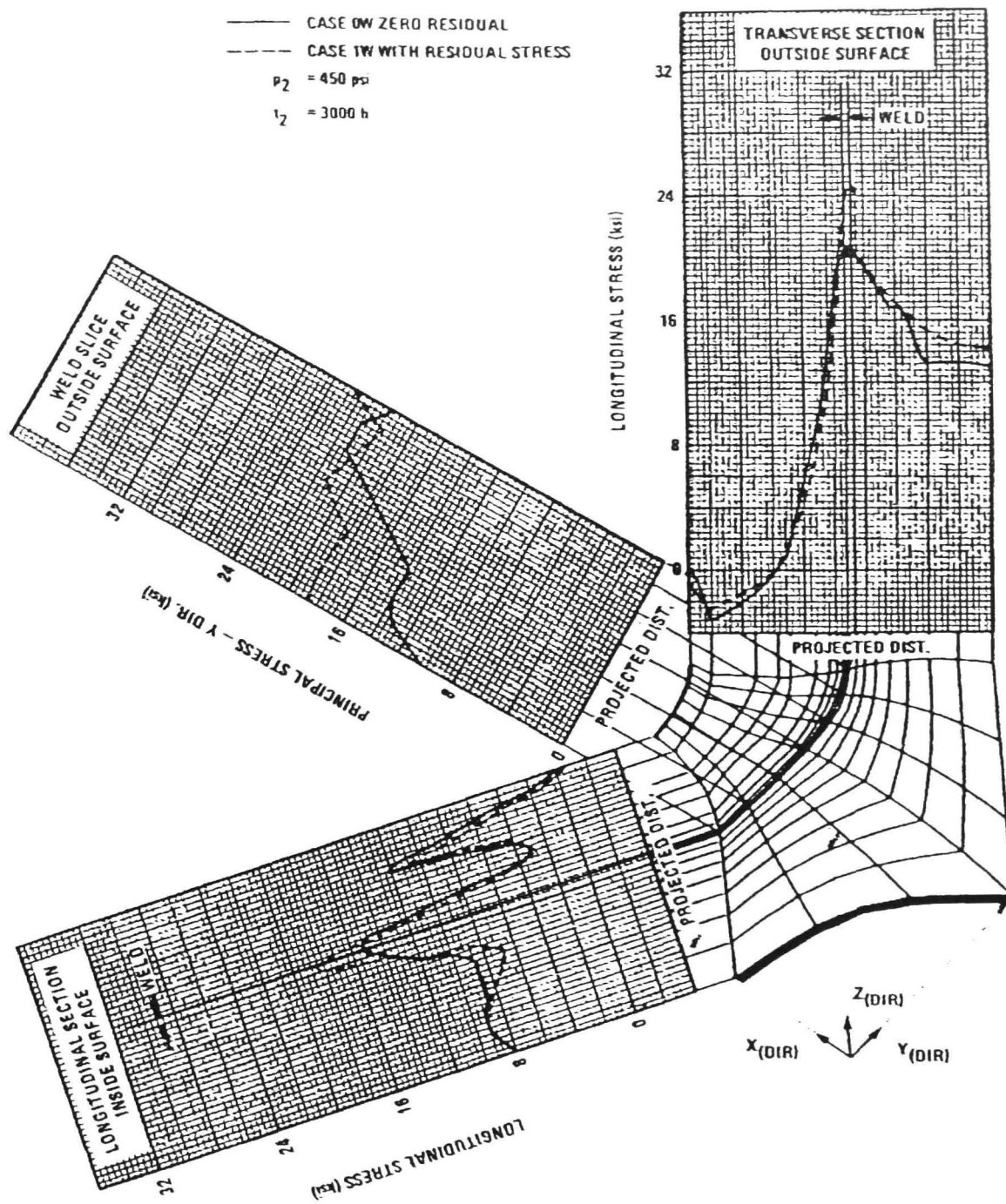


Figure 2.37. Comparison of FE longitudinal principal stresses with and without residual stress weld effects at 3000 hours for the welded branched pipe, including weldment material zones for the Type 304 stainless steel T-branched test vessel (Dhalla [121]).

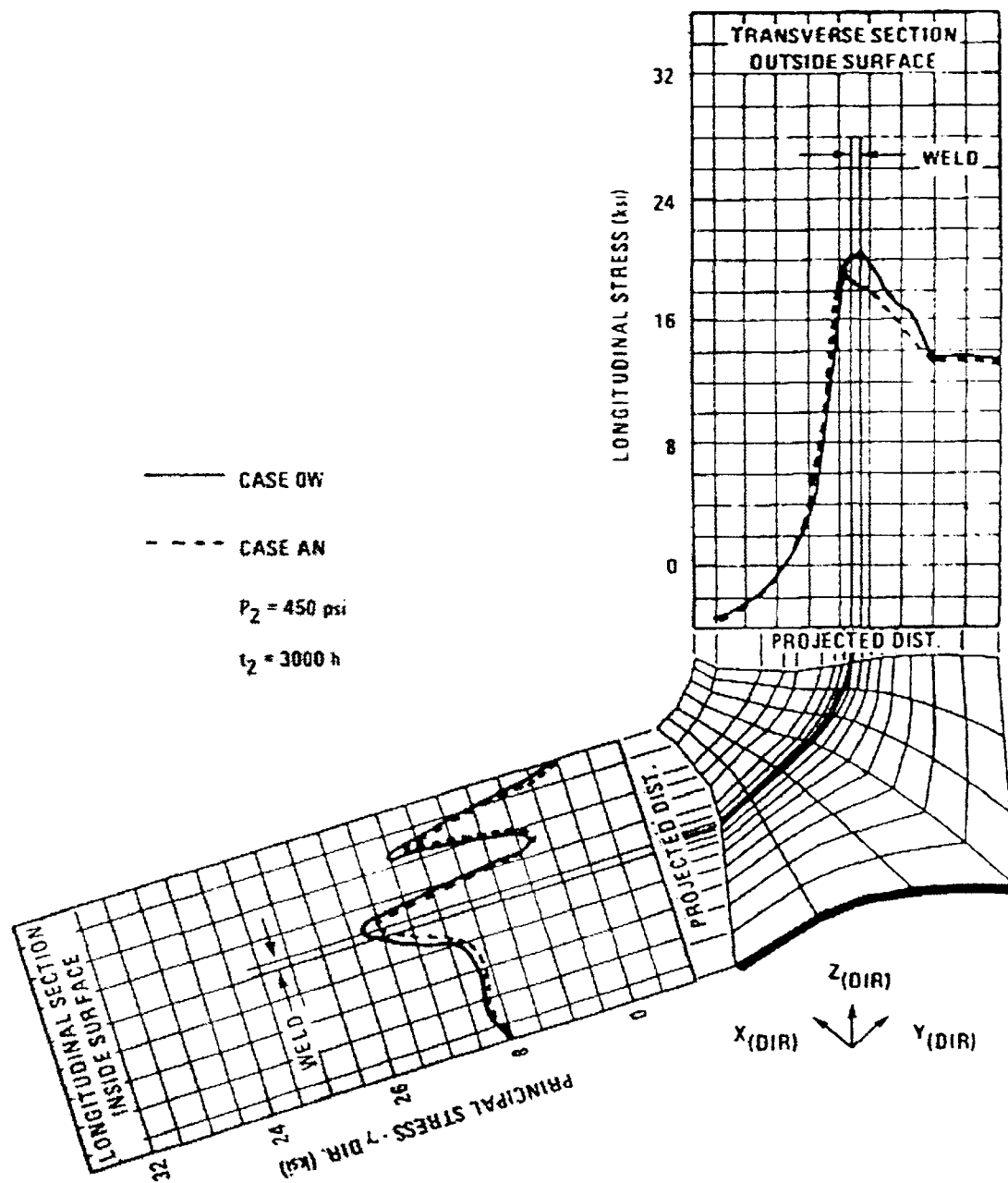


Figure 2.38. Comparison of FE longitudinal principal stresses with and without weldment creep properties at 3000 hours for the welded branched pipe, without residual stresses, for the Type 304 stainless steel T-branched test vessel (Dhalla [121]).

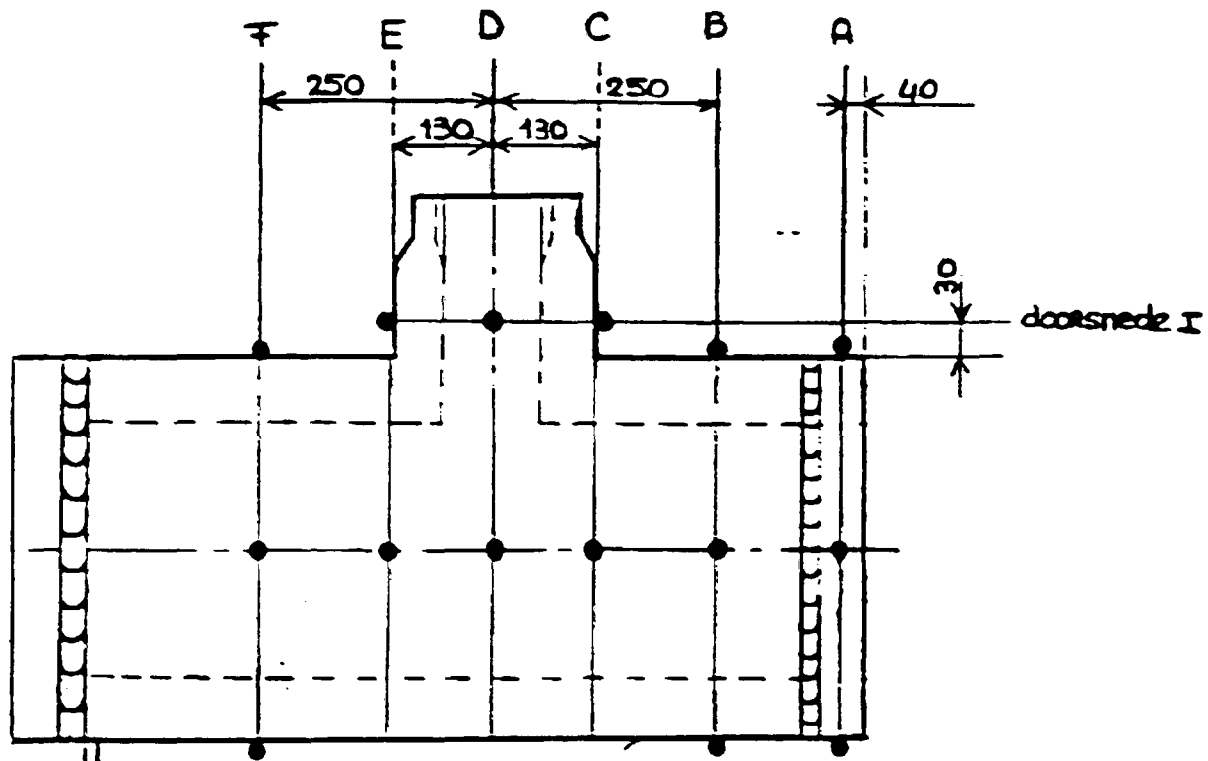
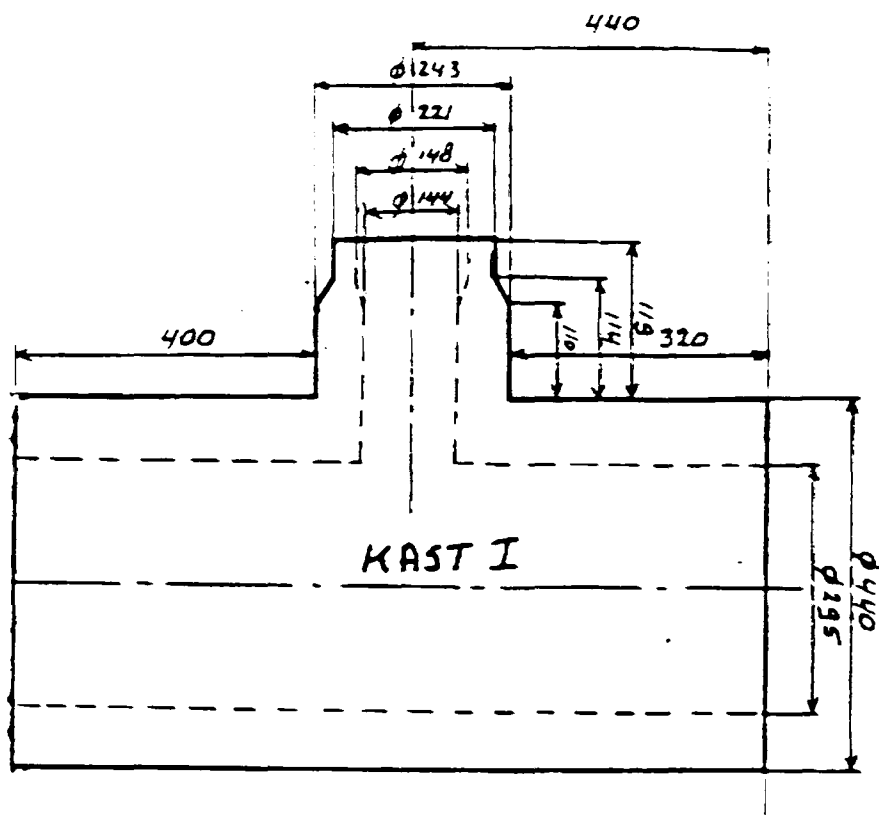
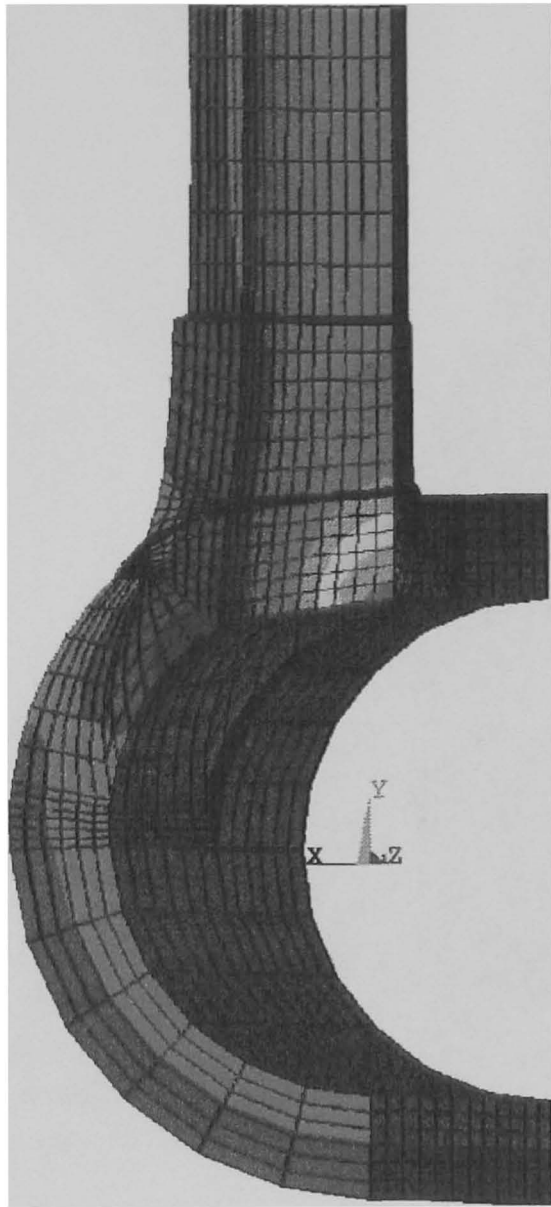


Figure 2.39. Geometry of 10CrMo910 T-branched pipe vessel used for FE modelling of weld repair (Li [122]).

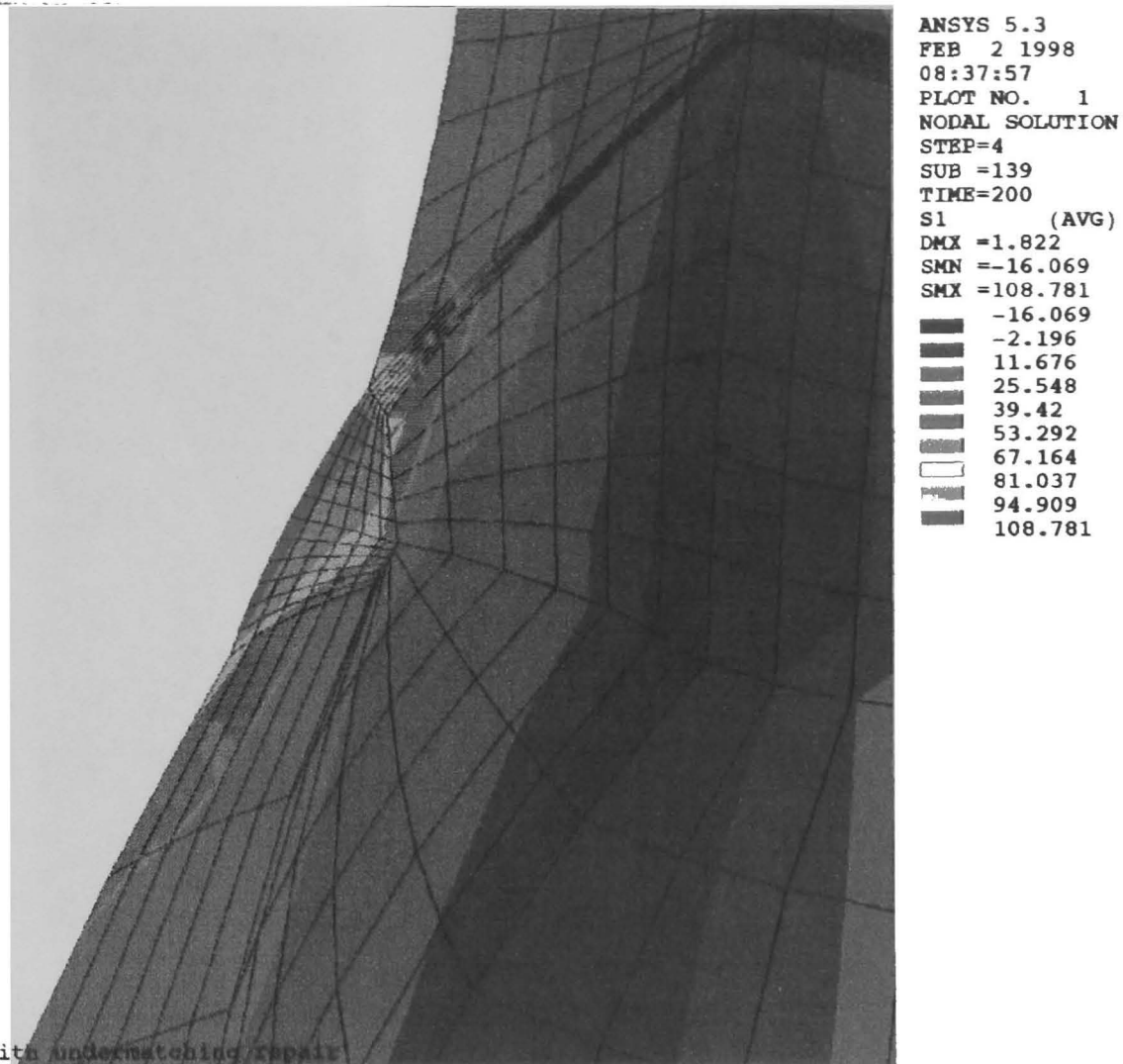


```

ANSYS 5.3
FEB 2 1998
08:57:32
PLOT NO. 1
NODAL SOLUTION
STEP=1
SUB =1
TIME=.100E-08
S1 (AVG)
DMX =.089926
SMN =3.38
SMX =160.093
3.38
20.792
38.205
55.617
73.03
90.443
107.855
125.268
142.68
160.093

```

Figure 2.41. Maximum principal elastic stress distribution for 10CrMo910 T-branched pipe vessel used for FE modelling of weld repair (Li [122]).



T-joint with undermatching repair
 Figure 2.42. Maximum principal steady-state creep stress distribution around the weld repair at the saddle region for under-matched 10CrMo910 T-branched pipe vessel used for FE modelling of a 13CrMo44 weld repair (Li [122]).

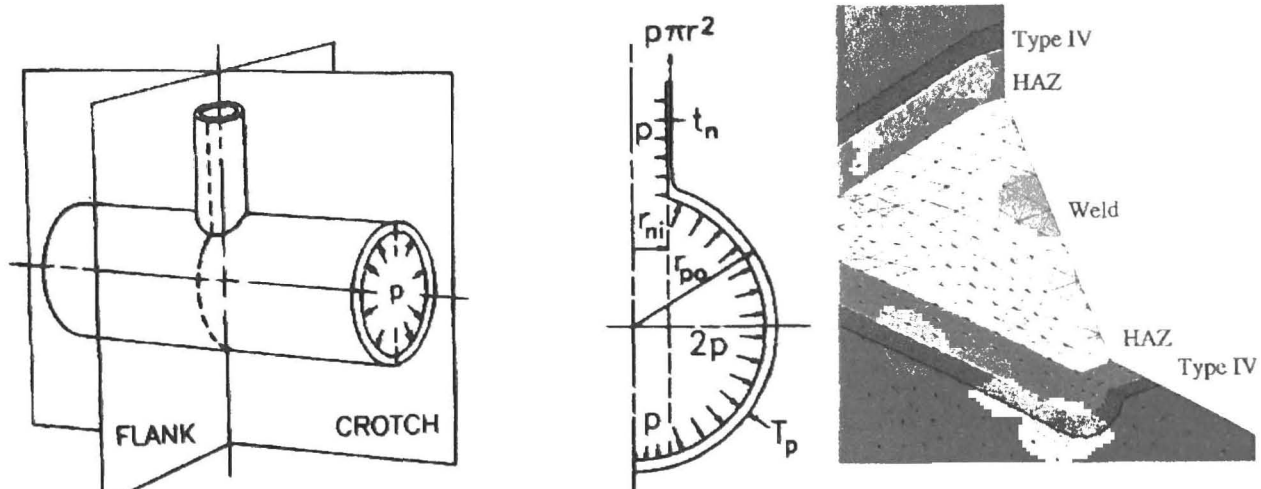


Figure 2.43. Finite element mesh and weldment geometry used by Hayhurst [87] for CDM calculations of a sphere-branch idealised intersection of a branch connection.

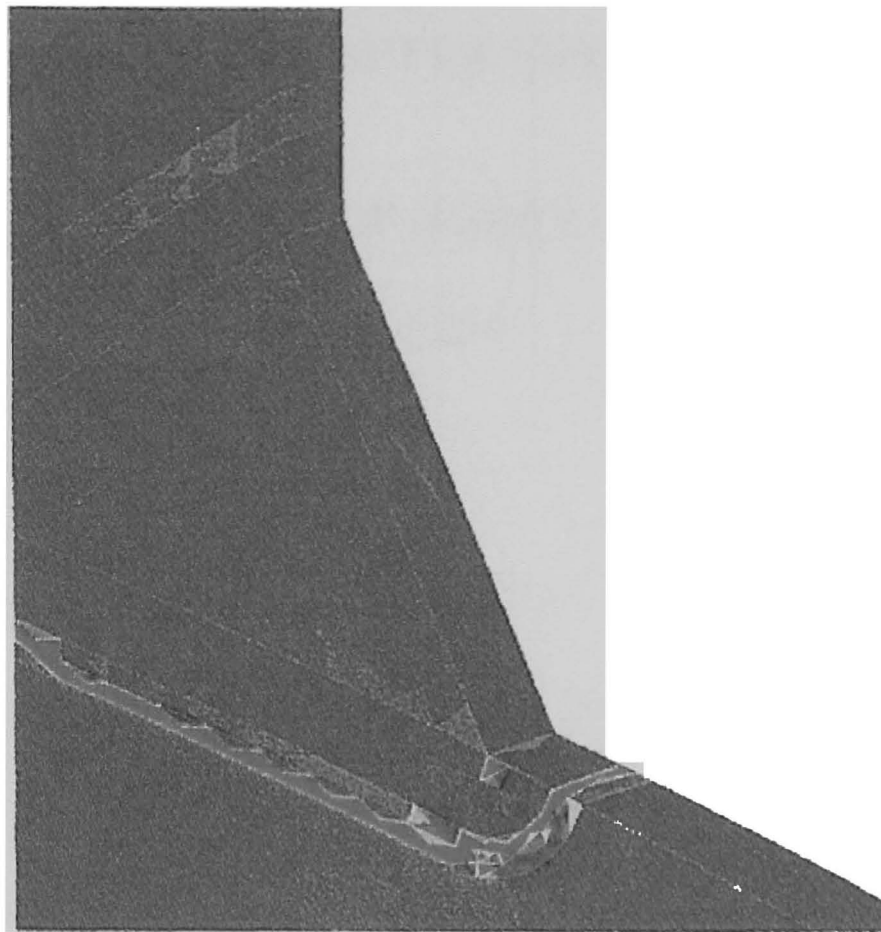


Figure 2.44. FE damage distribution from a CDM calculation of a sphere-branch idealised intersection of a branch connection (Hayhurst [87]).

CHAPTER THREE

CREEP BEHAVIOUR OF HOMOGENEOUS BRANCHED PIPES

3.1 General

Chapter Two describes how creep behaviour has been extensively researched and a large amount of knowledge has been gained, the bulk of this knowledge has been on a fundamental level, involving material property determination and analysis/design methods generally within the context of fairly simplified connection geometries. Section 2.6 identified that the understanding of the creep behaviour of realistic thick-walled branched pipe connections, with realistic material properties, is an area which needs additional research. This is the context of the present work. The sizes of such branches can vary significantly relative to that of the main steam pipe. The effect of specific dimensions and materials on the creep behaviour of the connection requires investigation using parametric studies, in particular, the dimensions; branch diameter, d , branch pipe thickness, t , and the weld size, and the material properties; steady-state Norton exponent, n , from Equation 2.3, and multi-axial rupture property, α , from Equation 2.8. The effects of these parameters on the steady-state creep stress distributions and peak stress values and positions are an important element to understanding this creep behaviour, for the purpose of improving creep life assessments. The understanding of these effects for

homogeneous branched pipe connections are required before the assessment of the inhomogeneous weldment is considered.

A large range of typical branched pipe geometries are considered within the investigation, varying from small branches, i.e. $d/D = 0.14$, up to equal branch-to-pipe diameter ratios, i.e. $d/D = 1$, for different branch thicknesses, t . For this study, the models assume a homogeneous material throughout, i.e. separate weld and heat affected zone material properties are not modelled, but the weld profile geometry is included and the effect of variations in the weld size is also studied. A range of material creep properties, covering different Norton's steady-state creep exponent value, n , from 3 to 9, and multi-axial rupture behaviour constant α values, from 0 to 1 are studied.

Exact analytical solutions cannot generally be obtained for the stress distributions within branched connections due to the complexity of the problem. The finite element (FE) method is therefore often used to analyse the behaviour of specific dimensions, loadings and materials of branched connections under steady-state creep conditions.

British design codes BS5500 [11] and BS1113 [12] base their design operating stresses for branched pipes on the elastic mean diameter hoop stress, σ_{mdh} , of the main pipe, as given, for example, by the following expression for the design operating stress, σ_b , of single, isolated branch connections:

$$\sigma_b = p_i \left[\frac{(D - 2T)(c \cdot a_1)}{2T\gamma} + 0.5 \right] \quad (3.1)$$

with the addition of a branch modification factor, Ca_1 , which depends on the branch and main pipe dimensions, p_i is the applied internal pressure, D and T are the main pipe mean diameter and wall thickness, respectively, and γ is a constant which depends on system loading. However, the effects of specific material properties on the internal stresses are not considered in the codes, which could greatly affect the accuracy of the codes life predictions. Booth [115] suggests the use of the inverse application of these codes to calculate rupture stresses at such connections and then using these with relevant rupture data to predict creep rupture lives. The term inverse use of the code is used because the codes are normally used in design purposes by fixing a level of stress within the branch which is acceptable for the material being used to fabricate the connection. Using this chosen level of stress within the code, the calculation of minimum thickness of the main and branch pipes is then made. The inverse use is the reverse of this procedure. Where all dimensions are known and a level of stress can then be predicted for the branched pipe. This study makes comparisons between the peak steady-state creep stresses within the components and the BS inverse code rupture stresses, as defined by Booth [115] using Equation 3.1, for various geometries and materials, to gain understanding of the conservatism of the BS codes.

The creep steady-state results are presented in the form of a normalised peak rupture stress, $\bar{\sigma}_r$, which is the maximum rupture stress within the connection divided by the mean diameter hoop stress of the main pipe, σ_{mdh} , where:

$$\sigma_{mdh} = \frac{p_i(D-T)}{2T} \quad (3.2)$$

A normalised equivalent stress, $\bar{\sigma}_{eq}$, and maximum principal stress, $\bar{\sigma}_1$, are similarly obtained. Hence, for the main pipe dimensions used throughout this study, i.e. $D = 355$ mm, $T = 65$ mm, with $p_i = 16.55$ MPa, the mean diameter hoop stress σ_{mdh} is 36.92 MPa. Such normalised forms of stress are instructive for comparative purposes.

3.2 Background theory

As explained in Section 2.3.2, uniaxial steady-state creep behaviour is commonly defined by Norton's law, which expresses the steady-state creep strain rate as an exponential function of stress, as shown by Equation 2.2. Where A and n are material constants and σ is the applied uniaxial stress. The present work is concerned with multiaxial stress-states and consequently the multiaxial creep strain rate is obtained using the multiaxial generalisation of Norton's creep law, which is shown by Equation 2.3. As proposed by Hyde and co-workers [33,34], from the steady-state stress distributions, a peak value of rupture stress within the component, σ_r , [10] can be calculated using Equation 2.8 to model material and component failure using the σ_{eq} , σ_1 and material property, α . This steady-state rupture stress can then be used with a rupture life equation, such as Equation 2.9 [33], to predict the life of the component.

Continuum damage mechanics methods have also been implemented within FE codes for analyses of the creep rupture process, e.g. [20,30,88]. However, although this approach provides more detailed results, there is a significant

computational overhead associated with such damage simulations and often the material constants required (i.e. M, m, ϕ, χ) may not be widely available. Previous steady-state investigations, e.g. [23,33,34], have shown the steady-state rupture approach to give reasonably conservative estimates of failure times of welds compared to the alternative CDM approach.

3.3 Geometries and FE models

Figure 3.1 is a scatter plot of statistical data showing the relationship between typical UK branch and main pipe radius to thickness ratios, as obtained from the three main UK power generation companies, namely Powergen, British Energy and Innogy [125-127]. The equal pressure line ($r_m/t = R_m/T$) (where R_m and r_m are the mean radius of the main and branch pipe, respectively and T and t are the main and branch pipe wall thickness, respectively) is shown on the graph to facilitate comparison between the general design of the branches with respect to pipe or branch strengthening, also, the data shows that the connections are generally near the equal pressure line for all three companies, the majority being above, showing a preference for branch strengthening. The majority of the data is situated around the small pipe and small branch ratios, i.e. $R_m/T=2$ and $r_m/t=2$, i.e. thick-walled connections.

This strengthening is used within branched pipe design and will be used in this investigation to reflect realistic connection geometries. The dimensions chosen were used to base the geometry close to the average radius/thickness ratios in Figure 3.1. Therefore the datum R_m/T and r_m/t value chosen was 2.23, which

corresponds to an equal pressure configuration of a typical UK ferretic CrMoV main steam pipe size of $D=355\text{mm}$ and $T=65\text{mm}$ [125-127]. This main pipe size was kept constant for all analyses, while the branch dimensions were varied to give branch pressure-strengthened, i.e. $R_m/T > r_m/t$, and main pipe pressure-strengthened, i.e. $R_m/T < r_m/t$, cases. The degree of strengthening was chosen to be 33% of R_m/T in both cases, i.e. $r_m/t = 1.5$ for branch strengthening and $r_m/t = 2.96$ for pipe strengthening. The branch thicknesses chosen for investigation were: 12.5mm (which is practically the smallest branch thickness used for this application), 20mm, 30mm, 40mm and 65mm (for the equal diameter pipe to branch connection). Figure 3.2 shows the geometry definition of the branched pipe configuration.

The size of the weld between the branch and the main pipe outer surfaces was defined by the parameters b_x (width) and b_y (height), shown in Figure 3.2, where these widths are maintained around the whole circumferences of branch and main pipe. The base case weld dimensions were fixed at $b_x = 25\text{mm}$ and $b_y = 30\text{mm}$ and these were also varied to investigate the size effect of the weld for different sizes of the branch. The weld dimensions chosen were typical for their application to main steam power plant [125-127].

Table 3.1 contains a summary of the dimensions used for the analyses carried out in the present investigation; the Norton material exponent, n , is also included. As shown in Table 3.1, the investigation is divided into a number of

different phases of analyses, each focussing on a different aspect, as described in the following:

Phase 1: Simultaneous investigation of the effect of branch diameter, d , and creep exponent, n , for a constant branch thickness of 12.5mm, including cases of pipe strengthening, branch strengthening and equal strength branches.

Phase 2: Same as Phase 1, but with a constant branch thickness of 20mm.

Phase 3: Investigation of weld size effect.

Phase 4: Same as Phase 1, but with a constant branch thickness of 30mm and constant n value of 6.

Phase 5: Same as Phase 4, but with a constant branch thickness of 40mm.

Phase 6: Equal branch to main pipe dimensions with a constant n value of 6.

The FE models used 20-noded brick elements with reduced integration to generate the required 3D branched pipe model. Global- and sub-modelling techniques were used to gain an efficient balance between solution accuracy and processing time. The sub-model incorporates the connection region with additional mesh refinement compared to the global-model. Examples of a global and sub-model are shown in Figures 3.3a and 3.3b, respectively. Preliminary global and sub-model analyses were run and the sub-model showed it was capable of producing reliable stress solutions at the highly stressed connection region. Mesh convergence studies were also carried out on various refined versions of the sub-model and a mesh that predicted accurate

creep stress values was chosen. Appendix 1 provides some general guidelines on how FE analysis can be utilized to effectively predict steady-state stress distributions.

For each of the geometries in Table 3.1 a global and a sub-model mesh were generated, except for the larger d/D ratios. For these cases, a more refined global model was used instead of the sub-model to reduce computational time, whilst the level of solution accuracy was maintained by mesh convergence studies of the new refined global mesh. The weld was modelled with the inclusion of radii at the weld edges (weld foot and neck) to model typical surface grinding, which is used to reduce high stress concentrations at this position. These weld radii, denoted as r_o and r_l for the weld neck and toe, respectively, are shown in Figure 3.2 and are fixed at 6mm for all geometry cases. All meshes were generated using an automatic mesh generation program developed by the author called GBRANCH and SBRANCH [128], which generates FE meshes of branched pipes for a large range of dimensions for the parameters defined in Figure 3.2.

The main and branch pipe were subjected to a typical internal pressure, p_i , of 16.55MPa and a mean axial end load, $\bar{\sigma}_a$, given by

$$\bar{\sigma}_a = p_i \left[\frac{1 \left(\frac{\text{diameter}}{\text{thickness}} \right) - 1}{2} \right]^2 / \left[\left(\frac{\text{diameter}}{\text{thickness}} \right) - 1 \right] \quad (3.3)$$

where the outside diameter to thickness ratio for the main pipe is defined as D/T , and the branch ratio is d/t . This axial end load corresponds to a closed end condition for the end of each pipe. The free ends of the main pipe and

branch were constrained to have uniform displacements in the axial directions. The analyses were performed using the ABAQUS FE code [28] and pre- and post-processing was carried out using the FEMGV package [129].

3.4 Material properties

To investigate the effects of Norton creep exponent, n , on the peak stress values and stress distributions within the homogeneous connections, n values of 3, 6 and 9 were used, for a range of geometries, as shown in Table 3.1. This range of n values is representative of materials commonly used for steam pipe applications [35,84]. In this study, specific attention is paid to materials with an n value of 6 as fossil-fuelled plants CrMoV materials typically have values close to this [35].

To find representative rupture stresses, σ_r , using Equation 2.8 a full range of the material constant α was used i.e. from 0 to 1 for all geometry cases. These peak σ_r were then plotted for different branch dimensions to establish the effect of α . The steady-state failure site was taken throughout to correspond to the position of peak FE σ_r in the connection [26].

3.5 Results

FE analyses were performed giving steady-state creep stress distributions for equivalent (von-Mises) stress, σ_{eq} , maximum principal stress, σ_1 , and rupture stress, σ_r . The peak values of σ_{eq} , σ_1 , and σ_r were obtained, the latter by a

combination of σ_{eq} and σ_1 using Equation 2.8, dependent on the value of α , for each geometry and material case shown in Table 3.1. The effects of geometry and material properties were then investigated. The peak rupture stresses were then compared to those predicted by the BS code [11,12] using Booth's [115] operating stresses for each geometry type, including the effect of different material properties, to establish the conservatism of the code, relative to the steady-state analyses. The BS system loading factor γ , of Equation 3.1 was assumed to be unity throughout, as additional system loading was not applied to the connections.

3.5.1 Stress distributions

Examples of typical σ_r (with $\alpha = 0.3$), σ_{eq} and σ_1 steady-state stress distributions within the sub-model connection are shown in Figures 3.4a, 3.4b and 3.4c, respectively. The distributions relate to analysis number 5 of Table 3.1 for branch dimensions and material of $d=68.3\text{mm}$ and $t=12.5\text{mm}$, and $n=6$, respectively. It can be seen that the distributions are non-uniform in all cases. The highest stress concentration region for σ_r and σ_{eq} are seen on the inside surface of the branch, along the longitudinal plane of symmetry (crotch-plane) and near to the inside bore of the main pipe (shown by point A in Figure 3.4b). The peak σ_1 value within the component was found on the same plane as the peak σ_{eq} and σ_r positions, but nearer the weld region and just inside from the inner-surface of the branch. The minimum σ_{eq} , σ_1 and σ_r stressed region was located in the main pipe section of the connection, near the intersection region on the plane of transverse symmetry (flank-plane), shown by point B in Figure

3.4b. The rupture, equivalent and maximum principal stress distributions in the weld region are relatively low compared to the high stress around point A. However, the stresses do increase around the weld foot (e.g. for analysis number 5, up to 66% of the σ_{eq} and σ_r values at point A). These higher stresses are produced by the relatively sharp weld outer edges, especially at the flank weld toe, represented by point C in Figure 3.4b. This emphasises how important effective weld grinding is to reduce stress concentrations at the weld toe. The effect of weld size on peak stress behaviour is dealt with in Section 3.5.4. Additionally, relatively high stresses were also found on the inside branch bore on the crotch-plane across the weld region, shown by point D in Figure 3.4b. Both of these high stress concentrations in the weld region are produced by geometry effects. These relatively high stresses therefore may dramatically affect the life and stress behaviour of the welded component when combined with different weld creep properties, producing larger mis-matches in stress across and along the weld. This is especially true when considering the weaker properties of the heat-affected zones (HAZ) and its effects on reducing creep life of the connection. Further study is therefore required in investigating the effect of such properties on stress behaviour, material mis-match and possible life reduction of the branched connection. These regions of high stress concentrations were common among all geometry and material ranges investigated within the study, therefore concluding that the weakest regions of thick-walled connections with r/t less than 3 will generally be located in these regions.

3.5.2 The effects of material properties

The effects of material properties on the stress distributions and peak stresses were investigated for several geometries (Phase 1 and 2 of Table 3.1); this involved varying the creep exponent value, n , within a realistic range and the variation of the material's α value.

The effect of the creep exponent value, n , on the peak normalised rupture stress within the component (with $\alpha = 0.3$) is shown in Figure 3.5 for several cases of different branch dimensions. The peak stresses were all found approximately at Position A of Figure 3.4b. The graph shows a plot of this stress against the reciprocal of creep exponent, i.e. $\frac{1}{n}$. The curves all follow a 'near linear' relationship described by Calladine [36]. The curves show that as the value of creep exponent is increased from 3 to 9 the peak stress within the component decreases by around 28% for the geometries considered. Calladine states that this result does not contradict intuition and holds as a general behaviour for all components [36].

The effect of the multi-axial rupture constant α on the peak rupture stress was investigated for varying branch diameters and thicknesses. Figures 3.6a and 3.6b show the variation of peak rupture stress over the full range of α (i.e. from 0 to 1) for branch thicknesses of 12.5 mm and 20 mm, respectively, and for different branch diameters with $n=6$. The rupture stress decreases uniformly from a maximum value at $\alpha=0$ to a minimum at approximately $\alpha=0.5$, but increases slightly as α approaches 1. This trend is seen to be

independent of branch dimensions. Note that the peak equivalent stress in the component ($\alpha = 0$) is larger than the peak maximum principal stress ($\alpha = 1$) due to the third principal stress being compressive in nature around the region of Position A. This position dominates the peak stress value in the range of $0 \leq \alpha \leq 0.5$. The small increase in σ_r for $\alpha > 0.5$ is due to the peak rupture stress position moving slightly closer to the weld connection region, i.e. moving away slightly from Point A, nearer to Point D of Figure 3.4b, where this position has a higher σ_1 concentration than point A (see Figures 3.4b and 3.4c).

3.5.3 The size effect of the branch

Within this investigation, the effect of varying two branch dimensions was studied. Firstly, the branch diameter and secondly the branch thickness. The ratio r/t was however maintained within a realistic range, i.e. $r_m/t=1.5, 2.23$ and 2.96 [125-127]. For this investigation all cases had a creep exponent, n , value of 6.

Calculations were performed for branch thicknesses $t=12.5\text{mm}, 20\text{mm}, 30\text{mm}, 40\text{mm}$ and 65mm . For all cases except $t=65\text{mm}$ (case 31 in Table 3.1), the above values were considered for the three r_m/t values. These are included in Table 3.1, namely, cases 2, 5, 8, 10, 12, 15, 18, 7 and 26 to 31. Constant weld dimensions of $b_x=25\text{mm}$ and $b_y=30\text{mm}$ were used throughout.

In all cases the peak σ_r , σ_1 and σ_{eq} values within the components occurred near point A, along the line y_0 , shown in Figure 3.4b, i.e. near the inside surface of the main pipe on the crotch plane. The peak σ_r , σ_1 and σ_{eq} stress positions therefore did not deviate significantly for the geometry range analysed. For example, the rupture and equivalent stress distributions along the line y_0 are shown in Figure 3.7 for a small branch size ($t=12.5\text{mm}$, $d=50\text{mm}$) and a large branch size ($t=40\text{mm}$, $d=160\text{mm}$). Note that the line y_0 starts from the inside crotch corner and at $y_0 = 65\text{mm}$ is equivalent to the wall thickness of the main pipe, this location is constant, as $T = 65\text{mm}$ is used throughout. The $y_0 = 65\text{mm}$ position is shown on the graph to distinguish this location for the two geometries. As the graph shows, despite the large difference in branch size similar stress distributions were obtained for both geometries and both types of stress. These plots show that the rupture and equivalent stress distributions vary by less than 10% across the main pipe wall thickness, along line y_0 , i.e. from $y_0 = 0\text{mm}$ to 65mm . Similarly, the peak rupture and equivalent stress positions were found to remain effectively unchanged along the line y_0 for all cases in Table 3.1. This position is approximately 11mm from the inside bore of the main pipe along line y_0 , as shown for example in Figure 3.7.

The effect of increasing branch diameter, in the form of d/D ratio, for constant branch thickness and with $n = 6$ is shown in Figures 3.8a, 3.8b and 3.8c. Four curves are shown for each, one for each branch thickness of 12.5mm, 20mm, 30mm and 40mm. Each curve consists of three points, corresponding to r_m/t

values of 1.5, 2.23 and 2.96. In addition, the result for a d/D value of 1 with $t=65\text{mm}$ is shown.

Figure 3.8a covers the d/D range of 0.14 to 1. The graph clearly shows that as d/D increases the peak equivalent stress also increases significantly, irrespective of the branch thickness. The curves are all approximately linear and as r/t increases with increasing t the stress increases sharply. This relationship is also evident in Figure 3.8b for the rupture stresses, using an α value of 0.3. The rupture stresses are always lower than the peak equivalent stresses, due to the principal stresses being lower than the equivalent stresses in the main pipe wall. The maximum principal stress variation is shown in Figure 3.8c, where the stresses are all lower than the equivalent stress by around 10%. The other important point to note from Figures 3.8a, 3.8b and 3.8c is that increasing t for a constant d/D leads to stress reduction, as expected. For example, changing t from 12.5mm to 20mm for $d/D=0.2$, reduces the peak equivalent stress from about $1.35 \sigma_{mdh}$ to about $1.25 \sigma_{mdh}$.

The variation of peak normalised rupture stress ($\alpha = 0.3$) versus branch thickness for different r_m/t values is shown in Figure 3.9. It is apparent that as branch thickness decreases the difference in stress between the large r/t values and the small r_m/t values decreases. This suggests that for small branch diameters the choice of branch thickness is less important than for large branch diameters. Thus, for example for $t=40\text{mm}$ there is a 35% difference between the large and small r_m/t values, whereas for $t=12.5\text{mm}$ the difference is only about 10%. In conclusion, as the branch diameter increases, the branch

thickness also has to increase significantly to ensure a small r_m/t value, which results in a minimal increase in peak stress. This is simply a manifestation of the effect of r_m/t on the hoop stress, which dominates the connection stresses.

3.5.4 The effect of weld size

Increasing weld size can be seen as an indirect way of strengthening the branched connection, by reducing the stress concentration around the connection region and thus reducing the peak rupture stress at the inside surface of the pipe. Calculations were performed for the standard dimensions of $b_x=25\text{mm}$ and $b_y=30\text{mm}$ (weld 2) as well as a smaller weld of $b_x = b_y = t$ (weld 1) for $t=12.5\text{mm}$ and $t=20\text{mm}$ cases. The variation of peak rupture stress, σ_r , versus branch diameter for these two thicknesses is shown in Figure 3.10. As expected, the peak rupture stresses reduce with increasing weld size, and this reduction becomes insignificant when the branch diameter is small. The peak stresses occur along the line y_0 near Point A of Figure 3.4b. The effect of increasing weld dimensions was more significant for the smaller branch thickness, i.e. $t=12.5\text{mm}$, due to the greater degree of structural strengthening for the smaller t value.

3.5.5 Comparison with British Standards and Booth's operating stresses

Comparing the predicted rupture, equivalent and maximum principal stresses to the elastic $\sigma_{m,th}$ value is important because BS codes [11.12] base their design/operating stresses on the latter. Note that branched pipe geometry

factor, $C\alpha_1$, is used to modify the hoop stress for branched pipes within BS codes (see Equation (3.1)) to obtain a operating/rupture stress, which is then used for lower bound life prediction. It is this BS rupture stress which must be compared to the FE rupture stresses to assess the accuracy and representative nature of the BS codes and their use in creep life assessments.

The normalised σ_r , σ_{eq} and σ_1 stresses predicted for all geometry cases are shown in Figures 3.8a, 3.8b, 3.8c and 3.9. It is clear from all four graphs that the predicted stresses are always larger than the elastic σ_{mdh} value, calculated using the main pipe dimensions. The normalised rupture stresses, with $\alpha = 0.3$ and $n = 6$ of Figure 3.8b show that for small branches (i.e. $d/D < 0.2$) the rupture stress is about 15% greater than σ_{mdh} , while for large branches, σ_r is greater than 40 % of σ_{mdh} . This shows that a branched pipe connection is always more highly stressed than a plain pipe with the same main pipe dimensions. Previous FE analyses by Hyde et al [26] of a homogeneous plain pipe, using the same main pipe dimensions as this investigation, showed that the peak rupture stress for a material with a creep exponent value of 6.1 and α of 0.3 was 30.4MPa. This is significantly less than both σ_{mdh} of the plain pipe (18% lower) and σ_r for the smallest sized branched connection (28% lower).

A comparison between the FE predicted rupture stresses (with $\alpha = 0.3$ for $n = 6$) and BS/Booth's rupture stresses [11,12,115] for the same connection geometries is shown in Figure 3.11. It can be seen that the FE rupture stresses are generally significantly higher than those of the BS code; differences of up

to 15% are shown. Using these higher BS code stresses would therefore predict non-conservative creep lives compared to the equivalent steady-state lives if based on a homogeneous connection. The code stresses do however follow the same trend as the peak FE steady-state rupture stresses, i.e. similar slope gradients, indicating that the BS5500 $C\alpha_1$ factors [11] are representative for predicting operating stresses within the range of branch sizes investigated. Investigation into whether BS code stress predictions used with multi-material weldment rupture data is conservative compared to the equivalent steady-state multi-material life predictions as the difference may well reduce due to the off-loading effects within the weld. This comparison is detailed in Chapter Four. Another problem with the BS code method is that it predicts stresses for non-specific material creep properties. As the creep exponent value decreases, the peak steady-state rupture stresses will increase, making the difference with the code estimates even larger. This trend is clearly shown in Figures 3.12a and 3.12b for α values of 0 ($\sigma_r = \sigma_{eq}$) and 1 ($\sigma_r = \sigma_1$) for cases 1 to 9 of Table 3.1. For the range of d/D investigated, as n decreases from 9 to 3 for the steady-state analyses the BS code stress predictions change from being around 5% lower than the steady-state, $\alpha=0$, prediction for $n = 9$, to around 10% lower for the $n = 6$ cases and around 30% lower for the $n = 3$ cases. The differences compared for the $\alpha=1$ steady-state stresses are similar over the d/D range considered, however differences of up to 20% lower stress predictions are determined for the small d/D ratio case. Therefore, for materials with low n values the inverse use of the BS code's rupture stresses are generally non-conservative compared to the steady-state predictions and could possibly be inaccurate in predicting creep rupture lives for homogeneous connections. A

30% lower BS code stress would significantly over-predict the creep life of the branched pipe using typical rupture data in a life equation such as Equation 2.9. A similar result would occur for materials with larger values of creep exponent, but to a lesser extent, i.e. $n > 6$, e.g. for Case 22 of Table 1, where $n = 9$ and the codes stress prediction is approximately 30% larger than the σ_r ($\alpha = 0$) prediction.

3.6 Discussion and conclusions

FE steady-state analyses for a large range of branch sizes were performed assuming a homogeneous material throughout. A range of creep exponent values from Norton's law was used (i.e. $n = 3, 6$ and 9) to assess peak rupture stresses within the connection. The effect of the weld materials was ignored to facilitate extensive geometrical investigations. For all of the geometries investigated, the peak rupture, equivalent and maximum principal stresses were located near to the main pipe inside surface, at the intersection region of the branch and main pipe inside surfaces (i.e. up from the inside crotch corner). The location of peak rupture stress, taken here to be the failure site, was approximately 11mm from the inside surface of the main pipe for all geometries considered. For a larger r_m/t value of 5, the peak rupture stress was located at the inside surface of the branch, away from the connection region. The magnitude of the associated rupture stress was very large compared to corresponding stresses for the other r_m/t values investigated (i.e. $r_m/t = 1.5, 2.23$ and 2.96), suggesting that large r_m/t values should be avoided for similar operating pressures. It was found that the rupture stress distribution did not

vary significantly for the range of branch sizes and material properties considered, and common stress concentration regions were identified for all.

The effect of varying branch dimensions on the salient stresses was found to be very significant. A set increase of 73% in branch diameter was more significant on the increase in peak stress value for larger thicknesses, where for a constant thickness the peak stresses varied from around 10% for the $t = 12.5\text{mm}$ cases, up to 35% for the $t = 40\text{mm}$ cases resulted. Increasing branch thickness resulted in a decreased peak stress value for constant branch diameter; the effect was more significant for larger diameters. For small branch diameters the effect of different branch thicknesses was comparatively small, e.g. an increase in σ_{eq} of around 7% was seen for a constant d/D value of 0.22 between the use of t values 12.5mm and 20mm, which is an increase in thickness of 60%. Similarly, a difference of around 15% in peak σ_{eq} was predicted for a constant d/D value of 0.55 between the t values of 30mm and 40mm, which is an increase in thickness of 33%. The variation of peak stress with branch diameter, for constant branch thickness, was found to be approximately linear, so that interpolation could be used.

The peak rupture stress within the component was predicted to decrease by around 28% with increasing n value from 3 to 9, while the position stayed relatively constant. The variation of peak stress with the inverse of the creep exponent was found to be approximately linear, thereby establishing validity of the Calladine [36] $1/n$ interpolation technique for predicting the maximum creep stress within a component. The effect of α on peak rupture stress was

found to be significant: as α increased from 0 to 0.5 the peak rupture stress magnitude decreased by about 8% for all geometries investigated, while the peak stress position stayed relatively unchanged. As α increased from 0.5 to 1 the peak rupture stress magnitude increased slightly due to the change in the peak rupture stress position towards the weld region and away from the inside bore of the main pipe.

Weld size was shown to have a significant effect on the peak rupture stress for large diameters with relatively small thicknesses, i.e. large r_m/t ratios. In addition, the weld profile was found to be an important factor in decreasing stress concentrations around the weld foot, i.e. removing sharp weld edges, helps avoid premature weld cracking.

Comparison of the FE peak rupture stresses with the BS code stresses [11,12,115] have clearly shown that the code stresses are generally significantly lower and perhaps too low for accurate rupture life predictions for homogeneous branched pipes, such as forged and cast connections. Additionally, the code predicted rupture stresses that were not material specific, this could jeopardise estimated life spans of the connections by being non-conservative for connection materials with Norton exponents within a wide range of 3 to 9, and especially for materials with lower n values.

The results obtained have clearly shown the effects of various geometric and material parameters for an isolated branched pipe under creep conditions. The steady-state method used predicts creep stresses within the secondary creep

stage and ignores tertiary creep stress redistribution. Therefore, the conservative nature of steady-state analyses can be seen as an attractive method for calculating stresses and failure lives [26,33,39]. The investigation incorporated a homogeneous material approach in order to investigate the general stress distributions within the connections. It was identified by the results that high stress concentrations existed in the weld region and this may have a significant effect on the failure behaviour of the connection when weaker weld materials are present. Further work considering more detailed multi-material steady-state FE models incorporating weld material properties (i.e. heat-affected zones (HAZ) and weld metal) are required to investigate and fully understand the complex stress and failure behaviour of welded branched connections. These aspects are dealt with in later chapters.

Table 3.1. Branch geometry analysis details, with constant main pipe dimensions of $D=355\text{mm}$, $T=65\text{mm}$ and $R_m/T = 2.23$.

PHASE	Analysis No.	t	d	n	d/D	t/T	b_x	b_y	r_m/t	Ratio of $r_m/t / R_m/T$
1	1	12.5	50.0	3	0.14	0.192	25	30	1.50	0.67
	2	12.5	50.0	6	0.14	0.192	25	30	1.50	0.67
	3	12.5	50.0	9	0.14	0.192	25	30	1.50	0.67
	4	12.5	68.3	3	0.19	0.192	25	30	2.23	1.00
	5	12.5	68.3	6	0.19	0.192	25	30	2.23	1.00
	6	12.5	68.3	9	0.19	0.192	25	30	2.23	1.00
	7	12.5	86.5	3	0.24	0.192	25	30	2.96	1.33
	8	12.5	86.5	6	0.24	0.192	25	30	2.96	1.33
	9	12.5	86.5	9	0.24	0.192	25	30	2.96	1.33
	10	12.5	138.5	6	0.39	0.192	25	30	4.74	2.13
2	11	20.0	80.0	3	0.225	0.308	25	30	1.50	0.67
	12	20.0	80.0	6	0.225	0.308	25	30	1.50	0.67
	13	20.0	80.0	9	0.225	0.308	25	30	1.50	0.67
	14	20.0	109.2	3	0.31	0.308	25	30	2.23	1.00
	15	20.0	109.2	6	0.31	0.308	25	30	2.23	1.00
	16	20.0	109.2	9	0.31	0.308	25	30	2.23	1.00
	17	20.0	138.5	3	0.39	0.308	25	30	2.96	1.33
	18	20.0	138.5	6	0.39	0.308	25	30	2.96	1.33
	19	20.0	138.5	9	0.39	0.308	25	30	2.96	1.33
3	20	12.5	50.0	6	0.14	0.192	12.5(t)	12.5(t)	1.50	0.67
	21	12.5	86.5	6	0.24	0.192	12.5(t)	12.5(t)	2.96	1.33
	22	12.5	138.5	6	0.39	0.192	12.5(t)	12.5(t)	4.74	2.13
	23	20.0	50.0	6	0.14	0.308	20(t)	20(t)	0.75	0.34
	24	20.0	80.0	6	0.225	0.308	20(t)	20(t)	1.50	0.67
	25	20.0	138.5	6	0.39	0.308	20(t)	20(t)	2.96	1.33
4	26	30.0	120.0	6	0.34	0.462	25	30	1.50	0.67
	27	30.0	163.9	6	0.46	0.462	25	30	2.23	1.00
	28	30.0	207.7	6	0.585	0.462	25	30	2.96	1.33
5	29	40.0	160.0	6	0.45	0.615	25	30	1.50	0.67
	30	40.0	218.5	6	0.615	0.615	25	30	2.23	1.00
	31	40.0	276.9	6	0.78	0.615	25	30	2.96	1.33
6	32	65.0	355.0	6	1.00	1.00	25	30	2.23	1.00

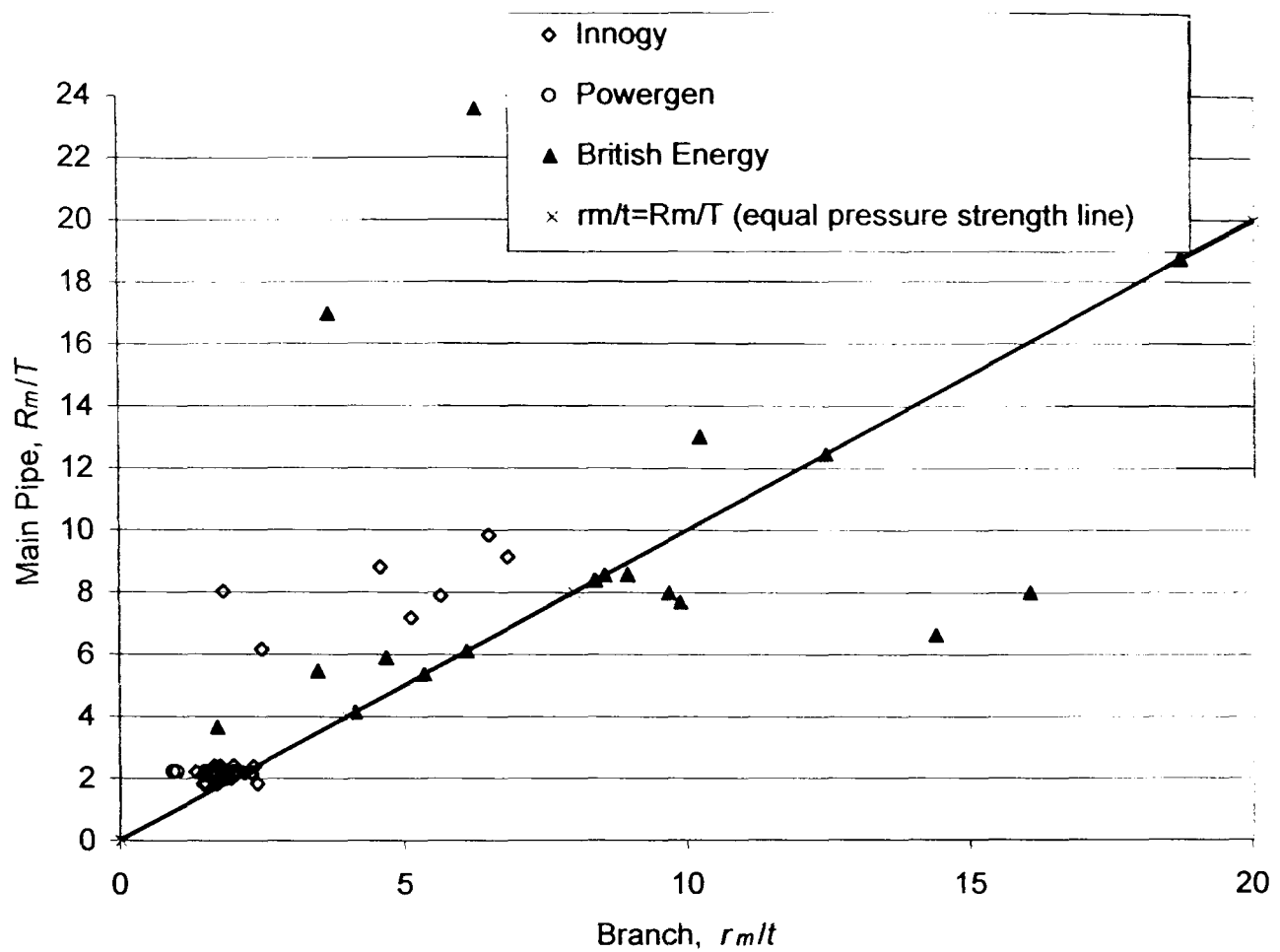


Figure 3.1. Scatter of sample geometries of r_m/t versus R_m/T for each branched pipe connection.

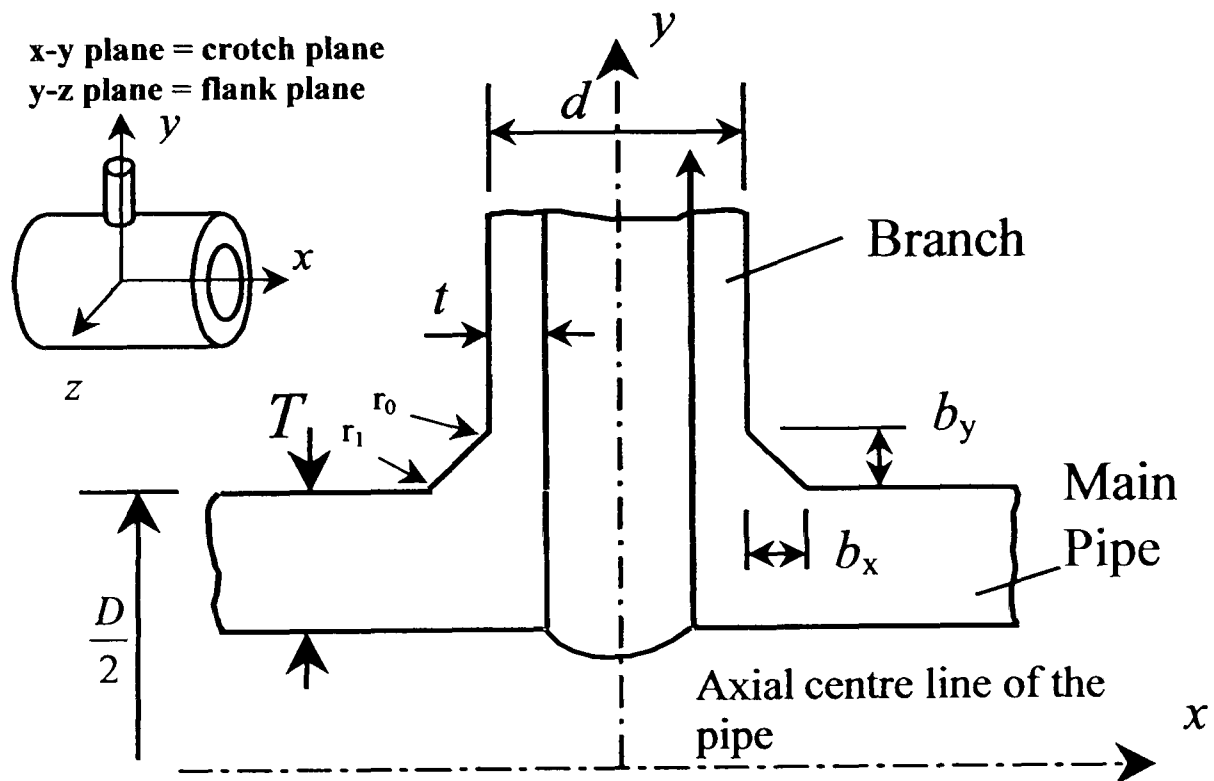


Figure 3.2. Diagram of the geometry and weld profile of the branched pipe connection.

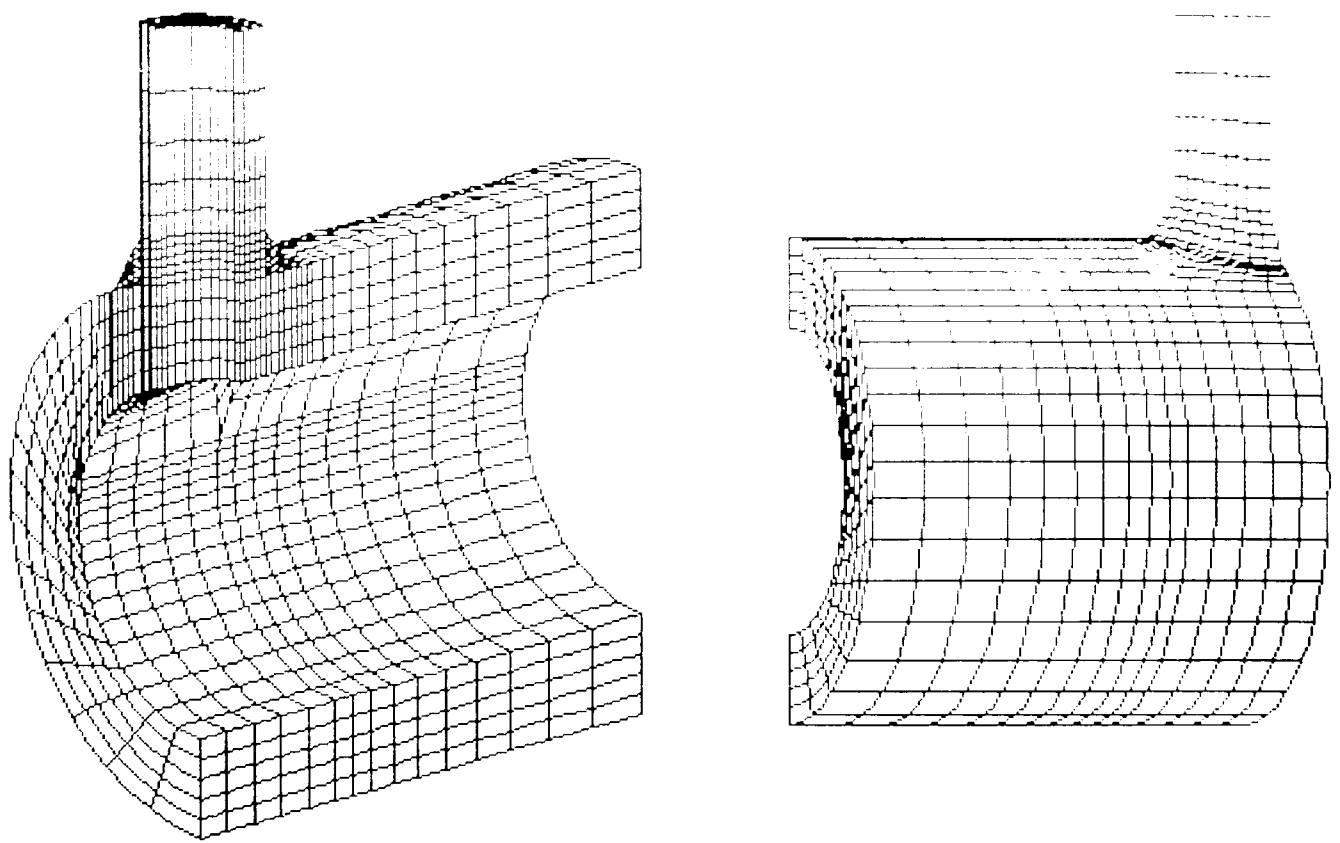


Figure 3.3a. Views of the global FE mesh of the isolated pipe to branch connection, $t=20\text{mm}$, $d=109.23\text{mm}$.

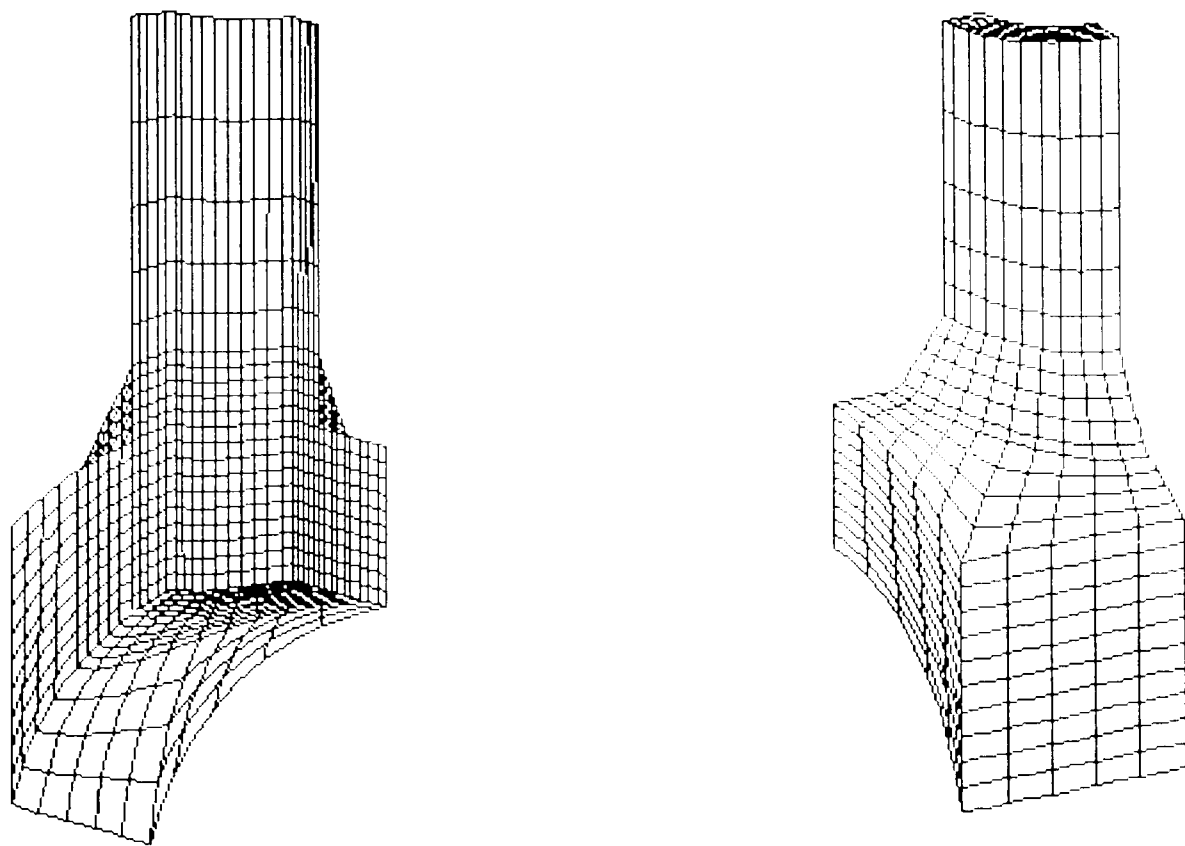


Figure 3.3b. Views of the refined FE mesh of the sub-model, $t=20\text{mm}$, $d=109.23\text{mm}$.

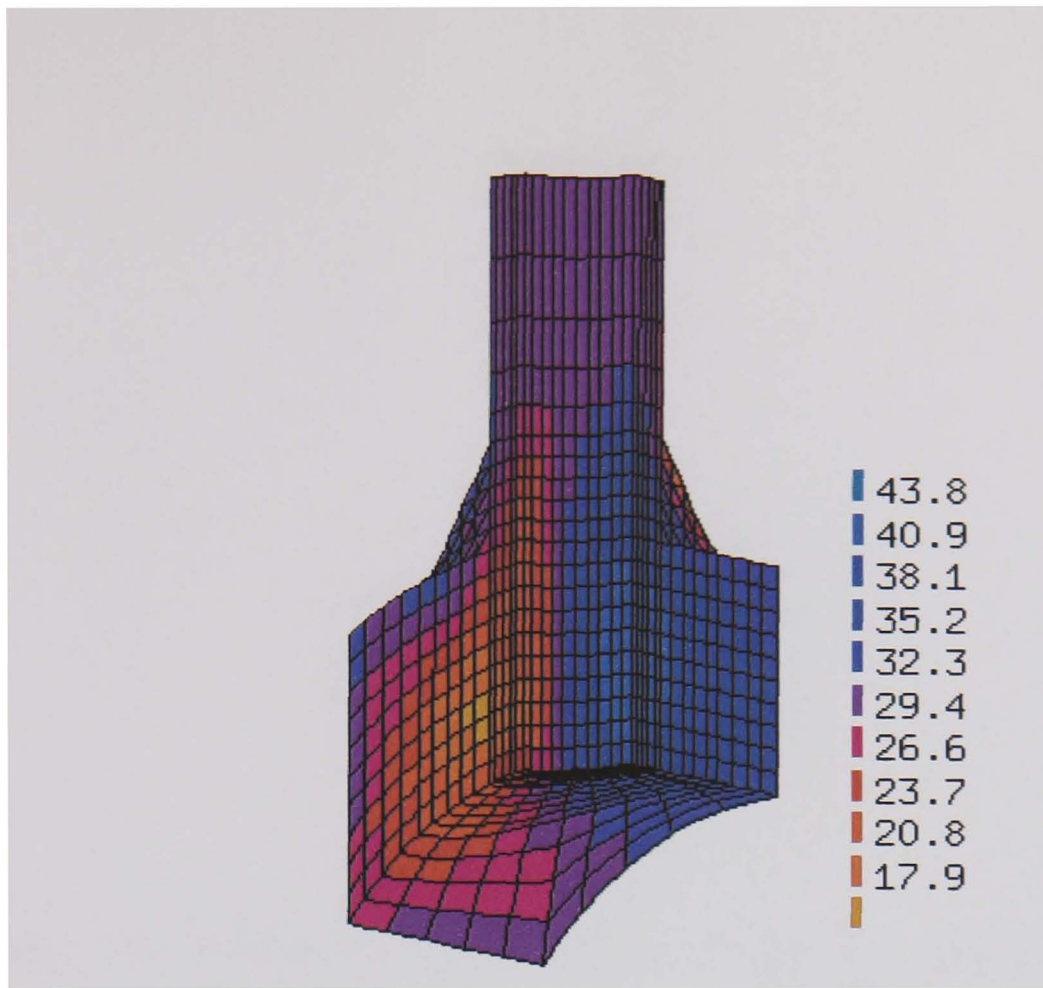


Figure 3.4a. Rupture stress, σ_r , ($\alpha=0.3$) distribution for analysis number 5, $d=68.3\text{mm}$, $t=12.5\text{mm}$ and $n=6$, units in MPa.

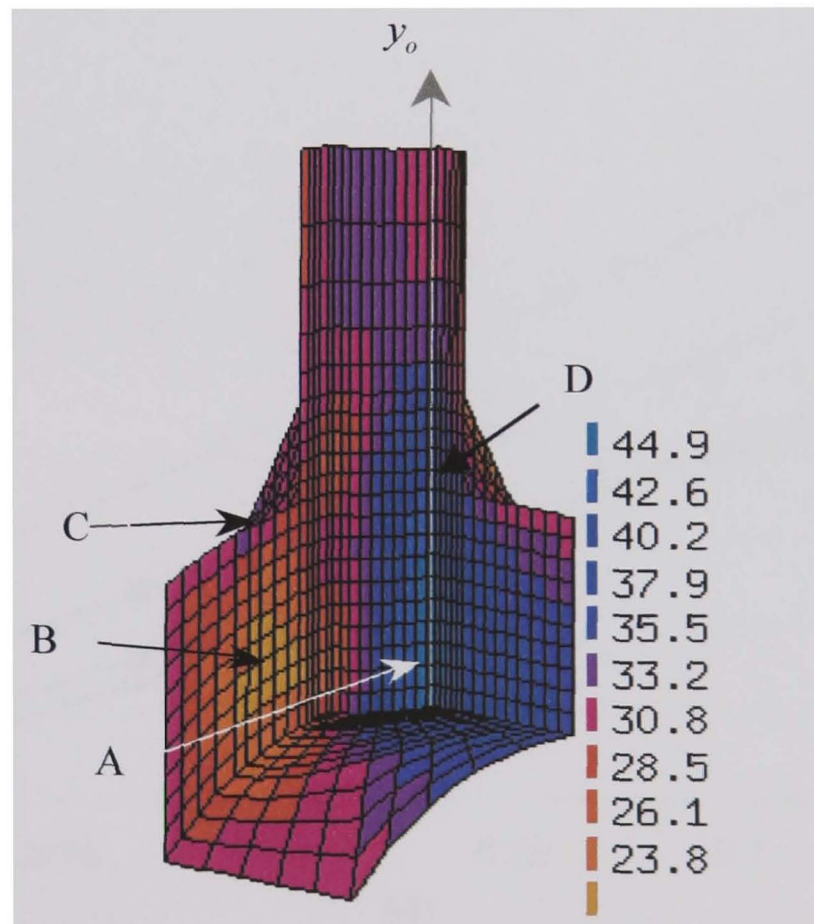


Figure 3.4b. Equivalent stress, σ_{eq} , ($\alpha=0$) distribution for analysis number 5, $d=68.3\text{mm}$, $t=12.5\text{mm}$ and $n=6$, units in MPa.

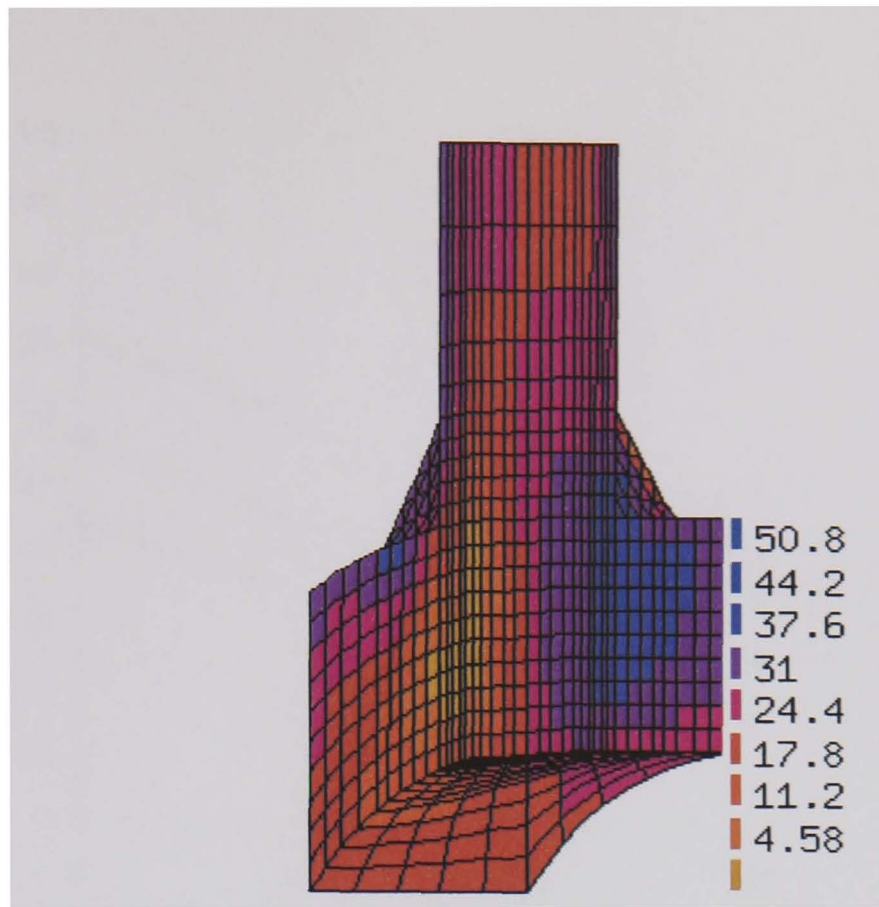


Figure 3.4c. Maximum principal stress, σ_1 , ($\alpha=1$) distribution for analysis number 5, $d=68.3\text{mm}$, $t=12.5\text{mm}$ and $n=6$, units in MPa.

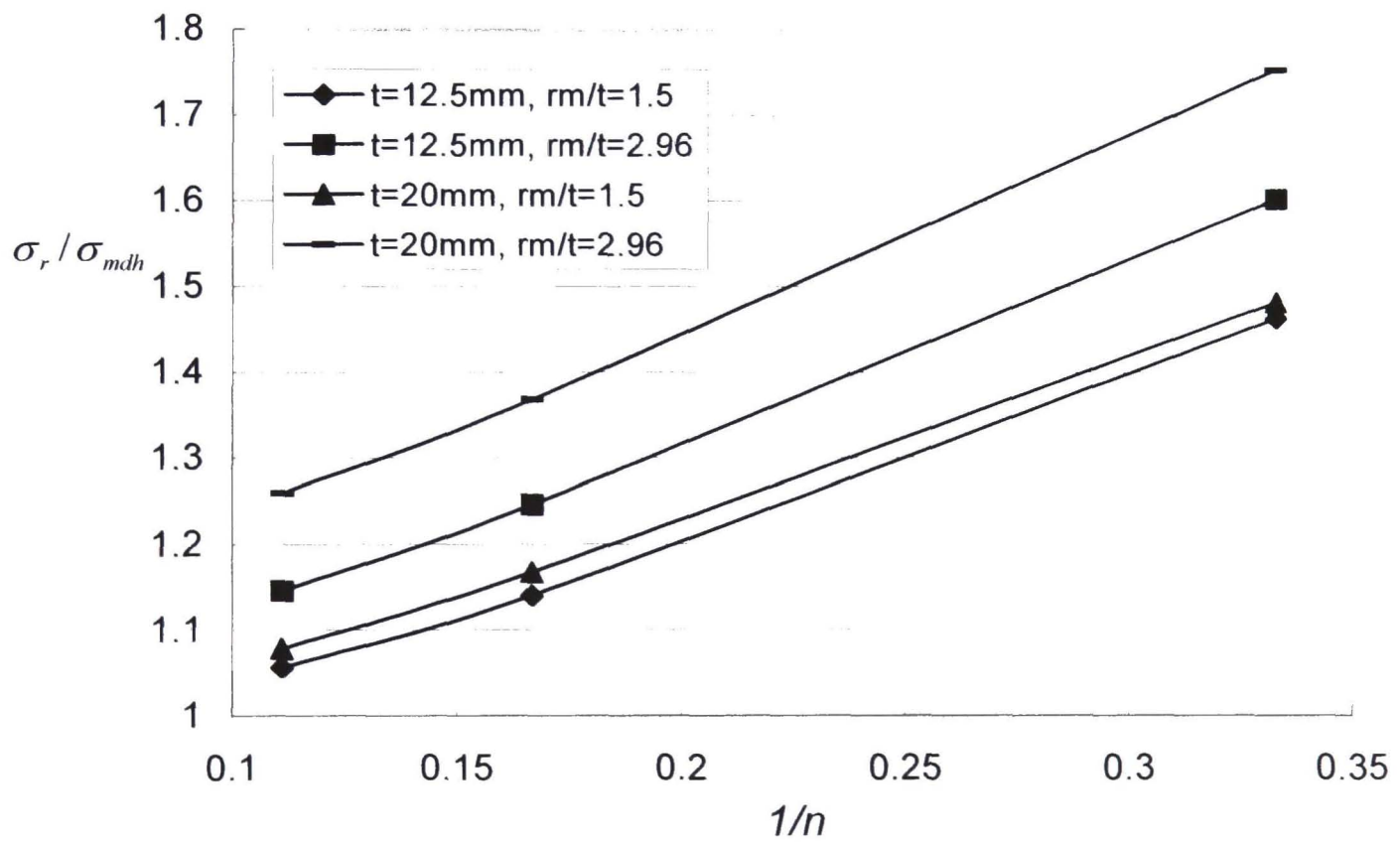


Figure 3.5. Peak normalised rupture stress variation with $1/n$ for varying branch dimensions, $\alpha=0.3$. Peak denotes the highest value within the whole component (around Position A of Figure.3.4b).

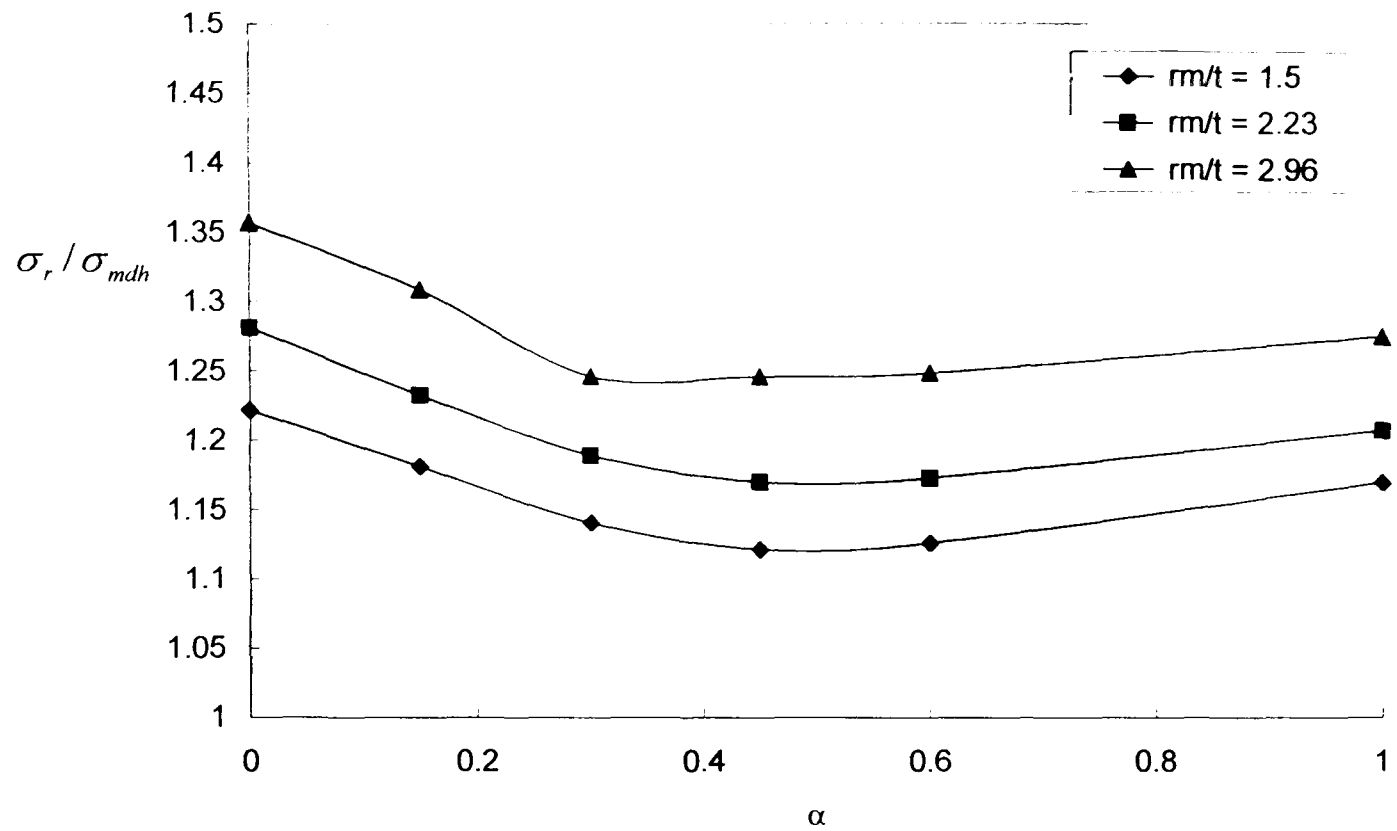


Figure 3.6a. Variation of peak normalised rupture stress with varying α value, for $n=6$ and $t=12.5\text{mm}$ cases.

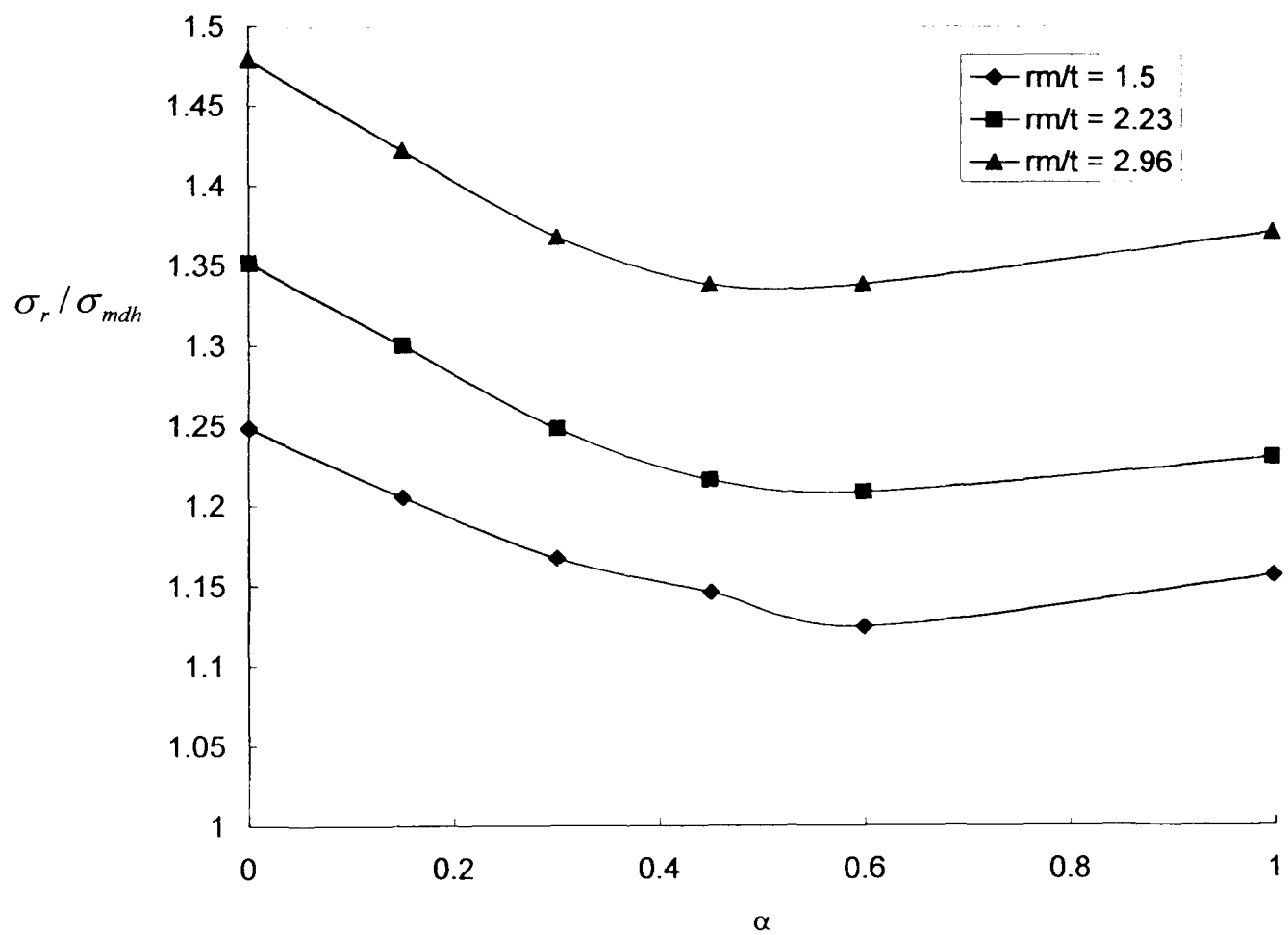


Figure 3.6b. Variation of peak normalised rupture stress for varying α values, for $n=6$ and $t=20\text{mm}$ cases.

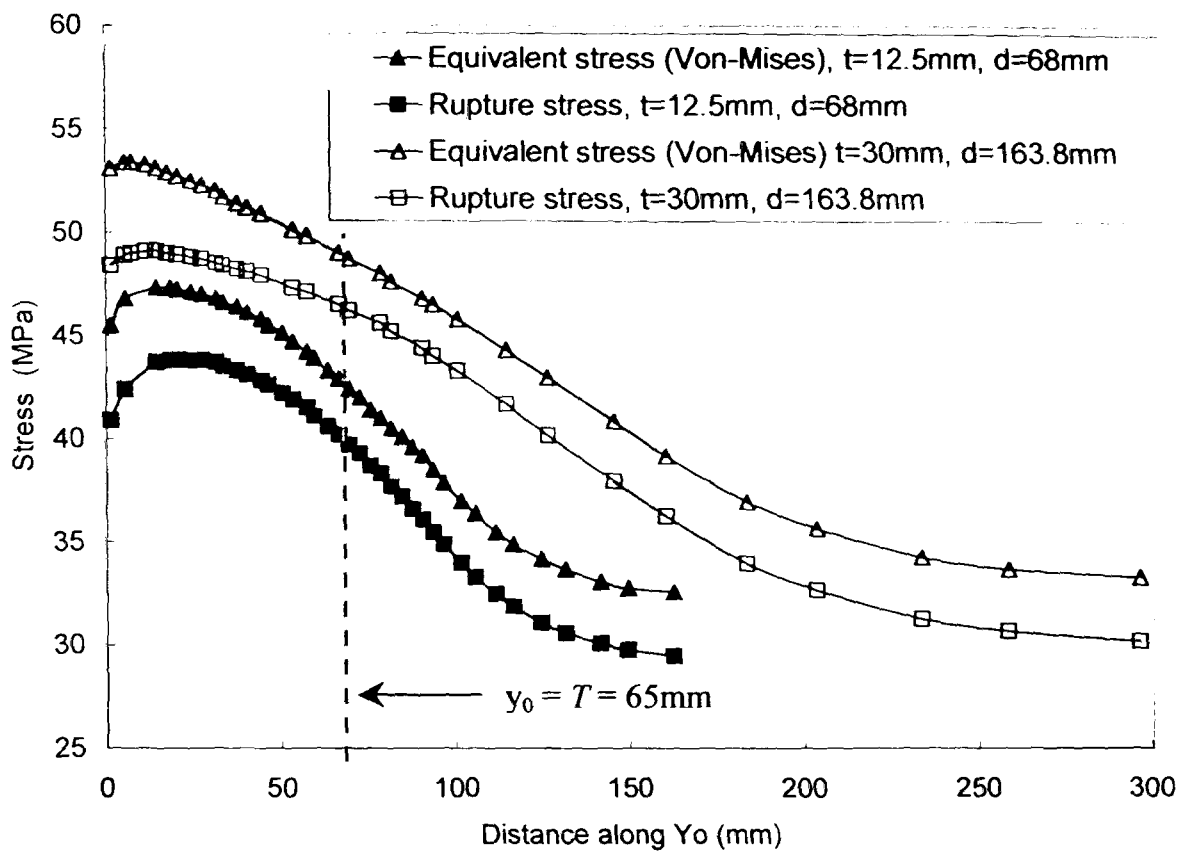


Figure 3.7. Distribution of equivalent ($\alpha = 0$) and rupture stress ($\alpha = 0.3$) along line, $n = 6$.

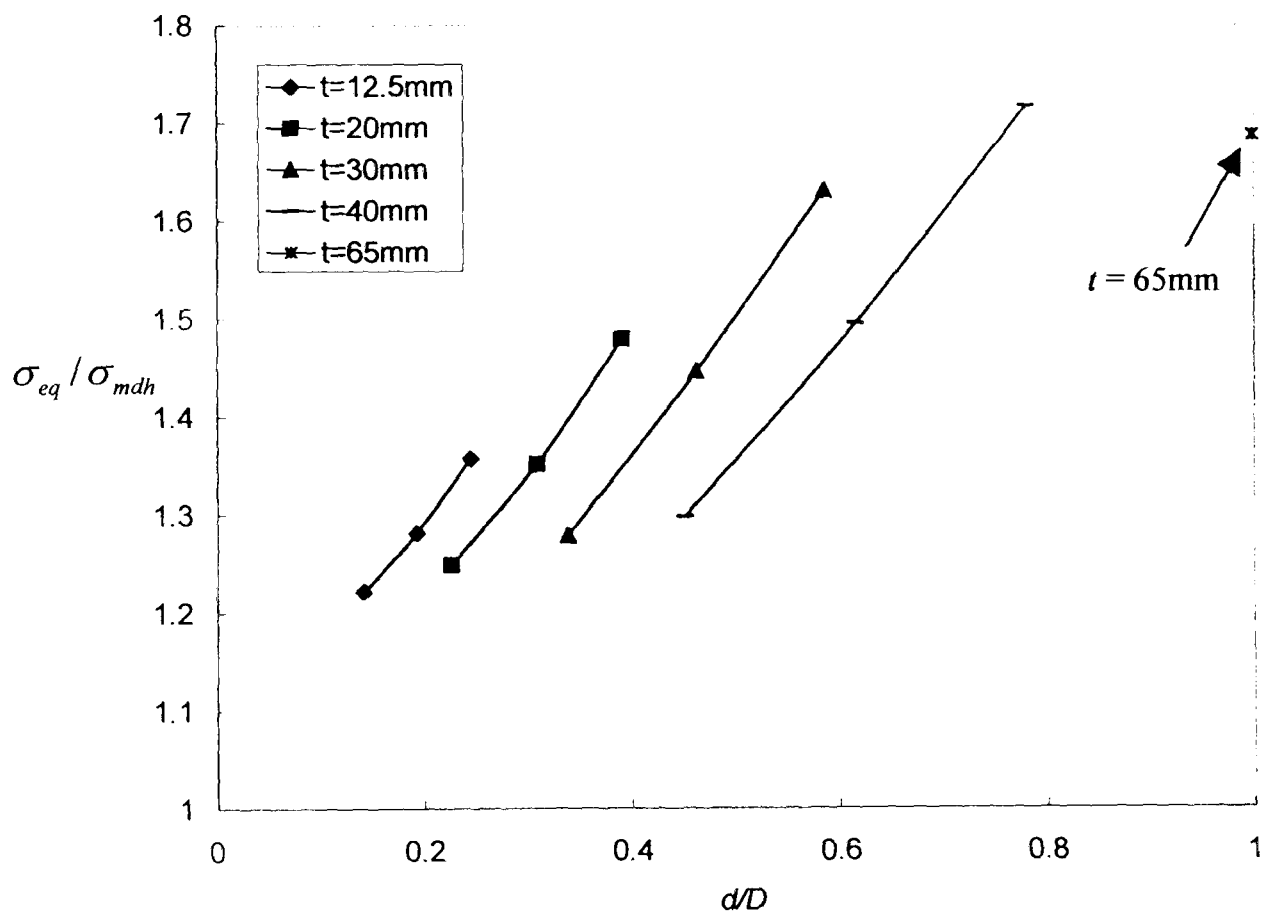


Figure 3.8a. Variation of peak normalised equivalent stress with increasing d/D ratio, for $n = 6$.

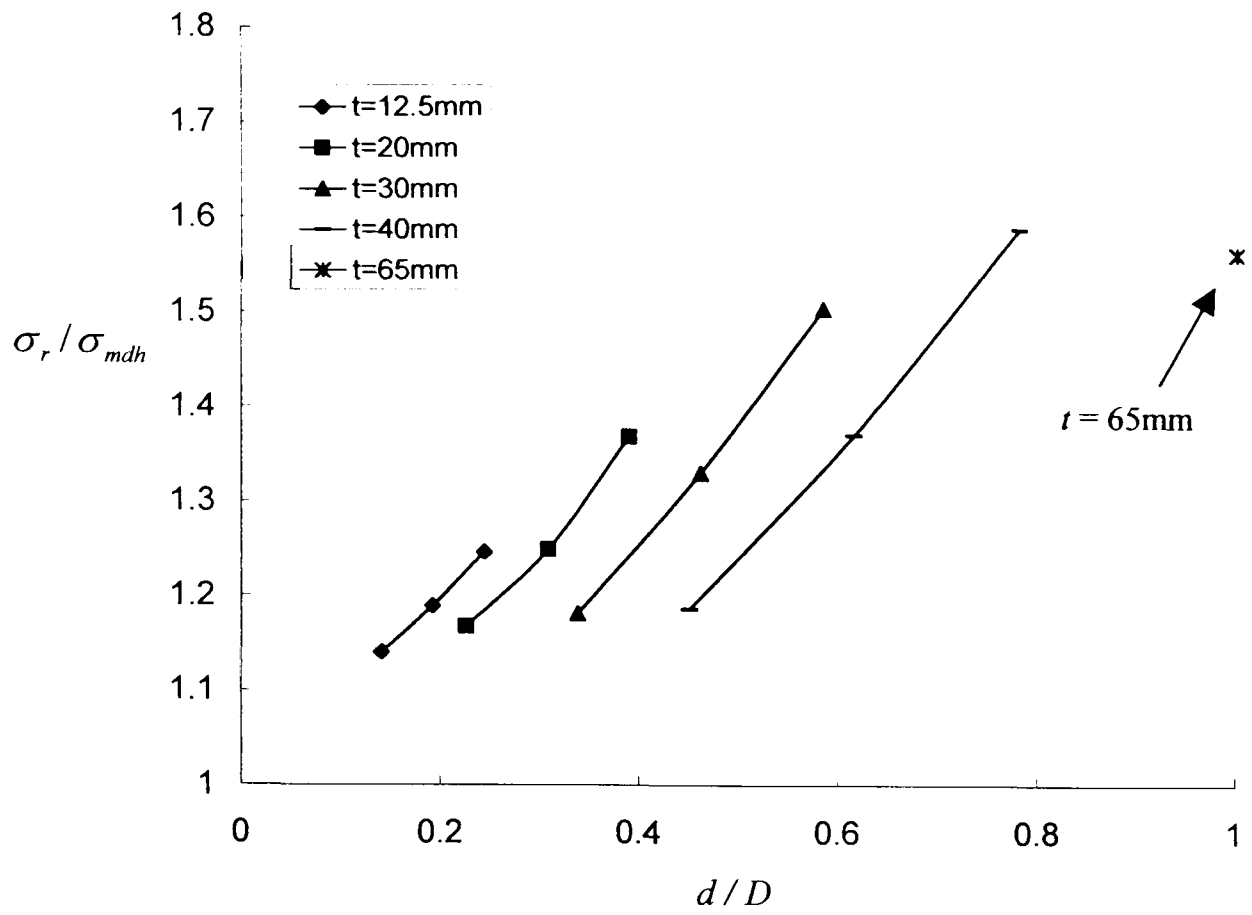


Figure 3.8b. Variation of peak normalised rupture stress with increasing d/D ratios for various thicknesses, for $n=6$ and $\alpha=0.3$.

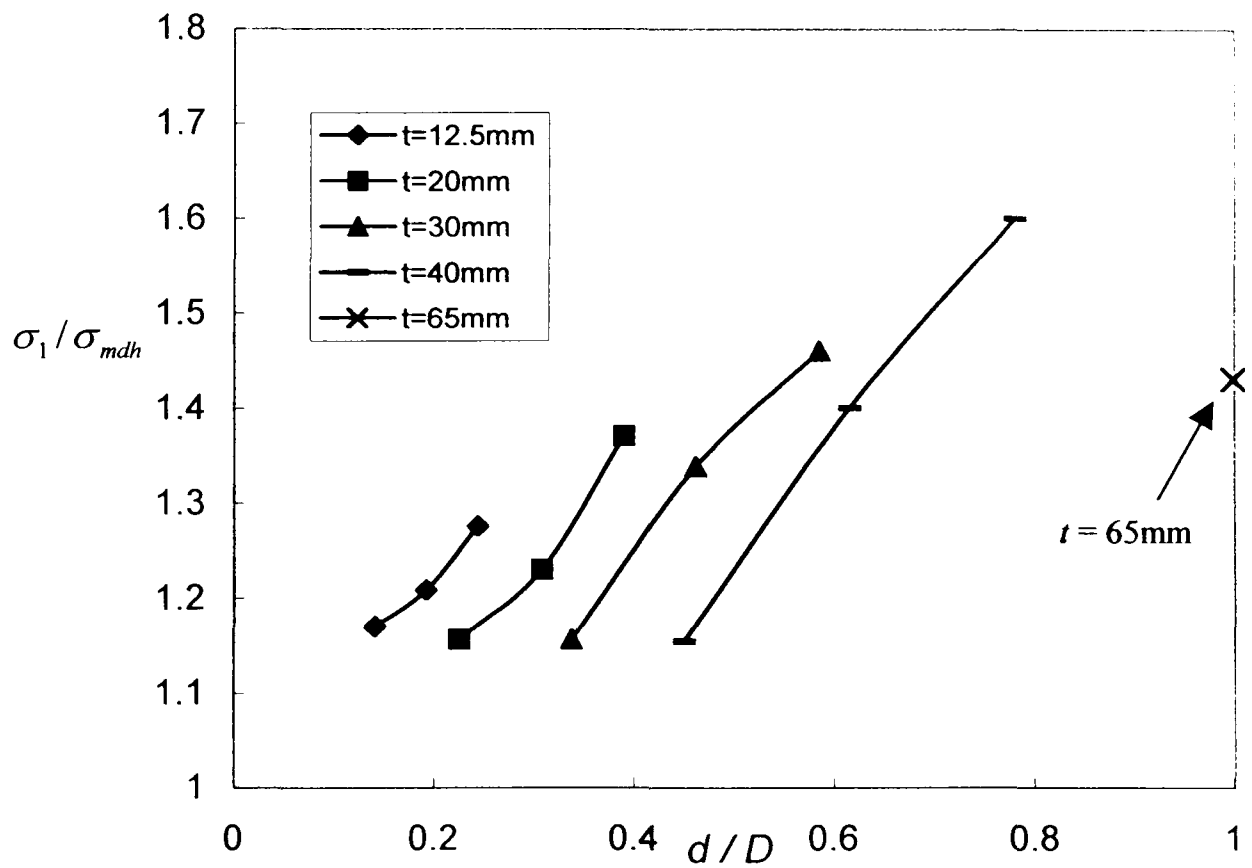


Figure 3.8c. Variation of peak normalised maximum principal stress with increasing d/D ratio, for $n=6$.

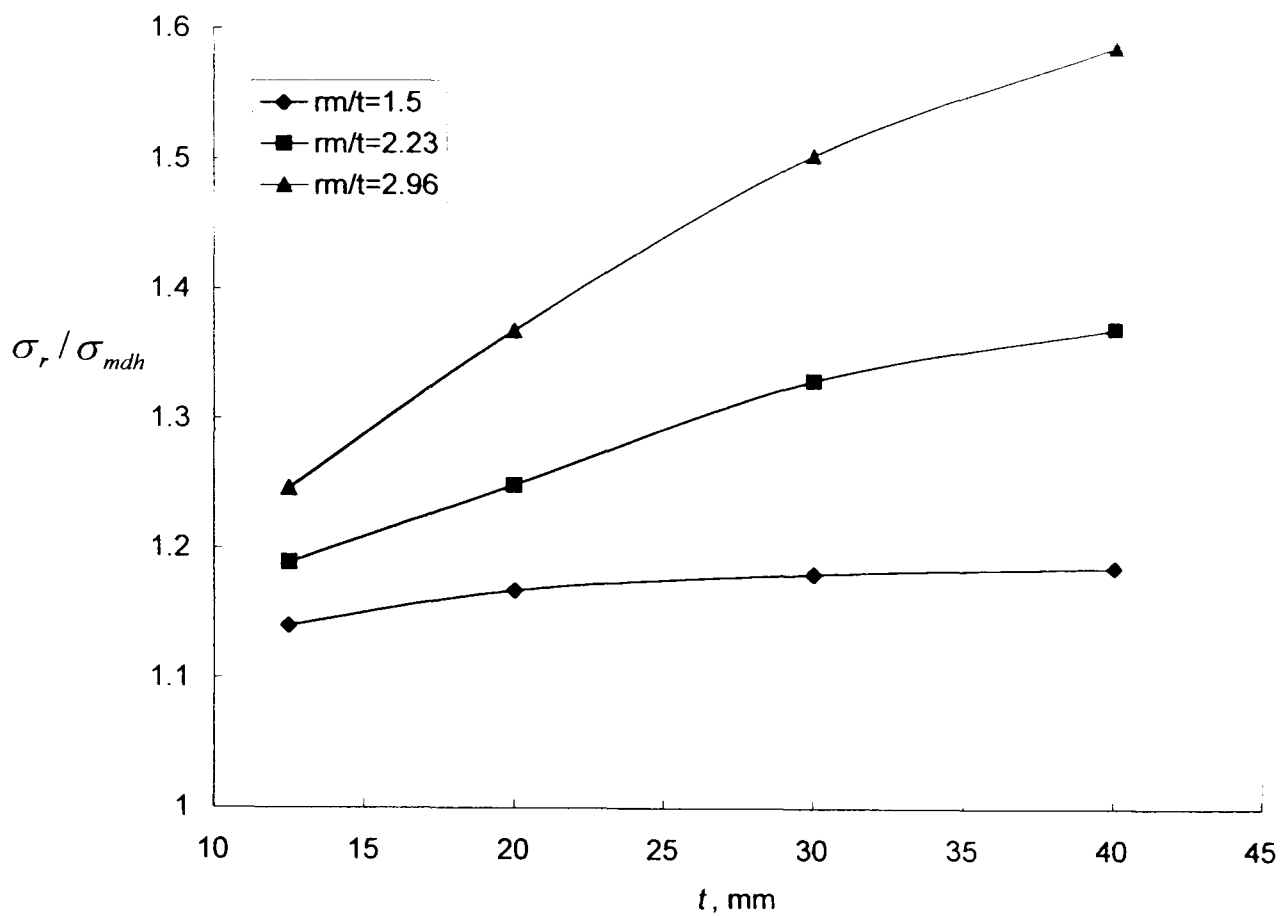


Figure 3.9. Variation of peak normalised rupture stress with constant r_m/t values for various branch thicknesses, $n=6$ and $\alpha=0.3$.

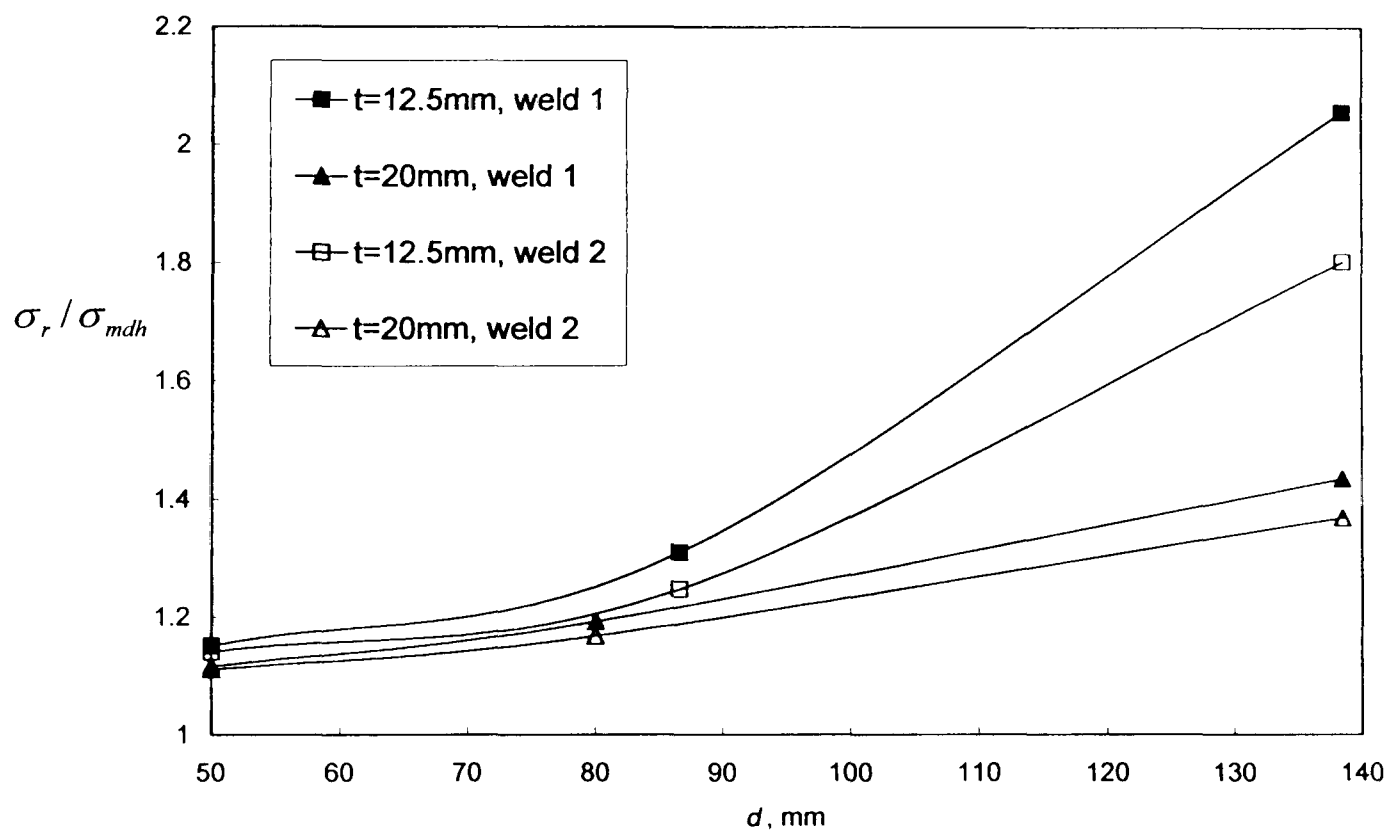


Figure 3.10. Variation of the peak rupture stresses with branch diameter, d for $t=12.5\text{mm}$ and $t=20\text{mm}$ using two weld sizes: weld 1: $b_x = b_y = t$; weld 2: $b_x = 25\text{mm}$ and $b_y = 30\text{mm}$, $n=6$ and $\alpha=0.3$.

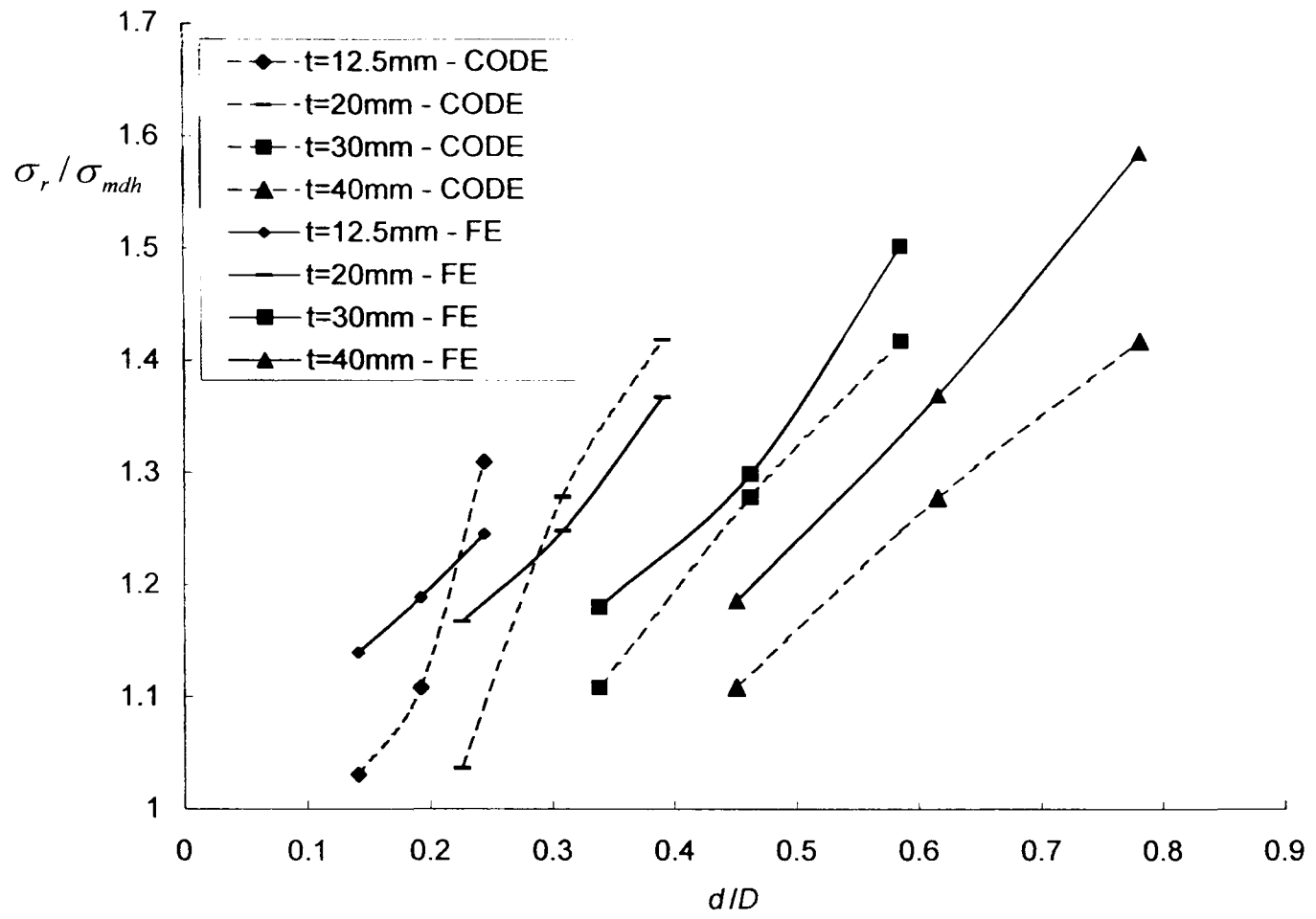


Figure 3.11. Comparison between the FE predicted peak normalised rupture stress and BS code operating stress [115], for various thicknesses with creep exponent of $n=6$ and $\alpha=0.3$.

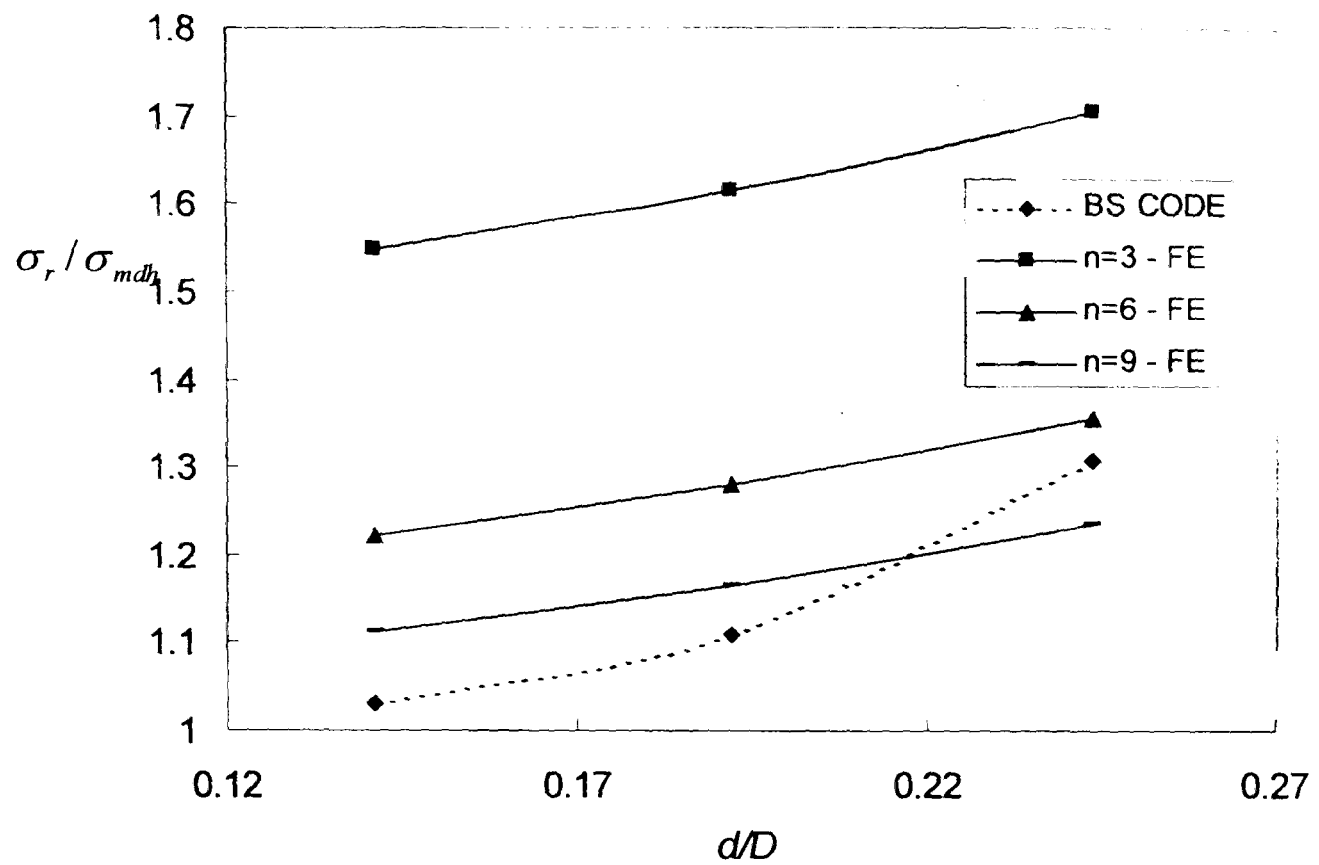


Figure 3.12a. Comparison between the FE predicted peak normalised rupture stress for $\alpha = 0$ and BS code operating stress [115] over a range of d/D for material with different creep exponent values, $t = 12.5\text{mm}$.

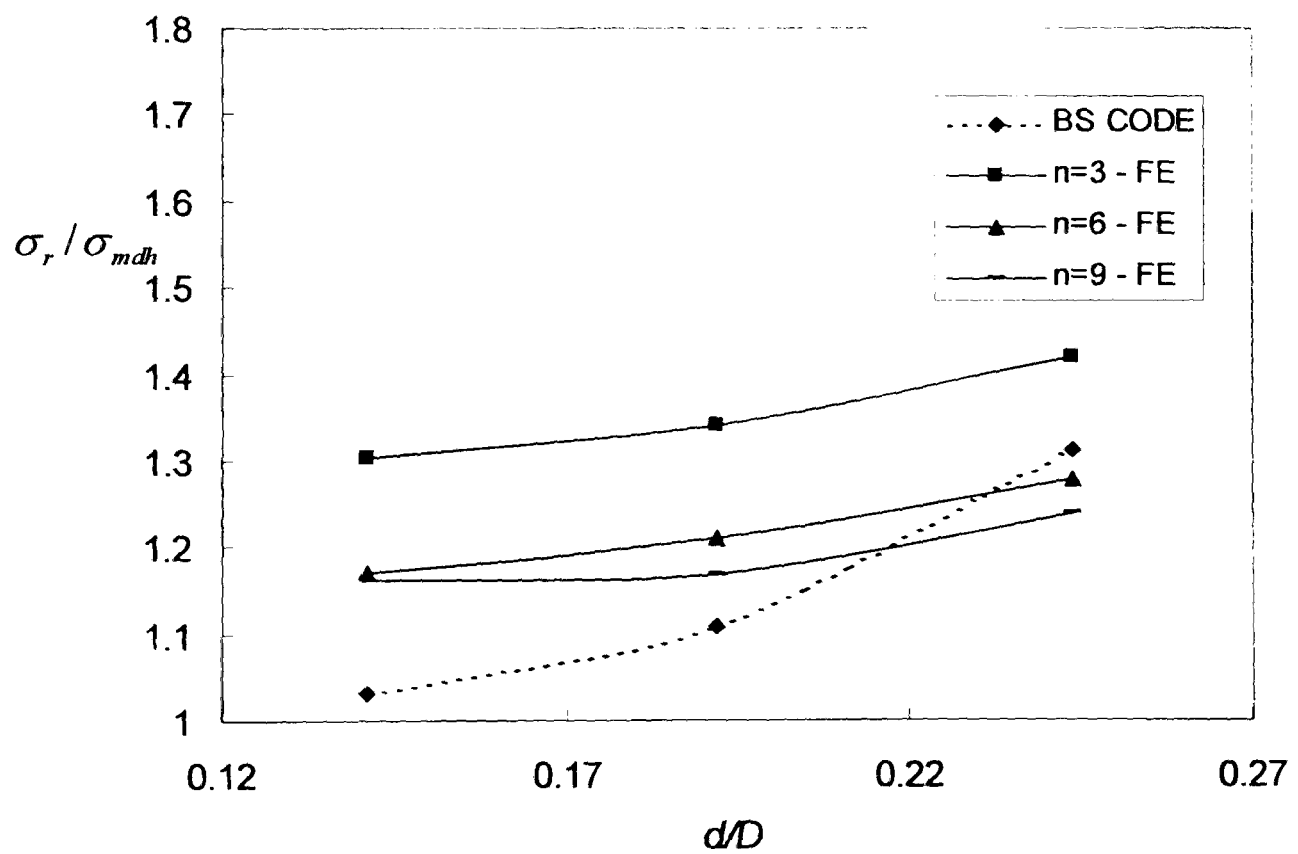


Figure 3.12b. Comparison between the FE predicted peak normalised rupture stress for $\alpha = 1$ and BS code operating stress [115] over a range of d/D for material with different creep exponent values, $t = 12.5\text{mm}$.

CHAPTER FOUR

CREEP BEHAVIOUR OF HETEROGENEOUS WELDED BRANCHED PIPES

4.1 Introduction

Chapter 3 identified that high stresses existed within the weld region of branched pipes and this may have a significant effect on the life of the weld when including in the effects of the weaker weld region of the HAZ, as well as the weld-mismatch effect. This chapter therefore is concerned with the steady-state, creep rupture behaviour of three different types of typical connections, incorporating the effects of the heterogeneous weld-related material zones, investigating the importance of the weld and its effect on the possible reduction in creep lives of the connections. The features considered are (i) a branched flat end cap, (ii) a branched hemi-spherical end cap and (iii) an isolated main pipe branch. The inclusion of PM, WM and HAZ weld steady-state and rupture properties are included in the analyses to model the stress and failure behaviour of the welded connections. Comparisons are made between the predicted heterogeneous multi-material weld component lives and the corresponding homogeneous connection predictions. The effect of varying branch diameter is also investigated on the creep stress and failure behaviour of the connections. The effect of material mis-match and how this affects failure behaviour is investigated. Comparisons are made between the single and multi-material steady-state failure lives and the inverse use of the BS codes

[11,12,115]. The term inverse use of the code is used because the codes are normally used in design purposes by fixing a level of stress within the branch which is acceptable for the material being used to fabricate the connection. Using this chosen level of stress within the code, the calculation of minimum thickness of the main and branch pipes is then made. The inverse use is the reverse of this procedure. Where all dimensions are known and a level of stress can then be predicted for the branched pipe. The BS codes BS5500 and BS1113 define an operating stress for different branch configurations, which is assumed as homogeneous. This operating stress can then be used as a design stress and also a stress to be used in creep life assessments. The importance of the inclusion of weld properties for creep life assessment of branched pipes is assessed.

Steady-state creep solutions, as described in Section 3.2, obtained using the multi-axial Norton creep law of Equation 2.3 were used to obtain the stress distributions within the connections and creep failure lives, t_f , were predicted using Equation 2.9, with steady-state peak rupture stresses, σ_r , defined by Equation 2.8 [24], for critical positions, using the appropriate uniaxial creep rupture material properties, e.g. Hyde et al [34,94]. The locations and values of the peak steady-state rupture stresses within each material zone are identified and the associated creep rupture lives are predicted using these peak values. The minimum life over all material zones is then taken as the multi-material component life and the corresponding location as the component's failure initiation site [94].

4.2 Geometry and material properties

Figures 4.1, 4.2 and 4.3 define the geometrical parameters for the three connection types studied. The values of D , T and t employed are 355mm, 65mm and 12.5mm, respectively, while the branch diameter, d , was varied from 55mm to 80mm. These dimensions are typical of UK fossil power plant. Figure 4.4 shows the assumed weld details for the three configurations. The five different material zones modelled are the branch and end cap parent material zones, designated PM^b and PM^p , respectively, the weld metal designated WM, and the branch and end cap heat-affected zones, designated HAZ^b and HAZ^p , respectively. These regions are defined by a number of geometrical parameters. The heat-affected zone widths, assumed to be equal, are defined by the parameter h . The angle θ defines the inclination of HAZ^b to the horizontal, the angle β defines the inclination of the weld outer surface to the horizontal, the parameters r_o and r_1 define the fillet radii created by weld neck and toe grinding and the additional parameters a , b and b_1 complete the geometry definition. The general shape of the weld is defined by the parameters b_x and b_y , as shown in Figure 4.3, for the example of the isolated branched pipe case. Table 4.1 defines the values of θ , β , a , b , b_1 , h , r_o and r_1 used throughout, while b_y was set equal to the branch thickness t .

Table 4.2 shows the relevant material properties obtained from creep tests on service exposed CrMoV pipe weldment material at 640°C [30]. Note that the HAZ^b and HAZ^p properties are assumed the same and likewise for the PM^b and PM^p zones. For this weldment the HAZ material is weaker than the PM and the WM is stronger than the PM with respect to the minimum creep strain rates

(i.e. $\dot{\epsilon}_{HAZ}^c > \dot{\epsilon}_{PM}^c > \dot{\epsilon}_{WM}^c$ for any given stress level) and rupture strength (i.e. $t_{HAZ}^f < t_{PM}^f < t_{WM}^f$ for a constant stresses below 70MPa) [30].

4.3 FE models

The flat and hemispherical end cap configurations can be analysed using axisymmetric models whereas a three-dimensional model is required for an isolated branched pipe. Quadratic elements with reduced integration were employed in all cases. Typical axisymmetric meshes for the hemi-spherical and flat end caps are shown in Figure 4.5 and 4.6, respectively. The sub-modelling technique was employed for the detailed weld region of the isolated branched pipe models to achieve the required high level of mesh refinement with satisfactory run-times. Mesh convergence studies established good correlation between the sub-model results and ‘converged’ fine mesh global model results; the latter however were prohibitively time-consuming for the parametric analyses. Figures 4.7(a) and 4.7(b) show the global-model and sub-model, respectively, for a typical isolated branched main pipe. Detailed attention has been given to ensuring compatible and uniform mesh design across the HAZ, PM and WM material mismatch boundaries. Weld toe and neck radii are used to eliminate sharp weld edges and therefore reduce unrealistic stress peaks. Careful interpretation of the time-dependent nodal stresses was used to ascertain when steady-state was achieved. The FE creep calculations were carried out using ABAQUS [28] finite element software. The pipes were loaded by an internal pressure of $p_i = 16.55\text{MPa}$ with an equivalent closed-end axial load applied to the end of the main pipe and branch. The three-

dimensional isolated branched main pipes were generated using an automatic mesh generation program called GBRANCH and SBRANCH [128] developed by the author. Appendix 1 provides some general guidelines on how FE analysis can be utilized to effectively predict steady-state stress distributions.

4.4 Stress distributions and high stress regions

4.4.1 Branched flat end cap

Figures 4.8 to 4.13 show the different views of the steady-state σ_{eq} , σ_1 and σ_r distributions within the $d = 55\text{mm}$ branched flat end cap.

Figures 4.8a and 4.8b show the main pipe σ_{eq} and σ_1 distributions, respectively. High σ_{eq} values occur on the inside surface of the main pipe, while high σ_1 values occur on the outside surface. High σ_{eq} and σ_1 stress concentrations were also predicted at the right-angled corner on the inside surface of the main pipe, due to the sharp change in the geometry, as shown in Figure 4.9. In reality, such a sharp corner would typically be avoided using a fillet so that these stress concentrations would generally not affect the component failure behaviour. Consequently, these stresses are not included in the lifing calculations. Figures 4.9a and 4.9b also show that the stresses along the branch pipe, away from the weld, are relatively low. The most significant σ_{eq} concentration region, in terms of affecting failure behaviour is at the weld on the inside surface of the branch, as shown in Figure 4.10a. High σ_{eq} values

were also found at the weld toe and neck. The highest σ_1 values in the weld are found near the outside surface at the weld toe and neck. due to the sharp change in geometry. It is clear from both contour plots that abrupt changes in stress magnitudes occur at the weld-related zone interfaces due to stress redistribution from the creep weak HAZ to the creep strong WM and PM regions.

Figures 4.11 to 4.13 show the rupture stress distributions in the HAZ^b and HAZ^p, WM and PM^b and PM^p zones, respectively, for the $d = 55\text{mm}$ case, where the different α values have been used for each particular weld related zone to calculate the rupture stress. The high rupture stresses in the HAZ^b and HAZ^p were predicted to occur near to but away from the outside surface (Figure 4.11). The HAZ^b had a slightly higher peak σ_r values than the HAZ^p, by around 7%, 11% and 16% for the $d= 55\text{mm}$, 70mm and 80mm branch cases, respectively, where similar peak stress positions were predicted for each case. Figure 4.12 displays the WM σ_r distribution within the WM, corresponding to an α value of 0.264. The highest stress regions were found at the inside surface, near the HAZ^b boundary and also at the weld toe. The peak σ_r value in the WM was found at the inside surface of the branch for the $d= 55\text{mm}$ case. The same peak WM stress position was also found for the $d= 70\text{mm}$ and 80mm geometry cases. Similar contours for the PM σ_r distributions, corresponding to an α value of 0.3, are shown in Figure 4.13 for the $d=55\text{mm}$ case, at various PM regions, i.e. (a) main pipe section, (b) end cap section, and (c) weld region. High stresses occurred at various positions, as shown, however the peak PM σ_r value was found in the main pipe section (i.e. PM^p) for the $d=55\text{mm}$ case.

For the larger diameters, $d=70\text{mm}$ and 80mm , the peak PM σ_r values were found at the same position in the PM^P region, just below the HAZ^P, as shown in Figure 4.13c by Position A.

4.4.2 Branched hemispherical end cap

The equivalent, maximum principal and rupture stress distributions for the $d=55\text{mm}$ branched hemispherical end cap configuration are shown in Figures 4.14 to 4.19.

The σ_{eq} and σ_1 stress distributions away from the connection region were predicted to be similar to those of the welded branched flat end cap, e.g. high σ_{eq} and σ_1 regions occur along the main pipe and branch pipe inside and outside surfaces, respectively. However, there are two important differences found between the two configurations. The first is that there is no obvious stress concentration at the joint between the end cap and the main pipe section for the hemispherical case, as shown in Figures 4.14 and 4.15. This is due to the fact that the hemispherical end cap has a significantly more gradual change in section at this position, in contrast to the sharp transition of the flat end cap. The second difference is that the hemispherical end cap weld regions have lower stress concentrations than the flat end cap cases, as shown by comparing Figure 4.16 to Figure 4.10. There is a σ_{eq} concentration at the inside surface of the WM, similar to that of the flat end cap, but the σ_{eq} and σ_1 values at the weld toe and neck are only about 20MPa and 15MPa, respectively, as compared to around 32MPa and 35MPa for the flat end cap case. As for the

flat end cap case, there is an abrupt change in stress across the PM/HAZ and HAZ/WM interfaces due to the material mis-match causing creep stress redistribution. However, the magnitude of stress difference is smaller in this case due to the smaller or negligible stress concentrations.

Figure 4.17 shows the rupture stress distribution in the HAZ using the α value of 0.49 for the $d=55\text{mm}$ case. The maximum σ_r value in the HAZ^p is only 14.7MPa as compared to a value of 18.5MPa in the HAZ^b. The latter is situated at the outside surface (weld neck). Similar distributions and identical peak σ_r positions were found for the $d=70\text{mm}$ and 80mm geometry cases. Figure 4.18 shows the σ_r distributions for the WM region, using the α value of 0.26. A relatively high σ_r concentration of up to 20.7MPa occurred at the weld neck, while the rest of the zone sees significantly lower stresses. Similar distributions were found for all three diameters investigated, where the peak σ_r value were found at the weld neck. Figure 4.19 shows the σ_r distribution in the PM zones, using the α value of 0.3. High σ_r values, of around 25MPa to 30MPa are predicted in the straight main pipe (PM^p) and branch sections (PM^b) and the peak value of 30.8MPa was found in the PM^p straight section, approximately mid-thickness. The PM σ_r values were relatively low in the weld region. Similar σ_r distributions and peak σ_r positions to that of the $d=50\text{mm}$ branch were again found for the larger $d=70\text{mm}$ and 80mm cases.

4.4.3 Isolated branched main pipe

The equivalent, maximum principal and rupture stress distributions for the $d=55\text{mm}$ connection region of the isolated branch configuration are shown in Figures 4.20 to 4.25. The stress distributions are significantly different to those of the branched end cap configurations. The stresses away from the connection region are relatively low so that discussion is concentrated on the connection region.

The σ_{eq} and σ_1 distributions on the flank and crotch planes and on the inner surface of the branch are shown in Figure 4.20. There are large σ_{eq} and σ_1 concentrations on the crotch plane, at the inside surface of the branch opening, up from the inner crotch corner. The maximum σ_1 position is half-way across the wall thickness of the main pipe, while the maximum σ_{eq} is about a quarter away across the main pipe wall. Comparatively lower σ_{eq} values occurred on the flank plane, apart from a concentration at the weld foot. Stresses were also comparatively lower in the near-connection section, away from the weld. Figures 4.21a and 4.21b display the weld-regions σ_{eq} and σ_1 distributions, respectively, on the inside surface. The σ_{eq} and σ_1 stresses display discontinuities of stress across the PM, HAZ and WM zone interfaces, due to mis-match in the materials properties, i.e. the weaker HAZ off-loads stress to the stronger PM and WM, especially at high stress regions. High σ_{eq} regions occur (i) at the weld toe on the flank plane and (ii) the inside surface on the crotch plane across the weld. High σ_1 values occurred (i) at the weld toe on

the flank plane, (ii) at the outer surface of the weld on the flank plane and (iii) across the weld at mid-branch thickness on the crotch plane. The outer surface σ_{eq} and σ_1 distributions are shown in Figures 4.22a and 4.22b. For both cases, stress concentrations occur circumferentially along the weld toe for about 45° from the flank plane. In each case, the highest stresses being predicted on the flank plane. The $d=70\text{mm}$ and 80mm branch cases showed very similar stress distributions to the $d=50\text{mm}$ case.

Rupture stress distributions for the HAZ^b and HAZ^p , using the α value of 0.49, are displayed in Figure 4.23. High σ_r values occur at (i) approximately across a third of the branch wall thickness from the inside surface, on the crotch plane, in both HAZs (Positions C and D in Figure 4.23a), (ii) in the HAZ^p at the weld toe, on the flank plane (Position B in Figure 2.23a) and (iii) at approximately 30° from the flank plane on the outside surface of the HAZ^p (Position E in Figure 2.23a). The peak σ_r position for the $d=55\text{mm}$ and 70mm branch diameter cases are in the HAZ^p at the weld toe, on the flank plane at Position B, while for the $d=80\text{mm}$ case it is located in the HAZ^b , on the crotch plane at Position D (Figure 4.23a). All three d values gave high HAZ σ_r values at the same four positions just mentioned. The differences in values for each d were small, i.e. less than 14%; therefore in practice multiple rupture sites at these positions could occur. However, the most likely sites for rupture initiation, and therefore crack initiation, leading to failure by steam leakage are the HAZ^p and HAZ^b positions C and D, on the crotch plane, due to the greater extent of high σ_r values across the wall thickness. Creep damage is therefore likely to grow

more quickly at these positions compared to the other two high σ_r positions, i.e. Positions B and E, since these two positions have just high local stresses. Continuum damage mechanics (CDM) analyses can provide more insight into the creep damage evolution at each of these sites.

Contour plots of the rupture stress for the WM, using the α value of 0.26, are shown in Figure 4.24. High stresses were found on the inner surface, crotch plane (see Figure 4.24b), and at the weld toe extending from the flank plane circumferentially along the outer surface to around 45° (Figure 4.24c). The peak WM σ_r position for all d values investigated was at the inner surface, crotch plane, close to the HAZ^P. These two peak stress locations are localized, with the rest of the WM experiencing significantly lower σ_r levels.

Figure 4.25 shows the rupture stress distributions for the PM regions, α value of 0.3. The highest σ_r locations are in the PM^P, approximately half main pipe wall thickness above the inside crotch corner and in the PM^b, on the inside surface of the branch, just above the HAZ^b, also on the crotch plane. As shown by all three contour plots, the rest of the PM regions have significantly lower stress levels. Similar trends were predicted for the $d=70\text{mm}$ and 80mm branch diameter cases.

4.5 Stress and life predictions

Tables 4.3 to 4.5 show the predicted peak rupture stresses and lives for each material zone for the three d values studied and for each branch configuration.

Figures 4.26 to 4.28 show the effect of branch diameter on the predicted multi-material peak rupture stresses graphically for the three configurations. The predicted stresses are presented normalised with the mean diameter elastic hoop stress, σ_{mdh} , of the main pipe, the resulting life predictions are also normalised with respect to the failure life, t_f^{mdh} , of the main plain pipe, based on σ_{mdh} and PM rupture properties. Increasing the branch diameter from 55mm to 80mm increases the peak stresses, approximately linearly, in all material zones; the largest increase of 70% occurs in the PM^b zone of the hemispherical end cap case; the PM^p zone is least affected in all cases. Significant differences, of 40% to 107% of the lowest stress values, are predicted between the different material zones of the three configurations. The highest values of peak rupture stress generally occur in the weld metal zone; the exception is the hemispherical end cap case, where the largest values occur in the PM^p, for low d values, and the PM^b, for high d values. The lowest peak stress values generally occur in the HAZ^p; the exception is isolated branched pipes with $d < 75$ mm, where the lowest values occur in the HAZ^b.

Figures 4.29 to 4.31 show the effect of branch diameter on predicted single and multi-material failure lives for the three branch configurations. For the multi-material cases, failure always occurs in the heat-affected zones, i.e. over the full range of d -values investigated in all three configurations. For the flat and hemi-spherical end cap cases this is in the HAZ^b, more specifically, near the PM^b/HAZ^b boundary and at approximately mid-branch wall thickness. For the isolated branch pipe, failure occurs on the crotch plane, i.e. x - y plane of symmetry (Figure 4.3), on the inner surface HAZ^b, near the PM^b/HAZ^b

boundary, for high d values, and in the HAZ^P, at approximately mid-branch wall thickness, near the PM^P/HAZ^P boundary for low d values.

The predicted failure life decreases significantly and monotonically with increasing branch diameter for all three configurations. For the hemispherical end-cap, the component's failure life ratio, t_f/t_f^{mdh} , decreases by 77% from 2.3 to 0.54 as d increases from 55mm to 80mm in the HAZ^b. For the flat end cap and isolated branched pipe cases, the corresponding respective life ratio decreases from 0.69 to 0.38 and from 0.34 to 0.19, i.e. by 45% in both cases. Thus, for both the flat end cap and isolated branch pipe cases, the predicted life is always less than that of a corresponding plain pipe creep life based on the elastic σ_{mdh} with PM properties. The hemispherical end cap is predicted to be stronger than the plain pipe for low d -values but weaker for high d -values. Also, Figures 4.29 to 4.31 show significant differences between the predicted failure lives of the different material zones, particularly between the HAZs and the other zones. For low d values, there can be an order of magnitude difference, depending on branch configuration and zone material.

For all three branch configurations, and for all d values studied, the single material predicted lives were greater (i.e. non-conservative) than the multi-material predictions. The single material predicted failure sites for the flat and hemispherical end cap cases are remote from the welded region, namely, in the pipe, for low d values, and in the branch, for high d values; for the isolated branch case the predicted failure site is near to the inside crotch corner. The multi-material lives range from about 25% of the single-material value to about

45% with increasing branch diameter for the flat end cap case, around 81% to 65% with increasing branch diameter for the hemispherical end cap case and approximately 80% to 74% with increasing d for the isolated branch case.

The comparative strength of each branch connection type, based on three-material creep assessments, is shown in Figure 4.32 in terms of failure life over the branch diameter range studied. The comparison clearly shows that there is a significant difference in strength between the three configurations. The weakest component is the isolated branched main pipe over all three branch diameter sizes, then the branched flat end cap and finally the strongest configuration is the branched hemispherical end cap. The isolated branch life is predicted to be around 85% lower and 50% lower than that of the hemispherical and flat end cap configurations lives, respectively, for the smallest, $d=55\text{mm}$, branch diameter. The difference in life between the isolated branched main pipe and the hemispherical case reduces with increasing branch diameter, reaching around 65% lower life for the former with $d=80\text{mm}$. However, the difference in creep life between the branched main pipe and branched flat end cap stays approximately steady at 50% lower.

4.6 Comparison with British Standard code life predictions

The steady-state single and multi-material life predictions for the three different configurations are compared to two different ways the British Standard (BS) [11,12,115] stress can be used for the prediction of creep rupture life, both based on the use of the inverse code method, as described by Booth [115]. Firstly, BS lives are predicted using the operating stress with the

weakest weldment material's rupture properties, i.e. for this weldment, the HAZ, as described by BS 7910 [131], this is denoted as BS Method *A*. Secondly, the BS predicted operating stresses [115] are used to predict creep rupture lives using the PM homogeneous rupture properties, this is denoted as BS Method *B*. The aim of the comparison is to identify whether the BS code Methods *A* and *B* life predictions are similar to the homogenous and multi-material steady-state predictions, thereby partially validating their use for branched pipe life assessments.

Results of the comparisons over the range of branch diameters are shown in Figures 4.33, 4.34 and 4.35 for the three branch configurations. It is clear from all three graphs that the use of BS Method *A* significantly under-predicts the rupture lives of the multi-material component compared to the single and multi-material steady-state predictions. For the cases of the flat and hemispherical branched end caps, the level of conservatism of the BS method *A* was very large, i.e. from about 10% to 35% that of the multi-material steady-state predictions over the d range investigated. The predicted isolated branched main pipe BS lives are improved compared to the end caps comparison, the conservatism is lower at around 60% to 80% that of the multi-material steady-state predictions. BS Method *B* life predictions, which is based on parent material data, were around 165%, 215% and 242% longer than Method *A*'s for the flat, hemispherical and isolated configurations, respectively. However these differences are small when compared with the differences with the single material steady-state life predictions for the flat and hemispherical branch end cap cases. When Method *B* life predictions for the end cap cases are compared

with the multi-material steady-state life predictions the lives are conservative for low values of branch diameter, d , but non-conservative for larger diameters. Method *B* predictions for the isolated branched main pipe are always non-conservative compared to the single material and multi-material steady-state predictions, lives of up to 75% longer are predicted compared to the single material steady-state lives. As highlighted in Chapter 3, the BS code was shown to be non-conservative compared to steady-state predictions for various single material isolated branched main pipe cases. For all three configurations, differences between the BS code predictions and single and multi-material steady-state lives due to the variation of branch diameter are small.

4.7 Conclusions

- Stress distributions were shown for various regions within each configuration. Significant stress discontinuities were produced due to material mis-match within the weldment for all cases. The highest stresses in the weld region were generally found in the WM and the lowest in the HAZs. Differences in equivalent stress of up to 30% to 40% between the PM, HAZ and PM zones occurred locally within the weld. Similar differences in maximum principal stress also occurred across the zones.
- Significant differences in equivalent and maximum principal stress distribution were found in the components and numerous high stress concentration regions were identified. These high stress regions were identified at the weld neck, weld toe and inside bore across the weld for the flat end cap cases, at the weld neck and inside bore for the hemispherical end cap cases and at the weld neck and toe on crotch and flank planes and

at the inside crotch bore for the isolated main pipe cases. Stress distribution trends were generally unaffected by change in branch diameter, although the peak stress values in each material zone generally increased with increasing branch diameter. For instance, for the failure dominant HAZ regions the peak rupture stress increased by around 58%, 20% and 11% for the flat end-cap, hemispherical end-cap and isolated main pipe configurations, respectively.

- It has been shown that for the typical CrMoV material properties used and the range of geometries investigated, the single-material steady-state life predictions are significantly higher than the three-material predictions, which include weld and heat affected zone properties, for three different branch-pipe configurations. Single material steady-state life predictions for the branched flat end-cap ranged from around 400% to 200% longer than the equivalent multi-material lives, over the branch diameter range investigated. For the hemispherical end-cap and isolated main pipe configurations, differences were lower, ranging from around 25% to 50% and 20% to 26%, respectively, over the diameter range. Concluding that the effect of the weldment material properties on failure life is very significant and the use of single material life assessments for welded connections are non-conservative for these cases.
- For all branch configurations and geometries considered, failure is predicted to occur in the heat-affected zones of the three-material models. Generally failure was predicted to initiate in the HAZ^b near the weld neck on the PM^b boundary, at the weld foot in the HAZ^p on the WM boundary for the flat end-cap cases and in the HAZ^p, either at the flank-plane weld

foot on the WM boundary or crotch-plane inside surface on the PM^p boundary, for low branch diameters, or in the HAZ^b at the crotch-plane weld neck on the PM^b boundary for larger branch diameters.

- The failure stresses increased approximately linearly, and the corresponding failure lives decreased significantly, with increasing branch diameter, for the single- and multi-material cases of the three branch configurations. For the geometries investigated, the flat end cap and branched main pipe failure lives were shown to be lower than those of a plain pipe based on σ_{mdh} . However, the hemi-spherical end cap life predictions indicated a transition from stronger to weaker behaviour for increasing branch diameter, compared with the plain pipe.
- The inverse use of the BS codes predicted conservative life estimates based on multi-material rupture properties compared to the single and multi-material steady-state life predictions. All BS multi-material life (Method *A*) predictions were lower by at least (i) 20% for the isolated branched main pipe and (ii) 65% for the two branched end cap configurations compared to the multi-material steady-state predictions. The BS life predictions based on single material properties (Method *B*) were generally very conservative compared to the single material steady-state lives for the branched flat and hemispherical cases. However, significantly non-conservative BS single material life predictions were predicted for the isolated branched main pipe cases. From these results, it has been shown that the inverse use of the BS codes based on multi-material rupture data is a conservative approach for predicting the multi-material lives of the welded branched pipes. It is for some cases however non-conservative to predict the creep rupture lives of

multi-material welded branched pipes using just single material BS life predictions, especially for the isolated main branched pipe. It is suggested that other creep life assessment methods are used for more accurate predictions, such as a steady-state method, a continuum damage mechanics approach or the R5 procedure [13].

Table 4.1. Values of weld geometrical parameters used

θ ($^{\circ}$)	β ($^{\circ}$)	a (mm)	b (mm)	b_1 (mm)	h (mm)	r_o (mm)	r_1 (mm)
45	45	2.5	3	3	1.5	6	6

Table 4.2. Material constants for the CrMoV weldment materials at 640 $^{\circ}$ C [30].

Material	A	n	M	χ	α
PM	6.5991×10^{-16}	6.1081	5.9981×10^{-14}	5.767	0.300
WM	9.7181×10^{-15}	5.2082	8.1202×10^{-13}	4.850	0.264
HAZ	1.7083×10^{-15}	6.1081	2.5000×10^{-9}	3.200	0.490

Note: $[\sigma] = \text{MPa}$; $[t] = \text{h}$, $[\dot{\epsilon}_{\min}^c] = \text{h}^{-1}$.

Table 4.3. Magnitudes and positions of peak steady-state stresses in each material zone and the rupture lives predicted obtained for the branched flat end cap, for three different branch diameters.

Branch Case	Zone	σ_{eq} (MPa)		σ_l (MPa)		σ_r (MPa)		t_f (hours)
		Value	Position	Value	Position	Value	Position	
$d=55$ $t=12.5$ (mm)	PM ^p	34.0	IS HAZ ^p /PM ^p	34.0	OS HAZ ^p /PM ^p	30.8	OS HAZ ^p /PM ^p	43403
	PM ^b	31.1	IS HAZ ^b /PM ^b	30.7	OS HAZ ^b /PM ^b	26.9	MID-OS HAZ ^b /PM ^b	94757
	HAZ ^p	26.6	IS HAZ ^p /PM ^p	27.6	OS HAZ ^p /PM ^p	25.2	OS HAZ ^p /PM ^p	13109
	HAZ ^b	26.7	IS HAZ ^b /PM ^b	35.6	OS HAZ ^b /PM ^b	27.0	MID-OS HAZ ^b /PM ^b	10512
	WM	33.9	IS HAZ ^p /WM	37.4	OS near HAZ ^b /WM	34.4	IS HAZ ^b /WM	43619
$d=70$ $t=12.5$ (mm)		σ_{eq} (MPa)		σ_l (MPa)		σ_r (MPa)		t_f (h)
	Zone	Value	Position	Value	Position	Value	Position	
	PM ^p	34.0	IS HAZ ^p /PM ^p	34.0	OS HAZ ^p /PM ^p	30.8	OS HAZ ^p /PM ^p	43403
	PM ^b	35.3	IS HAZ ^b /PM ^b	35.8	OS HAZ ^b /PM ^b	32.8	MID-OS HAZ ^b /PM ^b	30196
	HAZ ^p	28.6	IS HAZ ^p /PM ^p	27.9	OS HAZ ^p /PM ^p	26.5	OS HAZ ^p /PM ^p	11160
	HAZ ^b	29.2	IS HAZ ^b /PM ^b	36.3	OS HAZ ^b /PM ^b	29.6	MID-OS HAZ ^b /PM ^b	7584
WM	37.2	IS HAZ ^p /WM	45.5	OS near HAZ ^b /WM	38.8	IS HAZ ^b /WM	24333	
$d=80$ $t=12.5$ (mm)		σ_{eq} (MPa)		σ_l (MPa)		σ_r (MPa)		t_f (h)
	Zone	Value	Position	Value	Position	Value	Position	
	PM ^p	34.9	IS HAZ ^p /PM ^p	34.0	OS HAZ ^p /PM ^p	31.6	OS HAZ ^p /PM ^p	37437
	PM ^b	41.0	IS HAZ ^b /PM ^b	41.7	OS HAZ ^b /PM ^b	37.9	MID-OS HAZ ^b /PM ^b	13121
	HAZ ^p	30.7	IS HAZ ^p /PM ^p	28.3	OS HAZ ^p /PM ^p	27.9	OS HAZ ^p /PM ^p	9465
	HAZ ^b	32.0	IS HAZ ^b /PM ^b	36.9	OS HAZ ^b /PM ^b	32.5	MID-OS HAZ ^b /PM ^b	5808
	WM	40.2	IS HAZ ^p /WM	51.0	OS near HAZ ^b /WM	42.3	IS HAZ ^b /WM	16007

Note: OS = outer surface, IS = inner surface, MID = center, Materials interface. e.g. HAZ^p/WM

Table 4.4. Magnitudes and positions of peak steady-state stresses in each material zone and the rupture lives predicted obtained for the branched hemispherical end cap, for three different branch diameters.

Branch Case	Zone	σ_{eq} (MPa)		σ_l (MPa)		σ_r (MPa)		t_f (hours)
		Value	Position	Value	Position	Value	Position	
$d=55$ $t=12.5$ (mm)	PM ^p	34.0	IS straight section	34.0	OS straight section	30.8	OS straight section	43403
	PM ^b	26.2	IS remote section	25.0	OS remote section	22.5	OS remote section	265434
	HAZ ^p	20.0	IS HAZ ^p /WM	13.7	MID HAZ ^p /WM	14.7	MID HAZ ^p /WM	73561
	HAZ ^b	20.3	IS HAZ ^b /PM ^b	19.6	OS HAZ ^b /WM	18.5	OS HAZ ^b /WM	35246
	WM	24.2	IS HAZ ^b /WM	23.4	OS HAZ ^b /WM	20.7	OS HAZ ^b /WM	512040
$d=70$ $t=12.5$ (mm)		σ_{eq} (MPa)		σ_l (MPa)		σ_r (MPa)		t_f (h)
	Zone	Value	Position	Value	Position	Value	Position	
	PM ^p	34.0	IS straight section	34.0	OS straight section	30.8	OS straight section	43403
	PM ^b	35.1	IS remote section	35.2	OS remote section	31.9	OS remote section	35451
	HAZ ^p	26.0	IS HAZ ^p /WM	19.5	MID HAZ ^p /WM	20.6	MID HAZ ^p /WM	24985
	HAZ ^b	26.5	IS HAZ ^b /WM	26.7	OS HAZ ^b /WM	35.1	OS HAZ ^b /PM ^b	13277
WM	33.0	IS HAZ ^b /WM	29.0	OS HAZ ^b /WM	29.6	OS HAZ ^b /WM	90396	
$d=80$ $t=12.5$ (mm)		σ_{eq} (MPa)		σ_l (MPa)		σ_r (MPa)		t_f (h)
	Zone	Value	Position	Value	Position	Value	Position	
	PM ^p	34.0	IS straight section	34.0	OS straight section	30.8	OS straight section	43403
	PM ^b	40.9	IS remote section	42.2	OS remote section	38.2	OS remote section	12538
	HAZ ^p	30.0	IS HAZ ^p /WM	22.8	MID HAZ ^p /WM	24.5	MID HAZ ^p /WM	14346
	HAZ ^b	30.5	IS HAZ ^b /WM	31.2	OS HAZ ^b /WM	29.2	OS HAZ ^b /PM ^b	8182
	WM	39.0	IS HAZ ^b /WM	32.8	OS HAZ ^b /WM	35.1	OS HAZ ^b /WM	39559

Note: OS = outer surface, IS = inner surface, MID = Center, Materials interface, e.g. HAZ^p/WM

Table 4.5. Magnitudes and positions of peak steady-state stresses in each material zone and the rupture lives predicted obtained for the branched main pipe, for three different branch diameters.

Branch Case	Zone	σ_{eq} (MPa)		σ_l (MPa)		σ_r (MPa)		t_f (hours)
		Value	Position	Value	Position	Value	Position	
$d=55$ $t=12.5$ (mm)	PM ^p	46.3	IS pipe MID thickness CP	45.5	Near IS pipe MID thickness CP	43.1	IS pipe MID thickness CP	6251
	PM ^b	40.7	IS, HAZ ^b /PM ^b , CP	36.5	MID HAZ ^b /PM ^b , CP	37.6	IS, HAZ ^b /PM ^b , CP	13737
	HAZ ^p	36.2	IS, HAZ ^p /PM ^p , CP	36.3	Position B (Fig. 4.23)	36.1	Position B (Fig. 4.23)	4150
	HAZ ^b	35.5	IS, HAZ ^b /PM ^b , CP	32.2	MID HAZ ^b /PM ^b , CP	33.2	Position D (Fig. 4.23)	5425
	WM	47.5	IS, HAZ ^p /WM, CP	43.0	Weld toe, FP	45.0	IS, HAZ ^p /WM, CP	11858
$d=70$ $t=12.5$ (mm)		σ_{eq} (MPa)		σ_l (MPa)		σ_r (MPa)		t_f (h)
	Zone	Value	Position	Value	Position	Value	Position	
	PM ^p	48.8	IS pipe MID thickness CP	47.7	Near IS pipe MID thickness CP	45.5	IS pipe MID thickness CP	4573
	PM ^b	45.8	IS, CP, HAZ ^b /PM ^b	45.0	MID HAZ ^b /PM ^b , CP	43.0	IS, HAZ ^b /PM ^b , CP	6336
	HAZ ^p	40.0	IS, HAZ ^p /PM ^p , CP	39.8	MID, HAZ ^p /PM ^p , CP	37.9	Position C (Fig. 4.23)	3552
HAZ ^b	39.6	IS, HAZ ^b /PM ^b , CP	40.3	OS, HAZ ^b /WM, 45° CP to FP	37.7	Position D (Fig. 4.23)	3612	
WM	53.7	IS, HAZ ^p /WM, CP	51.5	Weld toe, FP	51.6	IS, HAZ ^p /WM, CP	6107	

Note: OS = outer surface, IS = inner surface, MID = Center, Materials interface, e.g. HAZ^p/WM, CP = crotch plane & FP = flank plane of the connection

Table 4.5. continued...

	Zone	σ_{eq} (MPa)		σ_1 (MPa)		σ_r (MPa)		t_f (h)
		Value	Position	Value	Position	Value	Position	
$d=80$	PM ^p	50.7	IS pipe MID thickness CP	49.0	Near IS pipe MID thickness CP	47.3	IS pipe MID thickness CP	3656
	PM ^b	48.7	IS, CP, HAZ ^b / PM ^b	50.1	MID HAZ ^p / PM ^p , CP	46.0	IS, HAZ ^b / PM ^b , CP	4294
$t=12.5$	HAZ ^p	42.2	IS, HAZ ^p /PM ^p , CP	41.9	MID, HAZ ^p / PM ^p , CP	40.0	Position C (Fig. 4.23)	2989
(mm)	HAZ ^b	42.0	IS, HAZ ^b / PM ^b , CP	45.2	OS, HAZ ^b / WM, 45° CP to FP	40.6	Position D (Fig. 4.23)	2850
	WM	57.4	IS, HAZ ^p /WM , CP	56.5	Weld neck, 45° CP to FP	55.3	IS, mid- width, CP	4365

Note: OS = outer surface, IS = inner surface, MID = Center, Materials interface, e.g. HAZ^p/WM, CP = crotch plane & FP = flank plane of the connection

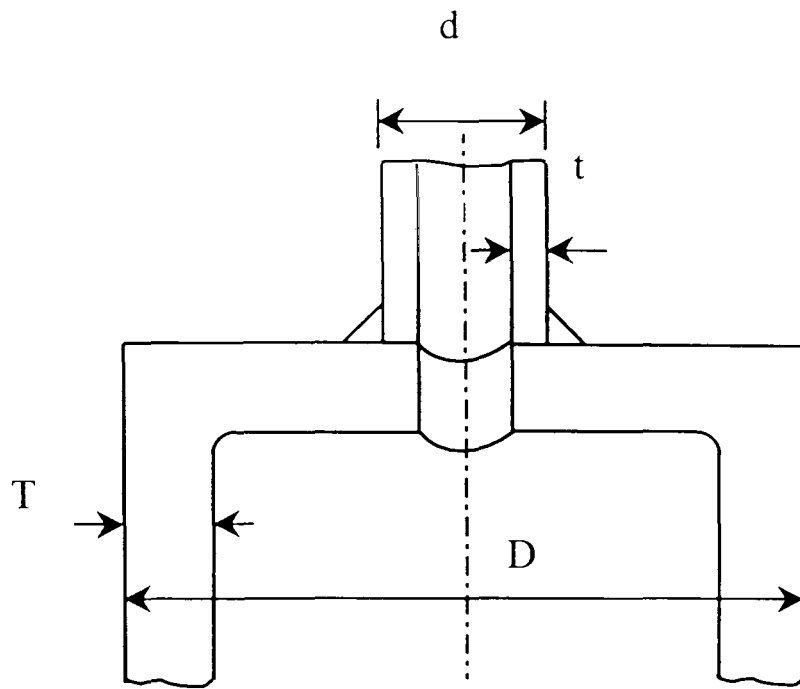


Figure 4.1. A flat end cap with a centralised branch penetration.

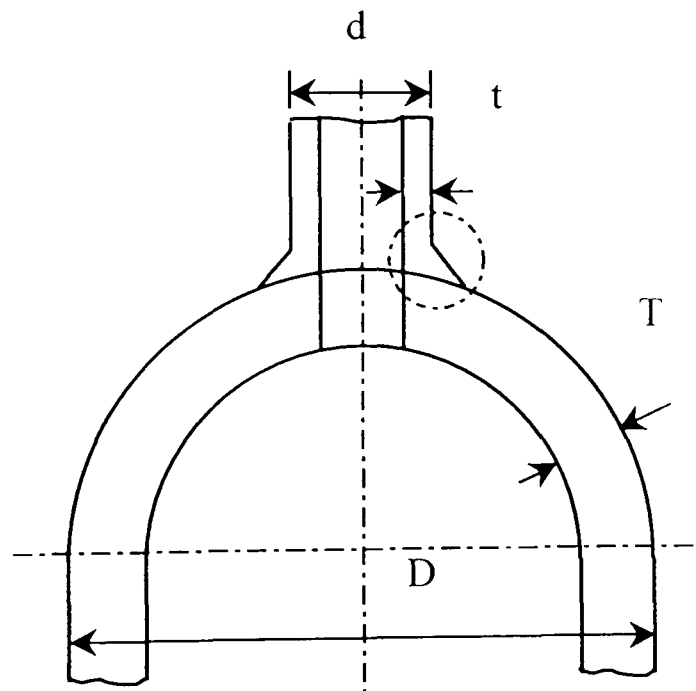


Figure 4.2. A hemispherical end cap with a centralised branch penetration.

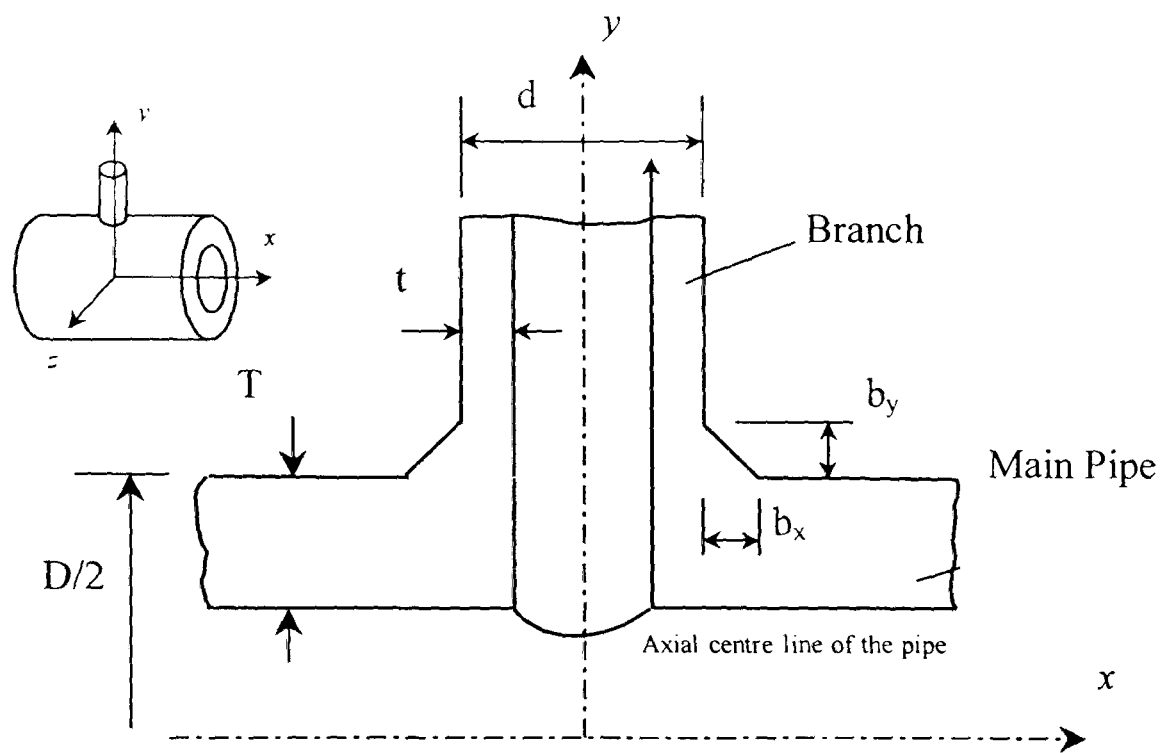


Figure 4.3. A main pipe with an isolated T-branch

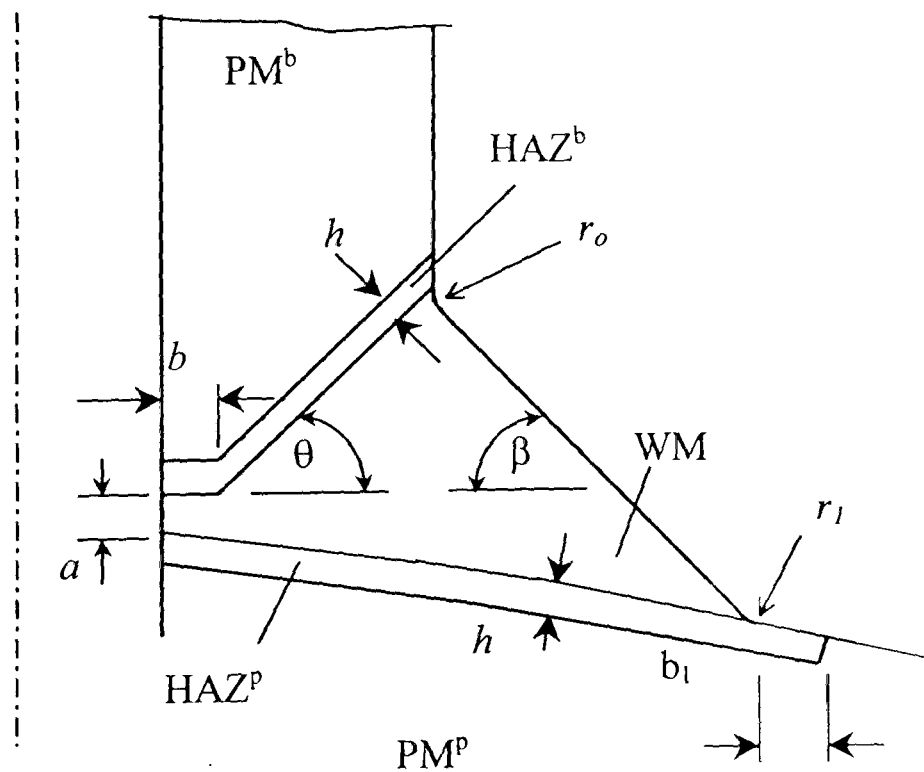


Figure 4.4. Definition of weld details

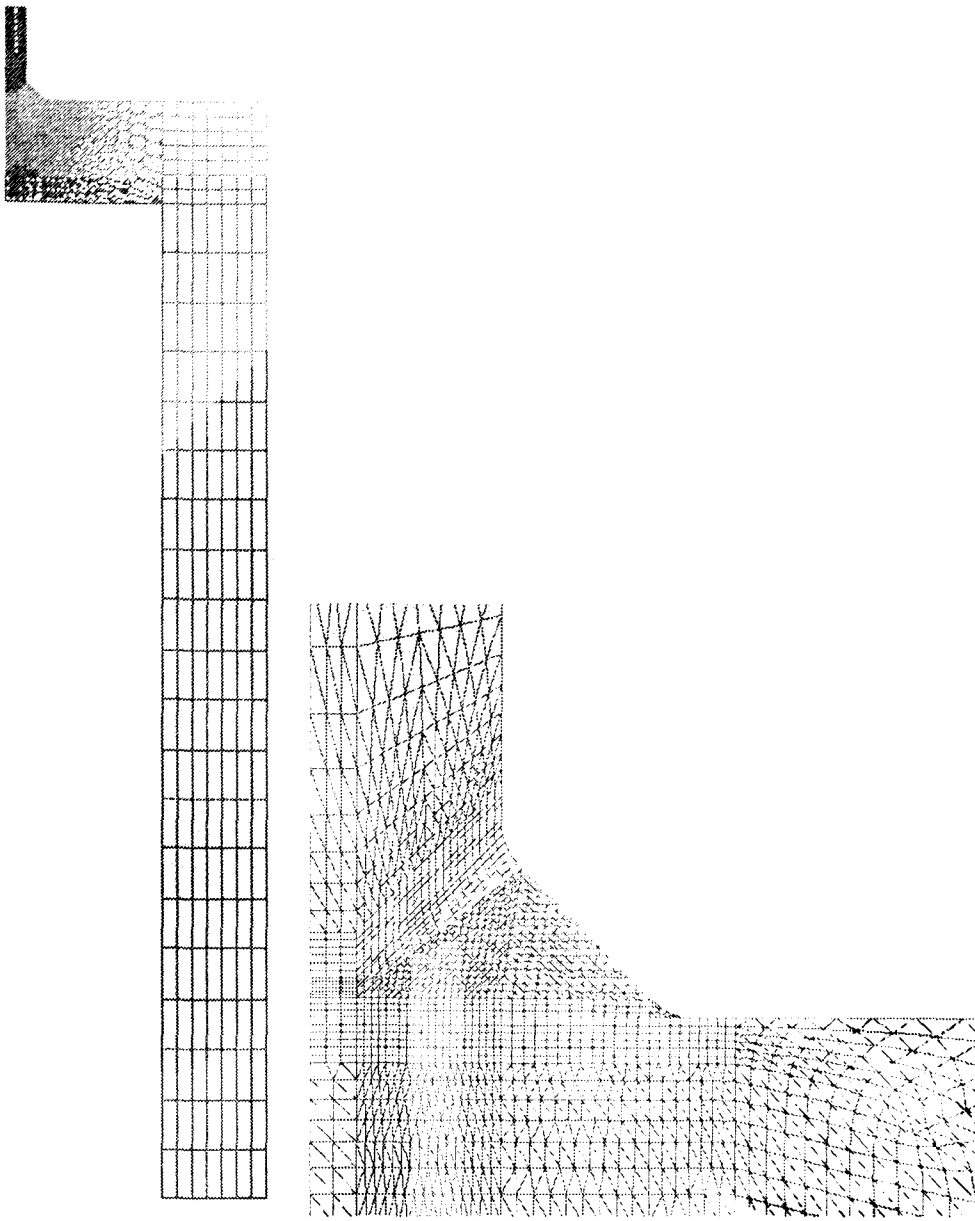


Figure 4.5. Axisymmetric FE mesh (part) of the flat end cap with centralised branch penetration.

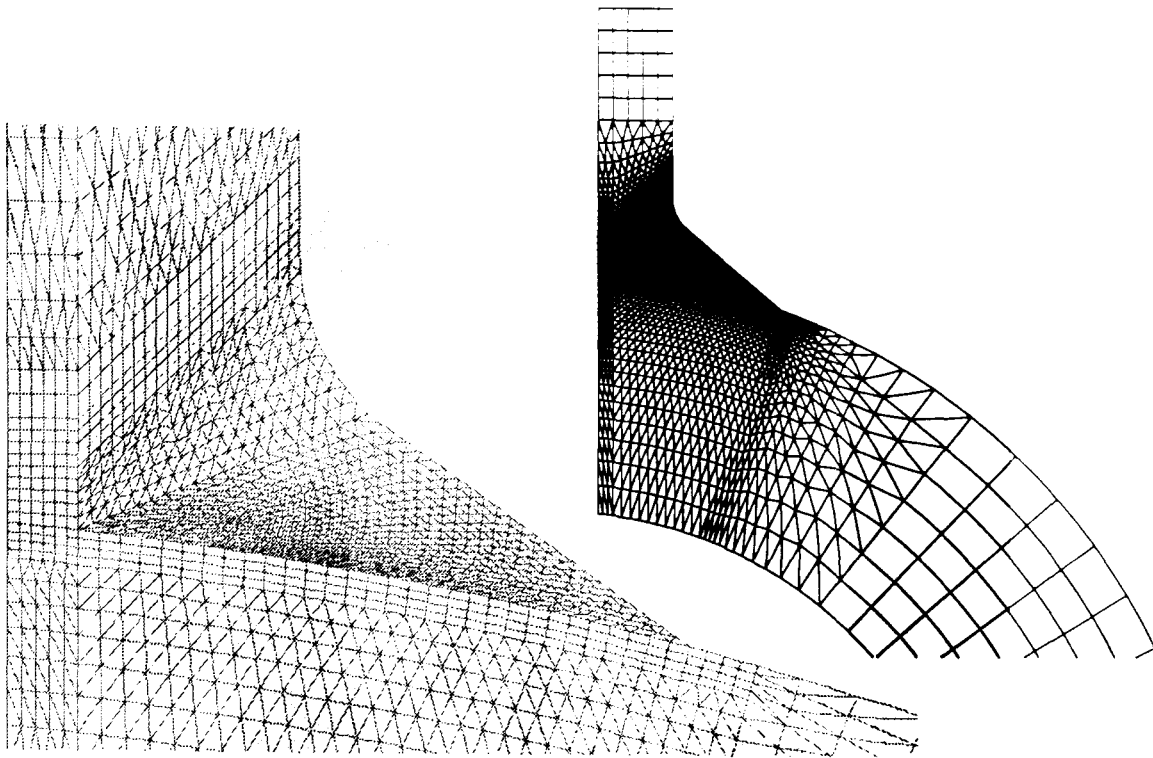


Figure 4.6. Axisymmetric FE mesh (part) of the hemi-spherical end cap with centralised branch penetration.

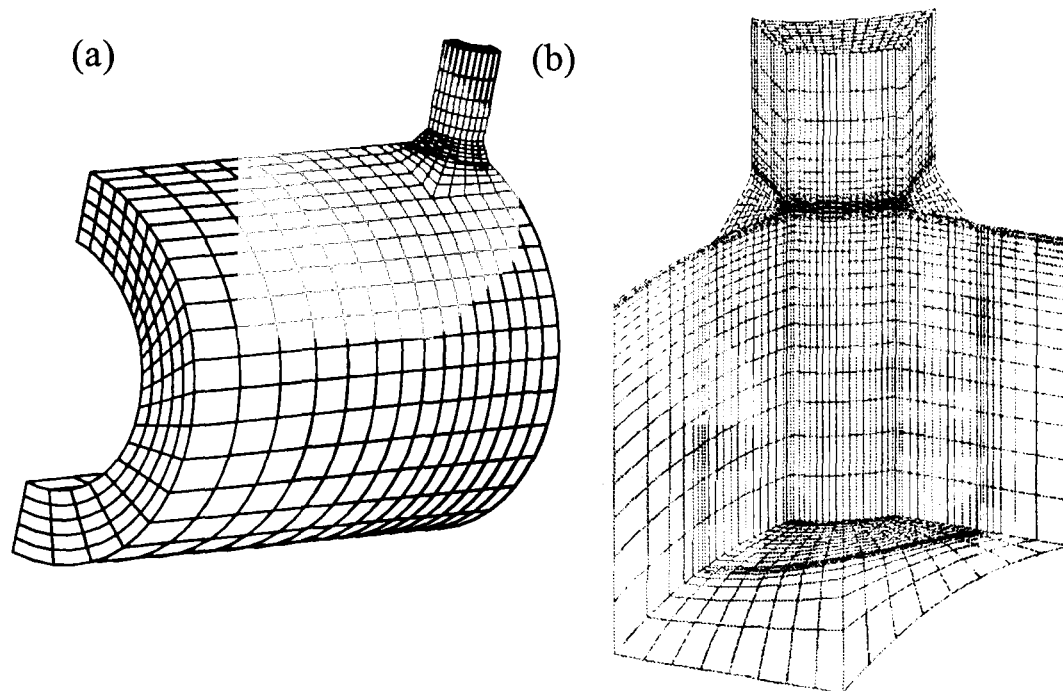


Figure 4.7. (a) Global model and (b) sub-model three-dimensional meshes for a pipe with an isolated branch.



Figure 4.8. Contour plots of the (a) equivalent (Von-Mises) stress (MPa) and (b) maximum principal stress (MPa) within the $d=55\text{mm}$ branched flat end cap, concentrating on the main pipe section.

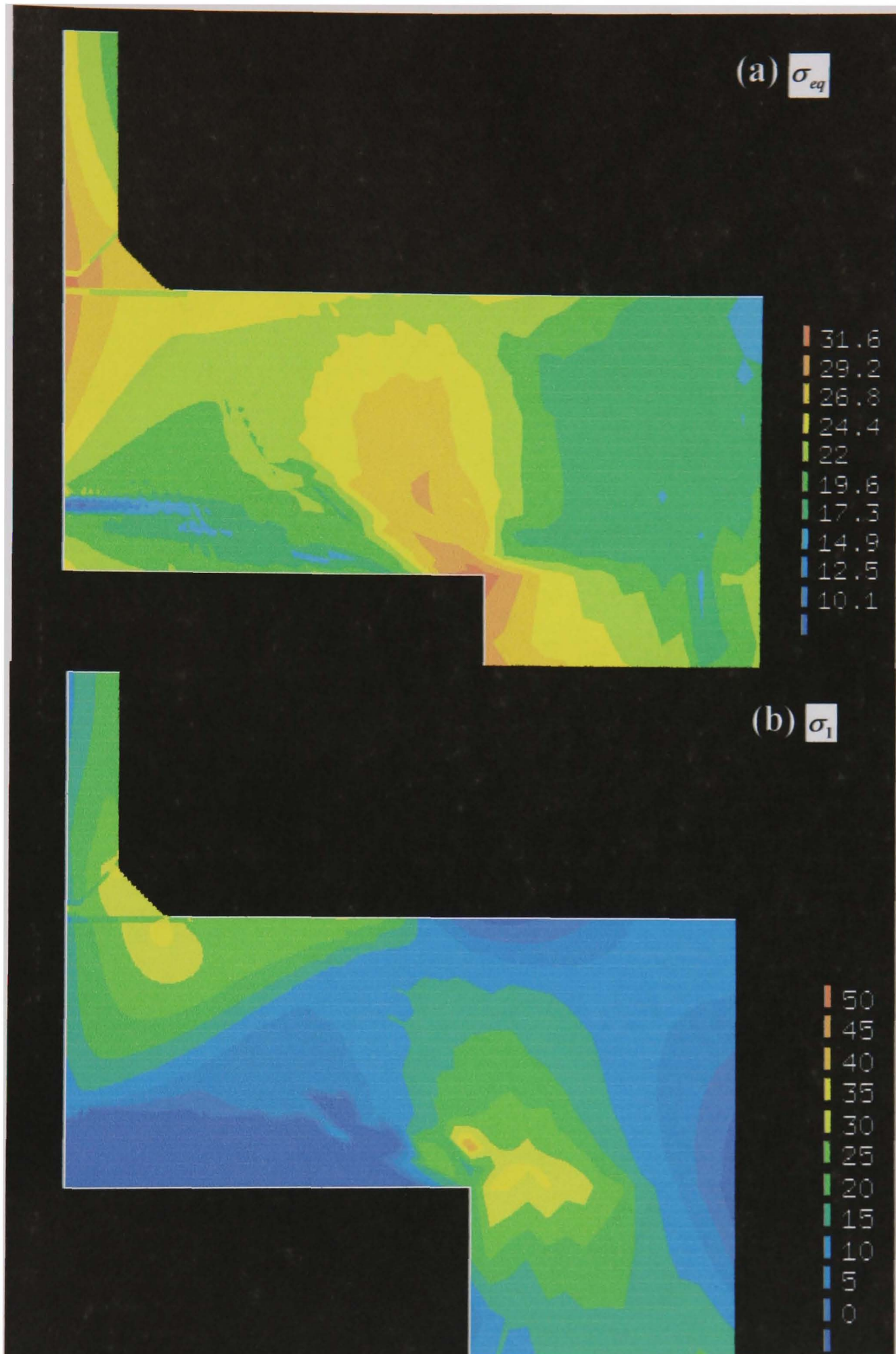


Figure 4.9. Contour plots of the (a) equivalent (Von-Mises) stress (MPa) and (b) maximum principal stress (MPa) within the $d=55\text{mm}$ branched flat end cap, concentrating on the end cap section.

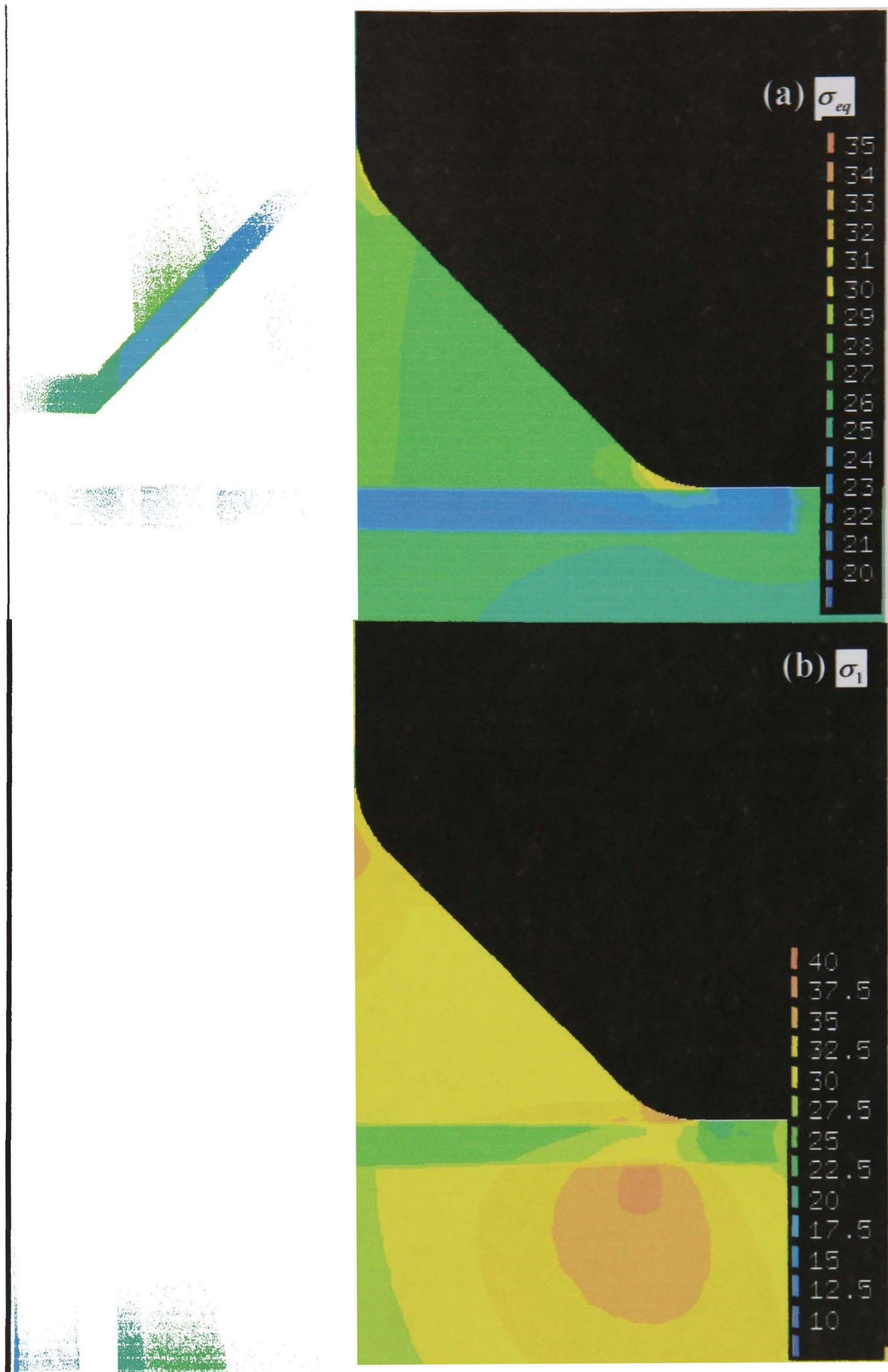


Figure 4.10. Contour plots of (a) equivalent (Von-Mises) stress (MPa) and (b) maximum principal stress (MPa) within the $d=55\text{mm}$ branched flat end cap, concentrating on the weld region.

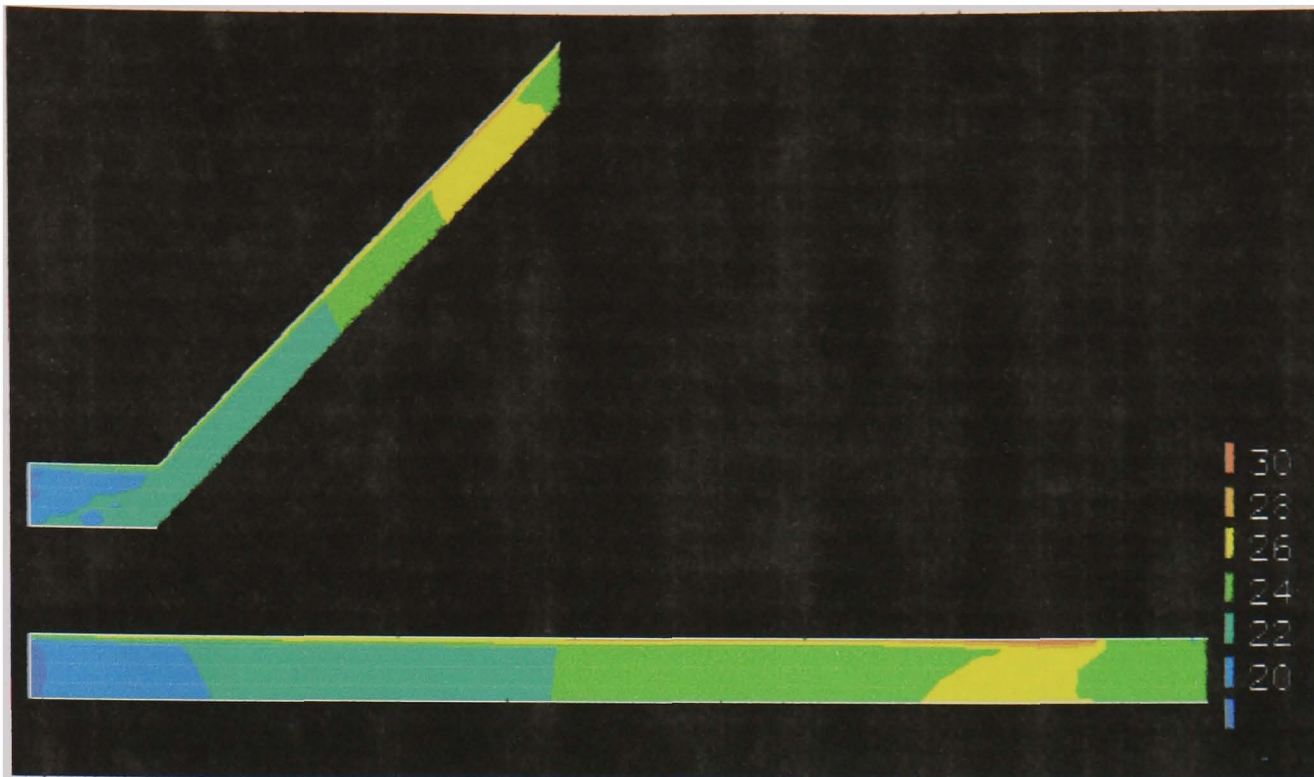


Figure 4.11. Contour plot of the HAZ regions rupture stress, calculated using the HAZ α -value ($\alpha=0.49$), for the $d=55\text{mm}$ branched flat end cap, stress in MPa.

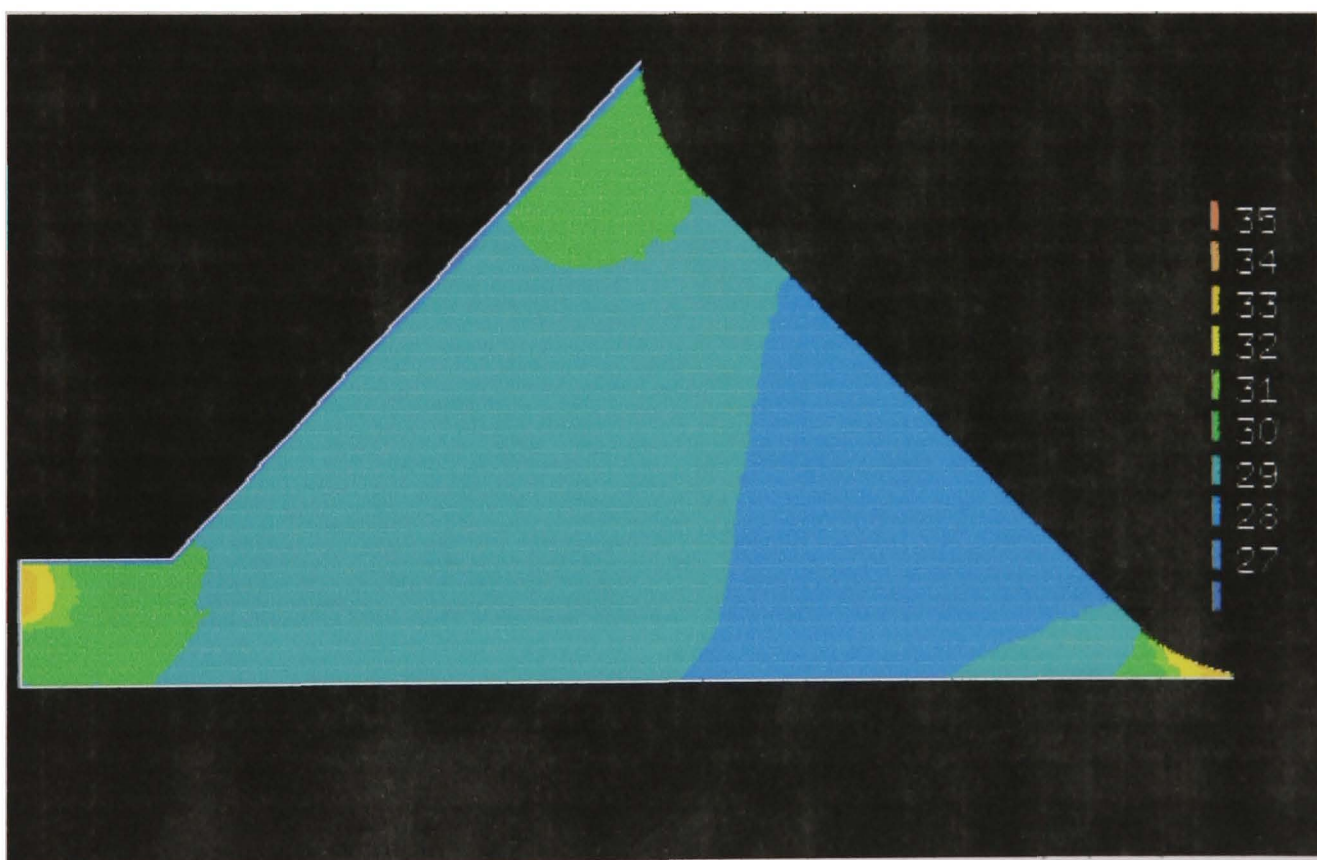


Figure 4.12. Contour plot of the WM region rupture stress, calculated using the WM α -value ($\alpha=0.26$), for the $d=55\text{mm}$ branched flat end cap, stress in MPa.

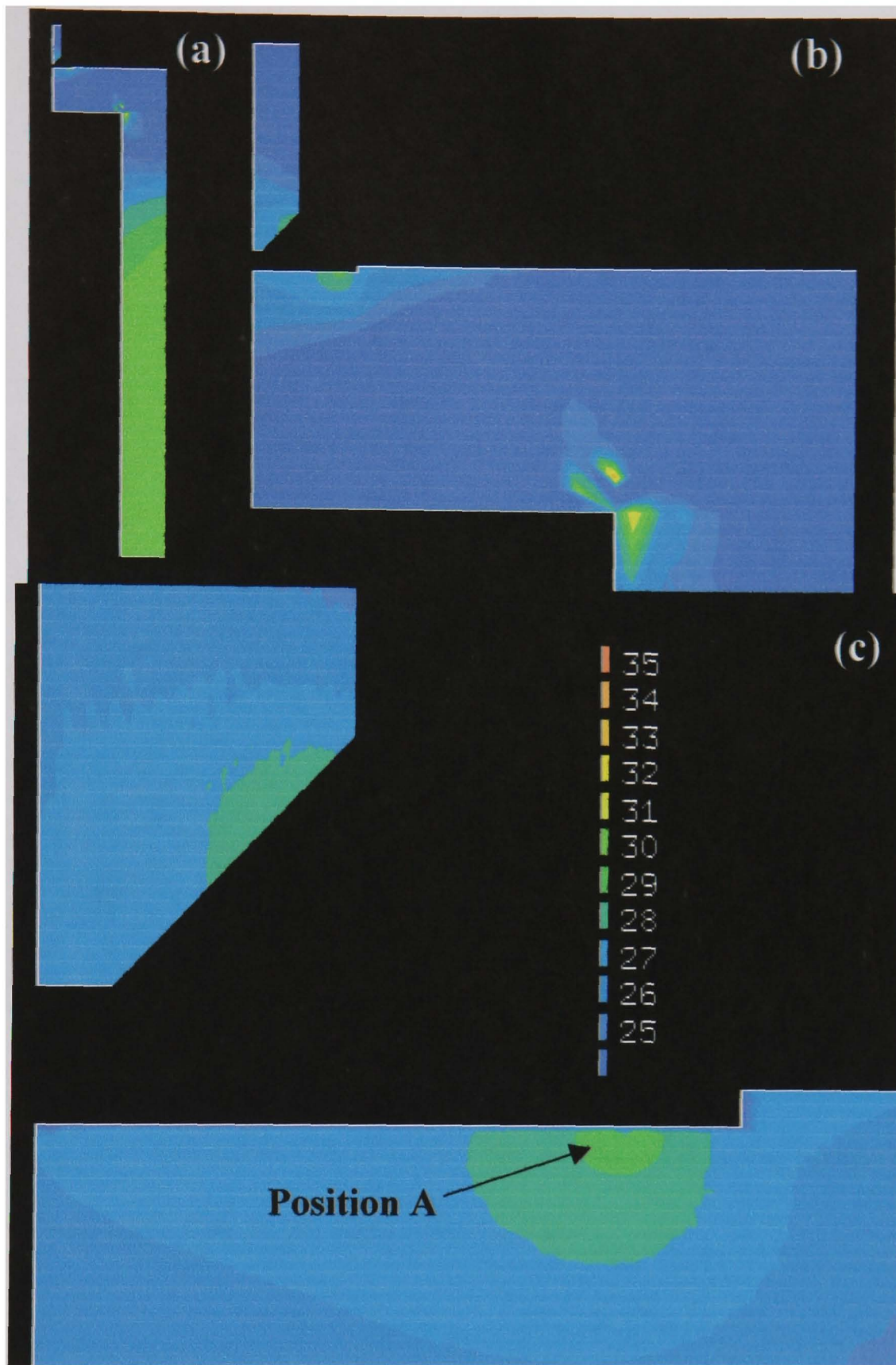


Figure 4.13. Contour plots of the PM regions rupture stress (MPa), calculated using the PM α -value ($\alpha=0.3$), within the (a) main pipe section, (b) the end cap section and (c) the weld region for the $d=55\text{mm}$ branched flat end-cap.



Figure 4.14. Contour plots of (a) equivalent (Von-Mises) stress (MPa) and (b) maximum principal stress (MPa) within the $d=55\text{mm}$ branched hemispherical end cap, concentrating on the main pipe section.

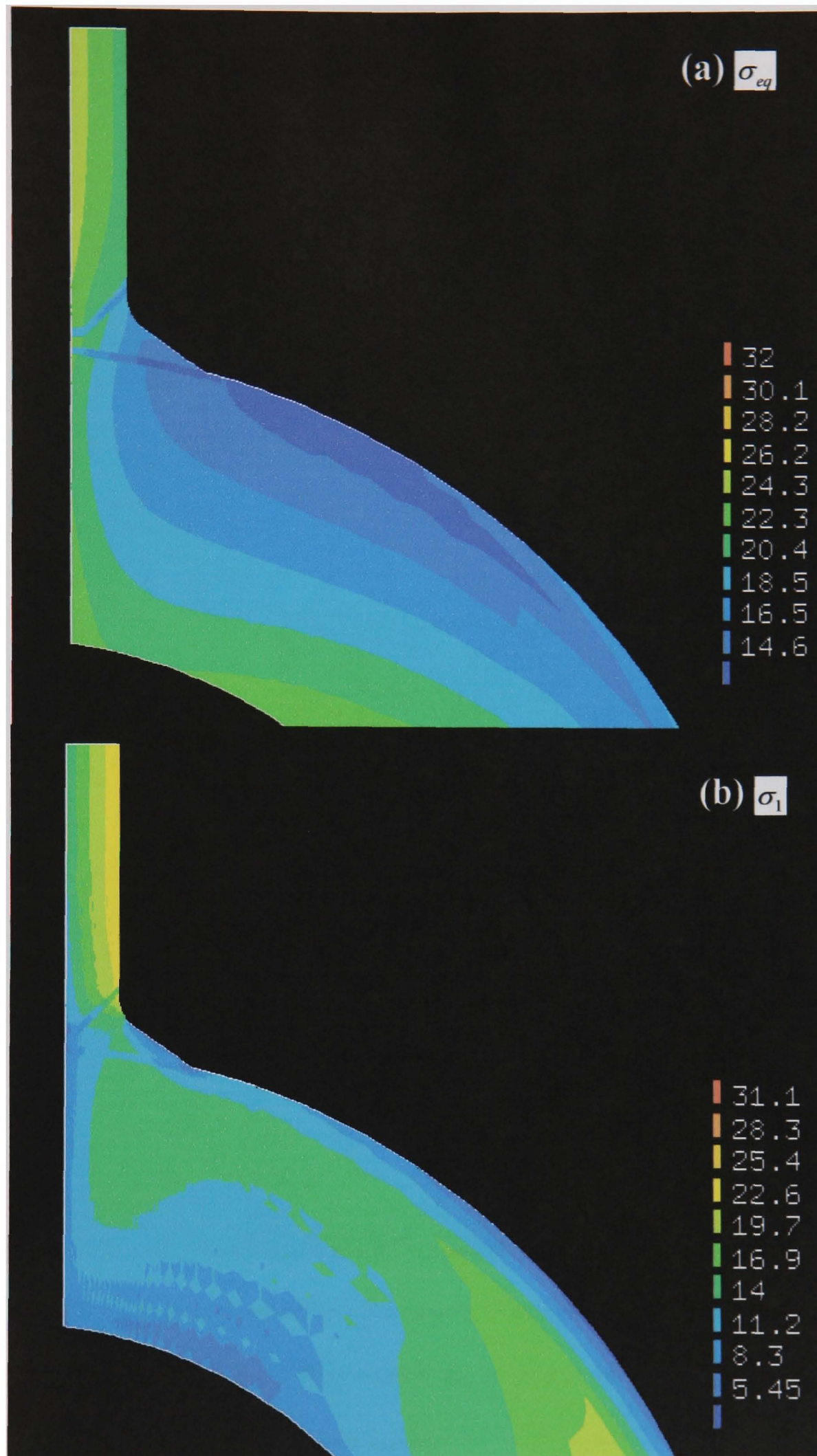


Figure 4.15. Contour plots of (a) equivalent (Von-Mises) stress (MPa) and (b) maximum principal stress (MPa) within the $d=55\text{mm}$ branched hemispherical end cap, concentrating on the end cap section.

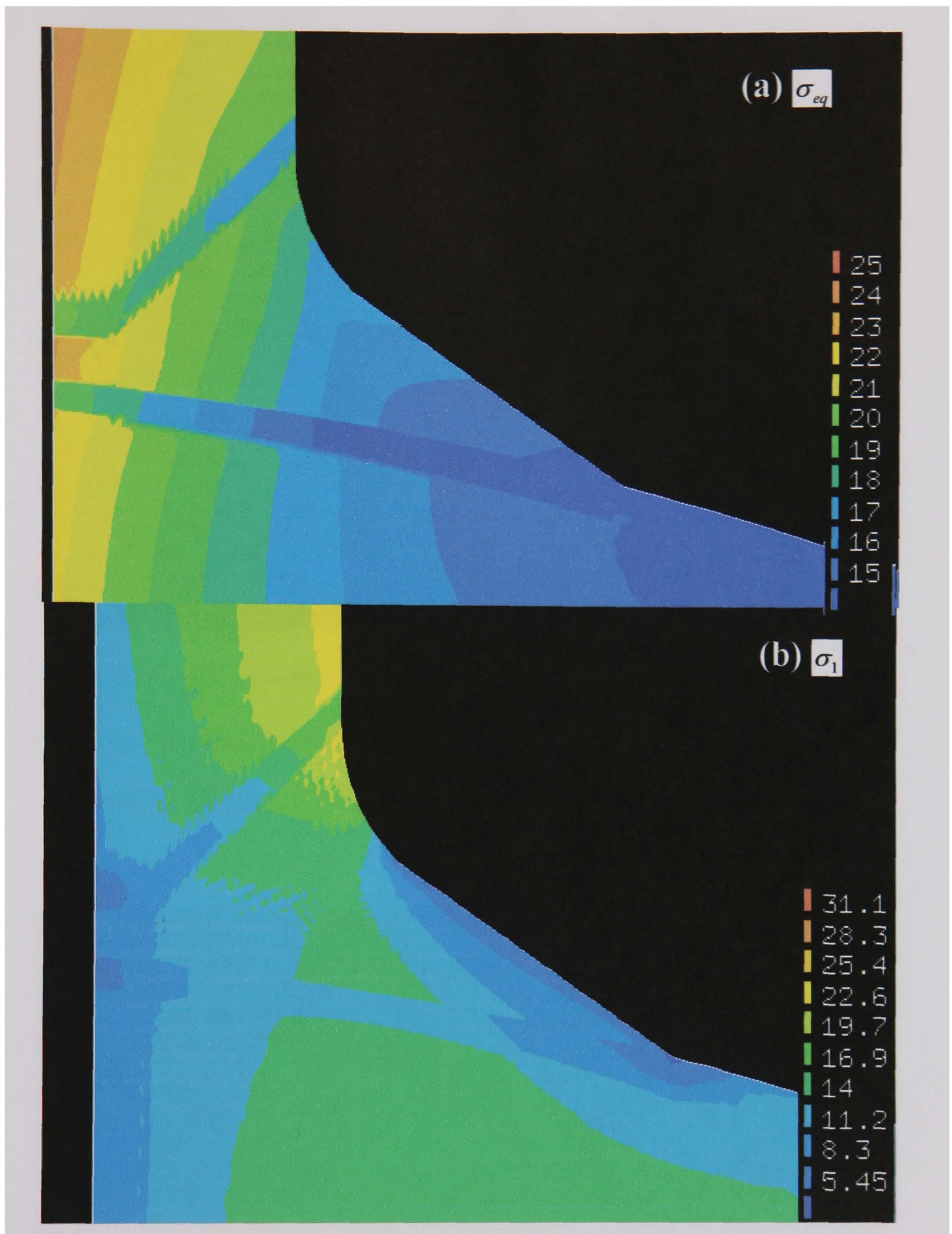


Figure 4.16. Contour plots of (a) equivalent (Von-Mises) stress (MPa) and (b) maximum principal stress (MPa) within the $d=55\text{mm}$ branched hemispherical end cap, concentrating on the weld region.

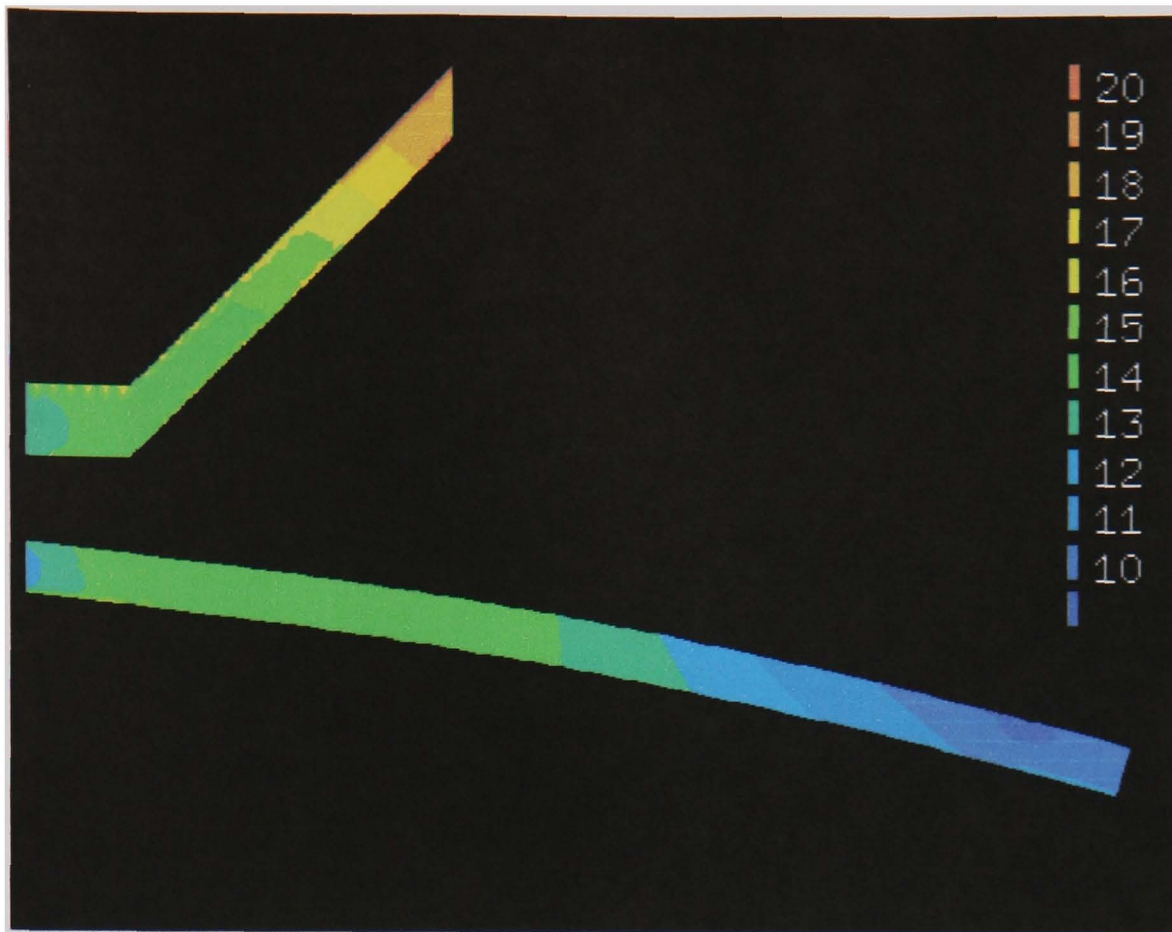


Figure 4.17. Contour plot of the HAZ regions rupture stress, calculated using the HAZ α -value ($\alpha=0.49$), for the $d=55\text{mm}$ branched hemi-spherical end cap, stress in MPa.

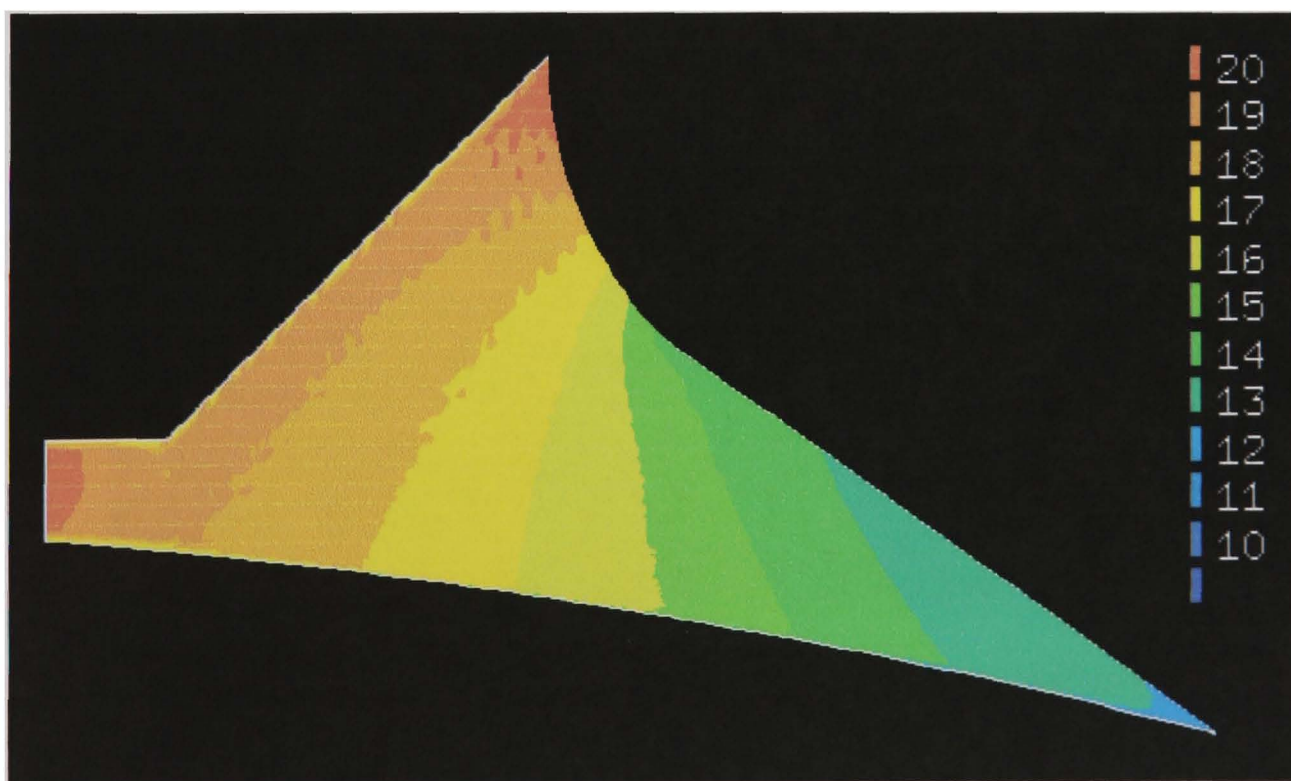


Figure 4.18. Contour plot of the WM region rupture stress, calculated using the WM α -value ($\alpha=0.26$), for the $d=55\text{mm}$ branched hemi-spherical end cap, stress in MPa.

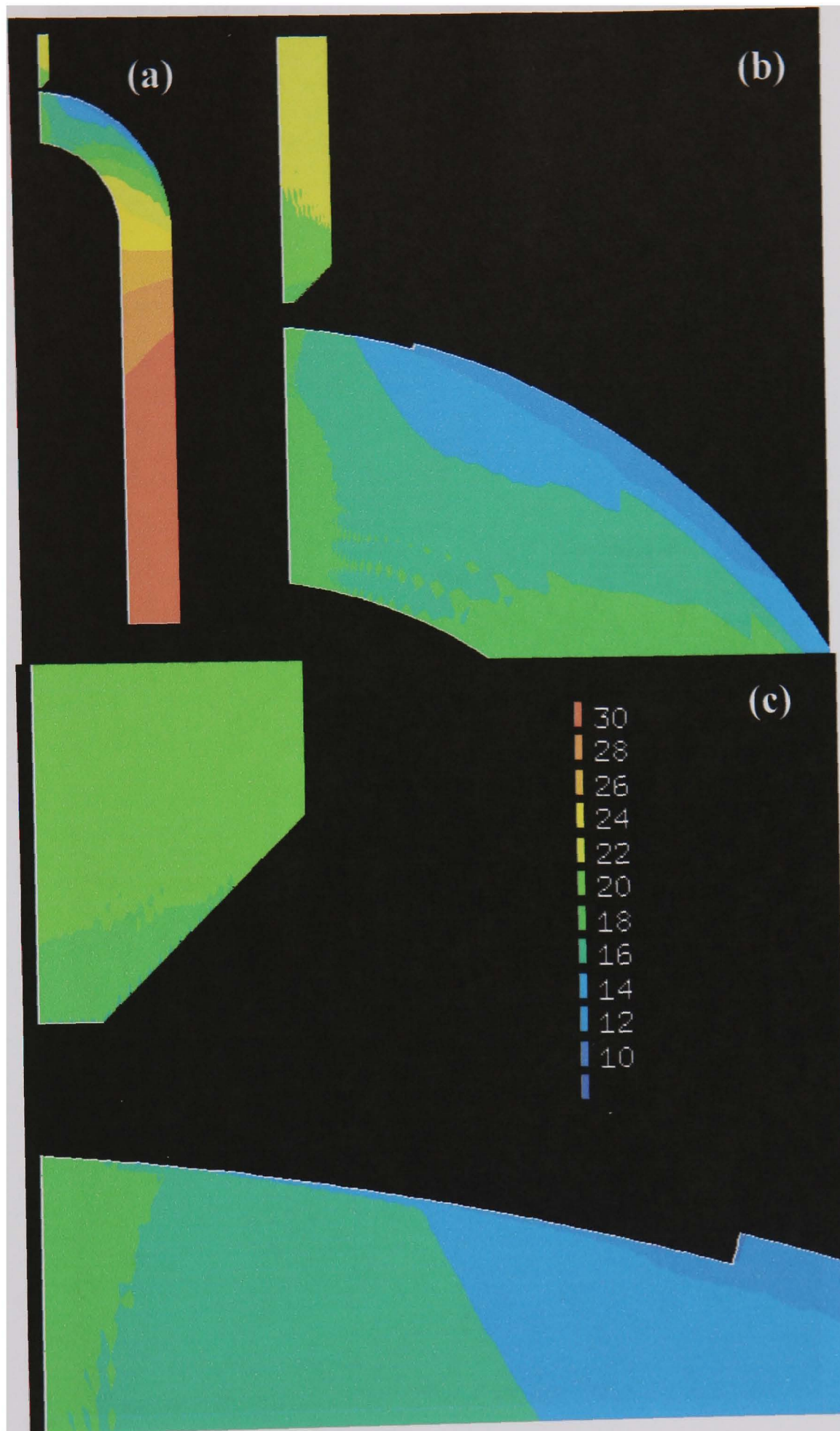


Figure 4.19. Contour plots of the PM regions rupture stress within the (a) main pipe section, (b) the end cap section and (c) the weld region. calculated using the PM α -value ($\alpha=0.3$), for the $d=55\text{mm}$ branched hemi-spherical end cap, stress in MPa.

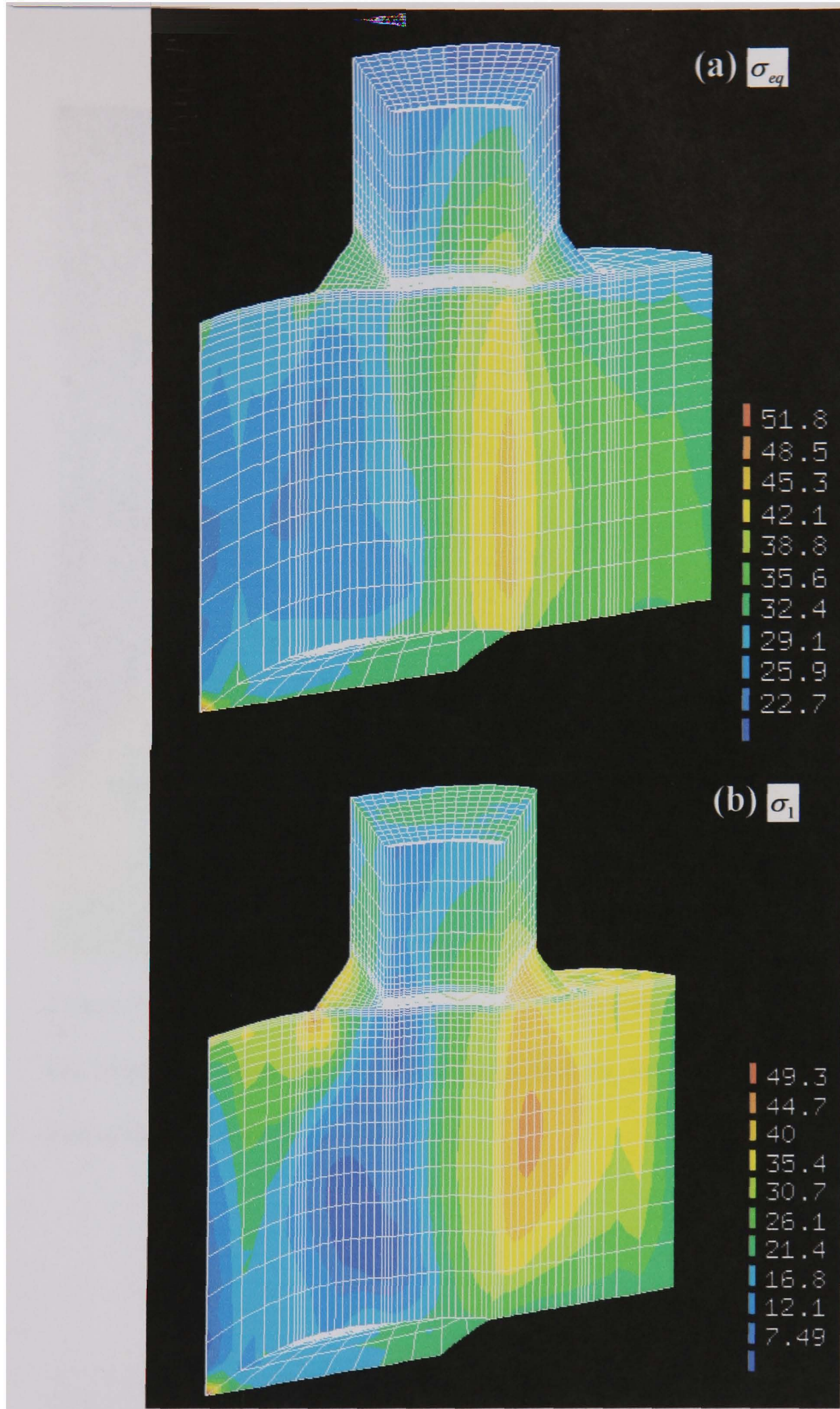


Figure 4.20. Sub-model contour plots of (a) equivalent (Von-Mises) stress and (b) maximum principal stress, (MPa), within the $d=55\text{mm}$ branched isolated main pipe main connection region.

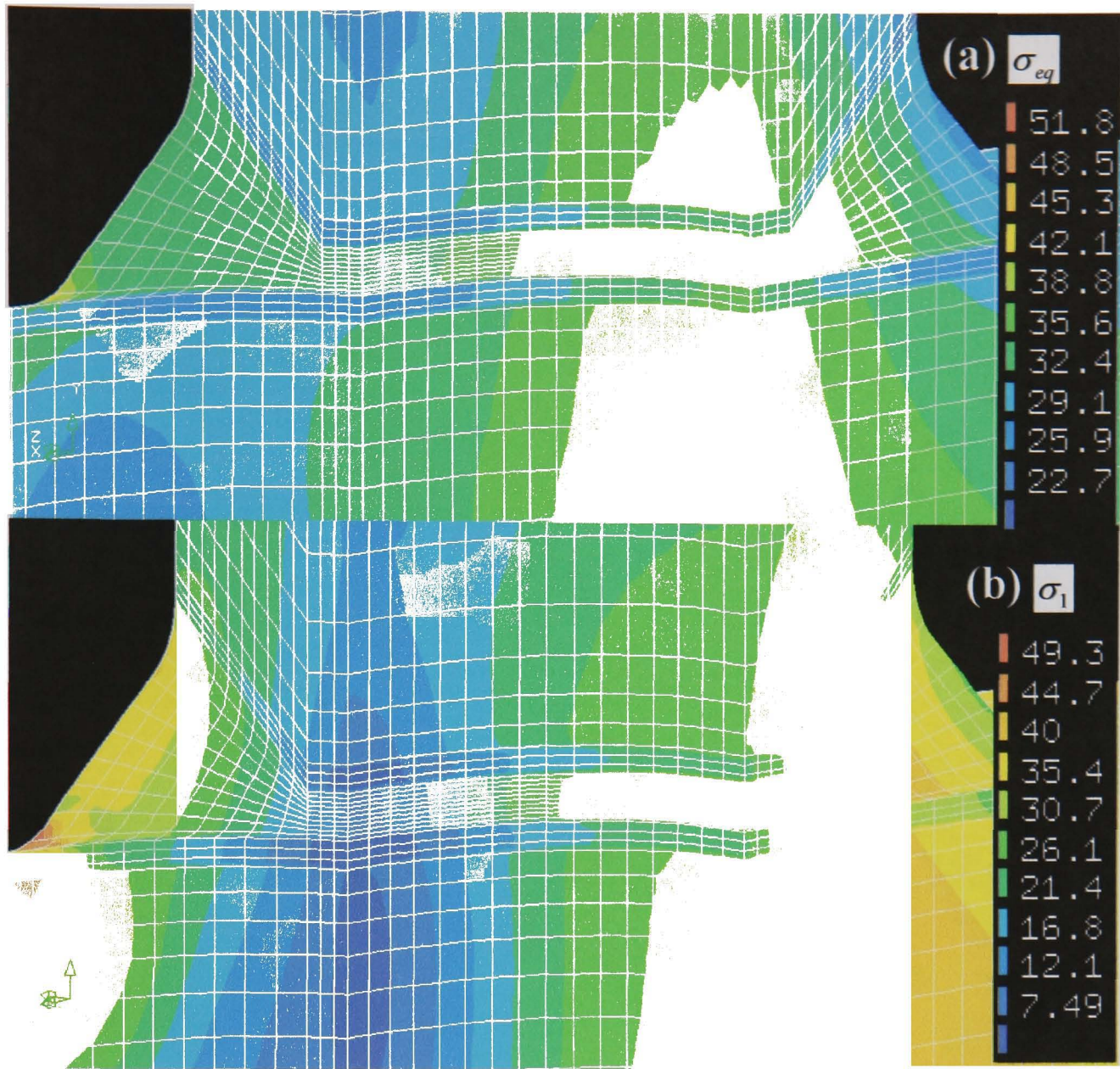


Figure 4.21. Sub-model contour plots of (a) equivalent (Von-Mises) stress and (b) maximum principal stress, (MPa), within the $d=55\text{mm}$ branched isolated main pipe inside surface weld region.

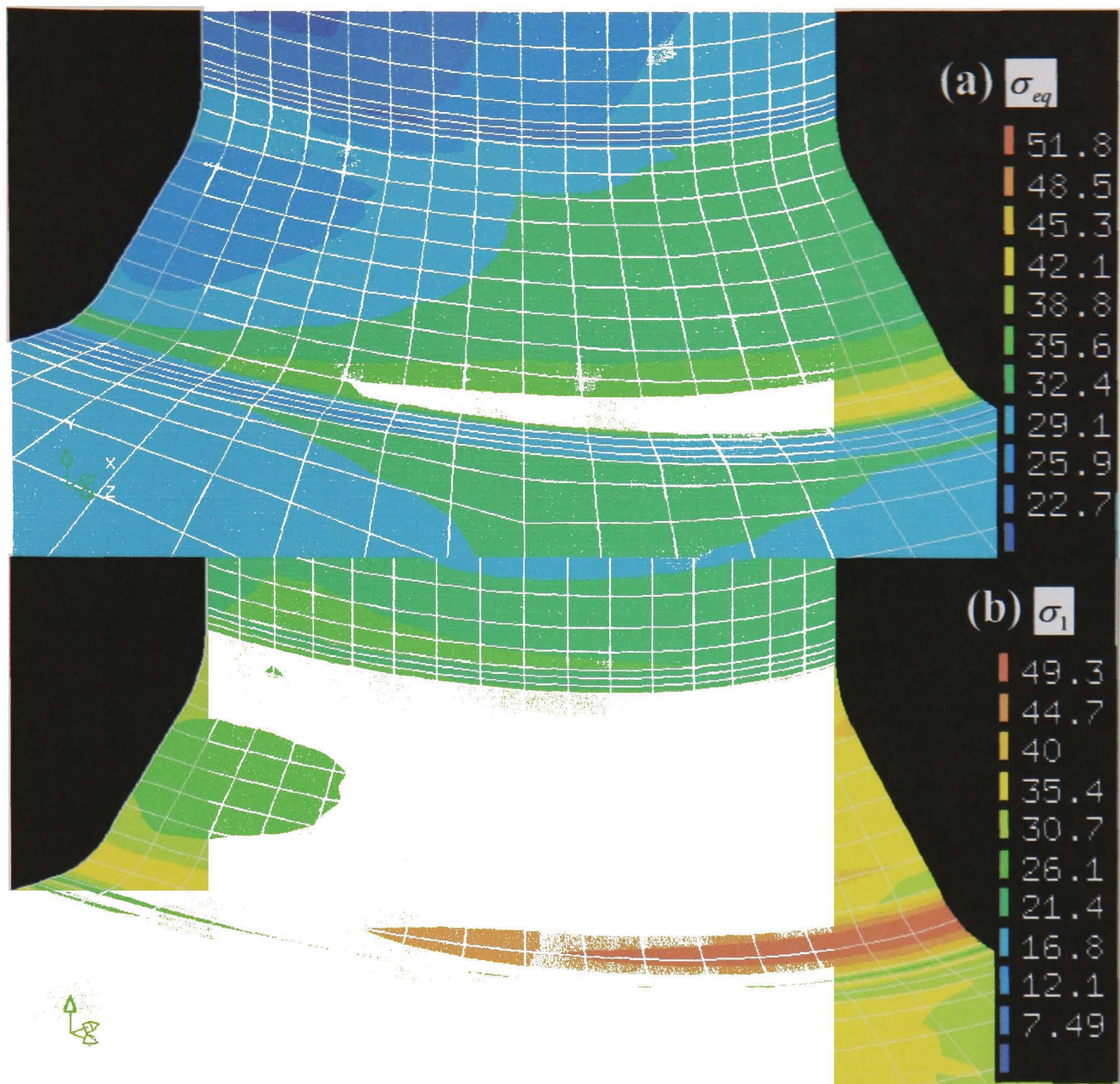


Figure 4.22. Sub-model contour plots of (a) equivalent (Von-Mises) stress and (b) maximum principal stress, (MPa), within the $d=55\text{mm}$ branched isolated main pipe outer surface weld region.

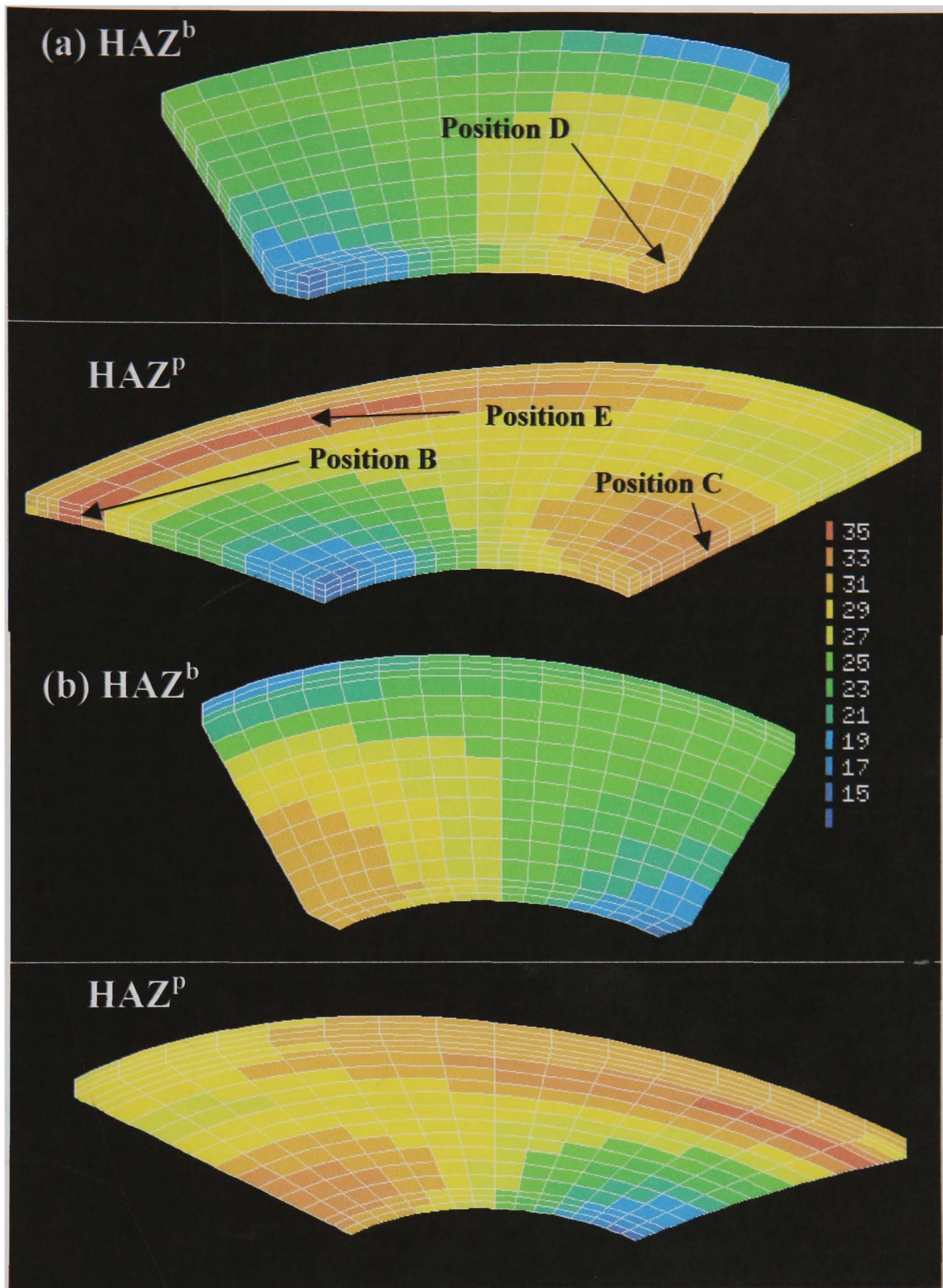


Figure 4.23. Sub-model contour plots of the HAZ^b (top) and HAZ^p (bottom) regions rupture stress distributions, calculated using the HAZ α -value ($\alpha=0.49$), at the (a) inside-bore top-surface view and (b) outside-bore bottom-surface view for the $d=55\text{mm}$ branched isolated main pipe.

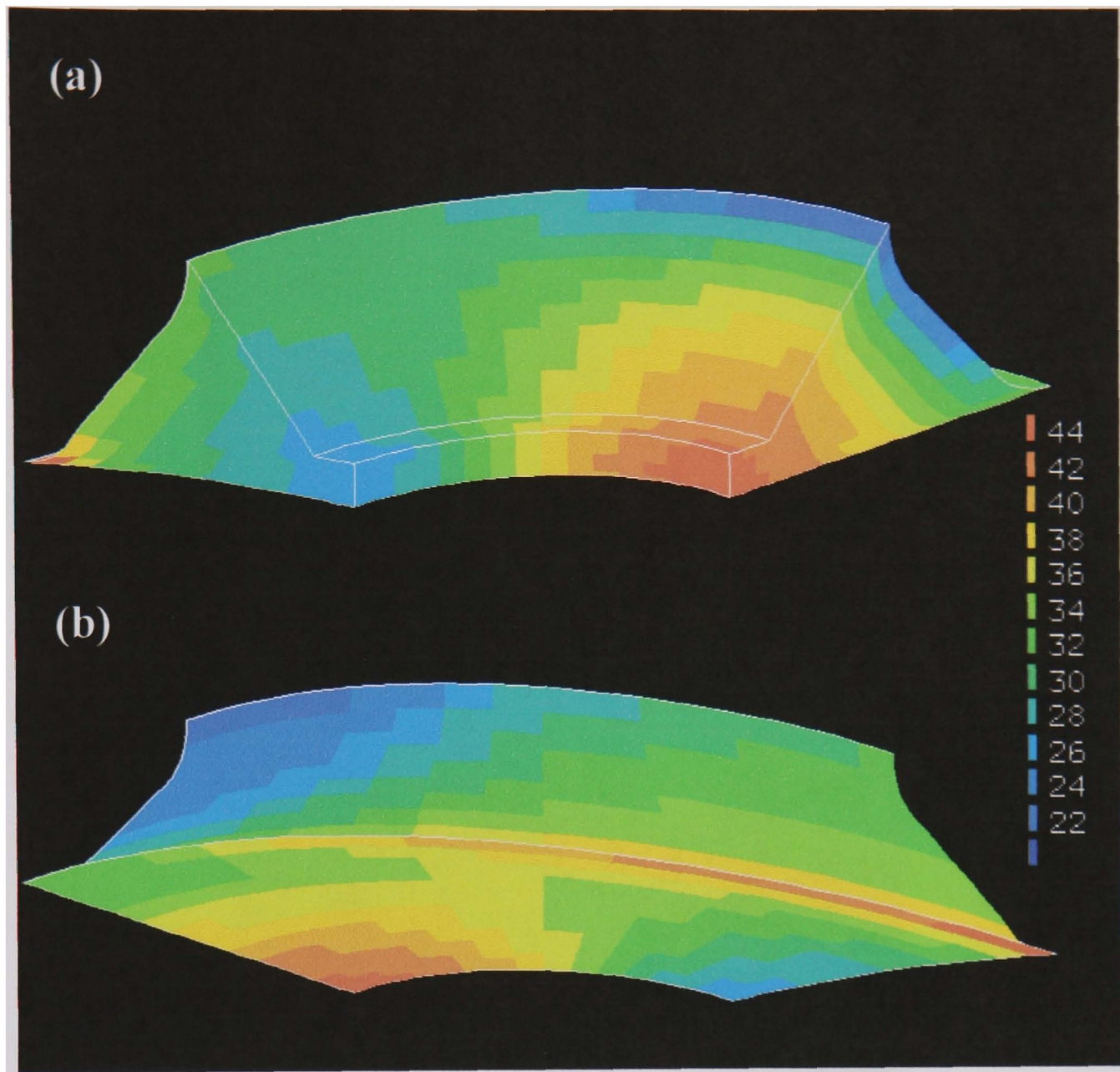


Figure 4.24. Sub-model contour plots of the WM region rupture stress, calculated using the WM α -value ($\alpha=0.26$), at the (a) inside-bore top-surface view and (b) outside-bore bottom-surface view for the $d=55\text{mm}$ branched isolated main pipe.

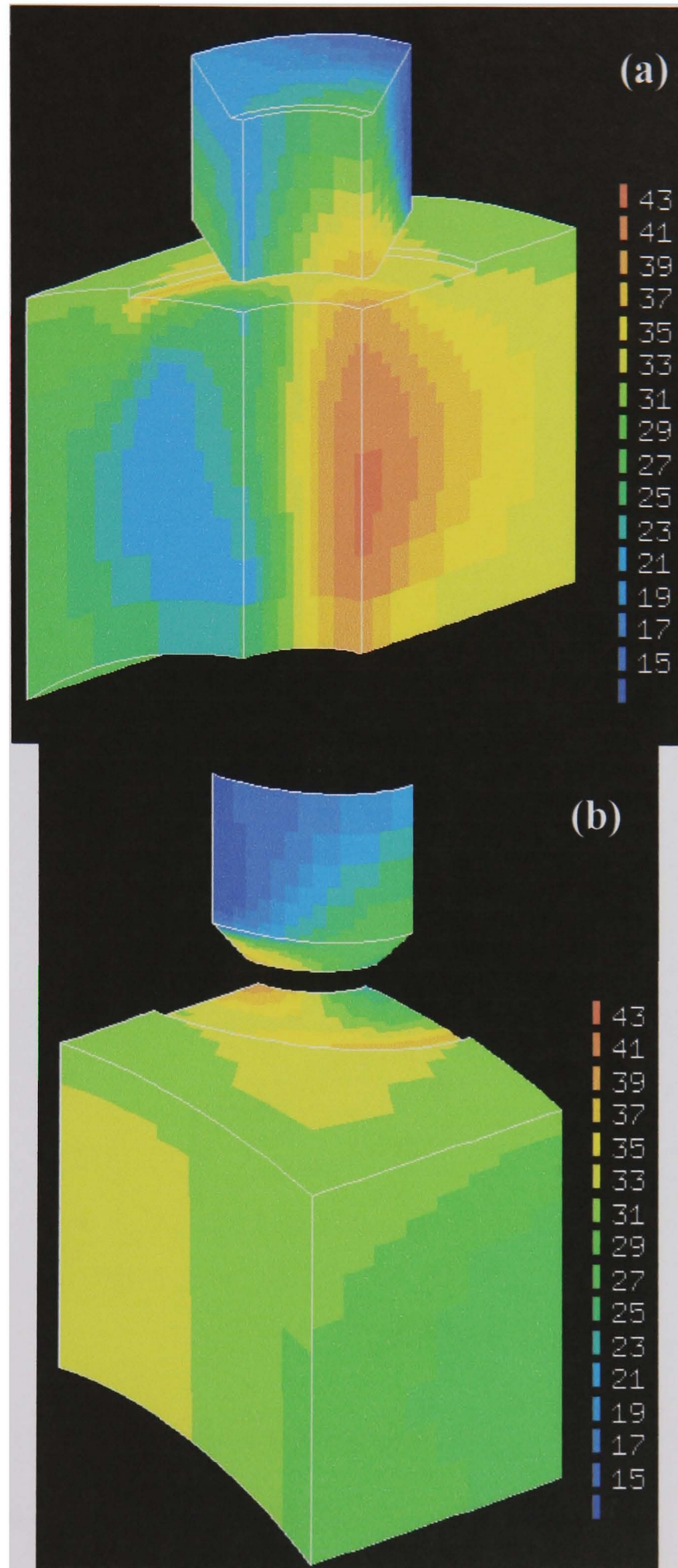


Figure 4.25. Sub-model contour plots of the PM regions rupture stress, calculated using the PM α -value ($\alpha=0.3$), within the (a) inside-bore surface view and (b) outside-bore surface view for the $d=55\text{mm}$ branched isolated main pipe.

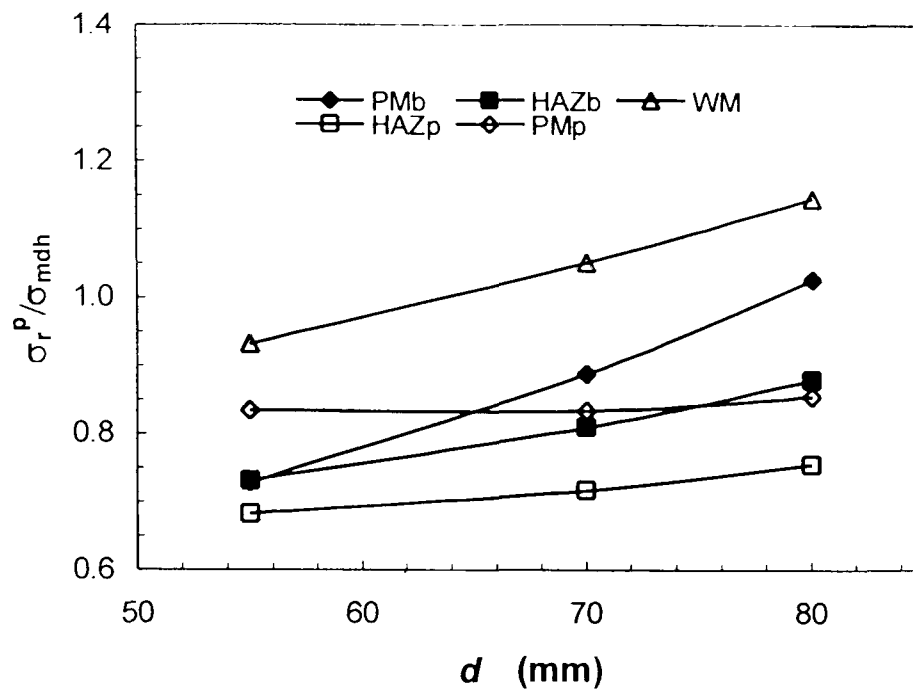


Figure 4.26. Effect of d on peak rupture stress, σ_r^P , in each zone for a branched flat end cap, ($\sigma_{mdh} = 36.9\text{MPa}$).

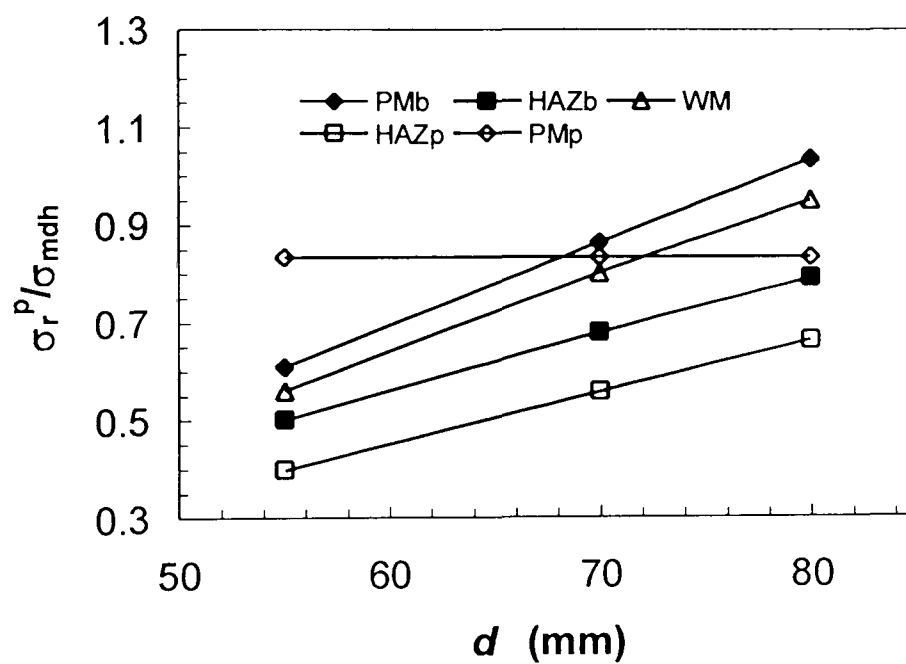


Figure 4.27. Effect of d on peak rupture stress, σ_r^P , in each zone for a branched hemispherical end cap, ($\sigma_{mdh} = 36.9\text{MPa}$).

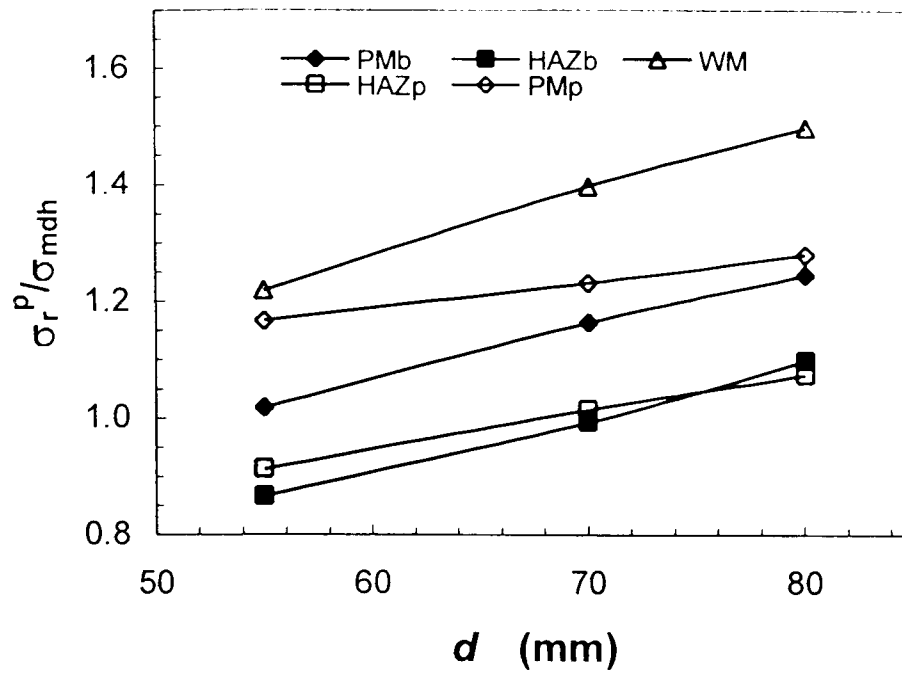


Figure 4.28. Effect of d on peak rupture stress, σ_r^P , for an isolated branched main pipe, ($\sigma_{mdh} = 36.9\text{MPa}$).

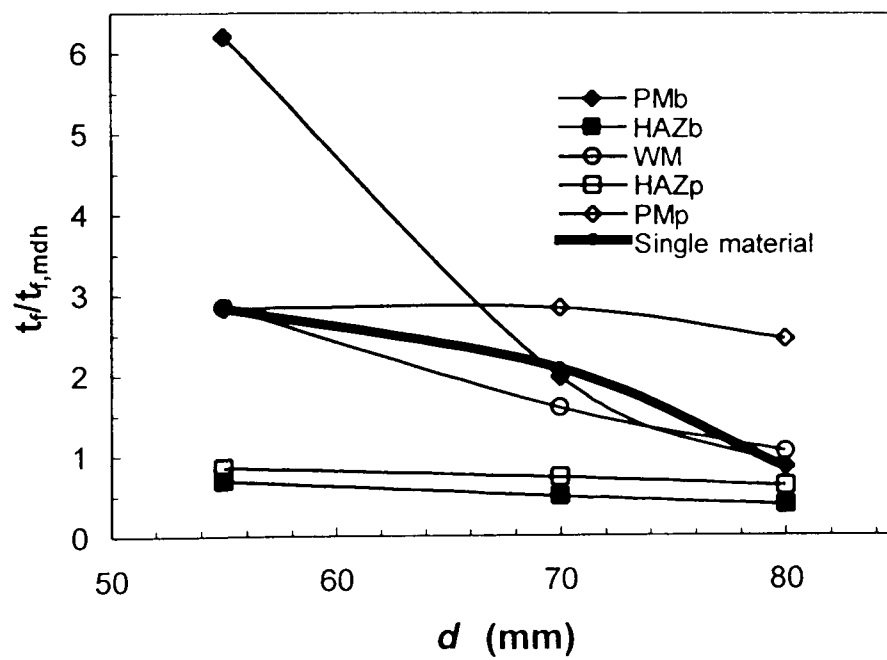


Figure 4.29. Effect of d on t_f for a branched flat end cap, ($t_{f,mdh} = 15261$ hours).

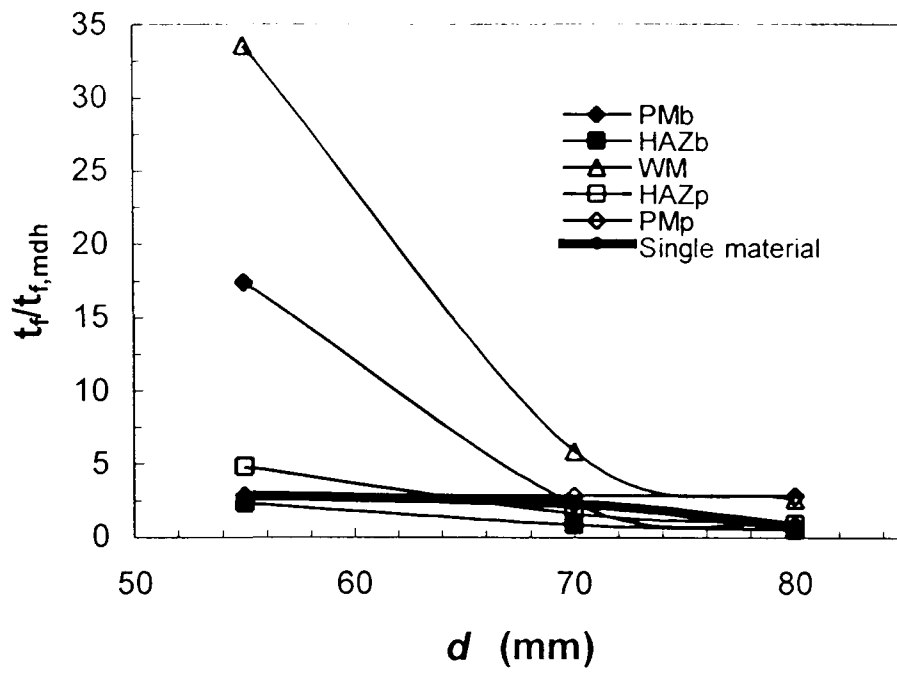


Figure 4.30. Effect of d on t_f for a branched hemispherical end cap, ($t_{f,mdh} = 15261$ hours).

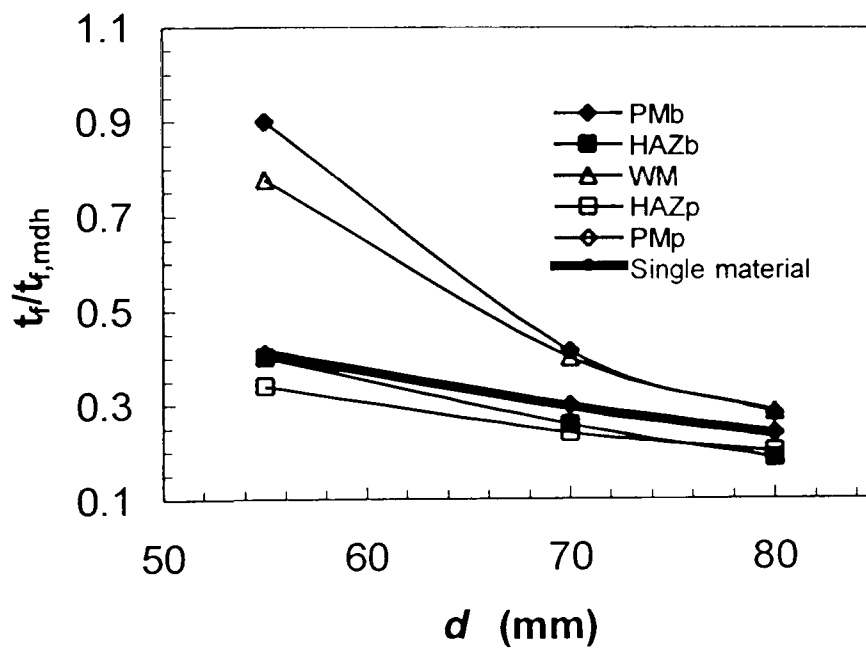


Figure 4.31. Effect of d on t_f for an isolated branched main pipe, ($t_{f,mdh} = 15261$ hours).

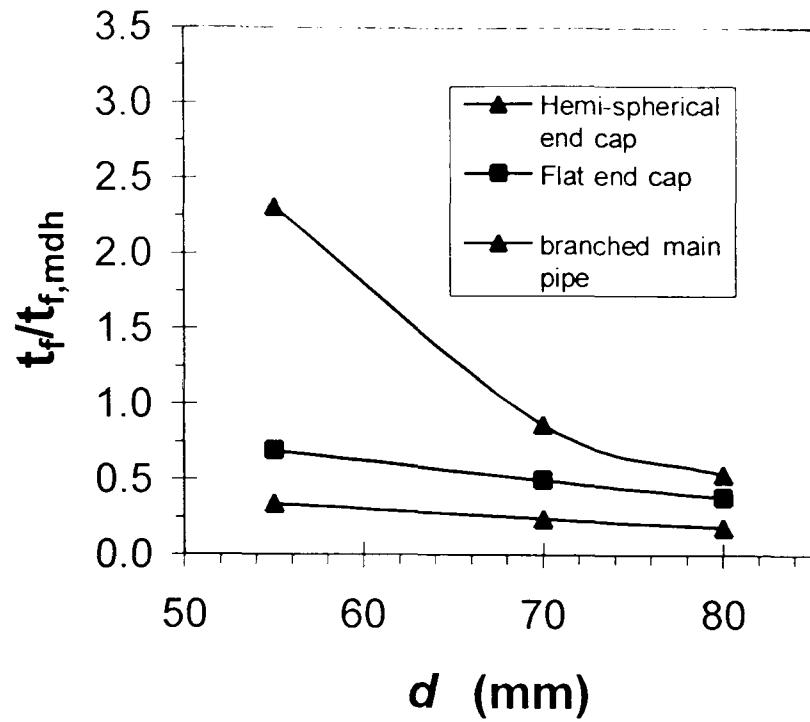


Figure 4.32. Comparative strengths of each connection type using 3-materials over varying d range in terms of failure life, ($t_{f,mdh} = 15261$ hours).

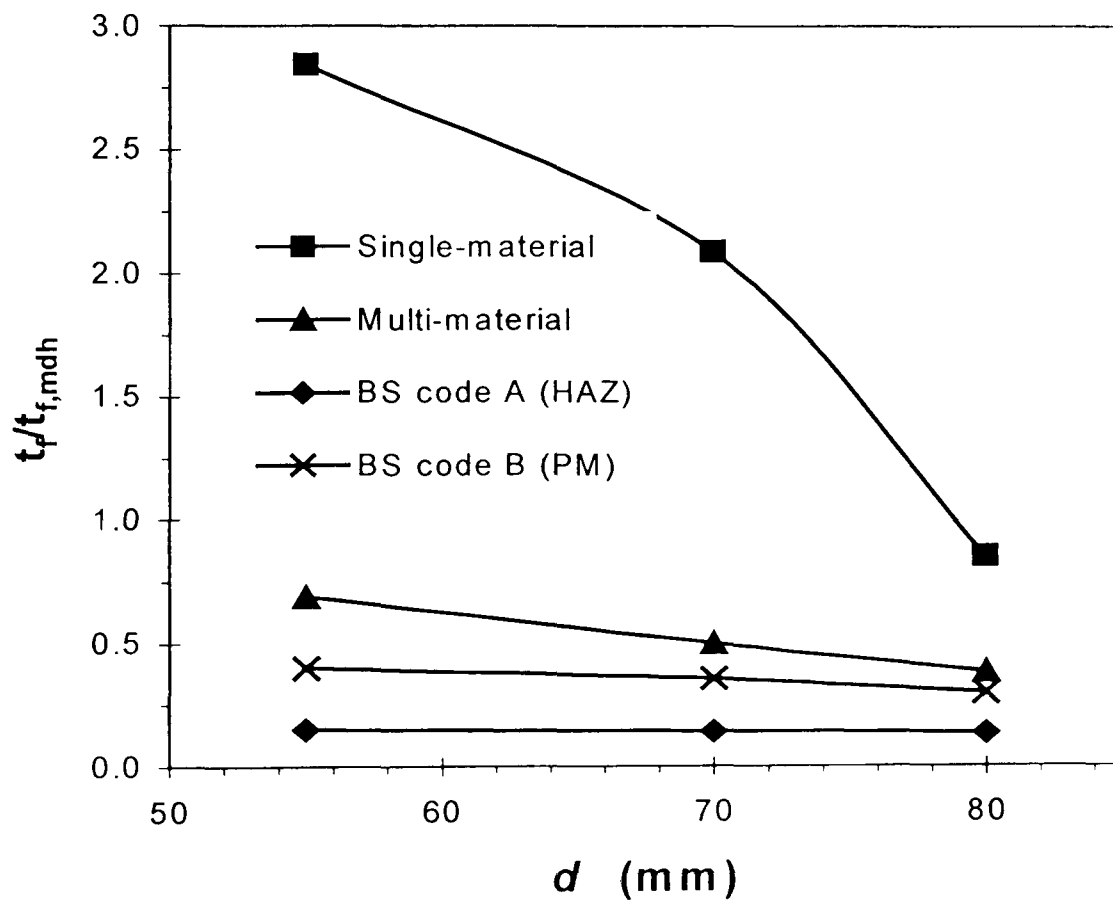


Figure 4.33. Comparison of BS code methods *A* and *B* rupture lives against single and 3-material steady-state lives with varying of d for a branched flat end cap, ($t_{f,mdh} = 15261$ hours).

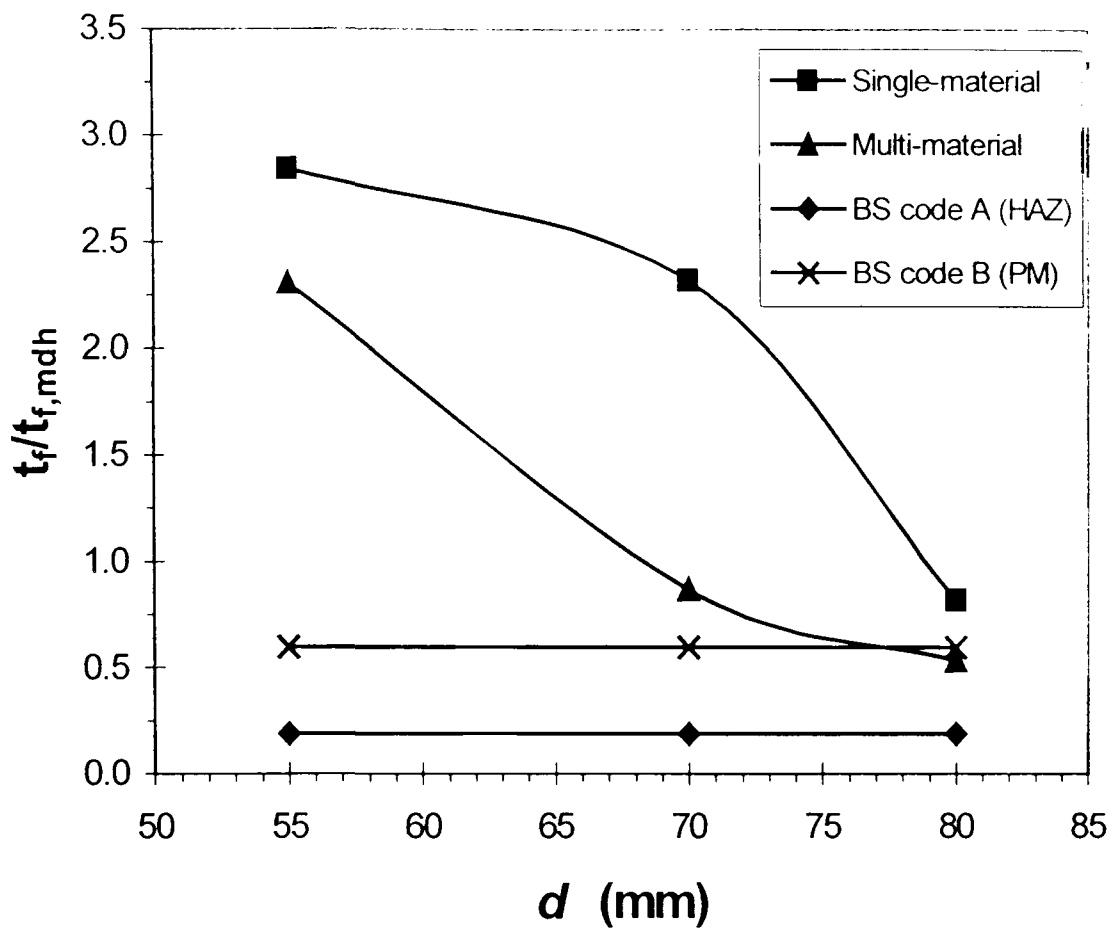


Figure 4.34. Comparison of BS code methods *A* and *B* rupture lives against single and 3-material steady-state lives with varying of *d* for a branched hemispherical end cap, ($t_{f,mdh} = 15261$ hours).

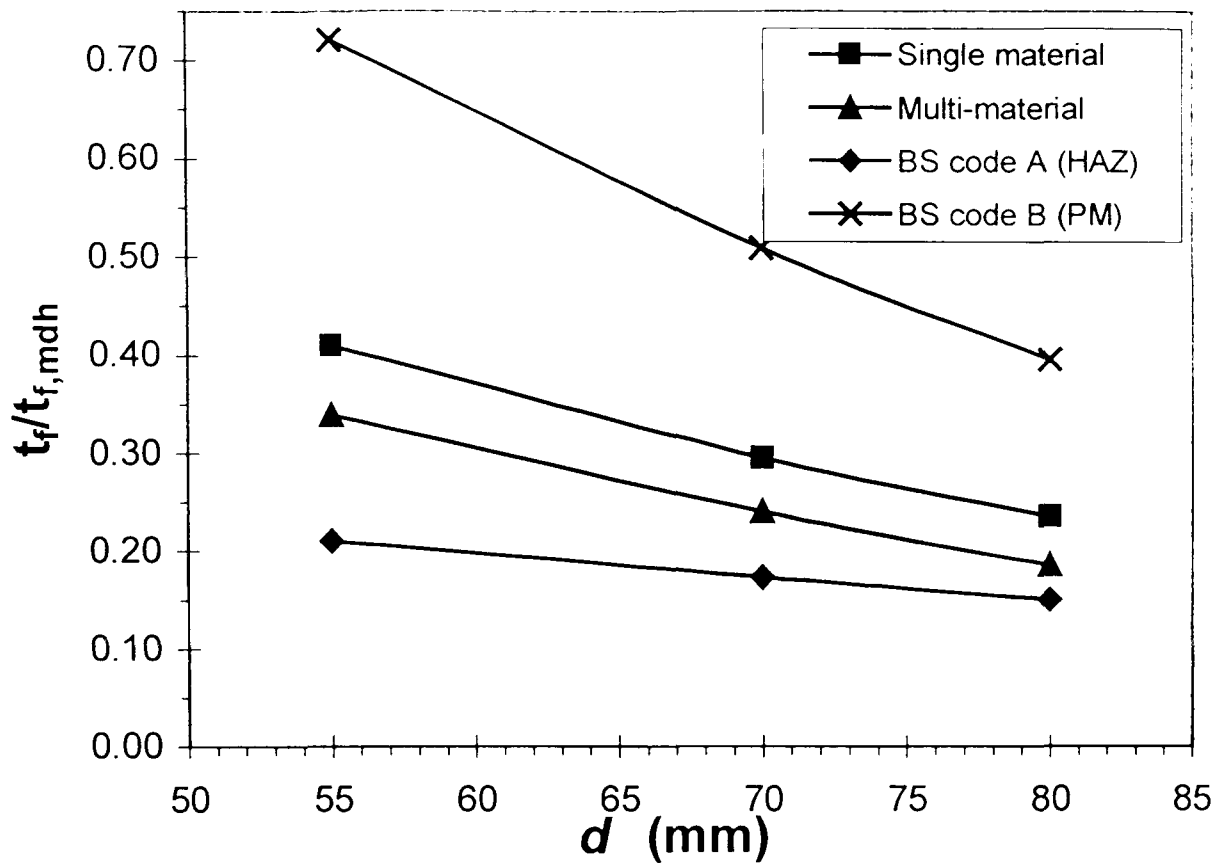


Figure 4.35. Comparison of BS code methods *A* and *B* rupture lives against single and 3-material lives with varying of d for an isolated branched main pipe, ($t_{f,mdh} = 15261$ hours).

CHAPTER FIVE

PARAMETRIC ANALYSIS OF STRESSES IN A WELDED BRANCHED PIPE UNDER CREEP CONDITIONS

5.1 Introduction

Chapter Four investigated the effects of geometry for a typical CMV weldment material set, at an operating temperature of 640°C, assessing the effects of geometry and presence of the weldment on failure. However, to investigate the effects of creep behaviour for different weldment materials (e.g. for assessing parent and weld filler material) on the mis-match of stress and the failure behaviour [8,24,26,69,99,132] within branched pipe weldments, parametric material analyses are required in order to improve knowledge for design and life assessment purposes. Under creep conditions, the stresses in a weld are strongly related to material inhomogeneity, which directly affects the failure life and position of the weld. Numerical analysis using the finite element (FE) method is often adopted to investigate the influence of material mismatch on the creep behaviour of welded components e.g. [26]. Analytical solutions can be obtained for the steady-state creep stresses in a number of simple multi-material components [104], e.g. beams in bending, multi-bar uniaxially loaded structures and pressurised cylinders. Based on these solutions, by a process of induction, a general formulation, based on Norton's creep law, for the steady-state stresses in multi-material structures has been proposed [35,102]. The method can be utilised to reduce significantly the number of calculations

required to cover the range of material constants in FE-based parametric analyses of welds. In addition, the method enables the results to be presented in a compact and easily manageable way. The approach has been applied to relatively simple welded components [100,102], but not to more complex components, such as welded branched pipes.

This chapter considers the general formulation combined with the approximately linear relationship between steady-state stress in a component and inverse of Norton creep exponent, n , to further reduce the computational overhead required in parametric multi-material studies. The latter approximation, first proposed by Calladine [36] for the maximum creep stress in a component, is well established for single material components and is commonly used in reference stress life assessment techniques, such as the R5 approach [13], to linearly interpolate stress for arbitrary values of n from known stresses corresponding to two other values of n . However, the approximation has not been previously applied for use within multi-material components to the author's knowledge. The use of the Calladine method presents an opportunity to significantly reduce the number of analyses required. This chapter firstly assesses the validity of the Calladine stress approximation for several positions of interest in a three-material welded branched pipe, i.e. not necessarily just for the maximum component stress. The applicability of the combined use of the Calladine approximation with the general formulation for the multi-material steady-state stresses is then investigated, followed by demonstration of the effect of variation of weldment properties on stresses, failure lives and failure positions of the component.

Then stress and life predictions obtained from the combined methods are compared with FE steady-state predictions, using three typical CrMoV weldment property sets and a steady-state creep rupture approach. Finally, the chapter presents the results of a systematic parametric stress analysis of four positions within common weld failure regions of the model in order to illustrate the application of the method to general and more practical situations, as well as providing practical information about the effect of branched pipe weld mismatch.

5.2 General formulation for multi-material creep stresses

It has been proposed [35,102] that a general expression for the steady-state creep stress at any given position within a multi-material component, for p different material zones, behaving according to Norton's law, is as follows:

$$\begin{aligned}
 & f_1(n_1, n_2, n_3, \dots, n_p, \text{dim}) \left(\frac{\dot{\epsilon}_{oi}}{\dot{\epsilon}_{o1}} \right)^{\frac{1}{n_1}} \left(\frac{\sigma_i}{\sigma_{nom}} \right)^{\frac{n_i}{n_1}} + f_2(n_1, n_2, n_3, \dots, n_p, \text{dim}) \left(\frac{\dot{\epsilon}_{oi}}{\dot{\epsilon}_{o2}} \right)^{\frac{1}{n_2}} \left(\frac{\sigma_i}{\sigma_{nom}} \right)^{\frac{n_i}{n_2}} + \\
 & f_3(n_1, n_2, n_3, \dots, n_p, \text{dim}) \left(\frac{\dot{\epsilon}_{oi}}{\dot{\epsilon}_{o3}} \right)^{\frac{1}{n_3}} \left(\frac{\sigma_i}{\sigma_{nom}} \right)^{\frac{n_i}{n_3}} + \dots \\
 & \dots + f_p(n_1, n_2, n_3, \dots, n_p, \text{dim}) \left(\frac{\dot{\epsilon}_{oi}}{\dot{\epsilon}_{op}} \right)^{\frac{1}{n_p}} \left(\frac{\sigma_i}{\sigma_{nom}} \right)^{\frac{n_i}{n_p}} - 1 = 0
 \end{aligned} \tag{5.1}$$

where σ_i is the stress at a chosen position in material i , $\dot{\epsilon}_{oi}$ and n_i are the Norton material constants for material i , σ_{nom} is a conveniently defined nominal stress and $f_1, f_2, f_3, \dots, f_p$ are unknown functions of Norton stress exponents and component dimensions. In this form of Norton creep law the material property $\dot{\epsilon}_{oi}$ is related to the A property of the un-normalised form of the Norton law of Equation 2.2, by $\dot{\epsilon}_{oi} = A \sigma_{nom}^{n_i}$. Equation 5.1 was induced

from the analytical solutions to a number of simple multi-material components obeying Norton's steady-state creep power law, in the form

$$\frac{\dot{\epsilon}_i^C}{\dot{\epsilon}_{oi}} = \left(\frac{\sigma_i}{\sigma_{nom}} \right)^{n_i} \quad (5.2)$$

It can be seen that the effects of the material $\frac{\dot{\epsilon}_{oi}}{\dot{\epsilon}_{oj}}$ ratios are explicitly defined

within the general equation. Equation 5.1 can be utilised to parametrically span a range of Norton material constants in multi-material parametric studies: previous applications have been used for a three-material cross-weld specimen [102] and a three-material welded main steam pipe [100]. The method is applied here to predict equivalent, maximum principal and rupture stresses at a series of critical positions in the significantly more challenging example of a three-material welded branched pipe. The rupture stress, σ_r , and creep life, t_f , are predicted using Equations 2.8 and 2.9, respectively, based on a steady-state multi-axial rupture stress approach [10,33,34]. The locations and values of the peak steady-state rupture stresses for various critical positions within each material zone can be identified and the associated creep rupture lives can then be predicted using these peak values. The minimum life over all material zones is then taken as the multi-material component life and the corresponding location as the component's failure initiation site.

As mentioned above, a novel aspect of the present work is the adoption of the (single-material) Calladine approach [36] for linear interpolation to a multi-material context. Thus, with respect to material 1, for example, to obtain the stress σ corresponding to a three-material set (n_1^C, n_2^A, n_3^A) , from known

stresses corresponding to three-material sets (n_1^A, n_2^A, n_3^A) and (n_1^B, n_2^A, n_3^A) , the multi-material interpolation equation can be expressed as follows:

$$\sigma(n_1^C, n_2^A, n_3^A) = \sigma(n_1^A, n_2^A, n_3^A) + \frac{\sigma(n_1^B, n_2^A, n_3^A) - \sigma(n_1^A, n_2^A, n_3^A)}{\frac{1}{n_1^B} - \frac{1}{n_1^A}} \left(\frac{1}{n_1^C} - \frac{1}{n_1^A} \right) \quad (5.3)$$

5.3 FE model of the welded branched pipe

A thick-walled, welded branched pipe, typical of fossil-fuel power plants was chosen for the study: the general geometry of the connection is shown in Figure 5.1, the assumed weld detail in Figure 5.2 and the corresponding dimensions used in the study are defined in Table 5.1. The values of D , T , d and t employed are 355mm, 65mm, 114mm and 20.8mm, respectively. The five different material zones modelled are the branch and main pipe parent material zones, designated PM^b and PM^p , respectively, the weld metal, designated WM, and the branch and main pipe heat-affected zones, designated HAZ^b and HAZ^p , respectively. The connection is a similar metal weld and therefore the HAZ^b and HAZ^p properties are assumed to be the same and likewise for the PM^b and PM^p zones, thus giving a three-material model of the connection. These regions are defined by a number of geometrical parameters. The heat-affected zone widths, assumed to be equal, are defined by the parameter h . The angle θ defines the inclination of HAZ^b to the horizontal, the angle β defines the inclination of the weld outer surface to the horizontal, the parameters r_o and r_i define the fillet radii created by weld neck and toe grinding and the additional parameters a , b and b_1 complete the geometry definition. The general shape of the weld is defined by the parameters b_s and

b_y , as shown in Figure 1, where b_y was set equal to the branch thickness, t . The loads applied to the model are an internal pressure, p_i , and a uniform axial end stress to the main pipe, $\bar{\sigma}_a$, which corresponds to a closed-ended condition. All three materials, i.e. PM, HAZ and WM, are assumed to obey a Norton power law of the form given in Equation 5.2. Similar to the models in Chapter 4, a symmetrical quarter of the branched connection was modelled using global and sub-modelling techniques for the weld region, both using twenty-noded quadratic three-dimensional brick elements with reduced integration as shown. Figures 5.3 and 5.4 show the global and sub-model, respectively, for the typical isolated branched pipe. The mesh chosen for the global and sub-model consisted of 4400 and 10500 elements, respectively. Detailed attention has been given to ensuring compatible and uniform mesh design across the HAZ, PM and WM material mismatch boundaries. Weld toe and neck radii are used to eliminate sharp weld edges and therefore reduce unrealistic stress peaks. Careful interpretation of the time-dependent nodal stresses was used to ascertain when steady-state was achieved. Appendix 1 provides some general guidelines on how FE analysis can be utilized to effectively predict steady-state stress distributions. The analyses were carried out using ABAQUS finite element software [28].

5.4 Analysis procedure

For a welded branched pipe consisting of three weldment materials (PM, HAZ and WM), Equation 5.1 reduces to the following:

$$f_1(n_{PM}, n_{HAZ}, n_{WM}) \left(\frac{\dot{\epsilon}_{oi}}{\dot{\epsilon}_{oPM}} \right)^{\frac{1}{n_{PM}}} \left(\frac{\sigma_i}{\sigma_{nom}} \right)^{n_{PM}} + f_2(n_{PM}, n_{HAZ}, n_{WM}) \left(\frac{\dot{\epsilon}_{oi}}{\dot{\epsilon}_{oHAZ}} \right)^{\frac{1}{n_{HAZ}}} \left(\frac{\sigma_i}{\sigma_{nom}} \right)^{n_{HAZ}} + f_3(n_{PM}, n_{HAZ}, n_{WM}) \left(\frac{\dot{\epsilon}_{oi}}{\dot{\epsilon}_{oWM}} \right)^{\frac{1}{n_{WM}}} \left(\frac{\sigma_i}{\sigma_{nom}} \right)^{n_{WM}} = 1 \quad (5.4)$$

where, for a given geometry, f_1, f_2 and f_3 are unknown functions of the stress exponents and σ_i is the stress measure of interest at any chosen position in material i . Materials 1, 2, 3 of Equation 5.1 correspond to the PM, HAZ and WM, respectively, so that $n_1 = n_{PM}$, $n_2 = n_{HAZ}$, $n_3 = n_{WM}$, $\dot{\epsilon}_{o1} = \dot{\epsilon}_{oPM}$, $\dot{\epsilon}_{o2} = \dot{\epsilon}_{oHAZ}$ and $\dot{\epsilon}_{o3} = \dot{\epsilon}_{oWM}$. Once the f_1, f_2 and f_3 functions are determined, this equation can clearly be used to determine the steady-state stress for arbitrary Norton material constants for the three-material component. The procedure described by Hyde and co-workers, e.g [35,102,104], required 81 steady-state FE creep calculations using the multi-material model to determine the f_1, f_2 and f_3 functions for three material components with different $\dot{\epsilon}_{oi}$ and n_i values. However, for complex geometries such as multi-material welded branched connections, even this number of analyses is a significant computational overhead. The use of the Calladine approximation can reduce this number to 24 analyses, as described in the following steps:

- I. Pick a suitable σ_{nom} which is dependent on load level, e.g. mean diameter hoop stress of the main pipe.
- II. Choose a stress measure of interest, e.g. equivalent (von-Mises) stress.
- III. Choose a position of interest in one of the material zones, e.g. one of positions A to I on Figure 5.4 to 5.6.

- IV. Choose two values of n corresponding to the extremes of the range to be spanned, in this case, these values are 3 and 10.
- V. Assign each of n_{PM} , n_{HAZ} and n_{WM} one of the latter two values, i.e. either 3 or 10. Thus, for example, set $(n_{PM}, n_{HAZ}, n_{WM}) = (3, 3, 3)$.
- VI. Choose three different pairs of values for $(\dot{\epsilon}_{oHAZ} / \dot{\epsilon}_{PM}, \dot{\epsilon}_{oHAZ} / \dot{\epsilon}_{WM})$, e.g. $(0.9, 0.95)$, $(1, 1.05)$ and $(1.1, 1.15)$, noting that $\dot{\epsilon}_{oi} / \dot{\epsilon}_{oi} = 1$ ($= \dot{\epsilon}_{oHAZ} / \dot{\epsilon}_{HAZ}$, in this case).
- VII. Run steady-state FE analyses for each of the three $(\dot{\epsilon}_{oHAZ} / \dot{\epsilon}_{PM}, \dot{\epsilon}_{oHAZ} / \dot{\epsilon}_{WM})$ pairs, using the chosen $(n_{PM}, n_{HAZ}, n_{WM})$ values from Step V.
- VIII. Using the three σ_i values from Step VII, the corresponding $(\dot{\epsilon}_{oHAZ} / \dot{\epsilon}_{PM}, \dot{\epsilon}_{oHAZ} / \dot{\epsilon}_{WM})$ values, the σ_{nom} value and the n_{PM} , n_{HAZ} and n_{WM} values in Equation 5.4, obtain three simultaneous equations in f_1 , f_2 and f_3 .
- IX. Solve the three simultaneous equations to obtain f_1 , f_2 and f_3 for the chosen $(n_{PM}, n_{HAZ}, n_{WM})$ values, e.g. $f_1(3,3,3)$, $f_2(3,3,3)$ and $f_3(3,3,3)$, in this case.
- X. Go back to step V and choose another permutation of $(n_{PM}, n_{HAZ}, n_{WM})$ using the two extreme n -values of 3 and 10, e.g. $(3, 3, 10)$, and follow Steps VI to IX to find the f_1 , f_2 and f_3 values for that combination. Do this for all eight permutations of $(n_{PM}, n_{HAZ}, n_{WM})$ on 3 and 10.
- XI. Thus, the complete set of f_1 , f_2 and f_3 values for the eight permutations of $(n_{PM}, n_{HAZ}, n_{WM})$ over the values of 3 and 10 are known.

e.g. see Table 5.2. These results can be used along with the Calladine approximation to give the stress for arbitrary material constants by following Steps XII and XIII.

- XII. The stresses corresponding to the eight ‘extreme’ $(n_{PM}, n_{HAZ}, n_{WM})$ value cases of Table 5.2 are first obtained, using Equation 5.4 and the f_1 , f_2 and f_3 values of Table 5.2 for arbitrary values of $\dot{\epsilon}_{oHAZ} / \dot{\epsilon}_{PM}$ and $\dot{\epsilon}_{oHAZ} / \dot{\epsilon}_{oWM}$. Clearly, these stresses are not directly related to an arbitrary n_{PM}, n_{HAZ}, n_{WM} combination.
- XIII. Linear interpolation, using Equation 5.3, is then employed between the stresses corresponding to these eight ‘extreme’ $(n_{PM}, n_{HAZ}, n_{WM})$ cases of Table 5.2 to predict the stress for an arbitrary n_{PM}, n_{HAZ}, n_{WM} combination, e.g. $(n_{PM}, n_{HAZ}, n_{WM}) = (4.1, 6.2, 5.4)$.
- XIV. Choose a different location or stress measure and repeat Steps V to XIII.

5.5 Results

5.5.1 Accuracy of the Calladine approximation

Figures 5.7 and 5.8 show the results of a series of FE calculations over the range $3 \leq n_{HAZ} \leq 10$ to assess approximate linearity of equivalent and maximum principal stresses with respect to $1/n_{HAZ}$ at three positions within the three-material weld region of the component. The three positions considered are positions A, B and C of Figure 5.6. A and B correspond to points in the branch parent material and weld metal, respectively, on the intersection of the x - y (crotch) plane and the inside branch bore. C corresponds to an adjacent HAZ.

point about 3 mm through the branch wall thickness, also on the x - y (crotch) plane. The corresponding (x,y,z) coordinates are also shown, for Cartesian axes centred on the intersection of branch and pipe central axes (see Figure 5.1). Figures 5.7a, 5.7b and 5.7c show the equivalent (von-Mises) stress versus $1/n_{HAZ}$ at these positions for three different $(\dot{\epsilon}_{oHAZ} / \dot{\epsilon}_{oPM}, \dot{\epsilon}_{oHAZ} / \dot{\epsilon}_{oWM})$ mismatch pairs of (0.1, 0.01), (1, 1), and (0.1, 0.1), corresponding to different degrees of weld-related material mis-match. The equivalent stress is normalised via the mean diameter hoop stress of the main pipe. It is clear that the equivalent stress varies approximately linearly with $1/n_{HAZ}$ for all cases. The dotted lines represent the linear interpolation lines between n_{HAZ} values of 3 and 10. It is shown that the largest differences between the linear approximation and the FE stress predictions occur at $1/n_{HAZ}$ midway between the two extremes of 0.1 and 0.33, i.e. at about $1/n_{HAZ} = 0.22$ ($n_{HAZ} = 4.5$). This is due to the nature of the curve produced by the FE predications. The differences between the linear approximation and FE stress predictions are generally small for the PM and WM positions A and B, respectively, at less than -2%. However, the largest difference associated with the HAZ Position C is much greater at about +35%, which corresponds to the $(\dot{\epsilon}_{oHAZ} / \dot{\epsilon}_{oPM}, \dot{\epsilon}_{oHAZ} / \dot{\epsilon}_{oWM}) = (0.1, 0.01)$ case of Figure 5.7c. Figures 5.8a, 5.8b and 5.8c show the corresponding variation of maximum principal stress with $1/n_{HAZ}$; similar trends are displayed. The greatest difference in this case is again about +35%, for the HAZ Position C corresponding to the $(\dot{\epsilon}_{oHAZ} / \dot{\epsilon}_{oPM}, \dot{\epsilon}_{oHAZ} / \dot{\epsilon}_{oWM}) = (0.1, 0.01)$ case of Figure 5.8c. For Positions A and B the effect of the material mis-match variation on the stress at these

positions is small and produced small differences between the linear approximation and FE predictions. However, the effects of varying the material mis-match, i.e. increasing $1/n_{HAZ}$, greatly increased the stress and the differences between the two methods, e.g. the stress increased about seven fold for the $\sigma_{eq}(\dot{\epsilon}_{oHAZ}/\dot{\epsilon}_{oPM}, \dot{\epsilon}_{oHAZ}/\dot{\epsilon}_{oWM}) = (0.1, 0.01)$ case and the differences peak at around 35%. The results therefore suggest that it is valid to use the Calladine approximation for equivalent or maximum principal stress at any position for the present three-material case as long as the cases use a low level of material mis-match between the three zones. Hence, caution must be taken when choosing the $\dot{\epsilon}_{oi}/\dot{\epsilon}_{oPM}$, $\dot{\epsilon}_{oi}/\dot{\epsilon}_{oHAZ}$ and $\dot{\epsilon}_{oi}/\dot{\epsilon}_{oWM}$ values in Steps VI described in the analysis procedure section, as Figures 5.7c and 5.8c both show that the errors may become larger with increasing material mis-match. This may be due to either the linear approximation relationship not holding or to the ineffectiveness of the mesh refinement level, or both. This aspect is discussed later in Section 5.5.2. Similar findings of an approximately linear relationship in stress would be expected if the variation of $1/n_{PM}$ or $1/n_{WM}$ was analysed and plotted.

5.5.2 Accuracy of the parametric analysis using the combined method

In order to demonstrate the parametric analysis capability of the method as described in Section 5.4, a selection of nine ‘critical’ locations within the multi-material, welded branched pipe have been chosen. These ‘critical’ points, labelled Positions A to I in Figures 5.4 to 5.6, correspond to regions close to observed ex-service branch creep failure locations [9,17] caused by

high stress and weak weld-related material, such as the HAZ Type IV region. The parametric analysis covers the practical range $3 \leq n_i \leq 10$, where again $i = 1, 2$ and 3 correspond to PM, WM and HAZ regions, respectively. using a typical internal pressure, p_i , of 16.55MPa. To illustrate the process, Table 5.2 shows the calculated f_1, f_2 and f_3 values corresponding to both the equivalent and maximum principal stresses, which are required to carry out the parametric analysis for Positions A to I of Figures 5.4 to 5.6. Throughout this study, the nominal stress used is the mean diameter hoop stress of the main pipe. Previous parametric analysis studies on a cross-weld creep specimen model [102] and a welded plain pipe model [100], both with three materials, using Equation 5.1, gave errors in stress of only about 2% compared to independent FE results. The present parametric procedure is different, due to the increased efficiency provided by the Calladine approximation and, equally importantly, the application is to a significantly more complex and realistic component. Validation of this enhanced procedure is again achieved via independent FE analyses. Three realistic weldment material sets are employed, as shown in Table 5.3. Set 1 is a service-aged CrMoV weldment at 640°C [30], Set 2 is an as-new CrMoV weldment at 640°C [30] and Set 3 is an as-new CrMoV weldment at 565°C [20,93]. Tables 5.4a, 5.4b and 5.4c show the comparison between the maximum principal and equivalent stresses as predicted by (i) the proposed new parametric procedure and (ii) independent FE steady-state analyses, for all nine positions A to I and for the three material sets of Table 5.3. The new parametric procedure accurately predicts equivalent, maximum principal and rupture stresses to within 3%, 4% and 3.5%, respectively, of the independently predicted FE values. Rupture lives

predicted using the rupture stresses are all within 8% of the independent FE-based values.

Section 5.5.1 highlights that large differences between the linear approximation and FE stress predictions resulted from cases of large material mis-matches, e.g. up to a 35% difference for HAZ Position C. It was noted that this could be due to either the linear approximation not holding or the ineffectiveness of the FE mesh used. However, the differences in stress between the two methods are much smaller (less than 4%) for the comparison of typical weldment properties shown in Table 5.4, even though the f values used were calculated using stresses obtained from large differences in n values of 3 and 10. It is thought that the stresses remain accurate compared to the FE predictions because the stresses used to calculate the f values were from FE analyses which used carefully chosen $\dot{\epsilon}_{oi} / \dot{\epsilon}_{oPM}$, $\dot{\epsilon}_{oi} / \dot{\epsilon}_{oHAZ}$ and $\dot{\epsilon}_{oi} / \dot{\epsilon}_{oWM}$ values to balance the level of material mis-match. Concluding that the linear approximation technique holds over a wide range of n for multi-material applications with relatively low levels of material mis-match, as seen for example in typical plant welds. It is therefore thought that the large differences of up to 35% between the approximation and the FE stress predictions for the HAZ Position C was due to inadequate mesh refinement for the high mis-match cases of $n_{HAZ} < 6$ in Figures 5.7c and 5.8c, since the mesh could not manage to predict accurate stresses when the differences in stresses across the zones were very large.

5.5.3 Results of a parametric analysis of stresses

The results of a systematic parametric analysis of the equivalent stress, σ_{eq} , and maximum principal stress, σ_1 , variation across the weld at critical positions A (PM^b), B (WM), D (HAZ^p) and F (WM) of Figure 5.5 and 5.6 are presented and used to illustrate the variations in stress which occur due to the difference in creep properties of the three weld materials. Detailed stress results of the parametric investigation are presented for the four positions with sample variation of material properties. The four positions are within regions of high stress concentration and are likely positions of creep failure [9, 17], e.g. for instance see Table 5.4 and Chapter 4 where failure occurs in the HAZ at Position D or at Position F in the WM, therefore the results are of practical interest. The σ_{eq} and σ_1 f_1, f_2, f_3 values calculated for the four positions for the 8 different combinations of n_{PM} , n_{HAZ} , n_{WM} , using n_i equal to 3 and 10 are displayed in Table 5.2 for convenience. Positions A and D within the PM^b and HAZ^p, respectively, were chosen to illustrate the parametric study technique by presenting and discussing the variations of equivalent stress with variation of PM, HAZ and WM material properties. Similar graphical presentation of results of parametric studies for the σ_{eq} of Positions B and F and σ_1 for all four positions are shown in Appendix 1, however the results are not discussed.

5.5.3.1 Effect of $\dot{\epsilon}_o$ ratios on σ_{eq} for Position A

Figures 5.9a and 5.9b present the variations of normalised equivalent stress, $\sigma_{eq} / \sigma_{nom}$, with $\dot{\epsilon}_{oPM} / \dot{\epsilon}_{oHAZ}$ ($0.001 < \dot{\epsilon}_{oPM} / \dot{\epsilon}_{oHAZ} < 1000$) for a range of $\dot{\epsilon}_{oPM} / \dot{\epsilon}_{oWM}$ ($0.001 < \dot{\epsilon}_{oPM} / \dot{\epsilon}_{oWM} < 1000$) for $(n_{PM}, n_{HAZ}, n_{WM}) = (3, 10, 10)$ and

(10,3,3) at Position A (PM^b). In general, the σ_{eq} value at this position decreases with increasing $\dot{\epsilon}_{oPM} / \dot{\epsilon}_{oHAZ}$ and $\dot{\epsilon}_{oPM} / \dot{\epsilon}_{oWM}$ ratios. As $\dot{\epsilon}_{oPM} / \dot{\epsilon}_{oHAZ}$ increases the stress decreases more rapidly for both $(n_{PM}, n_{HAZ}, n_{WM})$ cases. The effect of $\dot{\epsilon}_{oPM} / \dot{\epsilon}_{oWM}$ on stress is more significant when $\dot{\epsilon}_{oPM} / \dot{\epsilon}_{oHAZ}$ is small but rapidly reduces when $\dot{\epsilon}_{oPM} / \dot{\epsilon}_{oHAZ}$ is large. When $\dot{\epsilon}_{oPM} / \dot{\epsilon}_{oHAZ}$ is large, the σ_{eq} values become very small and are almost independent of $\dot{\epsilon}_{oPM} / \dot{\epsilon}_{oWM}$, except for the larger $\dot{\epsilon}_{oPM} / \dot{\epsilon}_{oWM}$ values. Deducing that when the PM is much weaker than the HAZ, the stress becomes small and is almost independent of the WM creep strength. The highest stresses occur for small $\dot{\epsilon}_{oPM} / \dot{\epsilon}_{oHAZ}$ and $\dot{\epsilon}_{oPM} / \dot{\epsilon}_{oWM}$ values and when the n_{PM} value is smallest, i.e. 3 in the $(n_{PM}, n_{HAZ}, n_{WM}) = (3, 10, 10)$ case, compared to the (10,3,3) case when n_{PM} is 10. The effect of $\dot{\epsilon}_{oPM} / \dot{\epsilon}_{oHAZ}$ and $\dot{\epsilon}_{oPM} / \dot{\epsilon}_{oWM}$ values on stress are much greater for the (3,10,10) case compared to the (10,3,3) case, where the largest difference in stress is around 30% for $\dot{\epsilon}_{oPM} / \dot{\epsilon}_{oHAZ} = \dot{\epsilon}_{oPM} / \dot{\epsilon}_{oWM} = 0.001$, where $\sigma_{eq} / \sigma_{nom} = 1.7$ and 1.28, respectively. This is due to the PM material being more ‘creep strong’ for the (3,10,10) case compared to the other two materials, therefore a larger extent of stress redistribution will occur.

5.5.3.2 Effect of n_i on σ_{eq} for Position A

Figures 5.10a, 5.10b, 5.10c and 5.10d show the normalised equivalent stress, $\sigma_{eq} / \sigma_{nom}$, at Position A against n_{WM} for a group of n_{PM} and n_{HAZ} combinations for four different $(\dot{\epsilon}_{oPM} / \dot{\epsilon}_{oHAZ}, \dot{\epsilon}_{oPM} / \dot{\epsilon}_{oWM})$ combinations of (100,0.01), (100,100), (0.01,100) and (0.01,0.01), respectively. It is clear from the graphs

that the equivalent stress generally decreases with increasing n_{WM} , the stress variation is less dependent on n_{WM} when the $\dot{\epsilon}_{oPM} / \dot{\epsilon}_{oWM}$ ratio is small (i.e. 0.01), shown in Figures 5.10a and 5.10d, compared to the larger $\dot{\epsilon}_{oPM} / \dot{\epsilon}_{oWM}$ of 100. The maximum stress variations over the n_{WM} range for the $(\dot{\epsilon}_{oPM} / \dot{\epsilon}_{oHAZ}, \dot{\epsilon}_{oPM} / \dot{\epsilon}_{oWM}) = (100, 0.01)$ and $(0.01, 0.01)$ cases are 11% and 3%, respectively, compared to 30% and 20% for the $(100, 100)$ and $(0.01, 100)$ cases, respectively. All four graphs show that the maximum stress variation over the n_{WM} range are found when n_{PM} is small (i.e. 3 in this case). Concluding that when the PM is ‘creep strong’ compared to the WM and/or HAZ the stress is highly dependent on the n_{WM} value. Additionally, it is shown in Figure 5.10 that n_{HAZ} has a significant effect on the stress when n_{WM} is large and n_{PM} small

Figures 5.11a, 5.11b and 5.11c display the variation of normalised equivalent stress with the variation of n_{PM} , for a range of $\dot{\epsilon}_{oPM} / \dot{\epsilon}_{oWM}$ and n_{WM} , with $n_{HAZ} = 6$ and $\dot{\epsilon}_{oPM} / \dot{\epsilon}_{oHAZ} = 0.01, 1$ and 100 , respectively. The effects of n_{PM} and n_{WM} on stress are clearly shown. In general, the equivalent stress decreases as n_{PM} is increased, except for the $\dot{\epsilon}_{oPM} / \dot{\epsilon}_{oHAZ}, \dot{\epsilon}_{oPM} / \dot{\epsilon}_{oWM}, n_{WM}$ case of $100, 100, 10$, respectively, in Figure 5.11c. The highest stresses occur in all three cases when $\dot{\epsilon}_{oPM} / \dot{\epsilon}_{oWM}$ is smallest, i.e. 0.01, and for constant $\dot{\epsilon}_{oPM} / \dot{\epsilon}_{oHAZ}, \dot{\epsilon}_{oPM} / \dot{\epsilon}_{oWM}$ and n_{PM} values, the stress increases with decreasing n_{WM} ; this increase is greatest when n_{PM} and $\dot{\epsilon}_{oPM} / \dot{\epsilon}_{oHAZ}$ are small. Comparing the three figures shows that increasing $\dot{\epsilon}_{oPM} / \dot{\epsilon}_{oHAZ}$ from 0.01 to 100 reduces the stress

insignificantly for all combinations of $\dot{\epsilon}_{oPM} / \dot{\epsilon}_{oWM}$, n_{PM} and n_{WM} values, e.g. a maximum stress reduction of around 10% was seen for the $\dot{\epsilon}_{oPM} / \dot{\epsilon}_{oWM} = 0.01$ and $n_{PM} = 3$ cases.

5.5.3.3 Effect of $\dot{\epsilon}_o$ ratios on σ_{eq} for Position D

Figures 5.12a and 5.12b present the variations of normalised equivalent stress, $\sigma_{eq} / \sigma_{nom}$, with $\dot{\epsilon}_{oHAZ} / \dot{\epsilon}_{oPM}$ ($0.001 < \dot{\epsilon}_{oHAZ} / \dot{\epsilon}_{oPM} < 1000$) for a range of $\dot{\epsilon}_{oHAZ} / \dot{\epsilon}_{oWM}$ ($0.001 < \dot{\epsilon}_{oHAZ} / \dot{\epsilon}_{oWM} < 1000$) for $(n_{PM}, n_{HAZ}, n_{WM}) = (10, 3, 10)$ and $(3, 10, 3)$ at position D (HAZ^p). From these graphs, the effect of $\dot{\epsilon}_o$ ratios can be clearly identified. In general, the σ_{eq} value at this position decreases with increasing $\dot{\epsilon}_{oHAZ} / \dot{\epsilon}_{oPM}$ and $\dot{\epsilon}_{oHAZ} / \dot{\epsilon}_{oWM}$ ratios. The effect of $\dot{\epsilon}_{oHAZ} / \dot{\epsilon}_{oWM}$ on stress is highly significant when $\dot{\epsilon}_{oHAZ} / \dot{\epsilon}_{oPM}$ is small but rapidly reduces when $\dot{\epsilon}_{oHAZ} / \dot{\epsilon}_{oPM}$ is large. When $\dot{\epsilon}_{oHAZ} / \dot{\epsilon}_{oPM}$ is large, the σ_{eq} values become very small and are almost independent of $\dot{\epsilon}_{oHAZ} / \dot{\epsilon}_{oWM}$. Deducing that when the HAZ is much weaker than the PM, the stress becomes small and is almost independent of the WM creep strength. The highest stresses occur for small $\dot{\epsilon}_{oHAZ} / \dot{\epsilon}_{oPM}$ and $\dot{\epsilon}_{oHAZ} / \dot{\epsilon}_{oWM}$ values and when the n_{HAZ} value is smallest, i.e. 3 in the $(n_{PM}, n_{HAZ}, n_{WM}) = (10, 3, 10)$ case, compared to the $(3, 10, 3)$ case when n_{HAZ} is 10. The effect of $\dot{\epsilon}_{oHAZ} / \dot{\epsilon}_{oPM}$ value on stress is much greater for the $(10, 3, 10)$ case compared to the $(3, 10, 3)$ case, where the largest difference between the two is around 600% for $\dot{\epsilon}_{oHAZ} / \dot{\epsilon}_{oPM} = \dot{\epsilon}_{oHAZ} / \dot{\epsilon}_{oWM} = 0.001$, where $\sigma_{eq} / \sigma_{nom} = 12.5$ and 2.1, respectively. This difference is due to the HAZ material being more ‘creep strong’ since it has a much lower creep exponent

value than the two materials for this case of (10,3,10) compared to the (3,10,3) case, therefore a larger extent of stress redistribution will result. As $\dot{\epsilon}_{oHAZ} / \dot{\epsilon}_{oPM}$ tends to infinity the stress for the $(n_{PM}, n_{HAZ}, n_{WM}) = (10,3,10)$ case tends to 0, while the stress for the $(n_{PM}, n_{HAZ}, n_{WM}) = (3,10,3)$ case tends to a larger value of around 0.5.

5.5.3.4 Effect of n_i on σ_{eq} for Position D

Figures 5.13a, 5.13b, 5.13c and 5.13d show the normalised equivalent stress, $\sigma_{eq} / \sigma_{nom}$, at Position D against n_{WM} value for a group of n_{PM} and n_{HAZ} combinations for four different $(\dot{\epsilon}_{oHAZ} / \dot{\epsilon}_{oPM}, \dot{\epsilon}_{oHAZ} / \dot{\epsilon}_{oWM})$ combinations of (100,0.01), (100,100), (0.01,100) and (0.01,0.01), respectively. It is clear from Figures 5.13a, 5.13b and 5.13d that the equivalent stress is practically independent of n_{WM} for all (n_{PM}, n_{HAZ}) combinations considered, where stress variations over the n_{WM} range are all less than 10%. This relationship for the HAZ position agrees with findings in other parametric weld studies of positions in the HAZ, e.g. for a welded plain pipe [100]. However, for the $(\dot{\epsilon}_{oHAZ} / \dot{\epsilon}_{oPM}, \dot{\epsilon}_{oHAZ} / \dot{\epsilon}_{oWM})$ combination of (0.01,100), shown in Figure 5.13c, the stress is significantly dependent on the n_{WM} value, as the stress sharply decreases for lower values of n_{WM} , i.e. from 3 to 10. The largest decrease in stress over the n_{WM} range from 10 to 3 is approximately 60% for the cases when $n_{HAZ} = 3$. When $n_{HAZ} = 6$ and 10 the decrease in stress from $n_{WM} = 10$ to 3 becomes less significant, at differences of 45% and 20%, respectively. The explanation for the large differences in stress over the varying n_{WM} range for

just this case, $(\dot{\epsilon}_{oHAZ} / \dot{\epsilon}_{oPM}, \dot{\epsilon}_{oHAZ} / \dot{\epsilon}_{oWM}) = (0.01, 100)$, and not the other three cases is that the WM is ‘creep strong’ compared to the HAZ. i.e. $\dot{\epsilon}_{oHAZ} / \dot{\epsilon}_{oWM} = 0.01$, and extremely ‘creep strong’ compared to the PM, i.e. $\dot{\epsilon}_{oWM} / \dot{\epsilon}_{oPM} = 0.0001$, therefore stress is redistributed extensively to the WM, resulting in the WM material properties, i.e. n_{WM} , having a significant effect on the level of stress redistribution between the three materials.

Figures 5.14a, 5.14b and 5.14c display the variation of normalised equivalent stress with the variation of n_{HAZ} , for a range of $\dot{\epsilon}_{oHAZ} / \dot{\epsilon}_{oPM}$ and n_{PM} , with $n_{WM} = 6$ and $\dot{\epsilon}_{oHAZ} / \dot{\epsilon}_{oWM} = 0.01, 1$ and 100 , respectively. The effects of n_{PM} and n_{HAZ} on stress are clearly shown. In all cases the equivalent stress varies with $\dot{\epsilon}_{oHAZ} / \dot{\epsilon}_{oPM}$ and n_{PM} more significantly when n_{HAZ} is small. The highest stresses occur in all three cases when $\dot{\epsilon}_{oHAZ} / \dot{\epsilon}_{oPM}$ is smallest, i.e. 0.01 , and for constant $\dot{\epsilon}_{oHAZ} / \dot{\epsilon}_{oPM}$, $\dot{\epsilon}_{oHAZ} / \dot{\epsilon}_{oWM}$ and n_{HAZ} values, the stress increases with increasing n_{PM} ; this increase is greatest when n_{HAZ} and $\dot{\epsilon}_{oHAZ} / \dot{\epsilon}_{oWM}$ are small. Comparing the three figures shows that increasing $\dot{\epsilon}_{oHAZ} / \dot{\epsilon}_{oWM}$ reduces the stress significantly for combinations with low $\dot{\epsilon}_{oHAZ} / \dot{\epsilon}_{oPM}$ and n_{HAZ} values, e.g. a stress reduction of around 70% for the $\dot{\epsilon}_{oHAZ} / \dot{\epsilon}_{oPM} = 0.01$ and $n_{HAZ} = 3$ cases.

5.6 Conclusions

For the three material sets and nine ‘critical’ locations considered, the parametric analysis procedure, which combines the previously-published general formulation for multi-material steady-state stresses with the Calladine

approximation, accurately predicts equivalent, maximum principal and rupture stresses to within 3%, 4% and 3.5% of independently-predicted FE values, respectively. Rupture lives are predicted to within 8% of the independent values. The benefit of using the Calladine approximation is that only 24 analyses are required to generate enough data for a complete parametric study of material properties for the three-material model, as opposed to 81 analyses for previous three-material studies [100,102] if Equation 5.1 were used without the use of the Calladine stress approximation, thus giving a reduction of 70% on the computational overhead.

A detailed parametric study of the equivalent and maximum principal stresses at four critical locations in the PM^b, WM, HAZ^p and WM, respectively, was presented (see Figures 5.4, 5.5 and 5.6). Where a study of the HAZ position was considered in more detail for the purpose of displaying the effectiveness of the proposed method. The parametric studies showed that the stresses were generally highly dependent on the level of material mis-match associated with the weld. There is a complex interaction between all of the material properties and the creep stresses, dependent not only on the material of interest, but on all three materials. The magnitude of stress is highly dependent on the $(n_{PM}, n_{HAZ}, n_{WM})$ combination and the $\dot{\epsilon}_{oi} / \dot{\epsilon}_{oj}$ ratio values, and proximity of position to the other materials, as well as the geometric effects on stress. It can be generally concluded that the stress variation with n_i at each of the four positions considered is highly dependent on the combination of the $\dot{\epsilon}_{oi} / \dot{\epsilon}_{oi}$ ratios and n_{PM}, n_{HAZ}, n_{WM} values. The stress redistribution behaviour depends

not only on material properties, but also on the relative sizes of the material zones. For instance, when the PM is 'creep weak' and the HAZ is 'creep strong', i.e. $\dot{\epsilon}_{oPM} / \dot{\epsilon}_{oHAZ} > 1$ and/or $n_{PM} > n_{HAZ}$, the stresses in the HAZ material will significantly increase. However, when the PM is 'creep strong' relative to the HAZ, the PM stresses will increase to a lesser extent due to the PM zone being larger. The behaviour found for the four positions in the three materials show similarities with other weld positions studied in cross-weld specimens and welded plain pipes [35,29,100].

Table 5.1. Dimensions of the welded branched pipe, dimensions in mm, if not otherwise stated.

D	T	d	t	b_x	b_y	r_1	r_0	a	b_1	β	θ	h	b
355	65	113.6	20.8	20.8	20.8	10	10	2.5	3	45°	45°	1.5	3

Table 5.2. Calculated f values for the equivalent and maximum principal stress at Positions A to I of Figure 5.4 to 5.6, for the eight 'extreme' (n_{PM} , n_{HAZ} , n_{WM}) combinations.

(a)PM^b Position A

$(n_{PM}, n_{HAZ}, n_{WM})$	σ_{eq}			σ_1		
	f_1	f_2	f_3	f_1	f_2	f_3
(3,3,3)	0.59367	0.01574	0.04767	0.68837	0.01455	0.07094
(3,3,10)	0.58397	0.01709	0.07062	0.69280	0.02030	0.06346
(3,10,3)	0.59320	0.01780	0.04818	0.69193	0.00450	0.07776
(3,10,10)	0.58287	0.01988	0.07094	0.68553	0.01227	0.08304
(10,3,3)	0.78235	0.01372	0.03431	1.03950	0.00000	0.08958
(10,3,10)	0.79697	0.00819	0.03399	1.01034	0.04509	0.05023
(10,10,3)	0.80004	0.00971	0.02421	1.00993	-0.01956	0.15749
(10,10,10)	0.79607	0.00856	0.03507	1.02669	0.00000	0.06974

(b)WM Position B

$(n_{PM}, n_{HAZ}, n_{WM})$	σ_{eq}			σ_1		
	f_1	f_2	f_3	f_1	f_2	f_3
(3,3,3)	0.56904	0.02293	0.05807	0.91028	-0.10649	-0.03282
(3,3,10)	0.52075	0.02078	0.13638	7.84311	-2.93870	-2.44821
(3,10,3)	0.57184	0.02431	0.05651	1.03348	-0.07815	-0.17557
(3,10,10)	0.54910	0.02982	0.08904	-8.90429	2.69176	4.53465
(10,3,3)	0.78790	0.01147	0.03432	0.96633	-0.01826	-0.02419
(10,3,10)	0.77698	0.01087	0.05127	1.08325	-0.12835	0.04356
(10,10,3)	0.79337	0.01292	0.03040	0.92343	-0.02292	-0.00499
(10,10,10)	0.78736	0.01280	0.41490	1.65893	-0.30642	-0.24173

(c)HAZ^b Position C

$(n_{PM}, n_{HAZ}, n_{WM})$	σ_{eq}			σ_1		
	f_1	f_2	f_3	f_1	f_2	f_3
(3,3,3)	0.59646	0.03822	0.06467	0.69653	0.05370	0.01591
(3,3,10)	0.59029	0.03786	0.08352	0.67323	0.01721	0.10482
(3,10,3)	0.58165	0.05288	0.06328	0.89879	0.21857	-0.21847
(3,10,10)	0.57089	0.06247	0.07628	1.04912	0.06161	-0.13150
(10,3,3)	0.79117	0.02073	0.04067	0.86310	0.00000	0.03781
(10,3,10)	0.79883	0.01389	0.04838	0.85533	-0.00288	0.05448
(10,10,3)	0.79155	0.02229	0.03771	0.98969	0.05959	-0.06671
(10,10,10)	0.79288	0.02354	0.04193	1.04135	-0.03793	0.01812

(d)HAZ^p Position D

$(n_{PM}, n_{HAZ}, n_{WM})$	σ_{eq}			σ_1		
	f_1	f_2	f_3	f_1	f_2	f_3
(3,3,3)	0.60046	0.02285	0.06497	0.73847	0.11491	-0.10648
(3,3,10)	0.59347	0.02588	0.08229	0.74709	0.07859	-0.05348
(3,10,3)	0.57693	0.02885	0.08322	0.87453	0.42918	-0.45522
(3,10,10)	0.56775	0.03797	0.10024	1.43976	0.66187	-1.18706
(10,3,3)	0.79808	0.01383	0.04256	0.88020	0.04934	-0.03435
(10,3,10)	0.79855	0.01184	0.04479	0.89696	0.01204	0.00201
(10,10,3)	0.79814	0.01397	0.03406	0.95190	0.12348	-0.10265
(10,10,10)	0.78816	0.01472	0.05125	1.12340	0.13564	-0.24408

(e)HAZ^b Position E

$(n_{PM}, n_{HAZ}, n_{WM})$	σ_{eq}			σ_1		
	f_1	f_2	f_3	f_1	f_2	f_3
(3,3,3)	0.73239	0.15073	0.03663	0.78365	-0.11425	0.22501
(3,3,10)	0.74129	0.14514	0.03926	0.71912	-0.05216	0.23410
(3,10,3)	0.68978	0.17183	0.03981	2.16234	-4.16162	2.76338
(3,10,10)	0.69814	0.18063	0.02961	0.74790	-0.86301	0.94733
(10,3,3)	0.83057	0.11794	-0.01063	0.90747	-0.08963	0.13482
(10,3,10)	0.87615	0.05485	0.01942	0.87917	-0.01363	0.08332
(10,10,3)	0.83062	0.07864	0.02622	2.07892	-2.12025	1.05650
(10,10,10)	0.84450	0.09185	0.00214	1.03709	-0.49026	0.45311

(f)WM Position F

$(n_{PM}, n_{HAZ}, n_{WM})$	σ_{eq}			σ_1		
	f_1	f_2	f_3	f_1	f_2	f_3
(3,3,3)	0.55269	0.03930	0.25880	0.61151	0.04416	0.09452
(3,3,10)	0.57543	0.03987	0.24286	0.80251	0.04136	-0.36293
(3,10,3)	0.54537	0.04870	0.26053	0.61924	0.04982	0.09244
(3,10,10)	0.54281	0.05861	0.26705	0.53748	0.05896	0.04267
(10,3,3)	0.76277	0.01846	0.12306	0.68304	0.02996	0.13724
(10,3,10)	0.77096	0.01978	0.12079	0.50197	0.04313	0.23329
(10,10,3)	0.77440	0.02154	0.11000	0.72780	0.02716	0.11263
(10,10,10)	0.77380	0.02520	0.11540	0.57075	0.05755	0.16875

(g)HAZ^p Position G

$(n_{PM}, n_{HAZ}, n_{WM})$	σ_{eq}			σ_1		
	f_1	f_2	f_3	f_1	f_2	f_3
(3,3,3)	0.86455	0.19979	-0.14271	0.87941	0.22660	-0.27515
(3,3,10)	0.90102	0.20480	-0.19398	0.71124	0.26359	-0.17075
(3,10,3)	0.79142	0.27905	-0.17375	0.69772	0.37055	-0.37247
(3,10,10)	0.83549	0.30717	-0.26448	0.69376	0.62360	-0.82270
(10,3,3)	1.00673	0.14561	-0.13412	0.97756	0.17527	-0.16581
(10,3,10)	1.03327	0.08460	-0.09078	1.07690	0.10173	-0.20067
(10,10,3)	1.00677	0.10151	-0.09795	0.97394	0.08639	-0.12234
(10,10,10)	1.01125	0.11773	-0.11429	1.07870	0.19115	-0.38532

(h)WM Position H

$(n_{PM}, n_{HAZ}, n_{WM})$	σ_{eq}			σ_1		
	f_1	f_2	f_3	f_1	f_2	f_3
(3,3,3)	0.78878	0.00512	0.12783	0.63261	-0.01080	0.15166
(3,3,10)	0.78563	0.00000	0.14506	0.51995	-0.03258	-0.00333
(3,10,3)	0.80006	0.00000	0.12758	0.84301	-1.91396	1.74302
(3,10,10)	0.85379	-0.01975	0.09430	0.48516	-0.08364	0.12870
(10,3,3)	0.93743	0.01127	0.05662	0.87898	0.01960	0.03524
(10,3,10)	0.96511	0.00570	0.04137	0.84317	0.00453	-0.03477
(10,10,3)	0.95816	0.00914	0.03843	0.90343	0.00547	0.02876
(10,10,10)	0.97165	0.00621	0.03737	0.83910	0.01628	-0.03350

(i)PM^P Position I

$(n_{PM}, n_{HAZ}, n_{WM})$	σ_{eq}			σ_1		
	f_1	f_2	f_3	f_1	f_2	f_3
(3,3,3)	0.54489	0.00839	0.03432	0.64718	0.01223	0.04999
(3,3,10)	0.54401	0.00798	0.04928	0.63511	0.01421	0.07114
(3,10,3)	0.54458	0.01240	0.03380	0.63633	0.01577	0.05834
(3,10,10)	0.53671	0.01468	0.05549	0.63542	0.01476	0.07234
(10,3,3)	0.77553	0.00371	0.02104	1.06238	0.04073	0.16539
(10,3,10)	0.77148	0.00458	0.03387	1.09436	0.02361	0.07270
(10,10,3)	0.77356	0.00899	0.02061	1.13294	0.02841	0.05619
(10,10,10)	0.75615	0.01198	0.04266	1.08694	0.02516	0.06290

Table 5.3. Material creep and rupture constants for three $\frac{1}{2}\text{Cr}\frac{1}{2}\text{Mo}\frac{1}{4}\text{V}:2\frac{1}{4}\text{Cr}1\text{Mo}$ material sets.

	Set 1: Service-aged @ 640°C			Set 2: As-new @ 640°C			Set 3: As-new @ 565°C		
	PM	HAZ	WM	PM	HAZ	WM	PM	HAZ	WM
$\dot{\epsilon}_{oi}$	6.599 $\times 10^{-16}$	1.708 $\times 10^{-15}$	9.718 $\times 10^{-15}$	3.208 $\times 10^{-18}$	1.044 $\times 10^{-15}$	6.459 $\times 10^{-17}$	2.853 $\times 10^{-16}$	1.551 $\times 10^{-13}$	5.308 $\times 10^{-15}$
n_i	6.108	6.108	5.208	7.269	6.108	6.430	4.897	3.369	4.368
m	0	0	0	0	0	0	-0.2031	-0.2148	-0.2031
M	5.998 $\times 10^{-14}$	2.500 $\times 10^{-9}$	8.120 $\times 10^{-13}$	4.823 $\times 10^{-12}$	9.660 $\times 10^{-10}$	5.794 $\times 10^{-11}$	1.452 $\times 10^{-10}$	3.259 $\times 10^{-9}$	8.858 $\times 10^{-10}$
α	0.30	0.49	0.26	0.33	0.49	0.42	0.60	0.43	0.43
χ	5.767	3.200	4.849	4.599	3.420	4.015	3.011	2.301	2.854

Table 5.4. Comparison of stresses and lives as predicted by multi-material, parametric procedure with independent FE results for (a) Material Set 1 (b) Material Set 2 and (c) Material Set 3. Units for σ are MPa and t_f are hours.

(a) Set 1 – Service-aged CrMoV @640°C

POSITION	Parametric procedure				FE				% difference			
	σ_{eq}	σ_1	σ_r	t_f	σ_{eq}	σ_1	σ_r	t_f	σ_{eq}	σ_1	σ_r	t_f
A (PM ^b)	47.0	37.2	44.0	5524	47.2	37.6	44.3	5322	-0.5	-1.1	-0.6	3.7
B (WM)	56.3	45.4	53.5	5134	55.5	46.0	53.0	5354	1.5	-1.3	0.9	-4.3
C (HAZ ^b)	39.4	34.5	37.0	3836	39.5	34.4	37.0	3835	-0.3	0.3	0.0	0.0
D (HAZ ^p)	39.6	36.3	38.0	3527	39.8	35.7	37.8	3584	-0.5	1.7	0.5	-1.6
E (HAZ ^b)	34.9	30.8	32.9	5580	34.5	32.0	33.3	5386	1.2	-3.8	-1.1	3.5
F (WM)	46.2	52.3	47.8	8852	46.4	50.3	47.4	9168	-0.4	3.8	0.8	-3.6
G (HAZ ^p)	33.2	39.4	36.2	4103	33.5	40.2	36.8	3908	-1.0	-2.0	-1.5	4.7
H (WM)	40.8	49.0	43.0	14861	41.5	49.5	43.6	13773	-1.7	-0.9	-1.5	7.3
I (PM ^p)	50.0	36.8	46.1	4265	50.1	37.9	46.4	4065	-0.1	-3.0	-0.8	4.7

(b) Set 2 – As-new CrMoV @640°C

POSITION	Parametric procedure				FE				% difference			
	σ_{eq}	σ_1	σ_r	t_f	σ_{eq}	σ_1	σ_r	t_f	σ_{eq}	σ_1	σ_r	t_f
A (PM ^b)	45.9	36.0	42.6	6630	46.0	36.1	42.7	6578	-0.1	-0.3	-0.2	0.8
B (WM)	48.6	37.0	43.8	4429	48.2	37.8	43.9	4401	0.9	-2.1	-0.2	0.6
C (HAZ ^b)	36.3	30.9	33.7	6205	36.4	30.8	33.7	6201	-0.3	0.4	0.0	0.1
D (HAZ ^p)	36.5	32.0	34.3	5818	36.6	31.9	34.3	5814	-0.3	0.3	0.0	0.1
E (HAZ ^b)	32.2	28.2	30.2	8942	32.1	29.0	30.6	8606	0.3	-2.8	-1.1	3.8
F (WM)	42.3	48.2	44.7	4068	42.4	46.6	44.2	4288	-0.3	3.3	1.3	-5.4
G (HAZ ^p)	29.7	34.5	32.1	7324	30.0	35.8	32.8	6743	-1.1	-3.7	-2.4	7.9
H (WM)	37.0	45.3	40.5	6075	37.5	45.0	40.6	5989	-1.3	0.7	-0.4	1.4
I (PM ^p)	48.4	34.8	43.9	5810	48.3	36.0	44.2	5612	0.2	-3.6	-0.8	3.4

(c) Set 3 – As-new CrMoV @ 565°C

POSITION	Parametric procedure				FE				% difference			
	σ_{eq}	σ_1	σ_r	t_f	σ_{eq}	σ_1	σ_r	t_f	σ_{eq}	σ_1	σ_r	t_f
A (PM ^b)	49.7	40.7	44.3	57308	50.4	41.0	44.8	55231	-1.5	-0.8	-1.1	3.6
B (WM)	42.4	31.7	37.8	26643	42.1	31.6	37.6	27112	0.7	0.5	0.6	-1.8
C (HAZ ^b)	44.3	38.2	41.7	42270	44.1	38.2	41.6	42525	0.4	0.1	0.3	-0.6
D (HAZ ^p)	44.6	38.1	41.8	41891	44.8	38.2	42.0	41600	-0.3	-0.2	-0.3	0.7
E (HAZ ^b)	34.5	34.3	34.4	65800	34.4	35.0	34.7	64599	0.2	-2.1	-0.8	1.8
F (WM)	36.4	40.9	38.4	25553	36.2	40.3	38.0	26355	0.7	1.6	1.1	-3.1
G (HAZ ^p)	29.6	32.8	31.0	83676	30.4	34.0	32.0	77912	-2.6	-3.8	-3.2	6.9
H (WM)	30.8	37.6	33.7	37058	31.3	37.8	34.1	35817	-1.8	-0.6	-1.2	3.3
I (PM ^p)	53.9	41.2	46.3	50102	54.0	42.3	47.0	47715	-0.2	-2.6	-1.5	4.8

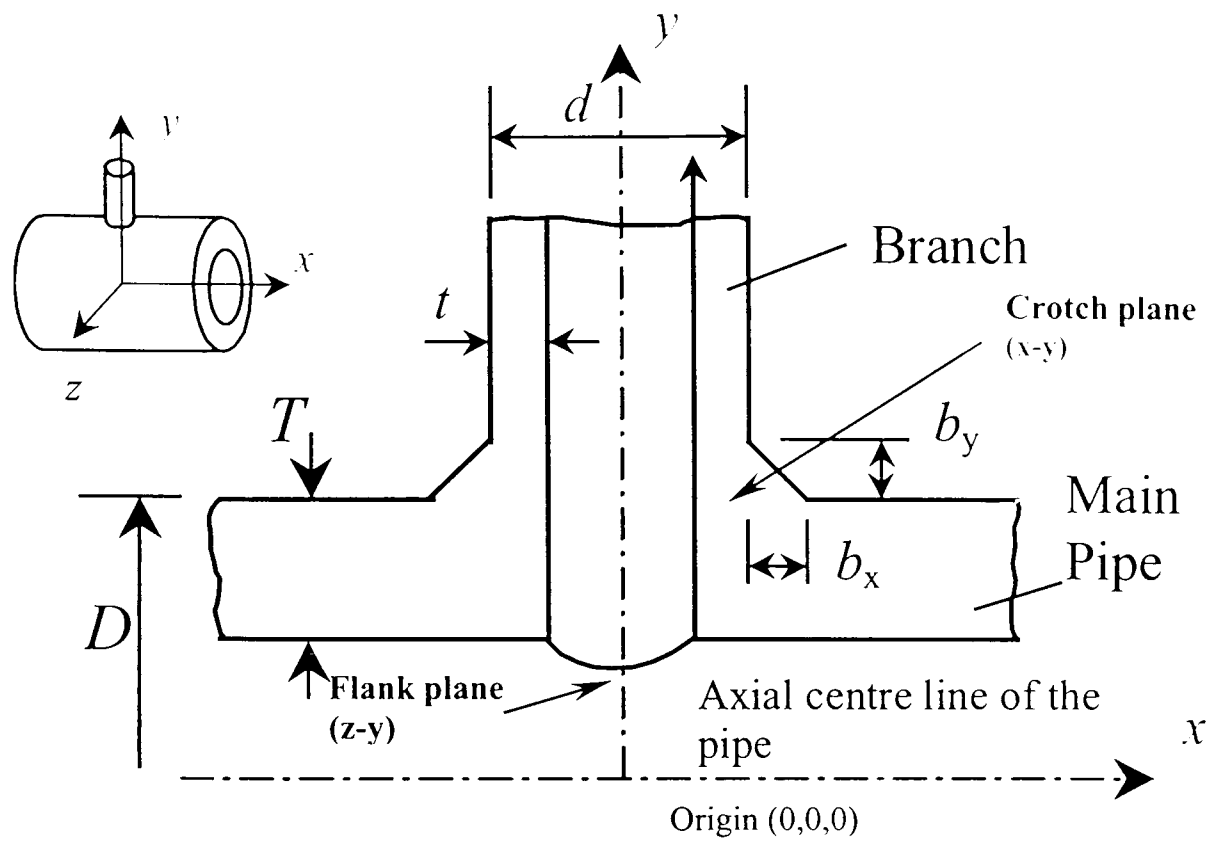


Figure 5.1. A main pipe with an isolated T-branch.

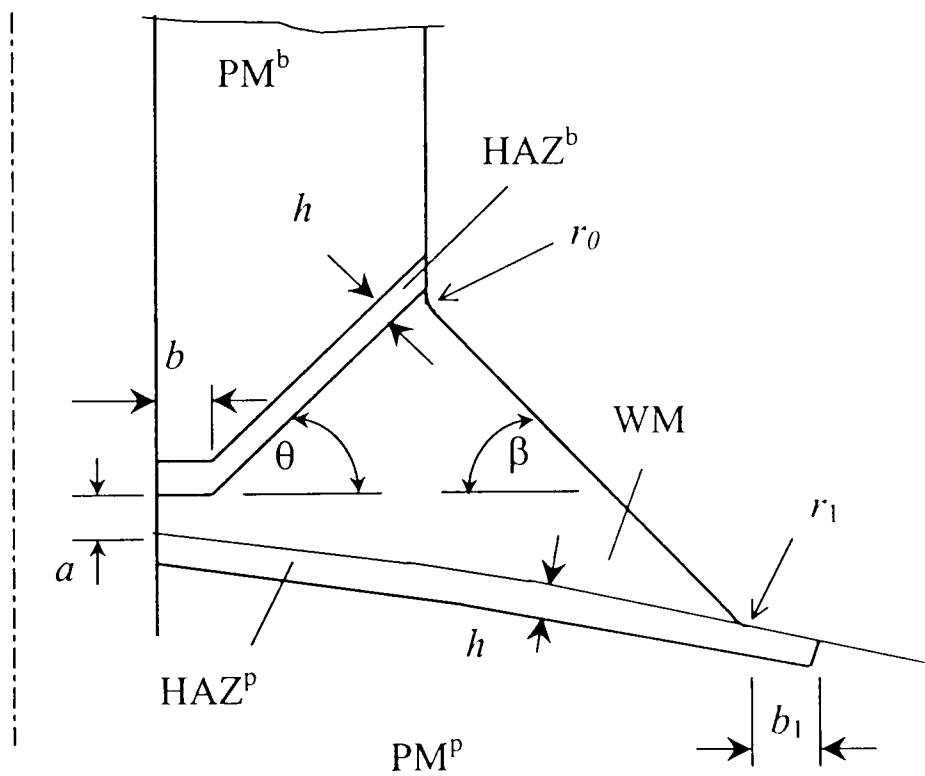


Figure 5.2. Definition of weld details.

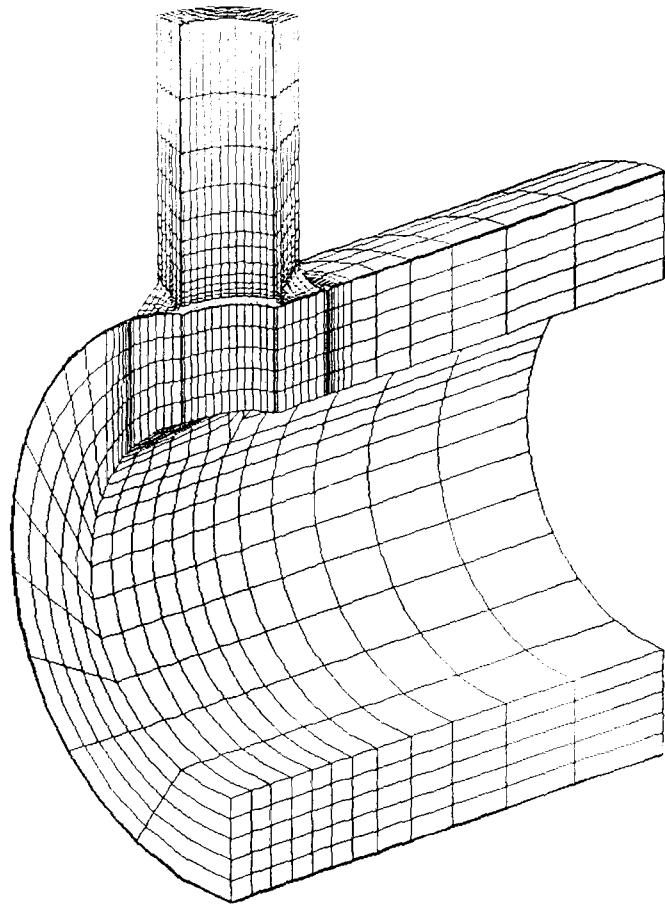


Figure 5.3. Global-model FE mesh.

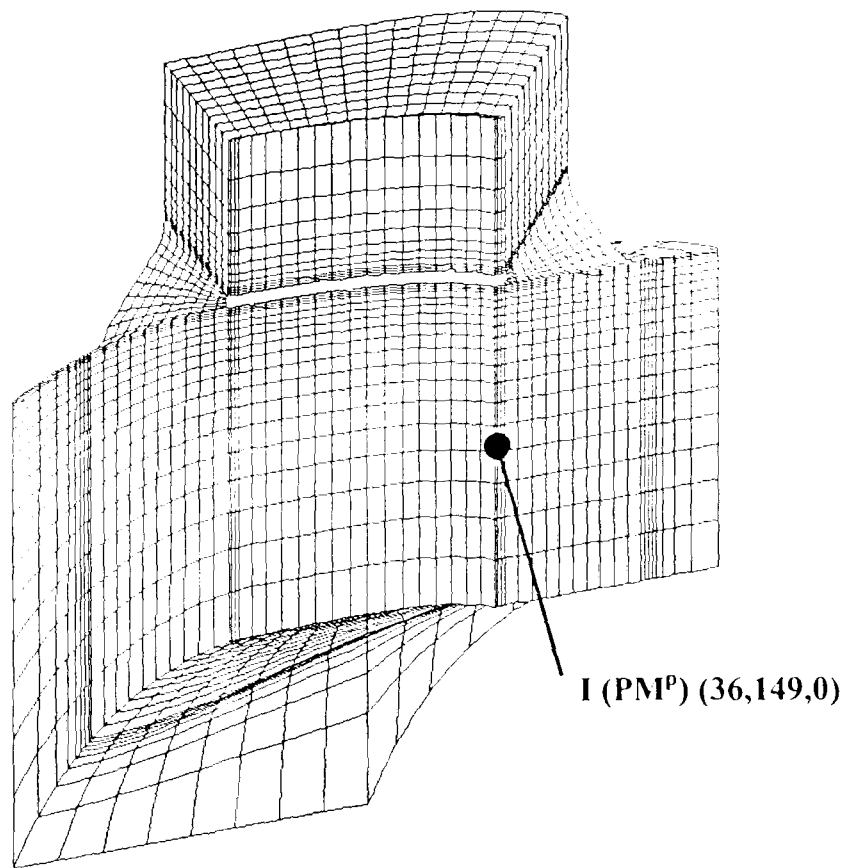


Figure 5.4. Sub-model FE mesh and position of interest **I** with Cartesian co-ordinates in mm

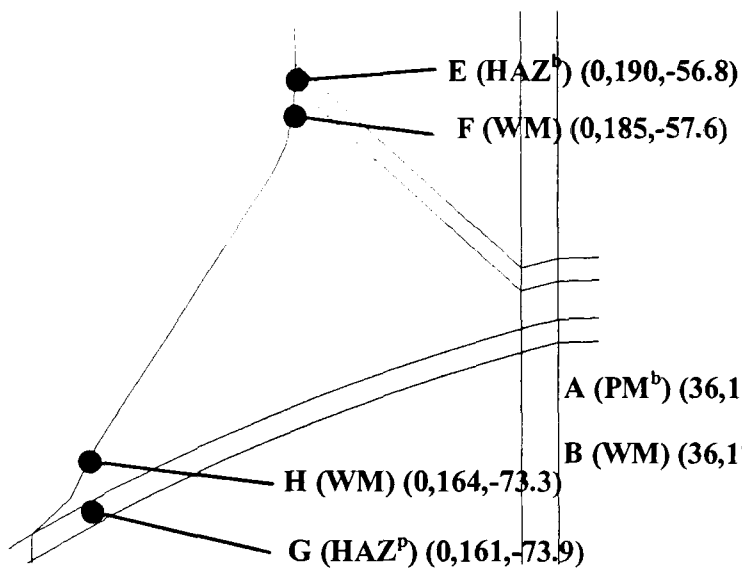


Figure 5.5. Positions of interest on the flank-plane ($y-z$) weld cross-section, with Cartesian co-ordinates in mm.

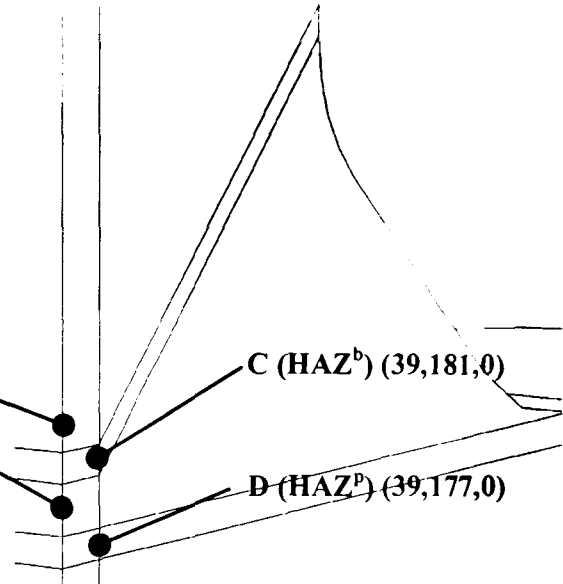
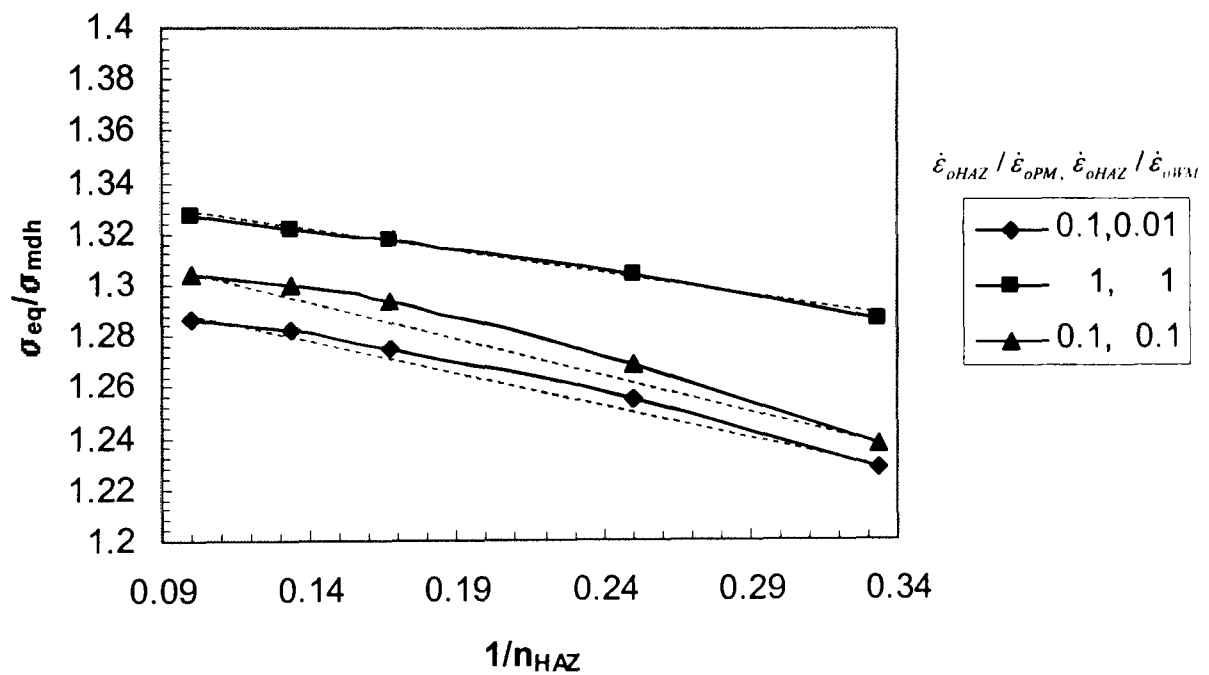
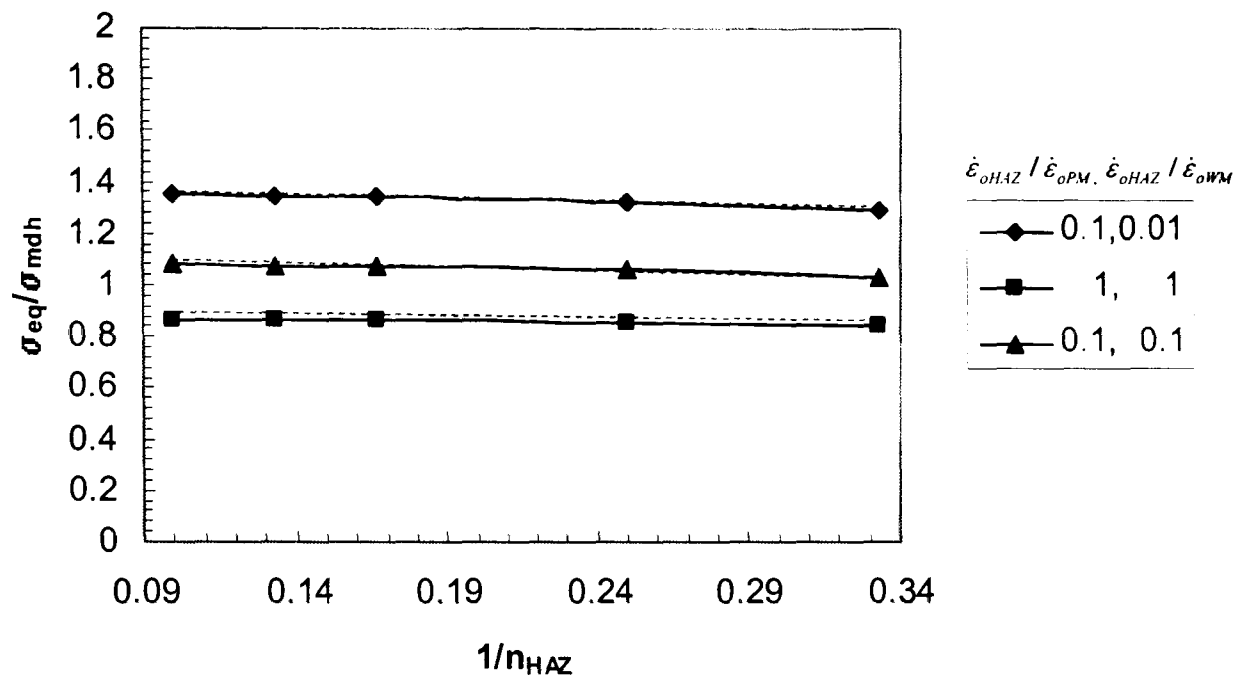


Figure 5.6. Positions of interest on the crotch-plane ($x-y$) weld cross-section, with Cartesian co-ordinates in mm.

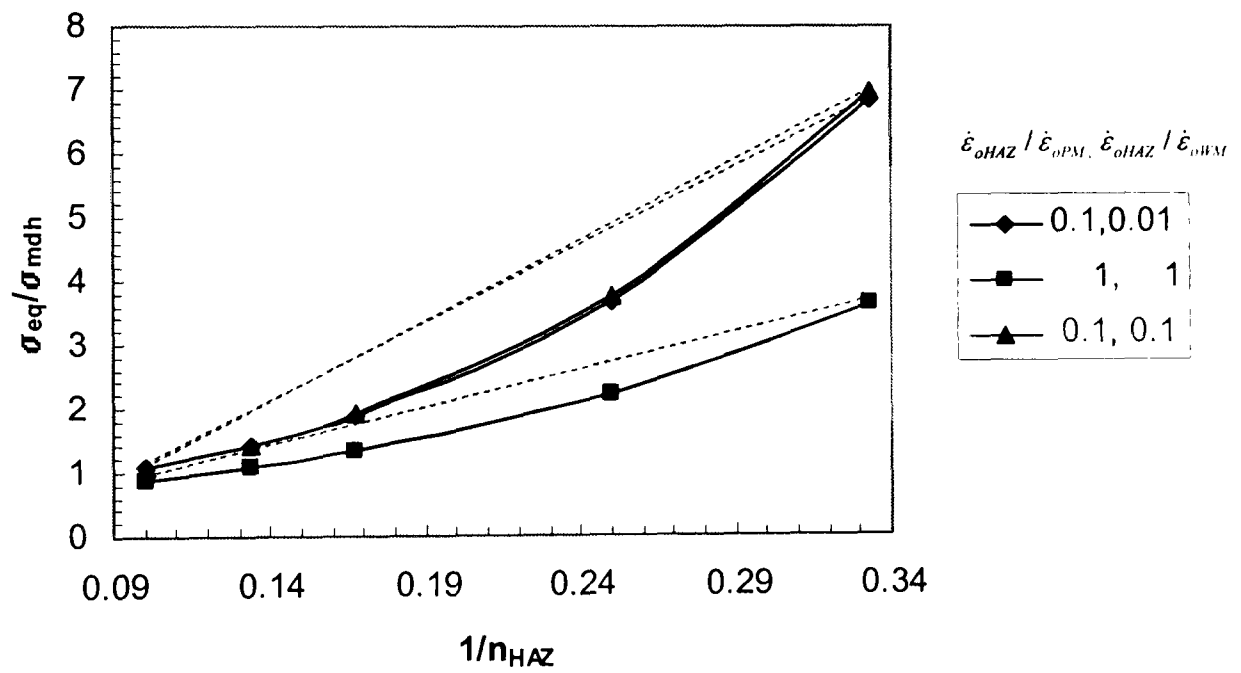


(a) Position A (PM^b)

Figure 5.7. Variation of steady-state equivalent von-Mises stress with $1/n_{HAZ}$, for three different $\dot{\epsilon}_{oHAZ} / \dot{\epsilon}_{oPM}, \dot{\epsilon}_{oHAZ} / \dot{\epsilon}_{oWM}$ ratios at positions A, B and C, $n_{PM} = 6$ and $n_{WM} = 10$.

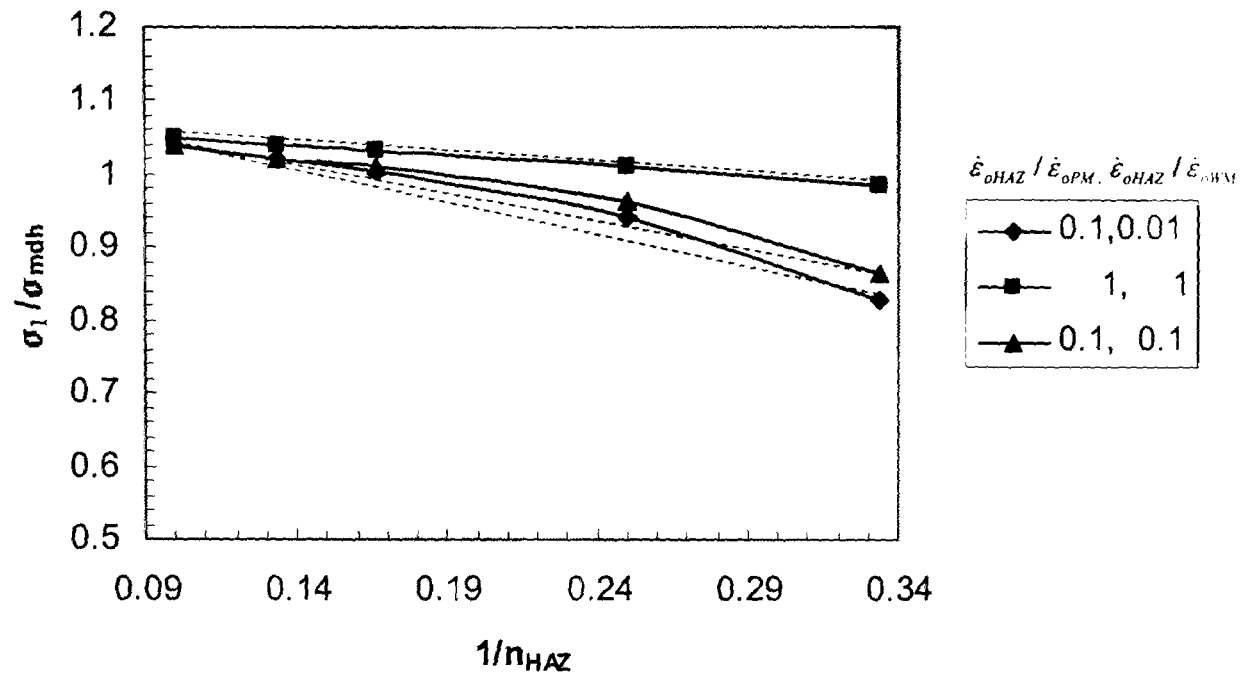


(b) Position B (WM)

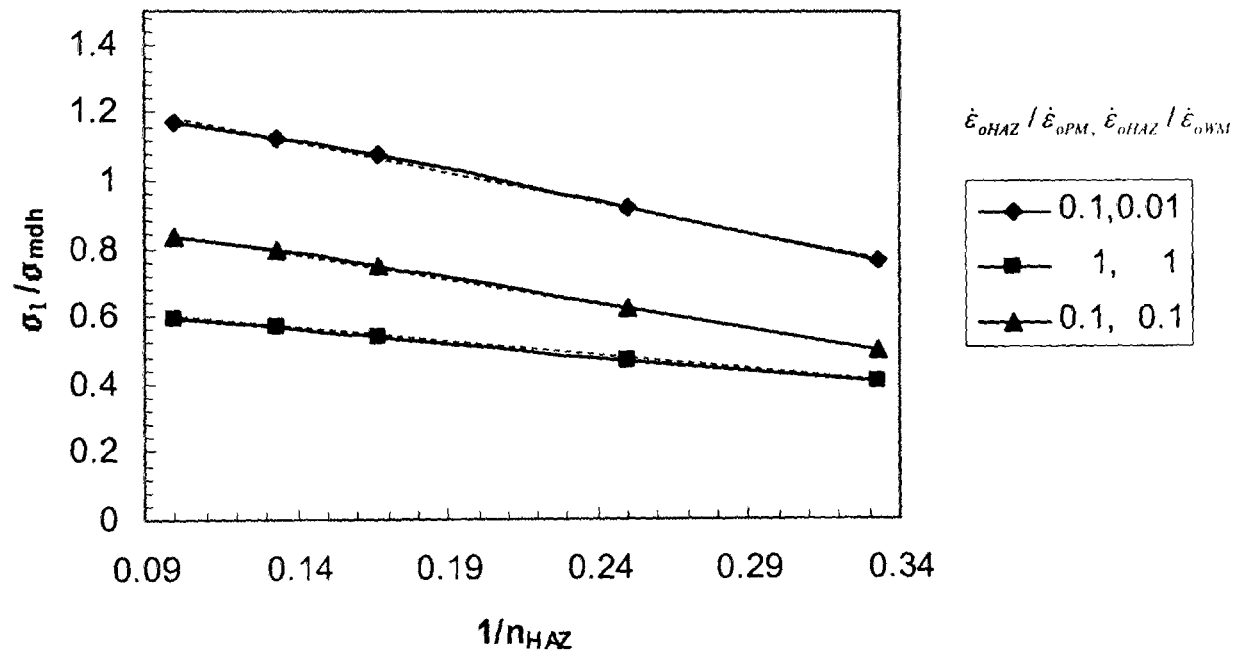


(c) Position C (HAZ^b)

Figure 5.7 continued. Variation of steady-state equivalent von-Mises stress with $1/n_{HAZ}$, for three different $\dot{\epsilon}_{oHAZ} / \dot{\epsilon}_{oPM}$, $\dot{\epsilon}_{oHAZ} / \dot{\epsilon}_{oWM}$ ratios at positions A, B and C, $n_{PM} = 6$ and $n_{WM} = 10$.

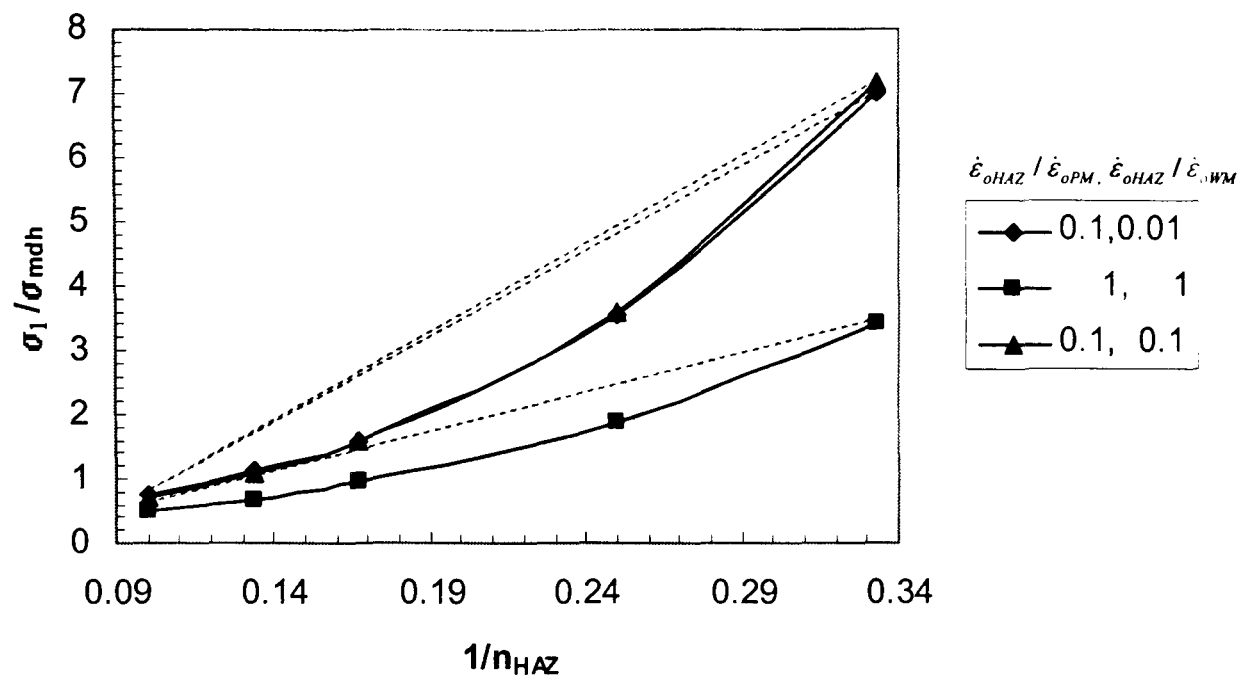


(a) Position A (PM^b)



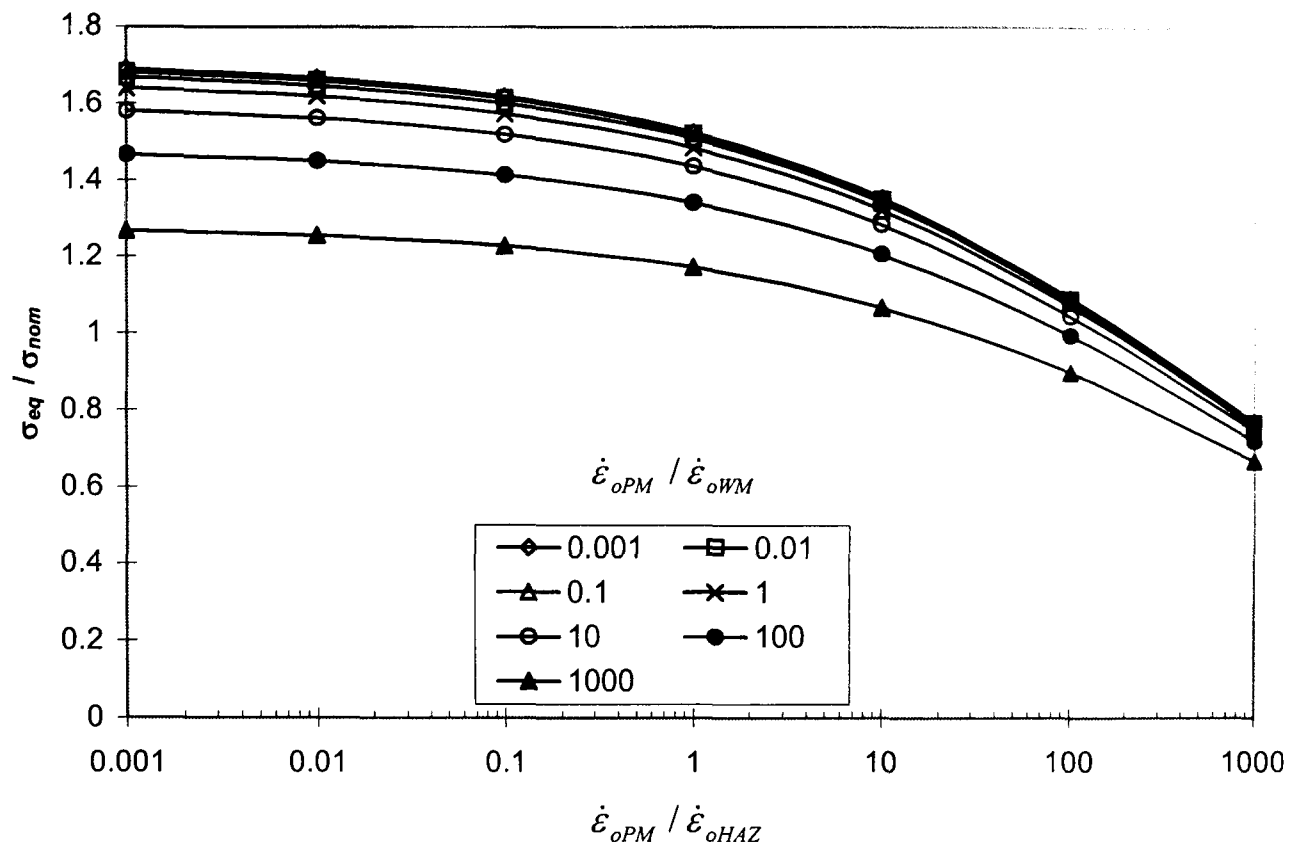
(b) Position B (WM)

Figure 5.8. Variation of steady-state maximum principal stress with $1/n_{HAZ}$, for three different $\dot{\epsilon}_{oHAZ} / \dot{\epsilon}_{oPM}$ and $\dot{\epsilon}_{oHAZ} / \dot{\epsilon}_{oWM}$ ratios at positions A, B and C, $n_{PM} = 6$ and $n_{WM} = 10$.

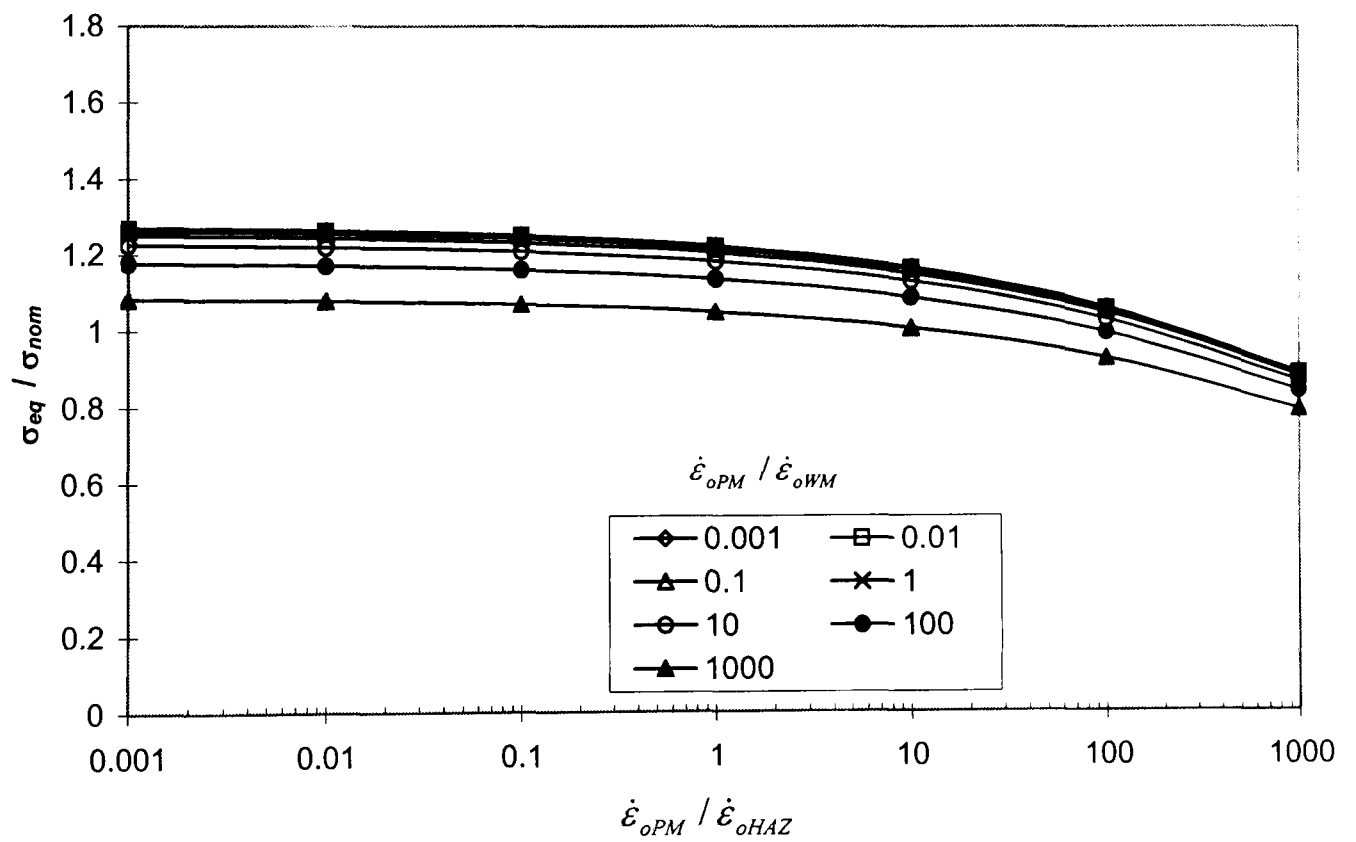


(c) Position C (HAZ^b)

Figure 5.8 continued. Variation of steady-state maximum principal stress with $1/n_{HAZ}$, for three different $\dot{\epsilon}_{oHAZ}/\dot{\epsilon}_{oPM}$ and $\dot{\epsilon}_{oHAZ}/\dot{\epsilon}_{oWM}$ ratios at positions A, B and C, $n_{PM} = 6$ and $n_{WM} = 10$.

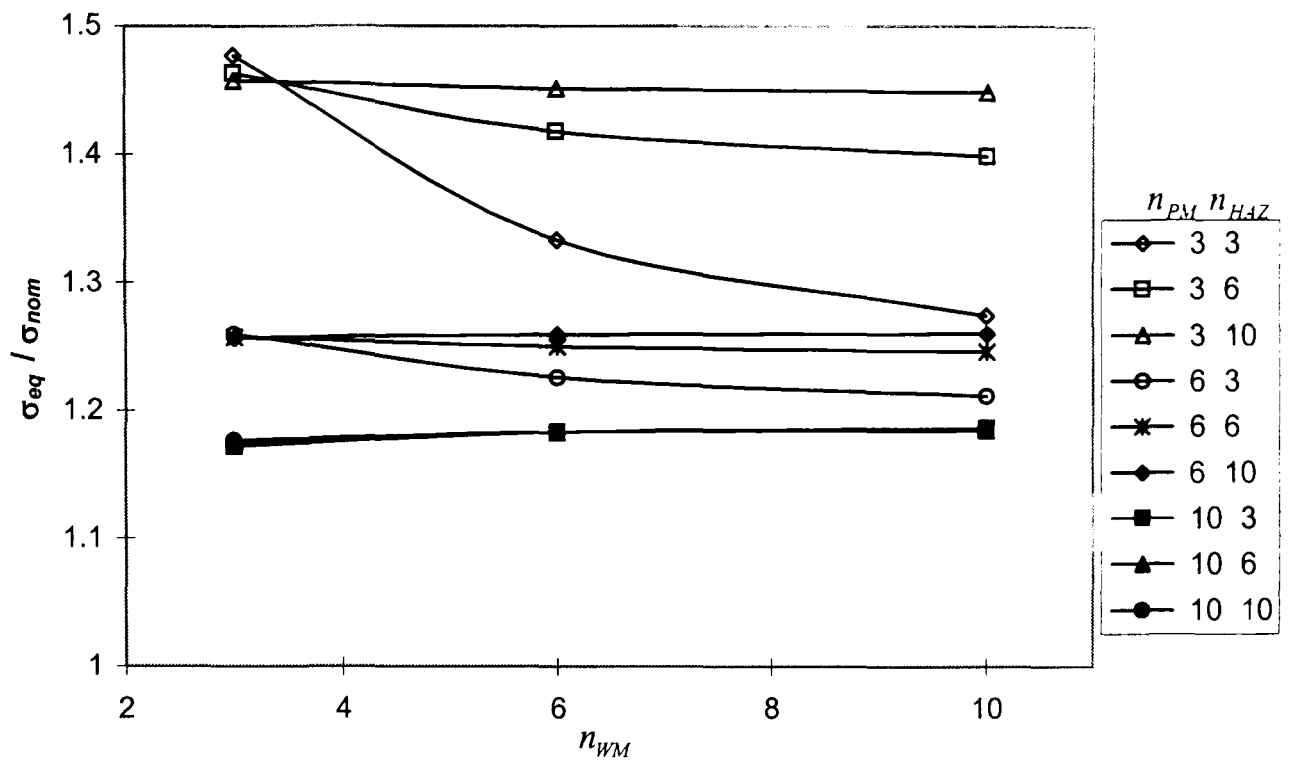


(a) $(n_{PM}, n_{HAZ}, n_{WM}) = (3, 10, 10)$

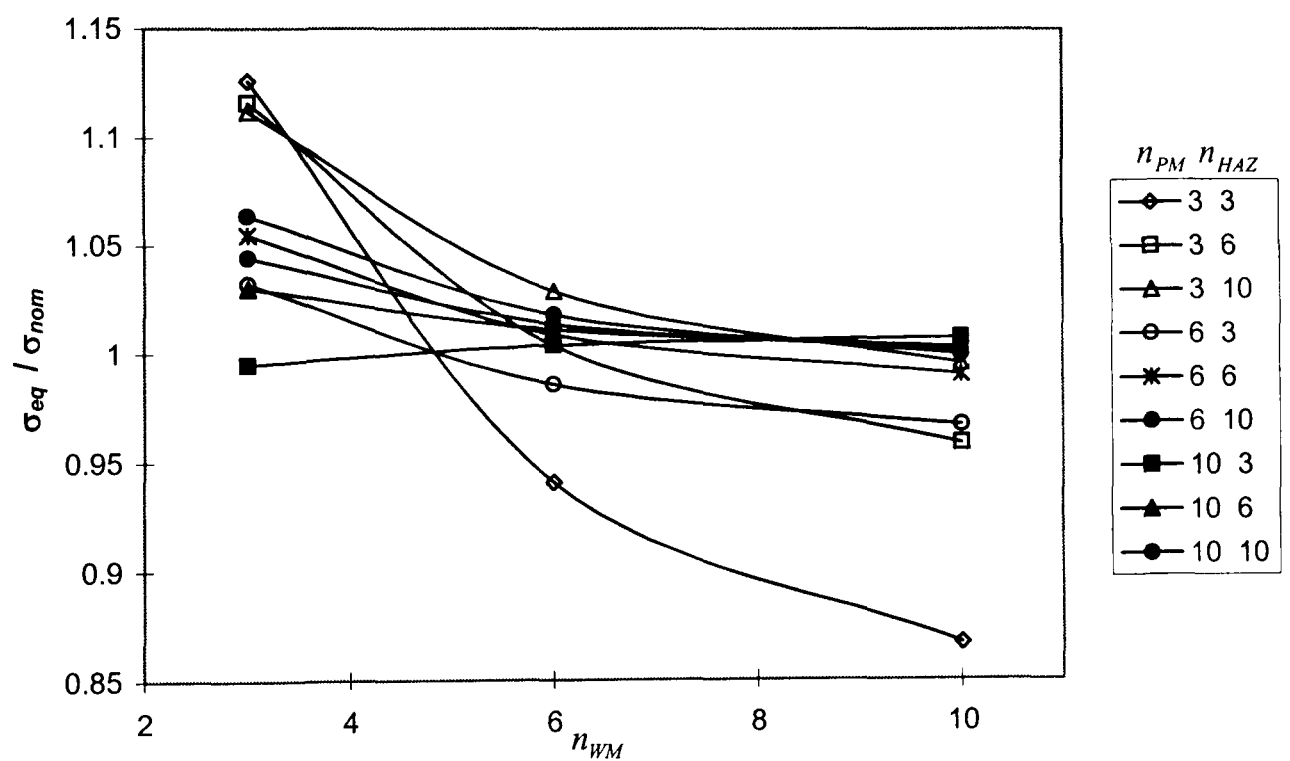


(b) $(n_{PM}, n_{HAZ}, n_{WM}) = (10, 3, 3)$

Figure 5.9. Variations of equivalent stress at Position A (PM^b) with $\dot{\epsilon}_{oPM} / \dot{\epsilon}_{oHAZ}$ and $\dot{\epsilon}_{oPM} / \dot{\epsilon}_{oWM}$ ratios for different $(n_{PM}, n_{HAZ}, n_{WM})$ combinations.

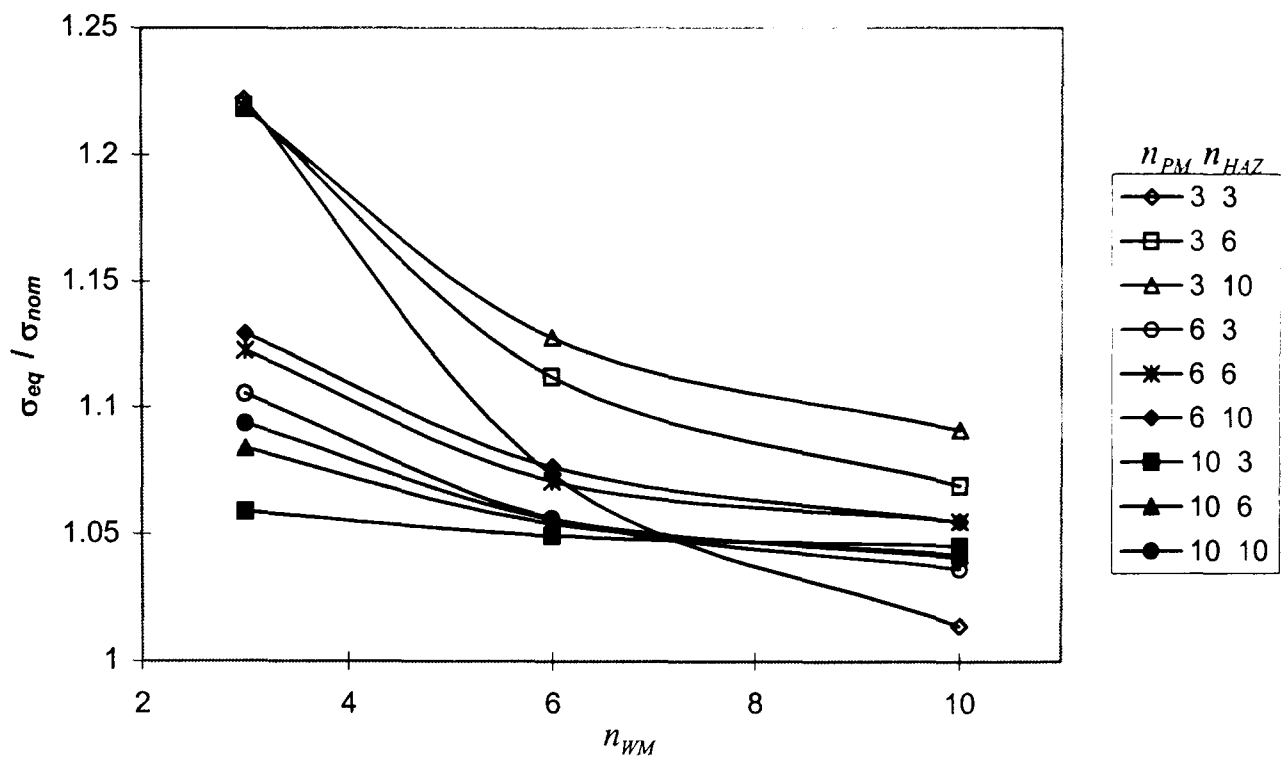


(a) $\dot{\epsilon}_{oPM} / \dot{\epsilon}_{oHAZ} = 100, \dot{\epsilon}_{oPM} / \dot{\epsilon}_{oWM} = 0.01$

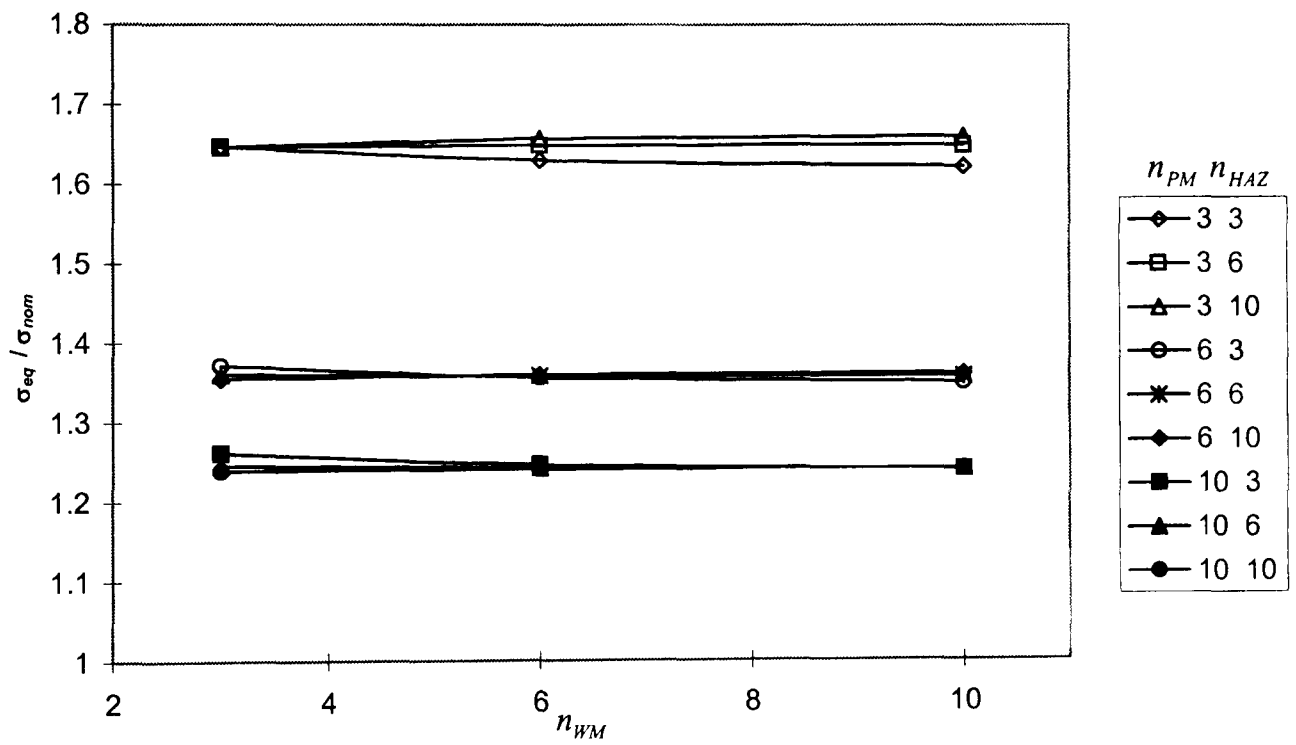


(b) $\dot{\epsilon}_{oPM} / \dot{\epsilon}_{oHAZ} = 100, \dot{\epsilon}_{oPM} / \dot{\epsilon}_{oWM} = 100$

Figure 5.10. Effect of n_{WM} on the equivalent stress at Position A (PM^b), for a range of n_{PM} and n_{HAZ} combinations, for four different $\dot{\epsilon}_{oPM} / \dot{\epsilon}_{oHAZ}$ and $\dot{\epsilon}_{oPM} / \dot{\epsilon}_{oWM}$ ratios.

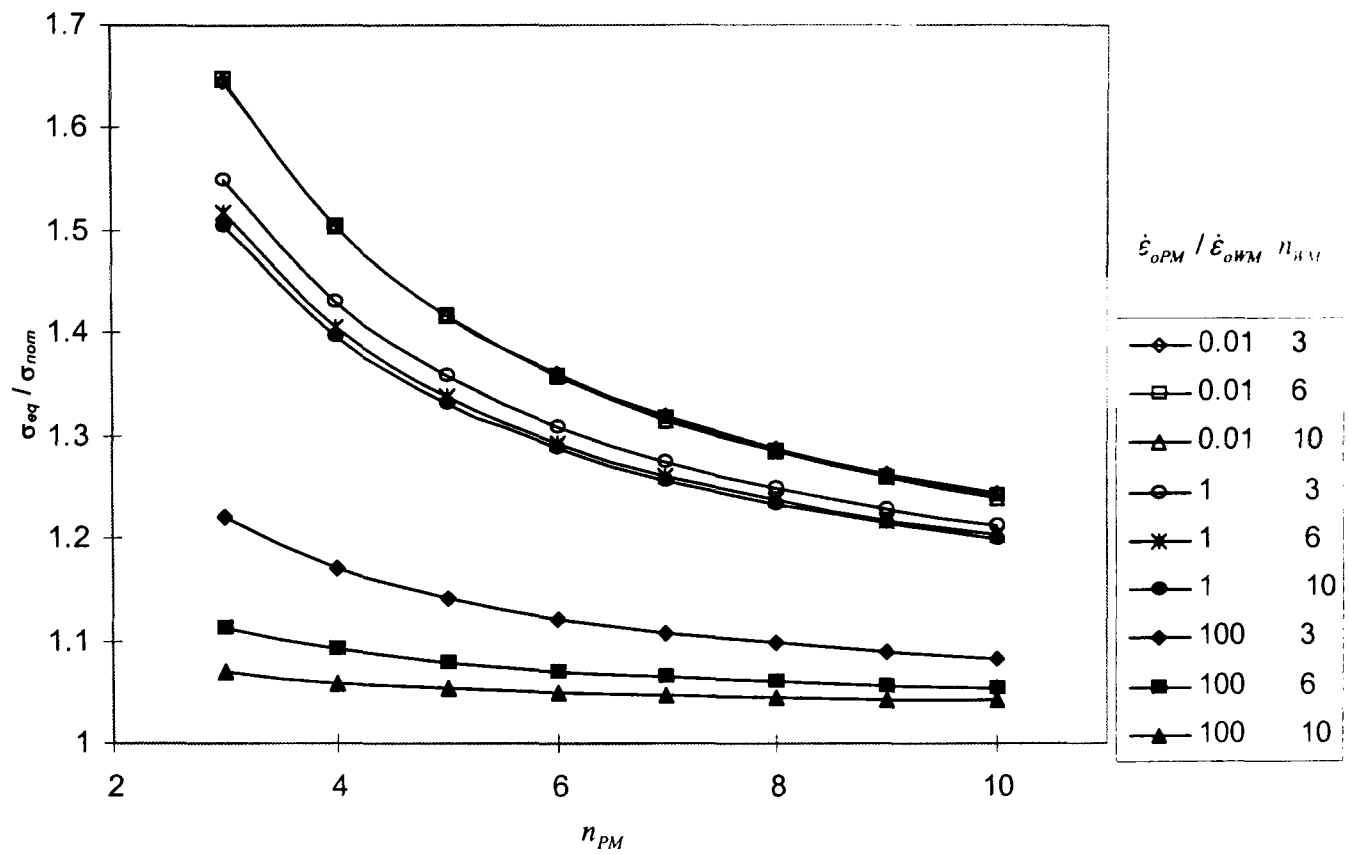


(c) $\dot{\epsilon}_{oPM} / \dot{\epsilon}_{oHAZ} = 0.01$, $\dot{\epsilon}_{oPM} / \dot{\epsilon}_{oWM} = 100$

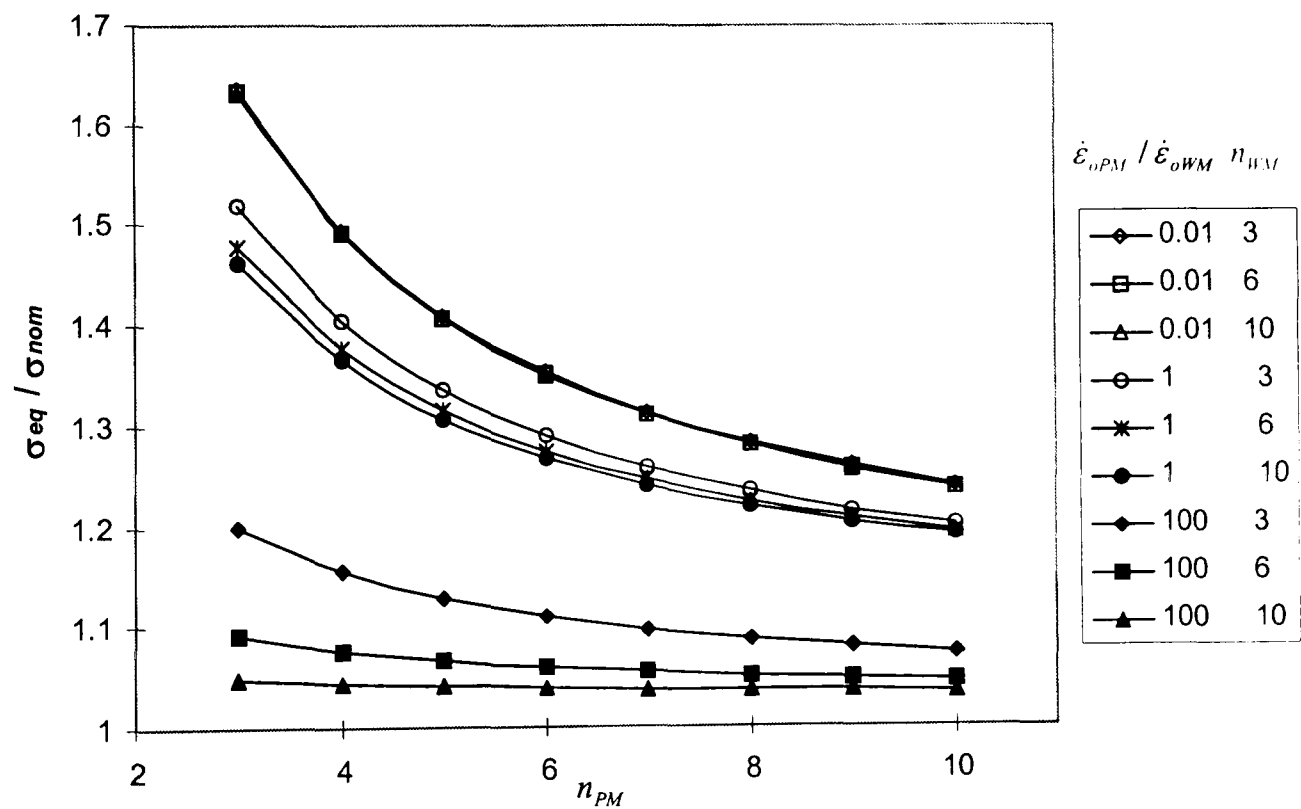


(d) $\dot{\epsilon}_{oPM} / \dot{\epsilon}_{oHAZ} = 0.01$, $\dot{\epsilon}_{oPM} / \dot{\epsilon}_{oWM} = 0.01$

Figure 5.10 continued. Effect of n_{WM} on the equivalent stress at Position A (PM^b), for a range of n_{PM} and n_{HAZ} combinations, for four different $\dot{\epsilon}_{oPM} / \dot{\epsilon}_{oHAZ}$ and $\dot{\epsilon}_{oPM} / \dot{\epsilon}_{oWM}$ ratios.



(a) $\dot{\epsilon}_{oPM} / \dot{\epsilon}_{oHAZ} = 0.01$



(b) $\dot{\epsilon}_{oPM} / \dot{\epsilon}_{oHAZ} = 1$

Figure 5.11. Effect of n_{PM} on the equivalent stress at Position A (PM^b), for a range of $\dot{\epsilon}_{oPM} / \dot{\epsilon}_{oWM}$ and n_{WM} combinations, with $n_{HAZ} = 6$, for three different $\dot{\epsilon}_{oPM} / \dot{\epsilon}_{oHAZ}$ ratios

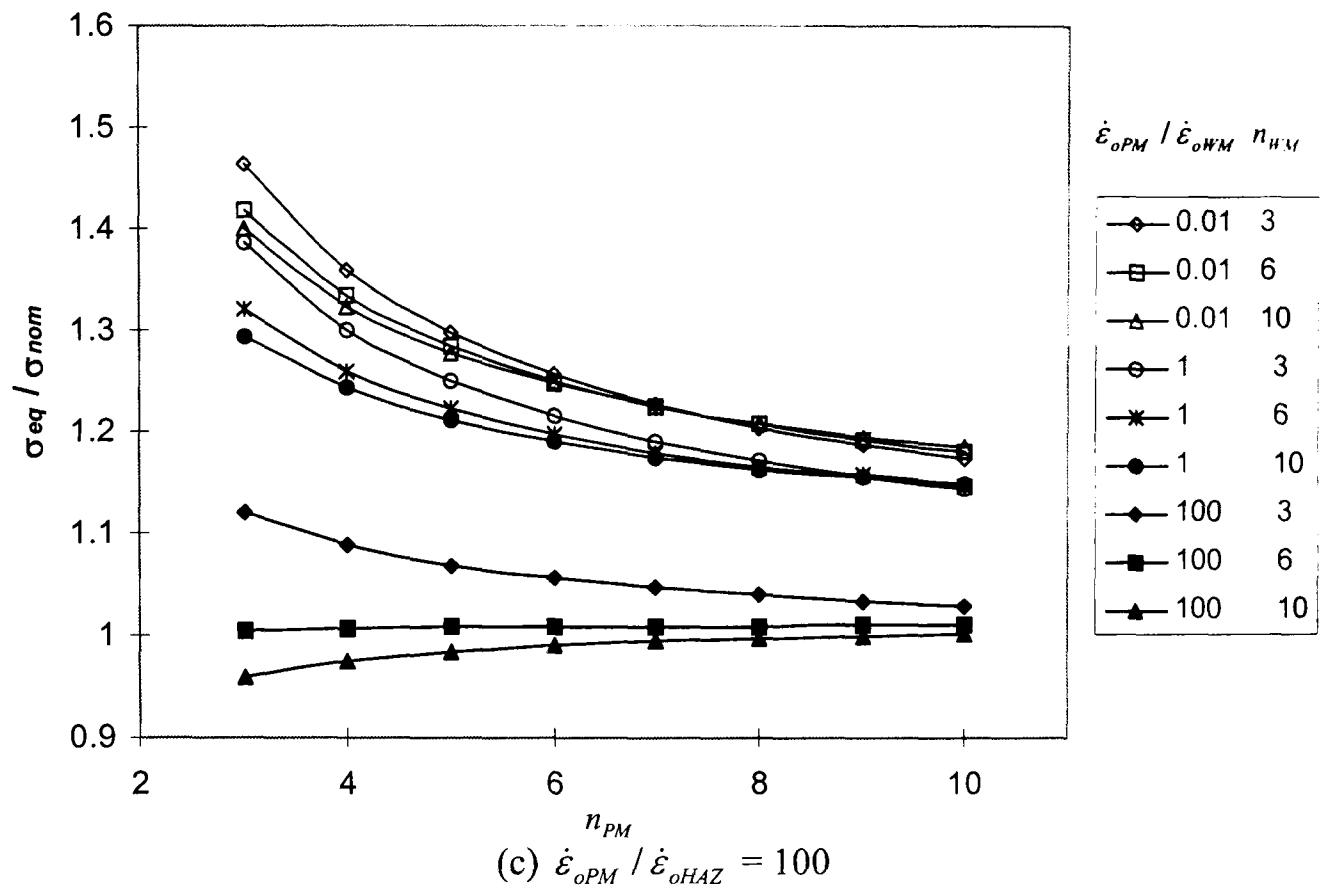
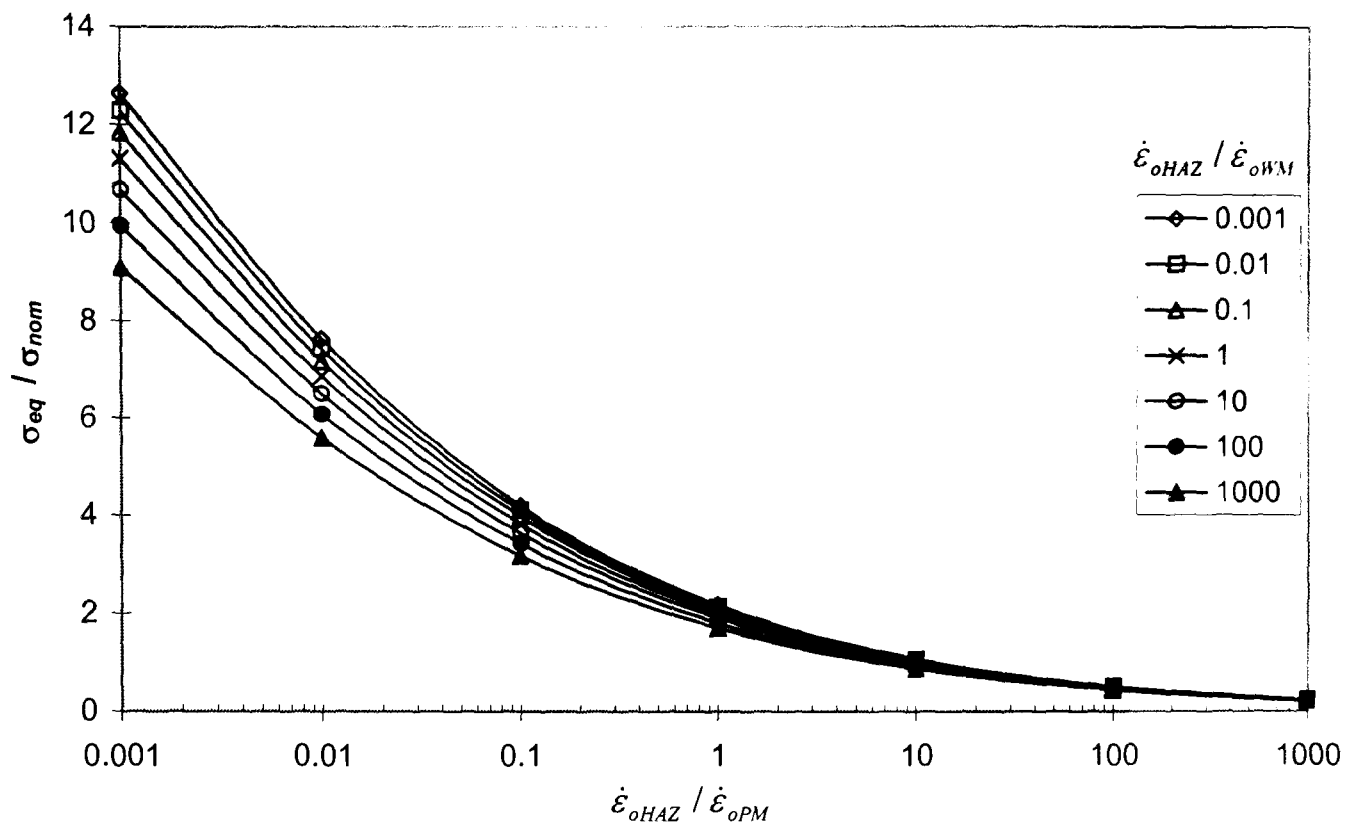
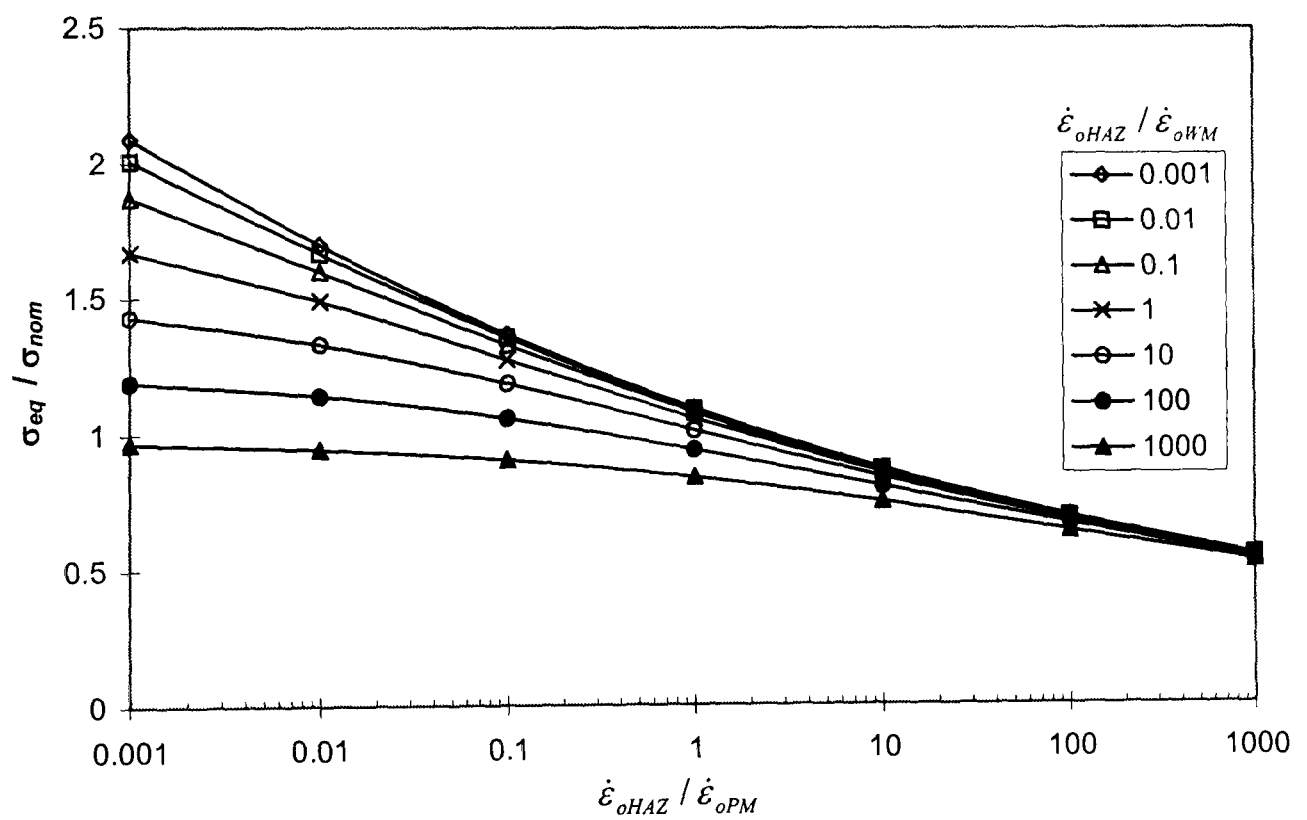


Figure 5.11 continued. Effect of n_{PM} on the equivalent stress at Position A (PM^b), for a range of $\dot{\epsilon}_{oPM} / \dot{\epsilon}_{oWM}$ and n_{WM} combinations, with $n_{HAZ} = 6$, for three different $\dot{\epsilon}_{oPM} / \dot{\epsilon}_{oHAZ}$ ratios

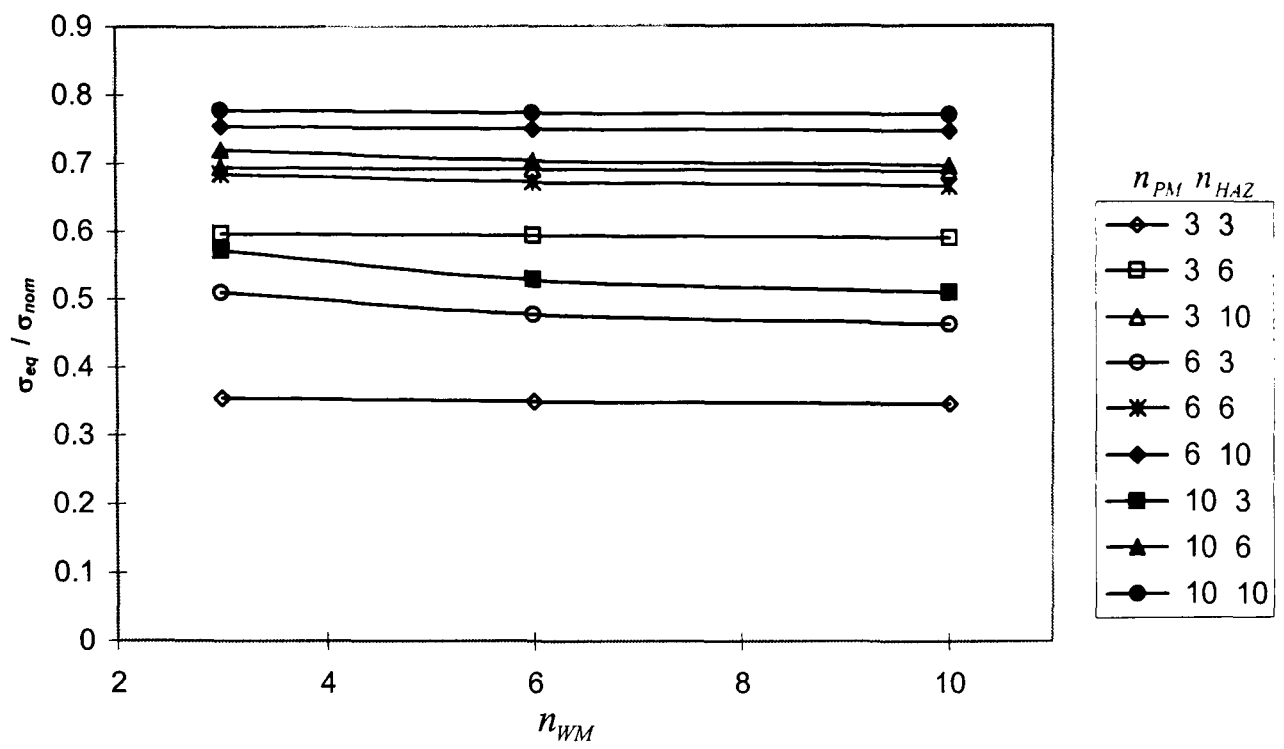


(a) $(n_{PM}, n_{HAZ}, n_{WM}) = (10, 3, 10)$

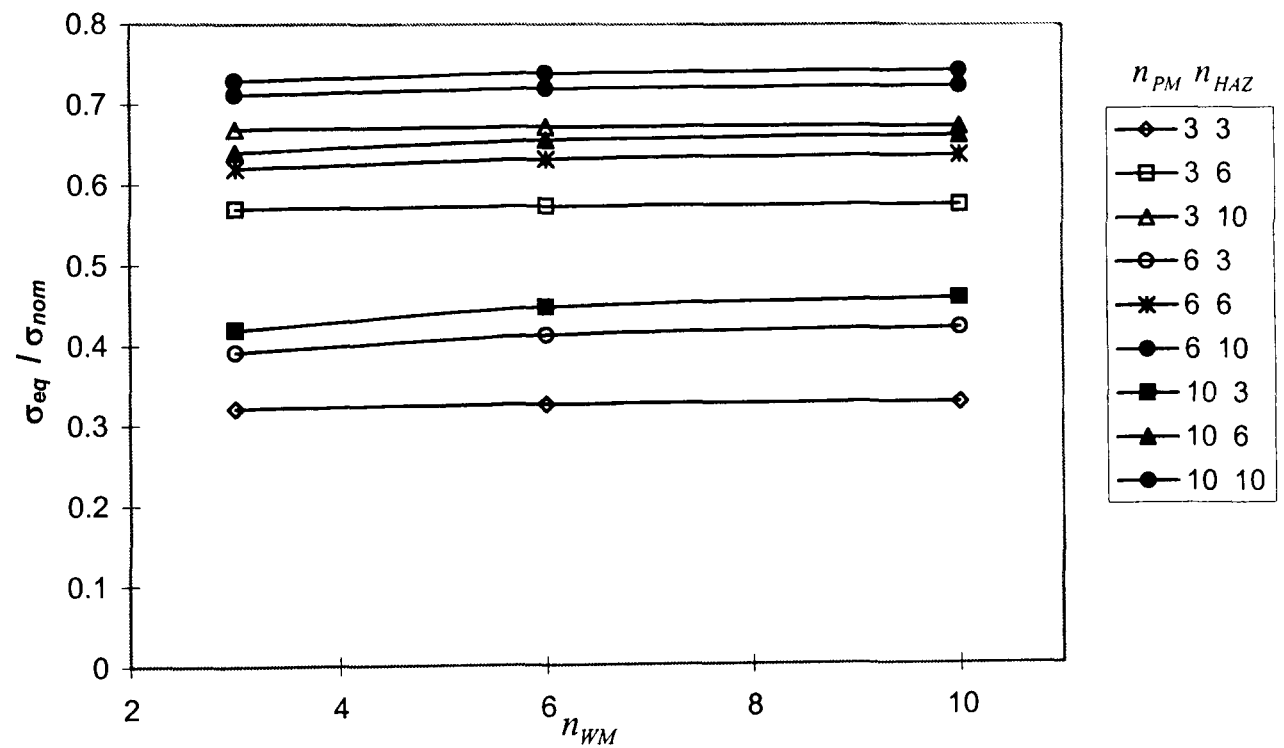


(b) $(n_{PM}, n_{HAZ}, n_{WM}) = (3, 10, 3)$

Figure 5.12. Variations of equivalent stress at Position D (HAZ^P) with $\dot{\epsilon}_{oHAZ} / \dot{\epsilon}_{oPM}$ and $\dot{\epsilon}_{oHAZ} / \dot{\epsilon}_{oWM}$ ratios for different $(n_{PM}, n_{HAZ}, n_{WM})$ combinations.

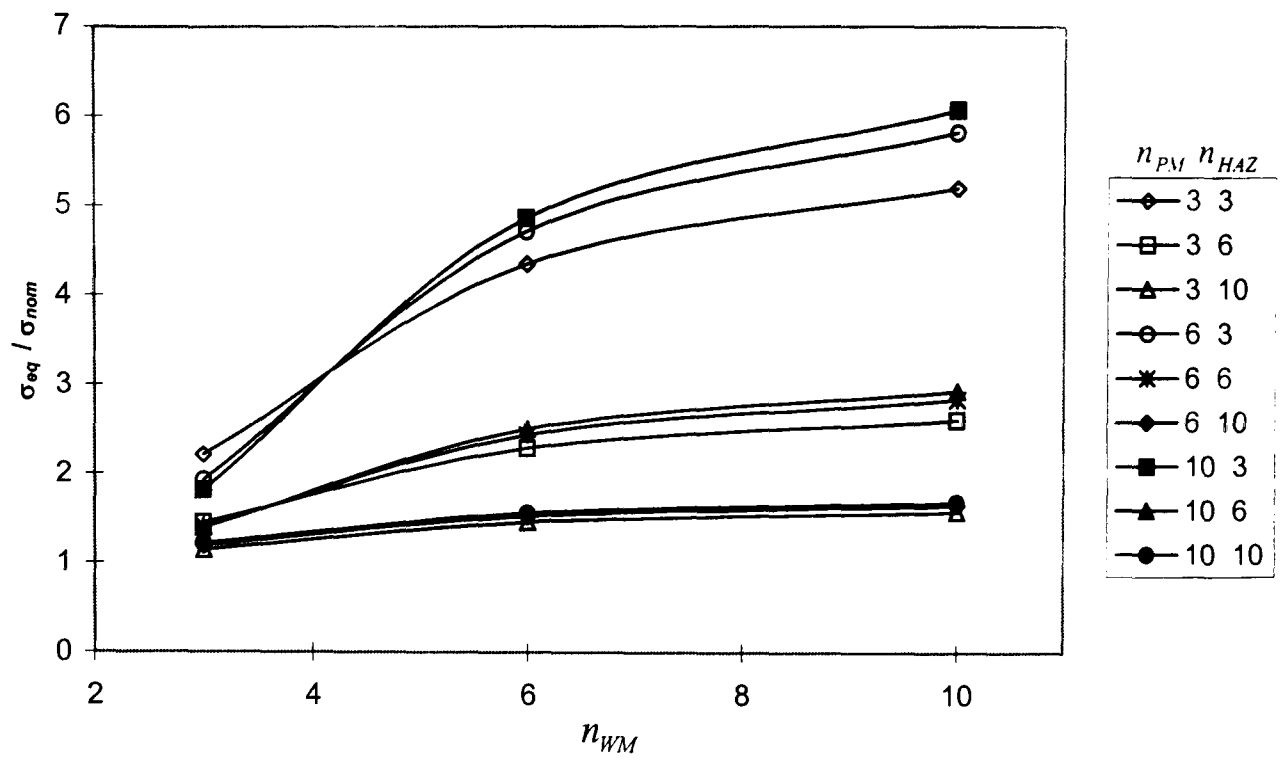


(a) $\dot{\epsilon}_{oHAZ} / \dot{\epsilon}_{oPM} = 100$, $\dot{\epsilon}_{oHAZ} / \dot{\epsilon}_{oWM} = 0.01$

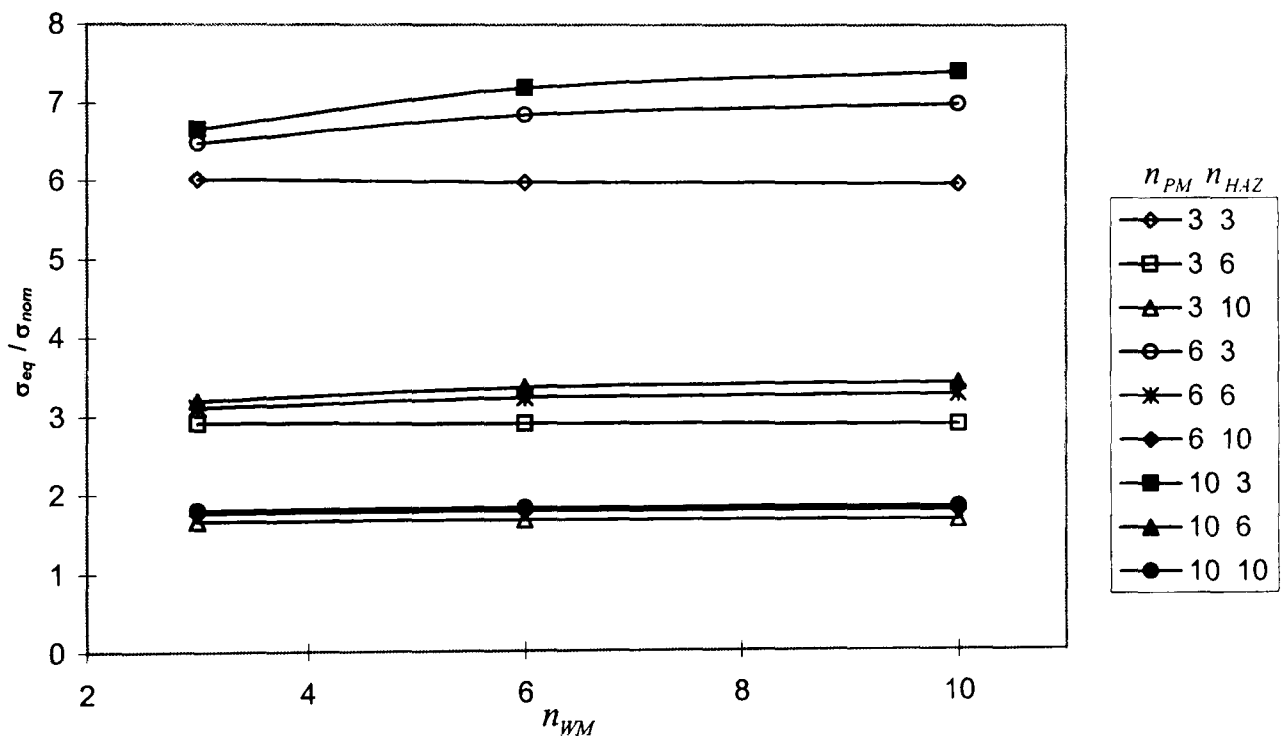


(b) $\dot{\epsilon}_{oHAZ} / \dot{\epsilon}_{oPM} = 100$, $\dot{\epsilon}_{oHAZ} / \dot{\epsilon}_{oWM} = 100$

Figure 5.13. Effect of n_{WM} on the equivalent stress at Position D (HAZ^p), for a range of n_{PM} and n_{HAZ} combinations, for four different $\dot{\epsilon}_{oHAZ} / \dot{\epsilon}_{oPM}$ and $\dot{\epsilon}_{oHAZ} / \dot{\epsilon}_{oWM}$ ratios.

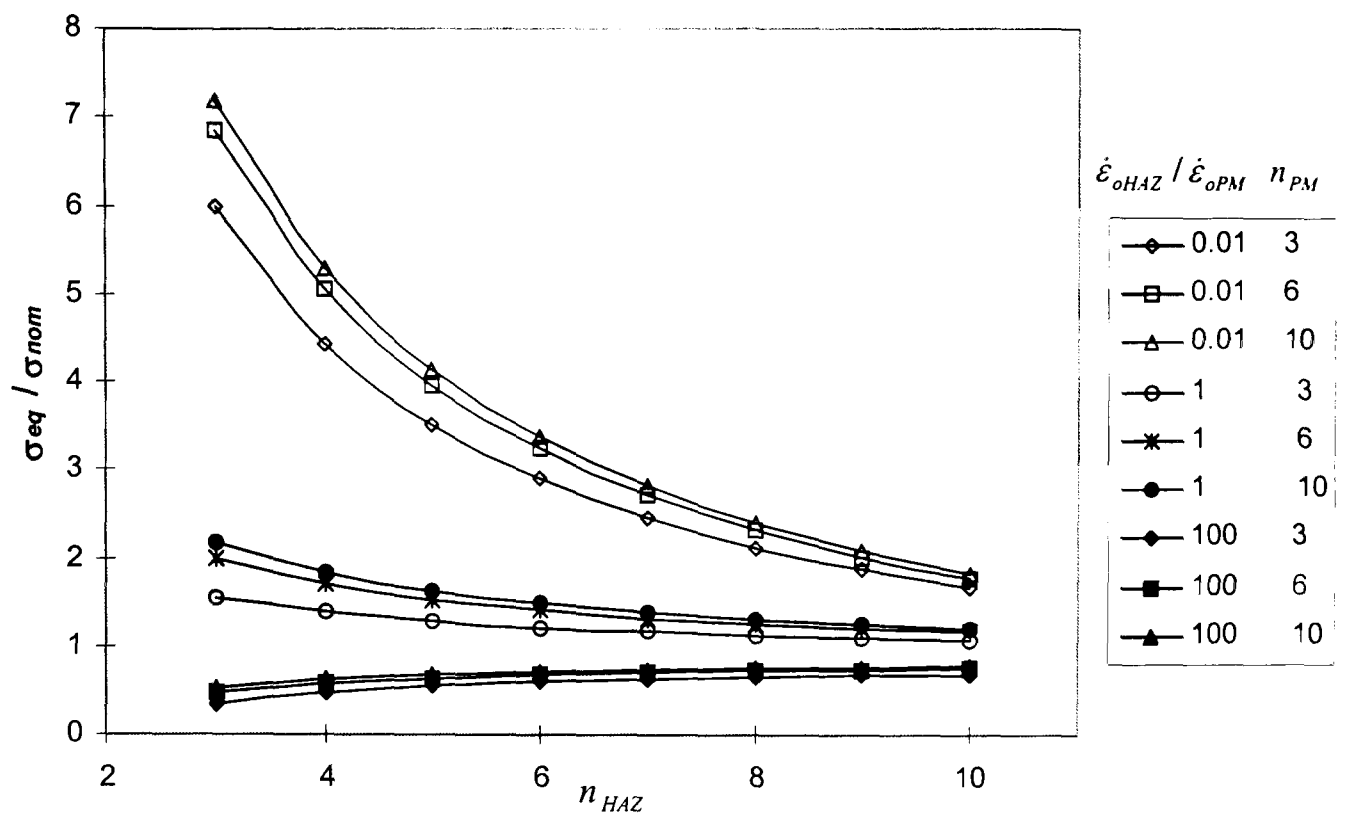


(c) $\dot{\epsilon}_{oHAZ} / \dot{\epsilon}_{oPM} = 0.01$, $\dot{\epsilon}_{oHAZ} / \dot{\epsilon}_{oWM} = 100$

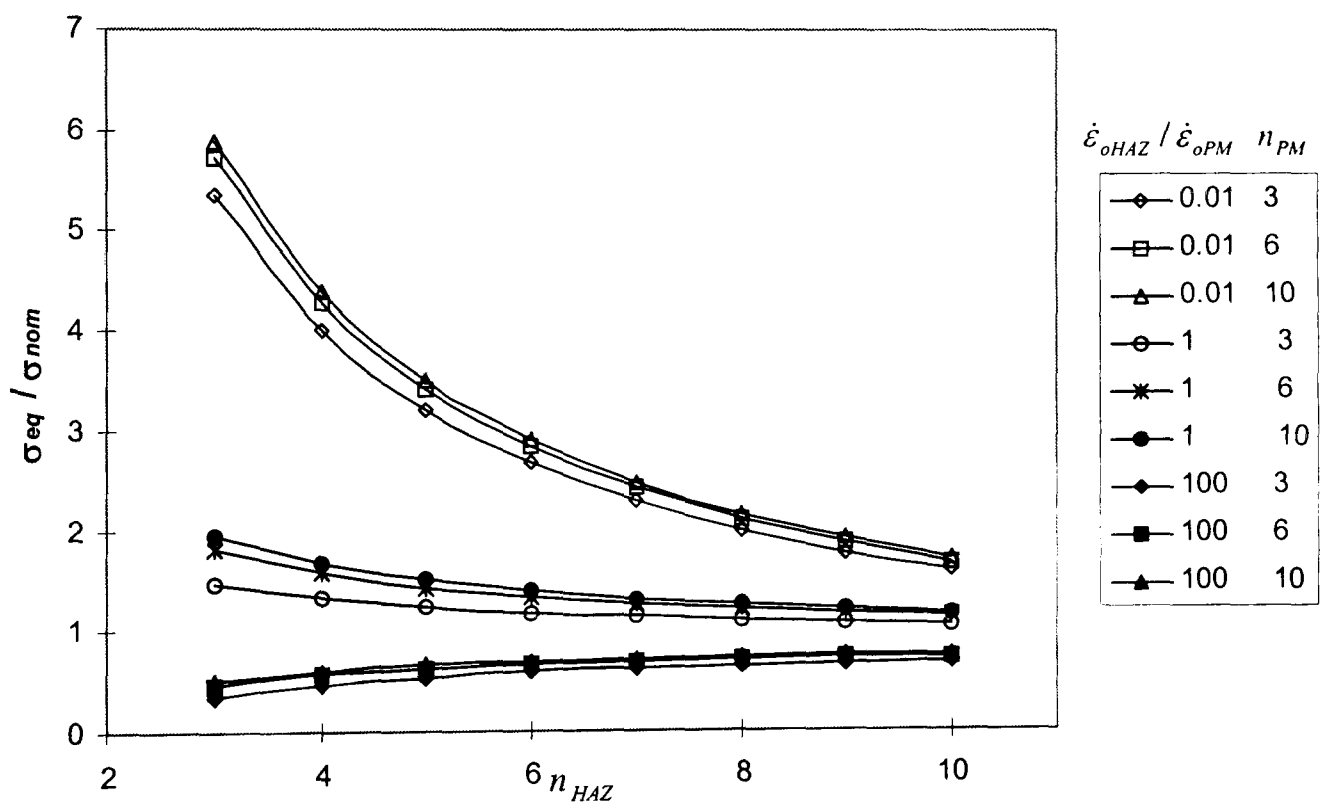


(d) $\dot{\epsilon}_{oHAZ} / \dot{\epsilon}_{oPM} = 0.01$, $\dot{\epsilon}_{oHAZ} / \dot{\epsilon}_{oWM} = 0.01$

Figure 5.13 continued. Effect of n_{WM} on the equivalent stress at Position D (HAZ^P), for a range of n_{PM} and n_{HAZ} combinations, for four different $\dot{\epsilon}_{oHAZ} / \dot{\epsilon}_{oPM}$ and $\dot{\epsilon}_{oHAZ} / \dot{\epsilon}_{oWM}$ ratios.

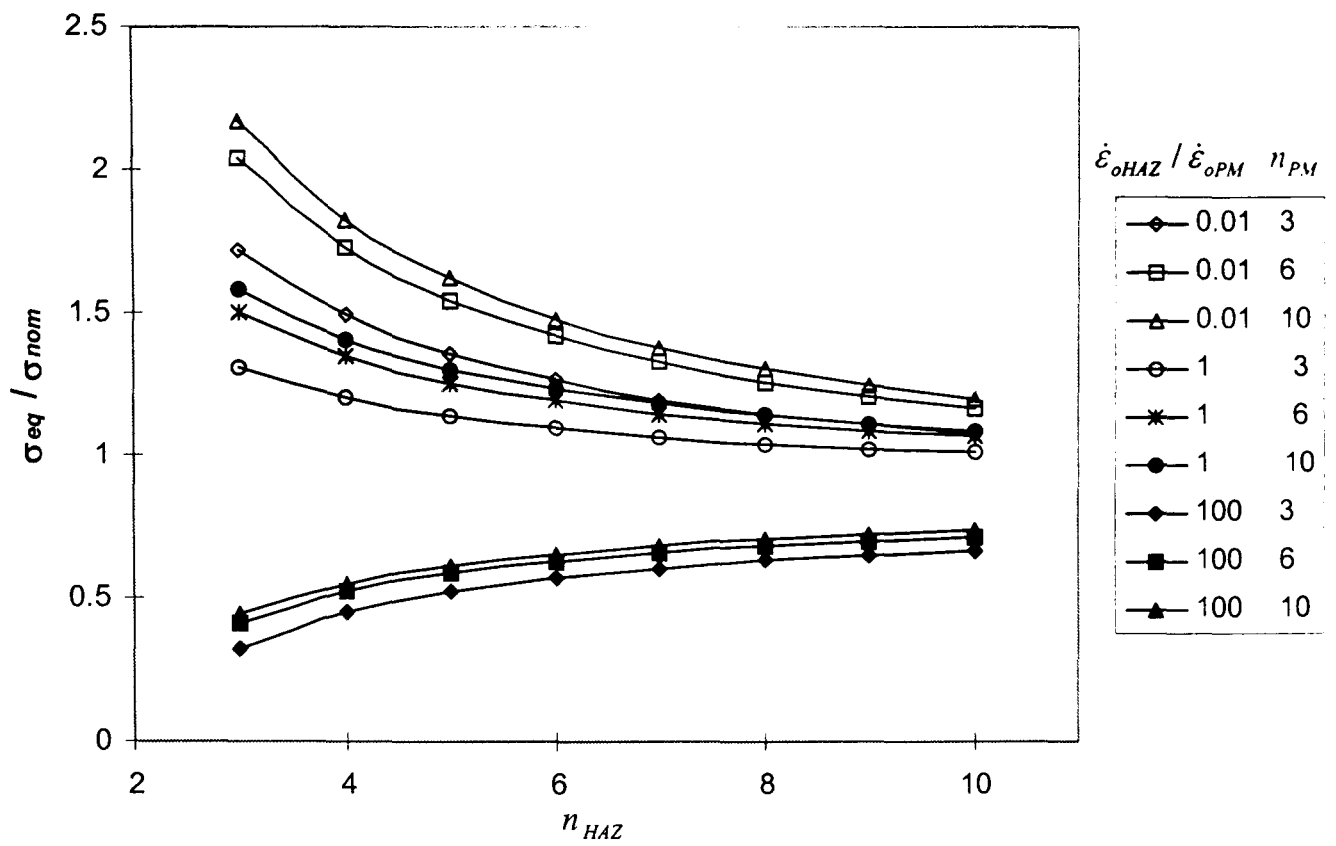


(a) $\dot{\epsilon}_{oHAZ} / \dot{\epsilon}_{oWM} = 0.01$



(b) $\dot{\epsilon}_{oHAZ} / \dot{\epsilon}_{oWM} = 1$

Figure 5.14. Effect of n_{HAZ} on the equivalent stress at Position D (HAZ^p), for a range of $\dot{\epsilon}_{oHAZ} / \dot{\epsilon}_{oPM}$ and n_{PM} combinations, with $n_{HAZ} = 6$, for three different $\dot{\epsilon}_{oHAZ} / \dot{\epsilon}_{oWM}$ ratios.



(c) $\dot{\epsilon}_{oHAZ} / \dot{\epsilon}_{oWM} = 100$

Figure 5.14 continued. Effect of n_{HAZ} on the equivalent stress at Position D (HAZ^P), for a range of $\dot{\epsilon}_{oHAZ} / \dot{\epsilon}_{oPM}$ and n_{PM} combinations, with $n_{HAZ} = 6$, for three different $\dot{\epsilon}_{oHAZ} / \dot{\epsilon}_{oWM}$ ratios.

CHAPTER SIX

CONTINUUM DAMAGE MECHANICS MODELLING OF CREEP IN WELDED BRANCHED PIPES

6.1 Introduction

For welded branched pipes, experience through in-plant and full-scale testing has shown that creep cracks and high damage regions commonly occur at the weld toe and neck, on the crotch and flank plane of the connections, as well as at the inside surface of the connection, in the weld region on the crotch plane, e.g. [9,17,18,113].

To effectively predict the creep life and cracking positions of in-situ components, relatively simple and quick calculations are required, where the finite element (FE) method is commonly used to run these creep calculations. In reality, a number of different creep calculations are used, some of which are more simplified than others. Two common methods are steady-state creep analysis, as employed in previous chapters, and continuum damage mechanics (CDM) analysis. The steady-state approach is less computationally intensive than the CDM approach [e.g. 31,33,34,53], and has been shown previously to predict conservative failure lives, by around 40% lower with identical failure positions for welded thick-walled steam pipes and cross-weld creep test specimens [26,33,34].

Chapters 3 to 5 use the steady-state rupture stress approach [34] for homogeneous and welded branched pipes, which assumes that the tertiary creep stage is small compared to the total life of the component. The CDM approach can model the primary, secondary and tertiary creep stages.

This chapter investigates the multi-material creep behaviour of two typical isolated welded branched pipes using the CDM approach and compares the failure results with the equivalent steady-state results. Two different material weldment sets, namely an as-new and a service-aged $\frac{1}{2}\text{Cr}\frac{1}{2}\text{Mo}\frac{1}{4}\text{V}:2\frac{1}{4}\text{Cr}1\text{Mo}$ weldment at 640°C , are investigated. The objective is to compare the performance of the steady-state and CDM approaches with respect to failure life, high-damage/rupture sites and final failure position. Details on the damage evolution at particular positions of the two branches are also addressed.

6.2 Material models

The CDM constitutive equations employed are based on the Kachanov theory [31], as described in Section 2.3.3 by Equations 2.6 and 2.7, σ_r is the creep rupture stress, defined by Equation 2.8, ω is the damage variable which varies from 0 (no damage) to 1 (failure) and $\dot{\omega}$ is the damage rate. A' , m , n' , M , ϕ and χ are the material constants required for the PM, WM and HAZ material zones. However, determinations of weldment material constants are difficult and are not widely available, especially for the small HAZ. Additionally, FE damage calculations are very time consuming. The application of the steady-

state rupture stress approach employed in this and previous chapters is described in detail in Chapters 2 to 4.

6.3 Geometry and FE models

The chosen branched pipe dimensions were typical of CrMoV UK power plant, with the branch being typical of small penetrations used for steam collection on header-tanks or for the purposes of pressure and temperature measurement tapping and the main pipe being typical of large main steam pipes or headers in the superheater section of plant. Figure 4.3 defines the geometrical parameters for the welded branched pipe studied. The values of D , T , d and t employed are 355mm, 65mm, 62.5mm and 12.5mm, respectively. The geometric weld parameters and notation are shown in Figure 4.4 and are fully described, along with the applied loadings of internal pressure and closed-end axial stress in Section 4.2. Table 6.1 defines the values of θ , β , a , b , b_1 , h , r_0 and r_1 used throughout, while b_x and b_y were set equal to the branch thickness, t . Note that the HAZ^b and HAZ^p properties are again assumed to be the same and likewise for the PM^b and PM^p zones. For the two welded branched pipe cases using material Sets 1 and 2, FE calculations were performed with an internal pressure of 16.55 MPa and the closed end axial load of 11.11MPa on the main pipe and 9.31MPa on the branch pipe.

The three-dimensional, quarter FE model used for the steady-state and CDM analyses is shown in Figure 6.1. The mesh used twenty-noded quadratic brick elements with reduced integration. Mesh refinement was used at the weld region and a total of 4500 elements were used. Detailed attention has been

given to ensuring compatible and uniform mesh design across the HAZ, PM and WM material mismatch boundaries. Weld toe and neck radii are used to eliminate sharp weld edges and therefore reduce unrealistic stress peaks. Careful interpretation of the time-dependent Gaussian stresses was used to ascertain when a steady-state was achieved. The same model was used for both the CDM and steady-state analyses. The mesh is relatively coarse compared to the sub-models used in Chapters 4 and 5 due to the computationally intensive CDM analyses requiring very long time scales to run for such a complex component and many time increments to model the tertiary creep stage. However, convergence studies showed that stress values within the weld were still reasonably accurate compared values predicted using the sub-model. The computer used for both analyses was a SGI[®] Origin and around one month of CPU time was required to reach sufficiently high damage levels within the welded branched pipes. A user-subroutine called *CREEP* [133] was employed with ABAQUS FE software to implement the CDM equations (i.e. Equations 2.6 to 2.8). The same routine has been previously applied to CDM analyses of V-welded straight pipe sections [133]. Appendix 1 provides some general guidelines on how FE analysis can be used to effectively predict steady-state stress distributions and how component failure can be defined using continuum damage mechanics analysis.

6.4 Material properties

The material constants used in the steady-state and damage FE analyses, via Equations 2.3, 2.6, 2.7 and 2.8, were obtained from uniaxial plain and notched

homogeneous and welded bar and indenting creep tests performed at 640°C [36,134], in the stress ranges of 40MPa to 70MPa, on the different constituent material zones of the two different types of weldment, i.e. (i) Set 1: Service-Aged and (ii) Set 2: As-New. The creep tests were performed on a $\frac{1}{2}\text{Cr}\frac{1}{2}\text{Mo}\frac{1}{4}\text{V}:2\frac{1}{4}\text{CrMo}$ weldment taken from an ex-service main steam pipe after 174,800 hours [36,134]. Suitability of the creep properties produced from the tests was assessed for FE steady-state and damage analyses and satisfactory results were found [36,134], i.e. FE creep test specimen models predicted similar creep strain, rupture life and rupture position compared to the experimental tests. The material constants used for the steady-state and damage analyses for the two weldment sets are shown in Table 6.2. The primary creep material constant m for the three zones, used in Equations 2.6 and 2.7, are equal to zero for these two weldment sets, as primary creep was negligible. Thus the A' and n' values for the damage equations are equal to the steady-state A and n values. For these two weldment sets the HAZ material is weaker than the PM and the WM is stronger than the PM with respect to the minimum creep strain rates (i.e. $\dot{\epsilon}_{HAZ}^c > \dot{\epsilon}_{PM}^c > \dot{\epsilon}_{WM}^c$ for any given stress level) and rupture strength (i.e. $t_{HAZ}^f < t_{PM}^f < t_{WM}^f$ for a constant stress at stresses below 70MPa) [34,134]. The HAZ material constants for both Set 1 and 2 weldment sets were obtained for the fine-grained HAZ region and not for the coarse-grained or a mixed HAZ region and therefore the results are assumed to be more representative of Type IV creep and damage behaviour [33,134].

6.5 Results

For the two branches, rupture initiation is assumed to have occurred according to the CDM analyses when a position had reached a damage level near unity, i.e. $\omega = 0.98$ in this case. Component failure is assumed to have occurred when a significant proportion of the wall thickness has reached a high level of damage, the criterion of 40% of wall-thickness greater than $\omega = 0.6$ was chosen, based on a compromise with analysis run-time. Previous results have shown [89,36,135] that when the damage level has penetrated through a significant proportion of the wall thickness, the damage rate across the remaining thickness will significantly increase so that the remaining operating time before final failure is very small compared to the total operating life. For the steady-state analyses, the rupture stress at each position is used to predict an assumed rupture initiation time. Additionally, the shortest rupture initiation life predicted over all positions and from all material zones is conservatively assumed to equal the component failure life.

6.5.1 Set 1: Service-aged connection predictions

Results for the continuum damage mechanics analysis, in the form of damage contour plots within the welded service-aged branch, are shown in Figures 6.2 and 6.3 at the component failure time of 7450 hours. High damage was confined to the weld HAZ region, as well as the inside bore, just up from the inside crotch corner. Several high damage regions in the HAZ^b and HAZ^p were predicted to occur on the flank and crotch plane on the outer and inner surfaces, as well as around the outer circumference. Component failure was

predicted to occur in both the HAZ^b and HAZ^p, on the crotch plane at 7450 hours (Figure 6.3), both near the boundary between HAZ and parent material. Figures 6.4 and 6.5 are graphs displaying the evolution of damage across the wall thickness of both failure regions, the HAZ^b and HAZ^p, respectively. For the HAZ^p region, the material first ruptured ($\omega=0.98$) at a position around a third across the thickness from the inner bore, at approximately 7310 hours. The damage then spread quickly from this point towards the inner and outer surfaces. For the HAZ^b failure region, the material initially ruptured at the outer surface, i.e. the weld neck, at about 6490 hours and then damage spread towards the inner surface. However, the damage at the center of the HAZ^b wall thickness did not increase as rapidly as the HAZ^p failure, due to the peaky nature of the weld neck stress concentration in the HAZ^b. Failure by steam leakage would be expected to occur a short time after this. Other high damage regions in the weldment are also predicted to occur. Of particular interest to in-situ monitoring is high damage (leading to shallow-depth cracks) on the HAZ^b or HAZ^p outer surfaces, at several locations around the connection's circumference. For this connection, high damage was found at these locations before failure had occurred, this may be of interest for inspection purposes. Figures 6.6 (a) to (e) display the damage evolution within the HAZ^b or HAZ^p zones for different times after initial material rupture, i.e. first occurrence of $\omega=0.98$, at Position F at 4650 hours (Figure 6.6(a)) until component failure at 7450 hours (Figure 6.6(e)). It is clear that the distinct rupture sites and their growth are shown from these damage contour plots. Table 6.3 also summarises the CDM results for critical Positions A to K of Figures 6.2, 6.3 and 6.6. If the damage at a position is lower than 0.98 at the time of component failure (i.e.

7450 hours) then the corresponding final damage value at this position is shown in the table. The order of failure of each position is also shown.

Contours of the steady-state creep rupture stress distributions for the Set 1 material combination are presented in Figures 6.7 to 6.9. Figures 6.7, 6.8 and 6.9 correspond to PM, HAZ and WM rupture stresses, respectively, using the corresponding α value for each material zone. Note that the contour plots for each zone exclude the other two material zones. The peak stress positions are similar to those of Chapter Four for similar service-aged branched pipes. The peak PM σ_r value occurs at Position *A* of Figure 6.7(b). The peak WM σ_r values occur at Position *B* and Position *C* of Figure 6.8. High HAZ σ_r values occur at eight positions, as shown in Figure 6.9.

The magnitudes of rupture stress at these HAZ positions are similar, suggesting that similar damage levels and therefore multiple rupture sites are likely to occur. Table 6.3 summarises the predicted steady-state rupture stresses and lives for each PM, HAZ and WM position. From these predicted lives, the order of failure for each of the positions has been made in the table, as well as the co-ordinates of each position. The steady-state results predict that the HAZ positions will rupture first, with Position *F* providing the lowest life of 2949 hours. The steady-state component failure life is therefore assumed to equal this value.

Comparison of the steady-state predictions with the CDM predictions are made in Table 6.3 and lead to a number of discussion points. Firstly, the peak

steady-state stress positions in the PM, WM and HAZ, shown in Figures 6.7, 6.8 and 6.9, respectively, correspond very closely to the peak damage locations of the CDM predictions, shown in Figures 6.2, 6.3 and 6.4, respectively. Secondly, it is clear from the results of Table 6.3 that the steady-state rupture life for each position is consistently conservative by between 33% to 44% relative to the CDM life predictions for each position. The resulting steady-state component failure life was 2949 hours, predicted to initiate at Position *F*, which is 60% conservative compared to the CDM predicted component life of 7450 hours, where peak damage also initiated at Position *F* and grew across the HAZ^b wall thickness. These results show that the steady-state approach can predict conservative rupture lives at critical positions, as well as a component failure life for the complex welded branched pipe case. In contrast to the simpler cases of welded straight pipes and cross-weld specimens, welded branched pipes have complex geometrical discontinuities around the weld due to sharp changes in geometry. This additional effect may affect the magnitude of stress redistribution during the tertiary stage compared to simpler components. However, the above results show that the steady-state approach still predicts accurate rupture lives and positions. Thirdly, a comparison of the order of rupture between the eleven peak stress and high damage positions (Positions *A* to *K*) via Table 6.3 shows that the steady-state order of failure is identical to that of the CDM.

6.5.2 Set 2: As-new connection predictions

Results for the continuum damage mechanics analysis in the form of damage contour plots within the weldment of the Set 2: As-new material branch are shown in Figures 6.10 and 6.11 at the component creep failure time of 10400 hours. As seen from the contour plots, high damage was mainly confined to the weld region; within this all material types (HAZ, WM and PM) have a significant level of damage, unlike the service-aged branch, where damage was mainly confined to the HAZ regions. Almost identical to the Set 1: service-aged damage predictions, several high damage regions in the HAZ^b and HAZ^p were predicted to occur on the flank and crotch plane, at the outer and inner surfaces, as well as around the outer circumference. However, high damage levels were also predicted on the crotch plane, near the outside surface of the WM and also in the WM, on the outer surface, at approximately 45° from the crotch to flank planes, in the longitudinal directions of the branch axis, as well as around the circumference of the weld edges, as shown in Figure 6.11b. The inside surface of the connection in the PM^p, up from the inside crotch corner also has high levels of damage. Component failure was predicted to occur both in the HAZ^b and HAZ^p on the crotch plane and on the PM boundary at approximately 10400 hours, as shown in Figure 6.11. However, the WM wall-thickness on the crotch plane could also control failure as a large majority of the thickness is approaching $\omega = 1$. Figures 6.12 and 6.13 are graphs displaying the evolution of damage across the wall thickness of both of these failure regions, the HAZ^b and HAZ^p, respectively. The damage evolution behaviour across the wall thickness for these two regions are similar to that of Set 1 CDM results. For the HAZ^p region, the material initially ruptured

($\omega=0.98$) at a position around a third across the thickness from the inner bore, at Position *D*, at approximately 10000 hours, the damage across the majority of the wall thickness at this time is relatively high, i.e. greater than 0.5. For the HAZ^b failure region, the material initially ruptured at the outer surface, i.e. at Position *F* on the weld neck, at about 6210 hours. Peak values of damage then spread in the HAZ^b towards the inner surface. However, the damage at the center of the HAZ^b wall thickness does not increase rapidly, unlike the HAZ^p wall thickness. The contour plots show for both HAZ^b and HAZ^p regions that high damage across the majority of the wall-thickness was predicted, and failure by steam leakage would occur in a relatively short time period after this time. Again, as for Set 1's findings, shallow-depth peak damage around the circumference of the HAZ^b weld neck was predicted and this it is expected that this would lead to possible circumferential creep crack growth in practice. Figures 6.14 (a) to (e) display the damage evolution within the HAZ^b or HAZ^p zones over different times from the initiation of $\omega=0.98$ at 6210 hours at Position *F* (Figure 6.14(a)) to component failure at 10400 hours (Figure 6.14(e)). Table 6.4 also summarises the CDM results for critical Positions *A* to *K* of Figures 6.10, 6.11 and 6.14. If the damage at a position is lower than 0.98 at the time of component failure (i.e. 10400 hours) then the corresponding final damage value at this position is shown in the table. The order of rupture for each position is also clearly shown in the table.

For the Set 2: As new weldment steady-state rupture stress distributions in the PM, WM and HAZ zones are shown in Figures 6.15, 6.16 and 6.17, respectively. The peak stress positions are very similar to those of the service-

aged connection (Set 1). The only difference relates to the Position C location on the weld foot, which occurs at 36° circumferentially from the flank plane for Set 2 as opposed to 5° for Set 1. Again, multiple similar high rupture stress locations and thus similar lives were predicted in the weld. Table 6.4 summarises the predicted steady-state rupture stresses and lives for each of the PM, HAZ and WM positions, i.e. Positions *A* to *K*. The steady-state Set 2 results differ from the Set 1 in that (i) the Set 2 HAZ failure lives are similar to those of the WM and PM lives, and (ii) the Set 2 HAZ lives are generally significantly longer than the Set 1 lives, as expected due to the weldment being as-new. The first position at which rupture is predicted is Position *F* in the HAZ^b at 5118 hours, followed by the PM^p Position *A* after approximately another 1300 hours. WM Positions *B* and *C* and HAZ Positions *D*, *H*, *J* and *K* are all predicted to fail at around the same time, just after Position *A*. Approximately 500 hours later the rest of the HAZ positions are predicted to fail. The resulting failure life of the component is therefore based on HAZ^b Position *F* rupture life of 5118 hours.

The steady-state rupture approach therefore predicted a component failure life of 5118 hours, initiating at Position *F*, which is conservative by about 50% compared to the CDM predicted component life of 10400 hours, which also initiated failure at Position *F*.

Table 6.4 summarises the peak damage values and associated rupture lives for Positions *A* to *K*, as shown in Figures 6.10, 6.11 and 6.14. Again, as done for Set 1, comparing the steady-state peak stress positions of Figures 6.15 to 6.17

within the PM, WM and HAZ^b or HAZ^p zones, respectively, with the peak damage locations, approximately identical rupture locations are predicted by both approaches. It is clear from Table 6.4 that at all positions the steady-state rupture lives are again conservative relative to the CDM predictions. In this case though, the steady-state predictions are much closer to the CDM, ranging from 18% to 37% less. The CDM 'order of rupture' predicts the HAZ^b Position *F* to rupture first, followed by HAZ Positions *K*, *J* and *H* and then HAZ^p Position *D* and PM^p Position *A*. The steady-state approach also predicted HAZ^b Position *F* to rupture first, but subsequent positions are different from those of the CDM predictions. This dissimilarity could be a result of the differences in stress redistribution in the tertiary creep stage of the CDM analysis.

6.6 Discussion

Application of the steady-state rupture approach of Hyde *et al* [26,33,34] to Set 1 and Set 2 welded branch pipe cases gave rupture lives for critical positions which were 44% to 18% conservative relative to the CDM life predictions. If the CDM component failure life is compared to the predicted steady-state component failure life, the steady-state predictions are conservative by around 50% to 60% for both Set 1 and Set 2 weldments. This level of conservatism for the steady-state approach is higher than previous comparisons for welded straight pipes and cross-weld test specimens, which were around 30% to 40% conservative [34,36]. For welded straight pipes and creep test specimens the stress-state across the wall thickness is relatively uniform so that the time for creep damage to spread across the wall-thickness is relatively small. However,

for the branched pipe cases, geometrical discontinuities cause high stress concentrations and a non-uniform stress distribution across the wall thickness, with comparatively larger time for damage to spread through the wall.

The predicted high damage locations from both analysis types are similar to those of numerous full-scale creep failure tests and typical of in-situ CrMoV thick-walled welded branched pipes [9,17,18,113], as described in Chapter Two. The general findings were that early high damage/creep cracks are commonly found to initiate along the HAZ weld toe and neck regions, on the flank and crotch planes and at about 45° circumferentially to the flank and crotch planes [9,17,18,113], while later cracks appear longitudinally on the WM outer surface around the circumference and longitudinally with the branch axis at the inside surface on the crotch plane, [e.g.17,18]. Typical crack locations in test branched pipe welds are shown in Figures 6.18 and 6.19, along with the cracking history of the weld shown in Figure 6.20.

6.7 Conclusions

The following conclusions can be derived from the work presented in this chapter:

1. Numerous high damage and therefore likely crack initiation sites are predicted in the HAZ weld regions for the typical welded branched pipe geometry analysed using (i) service-aged and (ii) as-new CrMoV weldment material properties at 640°C using CDM and steady-state analyses, these are:

- a. On the crotch plane, at the weld neck in the HAZ^b, on the PM boundary
 - b. On the crotch plane, approximately a third of the width of the wall thickness from the inside surface in the HAZ^p, on the PM boundary
 - c. Circumferentially in the HAZ^b
 - d. Within the WM, in the branch axial direction and also circumferential around the weld at various angles from the flank to crotch plane
2. The CDM and steady-state rupture approaches predicted identical high creep damage sites at multiple locations within the HAZ, WM and PM weld regions.
 3. The predicted steady-state rupture lives for various positions within the as-new weldment were within 18% of the CDM predictions for the same positions, whereas the differences were within 33% for the service-aged weldment. In both cases, the steady-state approach was conservative with respect to the CDM lives, this is expected since the inclusion of the tertiary creep stage is made in the CDM modeling and comparisons of steady-state and CDM approaches for simpler welded components in previous work have made similar conclusions.
 4. Component failure lives based on the steady-state rupture approach were approximately 50% to 60% lower than the CDM component failure lives for the two weldment sets. This level of conservatism is slightly higher than previous comparisons for typical welded plain pipes and cross-weld specimens, which gave steady-state underestimates of about 40% in life.

5. The 'order of rupture' for each location (Positions *A* to *K*) in the branched pipe predicted by both the steady-state and CDM approaches were similar for both weldment material sets.
6. Peak damage/creep crack initiation sites predicted by the steady-state and CDM approaches correspond closely to those of full-scale tests and in-situ experience of similar CrMoV welded branched pipes.

Table 6.1. Values of weld geometrical parameters used

θ ($^{\circ}$)	β ($^{\circ}$)	a (mm)	b (mm)	b_1 (mm)	h (mm)	r_0 (mm)	r_1 (mm)
45	45	2.5	3	3	1.5	6	6

Table 6.2. Material constants for the $\frac{1}{2}\text{Cr}\frac{1}{2}\text{Mo}\frac{1}{4}\text{V}:2\frac{1}{4}\text{CrMo}$ weldment materials at 640°C [134,36].

Material constant	Set 1: Service-aged @ 640°C			Set 2: As-new @ 640°C		
	PM	HAZ	WM	PM	HAZ	WM
A'	6.599×10^{-16}	1.708×10^{-15}	9.718×10^{-15}	3.208×10^{-18}	1.044×10^{-15}	6.459×10^{-17}
n'	6.108	6.108	5.208	7.269	6.108	6.430
m	0	0	0	0	0	0
M	5.998×10^{-14}	2.500×10^{-9}	8.120×10^{-13}	4.823×10^{-12}	9.660×10^{-10}	5.794×10^{-11}
ϕ	4.50	4.30	4.10	4.75	4.30	4.12
α	0.30	0.49	0.26	0.33	0.49	0.42
χ	5.767	3.200	4.849	4.599	3.420	4.015

Note: $[\sigma] = \text{MPa}$; $[t] = \text{h}$, $[\dot{\epsilon}_{\min}^c] = \text{h}^{-1}$.

Table 6.3. Steady-state and CDM failure predictions for Positions A to K for the CrMoV Set 1: Service-Aged weldment at 640° C, CDM component failure life equals 7450 hours.

Location			Steady-State				CDM		$t_{r(ss)}/t_{r(CDM)}$
Label	Material	Coordinate (x,y,z)	σ_{eq}	σ_1	σ_r	$t_{r(ss)}$ (hours) [rupture order]	ω	$t_{r(CDM)}$ (hours) [rupture order]	
A	PM	(-19,128,6)	45.4	42.5	44.5	5179 [9]	0.49	at 7450	N/A
B	WM	(-19,178,1)	49.4	46.6	48.6	8146 [10]	0.24	at 7450	N/A
C	WM	(-4,173,42)	42.0	50.7	44.3	12765 [11]	0.23	at 7450	N/A
D	HAZ ^p	(-30,176,1)	31.9	38.3	35.0	4582 [8]	0.98	7300 [8]	0.63
E	HAZ ^b	(-20,180,1)	36.8	35.0	35.9	4224 [7]	0.98	7280 [7]	0.58
F	HAZ ^b	(-30,189,1)	29.8	51.2	40.3	2949 [1]	0.98	4650 [1]	0.63
G	HAZ ^p	(-1, 171,40)	29.5	52.4	39.6	3086 [3]	0.98	5180 [3]	0.60
H	HAZ ^b	(-1,186,30)	29.6	46.8	37.7	3612 [5]	0.98	5860 [5]	0.62
I	HAZ ^p	(-30,175,28)	31.5	41.5	36.4	4041 [6]	0.98	7220 [6]	0.56
J	HAZ ^b	(-22,186,20)	29.1	47.1	37.9	3552 [4]	0.98	5690 [4]	0.64
K	HAZ ^p	(-20,172,36)	30.6	50.0	40.1	3001 [2]	0.98	4710 [2]	0.64

Note: [σ] = MPa, Origin of x-y-z axis is the intersection of the branch and main pipe axis

Table 6.4. Steady-state and CDM failure predictions for Positions A to K for the Set 2: CrMoV As-New weldment at 640° C, CDM component failure life is 10400 hours.

Location			Steady-State				CDM		
Label	Material	Coordinate (x,y,z)	σ_{eq}	σ_1	σ_r	$t_{r(ss)}$ (hours) [rupture order]	ω	$t_{r(CDM)}$ (hours) [rupture order]	$t_{r(ss)}/t_{r(CDM)}$
A	PM	(-19,128,6)	43.7	42.1	42.9	6445 [2]	0.98	10200 [6]	0.63
B	WM	(-19,178,1)	43.3	34.9	39.8	6504 [3]	0.62	at 10400	N/A
C	WM	(-25,174,34)	38.0	46.0	39.7	6570 [6]	0.62	at 10400	N/A
D	HAZ ^p	(-26,176,1)	30.7	34.8	32.7	6844 [8]	0.98	10000 [5]	0.68
E	HAZ ^b	(-21,181,13)	37.9	25.7	31.9	7445 [11]	0.56	at 10400	N/A
F	HAZ ^b	(-30,189,1)	28.2	45.0	35.0	5118 [1]	0.98	6210 [1]	0.82
G	HAZ ^p	(-1, 171,40)	27.1	37.5	32.2	7214 [9]	0.66	at 10400	N/A
H	HAZ ^b	(-1,186,30)	27.0	38.6	32.7	6843 [7]	0.98	9160 [4]	0.75
I	HAZ ^p	(-30,175,28)	28.5	35.6	32.0	7369 [10]	0.58	at 10400	N/A
J	HAZ ^b	(-22,186,20)	26.7	39.7	33.1	6565 [5]	0.98	8680 [3]	0.76
K	HAZ ^p	(-20,172,36)	27.7	38.8	33.1	6560 [4]	0.98	8570 [2]	0.77

Note: [σ] = MPa, Origin of x-y-z axis is the intersection of the branch and main pipe axis

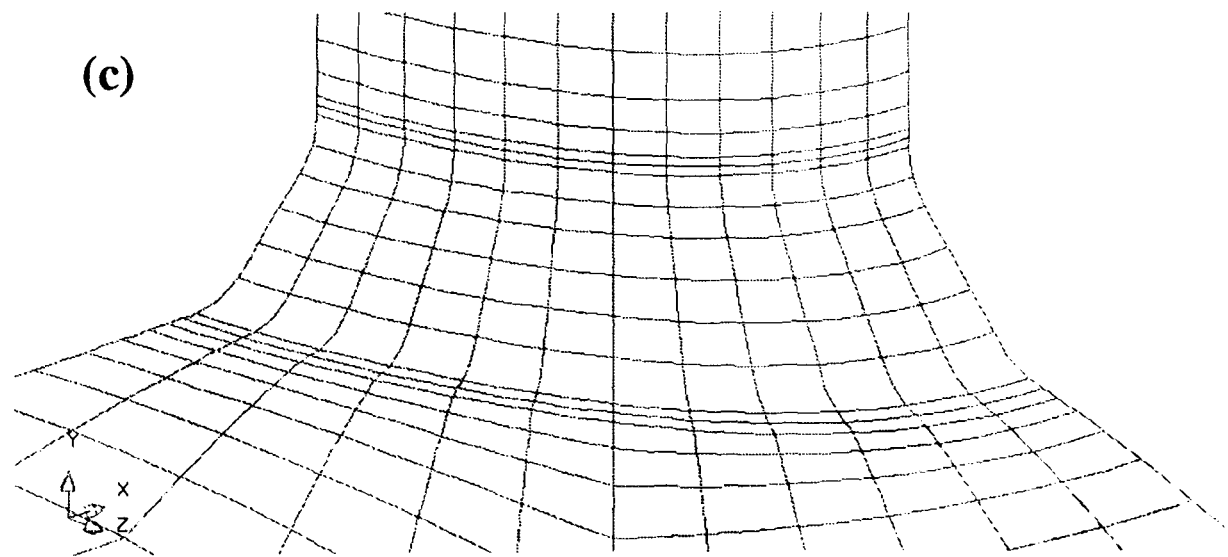
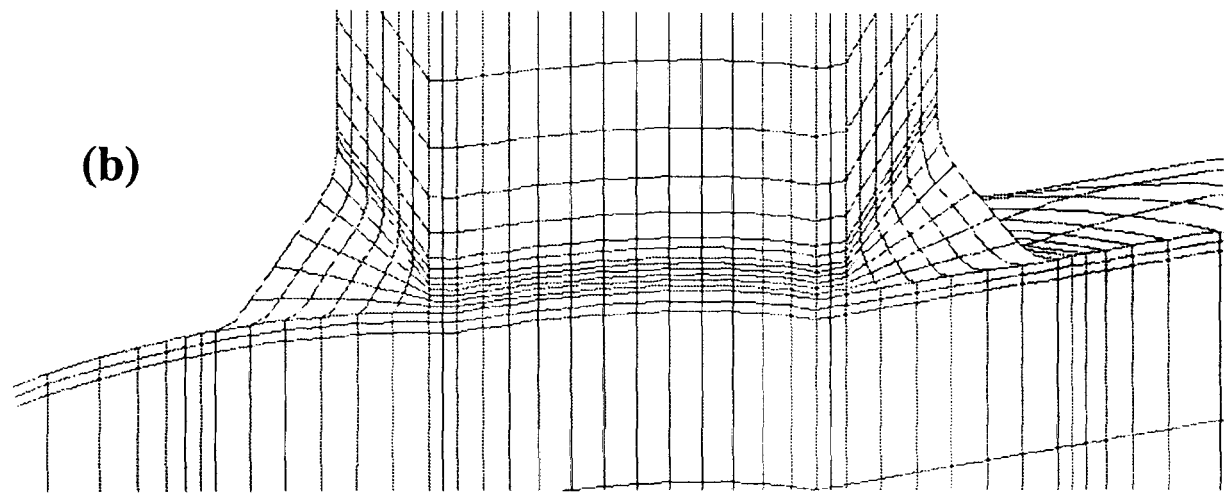
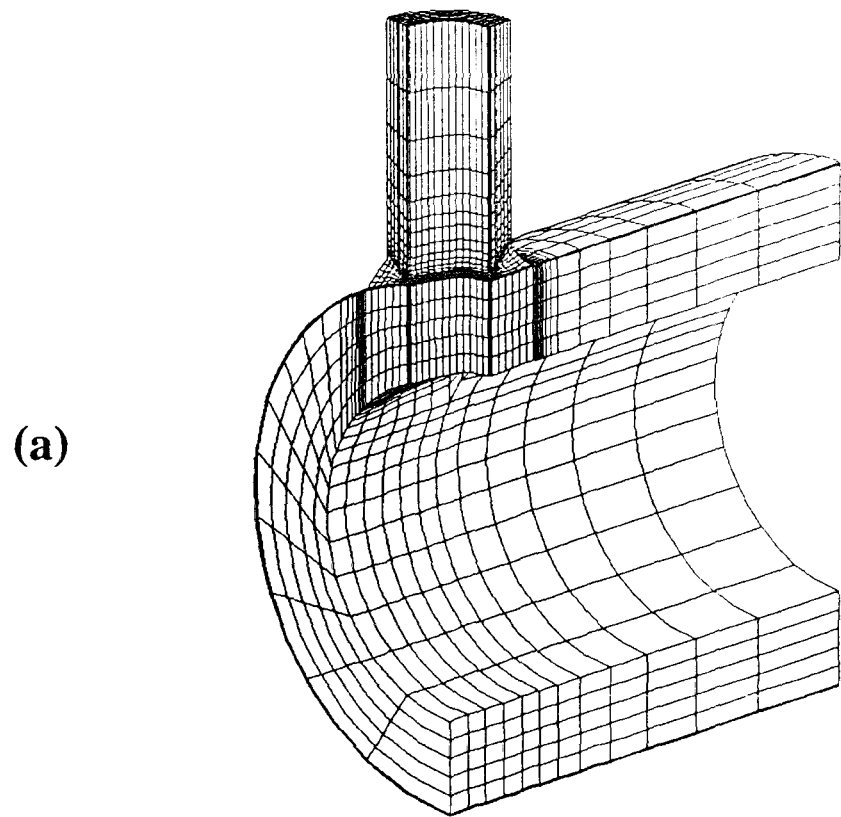


Figure 6.1. (a) FE model of a main pipe with an isolated branch; (b) zoom-in view of the inside weldment surface and (c) zoomed in-view of the outside weldment surface.

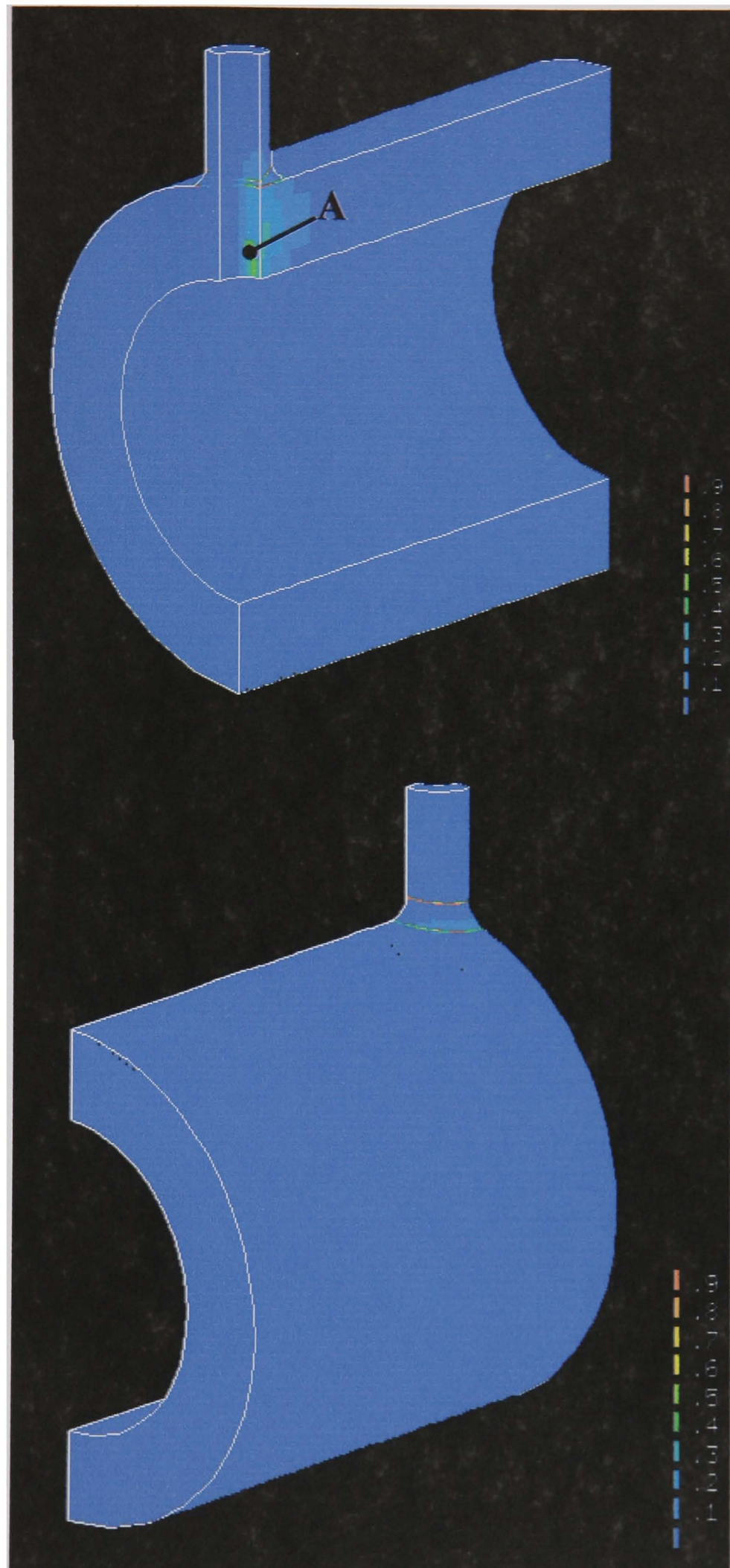


Figure 6.2. Inside and outside surface damage contour plots of the whole component for the Set 1: Service-aged material, at the failure life of 7450 hours.

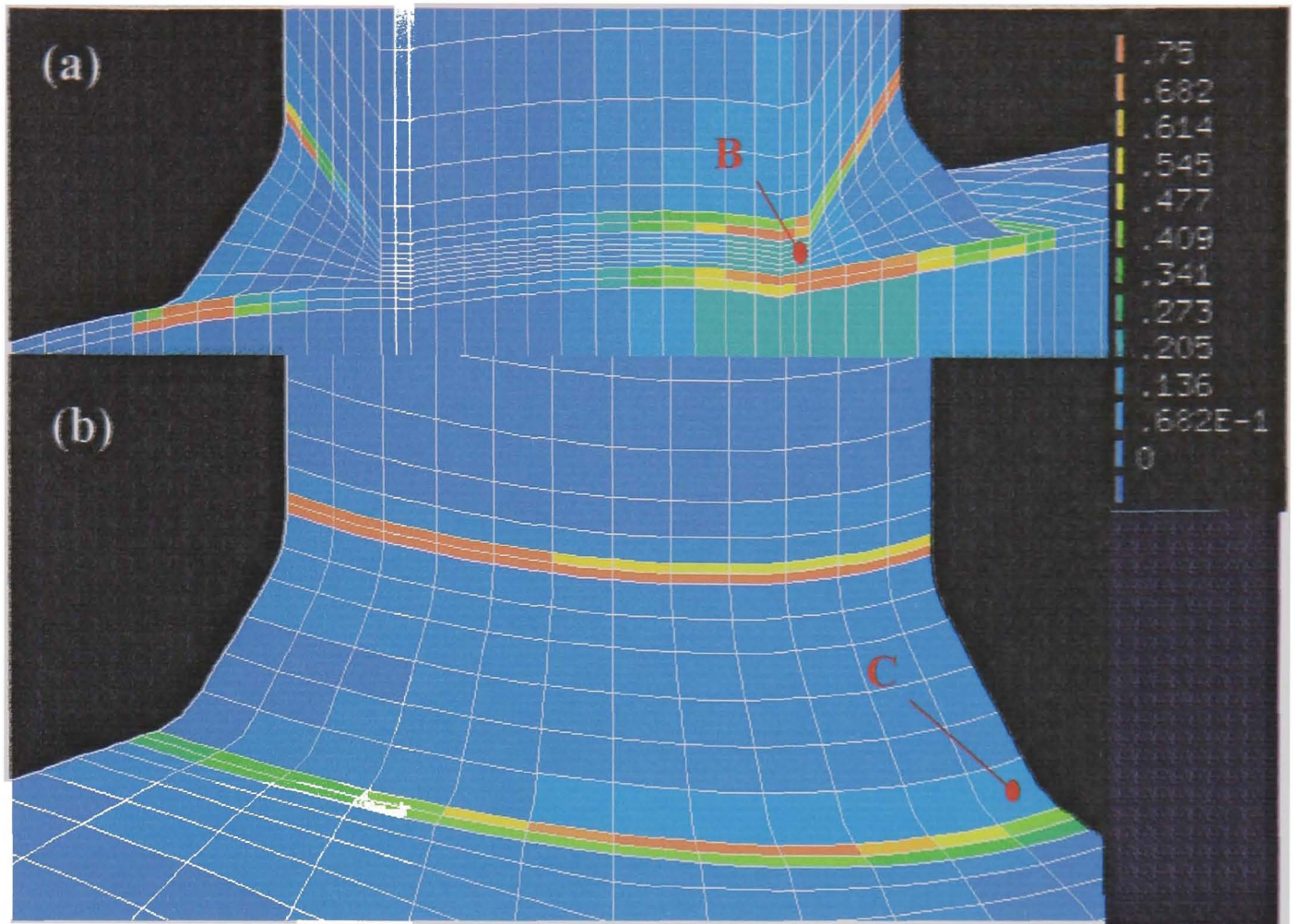


Figure 6.3. (a) Inside and (b) Outside surface damage contour plots of the weld region for the Set 1: Service-aged material at the failure life of 7450 hours.

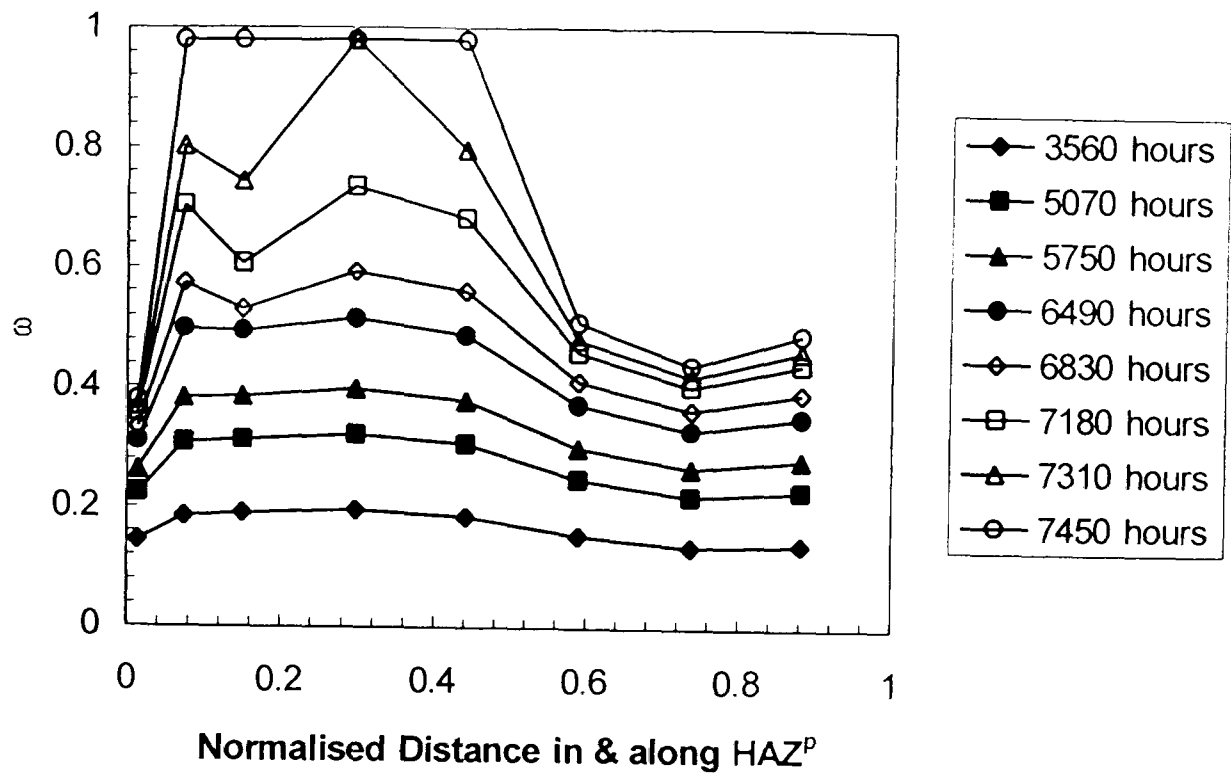


Figure 6.4. Damage evolution in the HAZ^P across the wall thickness on the crotch plane, from the inner to outer surface, along the HAZ^P/PM^P boundary for the Set 1: Service-aged weldment.

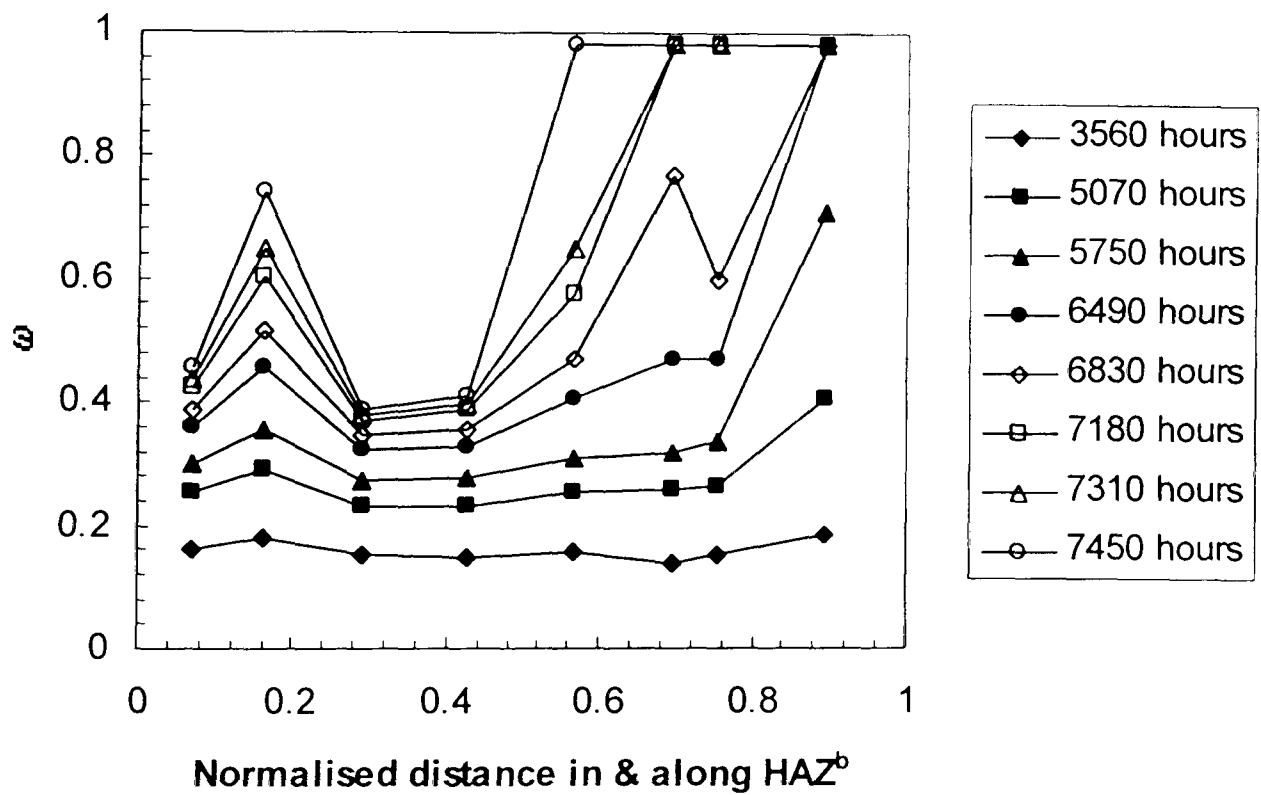
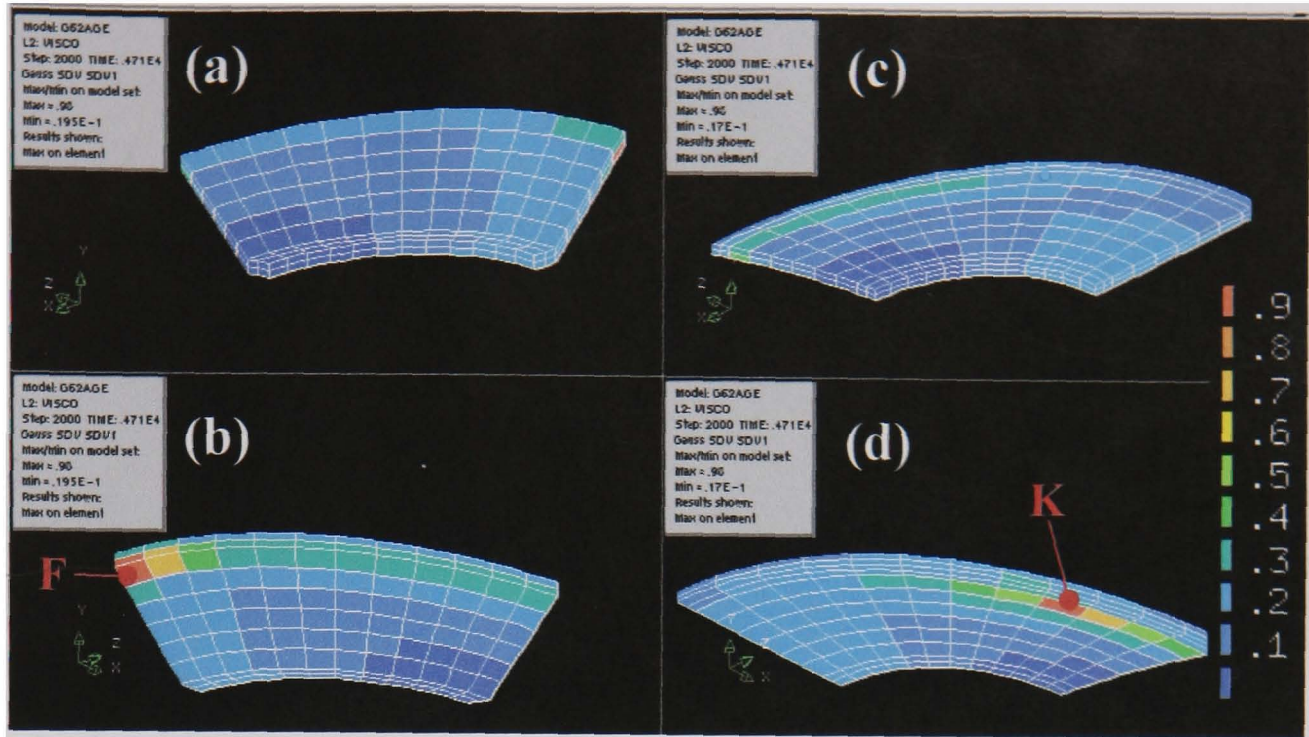
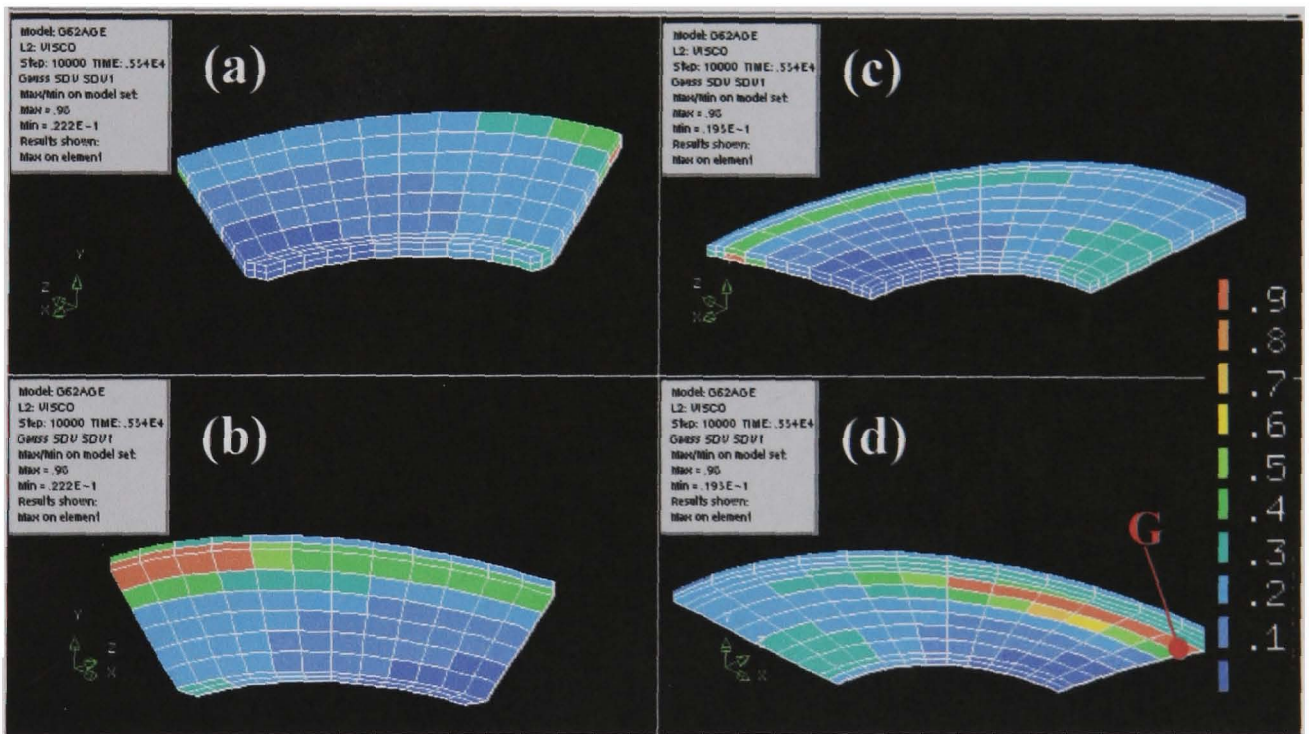


Figure 6.5. Damage evolution in the HAZ^b across the wall thickness on the crotch plane, from the inner to outer surface, along the HAZ^b/PM^b boundary for the Set 1: Service-aged weldment.

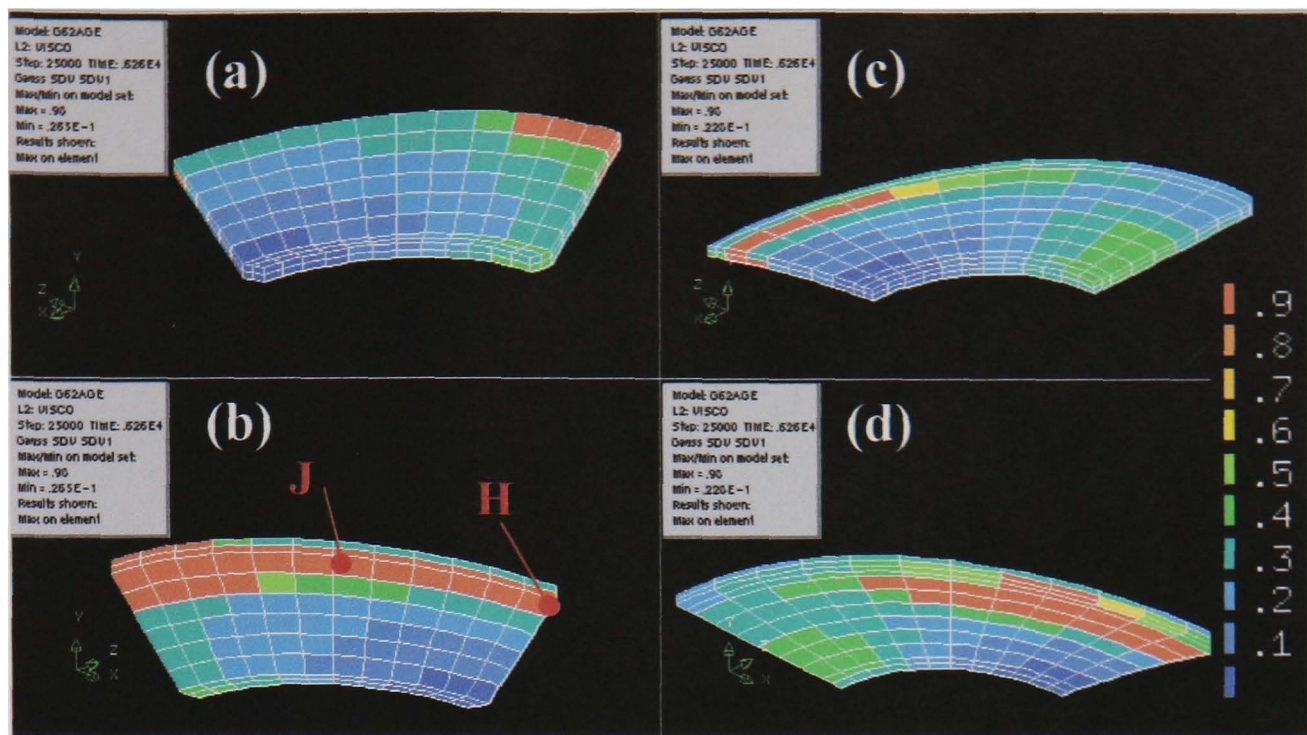


4710 hours

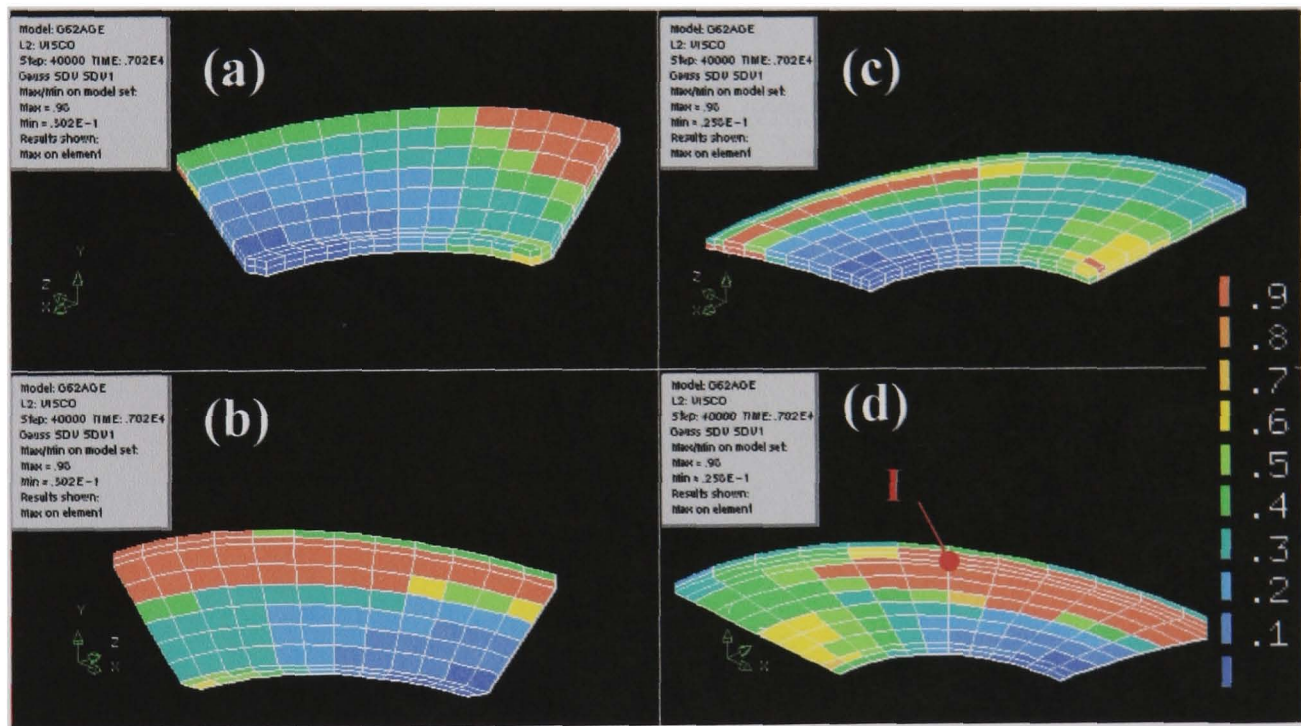


5430 hours

Figure 6.6. Damage evolution plots of the HAZ^b region (a) inner HAZ^b/PM^b surface view and (b) outer HAZ^b/WM surface view, and the HAZ^p region (c) inner HAZ^p/WM surface view and (d) outer HAZ^p/PM^p surface view for the Set 1: Service-aged branched pipe at various times. The failure locations of HAZ Positions D to K are identified.

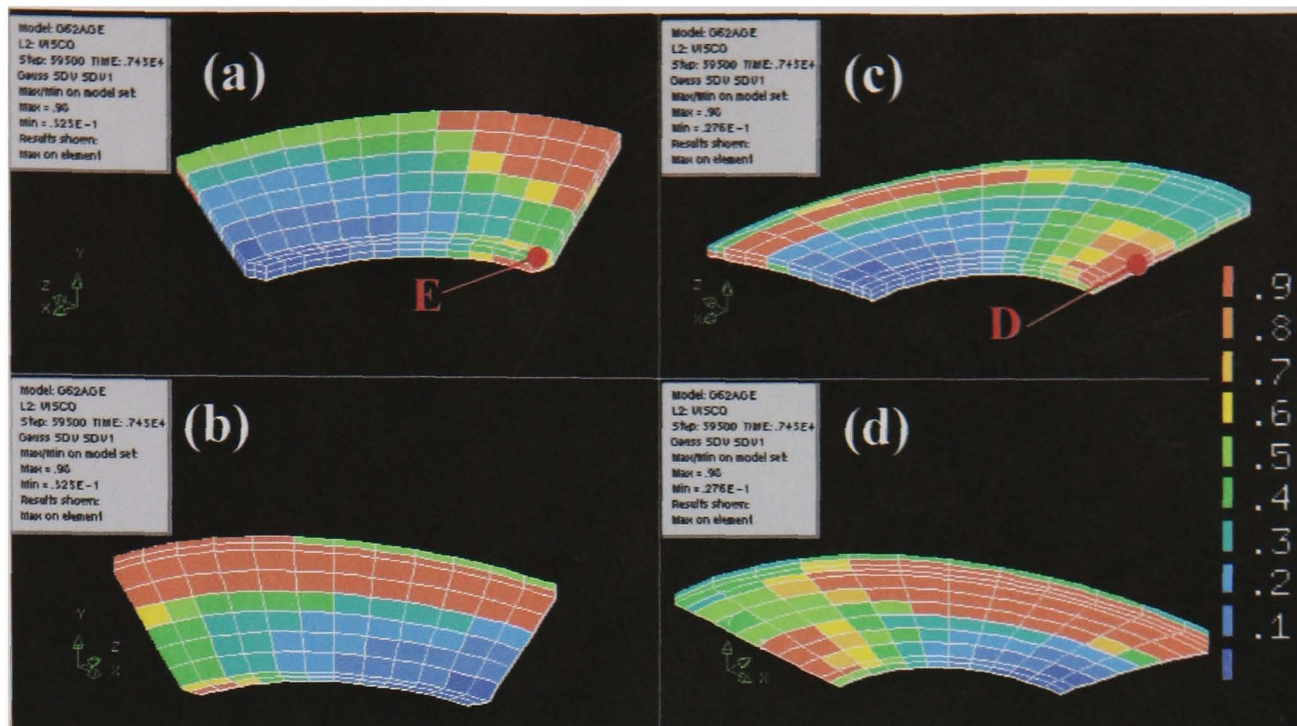


6260 hours



7020 hours

Figure 6.6 (continued). Damage evolution plots of the HAZ^b region (a) inner HAZ^b/PM^b surface view and (b) outer HAZ^b/WM surface view, and the HAZ^P region (c) inner HAZ^P/WM surface view and (d) outer HAZ^P/PM^P surface view for the Set 1: Service-aged branched pipe at various times. The failure locations of HAZ Positions D to K are identified.



7450 hours (component failure time)

Figure 6.6 (continued). Damage evolution plots of the HAZ^b region (a) inner HAZ^b/PM^b surface view and (b) outer HAZ^b/WM surface view, and the HAZ^p region (c) inner HAZ^p/WM surface view and (d) outer HAZ^p/PM^p surface view for the Set 1: Service-aged branched pipe at various times. The failure locations of HAZ Positions D to K are identified.

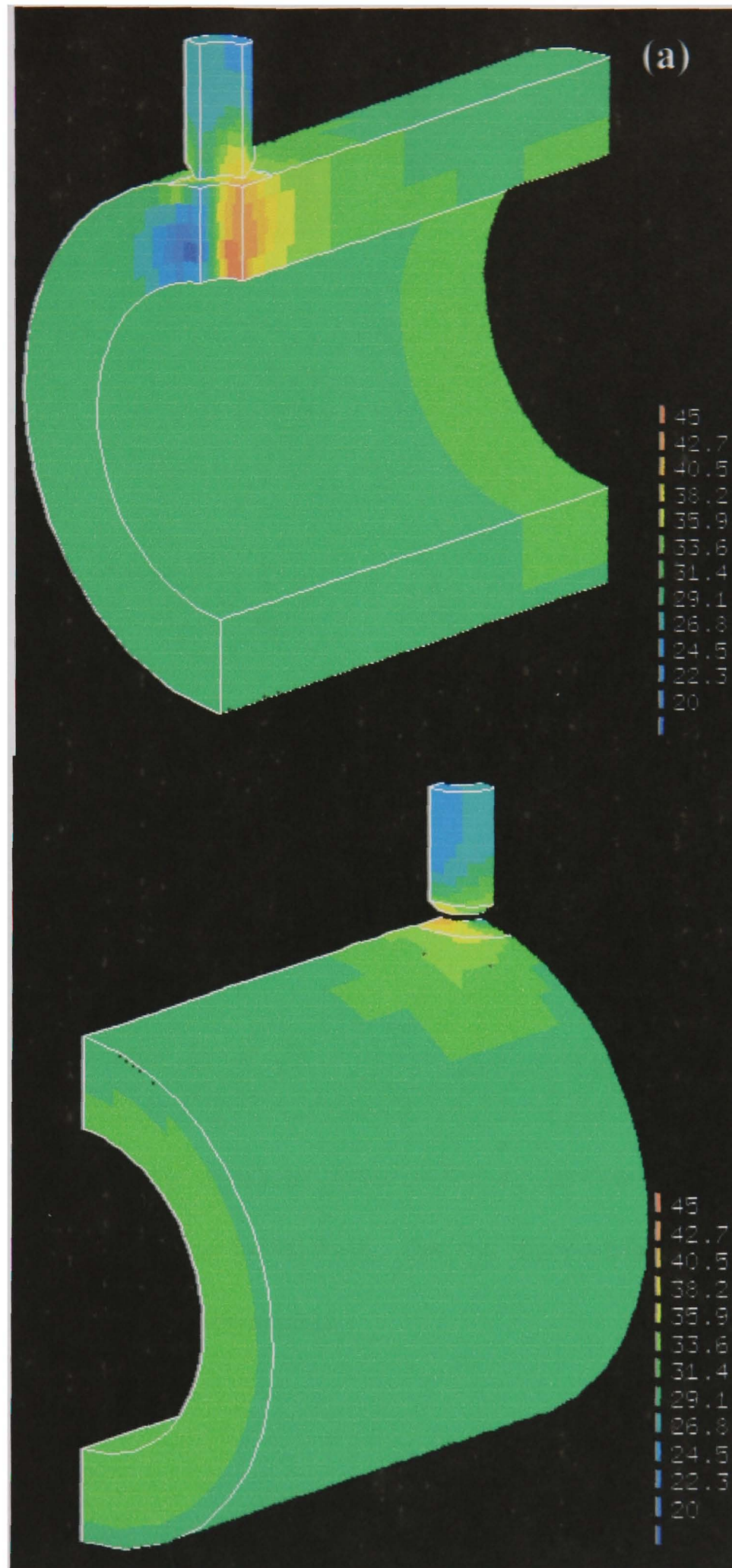


Figure 6.7. (a) Contour plots of Set 1: Service-aged material PM steady-state rupture stress ($\alpha=0.3$) on the inner and outer surfaces.

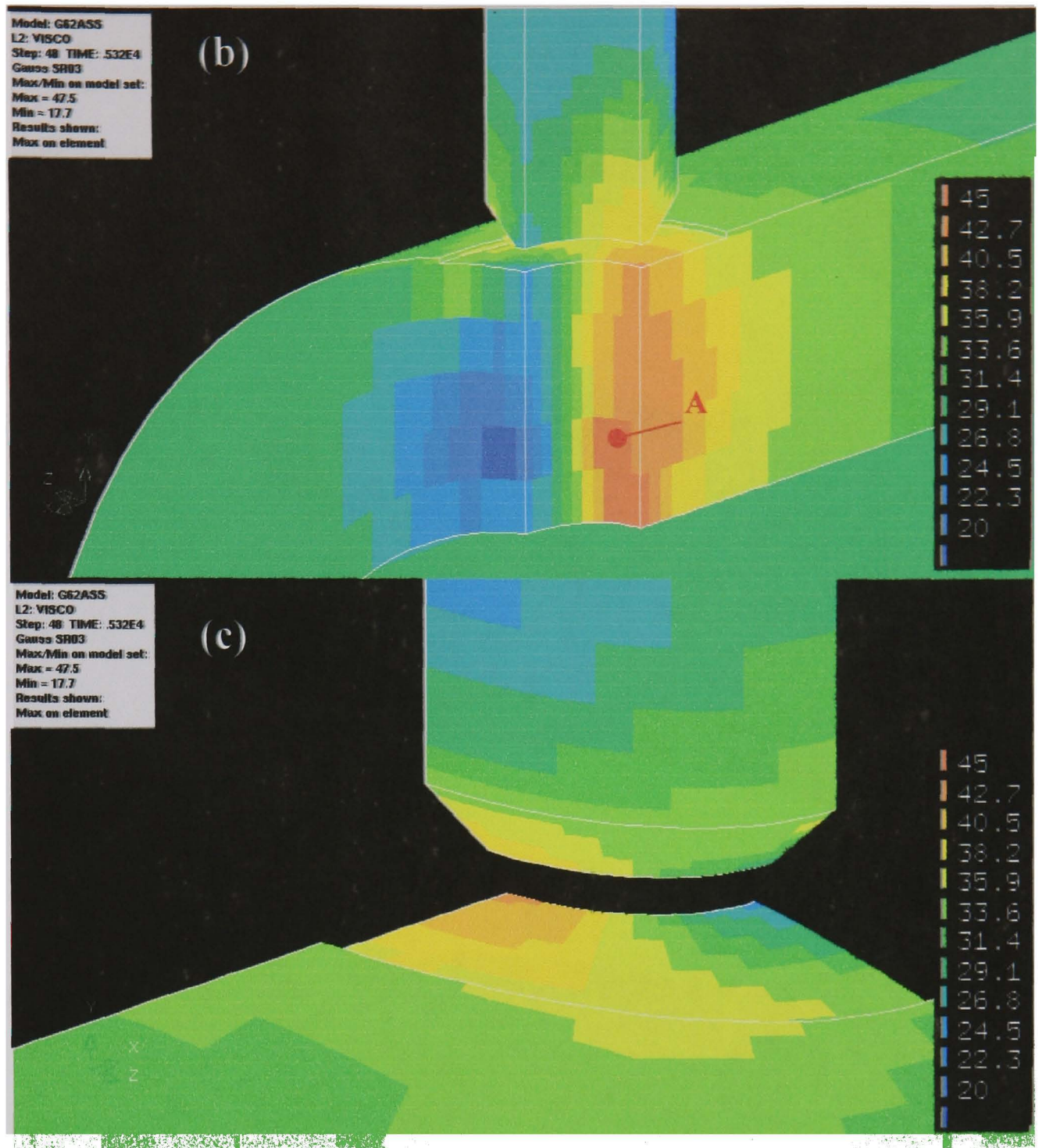


Figure 6.7 (continued). Contour plots of Set 1: Service-aged material PM steady-state rupture stress ($\alpha=0.3$) on the (b) inner-surface and (c) outer-surface weldment connection region.

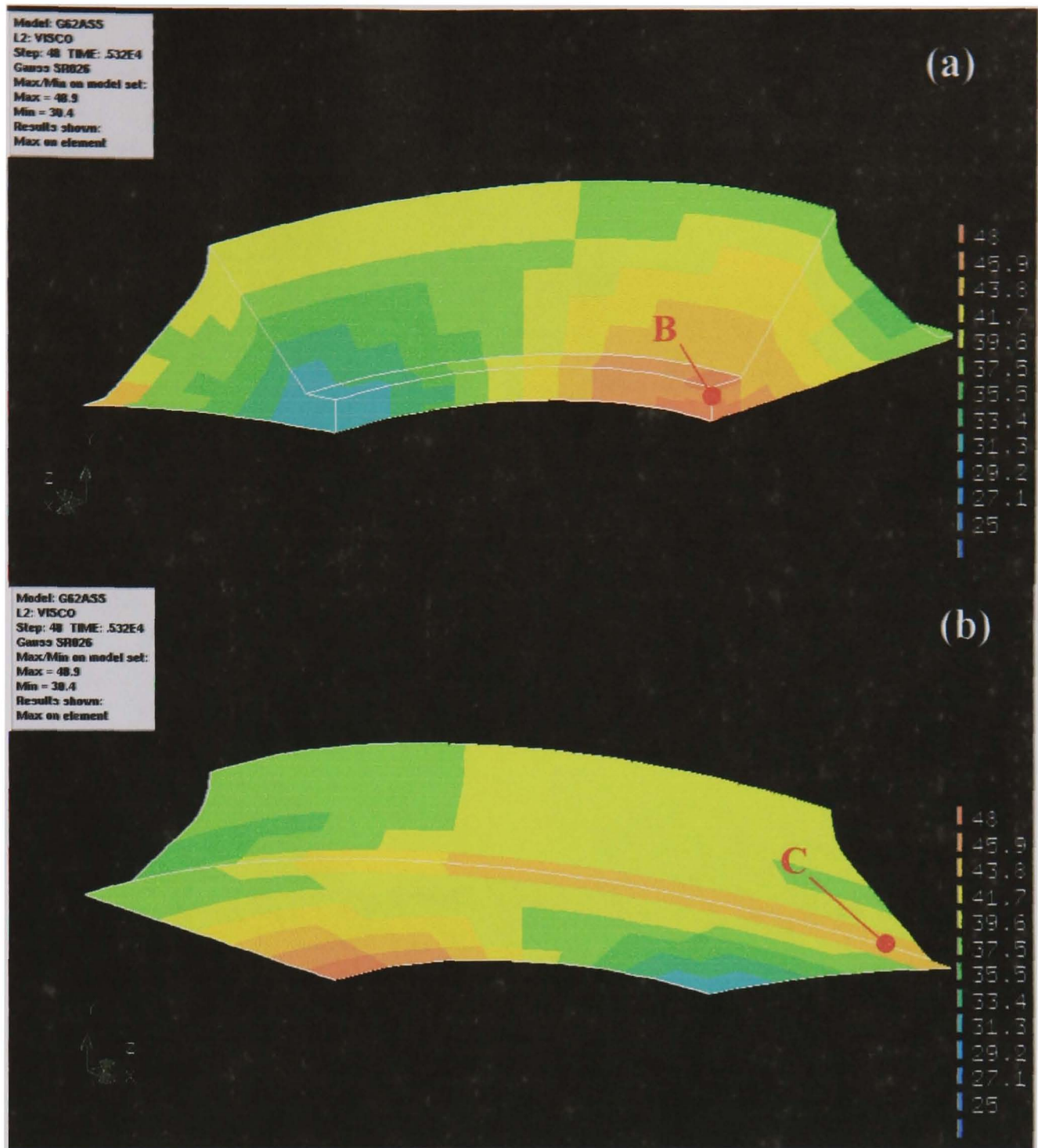


Figure 6.8. Contour plots of Set 1: Service-aged material WM steady-state rupture stress ($\alpha=0.26$) on the (a) the inner-top surface and (b) the outer-bottom surface.

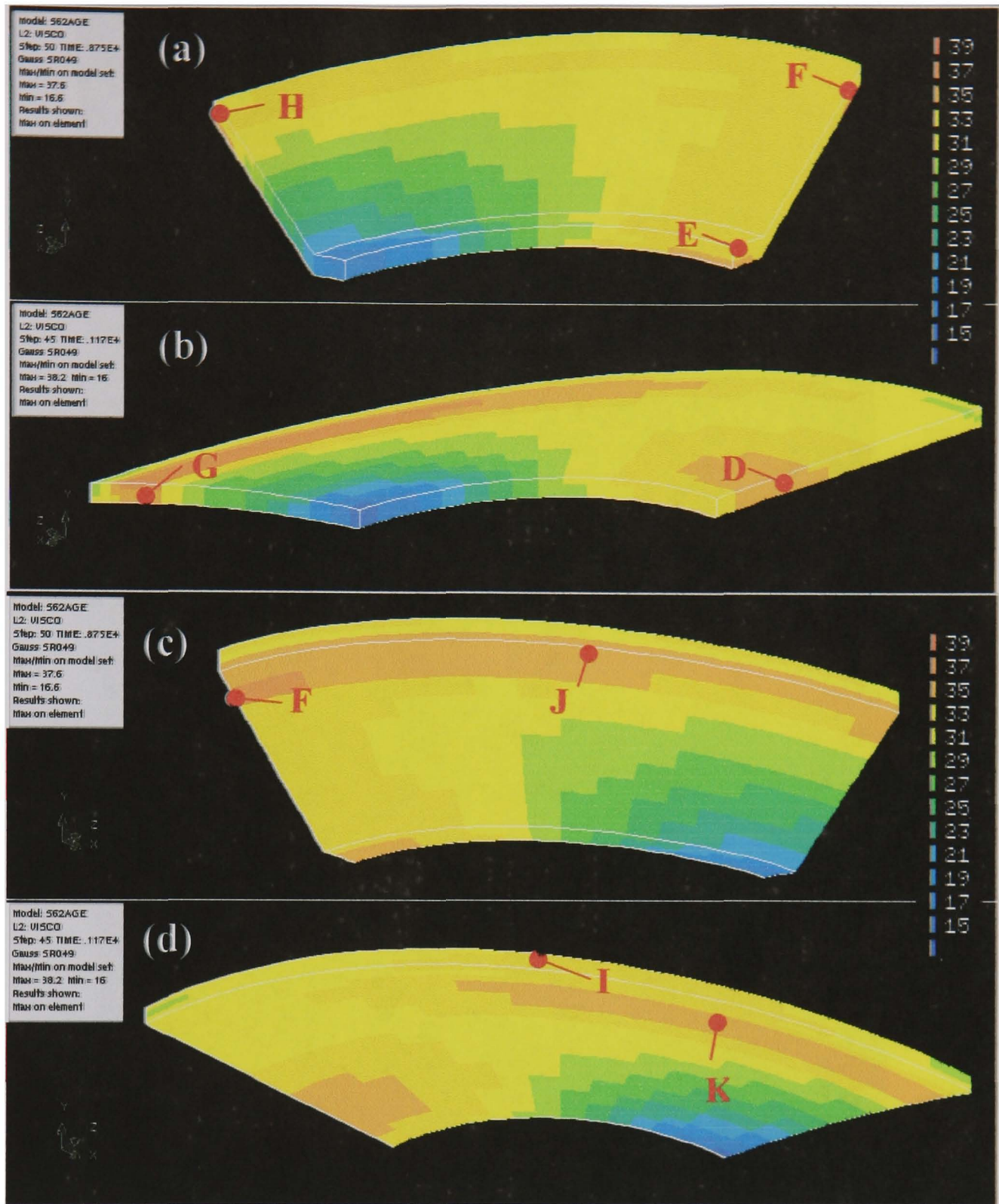


Figure 6.9. Steady-state rupture stress plots ($\alpha=0.49$) of the Set 1: Service-aged material connection, views of (a) the HAZ^b inner-top surface region, (b) the HAZ^P inner-top surface region, (c) the HAZ^b outer-bottom surface region and (d) the HAZ^P outer-bottom surface region.

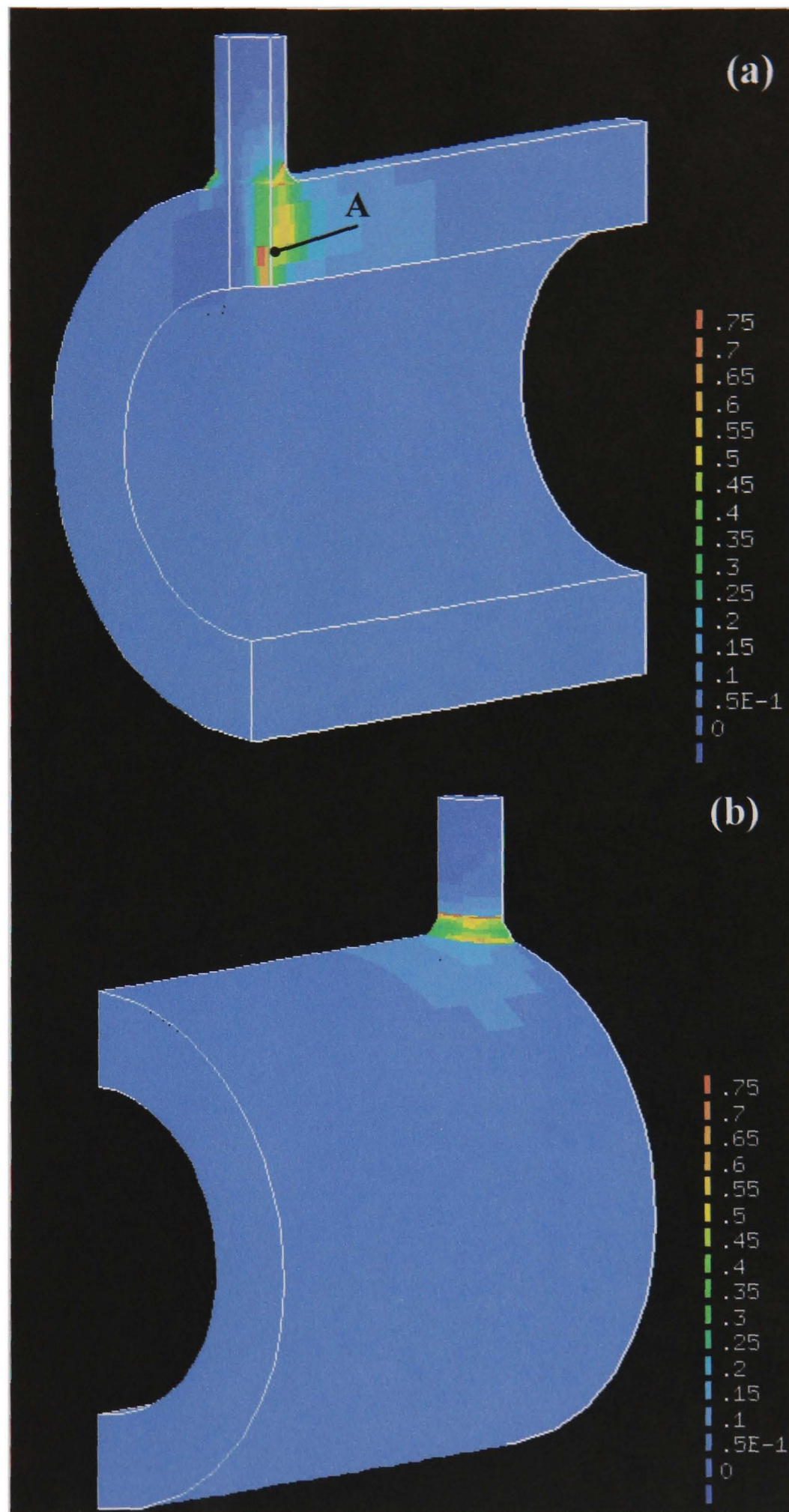


Figure 6.10. (a) Inside and (b) outside surface damage contour plots of the whole component for the Set 2: As-new material, at the failure life of 10400 hours.

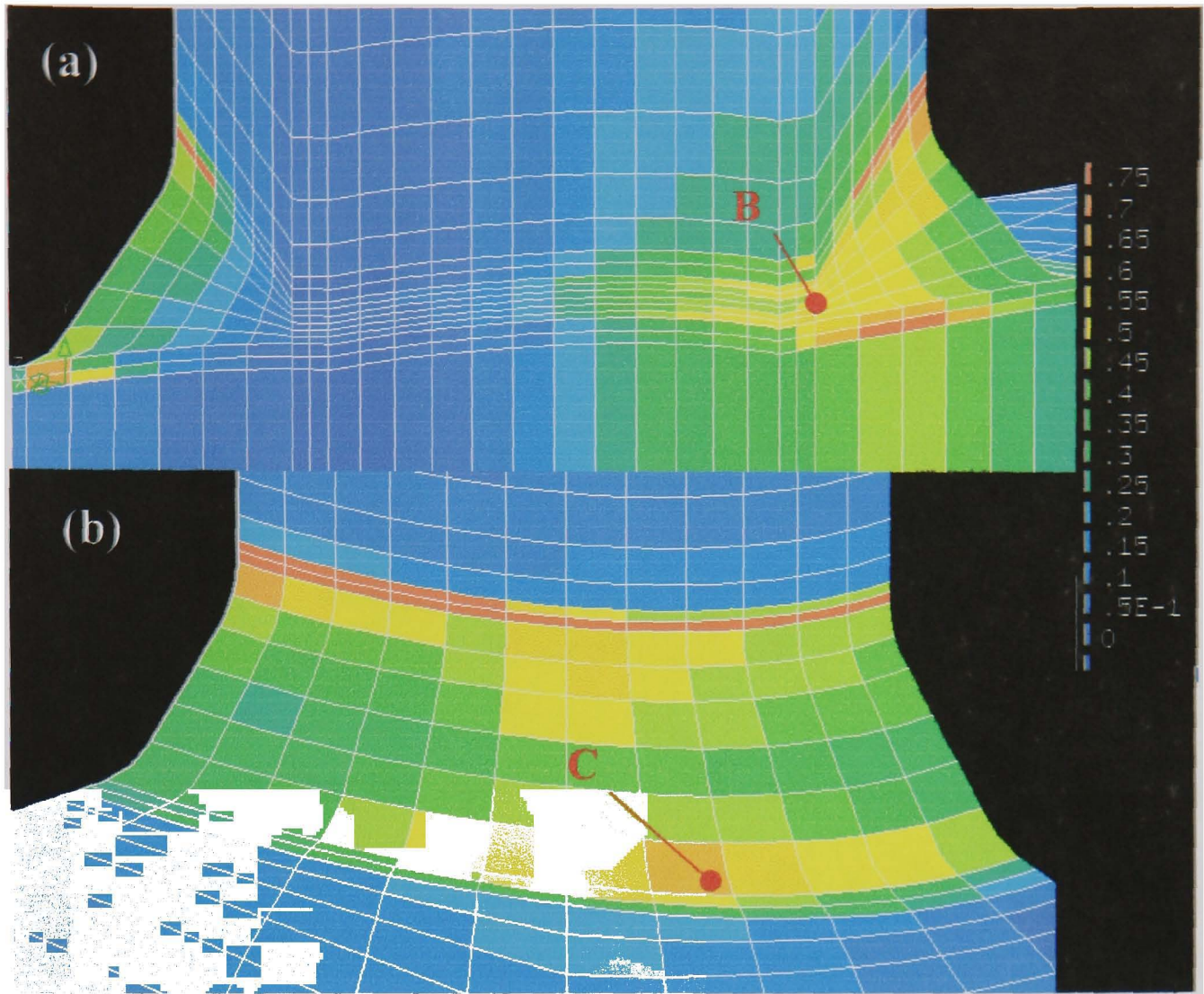


Figure 6.11. (a) Inside and (b) outside surface damage contour plots of the weld region for the Set 2: As-new material at the failure life of 10400 hours.

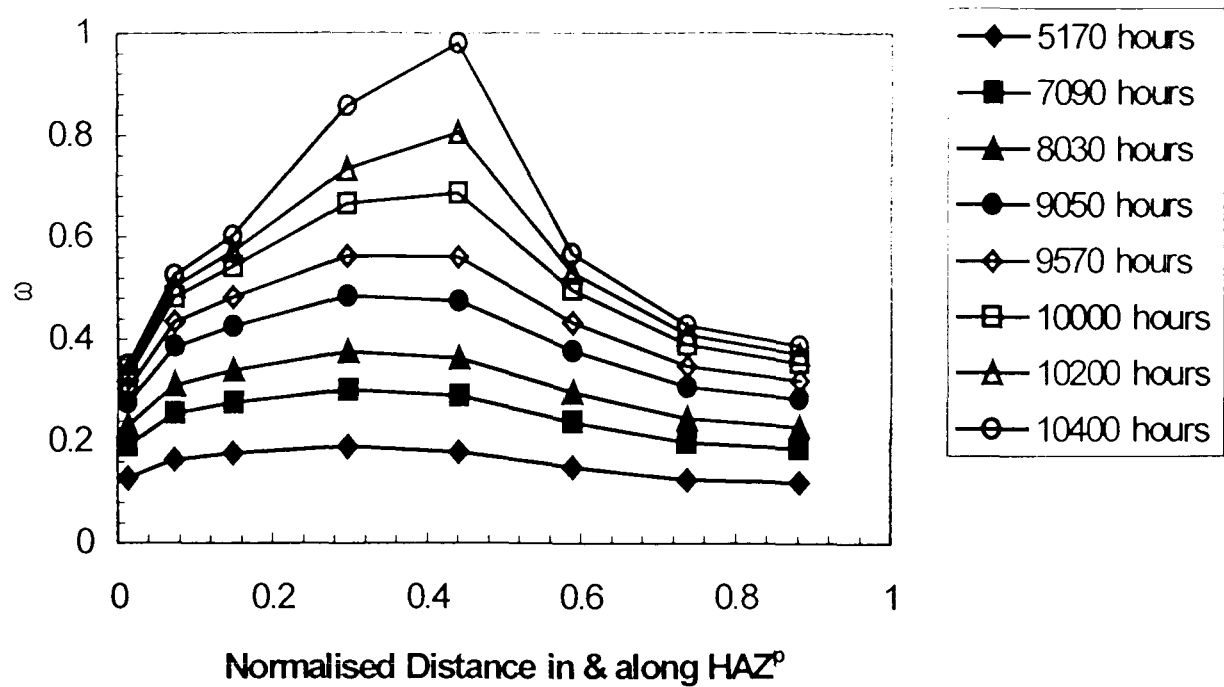


Figure 6.12. Damage evolution in the HAZ^p across the wall thickness on the crotch plane, from the inner to outer surface, along the HAZ^p/PM^p boundary for the Set 2: As-new weldment.

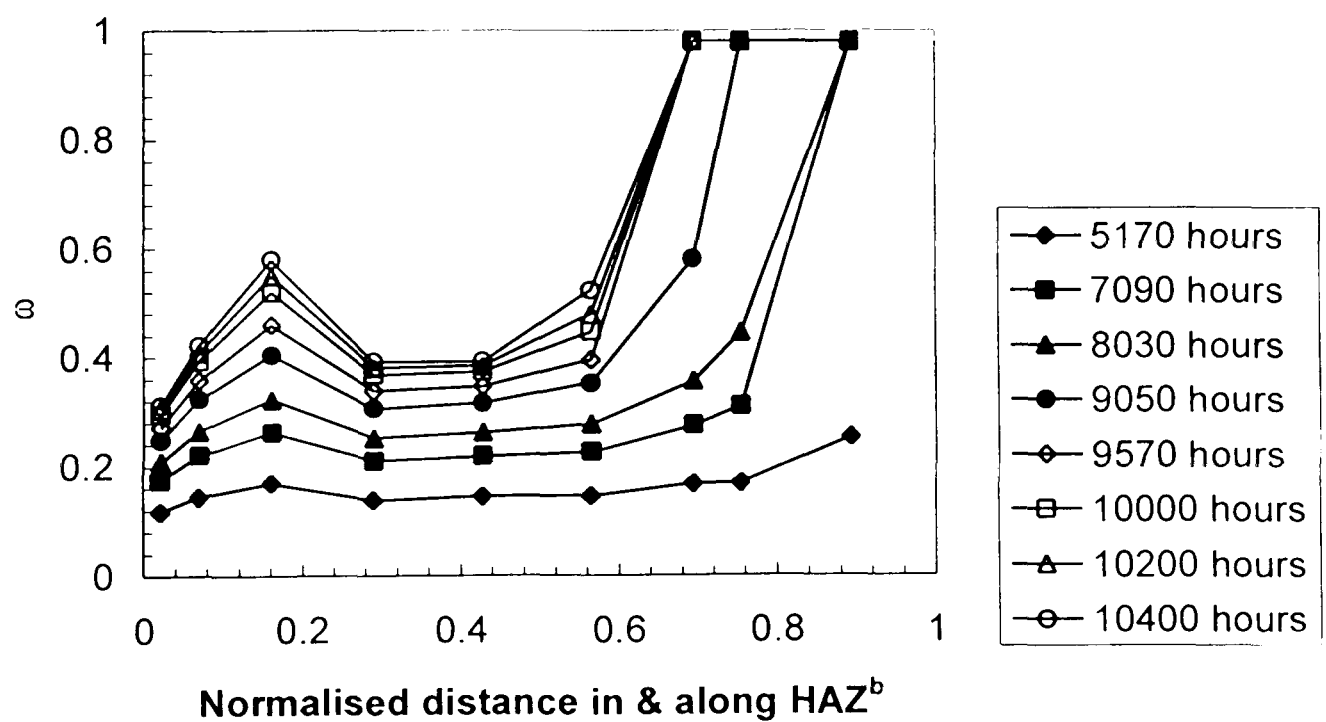
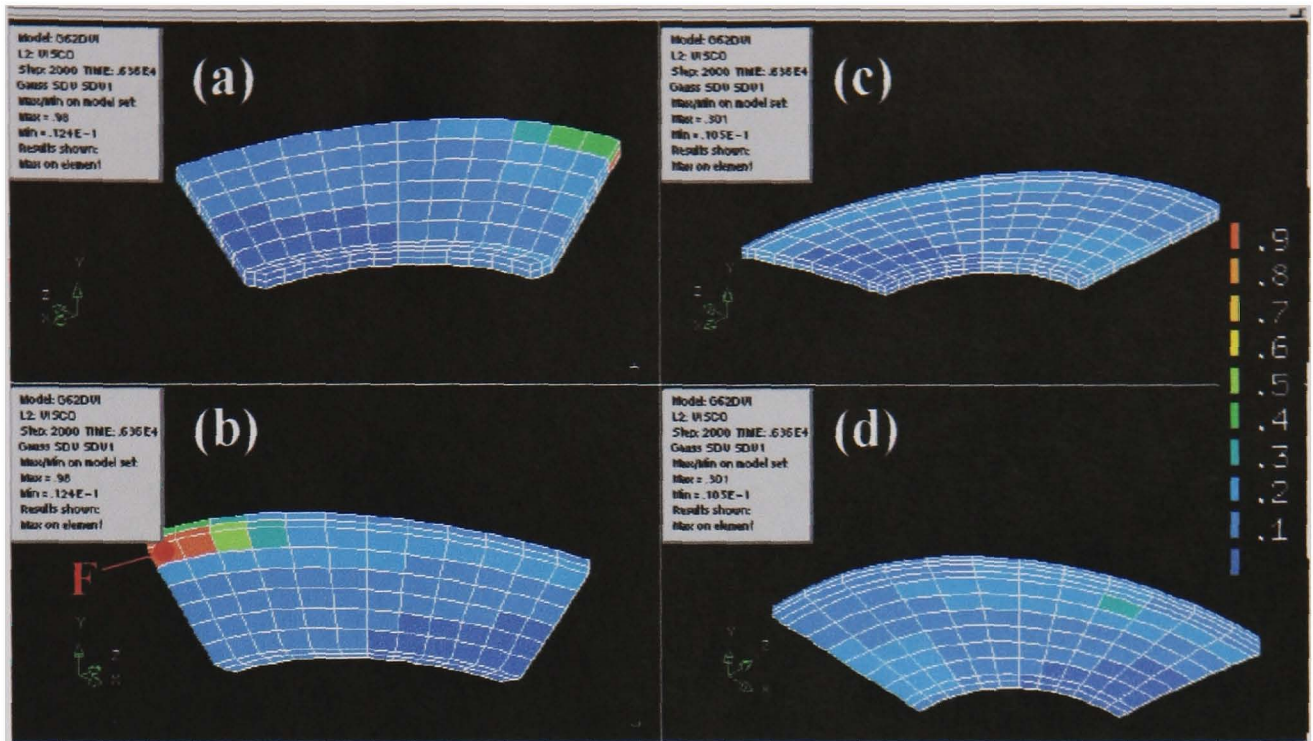
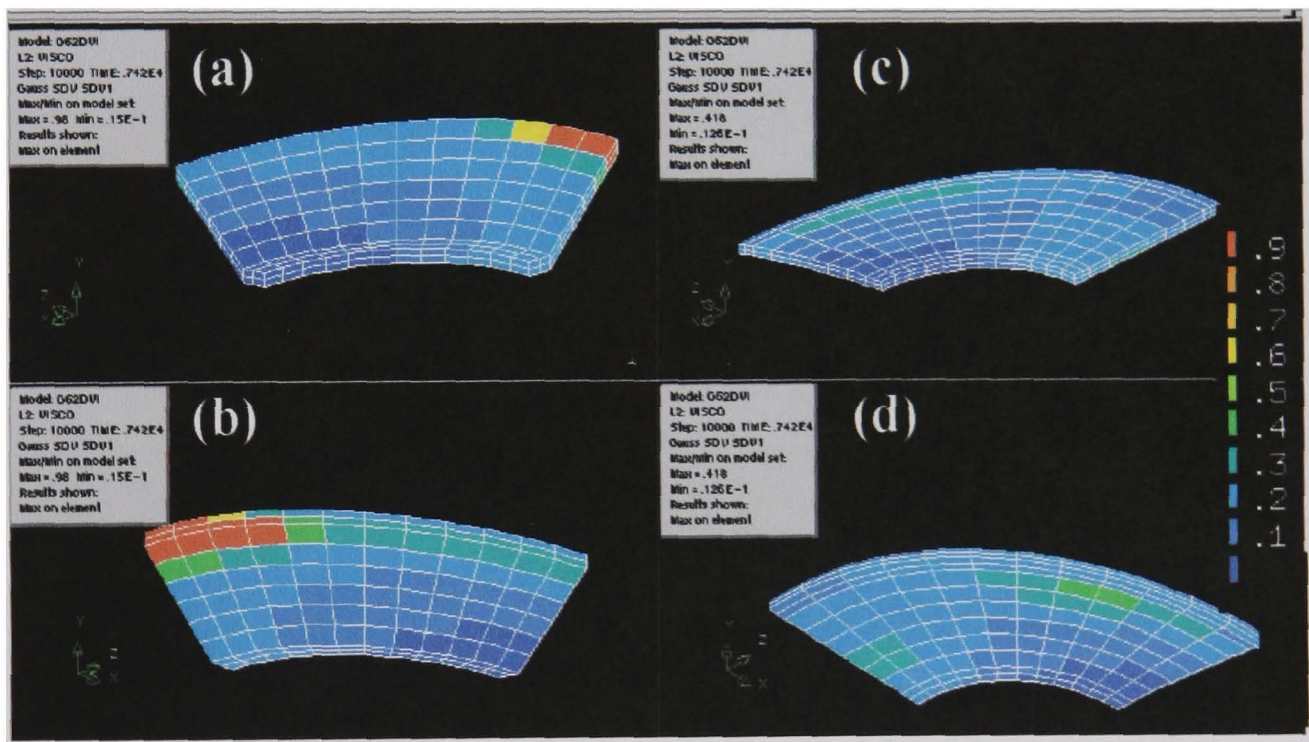


Figure 6.13. Damage evolution in the HAZ^b across the wall thickness on the crotch plane, from the inner to outer surface, along the HAZ^b/PM^b boundary for the Set 2: As-new weldment.

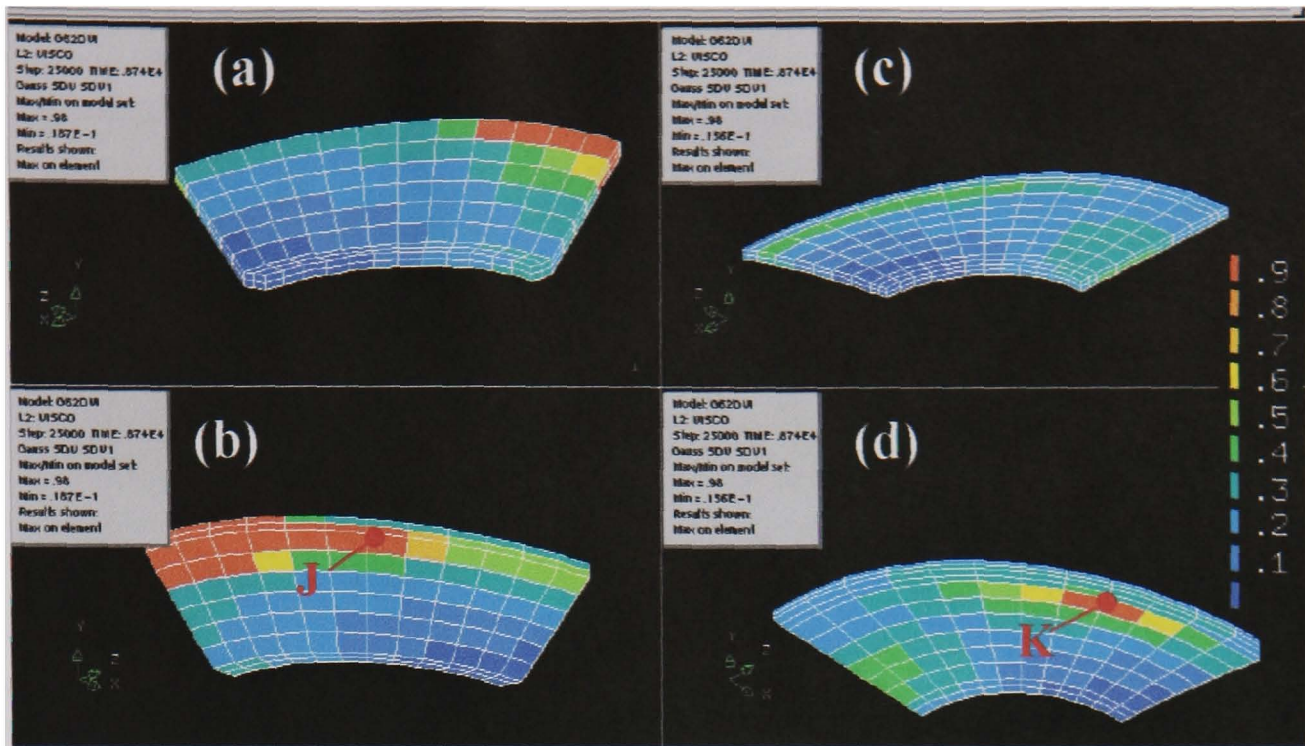


6360 hours

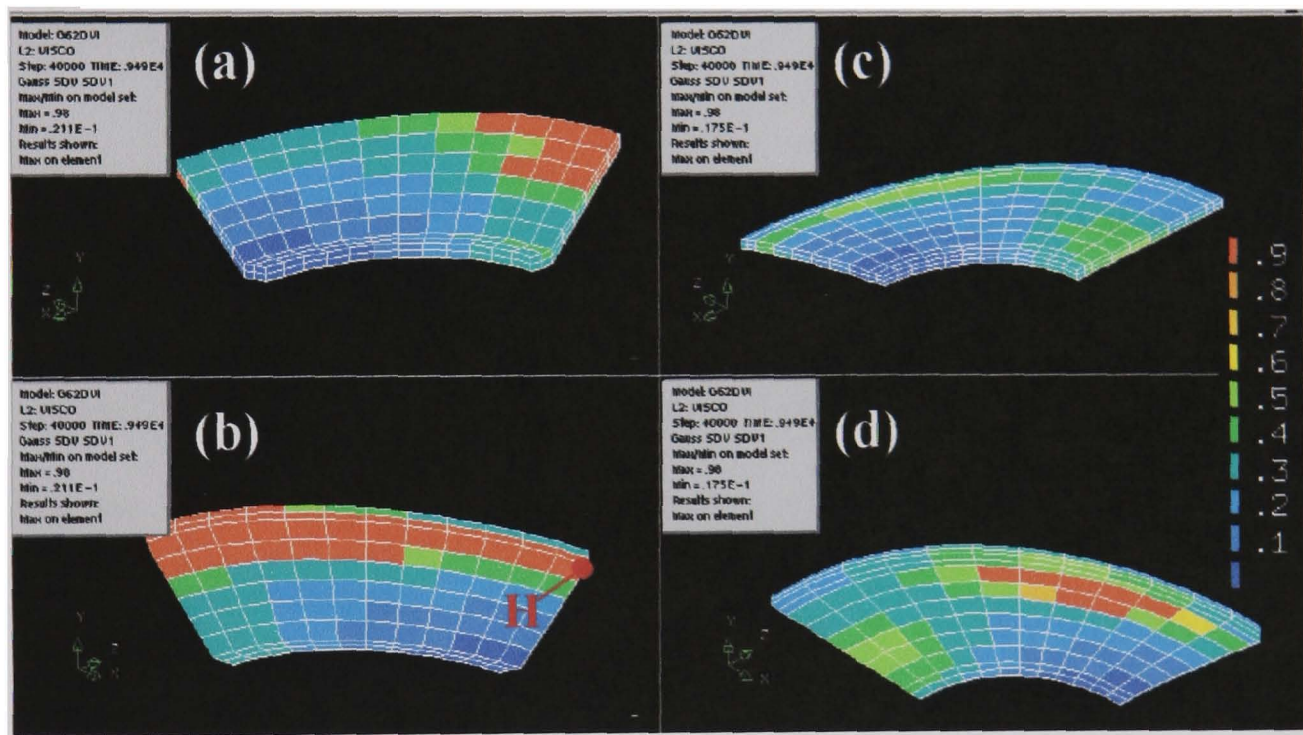


7420 hours

Figure 6.14. Damage evolution plots of the HAZ^b region (a) inner HAZ^b/PM^b surface view and (b) outer HAZ^b/WM surface view, and the HAZ^p region (c) inner HAZ^p/WM surface view and (d) outer HAZ^p/PM^p surface view for the Set 1: Service-aged branched pipe at various times. The failure locations of HAZ Positions D to K are identified.

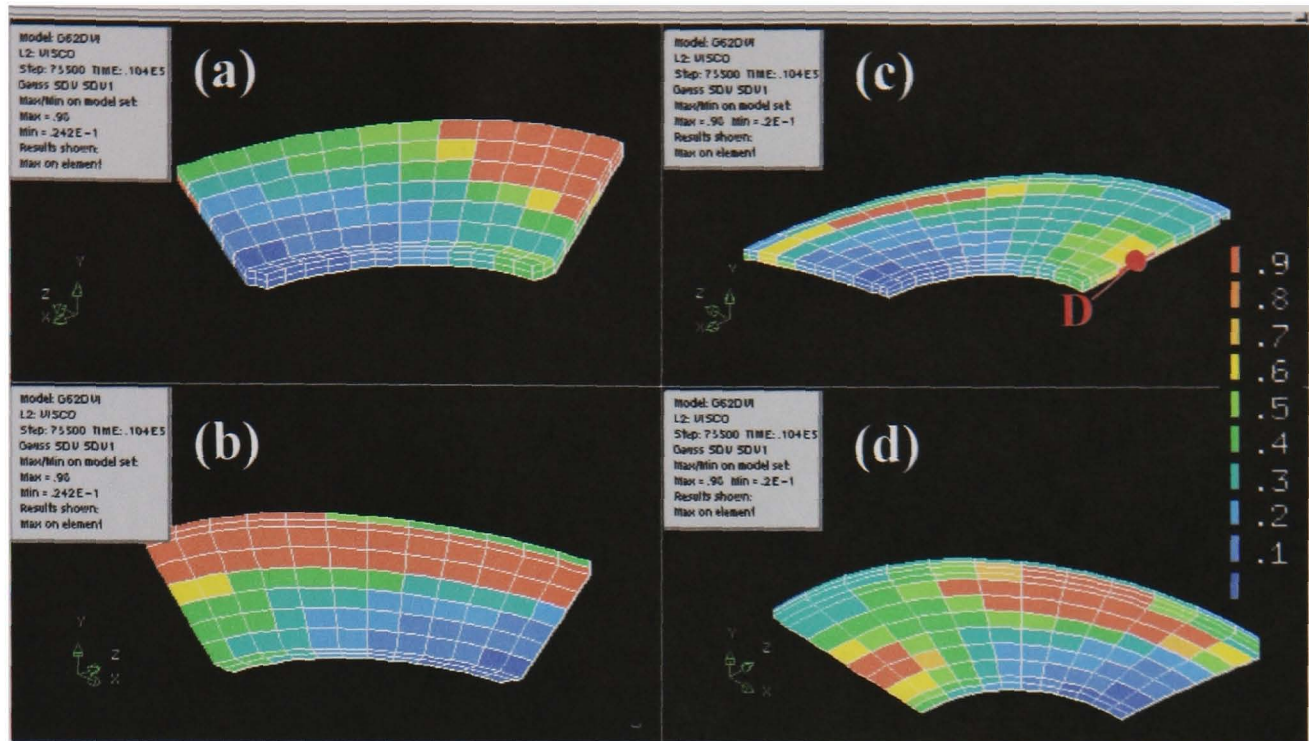


8740 hours



9490 hours

Figure 6.14 (continued). Damage evolution plots of the HAZ^b region (a) inner HAZ^b/PM^b surface view and (b) outer HAZ^b/WM surface view, and the HAZ^P region (c) inner HAZ^P/WM surface view and (d) outer HAZ^P/PM^P surface view for the Set 1: Service-aged branched pipe at various times. The failure locations of HAZ Positions D to K are identified.



10400 hours (component failure time)

Figure 6.14 (continued). Damage evolution plots of the HAZ^b region (a) inner HAZ^b/PM^b surface view and (b) outer HAZ^b/WM surface view, and the HAZ^p region (c) inner HAZ^p/WM surface view and (d) outer HAZ^p/PM^p surface view for the Set 1: Service-aged branched pipe at various times. The failure locations of HAZ Positions D to K are identified.

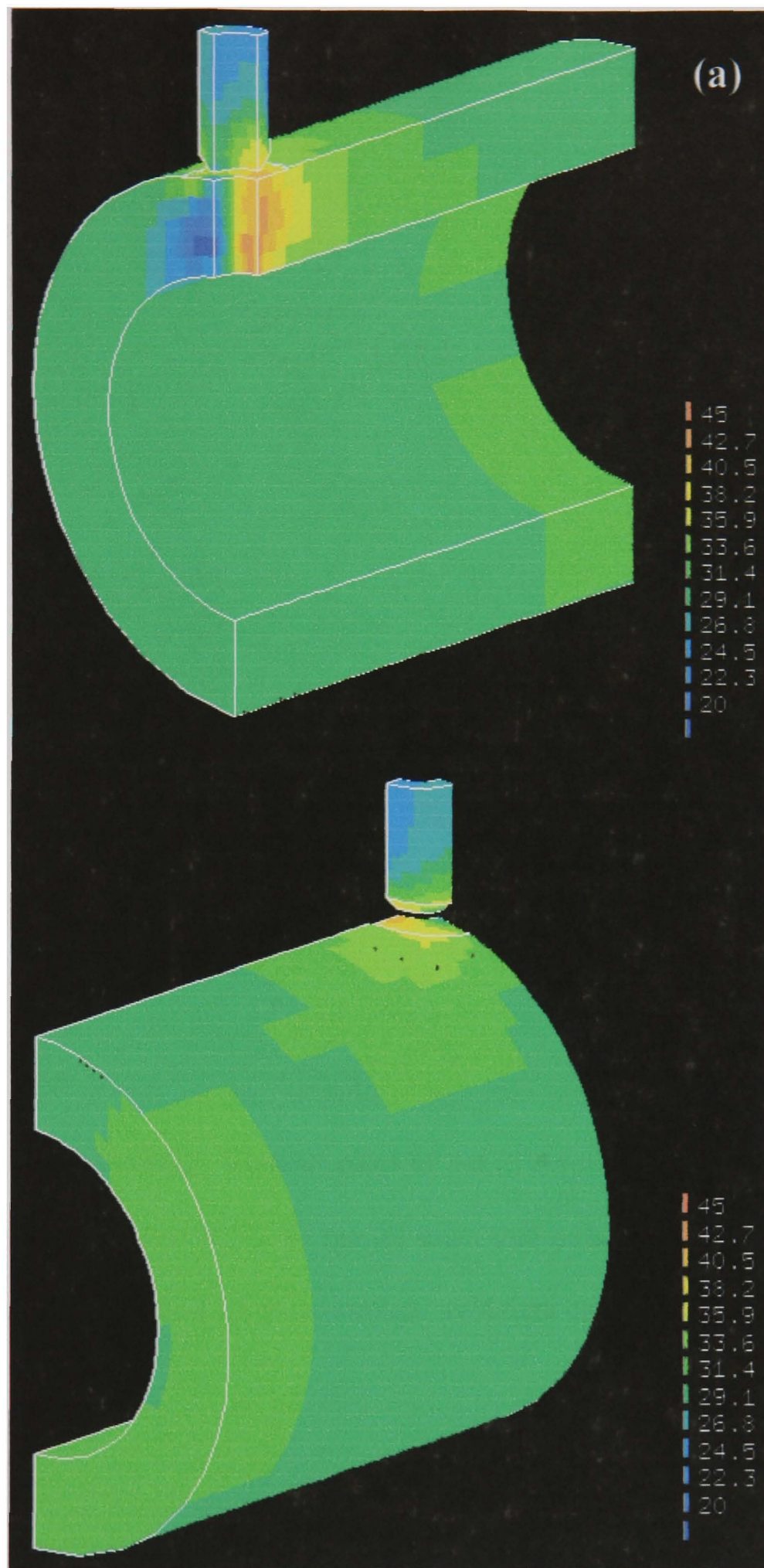


Figure 6.15. Contour plots of Set 2: As-new material PM steady-state rupture stress ($\alpha=0.33$) on the (a) inner and outer whole surface views, and (b) inner-surface and (c) outer-surface weldment connection region.

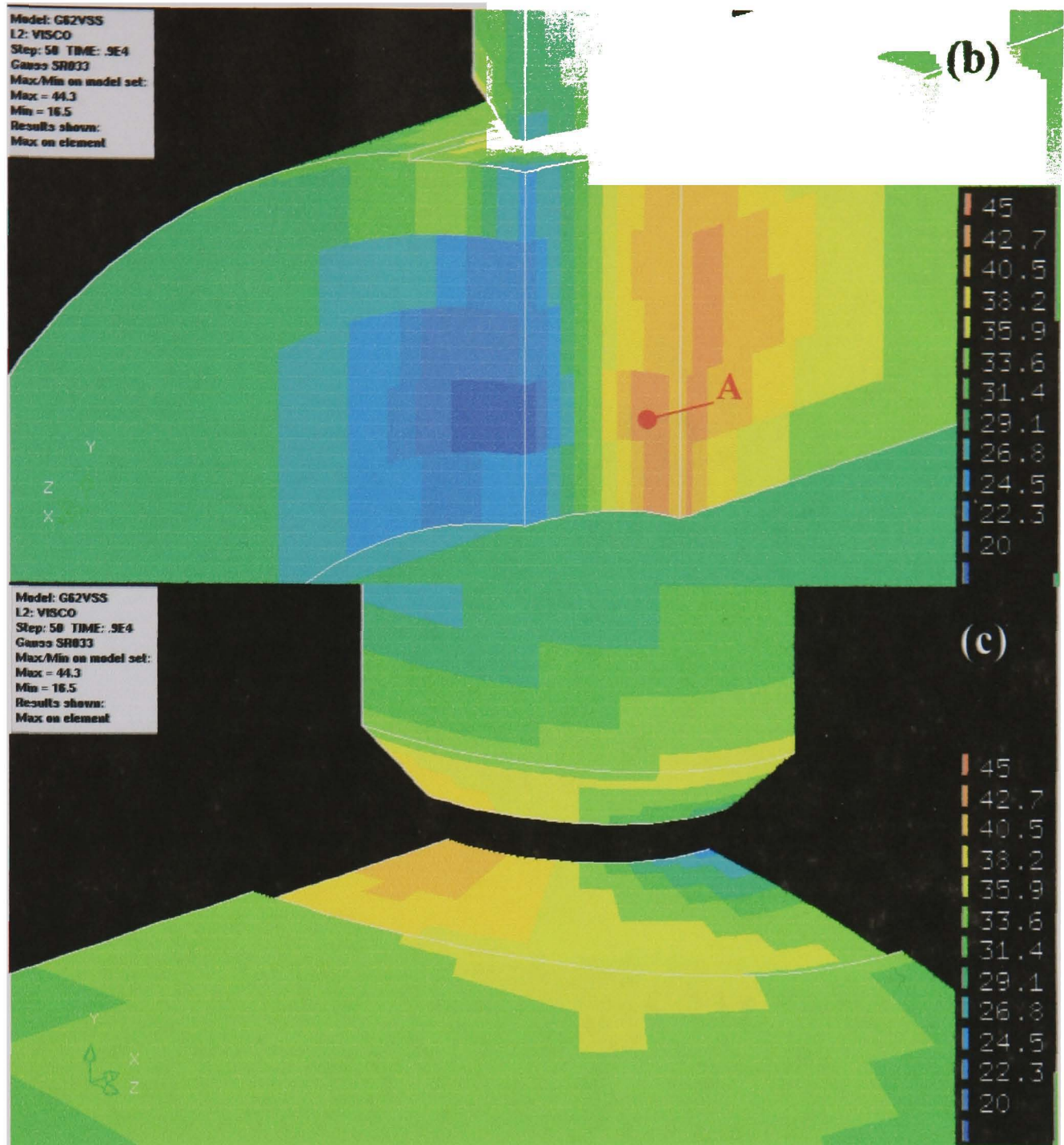


Figure 6.15 (continued). Contour plots of Set 2: As-new material PM steady-state rupture stress ($\alpha=0.33$) on the (a) inner and outer whole surface views, and (b) inner-surface and (c) outer-surface weldment connection region.

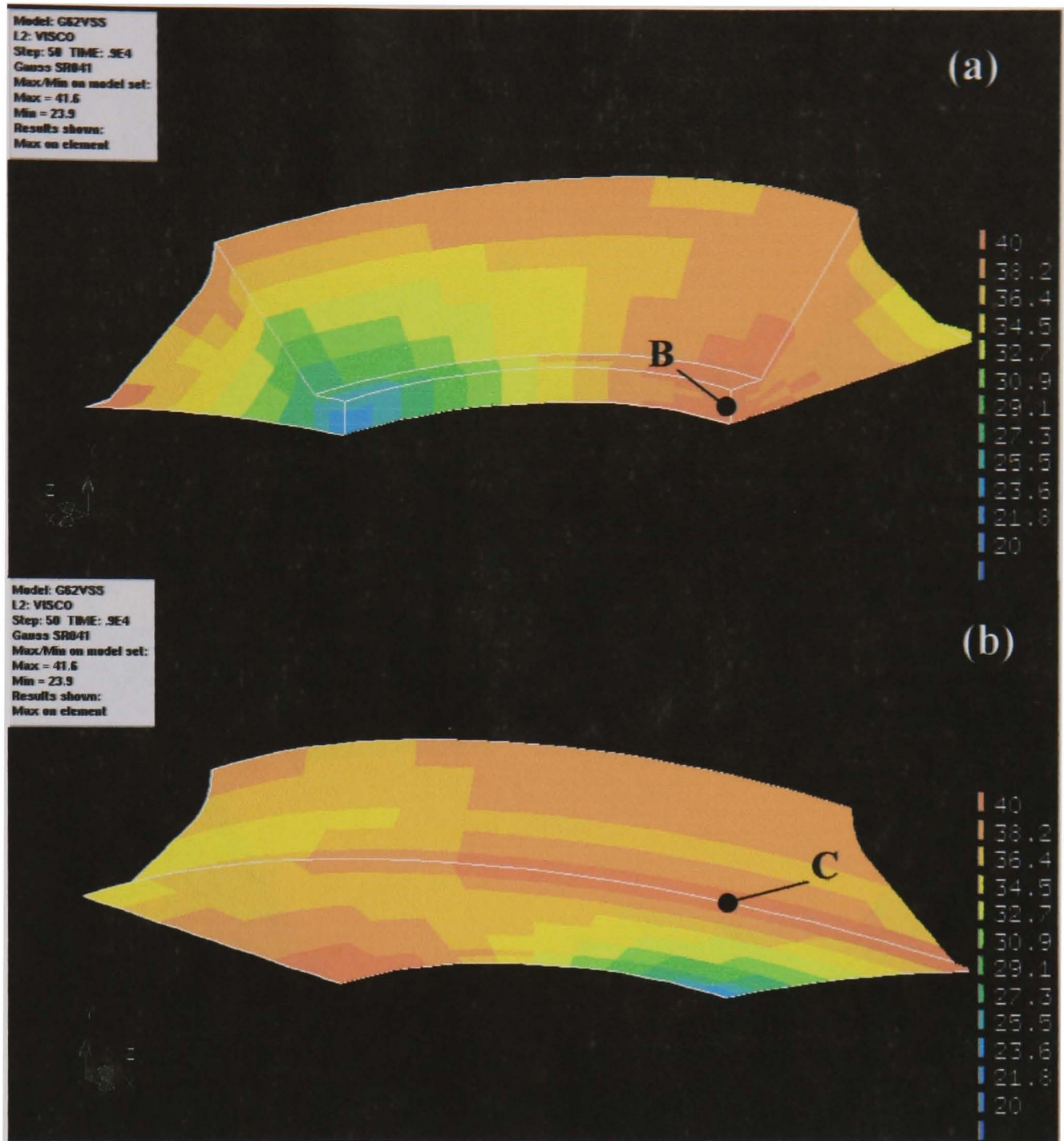


Figure 6.16. Contour plots of Set 2: As-new material WM steady-state rupture stress ($\alpha=0.417$) on the (a) the inner-top surface and (b) the outer-bottom surface.

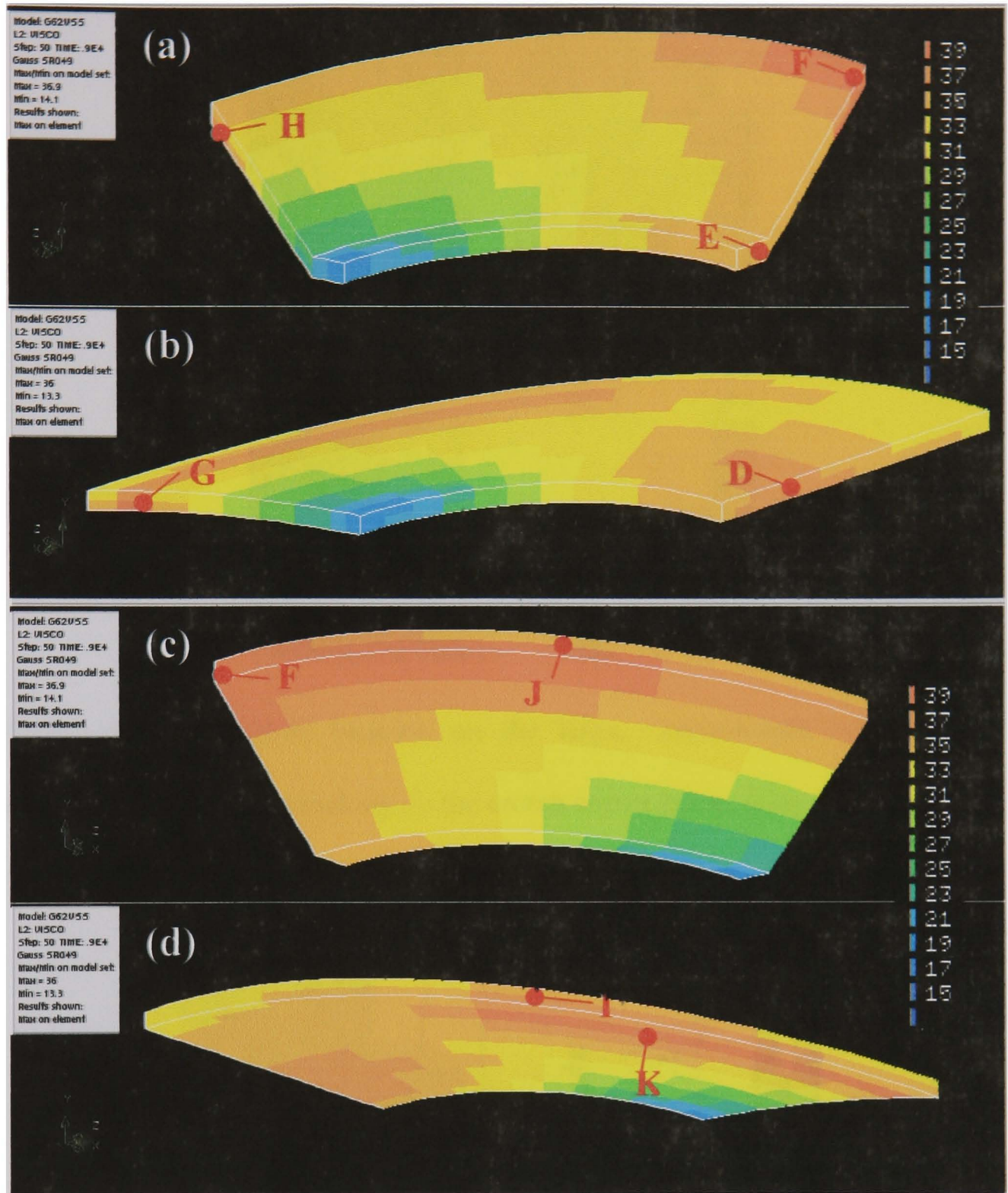


Figure 6.17. Steady-state rupture stress plots ($\alpha=0.49$) of the Set 2: As-new material connection, views of (a) the HAZ^b inner-top surface region, (b) the HAZ^P inner-top surface region, (c) the HAZ^b outer-bottom surface region and (d) the HAZ^P outer-bottom surface region.

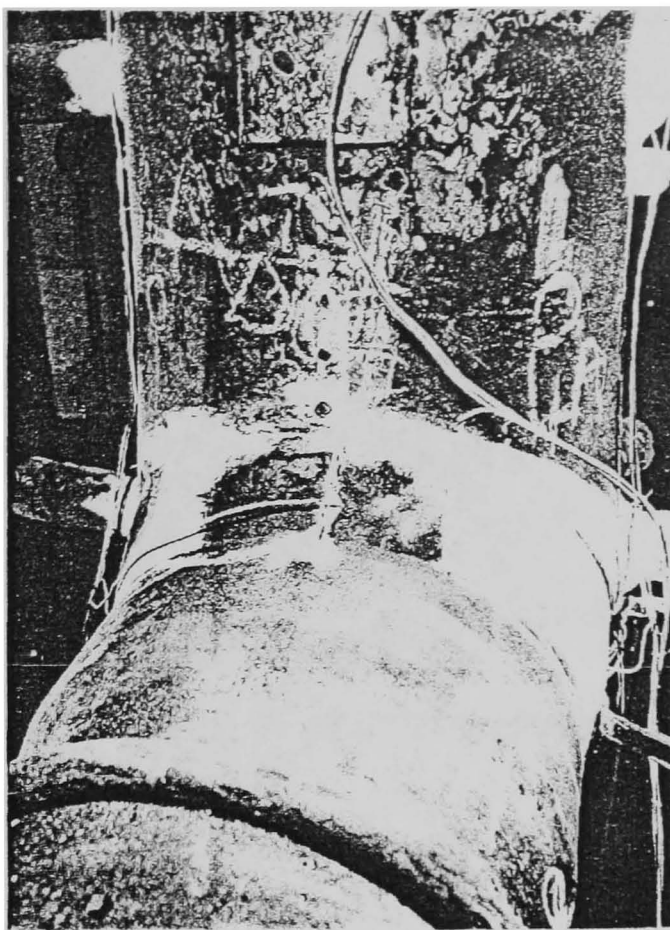


Figure 6.18. Failure location on the large, centre-length branch weld, transverse weld metal cracking on the crotch corner plane, (Day *et al* [1]).



Figure 6.19. Additional cracking locations on the large, centre-length header branch weld, circumferential and transverse weld metal cracks around the weld, (Day *et al* [1]).

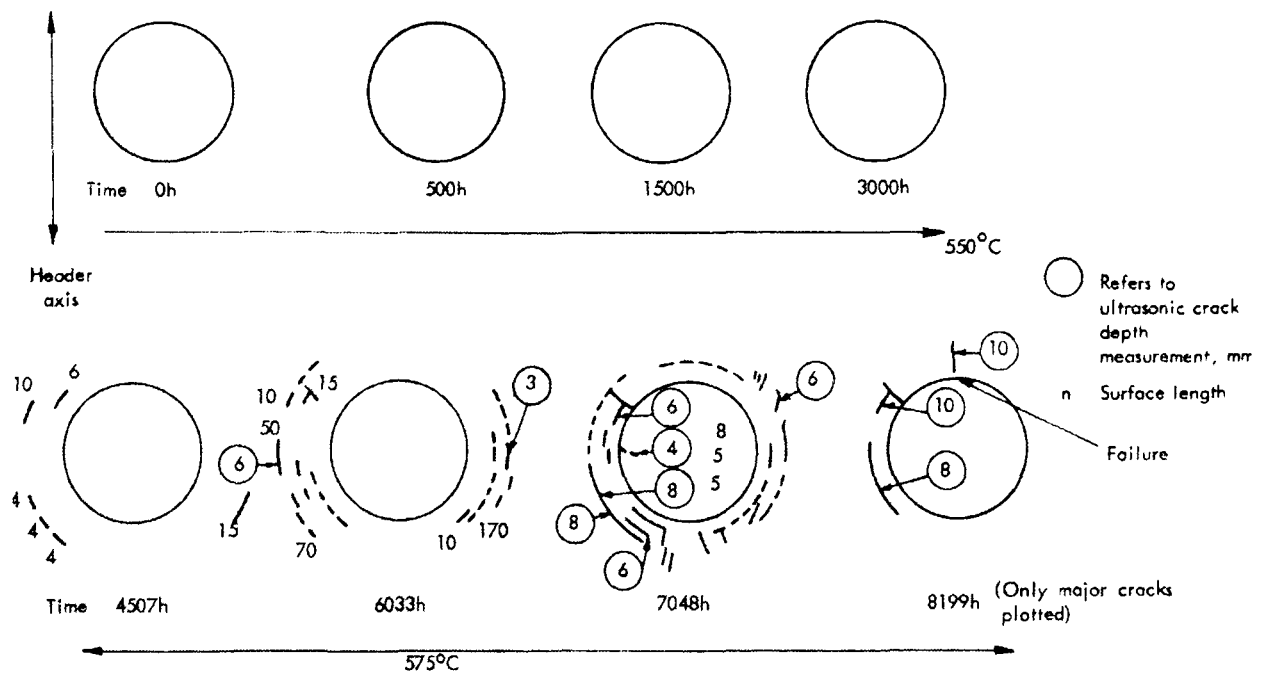


Figure 6.20. Cracking history of large, centre-length header branch weld, (Day *et al* [1]).

CHAPTER SEVEN

EVALUATION OF THE R5 CREEP LIFE ASSESSMENT APPROACH FOR SINGLE AND MULTI-MATERIAL COMPONENTS

7.1 Introduction

The aim of this chapter is to compare creep life predictions, based on British Energy's R5 assessment procedure [13], with the peak steady-state creep rupture stress approach and the damage mechanics approach. The R5 procedure uses an approximate reference stress approach based on the use of limit loads [50]. Volume 7 of R5 proposes two methods for the prediction of distinct reference stresses in the different material zones of multi-material components. The first is based on modifying the homogeneous rupture reference stress using a stress redistribution factor, k , for each weldment zone, as explained in Chapter 2. The second approach requires rupture strength stresses for the different material zones, used in a similar fashion to material distinct yield stresses within the limit load analysis. The physical basis of the second approach is not entirely clear. Assessment of the approach is therefore required and this is the main subject of this Chapter.

Several different components are used to assess the homogeneous and multi-material R5 procedures, investigation of the effects of relative dimensions and the numbers of constitutive materials are considered. The creep of relatively

simple components, i.e. 2-bar and 3-bar structures and a beam in pure bending, was investigated, as well as the realistic cases of pressurised welded plain and branched pipes. Analytical formulations, steady-state finite element analyses and continuum damage mechanics were used to predict rupture lives for the single and multi-material cases. The results permit comparisons of the three creep life assessment approaches, for both single and multi-material components. This chapter provides an assessment and some guidance on the use of the R5 approach for both single and multi-material components.

7.2 Background

Three of the main creep life assessment approaches associated with UK power plant applications are the R5's rupture reference stress approach, the steady-state creep approach and the continuum damage mechanics approach. Each approach has its advantages and disadvantages; for instance continuum damage mechanics requires a relatively large number of material creep constants to be determined in order to calculate a creep life which incorporates secondary and tertiary stages. These advantages and disadvantages will not be discussed any further here. However, the relative accuracy of each approach for single and multi-material components is required to validate and improve the understanding of each approach, especially for branched pipes. The R5's multi-material creep life predictions requires assessment against the other approaches. The R5 methodology uses a method of calculating a multi-material component's rupture life by modifying the homogeneous rupture reference stress. The physical basis behind the modifying of the approach to incorporate multi-material effects is unclear. Therefore investigations into the

accuracy of the approach are required to validate the method for multi-material applications. The following sections contain separate descriptions of the single and multi-material R5 approaches.

7.3 Overview of the R5 life assessment approach

A commonly used approach for creep life assessment of steam piping systems is based on the reference stress method (RSM), which is detailed in many publications, e.g. [39]. British Energy's R5 creep assessment procedure [13] uses such an approach and has been shown to give conservative but acceptably accurate estimates of rupture life for homogeneous branched pipes [114].

The creep rupture life of both homogeneous (e.g. plain pipes) and multi-material (e.g. welded pipes or welded branched connections) components are covered in various parts of the R5 procedure. For defect free single and multi-material components, creep rupture is assessed using a rupture reference stress, $\sigma_{\text{ref}}^{\text{R}}$, which is used to predict a rupture life, $t_{r(R5)}$.

7.3.1 R5 application to homogeneous components

The most common use of the R5 lifing technique is for homogeneous (single-material) components. The background of the R5 approach is explained in more detail in Section 2.3.4 of the literature review, as well as in published literature such as [13,50,63,64]. The reference stress is defined as

$$\sigma_{\text{ref}} = \frac{P\sigma_y}{P_1(\sigma_y)} \quad (7.1)$$

where P_L is the plastic collapse load defined for an elastic-perfectly plastic material with yield strength σ_y . Since $P_L(\sigma_y)$ is directly proportional to σ_y , the reference stress of Equation 7.1 is independent of σ_y ; it is proportional to P but the constant of proportionality, $[\sigma_y / P_L(\sigma_y)]$, depends on the geometry. Thus, an arbitrary value of σ_y can be used to obtain P_L , for example, in FE analyses.

R5 then uses a modified reference stress that incorporates the effect of stress concentrations to estimate the failure life of a homogeneous component under steady-state creep conditions and a steady load. A stress concentration factor, λ , is thus defined as

$$\lambda = \frac{\bar{\sigma}_{el,max}}{\sigma_{ref}} \quad (7.2)$$

where $\bar{\sigma}_{el,max}$ is the maximum value of the elastically calculated equivalent stress in the component. The equivalent stress is used to account for both uni-axial and multi-axial states of stress within components. Calladine [36] considered the effect of the steady-state creep exponent, n , on stress concentrations for a range of simple structures and deduced that the maximum steady-state stress varies approximately linearly with the inverse of n for values between the $n = \infty$ value and the $n = 1$ value. The maximum steady-state stress within a component at $n = \infty$ equals the reference stress and at $n = 1$ equals the maximum elastic stress. This relationship between the maximum steady-state stress and n value is used within the R5 procedure to define a rupture reference stress, σ_{ref}^R , and is defined as

$$\sigma_{ref}^R \approx \left(1 + \frac{1}{n}(\lambda - 1)\right) \sigma_{ref} \quad (7.3)$$

where n is the creep exponent for power law creep. The rupture reference stress therefore augments the reference stress to account for the effect of stress concentrations within a component. R5 states that Equation 7.3 should be used for all creep brittle materials, where overall creep rupture of a component may be assumed to occur when local rupture at the stress concentration occurs. However, for creep ductile materials there can be a significant time taken for damage to spread throughout a component after this local damage initiation, therefore the estimate of Equation 7.3 is too conservative and in this case, the rupture reference stress, σ_{ref}^R , takes the form

$$\sigma_{ref}^R = (1 + 0.13(\lambda - 1)) \sigma_{ref} \quad (7.4)$$

R5 also states that for creep ductile materials with n values greater than 7, the estimate of Equation 7.4 is over conservative and Equation 7.3 should be used. The rupture reference stress, σ_{ref}^R , which may take either the value defined by Equation 7.3 or Equation 7.4 depending on n and whether or not the material is creep brittle or ductile, is said to lead to improved accuracy compared with the simple use of just the reference stress, σ_{ref} .

The resulting rupture life is then calculated using a life equation based on material rupture properties and the reference rupture stress, such as

$$t_r = \frac{\sigma_{ref}^{R-\chi}}{M} \quad (7.5)$$

where M and χ are material properties.

7.3.2 R5 application to multi-material components

For multi-material components, Volume 7 of the R5 procedure predicts failure lives for each material zone by calculating different reference rupture stresses for each material zone, the lowest of the predicted lives is the predicted failure life of the component. The approach is based upon a modified version of the homogeneous reference rupture stress method, explained in the preceding section. The application of the R5 approach to multi-material components is outlined below.

For a component with i materials, Volume 7 of R5 assigns a different “rupture strength stress”, $\sigma_{y,i}$, (which is used in a similar manner as a yield stress in the homogeneous rupture reference stress approach) to each material zone, which is dependent on the corresponding rupture strength of that material and a chosen assessment time, t_r^* . The chosen assessment time is fixed for the “rupture strength stress” of each material as:

$$\sigma_{y,i} = (M_i \times t_r^*)^{-\frac{1}{\chi_i}} \quad (7.6)$$

where $\sigma_{y,i}$ is material i 's rupture strength stress, M_i and χ_i are the rupture properties of material i ; obtained from creep rupture tests. Note that British Energy [127] suggests that the assessment time, t_r^* , should be equal to the estimated design lifetime of the component and that an improved estimate of the component's predicted life, t_r , may be obtained by varying t_r^* . The choice of t_r^* and its effect on the accuracy of the component's predicted life requires investigation, and is therefore addressed below.

A limit load calculation is then performed for the multi-material component, assigning each material's $\sigma_{y,i}$ from Equation 7.6 to the corresponding material zone. The resulting mismatch limit load, P_L , from the limit load calculation, e.g. using FE analysis, which is a function of the mismatch between the $\sigma_{y,i}$ values and the geometry of each material zone, is used to predict a reference stress for each material zone using Equation 7.1. as follows:

$$\sigma_{ref,i} = \frac{P\sigma_{y,i}}{P_L(\sigma_{y_1}, \sigma_{y_2}, \dots, \sigma_{y_j})} \quad (7.7)$$

where P is the applied load and $P_L(\sigma_{y_1}, \sigma_{y_2}, \dots, \sigma_{y_j})$ is the mismatch limit load for j different material zones. For example, a three-material component ($i=3$) would have three different rupture strength stresses, $\sigma_{y_1}, \sigma_{y_2}, \sigma_{y_3}$, and three resulting reference stresses, $\sigma_{ref,1}, \sigma_{ref,2}, \sigma_{ref,3}$.

The corresponding rupture reference stresses for material i are then calculated using the n_i value or the 0.13 factor, the $\sigma_{ref,i}$ and the component stress concentration factor. The stress concentration factor, λ , is modified from the homogeneous version shown in Equation 7.2 due to the possibility of the stress concentration being in a part of the structure with a high rupture strength, which could otherwise lead to an unnecessarily pessimistic prediction [127]. The multi-material stress concentration factor used is defined as

$$\lambda = \frac{P_L}{P_y} \quad (7.8)$$

where P_L is the mismatch limit load and P_y is the load in which yield first occurs within any of the constitutive materials using the so-called rupture

strength stress of Equation 7.6. The rupture reference stress for each constitutive material within the component is then calculated using equations similar to Equations 7.3 and 7.4, as follows:

$$\bar{\sigma}_{ref,i}^R \approx \left(1 + \frac{1}{n_i} (\lambda - 1) \right) \sigma_{ref,i} \quad (7.9)$$

where the rupture reference stress for each material uses the corresponding n_i value and reference stress, $\sigma_{ref,i}$. Equation 7.9 is used in the same way as for homogeneous components, that is, it is used for all creep brittle materials and for ductile materials with n_i values greater than 7 [13]. Similarly to Equation 7.4, for homogeneous components made from creep ductile materials with n_i less than 7, the rupture reference stress version used for multi-material components is

$$\sigma_{ref,i}^R = (1 + 0.13(\lambda - 1)) \sigma_{ref,i} \quad (7.10)$$

where again, each material's reference stress is used to predict a rupture reference stress. For example, a three-material component behaving in a ductile fashion and having a n value less than 7 would produce three rupture reference stresses using Equation 7.10.

A separate rupture life is then obtained for each material using representative rupture properties in a rupture life equation, such as Equation 7.5. The lowest life predicted from all materials is then taken as the predicted rupture life of the whole component [127].

In the subsequent study, the multi-material reference stresses were calculated using an estimated design life, t_r^* , taken to be equal to the predicted steady-state component failure life. However, for each component considered, the effect of the choice of t_r^* on the predicted R5 rupture life was investigated using the following range:

$$t_r^* = 0.125t_{r(ss)}, 0.25t_{r(ss)}, t_{r(ss)}, 2t_{r(ss)} \text{ and } 4t_{r(ss)}$$

If the R5 reference stress approach can be shown to be satisfactorily conservative and relatively accurate for multi-material structures, compared to other assessment methods, such as the steady-state creep rupture stress approach [135] or damage mechanics approach [32,53], this would substantially simplify creep life calculations. This work primarily compares steady-state creep results with R5 reference stress results to assess the R5 procedure for homogeneous and multi-material components. The results of damage mechanics analyses are also used to give an indication of the level of conservatism of the steady-state creep and R5 approaches.

Within this investigation the limit loads and loads to first yield were calculated using small displacement theory, as suggested by R5 [13], and therefore the effects of non-linear geometry on the limit load is assumed negligible. The R5 rupture reference stresses are taken to correspond to an equivalent (von-Mises) stress. Hence, to provide a consistent comparison with the R5 stresses and lives, the steady-state and CDM approaches were obtained using the equivalent (von-Mises) stress, so that the use of the multi-axial rupture stress of Equation 2.8 is not considered. This signifies that the rupture behaviour of the material

under the control of the maximum principal stress or under equivalent (Von-Mises) stress is not considered for this work.

7.4 Single-material components

7.4.1 General

The components used to assess the validity of the R5 procedure against steady-state and CDM approaches for single materials are: -

1. An axially loaded 2-bar structure,
2. a thick-walled plain pipe, and
3. a thick-walled branched pipe.

The material used for the components is a typical fossil-fuelled power plant CMV material that is creep ductile and which has an n value less than seven; therefore Equation 7.4 is used in the R5 calculations. This material used is the parent material (PM) from a service-aged $\frac{1}{2}\text{Cr}\frac{1}{2}\text{Mo}\frac{1}{4}\text{V}:2\frac{1}{4}\text{Cr}1\text{Mo}$ pipe weldment at 640°C [30], as shown in Table 7.1.

7.4.2 Analytical formulations and FE models

With reference to the 2-bar structure shown in Figure 7.1, the analytical equation for calculating the limit load, P_L , is

$$P_L = \sigma_y (a_1 + a_2) \quad (7.11)$$

where a_1 and a_2 are the cross-sectional areas of the bars and σ_y is the yield stress of the material. The corresponding reference stress for the structure is

$$\sigma_{ref} = \frac{P}{(a_1 + a_2)} \quad (7.12)$$

where P is the chosen load level. The stress concentration factor is

$$\lambda = \frac{\sigma_{el,max}}{\sigma_{ref}} = \frac{a_1 + a_2}{(a_2 + \frac{L_2}{L_1} a_1)} \quad (7.13)$$

assuming that bar 2 fails first. Where L_1 and L_2 are the lengths of each bar. The corresponding rupture reference stress for the 2-bar structure is

$$\sigma_{ref}^R = (1 + 0.13(\lambda - 1)) \frac{P}{a_1 + a_2} \quad (7.14)$$

The steady-state stress formulation, based on Norton's power law, for the same 2-bar structure, for the stress in bar 2, σ_2 , is

$$\left(\frac{a_1}{a_1 + a_2} \right) \left(\frac{L_2}{L_1} \right)^{\frac{1}{n}} \left(\frac{\sigma_2}{\sigma_{nom}} \right) + \left(\frac{a_2}{a_1 + a_2} \right) \left(\frac{\sigma_2}{\sigma_{nom}} \right) - 1 = 0 \quad (7.15)$$

where

$$\sigma_{nom} = \frac{P}{(a_1 + a_2)}$$

The creep stress in bar 1 can be found using σ_2 , since the displacement rates of the bars are equal, i.e.

$$\dot{\epsilon}_1 L_1 = \dot{\epsilon}_2 L_2$$

therefore

$$\left(\frac{\sigma_1}{\sigma_{nom}} \right) = \left(\frac{L_2}{L_1} \right)^{\frac{1}{n}} \left(\frac{\sigma_2}{\sigma_{nom}} \right) \quad (7.16)$$

The damage mechanics prediction uses FE analysis to calculate the rupture life of the single material 2-bar structure. A user-subroutine called *CREEP* [133]

was employed with ABAQUS FE software [28] to implement the CDM equations (i.e. Equations 2.6 to 2.8). The same routine has been previously applied to CDM analyses of V-welded straight pipe sections [30]. The FE mesh used is shown in Figure 7.2, comprising of 31 2D 8-noded plane strain elements with reduced integration.

For the case of a welded pressurised plain pipe with an outer diameter of 355.6mm and wall thickness of 63.5mm, the lives for all three approaches were predicted using the FE analysis. The mesh is shown in Figure 7.3, weld zones are included in the mesh but only one material was modelled. The mesh comprises 2020 axisymmetric, 8- and 6-noded elements with reduced integration. The limit analysis used the modified RIKS [28] solution technique within ABAQUS, assuming elastic-perfectly-plastic material behaviour. The FE analyses provide a limit load pressure and maximum elastic equivalent stress for Equations 7.1 and 7.2. Where the limit load for this case is defined and obtained as the maximum load which the component can sustain, while ensuring small displacements are maintained within the component. This is termed the ‘global’ limit load by R5 [13]. The steady-state stress was calculated using Norton’s law, as described in previous Chapters and the CDM analysis used the *CREEP* user-subroutine [133].

For the case of a branched pipe, shown in Figures 7.4(a) and 7.4(b), which is a single-material model ignoring the weld properties, FE analyses were used to predict the rupture reference stress and the steady-state stress for the R5 and steady-state approaches, respectively. The *CREEP* damage sub-routine [133]

was used with Abaqus FE software [28] to predict the CDM life. The dimensions of the branched pipe are shown in Table 7.2. The FE limit load was again obtained by using the modified RIKS technique within ABAQUS. Again similarly, the limit load for this case is defined and obtained as the maximum load which the component can sustain, while ensuring small displacements are maintained within the component. The steady-state FE analysis used Norton's law. The FE models used are shown in Figure 7.5. Global and sub-modelling techniques were used for the steady-state analysis. The limit analysis used the global model only. The global model and sub model consisted of 4500 and 10500, 20-noded brick elements, respectively, with reduced integration.

Appendix 1 provides some general guidelines on how FE analysis can be used to effectively predict steady-state stress distributions and how component failure can be defined using continuum damage mechanics analysis.

7.4.3 Results

The single material 2-bar structure was subjected to a force, P , of 10 kN, with the dimensions shown in Table 7.3. The stress and life results obtained for all three approaches are presented in Table 7.4. It can be seen that the R5 rupture stress and failure life agree to within 2% and 8%, respectively, with the steady-state predictions.

The CDM predicted rupture life of 2493 hours, where a maximum damage level of $\omega = 0.84$ was reached across the section, shows that the R5 and

steady-state approaches were conservative, under-predicting the life by 17% and 22%, respectively, relative to the CDM prediction. The time taken for the damage level in the section to reach unity from 0.84 is expected to be small compared to the time taken to reach 0.84 from the undamaged state. Thus, the levels of conservatism stated above for the R5 and steady-state approaches would not be expected to increase significantly. The steady-state and damage analyses both predicted failure to occur in Bar 2.

The plain pipe was subjected to an internal pressure, p_i , of 16.55 MPa and axial end stress induced from a closed end condition. The stress and life results are presented in Table 7.5. The R5 and steady-state stresses agree to within 1% and the R5 approach predicted life was about 3.5% higher than that predicted by the steady-state approach.

The corresponding CDM component failure life was 31600 hours, the time at which the majority of the wall thickness had reaches a damage level greater than of $\omega = 0.7$. Thus, the R5 and steady-state approaches under-predict the life by about 30% and 32%, respectively, relative to the CDM life. The time taken for the damage level across the section to reach unity from the inside surface reaching 0.98 is expected to be small compared to the time taken for the inside surface to reach 0.98 from the undamaged state. Thus, the levels of conservatism stated above for the R5 and steady-state approaches would not be expected to increase significantly if a damage level of unity had been achieved across the wall. The steady-state and damage analyses predicted failure to initiate at the same position, namely the inside surface of the pipe.

The branched pipe was also subjected to an internal pressure, p_i , of 16.55 MPa with a closed end condition. The stress and life results of the R5 and steady-state approaches are presented in Table 7.6. The predicted R5 stress is lower than the steady-state stress by about 6%, which is a slightly larger difference than for the other two components. This larger difference in stress produces a R5 rupture life prediction which is 39% longer than that of the steady-state life prediction. The steady-state approach predicted failure to initiate just above the inside crotch corner on the inside surface of the connection, shown by point X in Figure 7.5(b).

The component life predicted by the CDM approach was 15000 hours, where component failure was defined as the time at which the majority of the wall-thickness had reached a damage level greater than 0.6. The peak damage ($\omega = 0.98$) initiated in the connection at point X in Figure 7.5(b), this is the same location as what was predicted by the steady-state approach. Thus, the R5 and steady-state approaches conservatively under-predicted the life by 62% and 72%, respectively, relative to the CDM life prediction. The steady-state and damage analyses predicted failure to initiate at the same position. The R5 and steady-state life predictions were both very conservative compared to the CDM prediction because the steady-state and R5 approaches are based on predicting the failure life for the position of highest equivalent stress, i.e. point X , and not on a failure life for net rupture across the wall. Hence, for this homogeneous material connection, Point X was located at a position of high local stress, while the stress levels across the rest of the wall-thickness was significantly

lower and therefore the difference in time between Point X failing and the net section failing is significant.

7.5 Multi-material components

7.5.1 General

The components used for the multi-material cases are: -

1. An axially loaded 2-bar structure,
2. an axially loaded 3-bar structure,
3. a beam in pure bending,
4. a thick-walled welded plain pipe and
5. a thick-walled welded branched pipe.

The weldment materials used are those detailed in Table 7.1 [26]. It is assumed that the Young's modulus for all of the materials are the same. Since all these materials are creep ductile [26,30] and have n values lower than 7, the R5 rupture reference stresses are calculated using Equation 7.10. The differences between the R5 and steady-state stresses and lives are investigated with respect to variations in component dimensions, material properties and the chosen design lifetime, t_r^* , used to calculate the R5 multi-material lives. Continuum damage mechanics calculations were also carried out for the cases of a 2-bar structure, welded plain pipe and welded branched pipes.

7.5.2 Analytical formulations and FE models

The analytical formulations and FE models used to calculate the rupture reference stresses and steady-state stresses, which are used to obtain life predictions based on the R5 and steady-state stress approaches for each component are described below. The FE models used for the CDM calculations of the 2-bar structure and welded plain and branched pipes are also described.

With reference to the 2-bar structure shown in Figure 7.1, where the material of bar 1 is different to that of bar 2, the analytical equation for calculating the limit load, P_L , of this 2-material component is:

$$P_L = \sigma_{y,1}a_1 + \sigma_{y,2}a_2 \quad (7.17)$$

where a_1 and a_2 are the cross-sectional areas of the bars and $\sigma_{y,1}$ and $\sigma_{y,2}$ are the rupture strength stresses of materials 1 and 2, respectively. Note that in this case $\sigma_{y,1}$ and $\sigma_{y,2}$ are given in Equation 7.6. The corresponding reference stresses are

$$\sigma_{ref,1} = \frac{P\sigma_{y,1}}{\sigma_{y,1}a_1 + \sigma_{y,2}a_2} \quad (7.18a)$$

$$\sigma_{ref,2} = \frac{P\sigma_{y,2}}{\sigma_{y,1}a_1 + \sigma_{y,2}a_2} \quad (7.18b)$$

where P is the chosen load level. The stress concentration factors, λ_i , for the two bars are:

$$\lambda_1 = \frac{P_L}{P_{y1}} = \frac{a_1 + \left(\frac{\sigma_{y2}}{\sigma_{y1}} \right) a_2}{a_1 + \left(\frac{L_1}{L_2} \right) a_2} \quad (7.19a)$$

$$\lambda_2 = \frac{P_L}{P_{y2}} = \frac{a_2 + \left(\frac{\sigma_{y1}}{\sigma_{y2}} \right) a_1}{a_2 + \left(\frac{L_2}{L_1} \right) a_1} \quad (7.19b)$$

where L_1 and L_2 are the lengths of each bar and $P_{y,1}$ and $P_{y,2}$ are the loads to first yield (reach the rupture strength stress level) of each bar. Note that the $P_{y,1}$ and $P_{y,2}$ expressions were derived from elastic analysis of the structure and using displacement compatibility and stress-strain relationships. The corresponding rupture reference stresses $\sigma_{ref,1}^R$ and $\sigma_{ref,2}^R$ are then given by

$$\sigma_{ref,1}^R = \left(1 + 0.13(\lambda_m - 1) \right) \frac{P \sigma_{y,1}}{\sigma_{y,1} a_1 + \sigma_{y,2} a_2} \quad (7.20a)$$

$$\sigma_{ref,2}^R = \left(1 + 0.13(\lambda_m - 1) \right) \frac{P \sigma_{y,2}}{\sigma_{y,1} a_1 + \sigma_{y,2} a_2} \quad (7.20b)$$

where λ_m is the stress concentration factor of the multi-material component and is chosen as the larger stress concentration value, λ_i , from Equations 7.19a and 7.19b.

Following the notation of Chapter 5, for the generalised steady-state solution to multi-material problems, based on a Norton's creep power-law in the form

$$\frac{\dot{\epsilon}^c}{\dot{\epsilon}_{0,i}} = \left(\frac{\sigma}{\sigma_{nom}} \right)^{n_i} \quad (7.21)$$

the steady-state stress in bar 2, σ_2 , is [102]: -

$$\left(\frac{a_1}{a_1 + a_2}\right)\left(\frac{L_2}{L_1}\right)^{\frac{1}{n_1}}\left(\frac{\dot{\epsilon}_{02}}{\dot{\epsilon}_{01}}\right)^{\frac{1}{n_1}}\left(\frac{\sigma_2}{\sigma_{nom}}\right)^{\frac{n_2}{n_1}} + \left(\frac{a_2}{a_1 + a_2}\right)\left(\frac{\sigma_2}{\sigma_{nom}}\right) - 1 = 0 \quad (7.22)$$

where σ_{nom} is a suitable nominal stress dependent on the load level, given here by;

$$\sigma_{nom} = \frac{P}{(a_1 + a_2)}$$

and where $\dot{\epsilon}_{0i} = A_i \sigma_{nom}^{n_i}$.

The stress in bar 1, σ_1 , can be obtained from compatibility of the displacement rates, as:

$$\left(\frac{\sigma_1}{\sigma_{nom}}\right) = \left(\frac{L_2}{L_1}\right)^{\frac{1}{n_1}}\left(\frac{\dot{\epsilon}_{02}}{\dot{\epsilon}_{01}}\right)^{\frac{1}{n_1}}\left(\frac{\sigma_2}{\sigma_{nom}}\right)^{\frac{n_2}{n_1}} \quad (7.23)$$

The FE mesh used for the CDM calculation is the same as that used for the single material mesh, shown in Figure 7.2, but using different material properties for each bar.

Figure 7.6 shows the 3-bar, 3-material structure. The analytical equation for the limit load, P_L , for this component is

$$P_L = \sigma_{y,1} a_1 + \sigma_{y,2} a_2 + \sigma_{y,3} a_3 \quad (7.24)$$

where a_1 , a_2 and a_3 are the cross-sectional areas of the bars and $\sigma_{y,1}$, $\sigma_{y,2}$ and $\sigma_{y,3}$ are the rupture strength stresses of material 1, 2 and 3, respectively, again obtained from Equation 7.6. The corresponding reference stresses for the three materials are

$$\sigma_{ref,1} = \frac{P\sigma_{y,1}}{\sigma_{y,1}a_1 + \sigma_{y,2}a_2 + \sigma_{y,3}a_3} \quad (7.25a)$$

$$\sigma_{ref,2} = \frac{P\sigma_{y,2}}{\sigma_{y,1}a_1 + \sigma_{y,2}a_2 + \sigma_{y,3}a_3} \quad (7.25b)$$

$$\sigma_{ref,3} = \frac{P\sigma_{y,3}}{\sigma_{y,1}a_1 + \sigma_{y,2}a_2 + \sigma_{y,3}a_3} \quad (7.25c)$$

The stress concentration factors, λ_i , for the three bars are:

$$\lambda_1 = \frac{P_L}{P_{y1}} = \frac{a_1 + \left(\frac{\sigma_{y2}}{\sigma_{y1}}\right)a_2 + \left(\frac{\sigma_{y3}}{\sigma_{y1}}\right)a_3}{a_1 + \left(\frac{L_1}{L_2}\right)a_2 + \left(\frac{L_1}{L_3}\right)a_3} \quad (7.26a)$$

$$\lambda_2 = \frac{P_L}{P_{y2}} = \frac{a_2 + \left(\frac{\sigma_{y1}}{\sigma_{y2}}\right)a_1 + \left(\frac{\sigma_{y3}}{\sigma_{y2}}\right)a_3}{a_2 + \left(\frac{L_2}{L_1}\right)a_1 + \left(\frac{L_2}{L_3}\right)a_3} \quad (7.26b)$$

$$\lambda_3 = \frac{P_L}{P_{y3}} = \frac{a_3 + \left(\frac{\sigma_{y1}}{\sigma_{y3}}\right)a_1 + \left(\frac{\sigma_{y2}}{\sigma_{y3}}\right)a_2}{a_3 + \left(\frac{L_3}{L_1}\right)a_1 + \left(\frac{L_3}{L_2}\right)a_2} \quad (7.26c)$$

with $P_{y,1}$, $P_{y,2}$ and $P_{y,3}$ as the loads to first yield of each bar (load to reach the rupture strength stress level). The corresponding rupture reference stresses

$\sigma_{ref,1}^R$, $\sigma_{ref,2}^R$ and $\sigma_{ref,3}^R$ are therefore

$$\sigma_{ref,1}^R = (1 + 0.13(\lambda_m - 1)) \frac{P\sigma_{y,1}}{\sigma_{y,1}a_1 + \sigma_{y,2}a_2 + \sigma_{y,3}a_3} \quad (7.27a)$$

$$\sigma_{ref,2}^R = (1 + 0.13(\lambda_m - 1)) \frac{P\sigma_{y,2}}{\sigma_{y,1}a_1 + \sigma_{y,2}a_2 + \sigma_{y,3}a_3} \quad (7.27b)$$

$$\sigma_{ref,3}^R = (1 + 0.13(\lambda_m - 1)) \frac{P\sigma_{y,3}}{\sigma_{y,1}a_1 + \sigma_{y,2}a_2 + \sigma_{y,3}a_3} \quad (7.27c)$$

where again λ_m is chosen as the largest stress concentration value, λ_i , from the Equations 7.27a, 7.27b and 7.27c values.

The steady-state stress in bar 2, σ_2 , is given by Hyde *et al* [102] as

$$\begin{aligned} & \left(\frac{a_1}{a_1 + a_2 + a_3} \right) \left(\frac{L_2}{L_1} \right)^{\frac{1}{n_1}} \left(\frac{\dot{\epsilon}_{02}}{\dot{\epsilon}_{01}} \right)^{\frac{1}{n_1}} \left(\frac{\sigma_2}{\sigma_{nom}} \right)^{\frac{n_2}{n_1}} + \left(\frac{a_3}{a_1 + a_2 + a_3} \right) \\ & \times \left(\frac{L_2}{L_3} \right)^{\frac{1}{n_3}} \left(\frac{\dot{\epsilon}_{02}}{\dot{\epsilon}_{03}} \right)^{\frac{1}{n_3}} \left(\frac{\sigma_2}{\sigma_{nom}} \right)^{\frac{n_2}{n_3}} + \left(\frac{a_2}{a_1 + a_2 + a_3} \right) \left(\frac{\sigma_2}{\sigma_{nom}} \right) - 1 = 0 \end{aligned} \quad (7.28)$$

where

$$\sigma_{nom} = \frac{P}{(a_1 + a_2 + a_3)}$$

The creep stress in bar 1, σ_1 , and bar 3, σ_3 , can be obtained in terms of σ_2 , using compatibility of displacement rates to give:

$$\left(\frac{\sigma_1}{\sigma_{nom}} \right) = \left(\frac{L_2}{L_1} \right)^{\frac{1}{n_1}} \left(\frac{\dot{\epsilon}_{02}}{\dot{\epsilon}_{01}} \right)^{\frac{1}{n_1}} \left(\frac{\sigma_2}{\sigma_{nom}} \right)^{\frac{n_2}{n_1}} \quad (7.29a)$$

and

$$\left(\frac{\sigma_3}{\sigma_{nom}} \right) = \left(\frac{L_2}{L_3} \right)^{\frac{1}{n_3}} \left(\frac{\dot{\epsilon}_{02}}{\dot{\epsilon}_{03}} \right)^{\frac{1}{n_3}} \left(\frac{\sigma_2}{\sigma_{nom}} \right)^{\frac{n_2}{n_3}} \quad (7.29b)$$

With reference to the 2 material beam in pure bending of Figure 7.7. the analytical equation for calculating the limit moment, \hat{M}_L , is

$$\hat{M}_L = \frac{\bar{d}^2}{4} (\bar{b}_1 \sigma_{y1} + (\bar{b}_2 - \bar{b}_1) \sigma_{y2}) \quad (7.30)$$

where \bar{b}_1 is the width of the material 1 zone, \bar{b}_2 is the total width of the beam, \bar{d} is the depth of the beam and $\sigma_{y,1}$ and $\sigma_{y,2}$ are the rupture strength stresses of materials 1 and 2, respectively. The corresponding reference stresses are

$$\sigma_{ref,1} = \frac{4\hat{M}\sigma_{y1}}{\bar{d}^2 (\bar{b}_1\sigma_{y1} + (\bar{b}_2 - \bar{b}_1)\sigma_{y2})} \quad (7.31a)$$

$$\sigma_{ref,2} = \frac{4\hat{M}\sigma_{y2}}{\bar{d}^2 (\bar{b}_1\sigma_{y1} + (\bar{b}_2 - \bar{b}_1)\sigma_{y2})} \quad (7.31b)$$

where \hat{M} is the chosen moment load. The stress concentration factors, λ_i , for the two materials are

$$\lambda_1 = \frac{\hat{M}_L}{\hat{M}_{y1}} = \frac{3(\bar{b}_1\sigma_{y1} + (\bar{b}_2 - \bar{b}_1)\sigma_{y2})}{2\sigma_{y1}\bar{b}_2} \quad (7.32a)$$

$$\lambda_2 = \frac{\hat{M}_L}{\hat{M}_{y2}} = \frac{3(\bar{b}_1\sigma_{y1} + (\bar{b}_2 - \bar{b}_1)\sigma_{y2})}{2\sigma_{y2}\bar{b}_2} \quad (7.32b)$$

$\hat{M}_{y,1}$ and $\hat{M}_{y,2}$ are the moment loads to first yield of each material (load level to reach the rupture strength stress) to . The corresponding rupture reference stresses $\sigma_{ref,1}^R$ and $\sigma_{ref,2}^R$ are therefore

$$\sigma_{ref,1}^R = (1 + 0.13(\lambda_m - 1)) \frac{\hat{M}\sigma_{y1}}{\frac{\bar{d}^2}{4} (\bar{b}_1\sigma_{y1} + (\bar{b}_2 - \bar{b}_1)\sigma_{y2})} \quad (7.33a)$$

$$\sigma_{ref,2}^R = (1 + 0.13(\lambda_m - 1)) \frac{\hat{M}\sigma_{y2}}{\frac{\bar{d}^2}{4} (\bar{b}_1\sigma_{y1} + (\bar{b}_2 - \bar{b}_1)\sigma_{y2})} \quad (7.33b)$$

where once again λ_m is chosen as the largest λ_i value from either Equation 7.32a or Equation 7.32b.

The maximum steady-state stress in material 2, σ_2 , which occurs at $y = \bar{d} / 2$, of the 2-material beam in pure bending is given by [102]: -

$$\left(\frac{\bar{b}_2 - \bar{b}_1}{\bar{b}_1} \right) \left(\frac{n_2}{2n_2 + 1} \right) \left(\frac{\sigma_2}{\sigma_{nom}} \right) + \left(\frac{n_1}{2n_1 + 1} \right) \left(\frac{\dot{\epsilon}_{02}}{\dot{\epsilon}_{01}} \right)^{\frac{1}{n_1}} \left(\frac{\sigma_2}{\sigma_{nom}} \right)^{\frac{n_2}{n_1}} - 1 = 0 \quad (7.34)$$

where the nominal stress is chosen as

$$\sigma_{nom} = \frac{2\hat{M}}{\bar{b}_1 \bar{d}^2}$$

The maximum creep stress in material 1, σ_1 , which occurs at $y = \bar{d} / 2$, can be expressed in terms of σ_2 using compatibility of strain rates i.e.

$$\dot{\epsilon}_1 = \dot{\epsilon}_2$$

Thus, from consideration of beam deformation

$$\left(\frac{\sigma_1}{\sigma_{nom}} \right) = \left(\frac{\dot{\epsilon}_{02}}{\dot{\epsilon}_{01}} \right)^{\frac{1}{n_1}} \left(\frac{\sigma_2}{\sigma_{nom}} \right)^{\frac{n_2}{n_1}} \quad (7.35)$$

For the case of a pressurised welded plain pipe, shown in Figure 7.8, the rupture lives for the three different approaches were calculated using FE analyses. The weld dimensions are; weld angle, θ_1 , of 15° , weld width, w_0 , of 46mm and HAZ width, h , of 4mm. The PM, HAZ and WM material properties are those of Table 7.1. The mesh used is shown in Figure 7.3. 8-noded and 6-noded axisymmetric isoparametric elements with reduced integration are employed throughout the mesh. In total there are 2020 elements and 4433 nodes in the model. The analysis methods are the same as those used for the homogeneous component.

The same FE model (Figure 7.5) and analysis methods as was used for the homogeneous analysis of Section 7.3 are used for the multi-material welded branched pipe analyses. The dimensions are shown in Table 7.2. The weldment materials used those of Table 7.1. Again, the analysis methods are the same as used for the homogeneous branch pipe.

7.5.3 Results

Table 7.7(a) shows the analysis input data for a series of ten cases to investigate the effect of varying a_1 / a_2 and L_1 / L_2 geometric ratios for the 2-material, 2-bar structure on the predictions obtained using the R5 procedure and the steady-state approach. In order to evaluate the effect of material mismatch, two material combinations are considered, as shown in Table 7.7b, referred to as Case A and Case B. Case A uses parent material properties (PM) for Bar 1 and weld metal properties (WM) for Bar 2, while Case B uses WM properties for Bar 1 and heat-affected zone (HAZ) properties for Bar 2. Thus, Case B has a greater mis-match in creep strength than Case A. The stress and life results for the ten cases are shown in Tables 7.8 and 7.9 for Cases A and B, respectively. Note that the predicted component failure lives, i.e. the lowest of the lives predicted from each of the two materials, along with the material in which the lowest failure life is predicted and the magnitude of the stress concentration factor, λ_i , are shown in addition. The results for each material case are explained below.

Figure 7.9 shows the effects of varying both a_1 / a_2 and L_1 / L_2 for the Case A material combination, on the ratio of R5 to steady-state rupture stress, i.e.

$\sigma_{ref}^R / \sigma_{r(SS)}$. It can be deduced from the graph that the R5 stress predictions diverge from the steady-state predictions when the geometries of the two bars differ significantly. With increasing a_1 / a_2 ratio, for $a_1 / a_2 > 1$, and with increasing L_1 / L_2 ratio, for $L_1 / L_2 > 1$, the R5 approach is seen to both over- and under-predict the rupture stress relative to the steady-state prediction by up to 8%.

Figure 7.10 shows the corresponding set of results for the Case B material combination. This combination gives an even larger difference between the R5 and steady-state rupture stresses. For this case, R5 over-predicts the rupture stress relative to the steady-state with increasing a_1 / a_2 and L_1 / L_2 ratios for $a_1 / a_2 > 1$ and $L_1 / L_2 > 1$ but in this case the over-predictions are larger than those for Case A. For example, for a_1 / a_2 and L_1 / L_2 values of 10, the R5 rupture stress is 24% greater than the steady-state value, as compared to 8% for the Case A material combination. For the cases when $a_1 / a_2 = 1$, the R5 stress is under predicted by about 17% compared to the steady-state stress.

Figures 7.11 and 7.12 display the corresponding R5 life predictions for each material case, respectively, compared to the steady-state predictions. A large R5 stress over-prediction relative to steady-state stress can produce a much smaller R5 life than the steady-state approach, e.g. for a_1 / a_2 and $L_1 / L_2 = 10$ using material Case B, the rupture stress is 24% larger than the steady-state prediction, producing a R5 life approximately 60% lower than the steady-state life. For $a_1 / a_2 = 1$, material Case B, R5 life predictions range from about 60%

to about 100% longer than the steady-state predictions, over the L_1 / L_2 range investigated.

Figure 7.13 and Table 7.10 display the dependency of the predicted R5 failure life on the choice of estimated design life. The graph shows the failure life curves of Bar 1 (PM) and Bar 2 (WM) for the Case 10 and Case A geometry and materials, respectively, which has a low degree of geometric mis-match. The component failure life is the lower life for any given t_r^* value. For the range of t_r^* investigated (i.e. $0.125t_{r(SS)}$ to $4t_{r(SS)}$), the variation of $t_{r(R5)}$ was less than 20%. The corresponding predicted lives varied from 12% shorter to 3% longer than the steady-state life of 3880 hours. The results show that the choice of t_r^* had only a small effect upon the predicted R5 life. The corresponding damage mechanics life for this geometry was 4436 hours (maximum $\omega = 0.98$ in one bar), relative to which the steady-state and R5 approaches are 12.5% lower and between 10% and 23% lower, respectively. The time taken for the damage level in both bars to reach 0.98 from one bar equal to 0.98 and the other less than 0.98 is expected to small compared to the time taken for one bar to reach unity from the undamaged state. Thus, the levels of conservatism stated above for the R5 and steady-state approaches would not be expected to increase significantly. Figure 7.14 shows the effect of t_r^* on the predicted R5 lives for the Case 6 and Case A geometry and materials, respectively, which has a higher degree of geometric mis-match. The largest failure life is 1400 hours and the lowest is 1100 hours for the range of t_r^* investigated. Again, the effect of t_r^* is seen to be relatively small, similar

to that of Case 10 predictions (Figure 7.13), this establishes that the inaccuracy of the R5 predictions for cases with high geometric mis-match, e.g. see Figures 7.12, does not appear to be entirely attributable to the choice of t_r^* .

The dimensions chosen for the comparison of the R5 and steady-state approaches of a 3-material 3-bar structure are shown in Table 7.11 for different geometric ratios. The a_1 / a_2 and L_1 / L_3 values are kept constant, so that the geometric variations of the structure are similar to those of the 2-bar structure. The materials chosen for Bars 1, 2 and 3 are PM, HAZ and WM, respectively. The effect of the variation of L_1 / L_2 and a_1 / a_2 on the R5 and steady-state rupture stresses are shown in Table 7.12 and Figure 7.15. The graph displays the change in stress ratio for the failure dominant HAZ material of Bar 2. The R5 approach always under-predicts the rupture stress relative to the steady-state approach, i.e. $\sigma_{ref}^R / \sigma_{r(SS)} < 1$, for all cases. As the a_1 / a_2 ratio increased from 1 to 4, the $\sigma_{ref}^R / \sigma_{r(SS)}$ ratio decreases significantly, and as the L_1 / L_2 ratio increases from 1 to 4, the $\sigma_{ref}^R / \sigma_{r(SS)}$ ratio increases significantly. The largest under-prediction by the R5 approach is about 34%, corresponding to the $L_1 / L_2 = 1$, $a_1 / a_2 = 4$ case (Case 3 of Table 7.7a). The corresponding effect on predicted failure life is seen to be even more significant, as shown in Figure 7.16 for the R5 to steady-state life ratio for all the cases shown in Table 7.11. The R5 approach significantly over-predicts the failure life relative to the steady-state approach, from about 70% to about 270%.

Figure 7.17 and Table 7.13 show the effect of t_r^* on the R5 failure life for Case 6 of Table 7.11. It is clear that, with varying t_r^* value, the minimum predicted R5 life over the three bars varies significantly, by about 275% from 4100 hours to 11250 hours. This is a more sizeable effect than for the 2-bar structure. The level of over-prediction of the R5 life with respect to the steady-state life is strongly dependent on t_r^* , ranging from 82% longer to about 400% longer.

For the 2-material beam of Figure 7.7, Table 7.14 shows the details for the different geometries considered. The dimensions are the width \bar{b}_1 of material zone 1 and the depth \bar{d} of the beam. Materials 1 and 2 used the HAZ and WM properties of Table 7.1. The effect of the variation of \bar{b}_1/\bar{b}_2 and \bar{d} is shown in Table 7.15 and Figure 7.18. Similar to the 3-bar structure results, the R5 approach under-predicts the rupture stress relative to the steady-state approach. The R5 under-prediction becomes more significant as \bar{b}_1/\bar{b}_2 is decreased and as \bar{d} is increased. When \bar{b}_1/\bar{b}_2 is near unity, the R5 and steady-state stress predictions are within about 20%, but when \bar{b}_1/\bar{b}_2 is decreased, the material 1 zone (HAZ) becomes smaller and the R5 stresses become as much as 45% lower than the steady-state stresses. These levels of R5 stress give longer failure lives, of up to seven times, compared with the steady-state life predictions, as shown in Figure 7.19 for these cases.

Figure 7.20 and Table 7.16 show the effect of t_r^* on the R5 life prediction for the geometry of Case 1 in Table 7.14. The R5 life varies significantly by around 66% across the $t_r^*/t_{r(ss)}$ range, from 3370 hours to 5600 hours, which

is similar to the range observed with the 3-bar structure. The R5 life predictions over the $t_r^* / t_{r(SS)}$ range are generally close to the steady-state life of 4870 hours, for $t_r^* / t_{r(SS)}$ values lower than about 2, with the maximum R5 value being around 15% longer. For $t_r^* / t_{r(SS)}$ values higher than 2, the R5 life becomes increasingly conservative by up to about 40%. However, the differences in life between the two approaches are still relatively small compared to the 2- and 3-bar structure examples.

The welded plain pipe and the welded branched pipe were both subjected to an internal pressure, p_i , of 16.55MPa and a closed end condition. For the welded plain pipe, the steady-state and R5 approaches predicted the failure life to be 7584 hours and 11005 hours, respectively for $t_r^* = t_{r(SS)}$. The R5 approach therefore over-predicts the life by 45% compared to the steady-state approach. The corresponding damage mechanics life was 13500 hours, at which the majority of the HAZ wall had reached a damage level greater than 0.8. Thus, the R5 and steady-state approaches were both conservative by 18% and 44%, respectively, relative to the equivalent damage life prediction. The time taken for the damage level across the HAZ to reach unity from the $t=13500$ hours (damage greater than 0.8 across HAZ) is expected to be small compared to the time taken from the undamaged state to 13500 hours, e.g. see [26.33,34]. Thus, the levels of conservatism stated above for the R5 and steady-state approaches would not be expected to increase significantly if a damage level of unity had been achieved across the HAZ wall. The steady-state and damage

calculations both predicted failure to occur at the same position, in the HAZ material at the inside surface at the PM interface, typical of Type IV cracking.

Table 7.17 and Figure 7.21 display the variation of R5 life with choice of t_r^* . It is clear that there is significant variation in R5 life of up to 130% of the minimum R5 life over the three zones. The lowest value is 5980 hours and the highest value is 13800hours. The latter corresponds to the intersection of the WM, PM and HAZ failure curves. Therefore, the R5 failure life ranges from 21% lower to 82% higher than the steady-state life and from 56% lower to 2% higher than the damage life depending on the t_r^* value. The results show that the R5 approach is generally conservative compared to the CDM approach, except for a small range of t_r^* values, and that they generally lie within about 80% of the steady-state predictions.

For the welded, three-material branched pipe, the steady-state and R5 approaches predicted failure lives of 4113 hours and 5000 hours, respectively, for $t_r^* = t_{r(SS)}$. The R5 approach therefore over-predicts the life by 20% compared to the steady-state result. The steady-state calculation predicted failure to occur in the main pipe side (crotch plane) of the pipe HAZ at the inside bore of the connection. The corresponding damage mechanics life prediction was 8700hours, at which time 40% of the HAZ^P wall had reached a damage level greater than 0.6 and where failure had initiated at the same position as the steady-state prediction, i.e. the inside surface. The R5 and steady-state lives were therefore both conservative by 44% and 53%, respectively, compared to the equivalent damage life. The time taken for the

damage level across the HAZ^P wall to reach unity from the $t=8700$ hours (damage greater than 0.6 across 40% of the HAZ^P wall) is expected to be small compared to the time taken from the undamaged state to 8700 hours. Thus, the levels of conservatism stated above for the R5 and steady-state approaches would not be expected to increase significantly if a damage level of unity had been achieved across the HAZ wall. Figure 7.22 and Table 7.18 display the variation of R5 failure life prediction with the choice of t_r^* , for the branched pipe. The graph shows that the R5 life ranged from 2640 hours to the maximum of 5850 hours for the t_r^* range investigated, i.e. 36% lower to 42% higher, respectively, than the steady-state life. The latter life corresponds to the intersection of the HAZ and PM failure curves. All R5 life predictions are therefore conservative compared to the CDM prediction over the t_r^* range considered.

7.6 Discussion

The application of the R5 rupture reference stress method to single-material components has been shown previously [13,114], to be an adequately conservative and effective method for estimating steady-state stresses and lives. In this Chapter, the R5 rupture life predictions for a 2-bar structure, a pressurised plain and branched pipe were non-conservative relative to the steady-state creep lives by 8%, 4% and 39%, respectively. The steady-state and R5 predictions for the 2-bar, plain and branched pipe components were all conservative relative to the CDM life predictions by at least 17%, 30% and 62%, respectively.

The results of the three approaches when applied to five different multi-material components have been presented. Comparisons of R5 and steady-state lives generally showed that the R5 approach either over- or under-predicted the lives relative to the steady-state approach. The R5 over- and under-predictions were very large in some cases, however relatively close for others. The comparison of the R5 lives for the typical power plant components of a welded plain and branched pipe with the other two approaches were relatively close, at 45% and 20%, respectively, higher compared to the steady-state lives and 18% and 44%, respectively, lower than the CDM predictions. These comparisons used a good estimate for t_r^* value, i.e. equal to the steady-state life prediction. These results are encouraging for the application of the R5 method to realistic power plant applications. The R5 approach under- and over-predicted lives for the 2-bar structure by around 60% and 100%, respectively, compared to steady-state predictions. The R5 life predictions for the 3-bar structure and beam were always higher than the predicted steady-state lives, ranging from 70% to 270% and 20% to 600% longer, respectively. The 2- and 3-bar structures and the 2-material beam case show that significant differences can occur between the R5 and steady-state approaches when considerable geometric and/or material mis-match is present. A possible explanation for the discrepancy between the R5 and steady-state predictions is that for components with large stress concentrations, produced by geometry and/or material mis-match, the effects of rupture properties, or geometries, of one or more zones, on the limit load can become negligible in comparison with the properties or geometries of the other zones. For instance, the reference stress for a very small volume zone is effectively independent of its own

geometry since it has negligible effect on the limit load. This may explain discrepancy between the R5 and the steady-state predictions when failure occurs in small volume zones, with associated large geometric stress concentrations across the zones, and for components with higher levels of material mis-match. Welded plain and branched pipes have small zones, e.g. the HAZ, but relatively accurate R5 lives were predicted for these cases since they did not have large geometric and/or material differences. More investigation is required to understand the discrepancy between the R5 and the steady-state predictions. The use of local collapse limit load solutions to predict multi-material reference stresses may improve the conservatism of the R5 life predictions for some cases compared to using global limit solutions, as used in this investigation. Local collapse denotes the applied load at which a local part of the component's wall thickness reaches its rupture strength stress across the whole wall. Global collapse denotes the applied load at which the whole component reaches its particular rupture strength stress and therefore cannot carry any more load.

For all the components analysed, the effect of the choice of the estimated design life, t_r^* , on the predicted R5 life, was investigated. The majority of these cases showed that the R5 failure life varied significantly over the range of t_r^* values. For instance, the welded plain pipe case gave R5 lives, which varied by up to 130% across the t_r^* range investigated. The results indicated that when the R5 multi-material method is used care must be taken in predicting an adequately conservative failure life by using a range of sensible t_r^* values. Additionally, for the plain and branched pipe cases the longest predicted R5

life, within the t_r^* range analysed, gave good agreement with the CDM predictions.

It should be noted that the difference between the homogeneous and 3-material steady-state life predictions is very small, less than 1%, for the branched pipe considered. This would partly suggest that life predictions of some branched pipe components could be approximated using a homogeneous life prediction only. However, the steady-state calculations in this Chapter used the equivalent stress to predict life and did not incorporate the rupture stress based on a multi-axial rupture behaviour based on the combination of equivalent and maximum principal stresses, via the material constant α , shown in Equation 2.8. Approximating the rupture stress in Equation 2.8 to the equivalent stress leads to a more conservative homogeneous life prediction of 4136 hours. When this is compared to the result for the same case using the PM α value of 0.3, as presented in Chapter 4, a life of 6251 hours is predicted, the consequence is therefore an increase in life of about 50%. The corresponding homogeneous R5 life for this branched pipe was 5754 hours, compared to the homogeneous steady-state life prediction based on just the equivalent stress, the R5 life is non-conservative by about 39%. However, compared to the steady-state homogeneous life prediction based on the use of the rupture stress of Equation 2.8, the R5 prediction is conservative by 8%. This provides additional reassurance that the R5 homogeneous approach predicts, with reasonable accuracy, the lives of single material branched pipes. However, it must be noted that as shown in Chapter 4, the steady-state life using weld properties for the same component is approximately 20% below the

homogeneous life, therefore the R5 homogeneous prediction is non-conservative compared to the 3-material steady-state rupture stress approach. Nevertheless, compared to the comparisons of steady-state and CDM life predictions presented in Chapter 6 the R5 approach is still a conservative approach for the branched pipes considered, since steady-state predictions were conservative by over 50% compared to the CDM approach.

Both single and multi-material applications of the R5 method have the disadvantage that the method doesn't supply information about the material and position of predicted failure. In addition, no information is given on the stress distributions across material boundaries to investigate the effects of material mis-match. These aspects are important for monitoring and assessing component life, and for improving component design. In contrast, steady-state and damage analyses can provide such detailed information.

7.7 Conclusions

The main conclusions drawn from the comparison of the R5 approach with the steady-state and CDM approaches for single and multi-material components are as follows:

1. The homogeneous R5 approach predicted over-estimates of life by 8%, 4% and 39% for the 2-bar structure, plain pipe and branched pipes case, respectively, compared to the steady-state approach. The R5 lives were all conservative compared to the corresponding CDM predicted lives by 17%, 30% and 62%, respectively. The application of the R5 rupture reference

stress approach to the typical power plant components studied is therefore conservative.

2. The multi-material R5 approach predicted conservative lives for the typical three-material power plant components of a welded plain pipe and welded branched pipe compared to the CDM approach. The R5 lives were relatively similar to the steady-state life predictions. The R5 plain pipe and branched pipe lives were conservative by 18% and 44%, respectively, compared to the CDM predictions, and over-predicted lives by 45% and 20%, respectively, compared to steady-state predictions, based on sensible choices of design life, t_r^* .
3. For the simple cases of 2- and 3-bar structures and beams in bending, the multi-material R5 approach gave lives which were either over- or under-predictions compared to the steady-state lives. These R5 lives remained relatively close to the corresponding steady-state and CDM predictions for most cases. However, the R5 life predictions were generally dissimilar to the steady-state lives when failure occurred in materials with high stress concentrations across the zones, produced by material mis-match and/or geometry. It is suggested that the multi-material R5 approach based on the use of a mis-match multi-material limit load be used for components with relatively low geometric stress concentrations and material mis-match. Further investigation is required into the reasons why the R5 predictions are in significant disagreement with the steady-state predictions for some geometric and material cases.
4. The choice of the estimated design lifetime, t_r^* , value used to predict a multi-material R5 failure life was generally found to be important. The

predicted R5 lives varied significantly with the choice of the t_r^* value: therefore it is suggested that a range of t_r^* values be used and the minimum life taken to give an adequately conservative life prediction.

Table 7.1 - Material steady-state and damage constants for the $\frac{1}{2}\text{Cr}\frac{1}{2}\text{Mo}\frac{1}{4}\text{V}:2\frac{1}{4}\text{Cr}1\text{Mo}$ service-aged weldment materials.

Material Constants	PM	HAZ	WM
$A' = A$	6.599×10^{-16}	1.708×10^{-15}	9.718×10^{-15}
$n' = n$	6.108	6.108	5.208
m	0	0	0
M	5.998×10^{-14}	2.500×10^{-9}	8.120×10^{-13}
ϕ	4.50	4.30	4.10
χ	5.767	3.2	4.849

Note: $[\sigma] = \text{MPa}$; $[t] = \text{h}$, $[\dot{\epsilon}_{\min}^c] = \text{h}^{-1}$.

Table 7.2 – Dimensions of the welded branched pipe

D	T	d	t	b_x	b_y	r_1	r_0	a	b	β	θ	h	b_1
355	65	55	12.5	12.5	12.5	10	10	2.5	3	45°	45°	1.5	3

Note: all dimensions in mm, unless otherwise stated.

Table 7.3 – Dimensions and load for the single material 2-bar structure.

a_1 (mm ²)	a_2 (mm ²)	L_1 (mm)	L_2 (mm)	P (kN)
100	100	1000	500	10

Table 7.4 – Single material, 2-bar structure results for the steady-state, R5 reference stress and damage mechanics approaches.

$\sigma_{r(SS)}$ (MPa)	$t_{r(SS)}$ (hours)	$\sigma_{ref(R5)}^R$ (MPa)	$t_{r(R5)}$ (hours)	$t_{r(CDM)}$ (hours)
52.83	1933	52.17	2079	2493

Table 7.5 – Single material, plain pipe results for the steady-state, R5 reference stress and damage mechanics approaches.

$\sigma_{r(SS)}$ (MPa)	$t_{r(SS)}$ (hours)	P_L/σ_y	λ	$\sigma_{ref}^R (R5)$ (MPa)	$t_{r(R5)}$ (hours)	$t_{r(CDM)}$ (hours)
34.80	21464	0.525	1.5	34.59	22226	31600

Table 7.6 – Single material, branched pipe results for the steady-state, R5 reference stress and damage mechanics approaches.

$\sigma_{r(SS)}$ (MPa)	$t_{r(SS)}$ (hours)	P_L/σ_y	λ	$\sigma_{ref}^R (R5)$ (MPa)	$t_{r(R5)}$ (hours)	$t_{r(CDM)}$ (hours)
46.30	4136	0.507	3.62	43.72	5754	15000

Table 7.7(a) – Geometric mis-match cases for 2-material 2-bar structure with varying dimensions and loads calculations.

Case	L_1/L_2	a_1/a_2	P (kN)	σ_{nom} (MPa)
1	1	1	5	25.0
2	1	5	5	41.7
3	1	10	5	45.5
4	5	1	5	25.0
5	5	5	5	41.7
6	5	10	5	45.5
7	10	1	5	25.0
8	10	5	5	41.7
9	10	10	5	45.5
10	2	1	10	50.0

Notes : 1. $a_1 = 100\text{mm}^2$, $L_1 = 1000\text{mm}$ for all cases

2. Young's moduli $E_1 = E_2$ for all cases

Table 7.7(b) – Material mis-match cases for the 2-material 2-bar structure

Case	Bar 1	Bar 2
A	PM	WM
B	WM	HAZ

Table 7.8 – Steady-state (SS) and R5 results for 2-material 2-bar structure, using Case A materials, where $t_r^* = t_{r(SS)}$.

Case	SS rupture stress, $\sigma_{r(SS)}$ (MPa)		R5 rupture stress, σ_{ref}^R (MPa)		Failure life, ($\times 1000$ hours)		λ
	PM	WM	PM	WM	$t_{r(SS)}$	$t_{r(R5)}$	
1	24.54	25.46	24.26	25.97	161 (PM)	171(WM)	1.04
2	40.77	46.15	40.62	47.87	8.61 (PM)	8.79(WM)	1.03
3	44.84	51.62	44.75	53.68	4.98 (PM)	5.03(PM)	1.02
4	21.04	58.96	25.83	28.07	100 (WM)	117(WM)	1.60
5	38.31	58.45	48.36	58.78	3.33 (WM)	3.22(PM)	2.56
6	43.26	67.41	56.11	69.78	1.67 (WM)	1.36(PM)	3.01
7	19.59	30.41	26.15	28.65	79.1 (WM)	106(WM)	1.74
8	37.13	64.37	52.43	64.73	2.08 (WM)	2.02(PM)	3.37
9	42.47	75.35	64.34	81.48	0.97 (WM)	0.62(PM)	4.40
10	43.84	56.66	46.53	56.30	3.88 (WM)	4.00(WM)	1.21

Table 7.9 – Steady-state (SS) and R5 results for 2-material 2-bar structure.

using Case B materials, where $t_r^* = t_{r(SS)}$.

Case	SS rupture stress, $\sigma_{r(SS)}$ (MPa)		R5 rupture stress, σ_{ref}^R (MPa)		Failure life. (×1000 hours)		λ
	WM	HAZ	WM	HAZ	$t_{r(SS)}$	$t_{r(R5)}$	
1	27.54	22.46	33.97	18.68	19.0(HAZ)	34.1(HAZ)	1.41
2	43.38	33.09	47.29	26.67	5.48 (HAZ)	7.78 (HAZ)	1.49
3	46.49	35.10	50.11	32.08	4.54 (HAZ)	6.05 (HAZ)	1.51
4	24.00	26.00	36.94	21.36	11.9 (HAZ)	22.3 (HAZ)	2.27
5	41.68	41.62	62.40	42.25	2.63 (HAZ)	2.43 (WM)	4.10
6	45.51	44.86	71.84	49.98	2.07 (HAZ)	1.23 (WM)	5.10
7	22.47	27.53	37.39	22.04	9.88 (HAZ)	20.1 (HAZ)	2.45
8	40.80	45.82	69.09	48.42	1.94 (HAZ)	1.48 (WM)	5.40
9	45.02	49.78	85.69	61.77	1.48 (HAZ)	0.520 (WM)	7.40
10	54.78	45.22	63.64	44.43	2.02 (HAZ)	2.14 (HAZ)	1.62

Table 7.10 – Results for the variation of t_r^* for the 2-material 2-bar structure using Case 10 geometry and Case A materials, where $t_{r(CDM)} = 4436$ hours and $t_{r(SS)} = 3880$ hours (failure in WM).

$t_r^* =$	t_r^* ($\times 1000$ hours)	R5 rupture stress (MPa)		R5 life ($\times 1000$ hours)		λ
		σ_{ref}^R PM	σ_{ref}^R WM	$t_{r(R5)}$ PM	$t_{r(R5)}$ WM	
$0.125 t_{r(SS)}$	0.49	44.61	57.77	5.13	3.53	1.18
$0.25 t_{r(SS)}$	0.97	45.25	57.28	4.72	3.68	1.19
$t_{r(SS)}$	3.88	46.53	56.30	4.02	4.00	1.21
$2 t_{r(SS)}$	7.76	47.18	55.81	3.71	4.18	1.23
$4 t_{r(SS)}$	15.52	47.85	55.32	3.42	4.36	1.24

Table 7.11 – Geometric mis-match cases for 3-material 3-bar structure with varying dimensions.

Case	L_1/L_2	a_1/a_2	σ_{nom} (MPa)
1	1	1	25.0
2	1	2	30.0
3	1	4	33.3
4	2	1	25.0
5	2	2	30.0
6	2	4	33.3
7	4	1	25.0
8	4	2	30.0
9	4	4	33.3

Notes : 1. $a_1 = 100\text{mm}^2$, $L_1=1000\text{mm}$, $P = 7.5\text{kN}$ for all cases

2. Young's moduli $E_1=E_2=E_3$ for all cases

3. $L_1/L_3 = 1$, $a_1/a_3 = 1$ for all cases

4. Materials of Bar 1, 2 and 3 are PM, HAZ and WM, respectively

Table 7.12 – Steady-state (SS) and R5 results for 3-material 3-bar structure.

where $t_r^* = t_{r(SS)}$.

Case	SS rupture stress, $\sigma_{r(SS)}$ (MPa)			R5 rupture stress, σ_{ref}^R (MPa)			Failure life ($\times 1000$ hours)		λ
	PM	HAZ	WM	PM	HAZ	WM	$t_{r(SS)}$	$t_{r(R5)}$	
1	25.84	22.12	27.05	28.70	18.01	32.92	19.9 (HAZ)	38.4(HAZ)	1.47
2	36.71	31.46	40.89	30.81	22.63	36.66	6.45 (HAZ)	18.5 (HAZ)	1.39
3	46.26	39.59	53.54	32.28	26.23	39.35	3.09 (HAZ)	11.5 (HAZ)	1.32
4	25.00	23.97	26.02	25.84	19.99	35.56	15.4 (HAZ)	27.5 (HAZ)	2.16
5	35.94	34.45	39.82	33.77	25.79	40.56	4.82 (HAZ)	12.2 (HAZ)	2.25
6	45.62	43.73	52.67	25.87	30.48	44.19	2.25 (HAZ)	7.13 (HAZ)	2.30
7	24.14	25.92	24.96	32.64	21.97	38.05	12.0 (HAZ)	20.3 (HAZ)	2.81
8	35.05	37.64	38.67	37.27	29.62	45.19	3.63 (HAZ)	7.81 (HAZ)	3.28
9	44.91	48.23	51.72	41.10	36.48	51.16	1.64 (HAZ)	4.01 (HAZ)	3.70

Table 7.13 – Results for the variation of t_r^* for the 3-material 3-bar structure using Case 6 geometry, where $t_{r(SS)} = 2250$ hours (failure in HAZ).

$t_r^* =$	t_r^* ($\times 1000$ hours)	R5 rupture stress, σ_{ref}^R (MPa)			R5 life, $t_{r(R5)}$ ($\times 1000$ hours)			λ
		PM	HAZ	WM	PM	HAZ	WM	
$0.125 t_{r(SS)}$	2.81	31.94	36.23	42.12	35.2	4.10	16.3	1.84
$0.25 t_{r(SS)}$	5.63	33.19	34.19	42.79	28.2	4.94	15.1	1.98
$t_{r(SS)}$	2.25	35.87	30.48	44.19	18.0	7.13	12.95	2.30
$2 t_{r(SS)}$	4.50	37.34	28.79	44.96	14.3	8.56	11.91	2.48
$4 t_{r(SS)}$	9.00	38.87	27.23	45.75	11.3	10.2	10.95	2.69

Table 7.14 – Geometric mis-match cases for 2-material beam in pure bending with varying dimensions.

Case	\bar{b}_1 / \bar{b}_2	\bar{d} (mm)	σ_{nom} (MPa)
1	0.83	10	20.0
2	0.83	15	8.9
3	0.83	20	5.0
4	0.50	10	33.3
5	0.50	15	14.8
6	0.50	20	8.3
7	0.33	10	50.0
8	0.33	15	22.2
9	0.33	20	12.5
10	0.17	10	100.0
11	0.17	15	44.4
12	0.17	20	25.0

Notes :

1. $\bar{b}_2 = 60\text{mm}$ and $\hat{M} = 50\text{Nm}$ for all cases
2. Young's moduli $E_1 = E_2$ for all cases
3. Materials of Material 1 and 2 are HAZ and WM, respectively.

Table 7.15 – Steady-state (SS) and R5 results for 2-material beam in pure bending, where $t_r^* = t_{r(SS)}$.

Case	SS rupture stress, $\sigma_{r(SS)}$ (MPa)		R5 rupture stress, σ_{ref}^R (MPa)		Failure life ($\times 1000$ hours)		λ
	HAZ	WM	HAZ	WM	$t_{r(SS)}$	$t_{r(R5)}$	
1	34.33	45.30	32.97	51.89	4.87 (HAZ)	5.55 (HAZ)	1.64
2	15.67	18.06	13.85	28.47	60.0 (HAZ)	89.1 (HAZ)	1.76
3	9.18	8.80	7.45	18.37	332 (HAZ)	646 (HAZ)	1.87
4	31.58	41.07	28.65	46.39	6.37 (HAZ)	8.70 (HAZ)	1.96
5	15.06	17.23	11.25	23.43	68.1 (HAZ)	173 (HAZ)	2.31
6	8.88	9.27	5.78	14.41	370 (HAZ)	1460 (HAZ)	2.62
7	30.46	39.37	26.84	44.01	7.15 (HAZ)	10.7 (HAZ)	2.13
8	14.79	16.87	10.34	21.66	72.2 (HAZ)	227 (HAZ)	2.60
9	8.84	9.23	5.25	13.12	374 (HAZ)	1985 (HAZ)	3.00
10	29.47	37.87	25.33	41.84	7.94 (HAZ)	13.1 (HAZ)	2.32
11	14.54	16.54	9.59	20.21	76.1 (HAZ)	289 (HAZ)	2.89
12	8.80	9.18	4.89	12.05	332 (HAZ)	2500 (HAZ)	3.33

Table 7.16 – Results for the variation of t_r^* for the 2-material beam in pure bending using Case 1 geometry, where $t_{r(SS)} = 4870$ hours (failure in HAZ).

$t_r^* =$	t_r^* ($\times 1000$ hours)	R5 rupture stress, σ_{ref}^R , (MPa)		R5 life, $t_{r(R5)}$ ($\times 1000$ hours)		λ
		HAZ	WM	HAZ	WM	
$0.125t_{r(SS)}$	6.09	34.29	43.27	4.89	14.3	1.56
$0.25t_{r(SS)}$	1.22	33.86	45.99	5.09	10.7	1.59
$t_{r(SS)}$	4.87	32.97	51.89	5.55	5.94	1.64
$2t_{r(SS)}$	9.74	32.47	54.97	5.83	4.49	1.70
$4t_{r(SS)}$	19.48	32.00	58.34	6.1	3.37	1.71

Table 7.17 – Results for the variation of t_r^* for the 3-material welded plain pipe, where $t_{r(SS)} = 7584$ hours and $t_{r(CDM)} = 13500$ hours (both HAZ failure).

$t_r^* =$ ($\times 1000$ hours)	SS rupture stress, $\sigma_{r(SS)}$ (MPa)			R5 rupture stress, σ_{ref}^R (MPa)			R5 life, $t_{r(R5)}$ ($\times 1000$ hours)			λ
	PM	HAZ	WM	PM	HAZ	WM	PM	HAZ	WM	
1.14	34.8	29.9	38.2	34.51	32.21	43.46	22.5	5.98	14.0	1.61
4.57				36.27	27.92	43.64	16.9	9.44	13.8	1.95
9.15				37.11	25.91	43.63	14.8	11.9	13.7	2.15
15.64				37.69	24.45	43.57	13.5	14.4	13.9	2.30
36.59				39.08	22.53	43.92	11.0	18.8	13.4	2.57

Table 7.18 – Results for the variation of t_r^* for the 3-material welded branched pipe, where $t_{r(SS)} = 4113$ hours and $t_{r(CDM)} = 8700$ hours (both HAZ^P failure).

$t_r^* =$ (×1000 hours)	SS rupture stress, $\sigma_{r(SS)}$ (MPa)			R5 reference rupture stress, σ_{ref}^R (MPa)			R5 life, $t_{r(R5)}$ (×1000 hours)			λ
	PM	HAZ	WM	PM	HAZ	WM	PM	HAZ	WM	
0.95	46.3	36.2	47.5	43.68	41.58	55.29	5.79	2.64	4.37	3.62
1.90				43.67	37.75	54.02	5.79	3.60	4.89	3.62
3.79				43.63	34.25	52.77	5.82	4.91	5.48	3.62
7.59				43.59	31.08	51.55	5.85	6.70	6.14	3.61
15.18				43.63	28.26	50.46	5.82	9.08	6.8	3.61
30.36				43.72	25.70	49.38	5.76	12.3	7.56	3.61

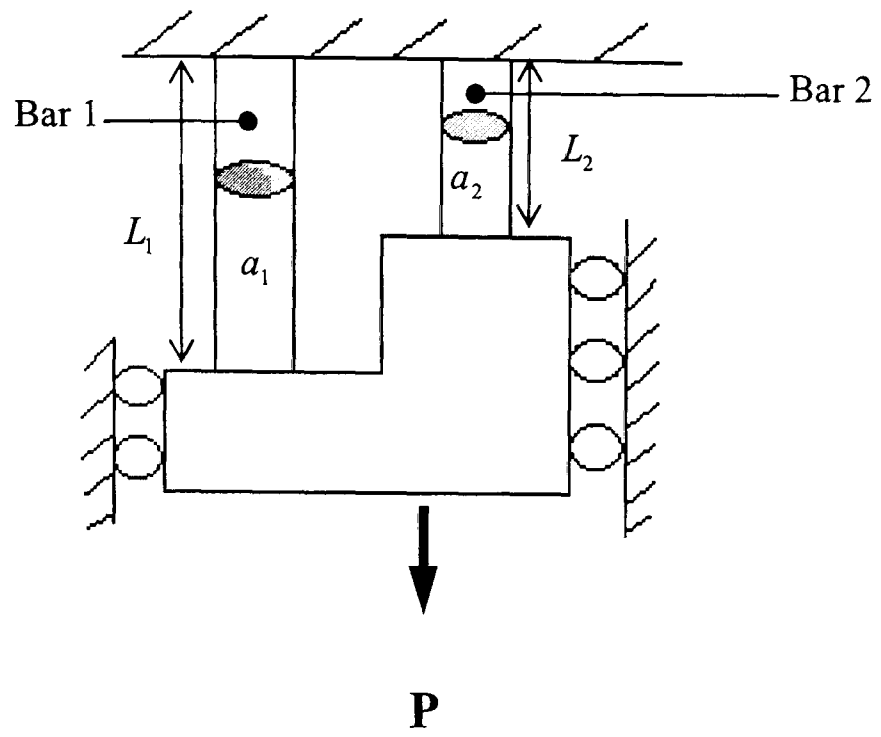


Figure 7.1. Schematic of 2-bar structure

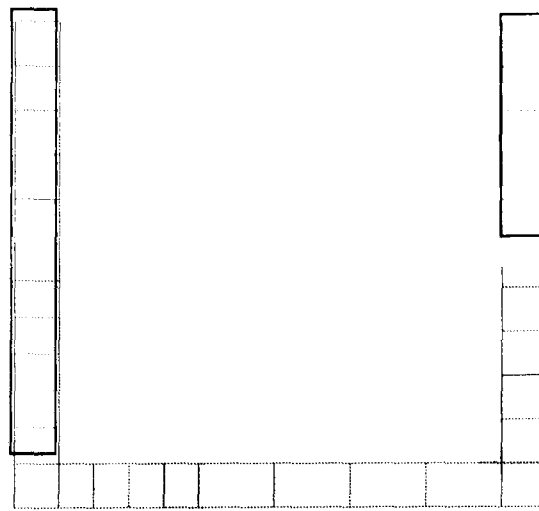


Figure 7.2. Finite element mesh of the 2-bar structure

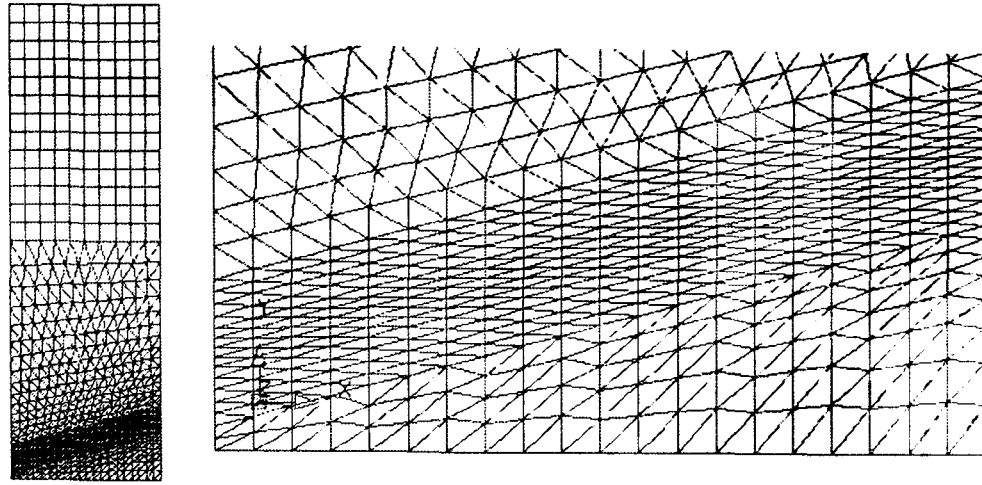


Figure 7.3. Axisymmetric finite element mesh of the plain pipe with weldment

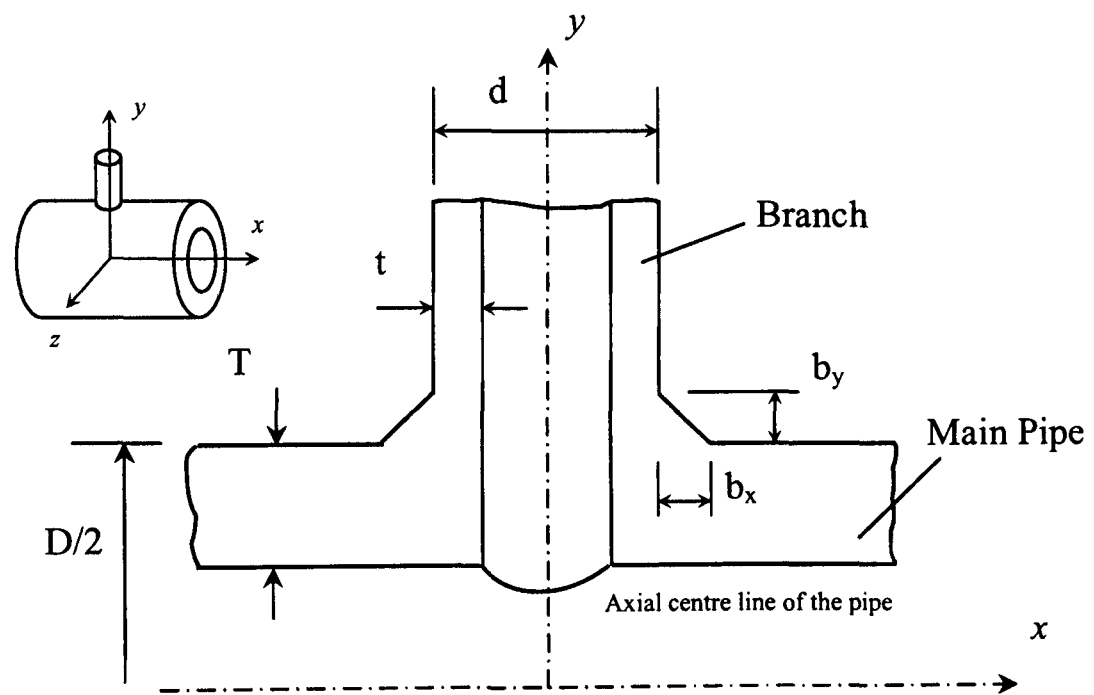


Figure 7.4 (a). Geometry and dimensions of the welded branched pipe.

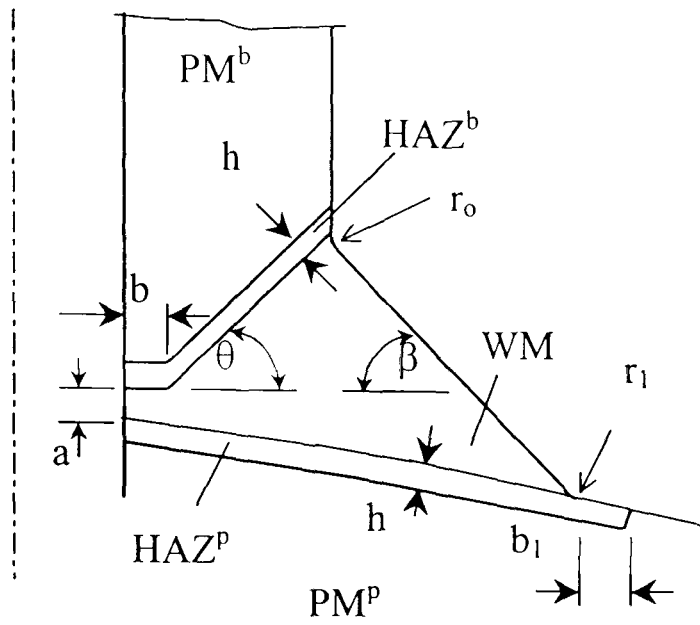
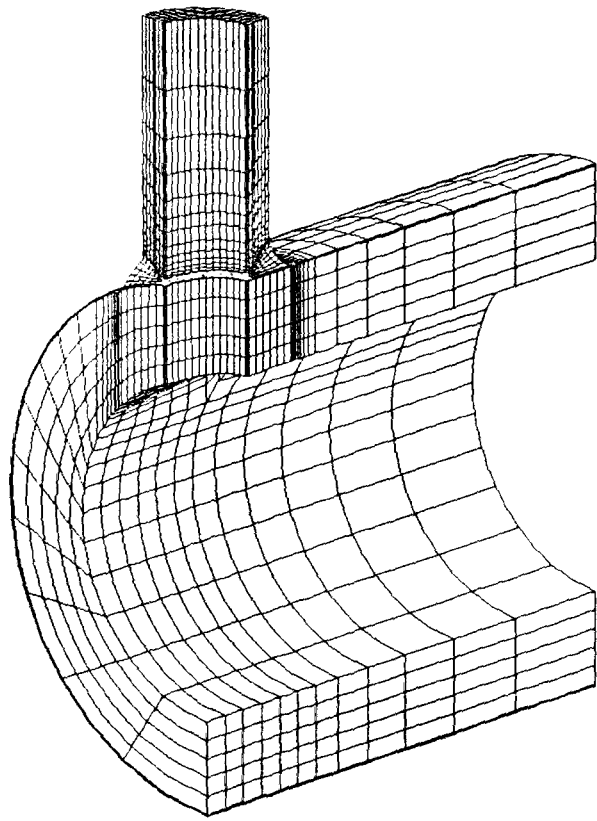
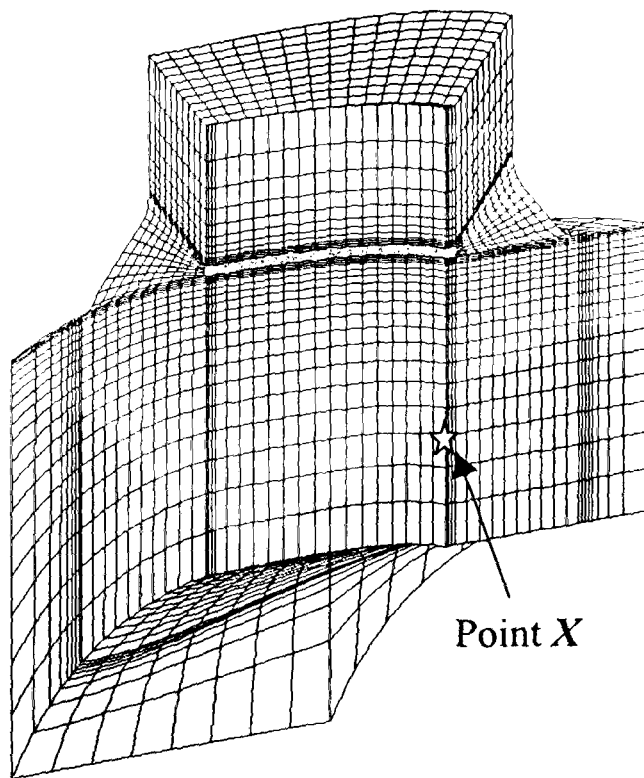


Figure 7.4 (b). Geometry and dimensions of the branched pipe weld region.



(a)



(b)

Figure 7.5. (a) Global-model and (b) Sub-model finite element meshes for the branched pipe geometry.

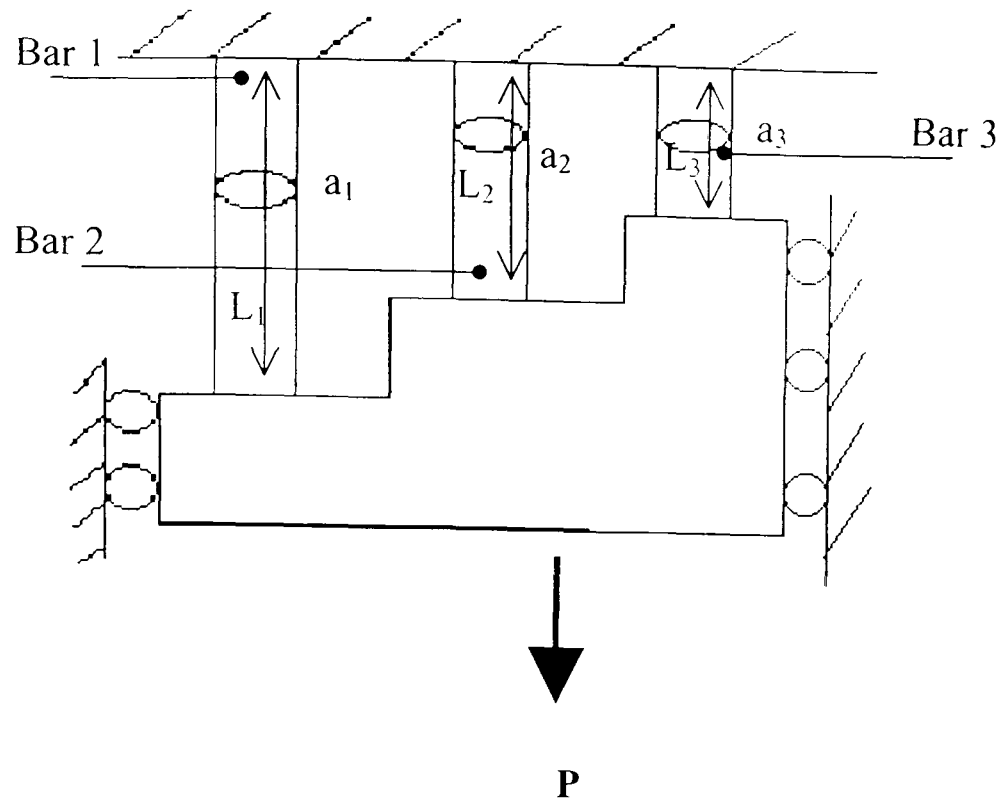


Figure 7.6. Schematic of 3-bar structure

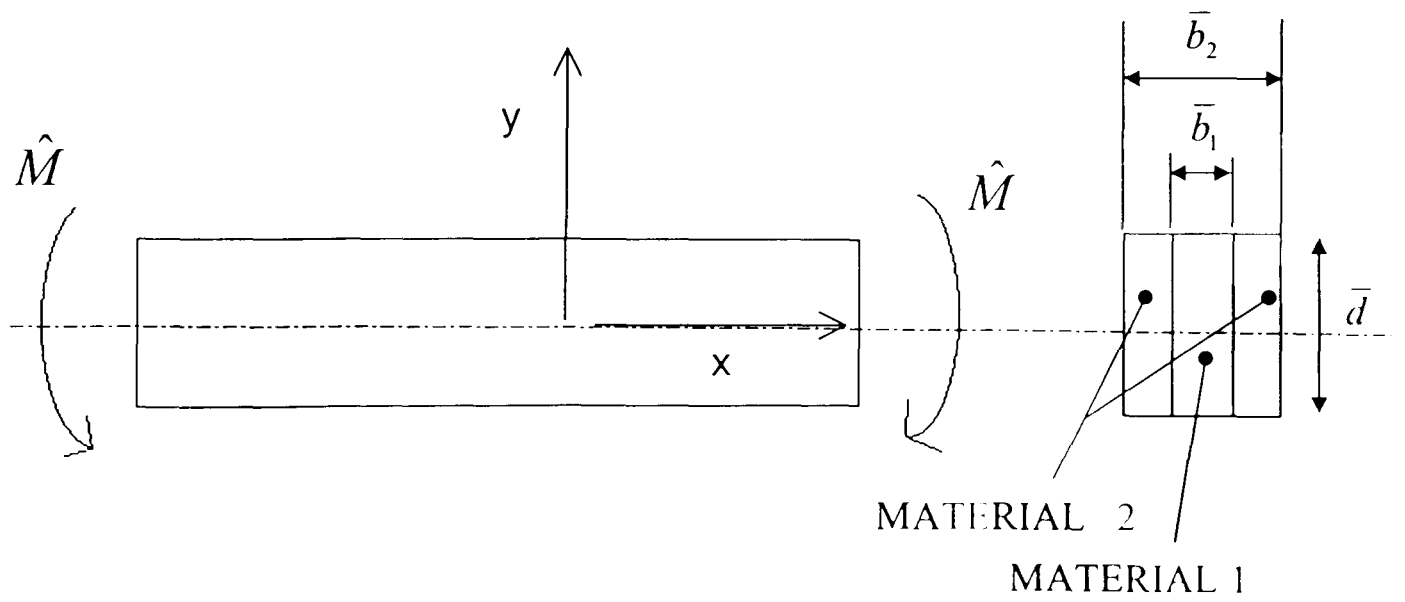


Figure 7.7. Schematic of 2-material beam in pure bending

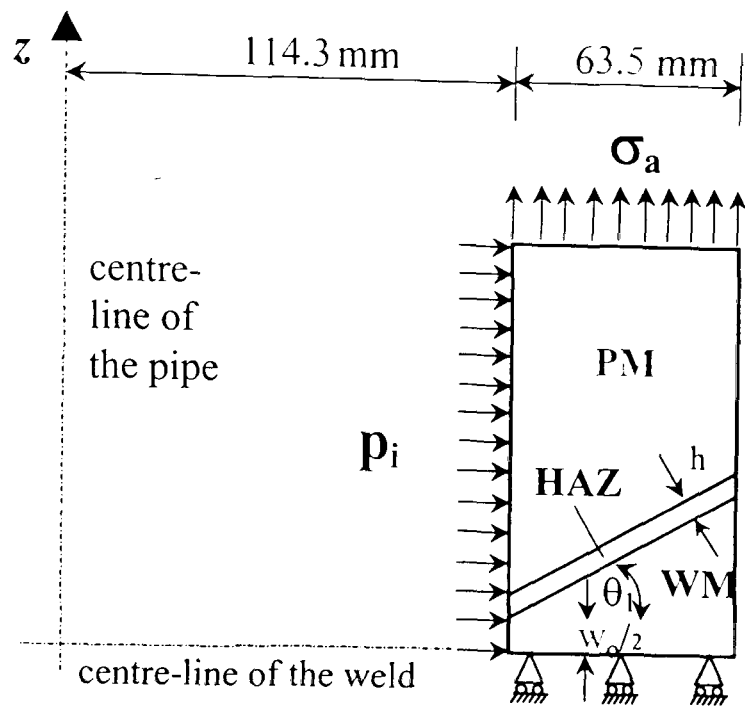


Figure 7.8. Axisymmetric geometry of the pipe weldment with a 15° weld angle and 4mm HAZ width loaded by internal pressure and axial end stress.

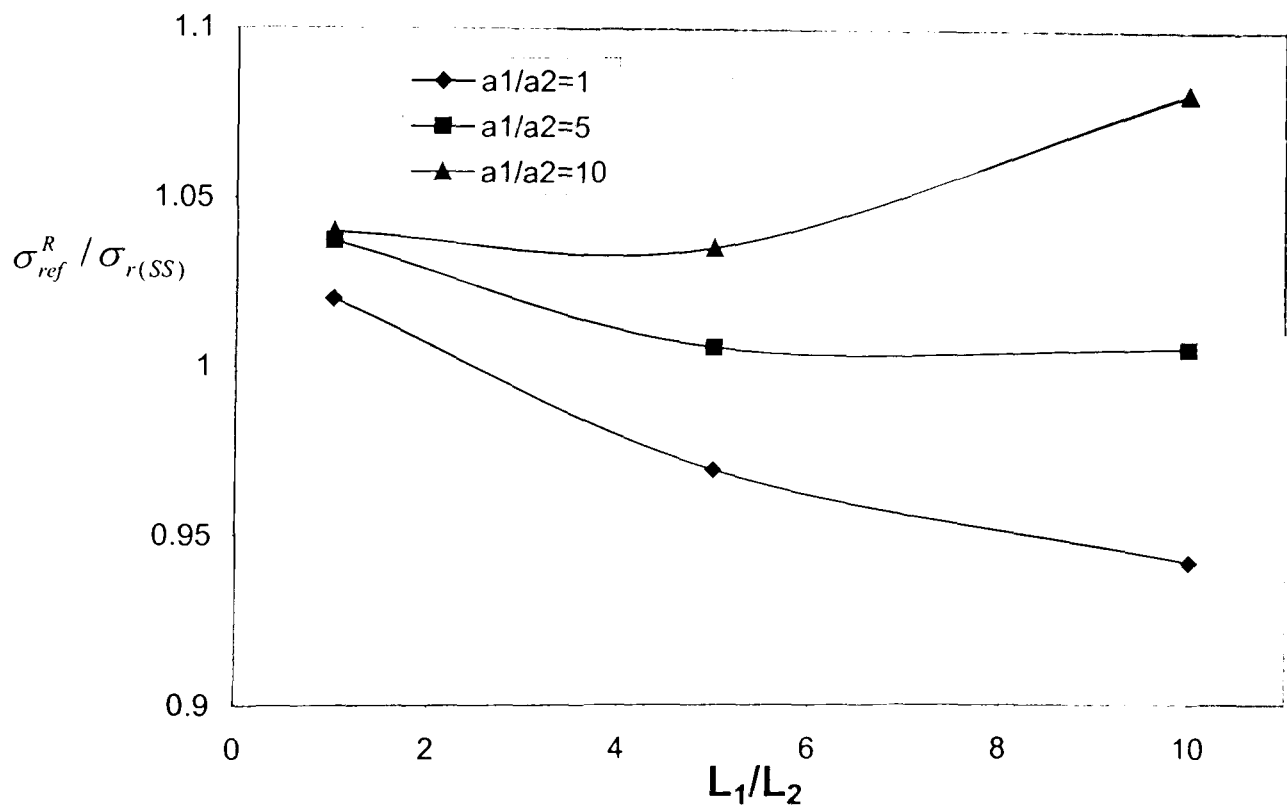


Figure 7.9. Effect of a_1/a_2 and L_1/L_2 ratios on R5 versus steady-state rupture stress ratio within Bar 2 (WM) for material Case A 2-material 2-bar structure,

$$t_r^* = t_{r(ss)}$$

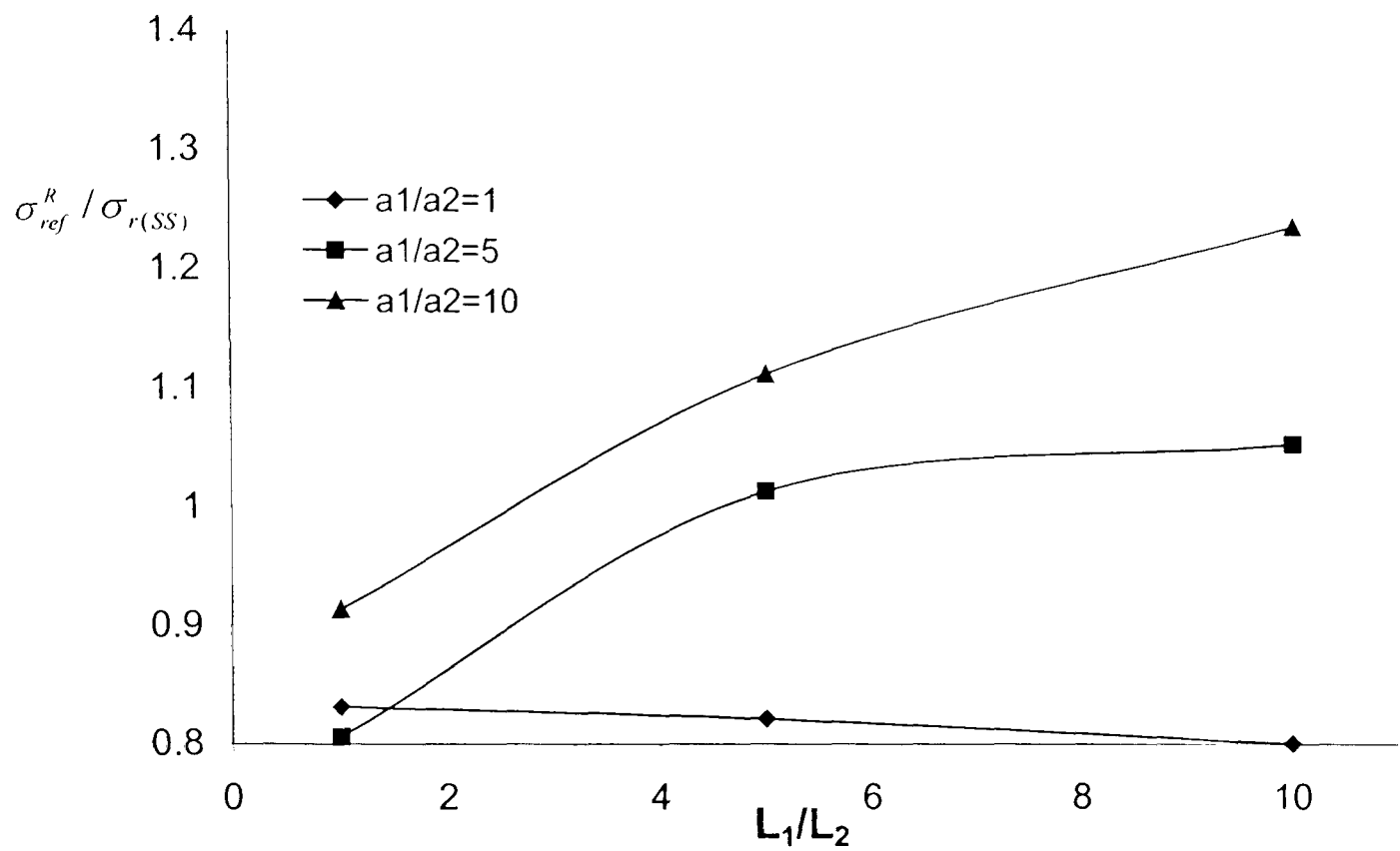


Figure 7.10. Effect of a_1/a_2 and L_1/L_2 ratios on R5 versus steady-state rupture stress ratio within Bar 2 (HAZ) for material Case B 2-material 2-bar structure,

$$t_r^* = t_{r(ss)}$$

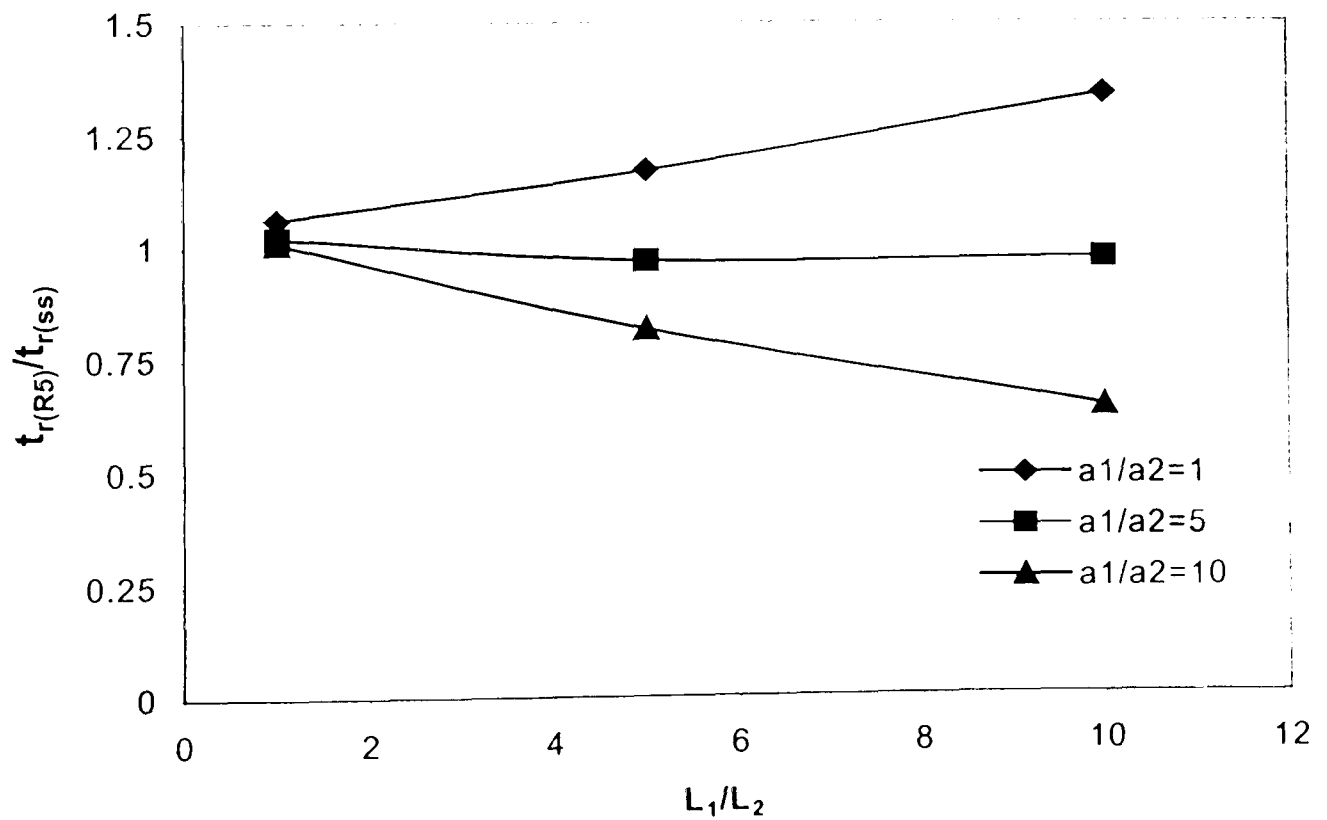


Figure 7.11. Effect of a_1/a_2 and L_1/L_2 ratios on R5 versus steady-state rupture life ratio for material Case A 2-material 2-bar structure, $t_r^* = t_{r(ss)}$

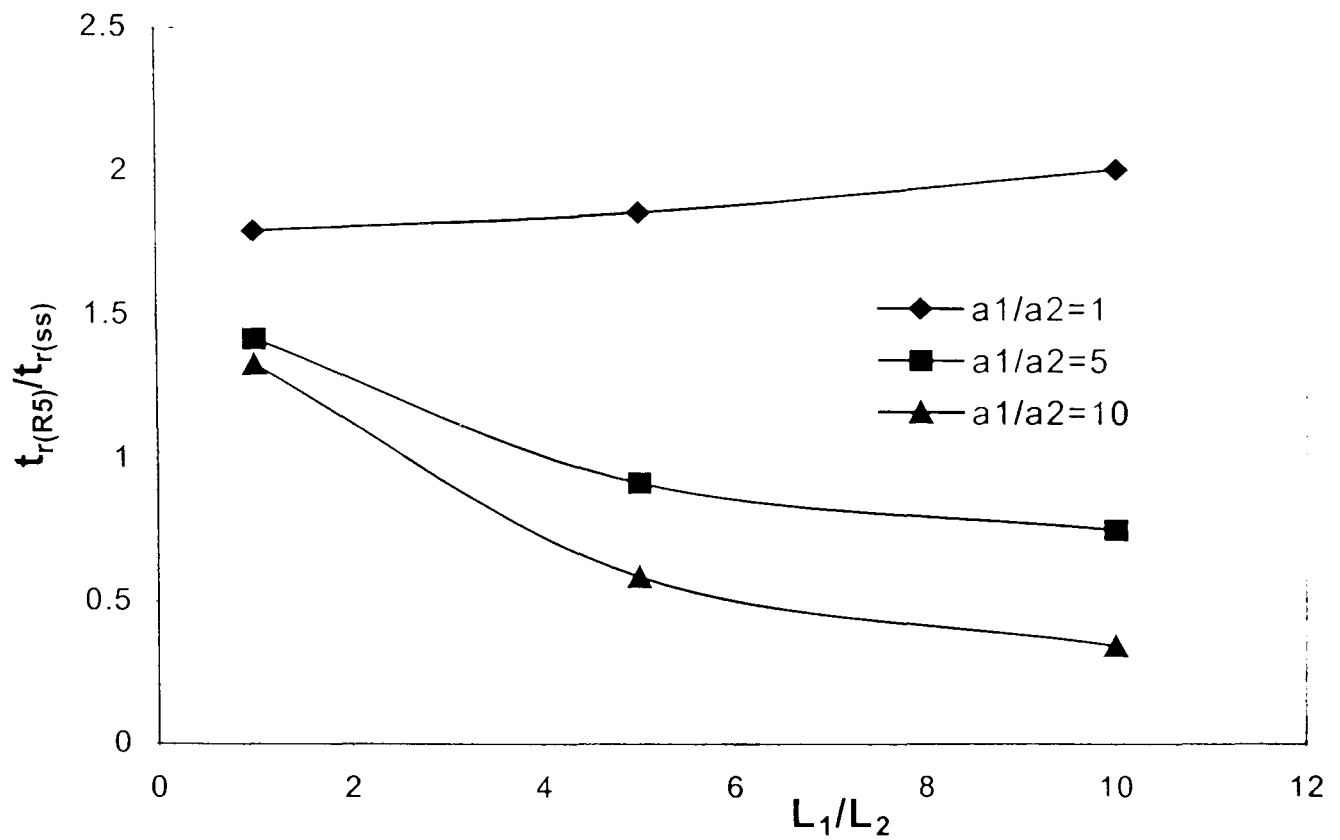


Figure 7.12. Effect of a_1/a_2 and L_1/L_2 ratios on R5 versus steady-state rupture life ratio for material Case B 2-material 2-bar structure, $t_r^* = t_{r(ss)}$.

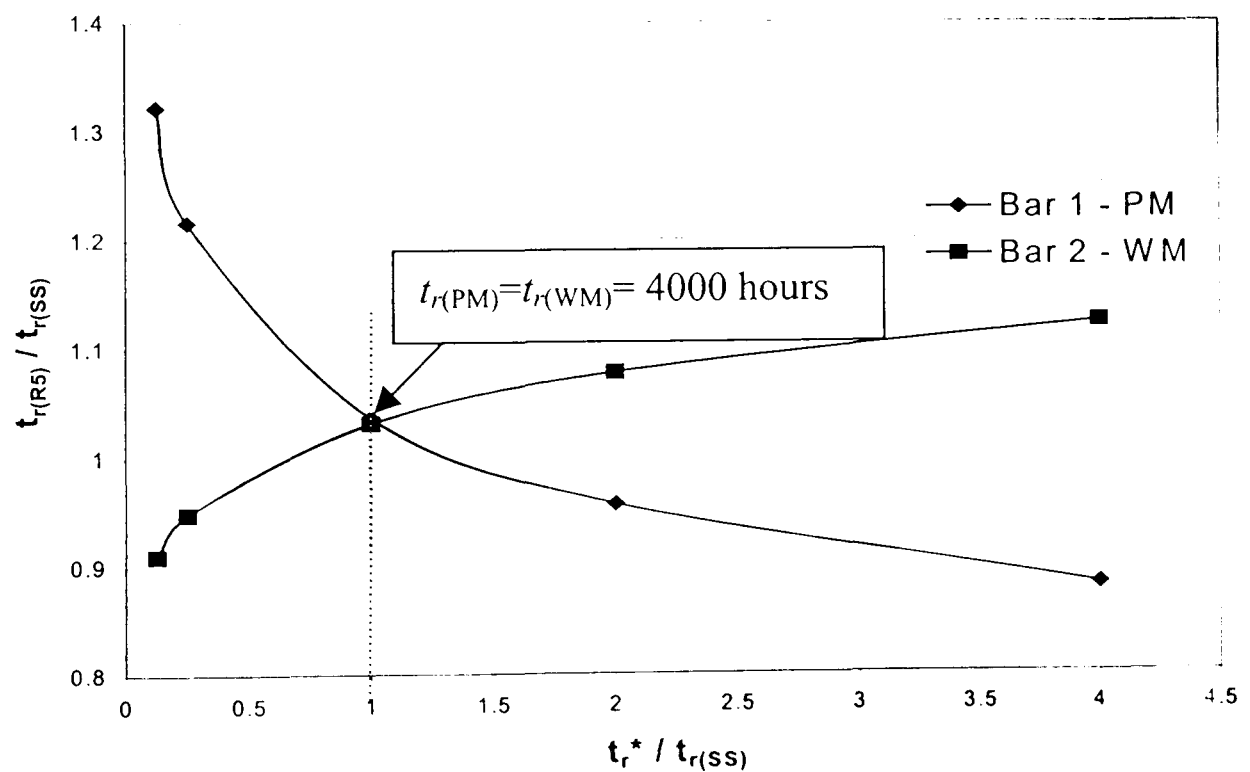


Figure 7.13. Effect of choice of t_r^* value on R5 life for 2-material, 2-bar structure with Case 10 geometry and Case A material combination, where $t_{r(ss)} = 3880$ hours.

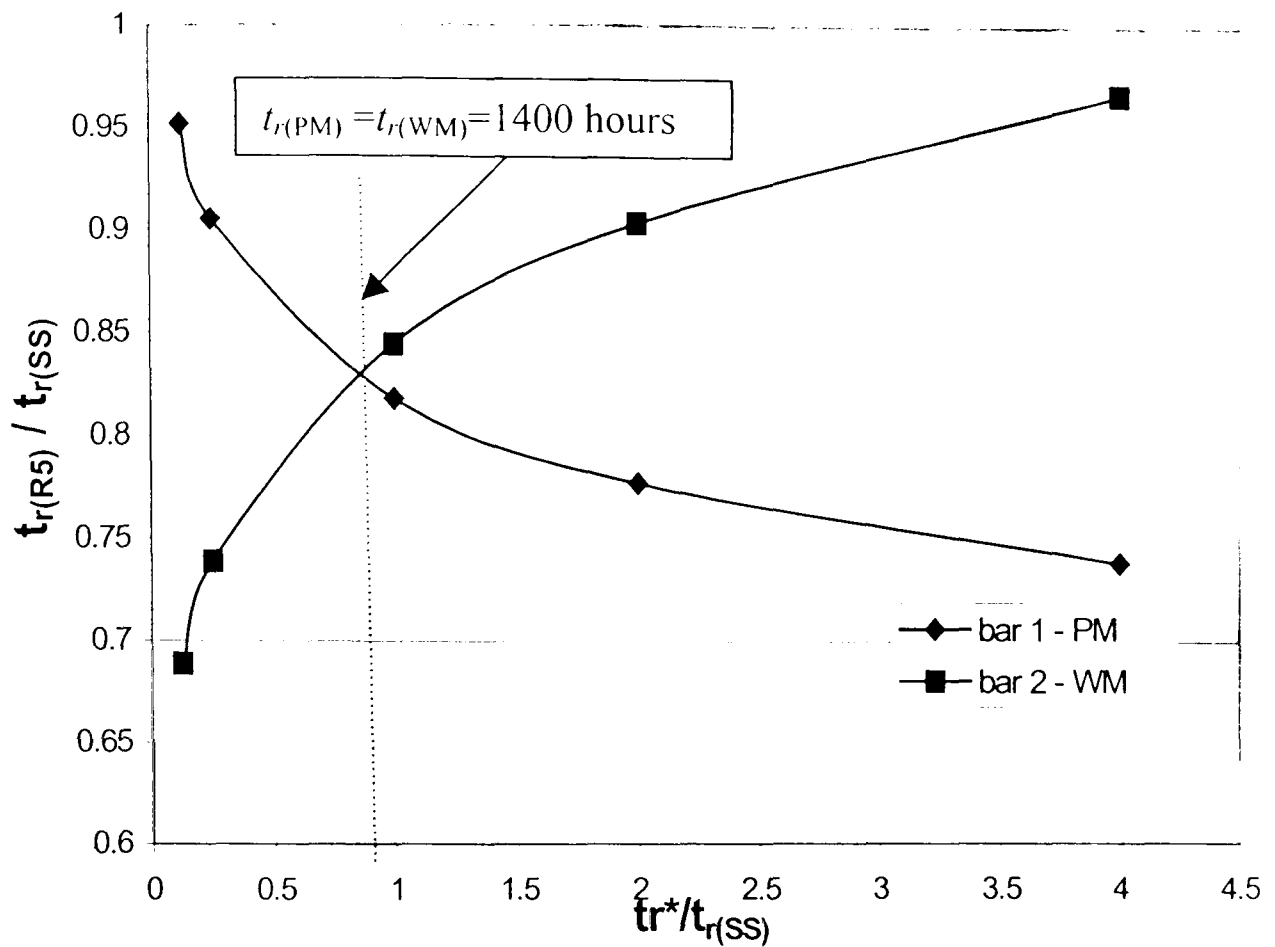


Figure 7.14. Effect of choice of t_r^* value on R5 life for 2-material, 2-bar structure with Case 6 geometry and Case A material combination, where $t_{r(SS)} = 1670$ hours.

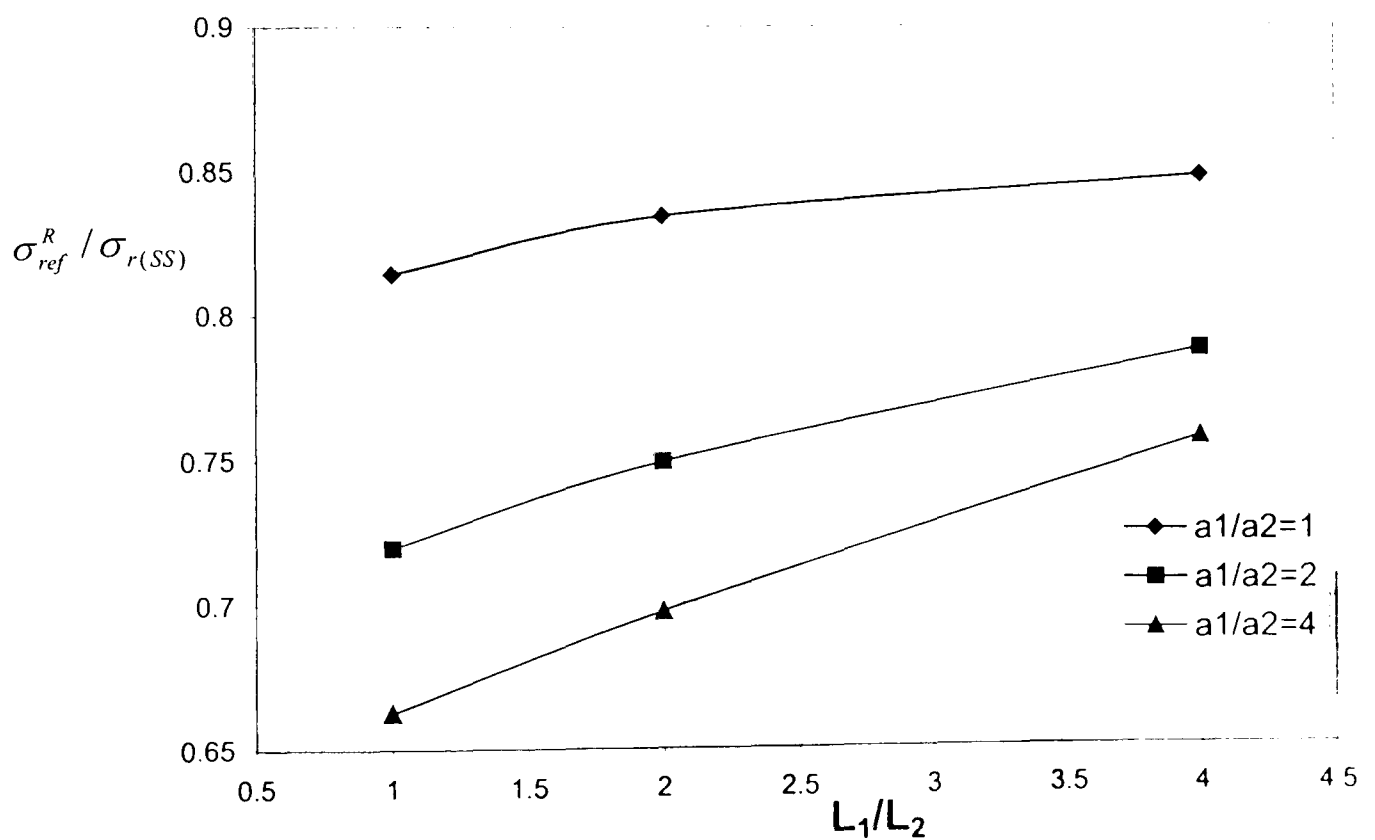


Figure 7.15. Effect of a_1/a_2 and L_1/L_2 ratios on R5 versus steady-state rupture stress ratio within Bar 2 (HAZ) for the 3-material 3-bar structure, $t_r^* = t_{r(SS)}$

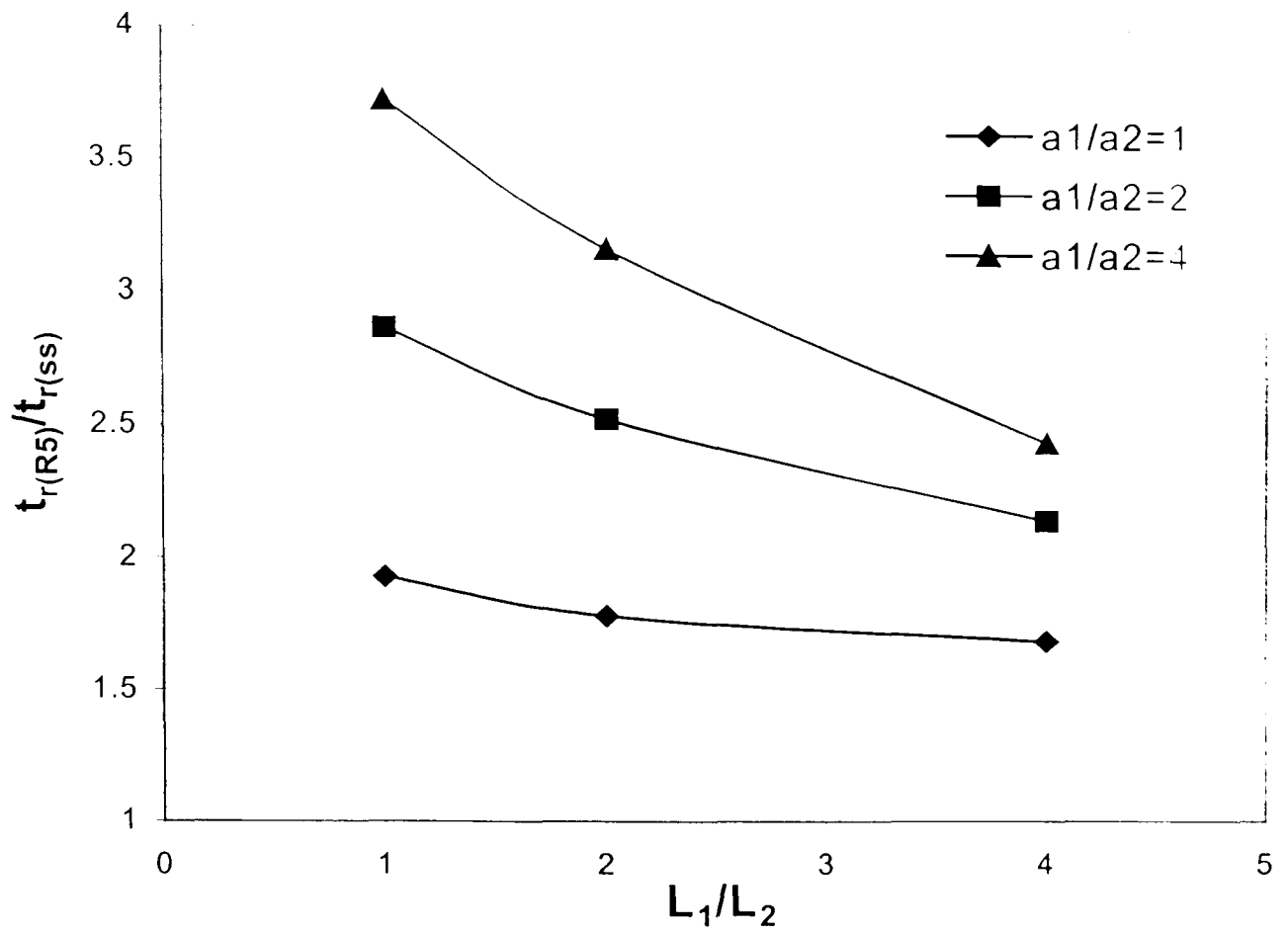


Figure 7.16. Effect of a_1/a_2 and L_1/L_2 ratios on R5 versus steady-state rupture life ratio for the 3-material 3-bar structure, $t_r^* = t_{r(ss)}$

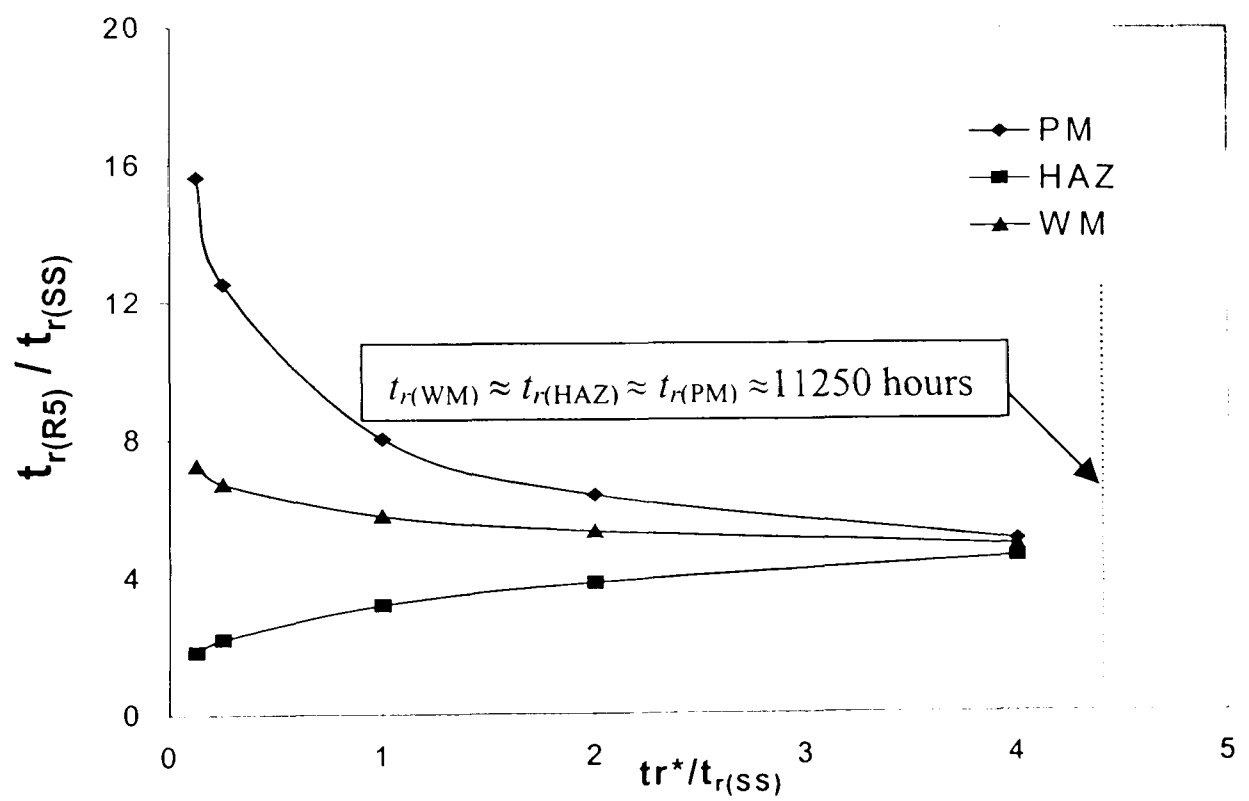


Figure 7.17. Effect of choice of t_r^* value on R5 life for 3-material, 3-bar structure with Case 6 geometry, where $t_{r(ss)} = 2250$ hours.

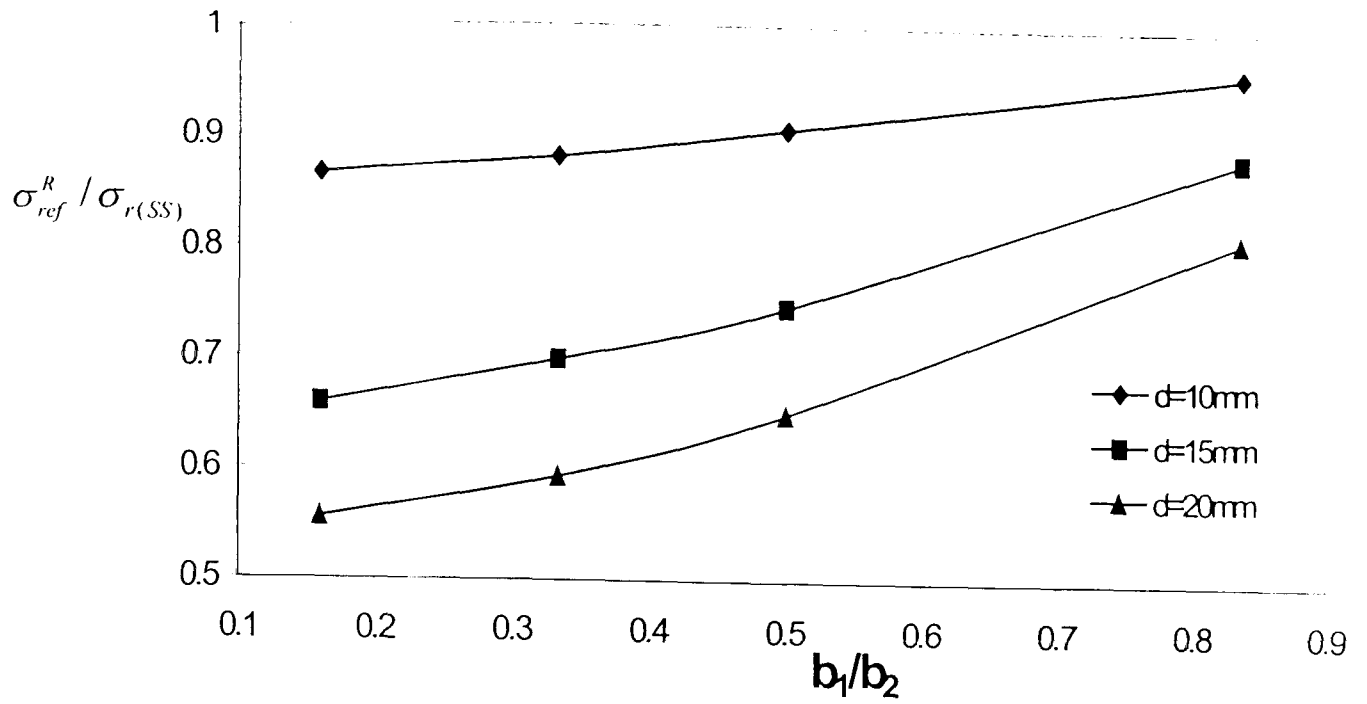


Figure 7.18. Effect of \bar{b}_1/\bar{b}_2 ratio and \bar{d} on R5 versus steady-state rupture stress ratio within Material 1 (HAZ) for 2-material beam in pure bending, $t_r^* = t_{r(ss)}$.

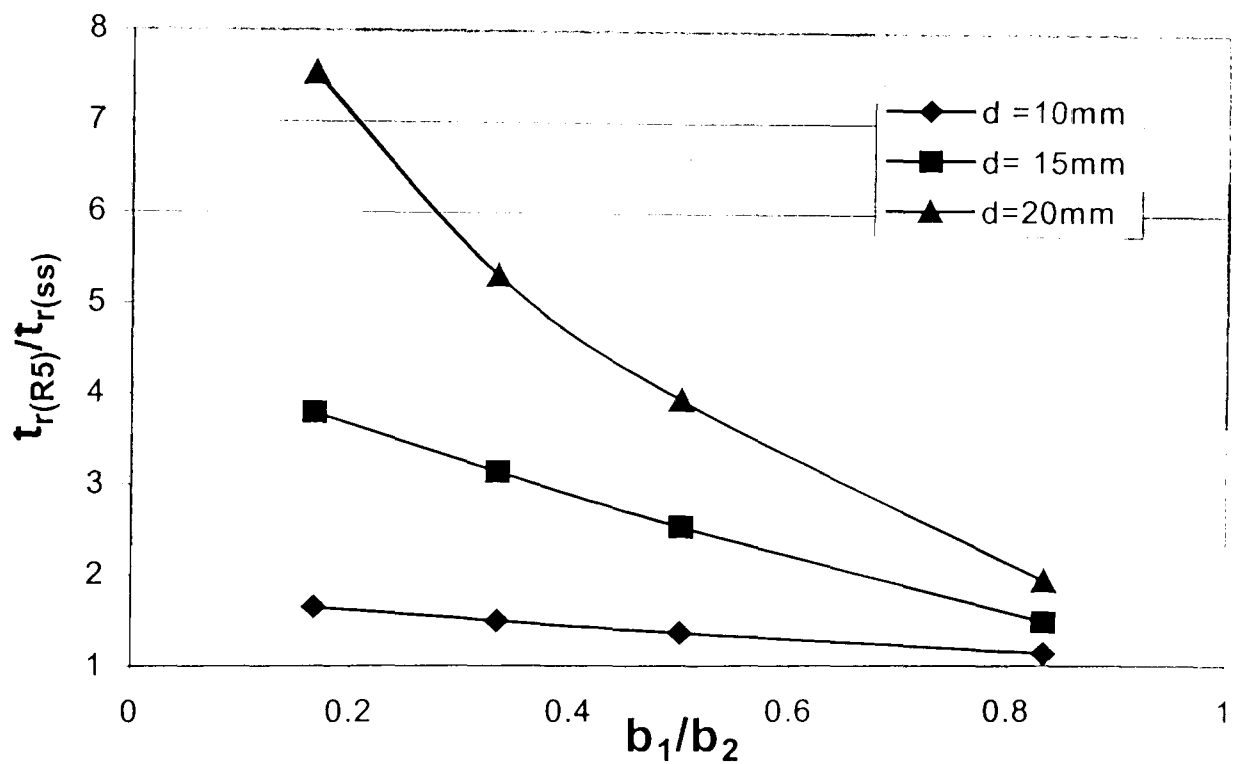


Figure 7.19. Effect of \bar{b}_1/\bar{b}_2 ratio and \bar{d} on R5 versus steady-state rupture life ratio for the 2-material beam in bending, $t_r^* = t_{r(ss)}$.

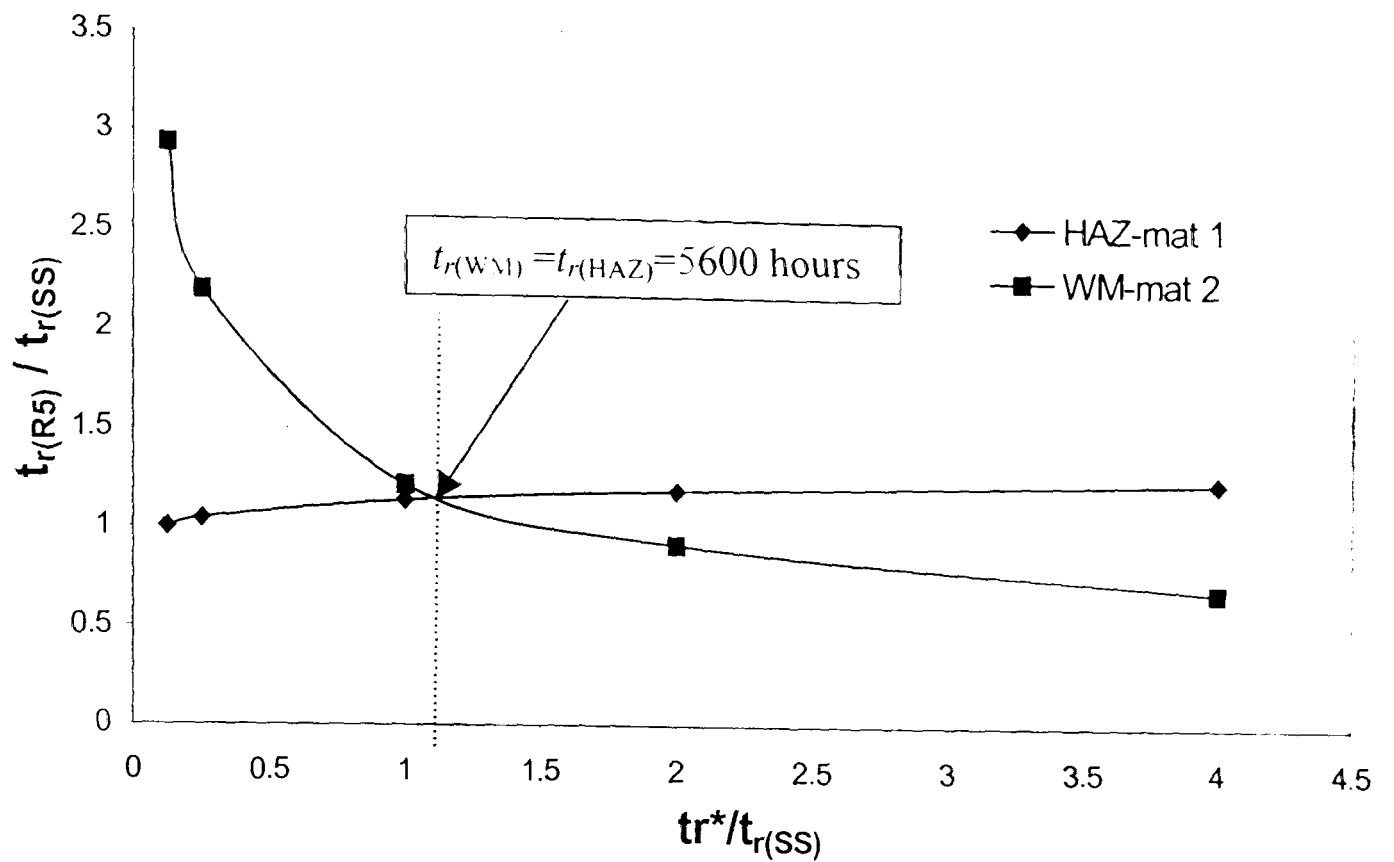


Figure 7.20. Effect of choice of t_r^* value on R5 life for 2-material, beam with Case 1 geometry, where $t_{r(SS)} = 4870$ hours.

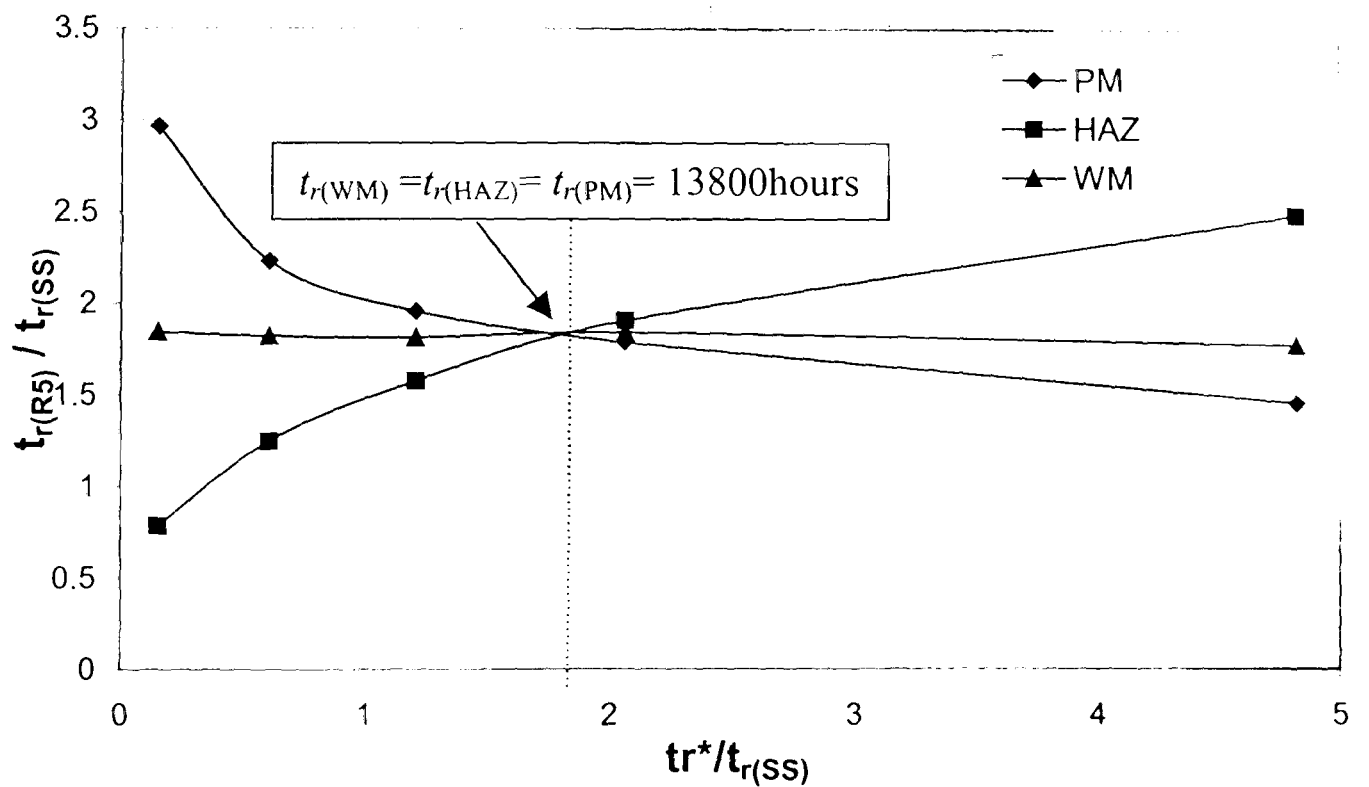


Figure 7.21. Effect of choice of t_r^* value on R5 life for 3-material, welded plain pipe, where $t_{r(SS)} = 7584$ hours.

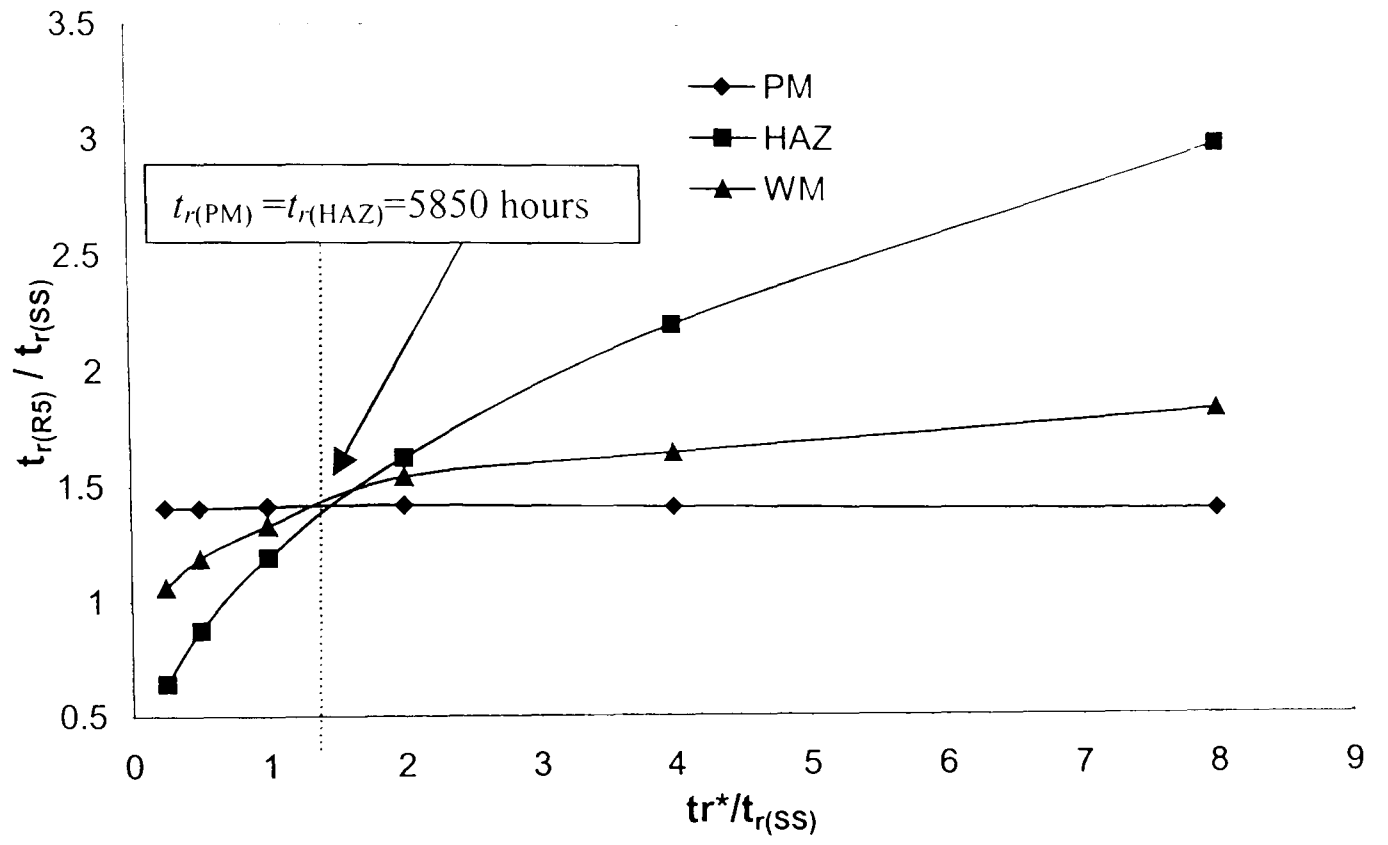


Figure 7.22. Effect of choice of t_r^* value on R5 life for 3-material, welded branched pipe, where $t_{r(SS)} = 4113$ hours.

CHAPTER EIGHT

DISCUSSION AND CONCLUSIONS

8.1 General discussion

The creep behaviour of branched pipes has been studied and presented within this thesis, considering homogeneous and multi-material welded connections. In general, the investigations into the effects of materials and geometrical parameters were based on steady-state creep analysis using Norton's law. The characteristics of the tri-axial stress state of homogeneous and welded (3-material) connections have been described. The importance of the distinct weld zones on the creep rupture strength of various connection types and sizes has also been investigated, as well as the conservatism of various approaches commonly used to predict the creep rupture lives of plant components. The discussion of these investigations is presented in detail at the end of each specific chapter. However, various general discussion points are described below.

The work generally utilizes Norton power-law and CDM material properties of a service-aged $\frac{1}{2}\text{Cr}\frac{1}{2}\text{Mo}\frac{1}{2}\text{V}$: $\frac{2}{4}\text{CrMo}$ weldment at 640°C , obtained from tests carried out by Hyde *et al* [30]. Although the materials and the stress range (40MPa to 70MPa) used to generate these properties are typical of power-plant applications, the temperature used is significantly above those seen in-situ, which are generally around 500°C to 560°C . This temperature of 640°C was

used in order to achieve acceptable creep test rupture times of less than approximately 2000 hours [23] while aiming to maintain the same creep mechanisms as those which exist at typical plant operating temperatures. It should therefore be noted that the resulting creep life predictions using these properties are significantly lower than the expected creep lives of in-situ components, due to this increased temperature. However, approximate extrapolation of failure times, to those of the operating temperatures may be possible if the creep activation energy is known.

The steady-state investigations define the creep rupture life as the operating life for local rupture of the material at a certain position to occur. The work does not however consider creep-crack growth, which will eventually lead to failure. In reality, the operating time for cracks to grow, causing failure, may be significant and hence creep-crack growth modelling should be used for cracked components, as described in the R5 procedure [13], for example. However, creep rupture assessments of components are widely used, since the vast majority of plant components are defect-free on a macroscopic level. The resulting rupture lives are often used to establish weld inspection intervals over the lifetime of the plant. These are used to identify which welds require inspection for the initiation of cracks and the accumulation of high creep damage. The accuracy and level of conservatism of the particular creep rupture approach used to predict these rupture lives will have a direct effect on the total number of welds that would need to be inspected and the number of cracked welds found, per number of welds inspected, for each of the intervals

over the plant lifetime. This important aspect has been one of the driving forces behind this work and is addressed in the majority of the Chapters.

The work has considered thick-walled branched pipes as these are the most commonly used in the main steam sections of power plant since thicker walls are required to withhold the high pressure steam. Although thin-walled branched pipes are more common in hot reheat sections of power plant piping, considerably more research into the creep behaviour of these types of connections had been carried out previously, e.g. [114,117,118,120], and thick-walled connections required additional attention.

Three-material creep modelling has been used to represent the variation of material properties across the weld, using a parent material, weld metal and heat-affected zone material. The work used creep properties representing the refined low temperature HAZ region instead of the coarse high temperature region; the former is generally weaker and prone to Type IV cracking. The weldment properties mainly considered within the work are for a service-aged weldment at 640°C. The HAZ regions of service-aged welds are generally tempered and softened from the as-new state [23], so that the HAZ material properties across the zone for this type of weld are practically constant [23], and hence the assumption of three materials as opposed to more is valid. However, the use of three materials is still a simplifying assumption, as the creep properties generally vary gradually across the weld and do not change abruptly as in the finite element models. Nonetheless, previous creep modelling of three/four-material butt-welded plain pipes by Sun [23] and

Perrin & Hayhurst [67] predicted rupture to occur at the same Type IV HAZ position as observed in-situ. This provides confidence in multi-material finite element creep modelling using a simplified number of distinct weld regions and simplified constitutive material behaviour models. It is assumed that the results for the plain pipes are applicable to branched pipes, as the work is identical in nature to [23] and [67], for example, i.e. same material models and properties, except for the geometry being branched pipes rather than plain pipes. Although direct comparisons with experimental results cannot be established for the work, since creep tests of branched pipes are prohibitively expensive and time-consuming, the work is based on established material models (Norton's law and CDM) and typical plant geometries and loadings.

The branched pipes considered in the work are loaded by internal steam pressure and axial end loads applied to the main pipe and the branch pipe, corresponding to closed ends. The steam used was at a pressure of 16.55MPa, which is typical of main-steam, power-plant piping. Although this type of loading is very common for typical plant components, some branched pipes may be subjected to additional in-plane and out-of-plane moment, torsion and axial end loads. These additional loads may significantly affect the creep behaviour of the connection. It was assumed that the components investigated in the work were subjected to near constant levels of temperature and loading. Such that the effects of creep relaxation, fatigue and other factors associated with variable temperature and load were negligible.

It was also assumed throughout the work that the welds assessed were adequately stress-relieved by post-weld heat treatment to remove residual stress distributions caused by the welding process. Post-weld heat treatments are commonly applied to power-plant high-temperature welds to remove the detrimental effect of these residual stresses.

8.2 General conclusions

The main conclusions of the work are summarised below:

1. The presence of a branch connecting to a pipe or an end-cap generally significantly reduces the creep strength compared to the corresponding plain pipe section. Creep life reductions of up to about 80% were predicted for the geometries considered compared to the life of equivalent plain pipes. The size of branch thickness and diameter also considerably affect the strength of the connection. For instance, typical reductions in creep life of about 25% to 60% were predicted on increasing the branch diameter by 45%, dependent on the connection type. However, the creep lives of hemispherical end caps joined with small centralised branches are predicted to have longer creep lives than that of the main pipe section, dependent on geometry and materials.
2. Steady-state creep stress distributions and stress magnitudes within the heat-affected zones, parent material and weld metal, of typical branched pipes, vary significantly and are highly dependent on the material properties of each zone and their interaction with the other zones. For instance, as shown by results in Chapter Four, for a typical $\frac{1}{2}$ CrMoV welded branched main pipe the peak rupture stress in the creep strong weld

zone is about 50% larger than that in the creep weak HAZ zones. The peak stress values within each zone are also very much dependent on the position within the geometry, as well as the dimensions of the connecting pipes and weld.

3. The existence of the weld-related material zones, i.e. weld metal, parent material and heat-affected zone, can drastically reduce the creep life of the welded connection compared to a homogeneous component. Typical reductions in predicted steady-state creep rupture life of about 75% for branched flat end-caps, 40% for branched hemispherical end caps and 23% for branched main pipes (connecting along the main pipe axis) are predicted when the effects of weld properties are included as compared to the equivalent homogeneous predictions.
4. Steady-state creep analysis using a peak rupture stress can be used with reasonable accuracy as an approximate prediction technique for the creep failure of welded branched pipes. The approach is conservative compared to CDM by about 18% to 36% for predicting rupture initiation lives at critical positions and around 50% to 60% conservative in predicting component failure lives for the typical branched pipes considered in the work. The steady-state approach also predicts consistent weld rupture initiation locations to those of the CDM approach.
5. CDM and steady-state analyses generally predict the various critical locations within the weld to rupture at discrete times in the same order within typical thick-walled branched pipes. The primary locations (i.e. earliest to rupture) for the $\frac{1}{2}$ CMV service-aged and as-new welds branches investigated are in the HAZ: (i) in the main pipe HAZ, circumferentially

around the weld edges, especially on the crotch and saddle planes and (ii) in the branch HAZ, near the inside bore on the crotch plane. For the as-new welds, damage approaching unity is also predicted to occur in the weld metal, on the crotch plane, near the inside surface, and longitudinally and circumferentially to the branch axis on the outer surface, at the weld edges, at approximately about 45° from crotch to flank plane.

6. Damage at the majority of the above locations is highly localised due to geometric discontinuities. Hence, CDM analyses predict that a significant time, e.g. about 35% of total life, will elapse between initial rupture at these locations and final component failure corresponding to rupture across the wall-thickness.
7. The R5 rupture reference stress approach can also be used as an approximate technique for creep life prediction of homogeneous thick-walled branched pipes. The approach predicts lives that are similar to the steady-state approach and are conservative compared to CDM lives.
8. The multi-material R5 rupture reference stress approach, based on a mismatch limit load, generally predicts creep failure lives that are conservative compared to CDM predictions for typical welded plain and branched pipes. However, for the components considered, the life predictions were generally significantly greater than those obtained from steady-state creep predictions.
9. The inverse use of the relevant British Standard codes BS5500 [11] and BS1113 [12], as described by Booth [115], results in conservative estimates of creep rupture lives for typical thick-walled branched pipes, based on multi-material weld rupture properties compared to equivalent multi-

material steady-state predictions. The predicted inverse BS multi-material lives were conservative by at least (i) 20% for isolated branched main pipes, (ii) 65% for branched flat end caps and (iii) 65% for hemispherical end caps, as compared to multi-material steady-state predictions. British standard life predictions for flat and hemispherical branched end caps based on homogeneous parent material rupture properties were always conservative compared to homogeneous material steady-state lives and were generally conservative compared to multi-material steady-state predictions. However, for the isolated branched main pipes studied, the homogeneous British code life predictions were non-conservative compared to homogeneous and multi-material steady-state lives for all of the typical branch geometries studied.

10. A rapid approximate method for estimating the steady-state creep stresses within multi-material welded branched pipes, for any combination of material properties, and at any position within the weld, is described and validated. This method, which was based on the general steady-state stress formulation of Hyde *et al* [102] and the Calladine approximation [36] for predicting the maximum stress in a power-law creeping structure, predicted rupture stresses and lives to within 4% and 8%, respectively, for several critical locations within a typical power-plant, multi-material branch weld.

CHAPTER NINE

FUTURE WORK

9.1 Parametric study of the creep behaviour for thick-walled branched steam pipes with additional loading

The current work has investigated the creep behaviour of thick-walled pipes under closed end pressure loading only. Although this is typical of many in-situ components, a large number of branched pipes will be subjected to additional in-plane and out-of-plane moment and torsion loads. These additional loads can be caused by the layout and weight of the pipework and the way it is supported. The presence of such loads may significantly increase the stresses in the weld region, causing premature failure and characteristic high damage/creep-crack locations. Homogeneous and heterogeneous material finite element investigations into the effects of these loads could be undertaken using similar approaches to those used in the current work. These investigations would require at least a symmetric half model of the connection opposed to the quarter models used in this work and a refined mesh for the inclusion of multi-material weld properties. These investigations may therefore require the acquisition of significantly higher specification of computer facilities than those currently available.

9.2 The creep behaviour of thin-walled branched pipes

Although thick-walled branched pipes are common in high-temperature plant, thin-walled branched pipes are also frequently used, for instance, in hot reheat sections of power plant piping. The majority of research on thin-walled connections has concentrated on the homogeneous reference stress behaviour and little on the creep behaviour of the weld within the connection. Creep investigations using such approaches as the steady-state and CDM methods could be used to investigate the creep strength of such connections.

9.3 The interaction effects between branch pipes

Along high-temperature piping sections small bore branches are often in close proximity to each other. Investigations into the proximity effects of multiple branches in the circumferential and axial directions, around and along the main pipe, on the creep behaviour of the connection is required. This work could include possible validation of established British Standard ligament efficiencies [11,12,115], which are used to modify the peak stress in an isolated branched pipe to that of a multi-branched pipe.

9.4 Assessment of R5 stress redistribution factors for weld zones

Chapter Seven contains an assessment of the homogeneous R5 rupture reference stress approach [13] and the multi-material references stress mismatch limit load approach for branched pipes, as well as other components; in general, conservative creep lives were predicted. However, R5 assesses weldments using a second approach, using stress redistribution factors, k , for each weld zone within CrMoV pipework. For instance, the $\frac{1}{2}\text{Cr}\frac{1}{2}\text{Mo}\frac{1}{4}\text{V}$ weld

zones addressed by the R5 approach are the parent material ($k = 1$), the weld metal ($k = 0.7$ or 1) and the Type IV ($k \leq 1$) and mixed/coarse ($k > 1$) HAZ regions.

The k factors are approximate values reflecting the off-loading effects across the various zones under steady-state creep conditions. The factors are used with the homogeneous reference stress to predict a rupture reference stress for each zone and this is used with the rupture data for each zone to predict a creep life. The current k values were established on the basis of typical stress redistribution behaviour of welded plain pipes. Since there may be a marked difference between the stress redistribution behaviour within the weld zones of branched pipes and plain pipes, especially at geometric discontinuities in the HAZ, it is suggested that an investigation into the applicability of the current R5 k values to typical CrMoV branched pipe welds should be carried out using typical steady-state weldment properties.

The use of the rapid general formulation of stress method and the ' f ' functions described in Chapter Five could be used to investigate this, as well as providing an alternative method to quickly assess the stress-redistribution behaviour of the three weld zones, using a wide range of CrMoV weldment sets. Additionally, the R5 documents that the k values should be used with welds under hoop stress dominance. If the weld is under axial stress dominance, when subjected to high moment loads, for example, the R5 documents that all weld zone k values are equal to unity, since stress-redistribution across the zones would be negligible, due the thinness of the HAZ regions and being near

perpendicular to the weld direction. This approach is applicable to all components including branches. The conditions leading to dominance of hoop stress or axial stress within the weld of a plain pipe is reasonably easy to identify for straight pipes. However, the conditions which lead to hoop or axial stress dominance within branched pipe welds is less clear as there are two sets of hoop and axial stresses acting, due to the presence of two pipes. The stresses at the welded connection region are hence a complex combination of all four of these “stress types”. For this reason, investigation into the stress redistribution behaviour of branched pipe welds under different loading modes is required to understand this relationship of “hoop or axial stress” dominance.

REFERENCES

- [1] Coleman, M. C. and Kimmins, S. T., The behaviour of $\frac{1}{2}\text{Cr}$ $\frac{1}{2}\text{Mo}$ $\frac{1}{4}\text{V}$ pipe weldments in high temperature plant, *Seminar on Life of welds at High Temperature*, IMechE, London, 1990.
- [2] Internet document, www.dti.gov.uk, 2003.
- [3] Internet document, www.energex.com.au, 2003.
- [4] PowerGen plc., UK.
- [5] Central Electricity Generating Board (CEGB), Modern power station practice Vol. 2: Mechanical, 2nd Edition, Pergamon, Oxford, UK, 1971.
- [6] Greenfield, P., *Creep of metals at high temperature*, M and B Monograph, ME/9, Mills & Boon Ltd, London, UK, 1972.
- [7] Evans, H.E., *Mechanisms of creep*, Elsevier Applied Science Publishers, London, UK, 1984.
- [8] Samuelson, L. A., Tu, S.-T. and Storesund, J., Life reduction in high temperature structures due to mis-match of weld and parent material creep properties, Proc. of *Mis-matching of welds, ESIS 17* (ed. by K.H Swalbe and M. Kocak), Mechanical Engineering Publications, London, UK, 1994, pp. 845-860.
- [9] Rotvel, F., Sampietn, C. Verelst, L., Wortel, H. and Zhi, L. Y., Header integrity assessment, *Proc. of VTT Symposium 184, Baltica IV Plant maintenance for managing life and performance, Vol. 1*. Helsinki. Sweden, 1998, pp.201-212.
- [10] Hayhurst, D. R., Creep rupture under multi-axial states of stress, *J. Mech. Phys. Solids*, **Vol. 20**, 1972, pp. 381-390.

- [11] BS5500, *Specification for unfired fusion welded pressure vessels*, BSI, London, UK, 1997.
- [12] BS1113, *Specification for water-tube generating plants*. BSI, London, UK, 1969.
- [13] British Energy Generation Ltd, R5: Assessment Procedure for the High Temperature Response of Structures, Issue 3 (editor: R. A. Ainsworth), British Energy Ltd., Gloucester, UK, 2003.
- [14] Nippon Steel Corporation, Japan.
- [15] Lynch, M. J., Limit loads of piping branch junctions with cracks. PhD thesis, The University of Liverpool, UK, 2001.
- [16] Dempster, I. and Ham, W. M., Damage assessment on failed BW48 pressure vessels: interim report:- stress rupture investigation, BPL project: RCP 4258/100/8428, Babcock Power report: 65/86/41, UK, 1987.
- [17] Sys, W., Creep rupture tests on cylinder to cylinder intersections, *Proc. of Int. Conf. on welding research related to power plant*, Southampton, UK, (ed. by N. F. Eaton and L. M. Wyatt), 1972, pp. 101-112.
- [18] Day, R. V., Rowley, T. and Williams, J. A., Examination of the determination and failure modes of an overheated 1Cr1/2Mo West Thurrock boiler header assembly of complex form, *CEGB report: R/M/R277*, UK, 1979.
- [19] Coleman, M. C., Parker, J. D. Walters, D. J. and Williams, J. A., The deformation behaviour of a thick walled pipe at elevated temperatures, *Proc. of Int. Conf. on Materials 3 (ICM3)*, Cambridge, UK, Vol. 2, ICM3, Pergamon Press, Oxford, UK, 1979.

- [20] Hall, F. R. and Hayhurst, D. R., Continuum damage mechanics modelling of high temperature deformation and failure in a pipe weldment, *Proc. R. Soc. London. A* 433, 1991, pp. 383-403.
- [21] Coleman, M. C. and Fidler, R., Testing of full-size steam plant components, *J. Strain Analysis*, Vol. 29, No. 3, IMechE, 1994, pp. 209-214.
- [22] Westwood, H. J. and Clark, M. A., Metallographic methods for creep life assessment of plant components, *Materials at high temperature*, Vol. 13, No. 3, 1995, pp.147-154.
- [23] Sun, W., Creep of service-aged welds, PhD thesis, The University of Nottingham, UK, 1996.
- [24] Vazda, D., On concentration effects in circumferential welds due to dissimilar creep properties, *Int. J. Pres. Ves. & Piping*, Vol. 73, 1997, pp. 119-126.
- [25] Singh, R. and Singh, S. R., Remaining creep life study of Cr-Mo-V main steam pipelines, *Int. J. Pres. Ves. & Piping*, Vol. 73, 1997, pp. 89-95.
- [26] Hyde, T. H. and Sun, W., Creep of welded pipes, *Proc. of IMechE*, Part E, Vol. 212, 1998, pp. 171 – 182.
- [27] Personal contact with Allen, D. (Powergen), Brett, S. (Innogy) and Budden, P. J. (British Energy), 2000-2003.
- [28] ABAQUS version 6.3, Hibbit, Karlsson & Sorensen, Inc, 2003.
- [29] Storesund, J. and Tu, S. T., Geometrical effect on creep in cross weld specimens, *Int. J. Pres. Ves. & Piping*, Vol. 62, 1995, pp. 179-193.
- [30] Hyde, T. H., Sun, W., Becker, A. A. and Williams, J. A., Creep continuum damage constitutive equations for the base, weld and heat-affected

zone materials of a service-aged 1/2Cr1/2Mo1/4V: 2¼Cr1Mo multi-pass weld at 640° C. *J. Strain Analysis*, **Vol. 32**, 1997, 273-285.

[31] Kachanov, L. M., *Theory of Creep* (English translation edited by A. J. Kennedy), National Lending Library, Boston Spa, USA, 1960.

[32] Hayhurst, D. R. and Perrin, I. J., CDM analysis of creep rupture in weldments, *Proc. of Engineering Mechanics*, 1, 1995, pp. 393-396.

[33] Sun, W., Hyde, T. H., Becker, A. A. and Williams, A. J., Comparison of the creep and damage failure prediction of the new, service-aged and repaired thick-walled circumferential CrMoV pipe welds using material properties at 640°C, *Int. J. Pres. Ves. & Piping*, **Vol. 77**, 2000, pp. 389-398.

[34] Hyde, T. H., Sun, W. and Becker, A. A., Assessment of the use of finite element creep steady-state stresses for predicting the creep life of welded pipes, *In: Proc. 4th Int. Conf. On Computational structures Technology* (edited by B. H. V. Topping), Civil-Comp Press, Edinburgh, UK, 1998, pp. 247-251.

[35] Tang, A. A., The Creep behaviour of cross-weld specimens and welded pipes, PhD thesis, The University of Nottingham, UK, 2000.

[36] Calladine, C.R., A rapid method for estimating the greatest stress in a structure subject to creep, *Proc, IMechE*, **Vol. 178**, 1963-1964, pp. 198–206.

[37] Evans, R. W. and Wilshire, B., *Introduction to Creep*, IOM, London, UK, 1993.

[38] Boyle, J. T. and Spence, J., *Stress analysis for creep*, Butterworths, London, UK, 1983.

[39] Penny, R. K. and Marriott, D. L., *Design for Creep*, second edition. Chapman & Hall, London, 1995.

- [40] Norton, F. H., The creep of steel at high temperatures, McGraw-Hill, London, UK, 1929.
- [41] McVetty, P. G., Creep of metals at elevated temperatures – the hyperbolic sine relation between stress and creep rate, *Trans. ASME*, Vol. 65, 1943.
- [42] Dorn, J. E., Some fundamental experiments on high temperature creep, *J. Mech. Phys. Solids*, Vol. 3, 1955.
- [43] Garofalo, F., Fundamentals of creep and creep rupture in metals, MacMillan, New York, USA, 1965.
- [44] Bailey, R. W., The utilisation of creep test data in engineering design, *Proc. IMechE*, Vol. 131, 1935.
- [45] Graham, A. and Walles, K. F. A, Relations between long and short time properties of a commercial alloy, *J. Iron & Steel Inst.*, Vol. 179, 1955.
- [46] Johnson, W. and Mellors, P. B., Plasticity for mechanical engineers, Van Nostrand Co., London, UK, 1962.
- [47] von Mises, R., *Gottinger Nachrichten Math.Phys. Klasse*, 1913, pp. 582.
- [48] Tresca, H., *Comptes Rendus Acad. Sci.*, Paris, France, Vol. 59, 1864, pp. 754.
- [49] Kraus, H., Creep analysis, John Wiley, New York, USA, 1980.
- [50] Sim, R. G., Creep of structures, PhD thesis, University of Cambridge, UK, 1968.
- [51] Evans, R. W. and Wilshire, B., Creep of Metals and Alloys, IOM, London, UK, 1985.

- [52] Rabotnov, Y. N., Creep problems in structural members, Amsterdam, Netherlands, 1969.
- [53] Hayhurst, D. R., The role of creep damage in structural mechanics, Engineering Approaches to High Temperature (edited by B. Wilshire & D. R. Owen), Pineridge Press, Swansea, UK, 1983.
- [54] ANSYS Version 5.3, Swanson Analysis Systems Inc., 1995.
- [55] Soderberg, C. R., Interpretation of creep tests on tubes, *Trans. ASME*, **Vol. 62**, 1941.
- [56] MacKenzie, A. C., On the use of a single uniaxial test to estimate deformation rates in some structures undergoing creep, *Int. J. Mech. Sci.*, **Vol. 10**, 1968, pp. 441 – 453.
- [57] Sim, R. G., Reference stress concepts in the analysis of structures during creep, *Int. J. Mech. Sci.*, **Vol. 13**, 1970, pp. 561-573.
- [58] Goodall, I. W., The behaviour of structures operating at high temperature with reference to remnant life estimation, *Symp. on the Prediction of Residual Lifetime of Constructions Operating at High Temperature*, Netherlands Institute of Welding, 1977.
- [59] Sun, W, Hyde, T. H., Becker, A. A. and Williams, A. J., Steady-state creep reference stresses for internally pressurised pipes for use in life prediction, *Int. J. Pres. Ves. & Piping*, **Vol. 79**, 2002, pp. 135-143.
- [60] Goodall, I. W. and Cockcroft, R. D. H., On bounding the life of structures subjected to steady load and operating in the creep range, *Int. J. Mech. Sci.*, **Vol. 15**, 1973, pp. 251-263.
- [61] Johnsson, A., An alternative definition of reference stress creep, IMechE Conference Publications, **Vol. 13**, 1973, pp. 205.1-205.7.

- [62] Goodall, I. W., Cockcroft, R. D. H. and Chubb, E. J., An approximate description of the creep rupture of structures, *Int. J. Mech. Sci.*, **Vol. 17**, 1975, pp. 351-360.
- [63] Goodall, I. W. and Ainsworth, R. A., Failure of structures by creep, *3rd Int. Conf. on Pres. Ves. Tech.*, Tokyo, Japan, ASME, **Vol. 2**, 1977, pp. 871-885.
- [64] Goodall, I. W., Leckie, F. A., Ponter, A. R. S. and Townley, C. H. A., The development of high temperature design methods based on reference stresses and bounding theorems, *ASME J Eng Material Technology*, **Vol. 101**, 1979, pp. 349 – 355.
- [65] Yehia, K. A., Reference stresses for impression creep and two material components, PhD Thesis, University of Nottingham, 1994.
- [66] Tu, S.-T., Segle, P. M. and Samuelson, L. A., Some aspects of the design of welded structures subjected to high temperature creep, *High Temperature Service and Time Dependent Failure*, ASME, 1993, PVP-**Vol. 262**.
- [67] Perrin, I. J., and Hayhurst, D. R., Creep constitutive equations for 1/2Cr1/2Mo1/4V ferritic steel in temperature range 600-675°C, *J. Strain Analysis*, **Vol. 31**, 1996, pp. 299-314.
- [68] Mitchell, K. C. and Brett, S. J., Review of ‘cold weld’ repair applications, *Proc. 3rd Int. HIDA and Integrity Conf.*, Lisbon, Portugal, 2002, pp. 125-132.
- [69] Perrin, I. J. and Hayhurst, D. R., Continuum damage mechanics analyses of the Type IV creep failure in ferritic steel, *Int. J. Pres. Ves & Piping*, 1999, **Vol. 76**, pp. 599-617.

- [70] Coleman, M. C., The structure of weldments and its relevance to high temperature failure, *Conf. Weldments: Physical Metallurgy and Failure Phenomena (Proc. 5th Bolton Landing Conference)*, Editor. Christoffel, R. F., Nippes, E. F. and Solomon, H. D., General Electric, USA, 1978, pp409-420.
- [71] Price, A. T and Williams, J. A., The influence of welding on the creep properties of steel, *Recent Advances in creep and fracture of engineering materials and structures*, Editor. Wilshire, B. and Owen, D. R. J., Pineridge Press, Swansea, 1982, pp.265.
- [72] Cane, B. J., Collaborative programme on the correlation of test data for high temperature design of welded steam pipes. Presentation and analysis of material data, CEGB report RD/L2101N81, CEGB, UK, 1981.
- [73] Egger, G., Ramteke, A., Coleman, M.C., Chew, B., Peter, G., Burblies, A., Hald, J., Jefferey, C., Rantala, J., De Witte, M. and Mohrmann, R., Analysis of creep in a welded 'P91' pressure vessel, *Int. J. Pres. Vess. & Piping*, **Vol. 60**, 1994, pp. 237.
- [74] Brett, S. J., Cracking experience in steam pipework welds in National Power, *Conf. on Materials welding technology in power plants*, 1994, Essen, Germany, VGB, 1994.
- [75] Wilson, J. D, Hawkes, M., James, P. and Pascoe, S., Degradation in ageing power plant components, *Parsons 2000 Conf. on Advanced Materials for 21st century turbines and power plant*, Cambridge, UK, 2000.
- [76] Schuller, H. J., Hagn, L. and Woitscheck, A., Cracking in the weld region of shaped components in hot steam pipelines – materials investigation, *Der Maschinenschaden*, **Vol. 47**, pp. 1-13.

- [77] Gooch, D. J. and Kimmins, S. T., Type IV cracking in $\frac{1}{2}\text{Cr}$ $\frac{1}{2}\text{Mo}$ $\frac{1}{4}\text{V}$ – $\frac{1}{4}\text{Cr}$ 1Mo weldments, *Conf. on Creep and Fracture of Engineering Materials and Structures*, Editors; Evans, R. W. and Wilshire, B., The Institute of Metals, London, UK, 1987, pp. 689-703.
- [78] Wu, R., Storesund, J., Sandstrom, R. and von Walden, E., Creep properties of 1Cr $\frac{1}{2}\text{Mo}$ steel welded joints with controlled microstructures, *Weld. World*, **Vol. 30**, 1992, pp. 239-336.
- [79] Middleton, C. J. and Metcalfe, E., A review of laboratory Type IV cracking data in high chromium ferritic steels. Steam plant for the 1990's, *Proc. IMechE*, No. C386/027, 1990.
- [80] Greenwell, B. S. and Taylor, J. W., The properties of candidate welds in 9CrMoNbV steel, *IMechE*, No. C386/041, 1990.
- [81] Otham, A. M. and Hayhurst, D. R., Multi-axial creep rupture of a model structure using a two parameter model, *Int. J. of Mech. Sci.*, **Vol. 32**, 1990, pp. 35-48.
- [82] Parker, J. D. and Stratford, G. C., Microstructure and performance of $1\frac{1}{4}\text{Cr}$ $\frac{1}{2}\text{Mo}$ steel weldments, *Materials at High Temperature*, **Vol. 13**, No. 1, 1995, pp. 37-45.
- [83] Etienne, C. F. and Heerings, J. H., Evaluation of the influence of welding on creep resistance (Strength reduction factor and lifetime reduction factor), IIW Meeting, doc. IX-1725-93, *Steel Research*, **Vol. 65**, No. 5, 1993, pp.187.
- [84] Hyde, T. H. and Tang, A. A., Creep analysis and life assessment using cross-weld creep specimens, *Int. Mat. Rev.*, **Vol. 43**, No. 6, 1998, pp.221.

- [85] Coleman, M. C., Parker, J. D. and Walters, D., The behaviour of ferritic weldments in thick section CrMoV pipe at elevated temperatures. *Int. J. Pres. Ves. & Piping*, **Vol. 18**, 1985, pp. 277-310.
- [86] Williams, J. A., The validation of procedures for assessing the life of components, *Conf. BALTICA 2: Life and Performance of High Temperature Materials and Structures, Helsinki, Finland*, Technical Research Centre of Finland (VTT), Espoo, Finland, 1992, Session 2c. Paper 2.
- [87] Hayhurst, D. R., Computational continuum damage mechanics: its use in the prediction of creep in structures – past, present and future, *Proc. of IUTAM Symposium on Creep in Structures*, Japan, 2000, pp. 175-188.
- [88] Storesund, J., Andersson, P., Samuelson, L. A. and Segle, P., Prediction of creep cracks in low alloy steel pipe welds by use of continuum damage mechanics approach, *4th Int. Colloquium on Ageing of Materials and Methods for the Assessment of Lifetimes of Engineering Plant*, Cape Town, South Africa, 1997, pp. 129-144.
- [89] Perrin, I. J., Hayhurst, D. R. and Ainsworth, R. A., Approximate creep rupture lifetimes of butt welded ferritic steel pressurised pipes, *Eur. J. Mech. A./ Solids*, **Vol. 19**, 2000, pp. 223-258.
- [90] Hyde, T. H., Sun, W., Becker, A. A. and Williams, J. A., Effect of weld angle on the creep behaviour of an internally pressurised thick walled CrMoV pipe weld, *Int. J. Pres. Ves. & Piping*, **Vol. 78**, 1997, pp. 365-372.
- [91] Samuelson, L. A., Segle, P. M., Andersson, P. and Storesund, J., Creep crack growth in welded components – a numerical study and comparison with the R5 procedure, *Int. J. Pres. Ves. & Piping*, **Vol. 78**, 1997, pp. 365-372.

- [92] Grittiths, J. E., The limit analysis of header geometries for application in remnant creep life assessments, Unclassified CEGB report, NER/SSD/R440, 1981.
- [93] Hyde, T. H., Williams, J. A. and Sun, W., Assessment of creep behaviour of a narrow gap weld, *Int. J. Pres. Ves. & Piping*, **Vol. 76**, 1999, pp. 515-525.
- [94] Hyde, T. H., Sun, W. and Williams, J. A., Prediction of creep failure life of internally pressurised thick walled CrMoV pipes, *Int. J. Pres. Ves. & Piping*, **Vol. 76**, 1999, pp. 925-933.
- [95] Walters, D. J. and Cockcroft, R. D. M., A stress analysis and failure criteria for high temperature butt welds, *Colloquium on Creep Behaviour of Welds in Boilers, Pressure Vessels and Piping*, IIW, Toronto, Canada, 1972.
- [96] Hyde, T. H., Sun, W. and Becker, A. A., Analysis of the impression creep test method using a rectangular indenter for determining the creep properties of welds, *Int. J. Mech. Sci.*, **Vol. 38**, 1996, pp. 1089-1102.
- [97] Hyde, T. H., Sun, W. and Becker, A. A., Creep of waisted and Notched cross-weld specimens, *Proc. of 7th Int. Conf. on Creep and Fracture of Engineering Materials and Structures*, California, USA, 1997, pp. 759-768.
- [98] Budden, P.J., Analysis of Type IV failures of three welded ferritic pressure vessels, *Int. J. Pres. Ves. & Piping*, **Vol. 75**, 1998, pp. 509-519.
- [99] Law, M. and Payten, W., Weld performance under creep using finite element modelling, *Int. J. Pres. Ves. & Piping*, **Vol. 72**, 1997, pp. 45-49.
- [100] Hyde, T. H., Sun, W. and Tang, A. A., A parametric analysis of stresses in a thick-walled pipe weld during steady-state creep, *Proc. of the 5th Int. Colloquium on Ageing Materials and Methods for Assessment of Lifetimes of*

Engineering Plant (edited by R. K. Penny), Cape Town, South Africa, 1999, pp. 231-246.

[101] Browne, R. J., Cane, B. J., Parker, J. D. and Walters, D. J., Creep failure analysis of butt welded tubes, *Proc. 1st Int. Conf. Creep & Fracture of Eng. Materials & Structures*, Swansea, UK, 1981, pp. 645-655.

[102] Hyde, T. H., Sun, W., Tang, A. A. and Budden, P. J., An inductive procedure for determining the stresses in multi-material components under steady-state creep, *J. Strain Analysis*, 2000, **Vol. 35**, pp. 347-358.

[103] Hyde, T. H., Sun, W., Tang, A. A., A general formulation of the steady-state creep deformation of multi-material structures, *Proc. of the 4th Int. Conf. on Modern Stress and Vibration Analysis* (Edited by A. A. Becker), Nottingham, UK, 2000, pp. 481-492.

[104] Hyde, T. H., Sun, W., Tang, A. A., Parametric analysis of stresses and deformations in a pipe with a circumferential weld under creep conditions, *Proc. of the Int. Conf. on Integrity of High Temperature Welds*, Nottingham, UK, 1998, pp. 323-332.

[105] Tu, S.-T. and Sandstrom, R., Numerical simulation of creep exhaustion of weldments and some design considerations, *5th Int. Conf. on Creep and Fracture of Engineering Materials and Structures* (Editors: B. Wilshire and R. W. Evans), Swansea, UK, 1993.

[106] Hyde, T. H. and Sun, W., Effect of bending load on the failure behaviour of pressurised thick-walled CrMoV pipe weldment, *Int. J. Pres. Ves. & Piping*, 2002, **Vol. 79**, pp. 331-339.

- [107] Wang, Z. P. and Hayhurst, D. R., The use of supercomputer modelling of high temperature failure in a pipe welds to optimise weld and HAZ selection, *Proc. Royal Soc. Lond.*, A446, 1994, pp. 127-148.
- [108] Patel, R. D., Laham, S. A. and Budden, P. J., R5 creep life assessment of welded trunnion and large bore branch components, *Proc. of 9th Int. Conf. Creep and Fracture of Engineering Materials & Structures* (Editor: J. D. Parker), Swansea, UK, 2001, pp. 567-577.
- [109] Dhalla, A. K., Influence of weld factors on creep-rupture cracking at elevated temperature, *J. Pres. Ves. Technology*, ASME, 1991, **Vol. 113**, pp. 195-209.
- [110] Lynch, M. A., Moffat, D. G. and Moreton, D. N., Limit loads for cracked piping branch junctions under pressure and branch out-of-plane bending, *Int. J. Pres. Ves. & Piping*, **Vol. 77**, 2000, pp. 185-194.
- [111] Storesund, J., Wu, R. and Sandstrom, R., Through thickness distribution of creep damage in a service-exposed double T-joint of $\frac{1}{2}\text{Cr}\frac{1}{2}\text{Mo}\frac{1}{4}\text{V}$ steel, *Proc. of 7th Int. Conf. of Pres. Ves. Technology*, **Vol. 1**, Dusseldorf, Germany, 1992, pp.772-789.
- [112] Bendick, W. and Weber, H., Entwicklung einer Zeitstandscharakteristik und ihre Auswirkung auf Bauteilverhalten, *VGB Conf. Residual Service Life*, Mannheim, Germany, **Vol. 30**, 1992.
- [113] van Wortel, J. C. and Arav, F., Effectiveness of repair welding without post weld heat treatment of creep damaged $1\text{Cr}\frac{1}{2}\text{Mo}$ and $2\frac{1}{4}\text{Cr}1\text{Mo}$ components, *Int. Conf. on Pres. Ves. Technology*, **Vol. 1**, ASME, 1996, pp.41-49.

- [114] Budden, P. J. and Goodall, I. W., The creep life of cylinder/cylinder connections, *2nd Int. Conf. on Pipework Eng. and Operation*, IMechE, February 1989.
- [115] Booth, S.J., The calculation of operating stresses at branches and end-caps in boiler headers for use in GOM 101 creep life assessment, CEGB Report, SWR/SSD 10447/N/84, 1984.
- [116] Brown, T. B., Creep rupture testing of welded nozzle connections, *Conf. Designing High Temperature Materials*, Paper 16 (Inst. Metals), Univ. of Sheffield, UK, 1983.
- [117] Moffat, D. G., Experimental stress analysis of four fabricated equal diameter branch intersections subjected to moment loadings and the implications on branch junction design, *Proc. IMechE*, 1985, **Vol. 199**(4), pp. 261-284.
- [118] Lynch, M. A., Moffat, D. G. and Moreton, D. N., Limit loads for cracked branch junctions under pressure and branch out-of-plane bending, *Int. J. Pres. Ves. & Piping*, 2000, **Vol. 77**, pp. 185-194.
- [119] Fuzhen, X., Peining, L. and Shan-Tung, T., An estimation of plastic limit load of cracked equal diameter welded piping branch junctions under internal pressure, *Proc. Int. Conf. on Eng. Struct. Int. Assessment*, Manchester, UK, 2002, pp. 165-174.
- [120] Gritths, J. E., The limit analysis of header geometries for application in remanent life creep life assessments, CEGB report NER/SSD/R440, 1981.
- [121] Dhalla, A. K., Influence of weld factors on creep-rupture cracking at elevated temperatures, *J. Pre. Ves. Technology*, Trans. ASME, 1991, **Vol. 113**, pp. 194-209.

- [122] Li, Y. Z., Modelling for Life Assessment of local weld repair of 10CrMo44 T-joints by using matched and under-matched weld metal. Report No. 98570002-KPG/I&M 98-1143, KEMA Power Generation, 1998.
- [123] van Wortel, J. C., Effectiveness repair of in-service components by grinding or by welding without PWHT, *Arbeitsgemeinschaft für Hochtemperaturwerkstoffe*, VDEh, Dusseldorf, Germany, pp. 67-82.
- [124] Hayhurst, D. R. and Miller, D. A., The use of creep continuum damage mechanics to predict damage evolution and failure in welded vessels, *Remnant Life Prediction*, I.MechE, Seminar Pub., 1998, **Vol.4**, pp. 117-132.
- [125] Allen, D., Personal communication, PowerTech, PowerGen plc., 2000-2003.
- [126] Brett, S. J., Personal communication, Innogy plc., 2000-2003.
- [127] Budden, P. J., Personal communication, British Energy plc., 2000-2003.
- [128] Rayner, G., GBRANCH & SBRANCH: Automatic FE mesh generation of branched pipe models, The University of Nottingham, UK, 2001.
- [129] FEMGV Version 4.1, Femsys Ltd, 1996.
- [130] Hyde, T. H., Sun, W., Leen, S. B. and Rayner, G., FE analysis of the creep of branched pipes, *The Colloquium of Pressure Vessel Technology*, Glasgow, May 2003.
- [131] BS7910: *Guide on methods for assessing the acceptability of flaws in metallic structures*, British Standards Institute, London, UK, 1999.
- [132] Nicol, D. A. C. and Williams, J. A., The creep behaviour of cross-weld specimens under axial loadings, *Res. Mechanics*, **Vol. 14**, 1985, pp. 197-223.

[133] Sun, W.. Validation of a simplified FE damage code using user subroutine CREEP within ABAQUS, ESR21 Progress Report. The University of Nottingham, January 2001.

[134] Hyde, T. H., Sun, W. and Williams, J. A., Creep behaviour of parent weld and HAZ materials of new, service-aged and repaired $\frac{1}{2}\text{Cr}\frac{1}{2}\text{Mo}\frac{1}{4}\text{V}$: $2\frac{1}{2}\text{Cr}1\text{Mo}$ pipe welds at 640°C, *Material High Temperature*, 1999, **Vol, 16(3)**, pp. 117-129.

[135] Hyde, T. H., Sun, W. and Becker, A. A., Failure prediction for multi-material creep test specimens using a steady-state creep rupture stress, *Int. J. Mech. Sci.*, 2000, **Vol. 42(3)**, pp. 401-423.

APPENDIX 1

GUIDELINES FOR STEADY-STATE AND CONTINUUM DAMAGE MECHANICS FINITE ELEMENT ANALYSIS

A1.1 Steady-State Creep Analysis Guidelines

Within the work presented in this thesis finite element (FE) steady-state creep analyses have been used to calculate steady-state creep stress distributions. Many commercial finite element software packages have in-built steady-state material models, such as Norton's law. This thesis has used Norton's law for calculation of steady-state creep stresses with Abaqus FE software [28].

The FE calculation requires two steps to calculate the steady-state creep stress state. The first step calculates the elastic strain and stress state within the component. This stress state is equivalent to a creep time of zero. Once the calculation of the elastic stresses and strains within the component has been achieved, the second stage is for the FE calculation to introduce creep strains over a finite number of time increments. This second stage is responsible for the calculation of stress redistribution within the component from the initial elastic state to the steady-state creep state. Compatibility of the elastic and creep strains within the component must be achieved. To attain this, stresses at high elastic stress positions off-load to lower elastically stressed positions to maintain this compatibility; this is the nature of stress redistribution, see Figure A1.1 as example of stress redistribution. Additionally, while some positions

have reached a steady-state, others may have not, therefore care must be taken to ensure the whole component has reached steady-state. The FE computation introduces small levels of creep strains to the elastic strain state within the component over small increments of creep time. Small time increments are used as the effects of creep strain on the level of off-loading will be large initially and then reduce over time as the stresses eventually redistribute to reach a steady-state. As the creep time increases during the analysis, the amount of time required per time increment to calculate the new stress state will also increase due to the magnitude of stress redistribution decreasing, see Figure A1.1. Some guidelines on running steady-state analysis are listed below.

- When conducting steady-state creep FE analysis the Norton law material properties A and n are required to calculate the magnitude of creep strain over time (see Equation 2.2). For single material analysis the material's stress index value, n , has an effect on the magnitude of stress redistribution and therefore on the peak values. However, the A material property has no effect on the stress level. Both A and n effect the time that stress redistribution takes to complete. For instance, having a low value of n , say 3, and low value A , say 1×10^{-50} , increases the time required to reach steady-state compared to a material having high values of n and A , since the creep strain rates will be very small and will therefore require longer to exceed the elastic strains within the component and thus achieve a steady-state. Since high values of A and n , would take very different creep times to reach a steady-state than low

values the time controlling parameters, e.g. number of time increments to be used, total creep time and the creep strain tolerance. of the FE analysis must be stated correctly in the step data card of the analysis input file, as well as being chosen effectively to reduce the CPU run time, see Figure A1.2 for a typical Abaqus [28] creep step card. Note that although the size of each time increment is generally controlled automatically by the FE software, the user does have some control of these time parameters as stated above. For instance, a material with low A and n values requires 15'000 hours to reach a steady-state in a component. Hence a larger initial time increment, e.g. 0.01 hours, and a longer total creep time, e.g. 18'000 hours, needs to be stated in the input file for the analysis to reach a steady-state and to optimise the computation. Materials with larger values of these material properties would require the inverse. If a small time increment was chosen for the low A and n analysis, the first number of time increments would be small and would require more time increments and CPU processing time to reach the same creep time of 16,000 hours as choosing an increment of 0.01 hours, for example. Alternatively, if the creep time was set to 10'000 hours for this analysis, steady-state would not be achieved and the analysis would be classed as a failure. In conclusion, appropriate user defined time parameter values are required to achieve a successful analysis that has reached steady-state in a satisfactory CPU run time. Similar guidelines as described above apply to multi-material steady-state analysis, except a general knowledge of the level of mismatch between the different materials are required to estimate the time

for steady-state to be reached, as one material may creep quickly (i.e. high A and n values), while another creeps slowly (i.e. low A and n values). As a general guideline, the total creep time required to run the multi-material analysis to a steady-state will be slightly shorter than that of the time required to run an analysis in which the component was analysed using just the slower creeping material in a single material analysis. The creep strain tolerance and initial time increment required for this multi-material analysis would be similar to that used if the component were analysed using just the quickly creeping material in a single material analysis. Hence, the analysis time parameters (time increments, total time, creep strain tolerance) should reflect this.

- To decide whether a steady-state has been achieved within the component several steps are required in the post-processing stage of the analysis. Firstly, choose several positions within the component which are in very different locations within the component and then plot the variation of several different stress types at these positions (e.g. equivalent and the principal stresses) with creep time. As the time increases, the stress should smooth out to a steady state for all stress types and at all positions. A tolerance can be used to manually determine when this steady-state is achieved. For instance, for the steady-state analyses in this thesis, a tolerance of 0.5% was used, i.e. steady-state was achieved within the whole component when all stress types at the positions chosen varied by less than 0.5% with creep time. To reduce the time in determining when steady-state has been achieved a computer program can be used while the analysis is running to check

the variation of stresses, which uses such a tolerance to stop the analysis. This program could be used via an FE user defined sub-routine.

A1.2 FE Continuum Damage Mechanics Creep Analysis Guidelines

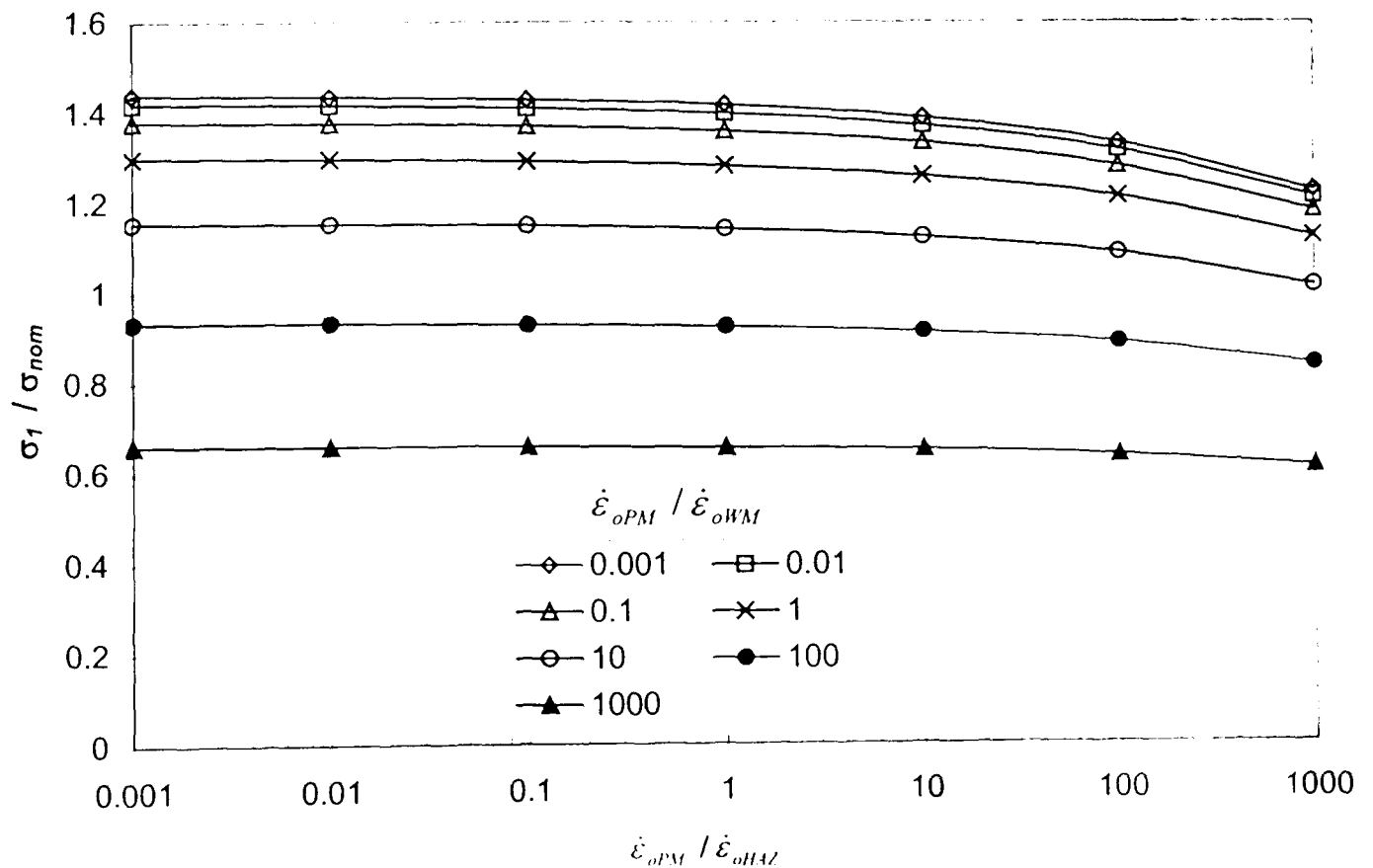
FE continuum damage mechanics (CDM) computations are very intensive on computer resources as they require thousands of small time increments throughout the analysis because of the need for continuous stress redistribution to maintain the compatibility of strain within the component to model the tertiary creep stage of the material. The analysis becomes very intensive when damage at positions within the material reaches values near one. This is due to the material reaching failure and hence the creep strain rates become very large, requiring a very large amount of off-loading from this position to the local, less damaged regions around it. At this point in the analysis, the time increments become very small and typically require hundreds of increments to model tens of hours in creep time. Even though a position fails by reaching a damage level of one, this doesn't necessarily mean that the whole component has failed, as the rest of the component can be relatively undamaged and can still carry load. Take a plain pipe for example; the peak damage may be located on the outer surface, as the peak rupture stress may be located there, but the rest of the wall thickness may still be relatively undamaged at this point in time. However, as time goes on, the outer surface damage will increasingly off-load onto the rest of wall and thus damage will spread across the wall. At certain point in time the whole wall will eventually reach a damage level of

unity and this is defined as the failure time of the whole component. However, in computational terms this would require a very large amount of increments and CPU processing time even for a simple component as a plain pipe. For CDM analysis of more complex components, such as branched pipes, the achievement of complete failure across the wall of the connection would require even more time. Previous FE CDM studies of components such as welded pipes, cross-weld test specimens, e.g. [26,30,33,34], have concluded that the creep time taken from one position failing within the component, i.e. (to reach a damage level of 1), to the rest of the cross section failing is small relative to the creep time taken for the first position to fail. This means that a conservative CDM estimate of component failure life can be obtained by ensuring that the majority of a component's cross section has nearly reached failure, while at the same time severely limiting the CPU run time required to achieve an accurate CDM component failure life. In this thesis, this approach has been adopted for all CDM calculations that have been reported on. For the multi-material branched pipes analyses, the component failure life was defined as the creep time that was required for 40% of the HAZ, across the wall thickness, to reach a damage level greater than 0.6, see Figures 6.4 and 6.5 for example. A similar condition was defined for single-material branched pipes. For the two bar structure, the component failure life was defined as a damage level of least 0.8 was reached in one of the bars. Lastly, for single material and multi-material welded plain pipes the condition for CDM component failure life was that the majority of the wall reaches a damage level greater than 0.7.

APPENDIX 2

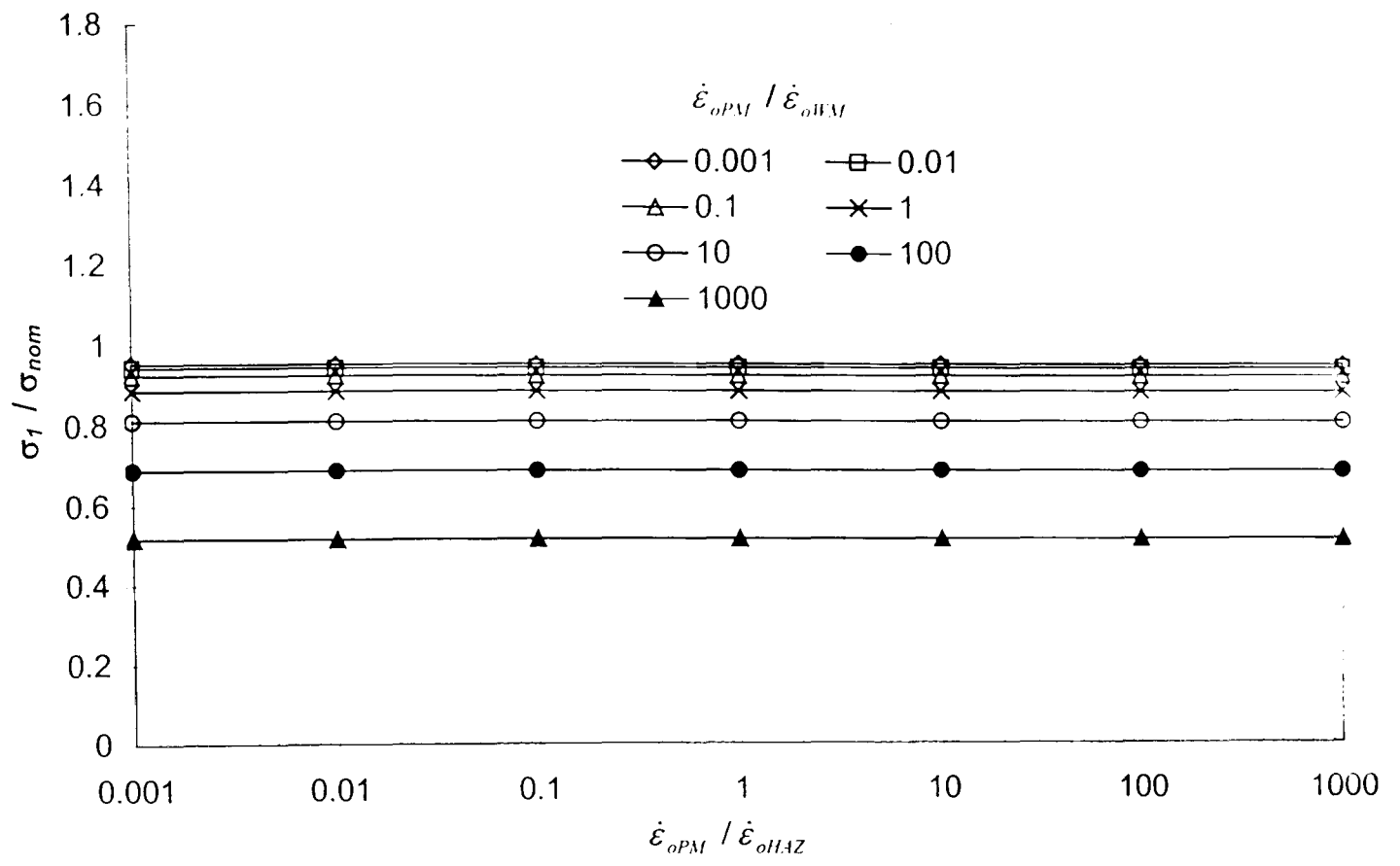
THE RESULTS OF A PARAMETRIC STUDY OF MATERIALS ON σ_{eq} AND σ_1 FOR POSITIONS A, B, D AND F FROM CHAPTER 5

This appendix shows a continuation of the parametric study, as described in Chapter 5, of the effect of material properties $\dot{\epsilon}_{oi}$ and n_i for the PM, HAZ and WM weld zones on the equivalent and maximum principal stress for four critical positions (Positions A(PM^b), B(WM), D(HAZ^p) and F(WM)) within a typical three-material, branched pipe weld.



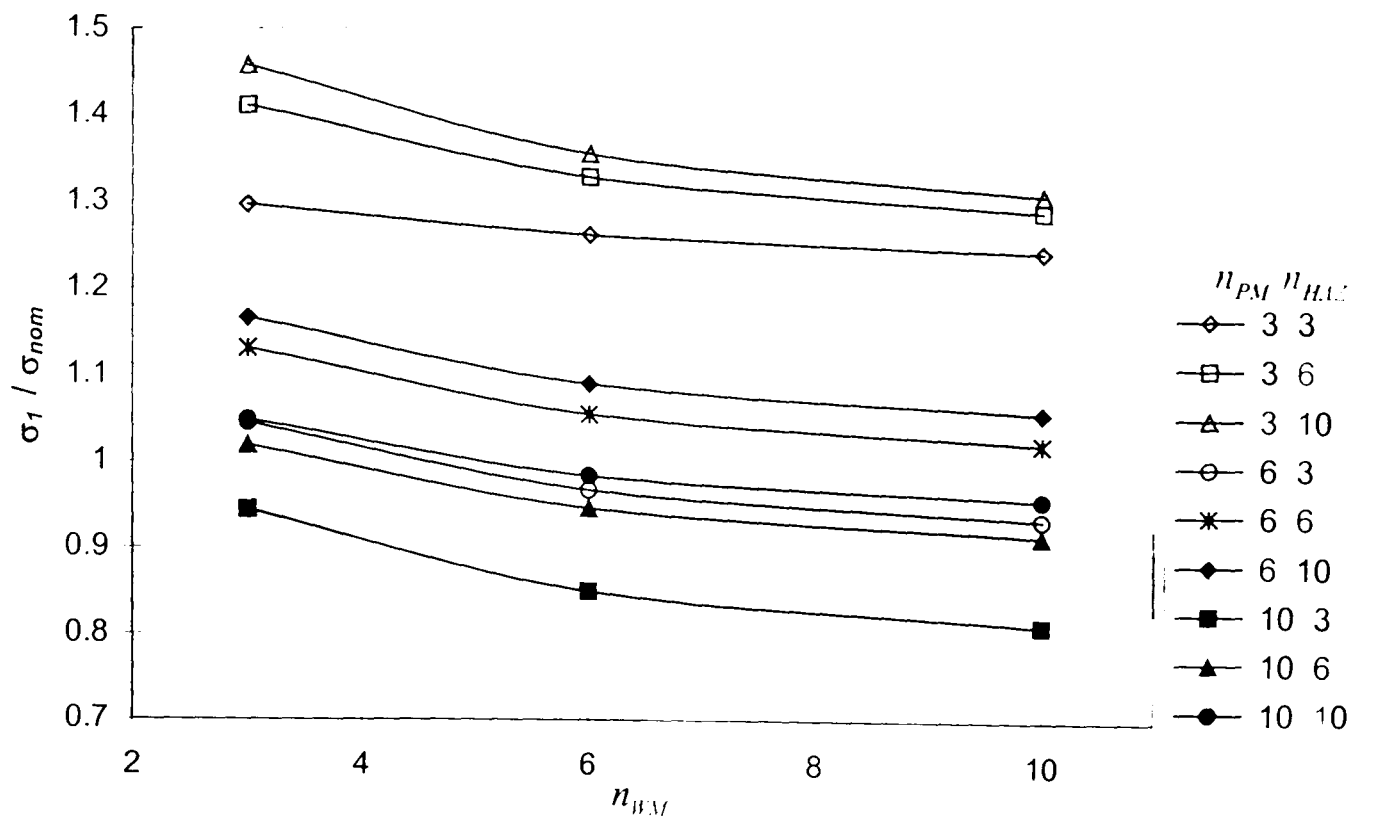
(a) $(n_{PM}, n_{HAZ}, n_{WM}) = (3, 10, 10)$

Figure A2.1. Variations of maximum principal stress at Position A (PM^b) with $\dot{\epsilon}_{oPM} / \dot{\epsilon}_{oHAZ}$ and $\dot{\epsilon}_{oPM} / \dot{\epsilon}_{oWM}$ ratios for different $(n_{PM}, n_{HAZ}, n_{WM})$ combinations.

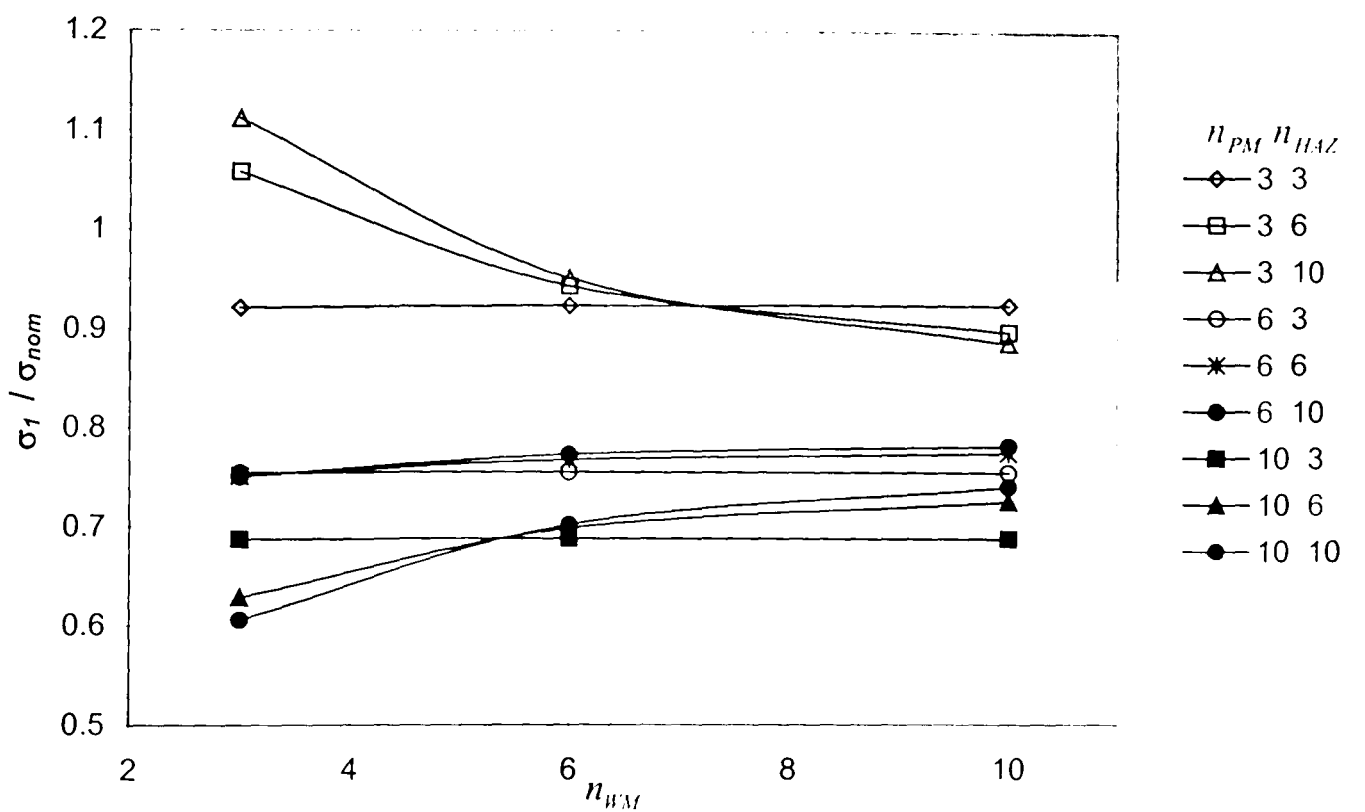


(b) $(n_{PM}, n_{HAZ}, n_{WM}) = (10, 3, 3)$

Figure A2.1 continued. Variations of maximum principal stress at Position A (PM^b) with $\dot{\epsilon}_{oPM} / \dot{\epsilon}_{oHAZ}$ and $\dot{\epsilon}_{oPM} / \dot{\epsilon}_{oWM}$ ratios for different $(n_{PM}, n_{HAZ}, n_{WM})$ combinations.

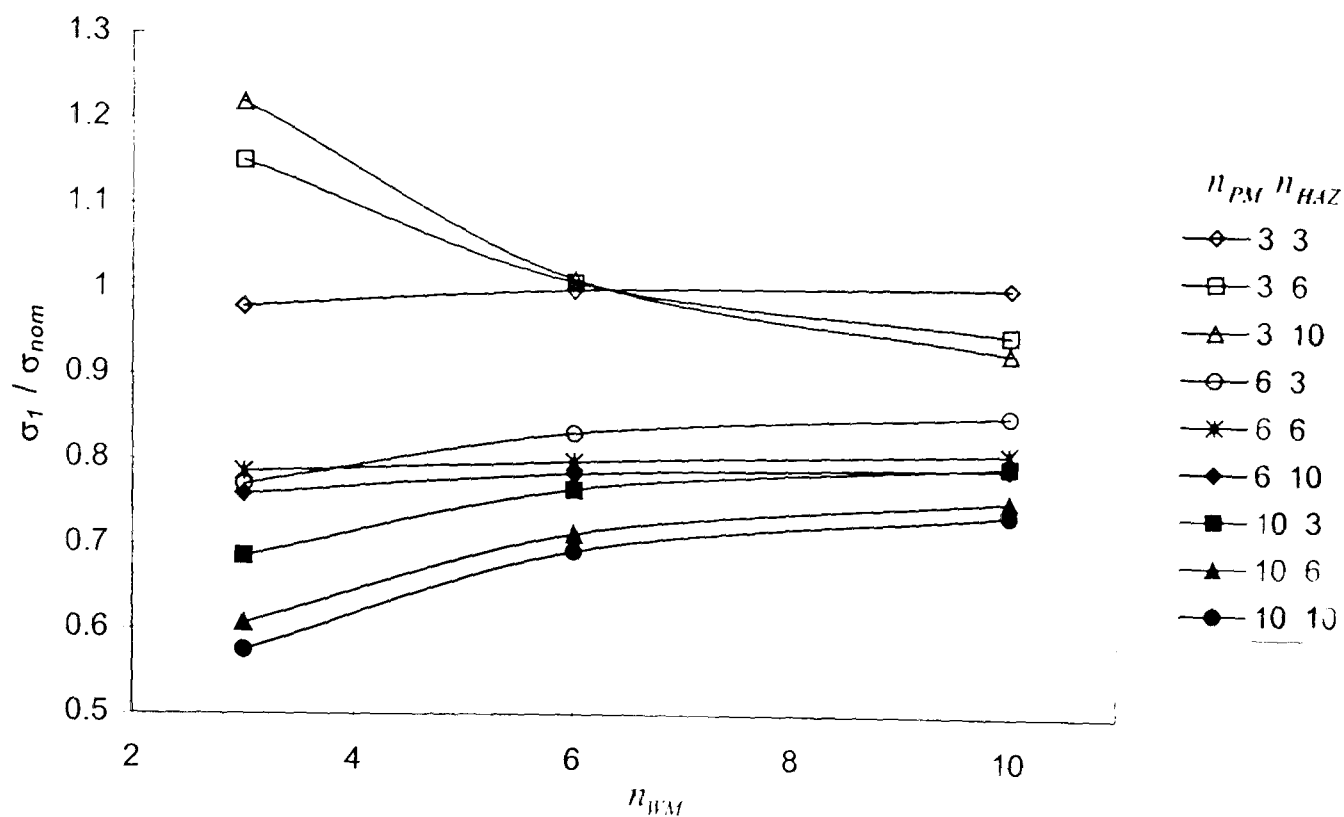


(a) $\dot{\epsilon}_{oPM} / \dot{\epsilon}_{oHAZ} = 100, \dot{\epsilon}_{oPM} / \dot{\epsilon}_{oWM} = 0.01$

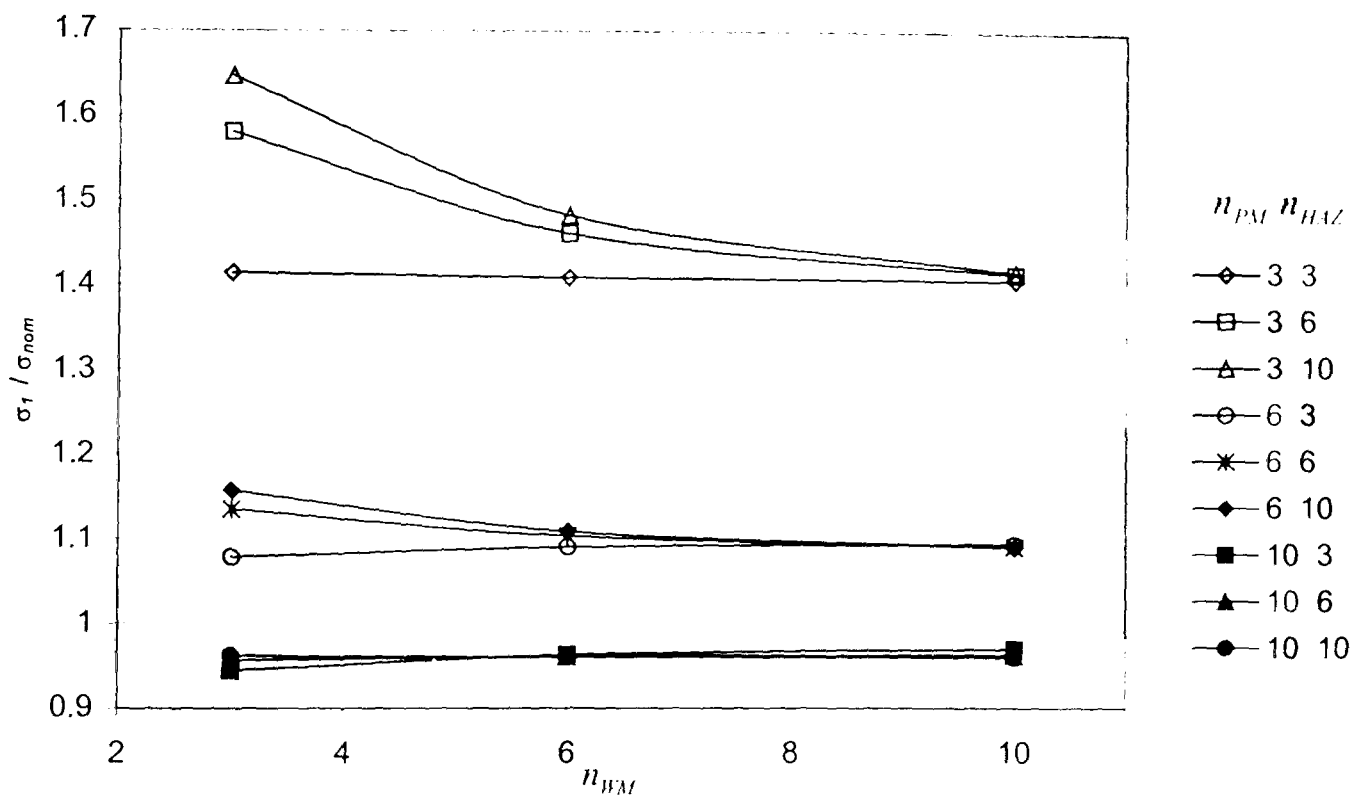


(b) $\dot{\epsilon}_{oPM} / \dot{\epsilon}_{oHAZ} = 100, \dot{\epsilon}_{oPM} / \dot{\epsilon}_{oWM} = 100$

Figure A2.2. Effect of n_{WM} on the maximum principal stress at Position A (PM^b), for a range of n_{PM} and n_{HAZ} combinations, for four different $\dot{\epsilon}_{oPM} / \dot{\epsilon}_{oHAZ}$ and $\dot{\epsilon}_{oPM} / \dot{\epsilon}_{oWM}$ ratios.



(c) $\dot{\epsilon}_{oPM} / \dot{\epsilon}_{oHAZ} = 0.01$, $\dot{\epsilon}_{oPM} / \dot{\epsilon}_{oWM} = 100$



(d) $\dot{\epsilon}_{oPM} / \dot{\epsilon}_{oHAZ} = 0.01$, $\dot{\epsilon}_{oPM} / \dot{\epsilon}_{oWM} = 0.01$

Figure A2.2 continued. Effect of n_{WM} on the maximum principal stress at Position A (PM^b), for a range of n_{PM} and n_{HAZ} combinations, for four different $\dot{\epsilon}_{oPM} / \dot{\epsilon}_{oHAZ}$ and $\dot{\epsilon}_{oPM} / \dot{\epsilon}_{oWM}$ ratios.

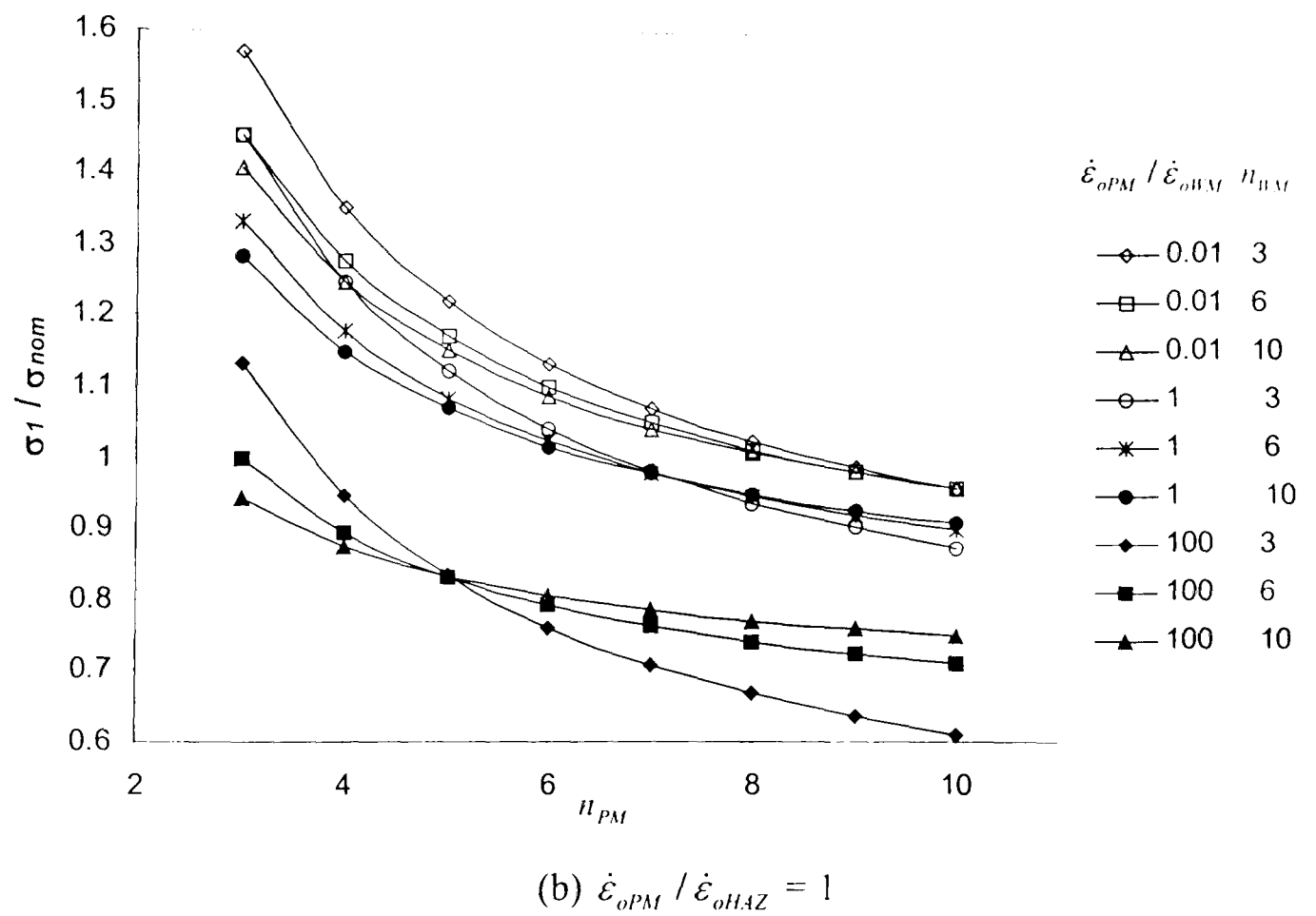
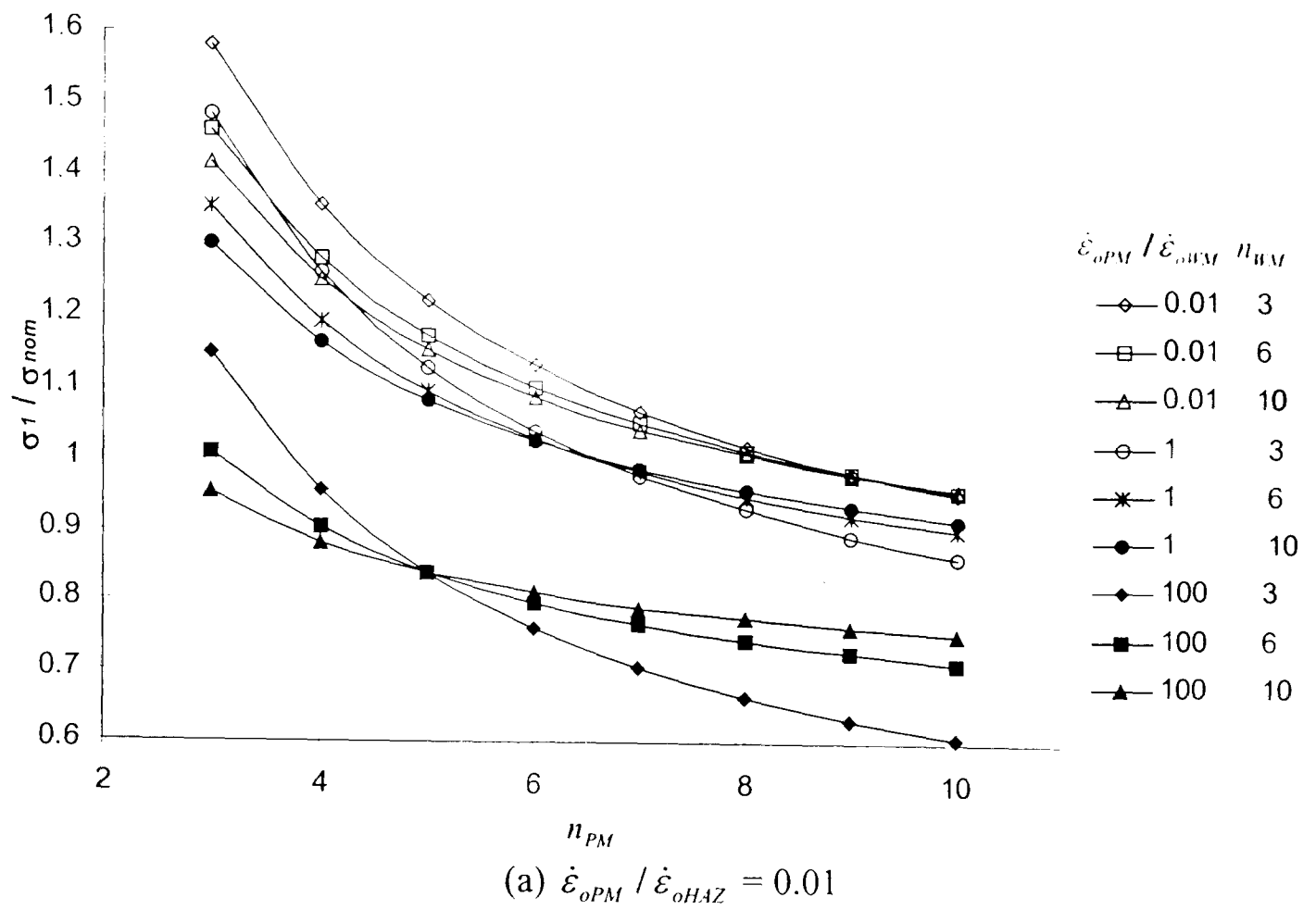


Figure A2.3. Effect of n_{PM} on the maximum principal stress at Position A (PM^b), for a range of $\dot{\epsilon}_{oPM} / \dot{\epsilon}_{oWM}$ and n_{WM} combinations, with $n_{HAZ} = 6$, for three different $\dot{\epsilon}_{oPM} / \dot{\epsilon}_{oHAZ}$ ratios

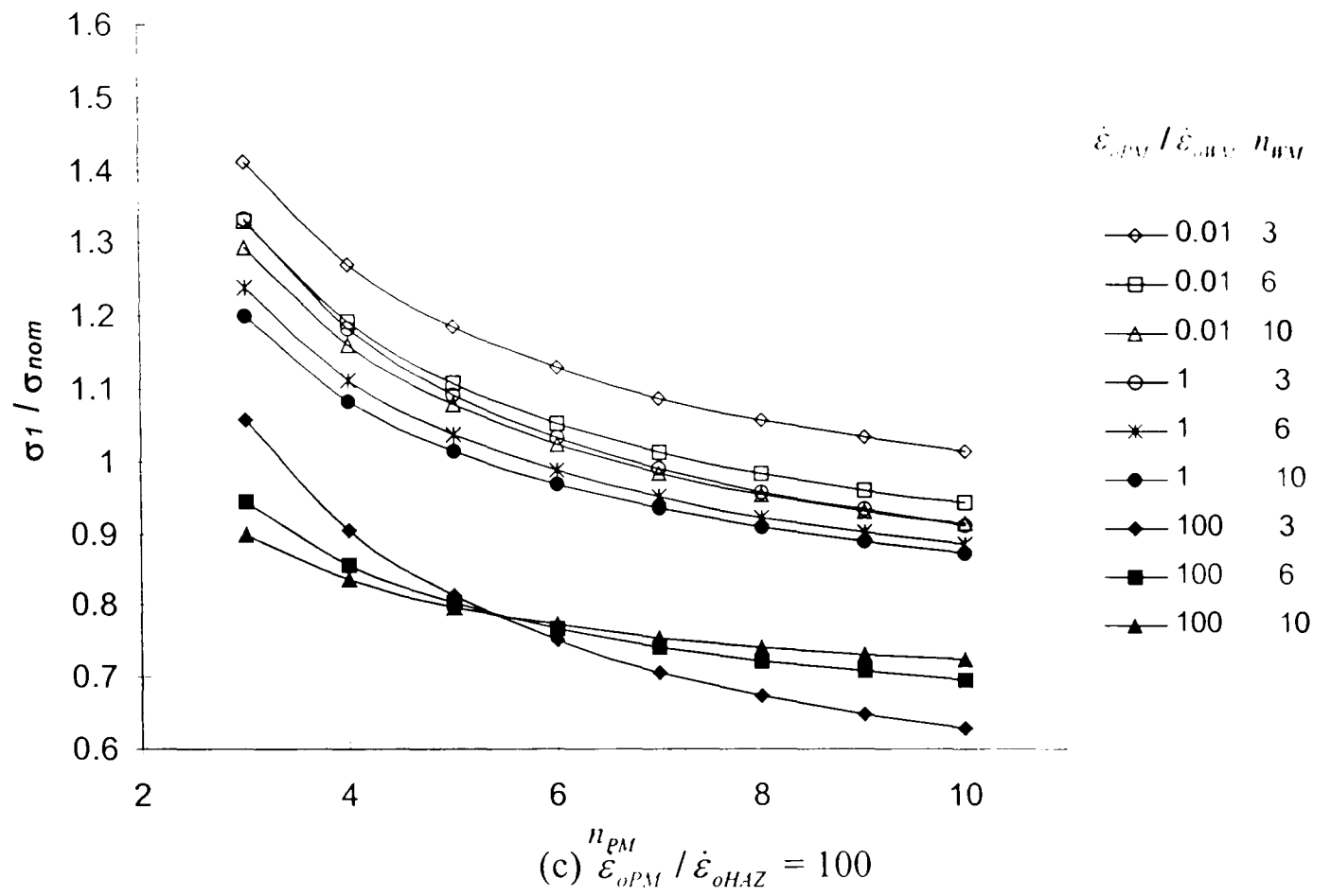
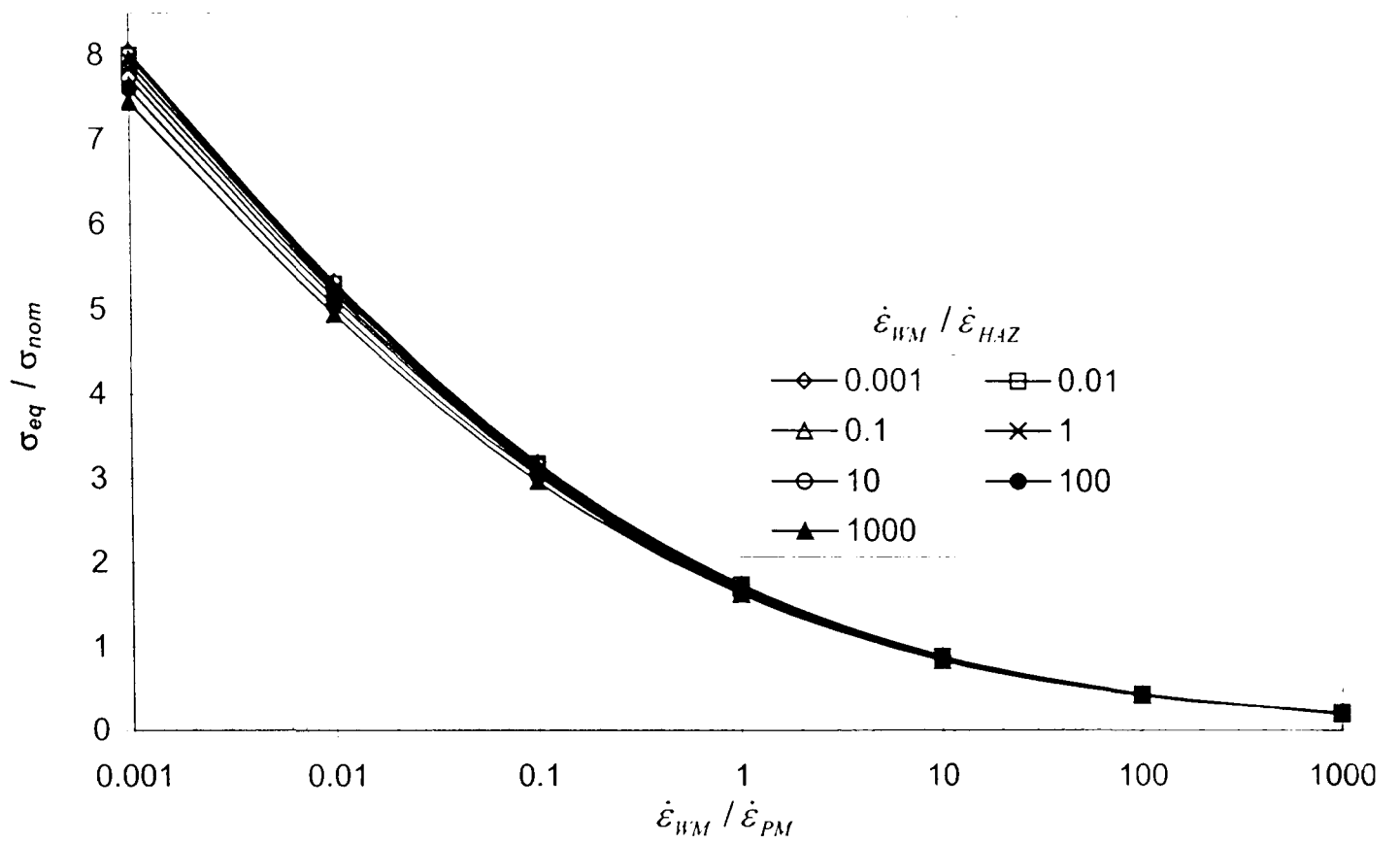
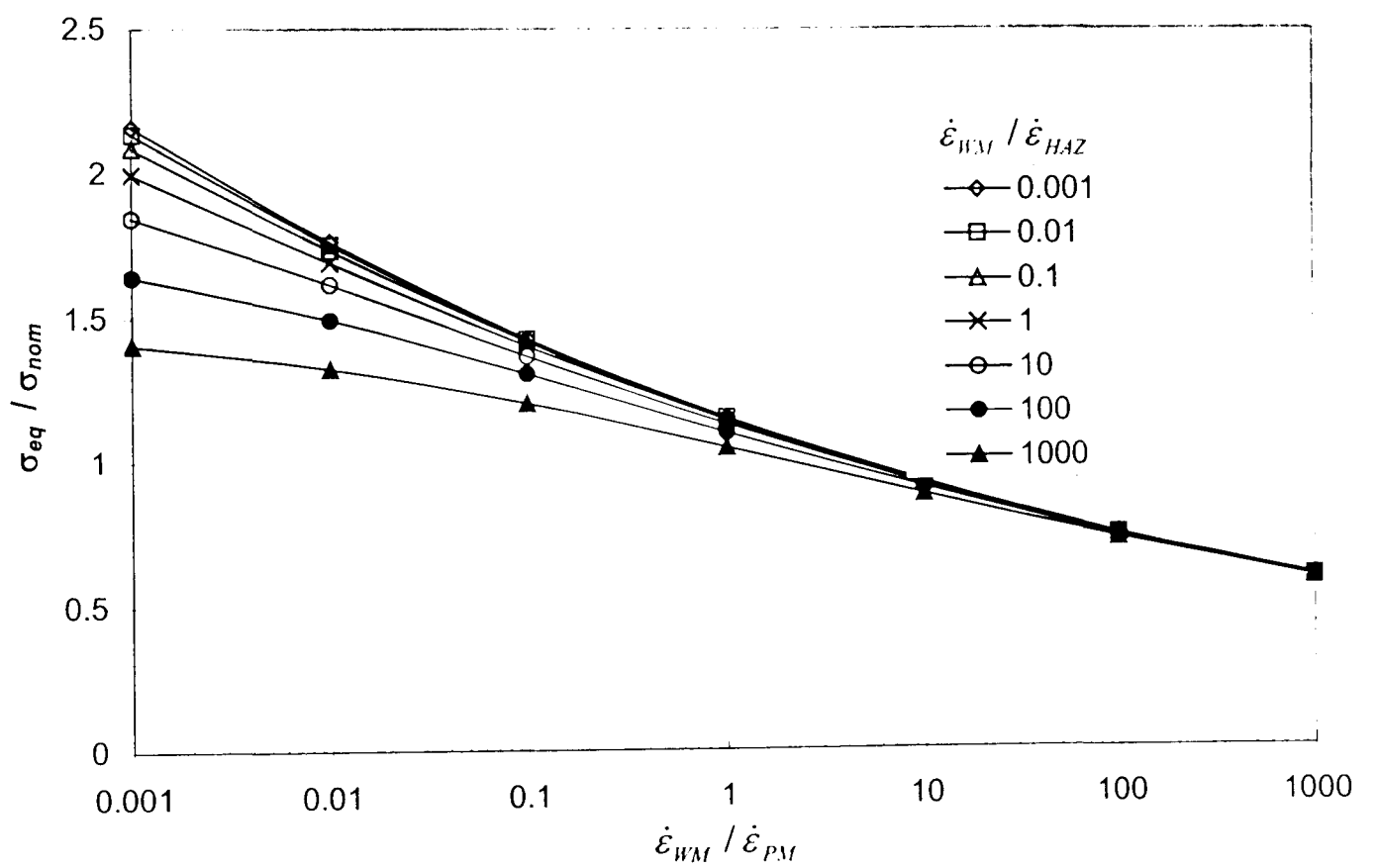


Figure A2.3 continued. Effect of n_{PM} on the maximum principal stress at Position A (PM^b), for a range of $\dot{\epsilon}_{oPM} / \dot{\epsilon}_{oHM}$ and n_{WM} combinations, with $n_{HAZ} = 6$, for three different $\dot{\epsilon}_{oPM} / \dot{\epsilon}_{oHAZ}$ ratios

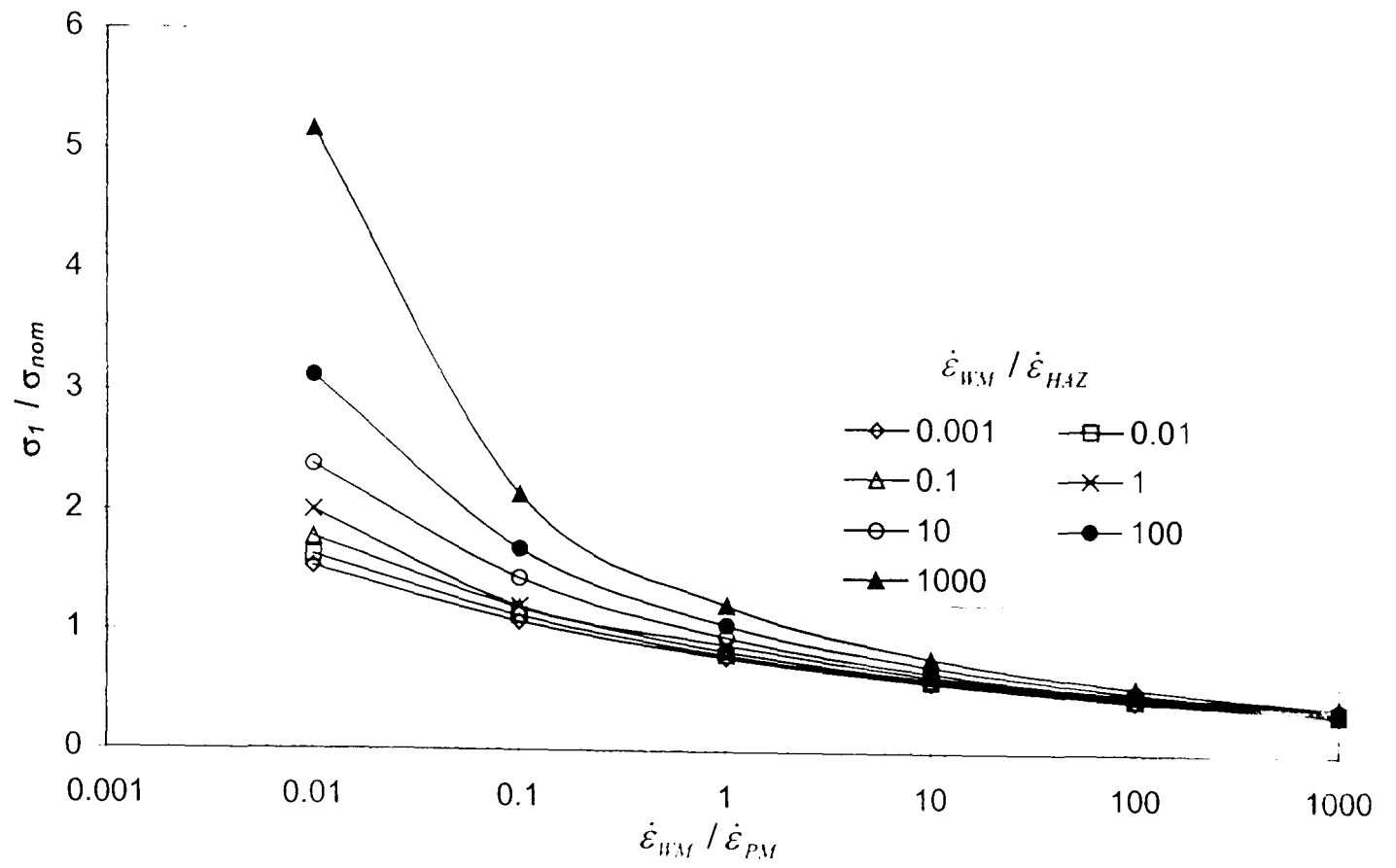


(a) $(n_{PM}, n_{HAZ}, n_{WM}) = (10, 10, 3)$

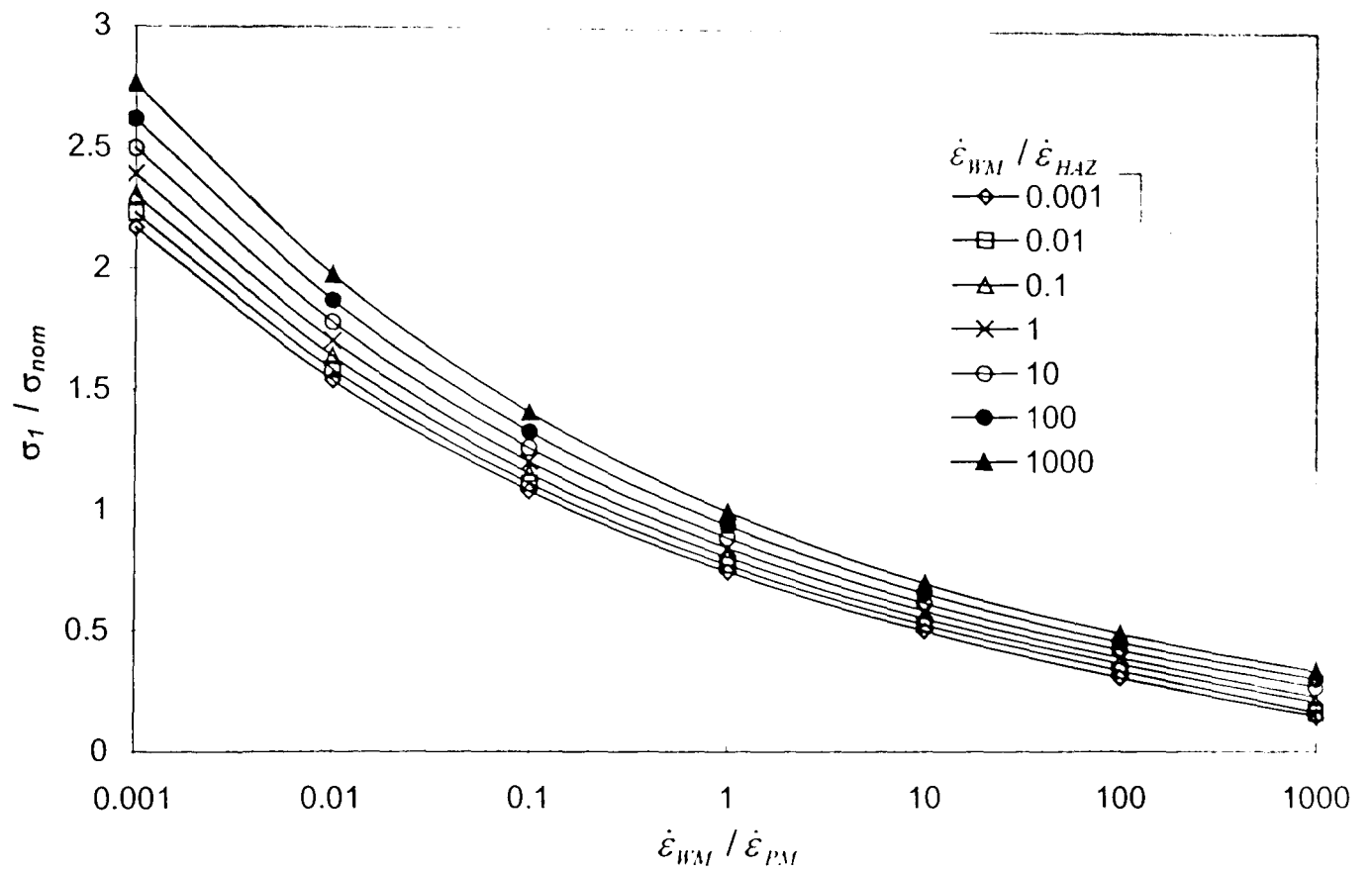


(b) $(n_{PM}, n_{HAZ}, n_{WM}) = (3, 3, 10)$

Figure A2.4. Variations of equivalent stress at Position B (WM) with $\dot{\epsilon}_{oWM} / \dot{\epsilon}_{oPM}$ and $\dot{\epsilon}_{oWM} / \dot{\epsilon}_{oHAZ}$ ratios for different $(n_{PM}, n_{HAZ}, n_{WM})$ combinations.

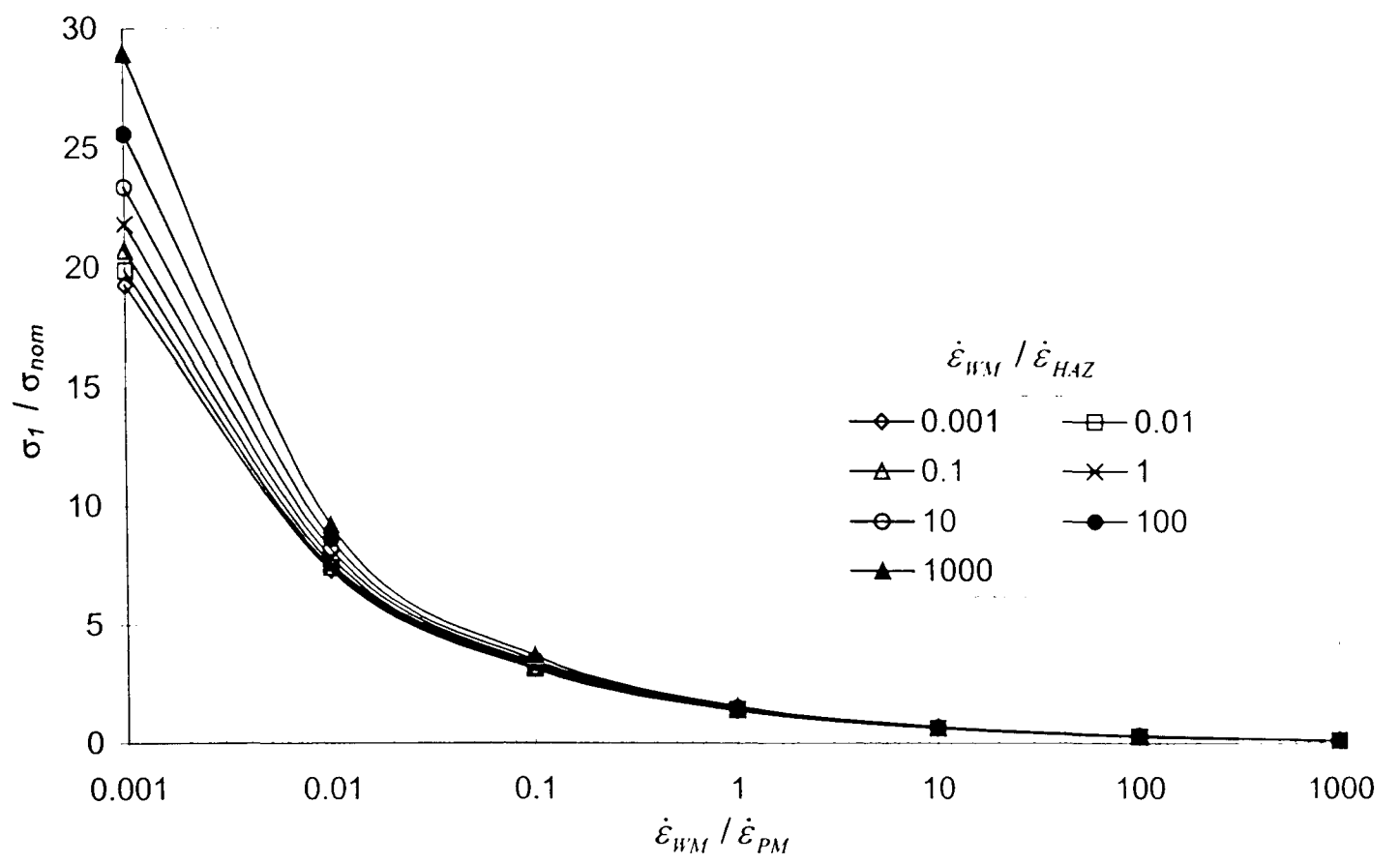


(a) $(n_{PM}, n_{HAZ}, n_{WM}) = (10, 10, 10)$



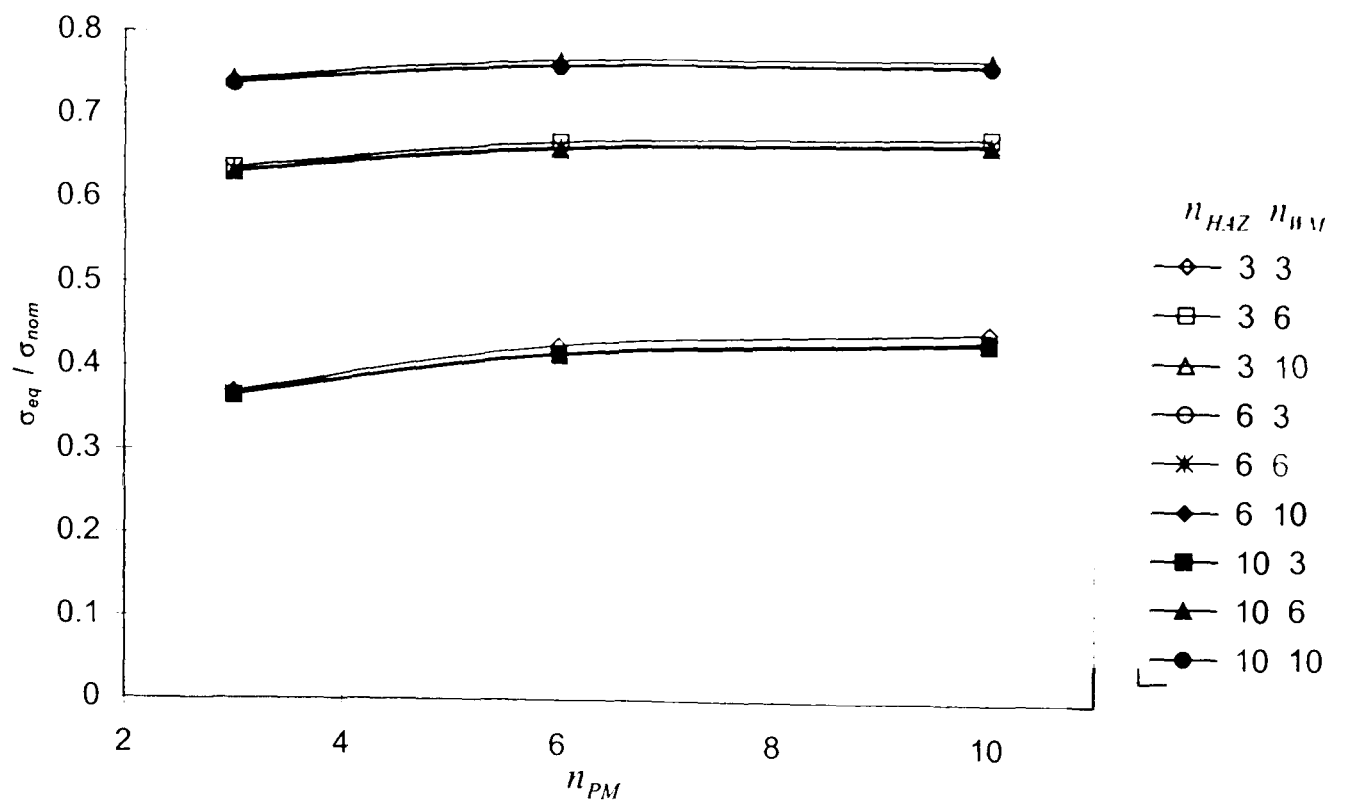
(b) $(n_{PM}, n_{HAZ}, n_{WM}) = (3, 10, 10)$

Figure A2.5. Variations of maximum principal stress at Position B (WM) with $\dot{\epsilon}_{oWM} / \dot{\epsilon}_{oPM}$ and $\dot{\epsilon}_{oWM} / \dot{\epsilon}_{oHAZ}$ ratios for different $(n_{PM}, n_{HAZ}, n_{WM})$ combinations.

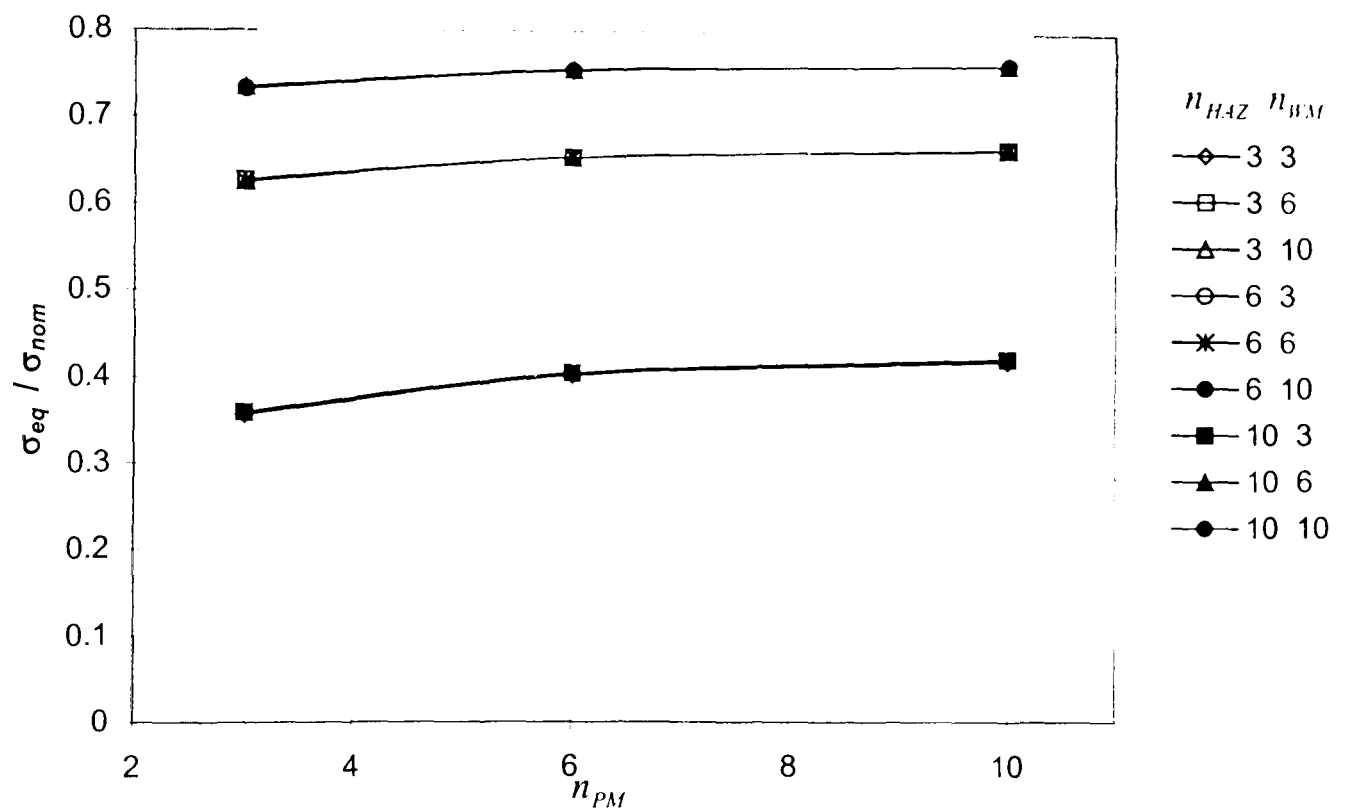


(c) $(n_{PM}, n_{HAZ}, n_{WM}) = (3, 10, 3)$

Figure A2.5 continued. Variations of maximum principal stress at Position 3 (WM) with $\dot{\epsilon}_{oWM} / \dot{\epsilon}_{oPM}$ and $\dot{\epsilon}_{oWM} / \dot{\epsilon}_{oHAZ}$ ratios for different $(n_{PM}, n_{HAZ}, n_{WM})$ combinations.

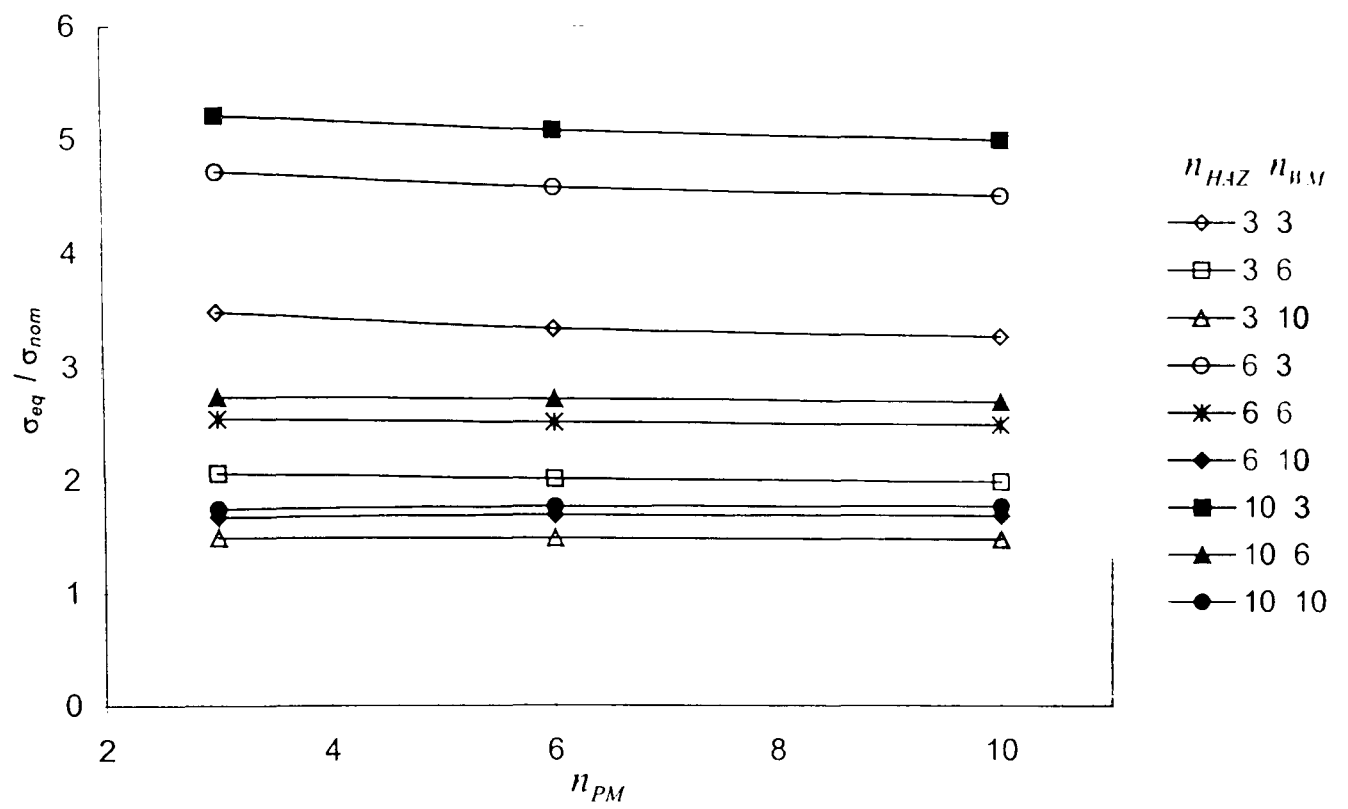


(a) $\dot{\epsilon}_{oWM} / \dot{\epsilon}_{oPM} = 100$, $\dot{\epsilon}_{oWM} / \dot{\epsilon}_{oHAZ} = 0.01$

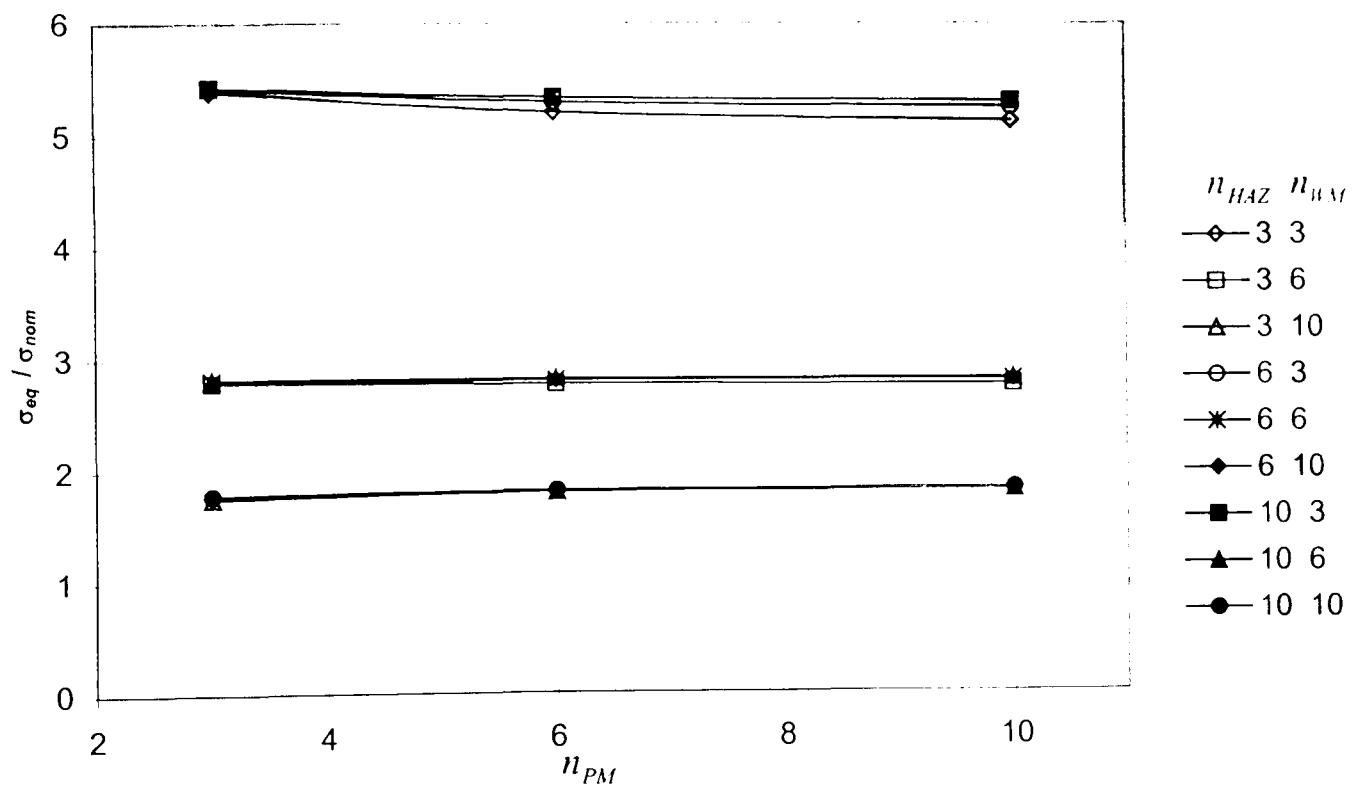


(b) $\dot{\epsilon}_{oWM} / \dot{\epsilon}_{oPM} = 100$, $\dot{\epsilon}_{oWM} / \dot{\epsilon}_{oHAZ} = 100$

Figure A2.6. Effect of n_{PM} on the equivalent stress at Position B (WM), for a range of n_{HAZ} and n_{WM} combinations, for four different $\dot{\epsilon}_{oWM} / \dot{\epsilon}_{oPM}$ and $\dot{\epsilon}_{oWM} / \dot{\epsilon}_{oHAZ}$ ratios.



(c) $\dot{\epsilon}_{oWM} / \dot{\epsilon}_{oPM} = 0.01$, $\dot{\epsilon}_{oWM} / \dot{\epsilon}_{oHAZ} = 100$



(d) $\dot{\epsilon}_{oWM} / \dot{\epsilon}_{oPM} = 0.01$, $\dot{\epsilon}_{oWM} / \dot{\epsilon}_{oHAZ} = 0.01$

Figure A2.6 continued. Effect of n_{PM} on the equivalent stress at Position B (WM), for a range of n_{HAZ} and n_{WM} combinations, for four different $\dot{\epsilon}_{oWM} / \dot{\epsilon}_{oPM}$ and $\dot{\epsilon}_{oWM} / \dot{\epsilon}_{oHAZ}$ ratios.

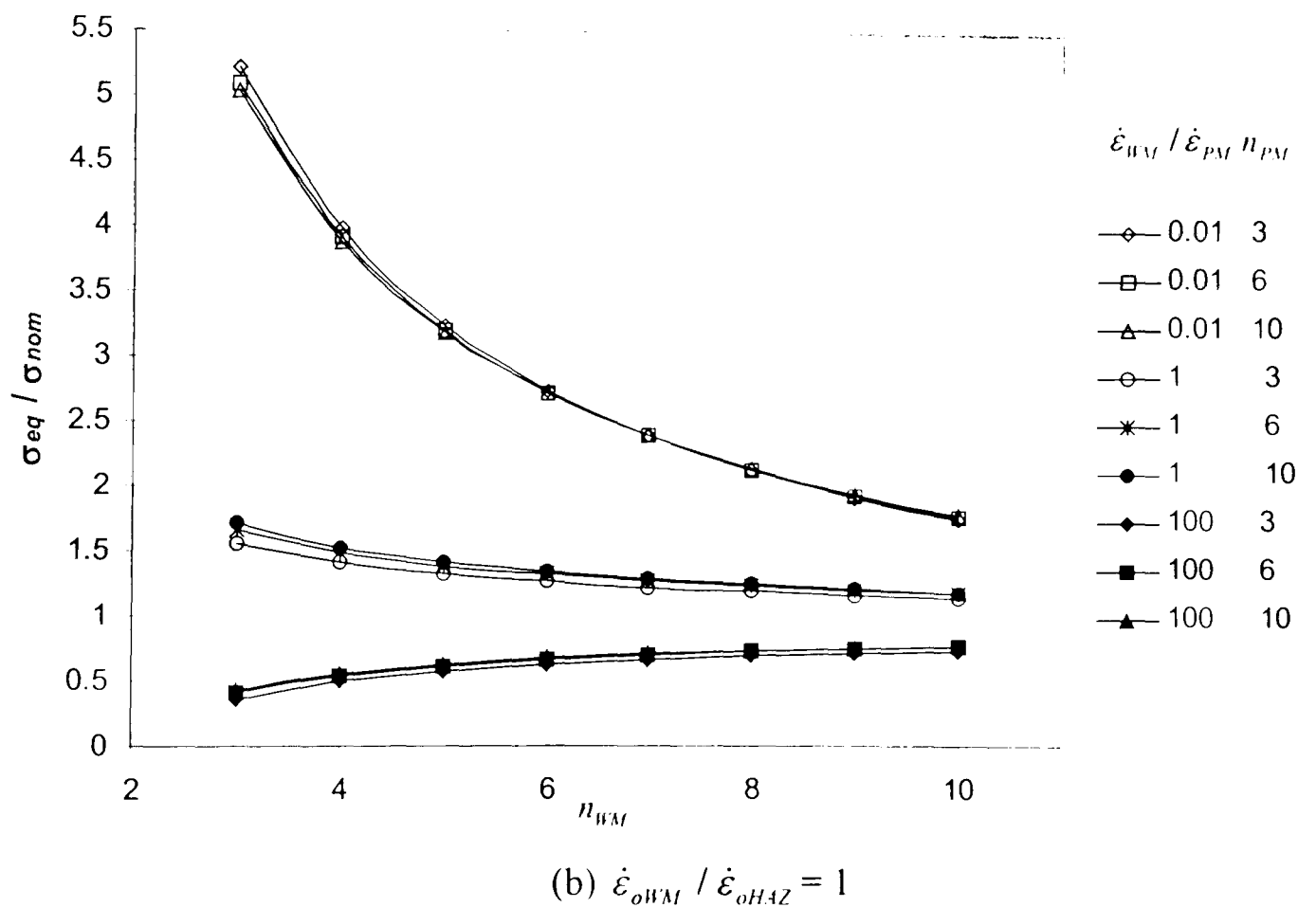
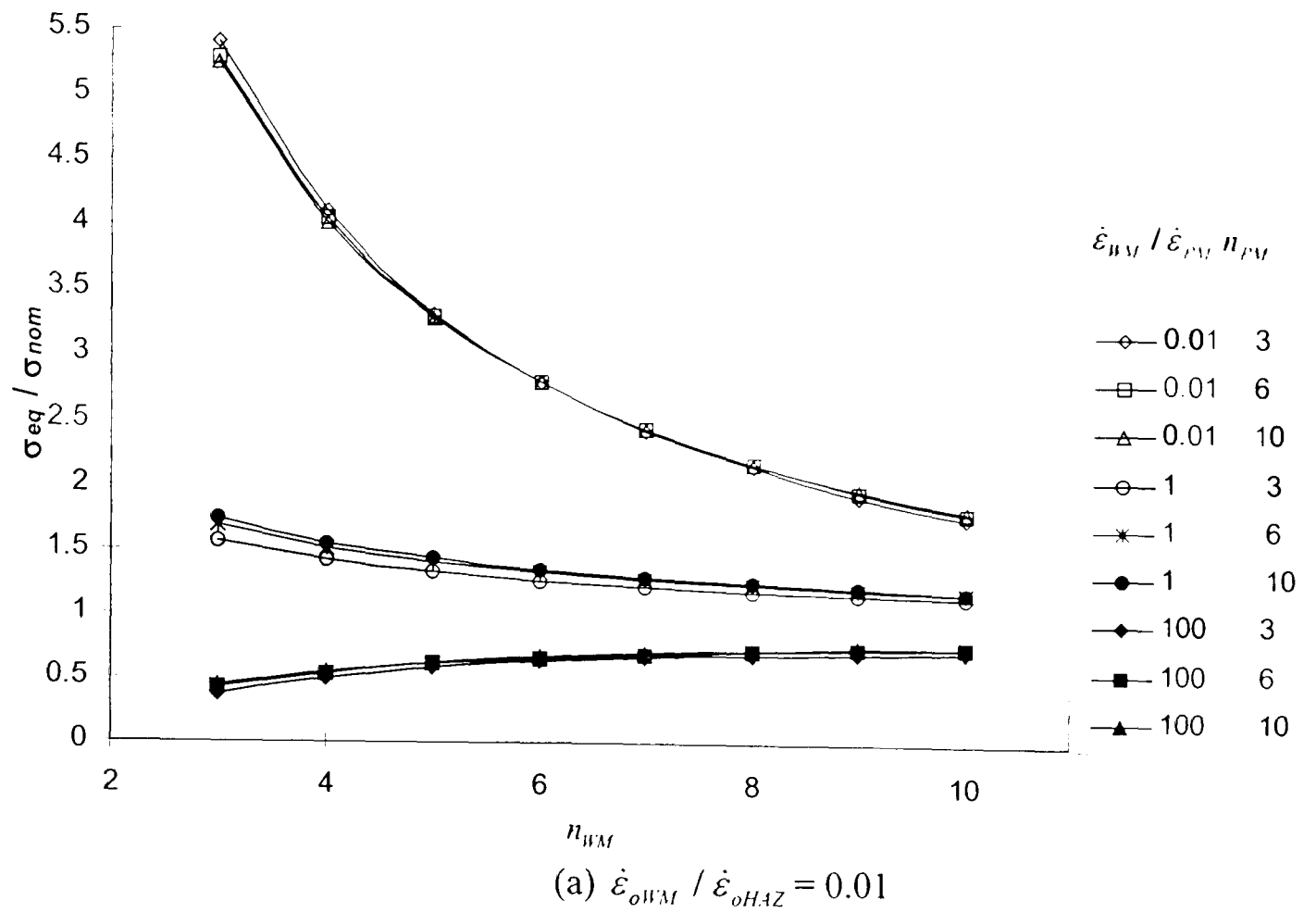


Figure A2.7. Effect of n_{WM} on the equivalent stress at Position B (WM), for a range of $\dot{\epsilon}_{oWM} / \dot{\epsilon}_{oPM}$ and n_{PM} combinations, with $n_{HAZ} = 6$, for three different $\dot{\epsilon}_{oWM} / \dot{\epsilon}_{oHAZ}$ ratios.

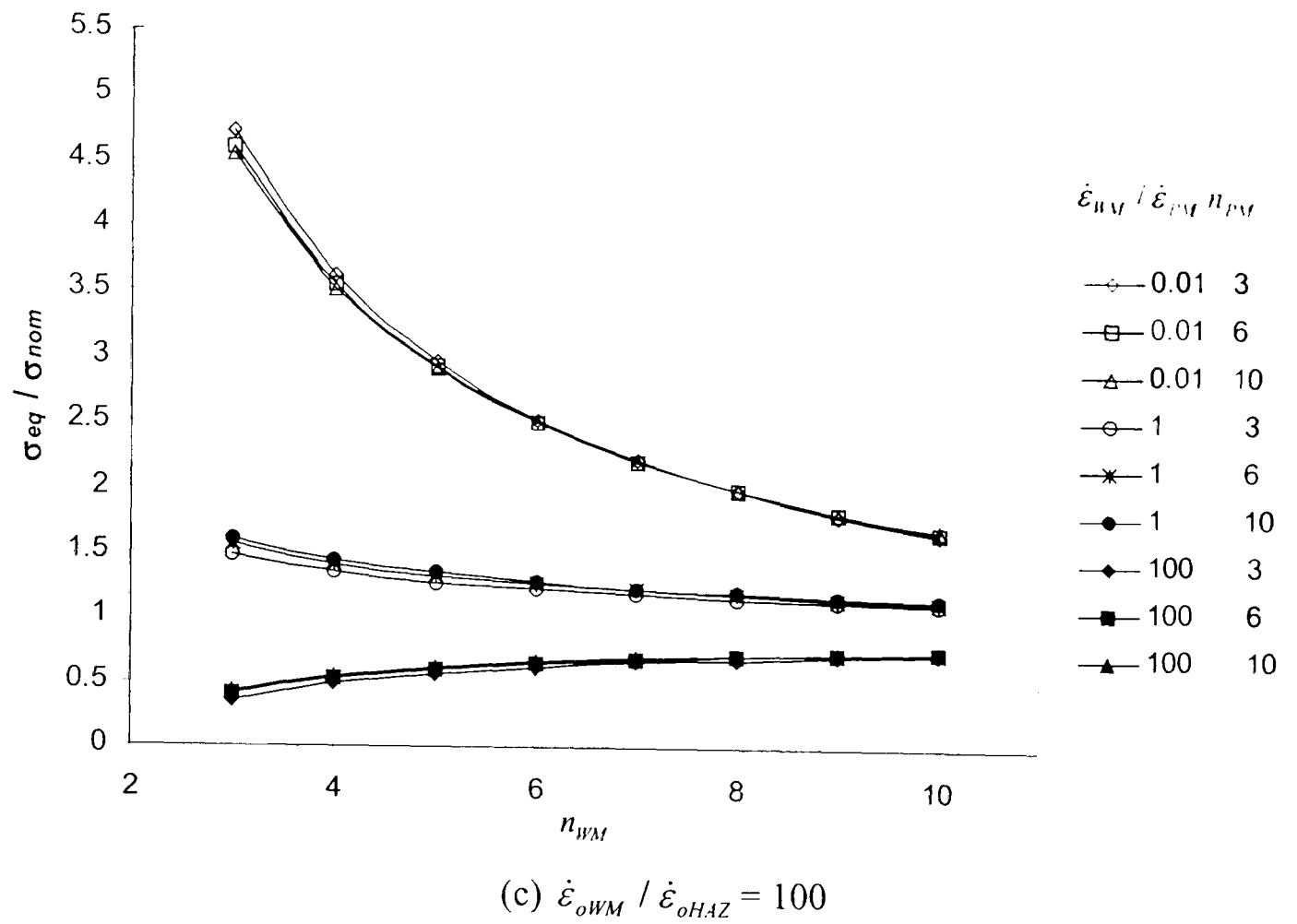


Figure A2.7 continued. Effect of n_{WM} on the equivalent stress at Position B (WM), for a range of $\dot{\epsilon}_{oWM} / \dot{\epsilon}_{oPM}$ and n_{PM} combinations, with $n_{HAZ} = 6$, for three different $\dot{\epsilon}_{oWM} / \dot{\epsilon}_{oHAZ}$ ratios.

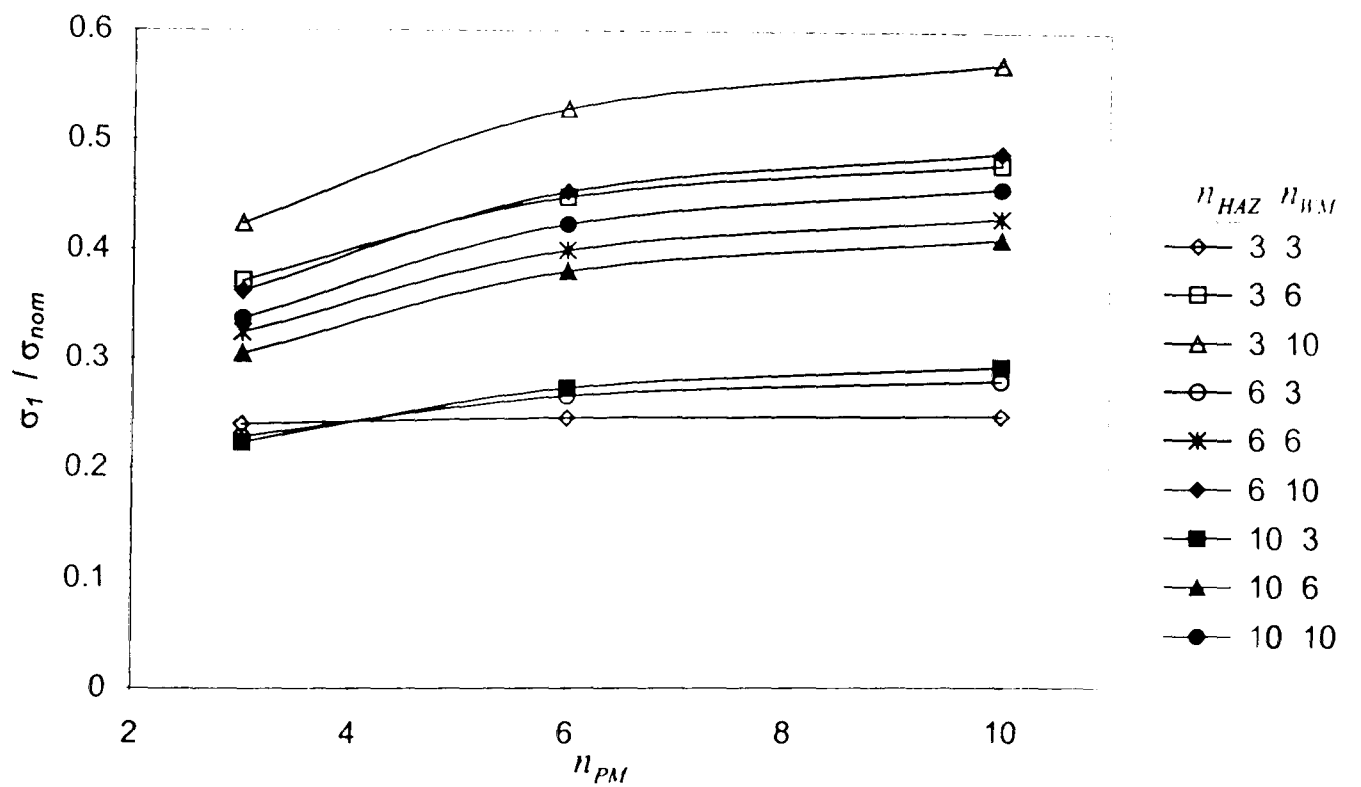


Figure A2.8. Effect of n_{PM} on the maximum principal stress at Position B (WM), for a range of n_{HAZ} and n_{WM} combinations, for $\dot{\epsilon}_{oWM} / \dot{\epsilon}_{oPM} = 100$ and $\dot{\epsilon}_{oWM} / \dot{\epsilon}_{oHAZ} = 100$.

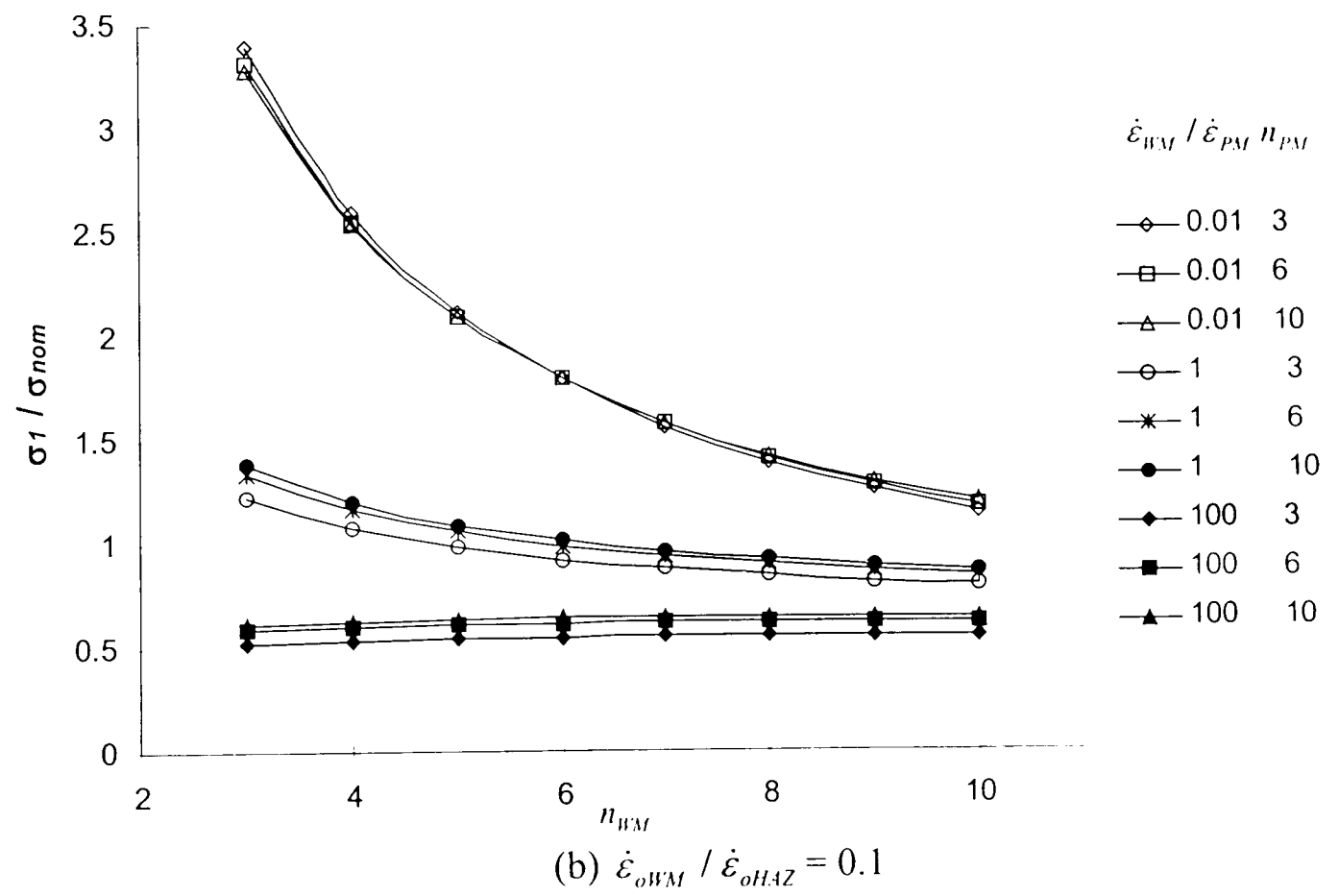
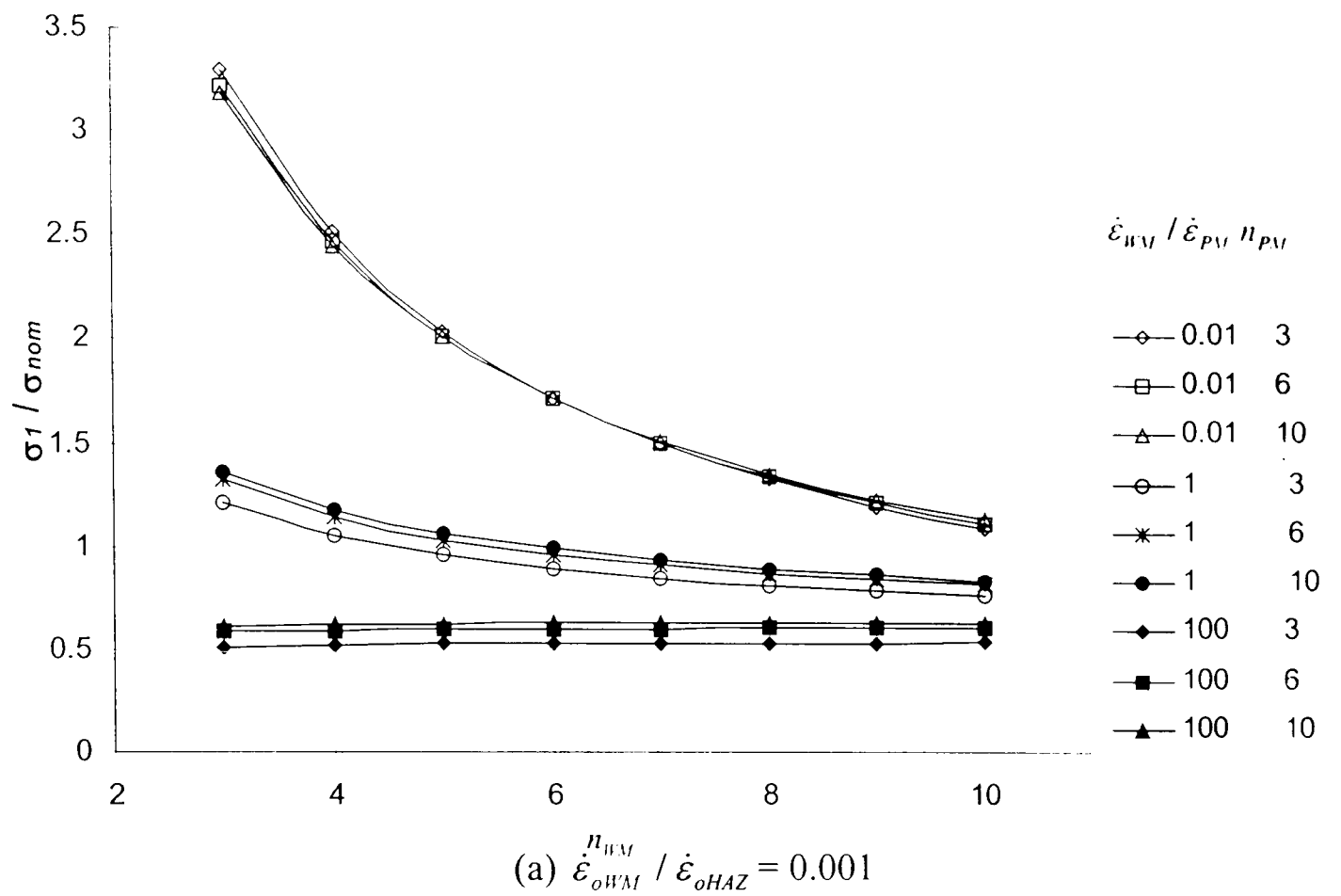
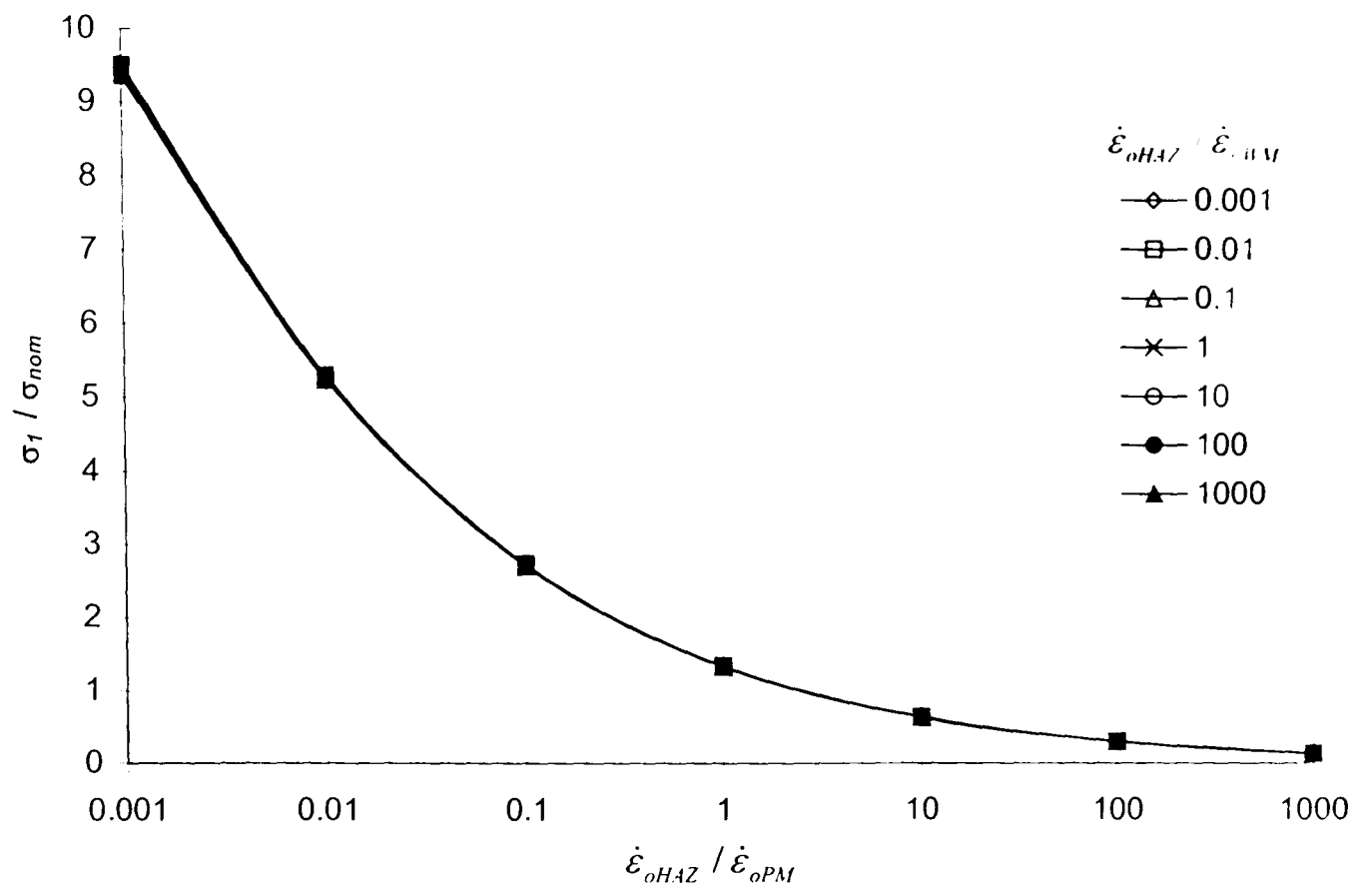
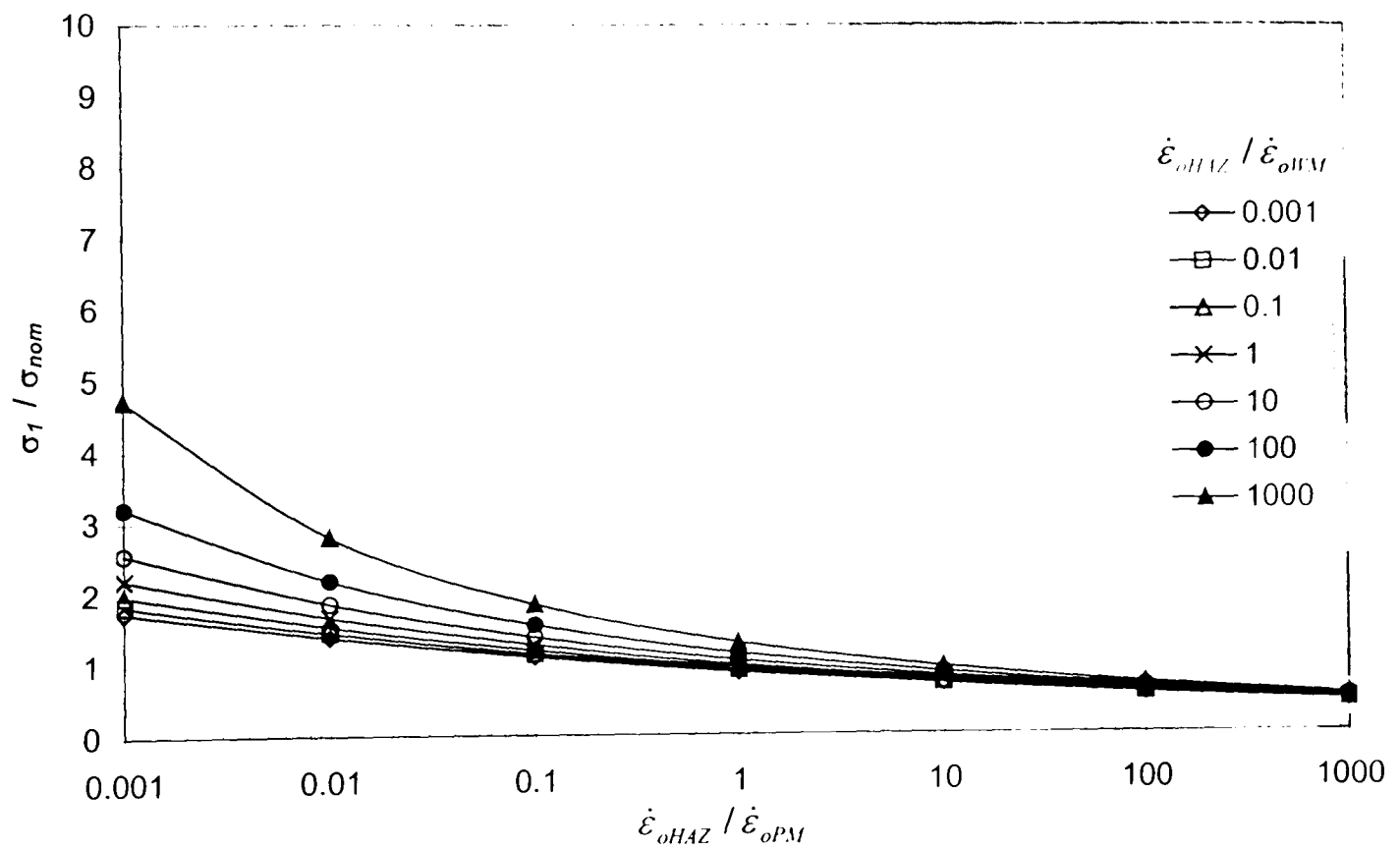


Figure A2.9. Effect of n_{WM} on the maximum principal stress at Position B (WM), for a range of $\dot{\epsilon}_{oWM} / \dot{\epsilon}_{oPM}$ and n_{PM} combinations, with $n_{HAZ} = 6$, for three different $\dot{\epsilon}_{oWM} / \dot{\epsilon}_{oHAZ}$ ratios.

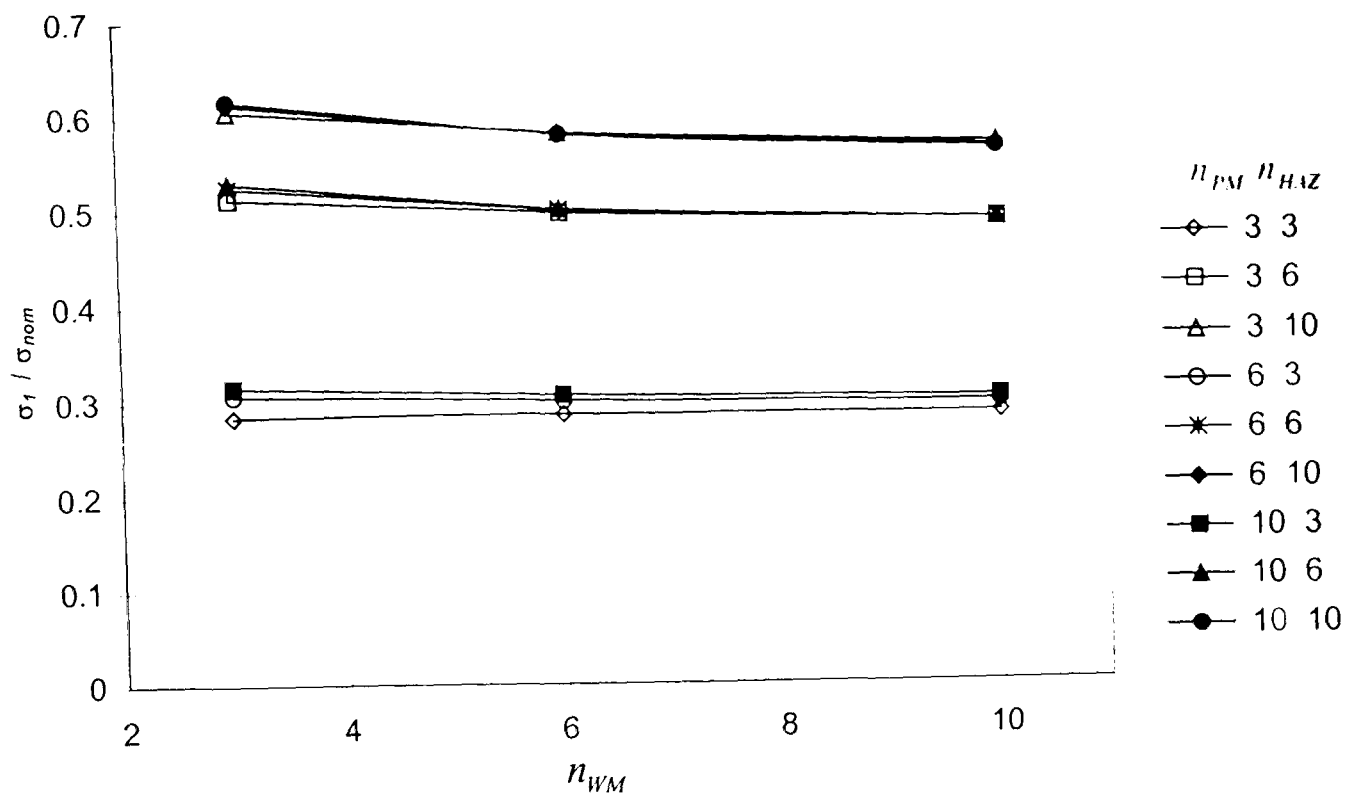


(a) $(n_{PM}, n_{HAZ}, n_{WM}) = (10, 3, 10)$

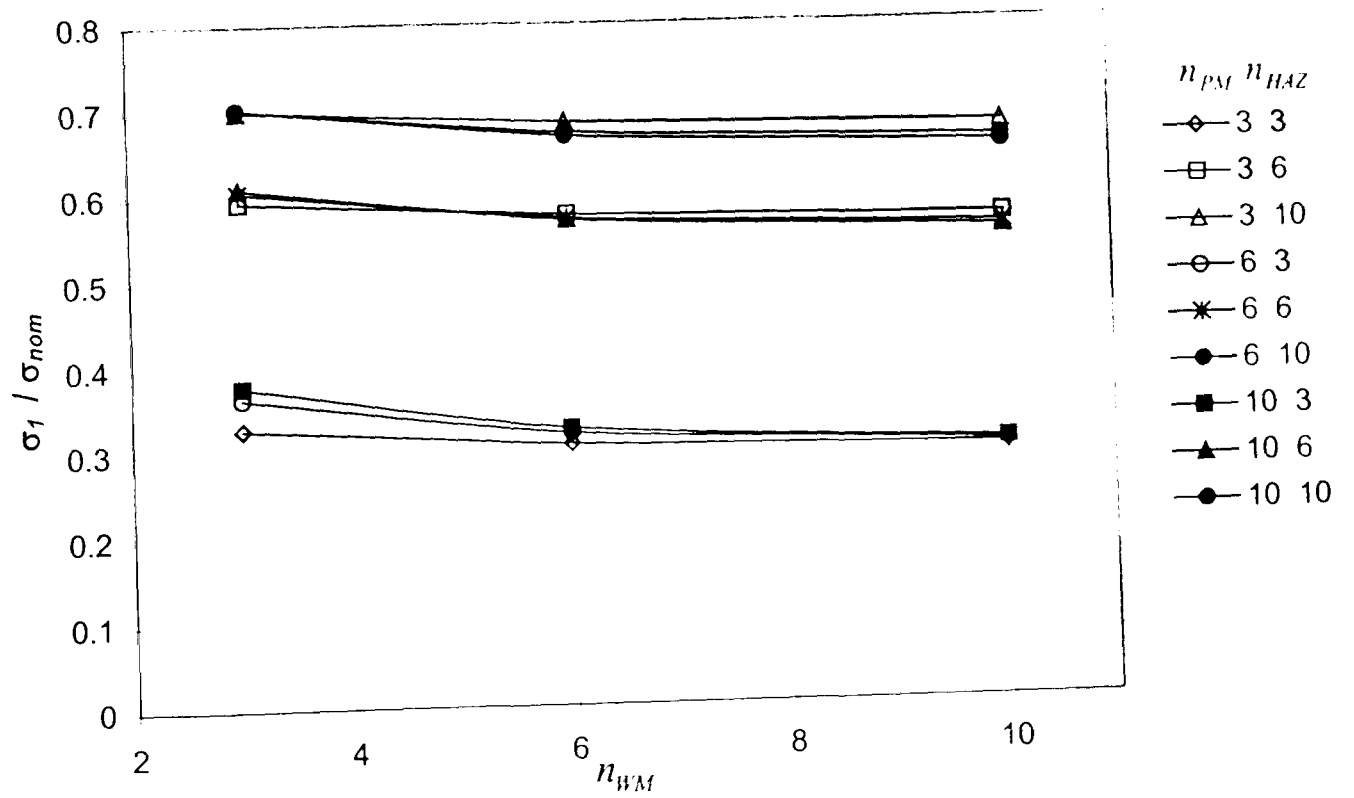


(b) $(n_{PM}, n_{HAZ}, n_{WM}) = (3, 10, 3)$

Figure A2.10. Variations of maximum principal stress at Position D (HAZ^P) with $\dot{\epsilon}_{oHAZ} / \dot{\epsilon}_{oPM}$ and $\dot{\epsilon}_{oHAZ} / \dot{\epsilon}_{oWM}$ ratios for different $(n_{PM}, n_{HAZ}, n_{WM})$ combinations.

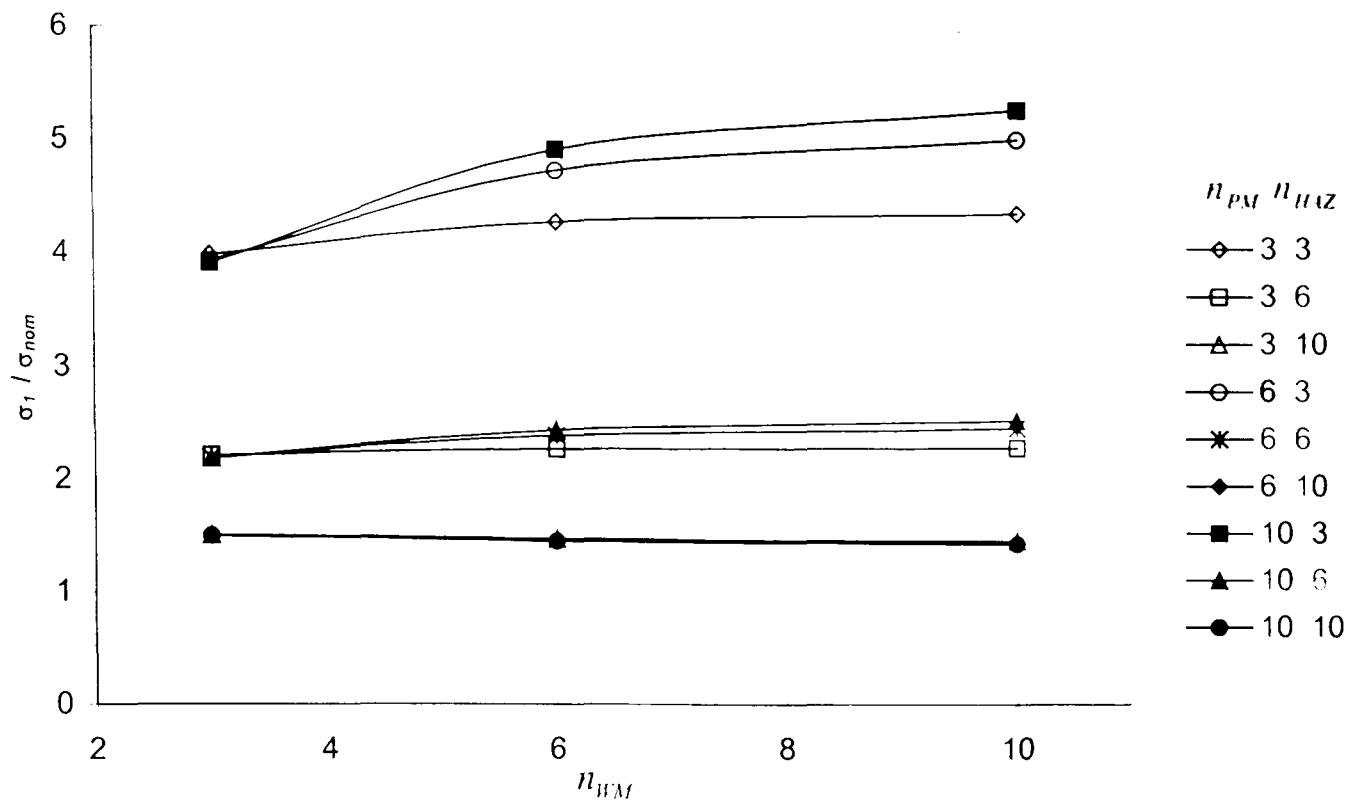


(a) $\dot{\epsilon}_{oHAZ} / \dot{\epsilon}_{oPM} = 100, \dot{\epsilon}_{oHAZ} / \dot{\epsilon}_{oWM} = 0.01$



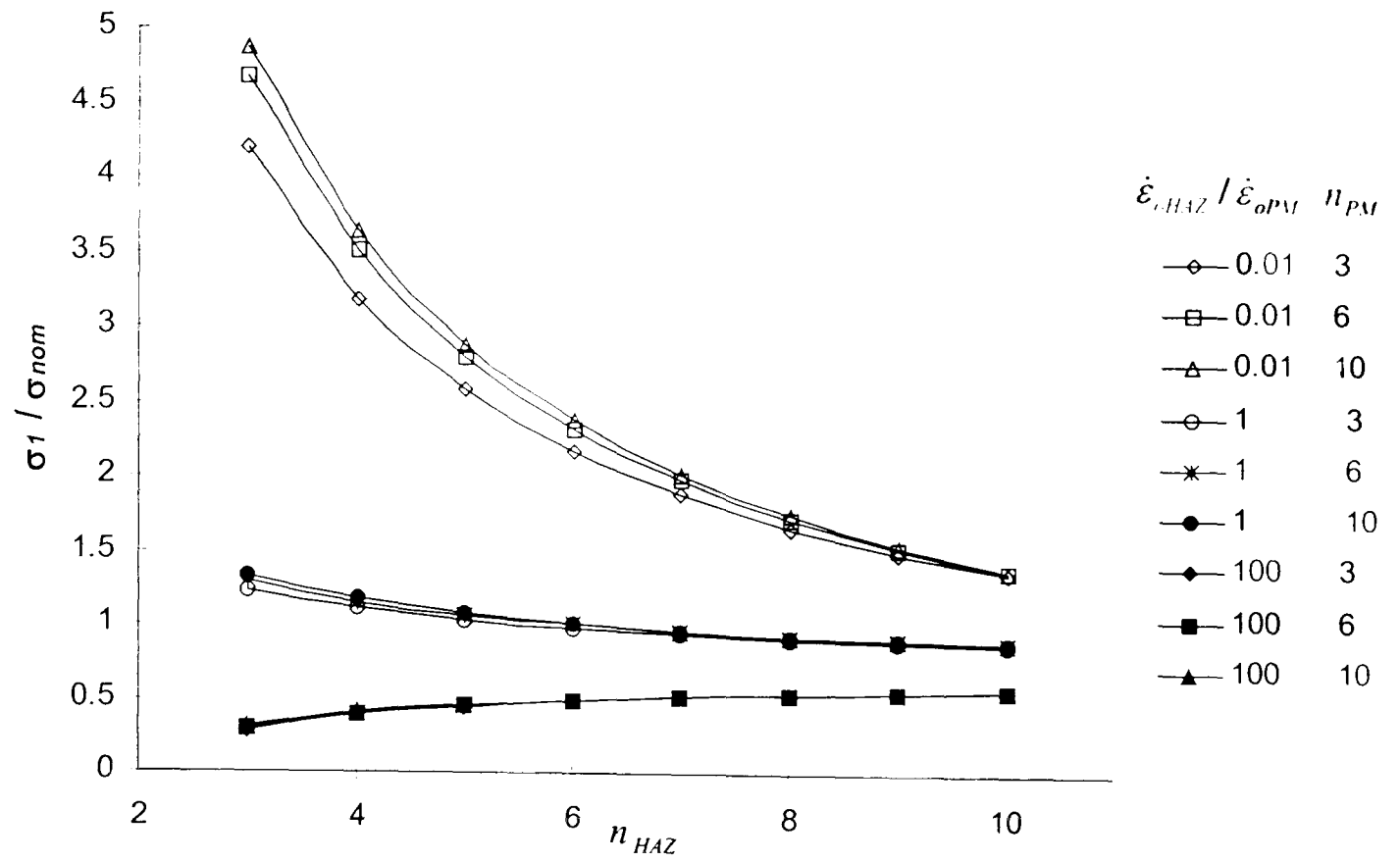
(b) $\dot{\epsilon}_{oHAZ} / \dot{\epsilon}_{oPM} = 100, \dot{\epsilon}_{oHAZ} / \dot{\epsilon}_{oWM} = 100$

Figure A2.11. Effect of n_{WM} on the maximum principal stress at Position D (HAZ^p), for a range of n_{PM} and n_{HAZ} combinations, for three different $\dot{\epsilon}_{oHAZ} / \dot{\epsilon}_{oPM}$ and $\dot{\epsilon}_{oHAZ} / \dot{\epsilon}_{oWM}$ ratios.

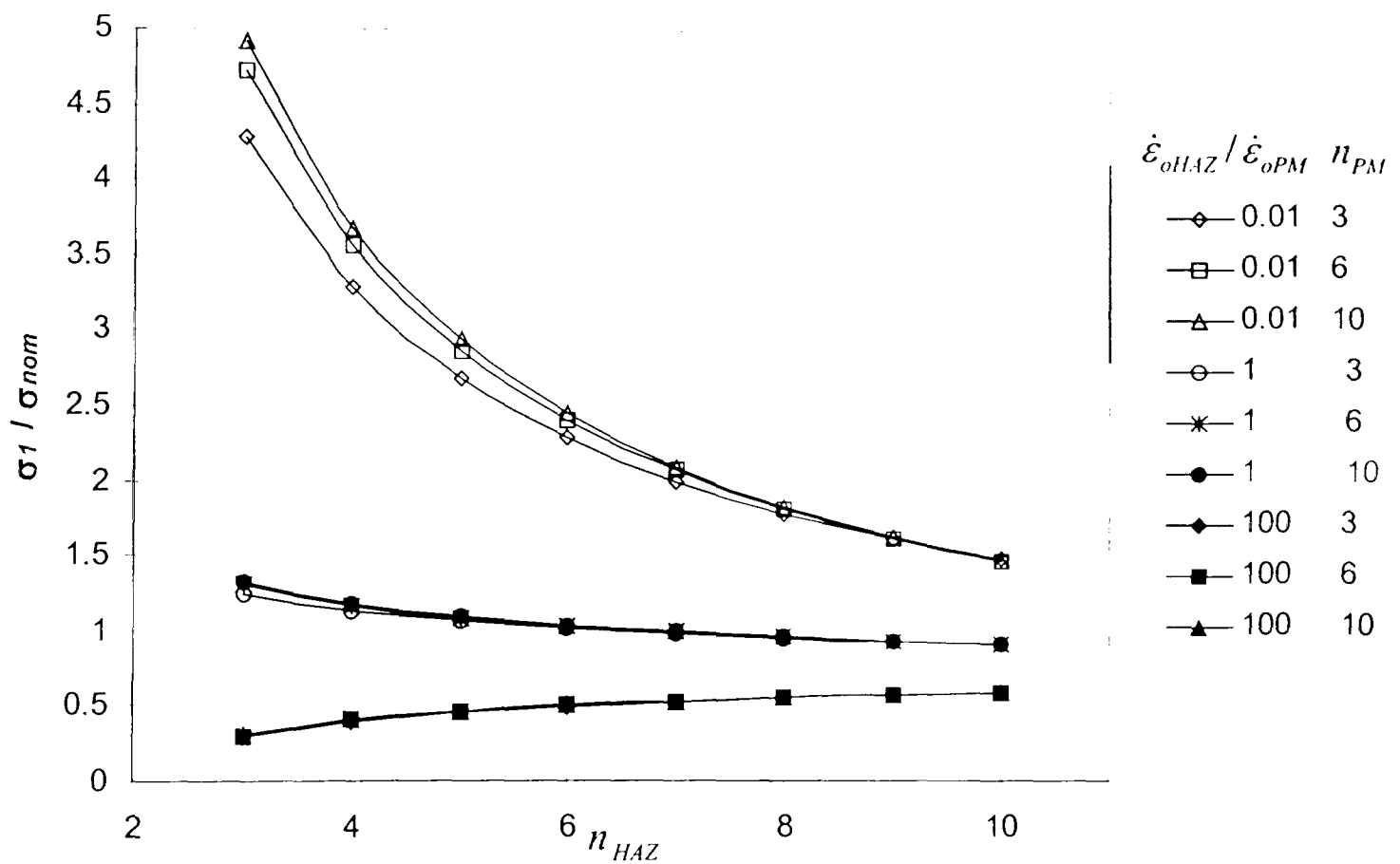


(c) $\dot{\epsilon}_{oHAZ} / \dot{\epsilon}_{oPM} = 0.01$, $\dot{\epsilon}_{oHAZ} / \dot{\epsilon}_{oWM} = 100$

Figure A2.11 continued. Effect of n_{WM} on the maximum principal stress at Position D (HAZ^p), for a range of n_{PM} and n_{HAZ} combinations, for three different $\dot{\epsilon}_{oHAZ} / \dot{\epsilon}_{oPM}$ and $\dot{\epsilon}_{oHAZ} / \dot{\epsilon}_{oWM}$ ratios.

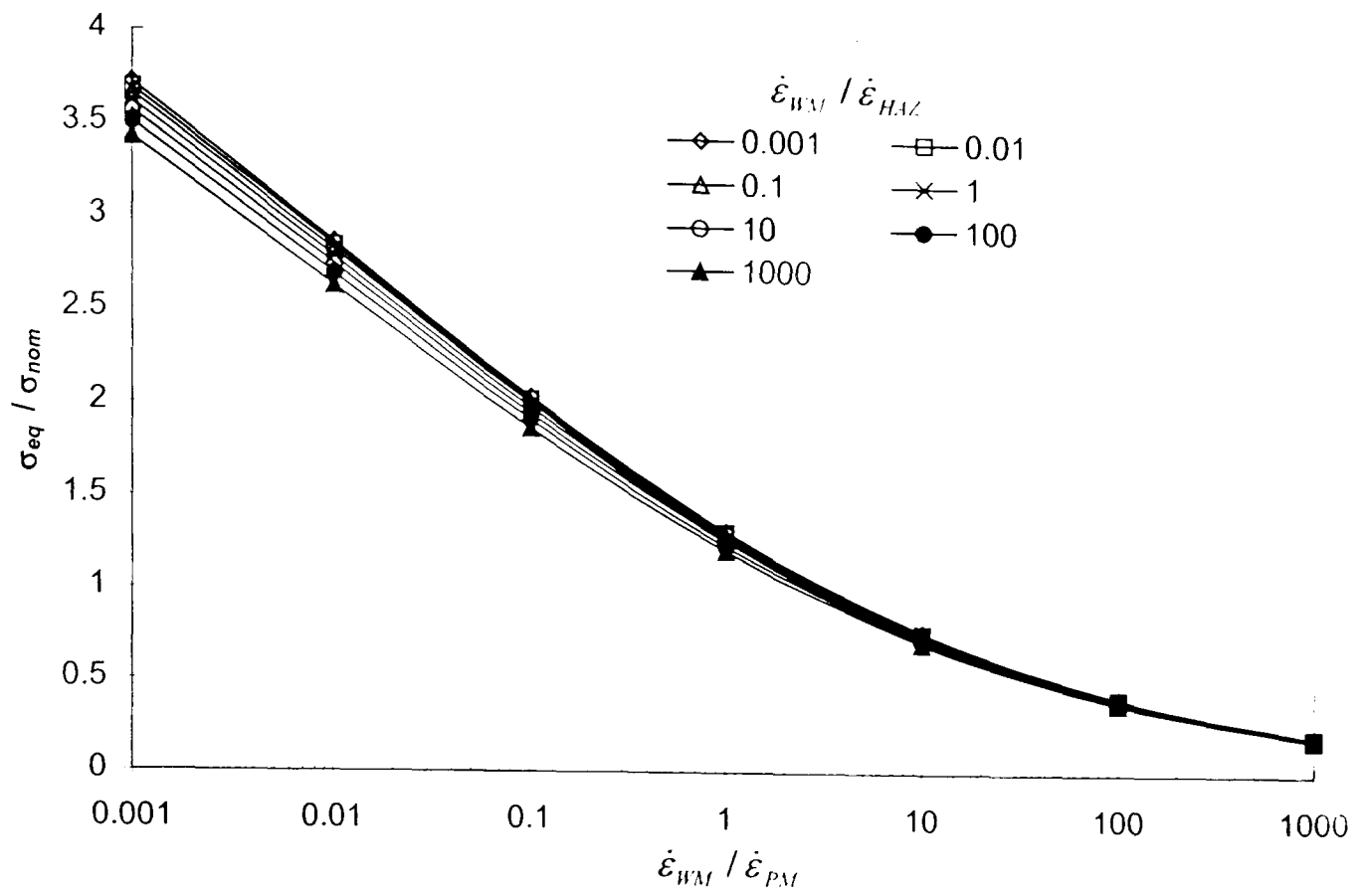


(a) $\dot{\epsilon}_{oHAZ} / \dot{\epsilon}_{oWM} = 0.01$

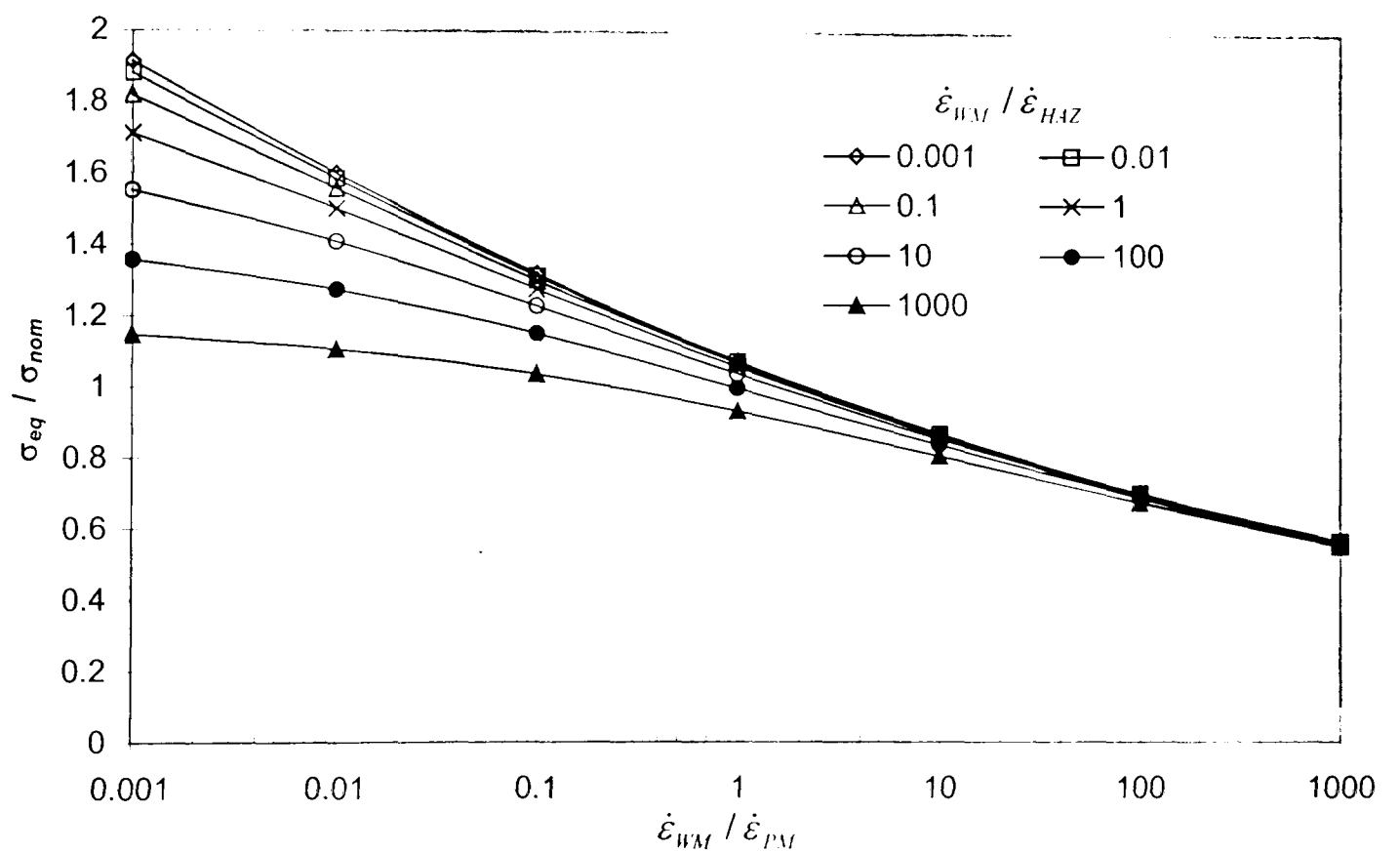


(b) $\dot{\epsilon}_{oHAZ} / \dot{\epsilon}_{oWM} = 1$

Figure A2.12. Effect of n_{HAZ} on the maximum principal stress at Position D (HAZ^P), for a range of $\dot{\epsilon}_{oHAZ} / \dot{\epsilon}_{oPM}$ and n_{PM} combinations, with $n_{HAZ} = 6$, for two different $\dot{\epsilon}_{oHAZ} / \dot{\epsilon}_{oWM}$ ratios.

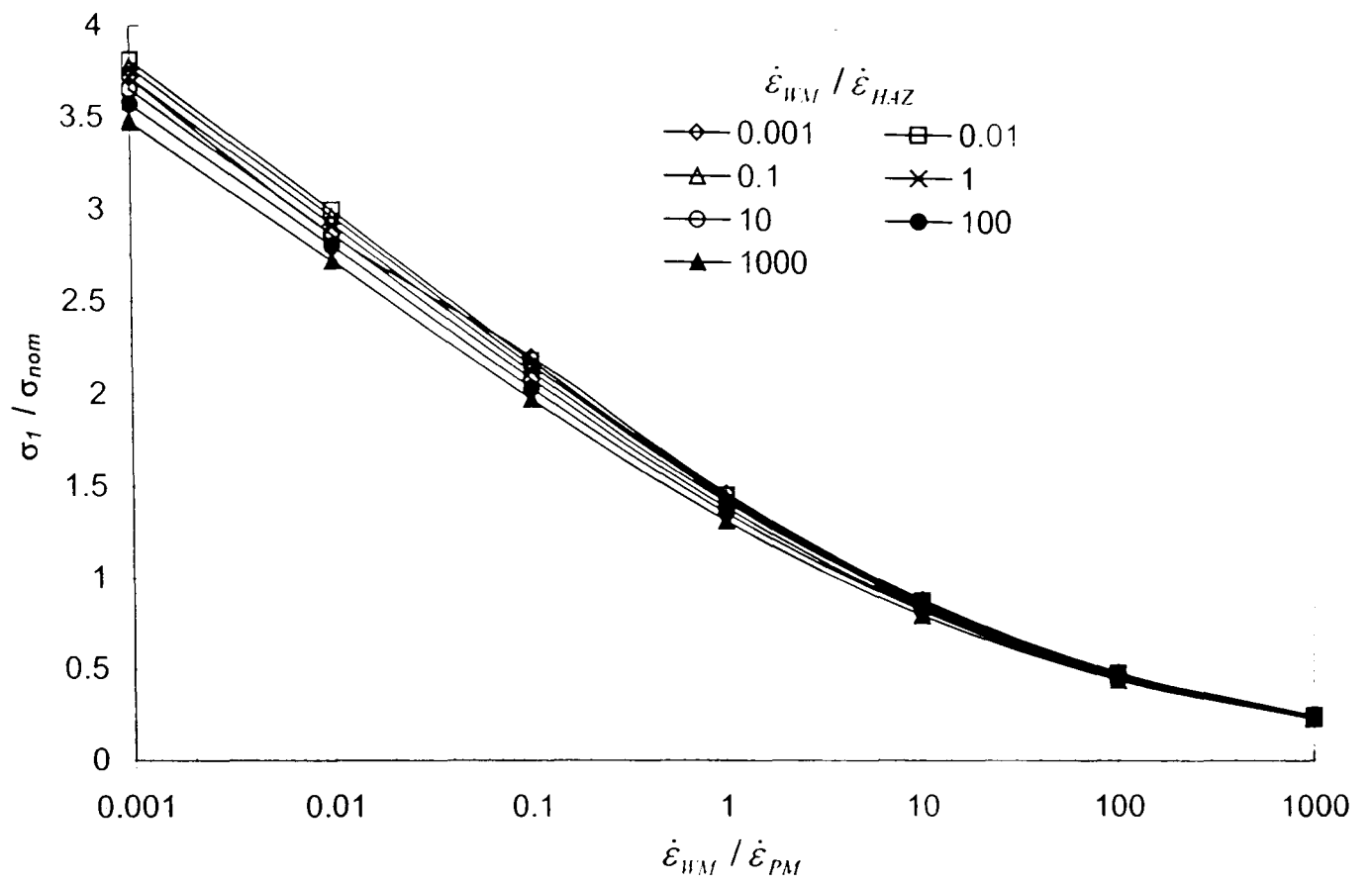


(a) $(n_{PM}, n_{HAZ}, n_{WM}) = (10, 10, 3)$

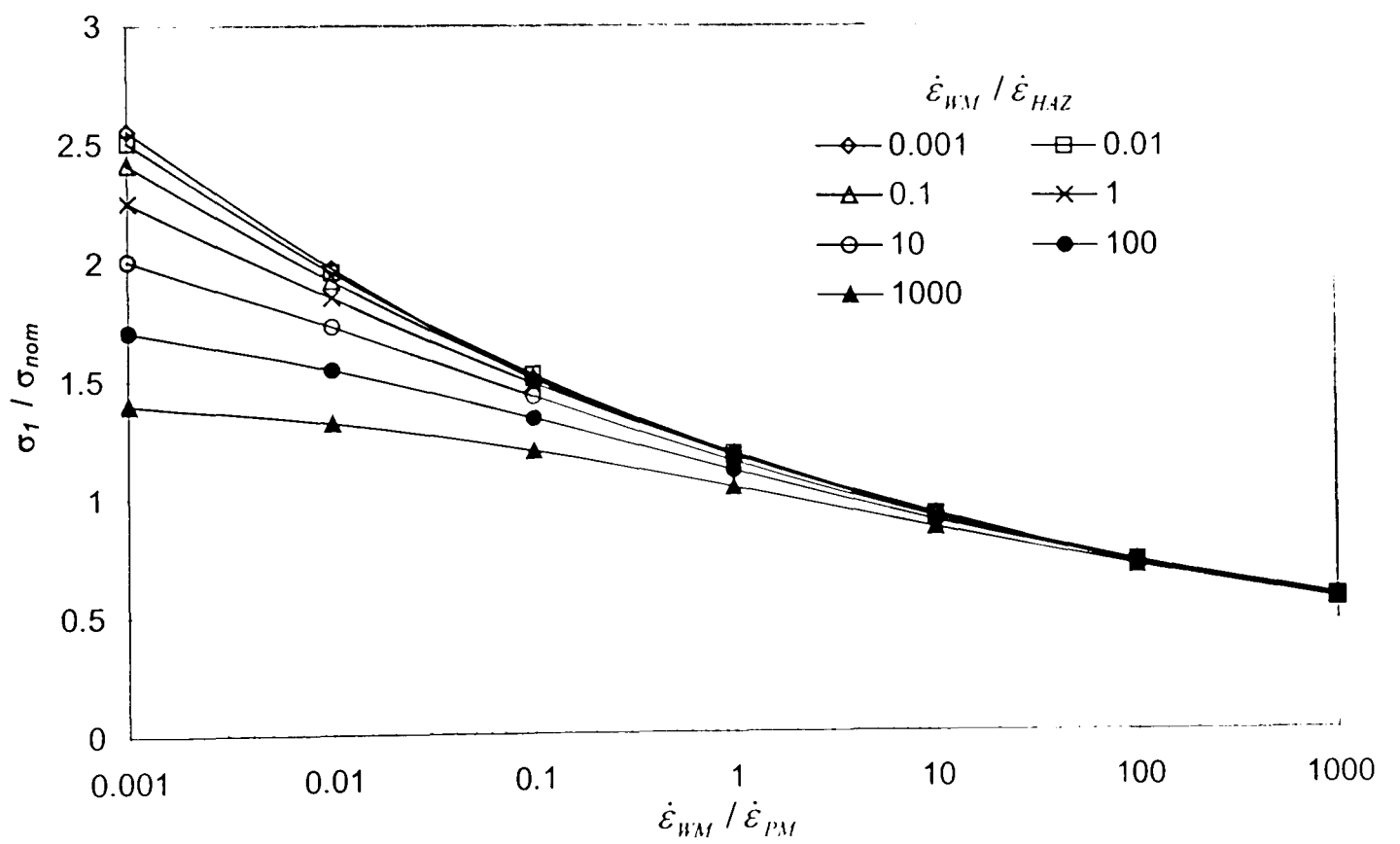


(b) $(n_{PM}, n_{HAZ}, n_{WM}) = (3, 3, 10)$

Figure A2.13. Variations of equivalent stress at Position F (WM) with $\dot{\epsilon}_{oWM} / \dot{\epsilon}_{oPM}$ and $\dot{\epsilon}_{oWM} / \dot{\epsilon}_{oHAZ}$ ratios for different $(n_{PM}, n_{HAZ}, n_{WM})$ combinations.

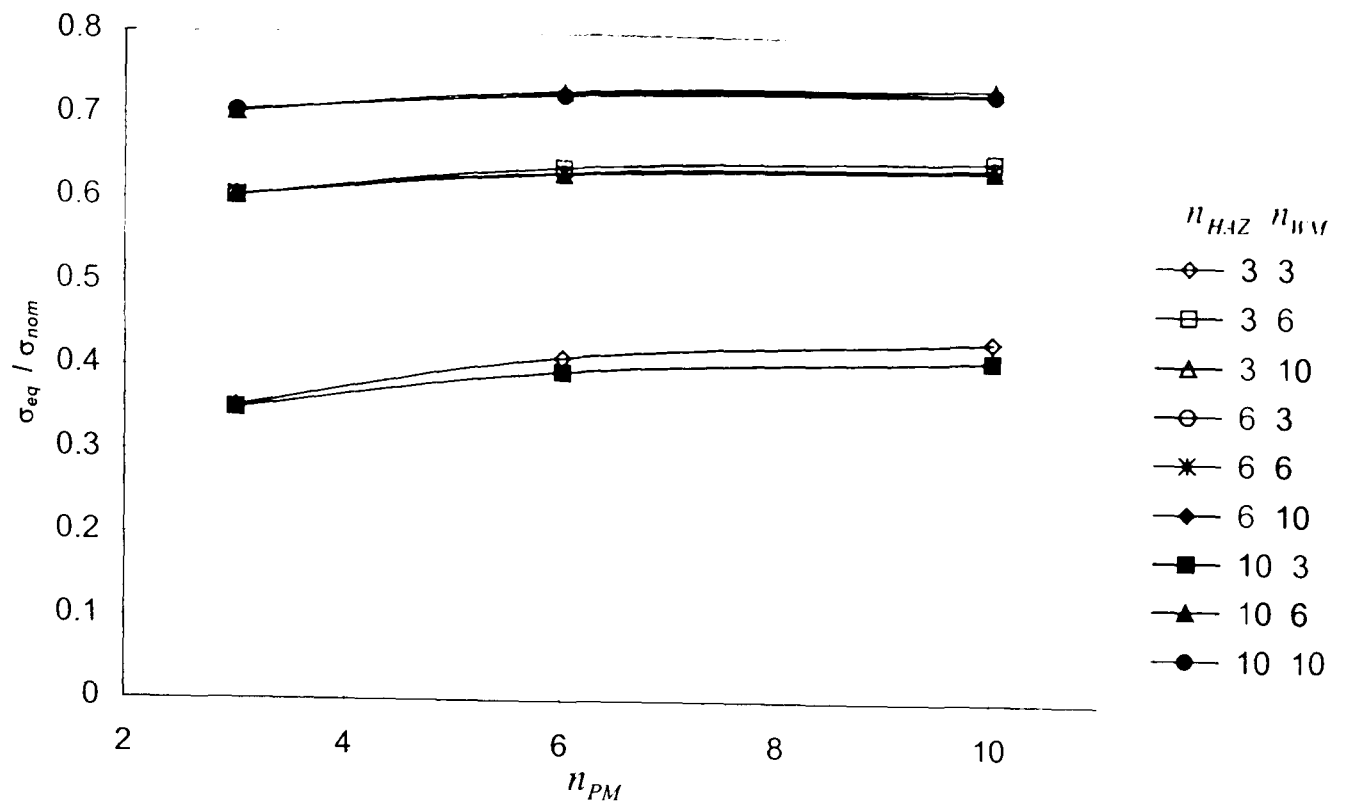


(a) $(n_{PM}, n_{HAZ}, n_{WM}) = (10, 10, 3)$

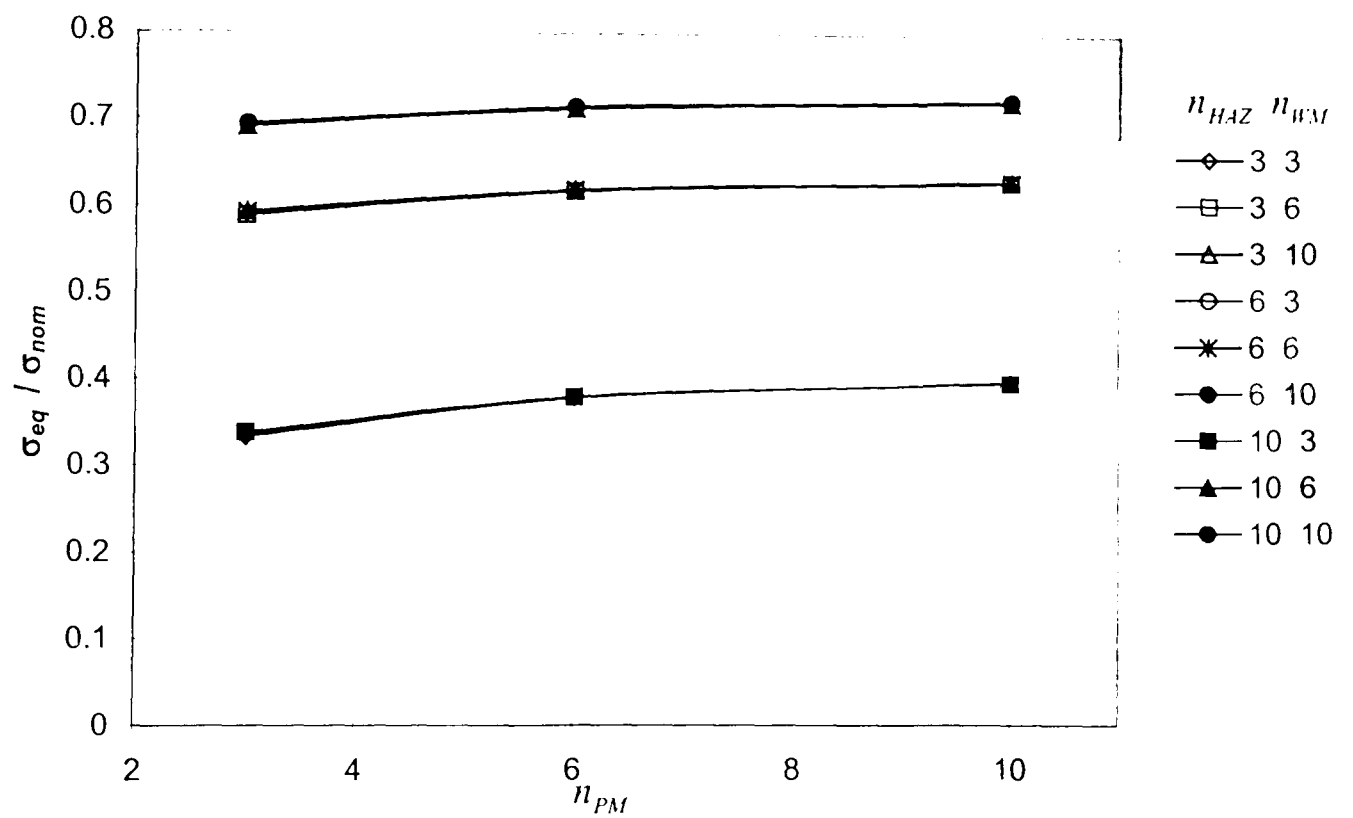


(b) $(n_{PM}, n_{HAZ}, n_{WM}) = (3, 3, 10)$

Figure A2.14. Variations of maximum principal stress at Position F (WM) with $\dot{\epsilon}_{oWM} / \dot{\epsilon}_{oPM}$ and $\dot{\epsilon}_{oWM} / \dot{\epsilon}_{oHAZ}$ ratios for different $(n_{PM}, n_{HAZ}, n_{WM})$ combinations.



(a) $\dot{\epsilon}_{oWM} / \dot{\epsilon}_{oPM} = 100$, $\dot{\epsilon}_{oWM} / \dot{\epsilon}_{oHAZ} = 0.01$



(b) $\dot{\epsilon}_{oWM} / \dot{\epsilon}_{oPM} = 100$, $\dot{\epsilon}_{oWM} / \dot{\epsilon}_{oHAZ} = 100$

Figure A2.15. Effect of n_{PM} on the equivalent stress at Position F (WM), for a range of n_{HAZ} and n_{WM} combinations, for four different $\dot{\epsilon}_{oWM} / \dot{\epsilon}_{oPM}$ and $\dot{\epsilon}_{oWM} / \dot{\epsilon}_{oHAZ}$ ratios.

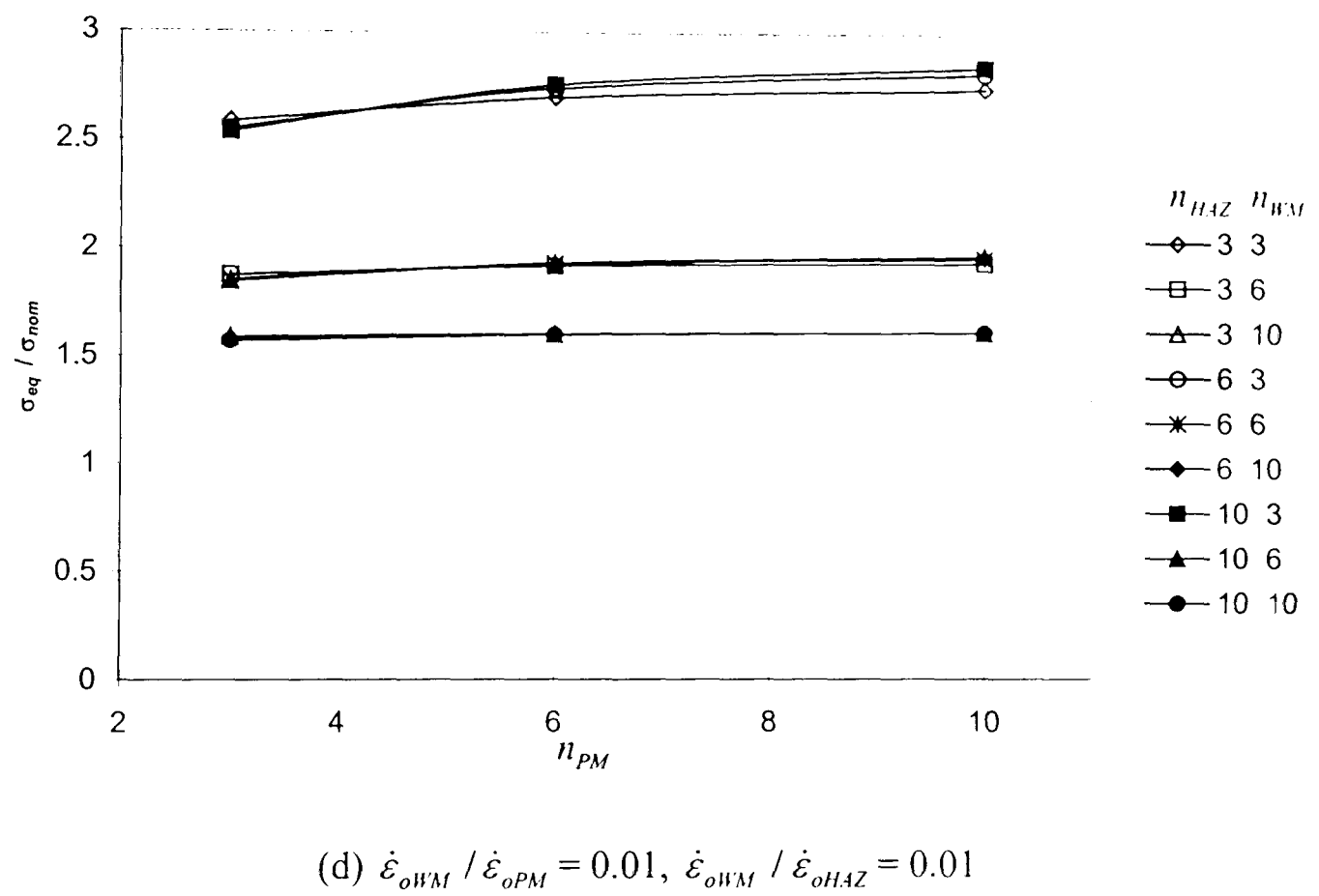
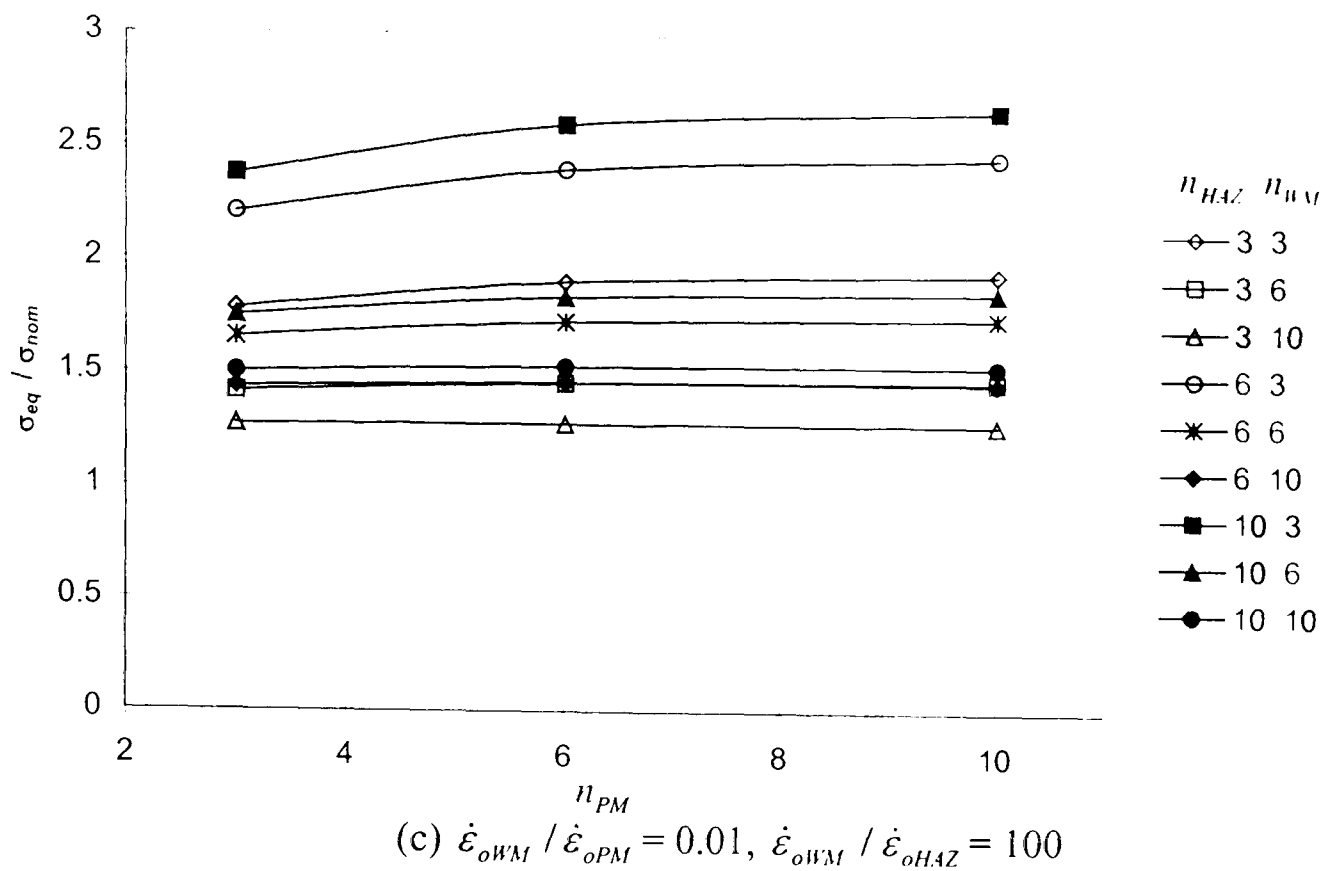


Figure A2.15 continued. Effect of n_{PM} on the equivalent stress at Position 1 (WM), for a range of n_{HAZ} and n_{WM} combinations, for four different $\dot{\epsilon}_{oWM} / \dot{\epsilon}_{oPM}$ and $\dot{\epsilon}_{oWM} / \dot{\epsilon}_{oHAZ}$ ratios.

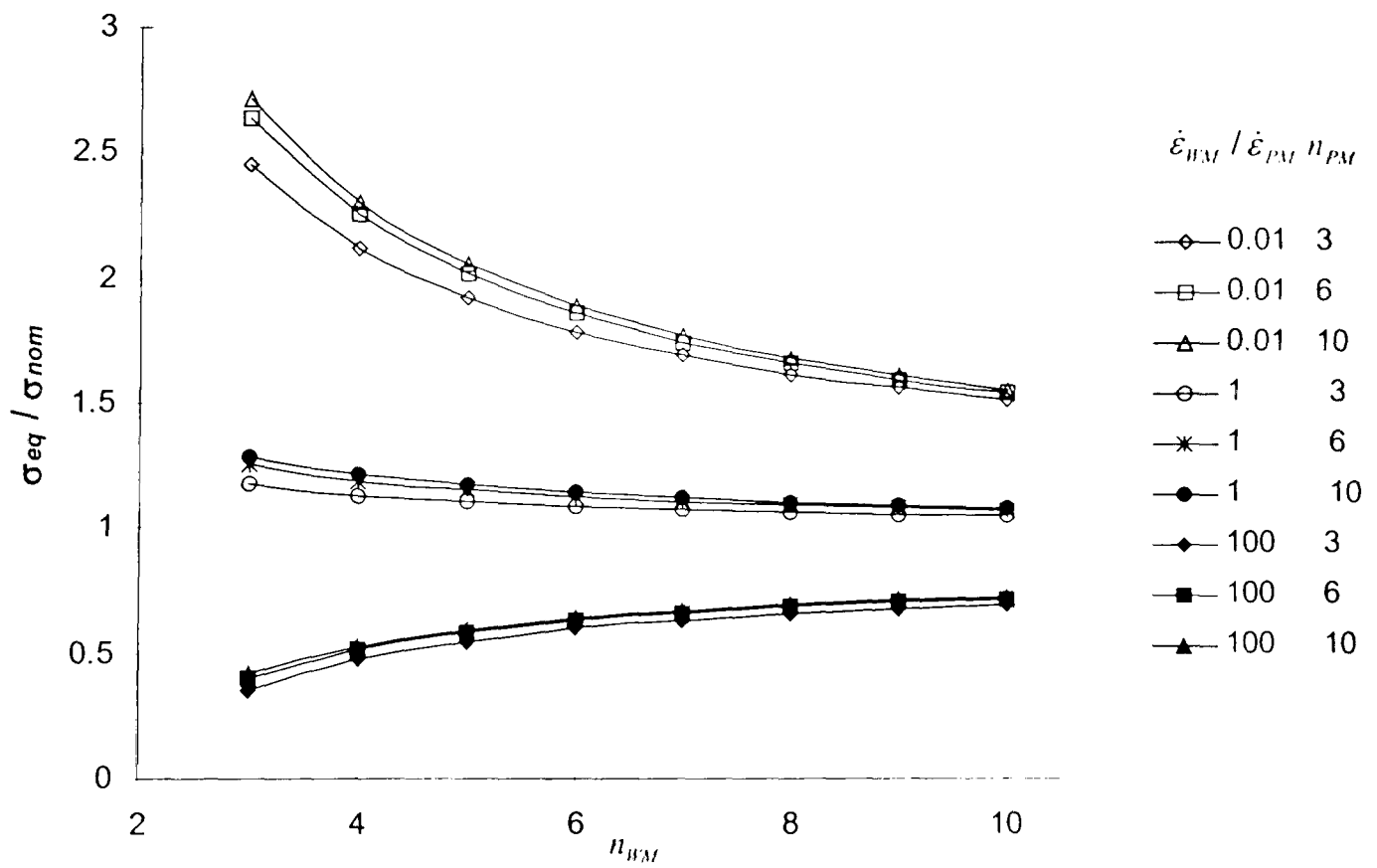
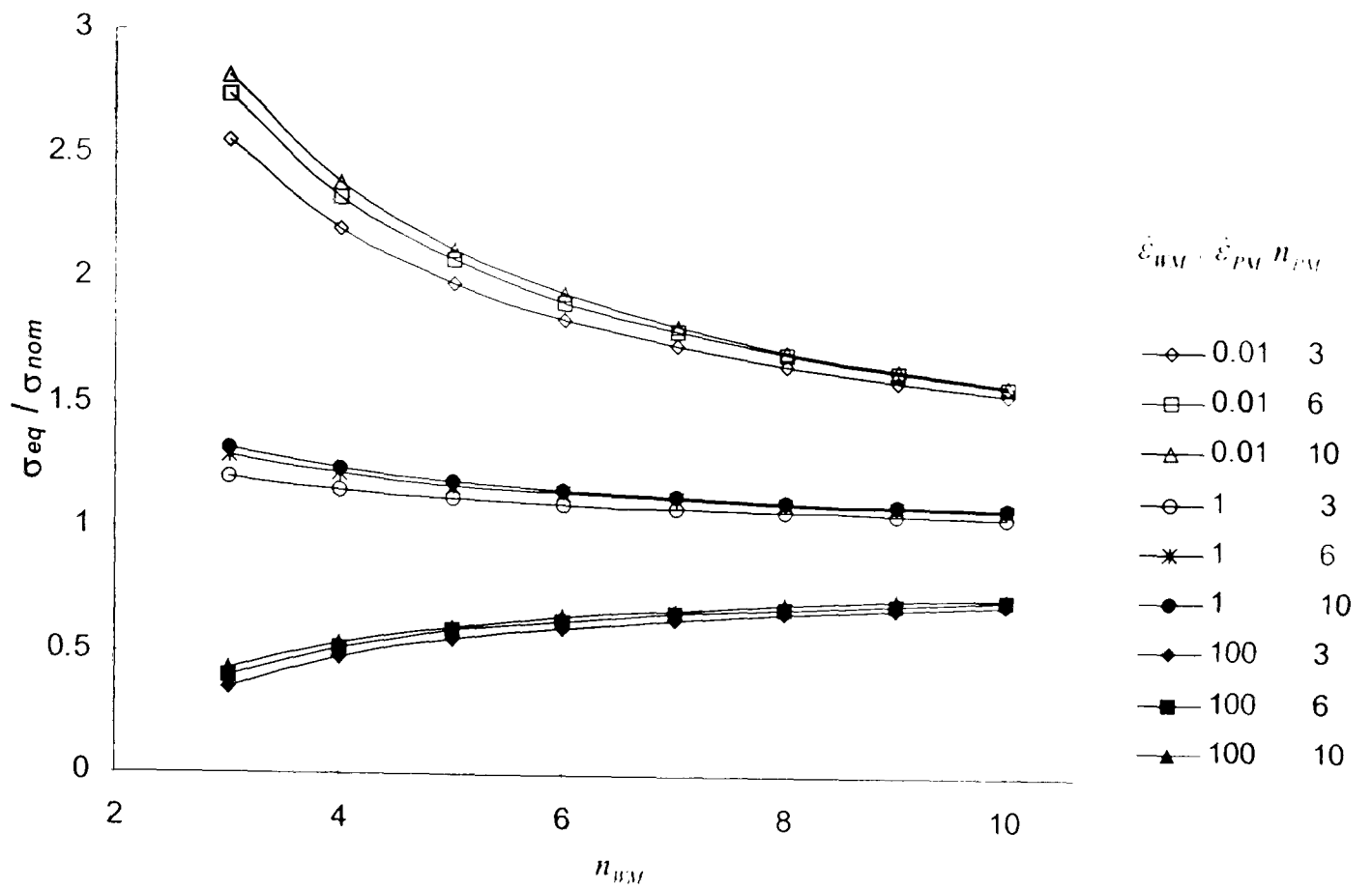


Figure A2.16. Effect of n_{WM} on the equivalent stress at Position F (WM), for a range of $\dot{\epsilon}_{oWM} / \dot{\epsilon}_{oPM}$ and n_{PM} combinations, with $n_{HAZ} = 6$, for three different $\dot{\epsilon}_{oWM} / \dot{\epsilon}_{oHAZ}$ ratios.

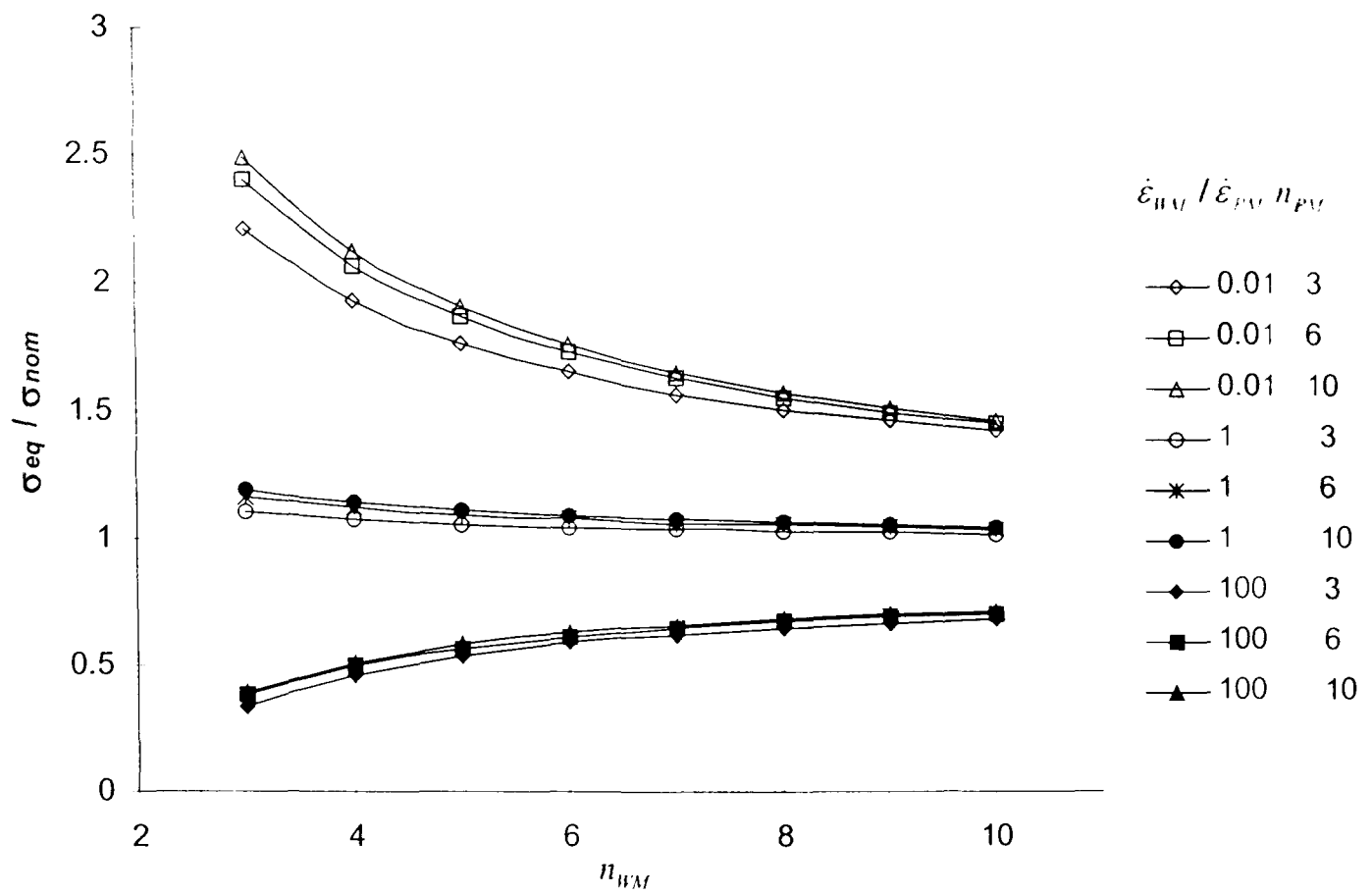


Figure A2.16 continued. Effect of n_{WM} on the equivalent stress at Position F (WM), for a range of $\dot{\epsilon}_{oWM} / \dot{\epsilon}_{oPM}$ and n_{PM} combinations, with $n_{HAZ} = 6$, for three different $\dot{\epsilon}_{oWM} / \dot{\epsilon}_{oHAZ}$ ratios.

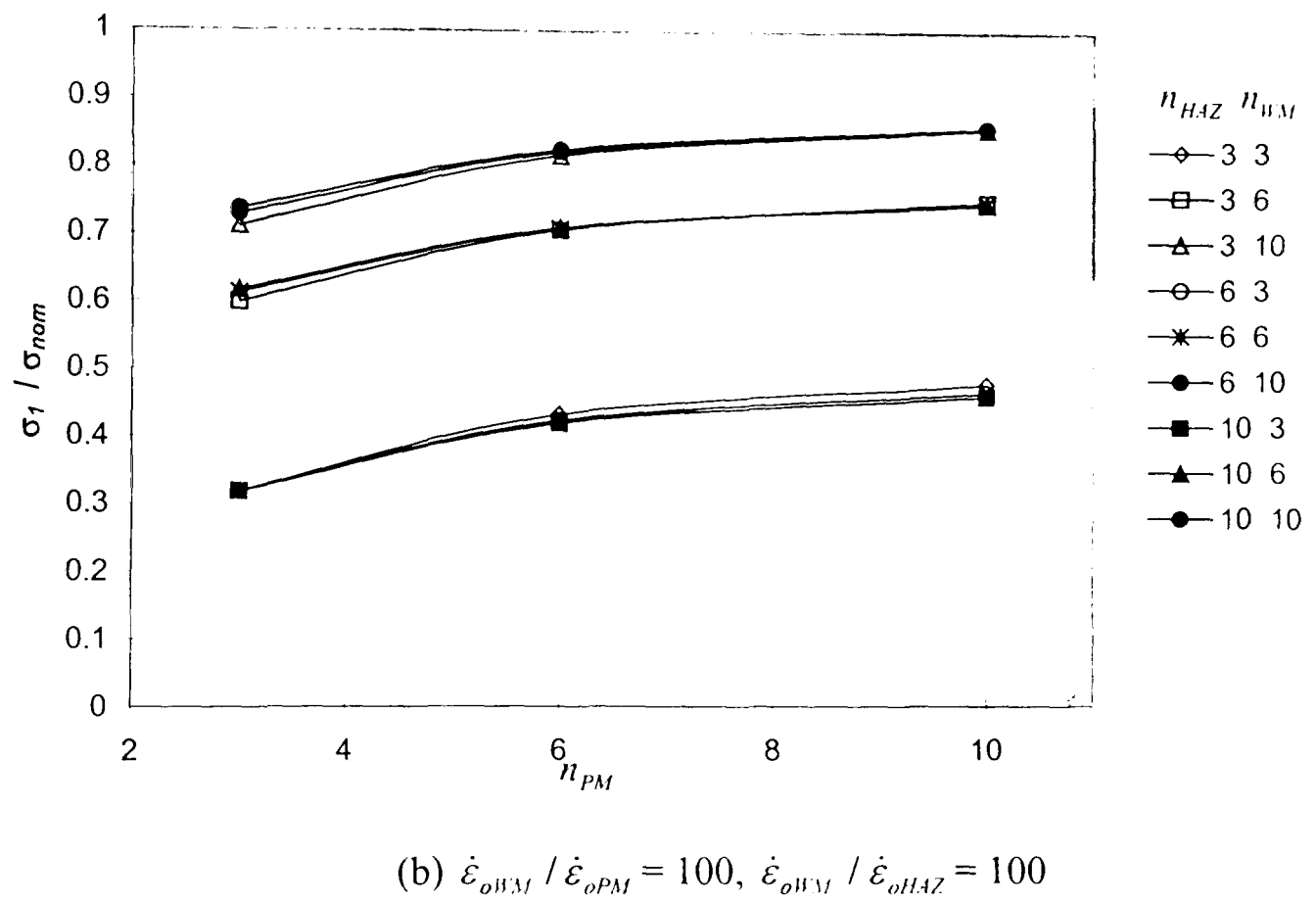
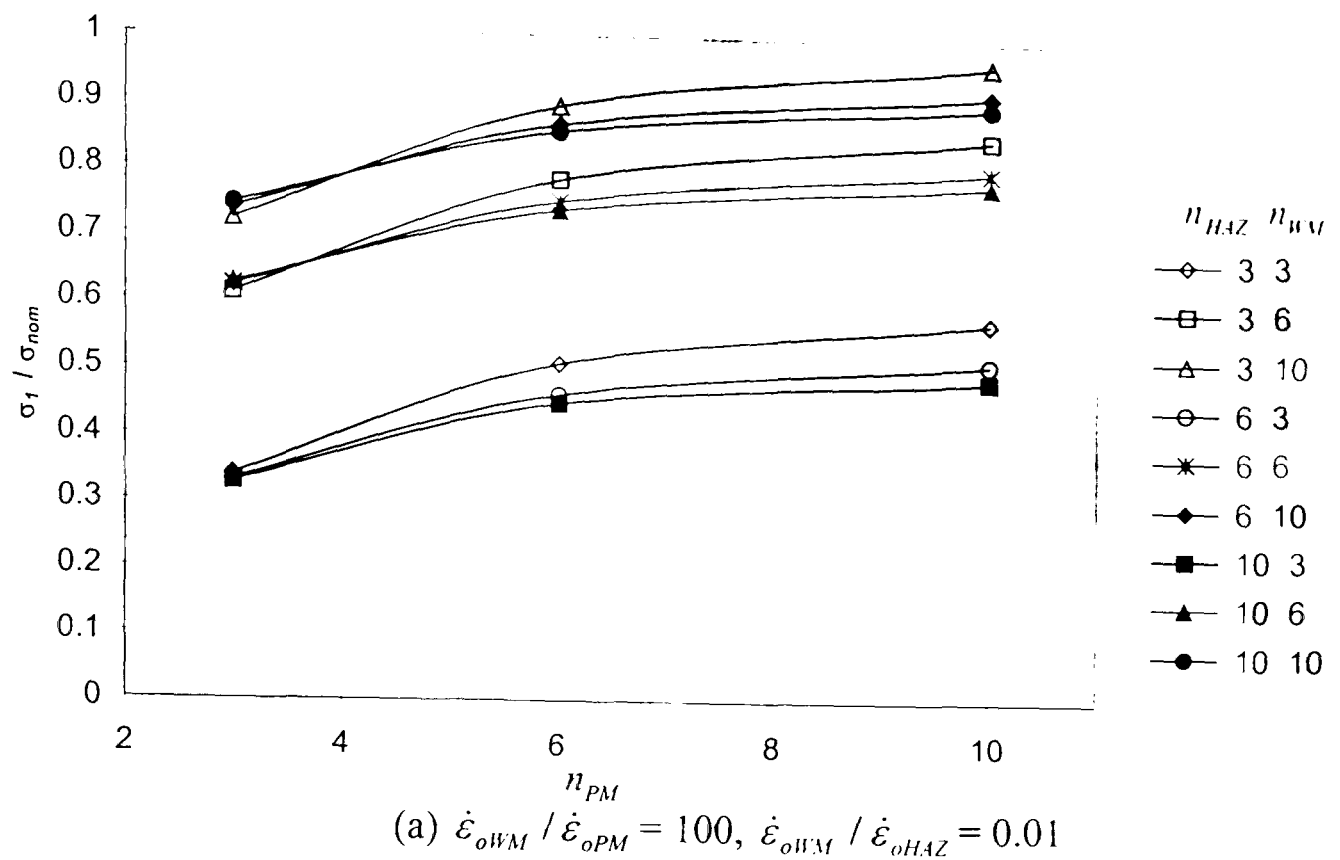
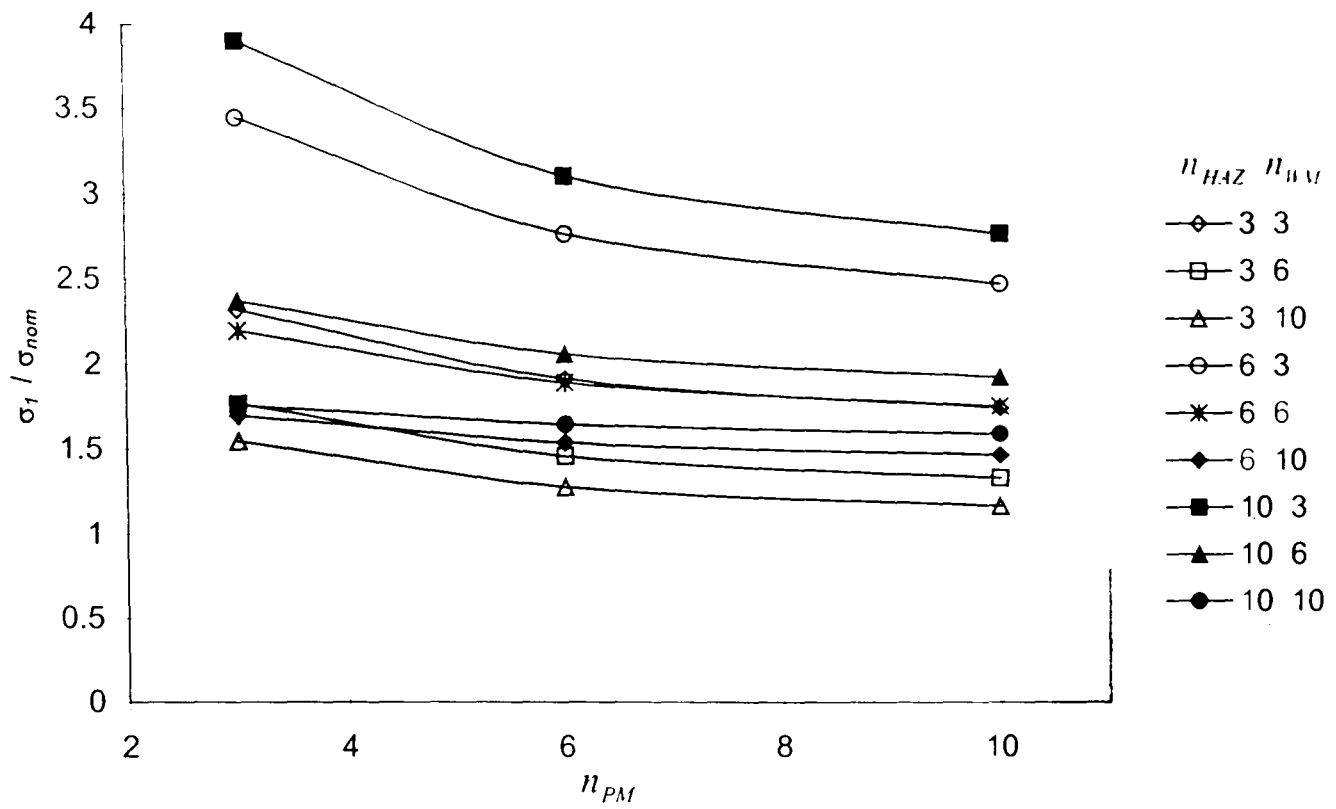
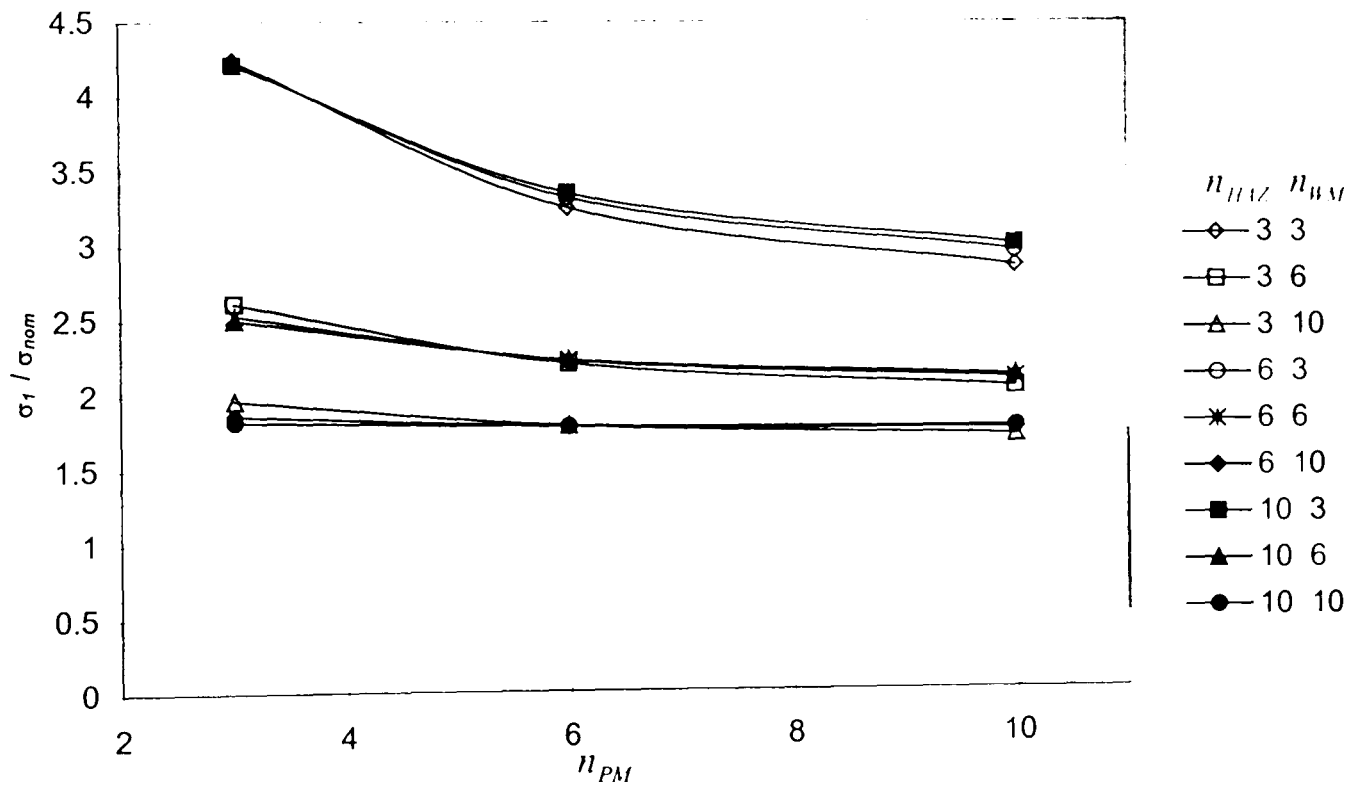


Figure A2.17. Effect of n_{PM} on the maximum principal stress at Position F (WM), for a range of n_{HAZ} and n_{WM} combinations, for four different $\dot{\epsilon}_{oWM} / \dot{\epsilon}_{oPM}$ and $\dot{\epsilon}_{oWM} / \dot{\epsilon}_{oHAZ}$ ratios.

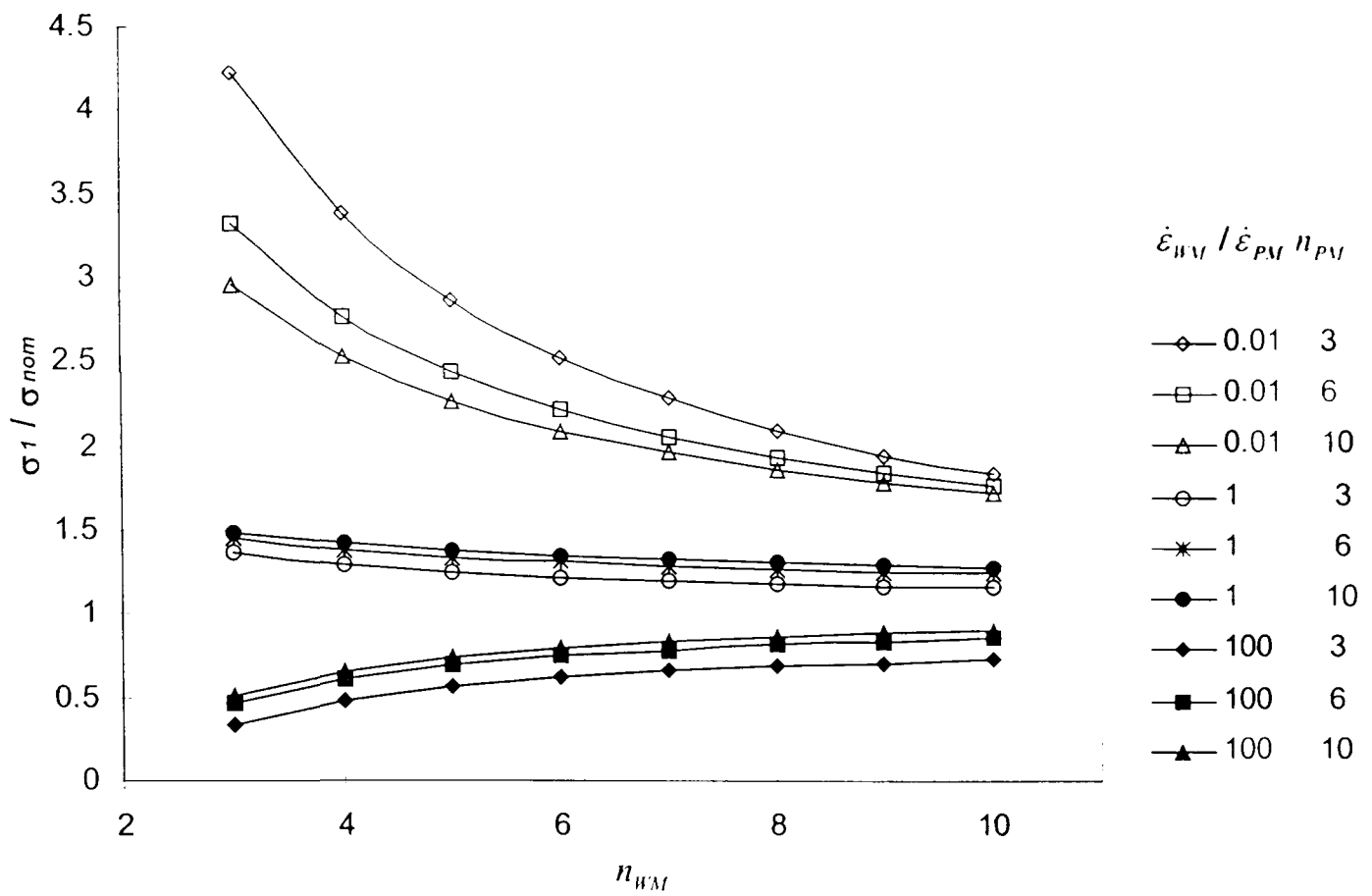


(c) $\dot{\epsilon}_{oWM} / \dot{\epsilon}_{oPM} = 0.01$, $\dot{\epsilon}_{oWM} / \dot{\epsilon}_{oHAZ} = 100$

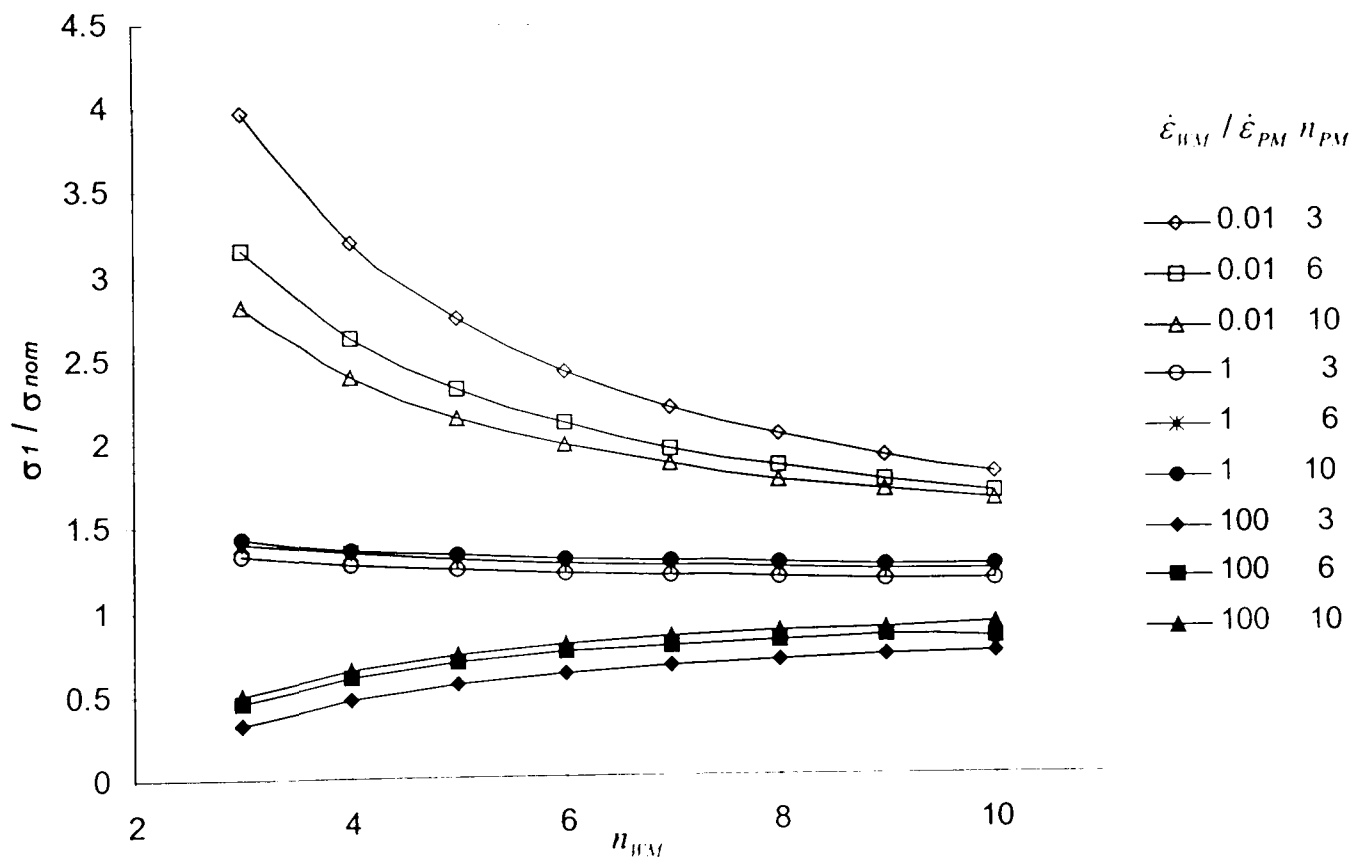


(d) $\dot{\epsilon}_{oWM} / \dot{\epsilon}_{oPM} = 0.01$, $\dot{\epsilon}_{oWM} / \dot{\epsilon}_{oHAZ} = 0.01$

Figure A2.17 continued. Effect of n_{PM} on the maximum principal stress at Position F (WM), for a range of n_{HAZ} and n_{WM} combinations, for four different $\dot{\epsilon}_{oWM} / \dot{\epsilon}_{oPM}$ and $\dot{\epsilon}_{oWM} / \dot{\epsilon}_{oHAZ}$ ratios.

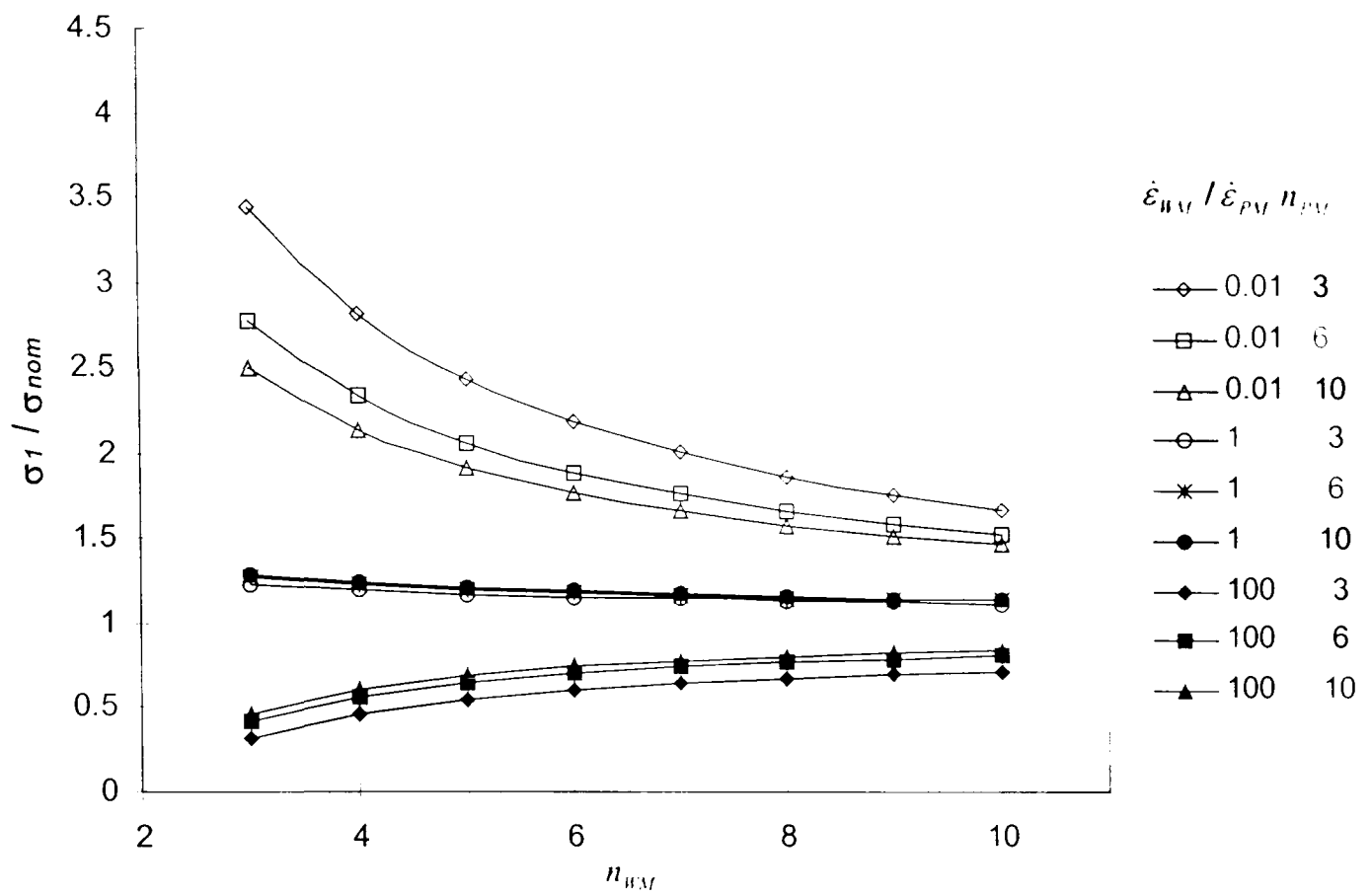


(a) $\dot{\epsilon}_{oWM} / \dot{\epsilon}_{oHAZ} = 0.01$



(b) $\dot{\epsilon}_{oWM} / \dot{\epsilon}_{oHAZ} = 1$

Figure A2.18. Effect of n_{WM} on the maximum principal stress at Position F (WM), for a range of $\dot{\epsilon}_{oWM} / \dot{\epsilon}_{oPM}$ and n_{PM} combinations, with $n_{HAZ} = 6$, for three different $\dot{\epsilon}_{oWM} / \dot{\epsilon}_{oHAZ}$ ratios.



(c) $\dot{\epsilon}_{oWM} / \dot{\epsilon}_{oHAZ} = 100$

Figure A2.18 continued. Effect of n_{WM} on the maximum principal stress at Position F (WM), for a range of $\dot{\epsilon}_{oWM} / \dot{\epsilon}_{oPM}$ and n_{PM} combinations, with $n_{HAZ} = 6$, for three different $\dot{\epsilon}_{oWM} / \dot{\epsilon}_{oHAZ}$ ratios.